TECHNICAL UNIVERSITY OF CARTAGENA

DEPARTMENT OF COMMUNICATIONS AND INFORMATION TECHNOLOGIES

TECHNICAL UNIVERSITY
OF CARTAGENA

E.T.S.I.T

Novel Integral Equation Methods Applied to the Analysis of New Guiding and Radiating Structures and Optically-Inspired Phenomena at Microwaves

(Doctoral Thesis)

Dissertation written by

Juan Sebastián GÓMEZ-DÍAZ

under the surpervision of

Prof. Alejandro Álvarez-Melcón

Prof. Christophe Caloz

Cartagena, May 2011

UNIVERSIDAD POLITÉCNICA DE CARTAGENA

AUTORIZACIÓN DE LA PRESENTACIÓN DE LA TESIS DOCTORAL POR EL DIRECTOR/A

D. Alejandro Álvarez Melcón, Profesor Doctor del Área de Teoría de la Señal y Comunicaciones en el Departamento de Tecnologías de la Información y las Comunicaciones (TIC)

A U T O R I Z A:

La presentación de la Tesis Doctoral titulada "**Novel Integral Equation Methods Applied to the Analysis of New Guiding and Radiating Structures and Optically-Inspired Phenomena at Microwaves**", realizada por D./Dª. Juan Sebastián Gómez Díaz, bajo mi dirección y supervisión, en el Departamento de Tecnologías de la Información y las Comunicaciones, y que presenta para la obtención del grado de Doctor por la Universidad Politécnica de Cartagena.

En Cartagena, a 5 de Mayo de 2011

EL/LA DIRECTOR/A DE TESIS

[redacted]

Fdo.: Alejandro Álvarez Melcón

UNIVERSIDAD POLITÉCNICA DE CARTAGENA

AUTORIZACIÓN DE LA PRESENTACIÓN DE LA TESIS DOCTORAL POR EL DIRECTOR/A

D/Dª. Christophe Caloz, Profesor/a Doctor/a del Departamento Poly-Grames en la École Polytechnique de Montréal,

A U T O R I Z A:

La presentación de la Tesis Doctoral titulada "**Novel Integral Equation Methods Applied to the Analysis of New Guiding and Radiating Structures and Optically-Inspired Phenomena at Microwaves**"", realizada por D./Dª. Juan Sebastián Gómez Díaz, bajo mi dirección y supervisión, en el Departamento de Tecnologías de la Información y las Comunicaciones, y que presenta para la obtención del grado de Doctor por la Universidad Politécnica de Cartagena.

En Montreal, a 5 de Mayo de 2011

EL/LA DIRECTOR/A DE TESIS

Fdo.: Christophe Caloz

UNIVERSIDAD POLITÉCNICA DE CARTAGENA
Comisión de Doctorado

AUTORIZACIÓN DE LA PRESENTACIÓN DE LA TESIS DOCTORAL POR LA COMISIÓN ACADÉMICA RESPONSABLE DEL PROGRAMA

D. Francisco Ortiz Zaragoza, Coordinador de la Comisión Académica del Programa de Teoría de la Información y las Comunicaciones

INFORMA:

Que la Tesis Doctoral titulada "**Novel Integral Equation Methods Applied to the Analysis of New Guiding and Radiating Structures and Optically-Inspired Phenomena at Microwaves**", ha sido realizada por D. Juan Sebastián Gómez Díaz, bajo la dirección y supervisión de D. Alejandro Álvarez Melcón y D. Christophe Caloz y que la Comisión Académica ha dado su conformidad para que sea presentada ante la Comisión de Doctorado.

La rama de conocimiento por la que esta tesis ha sido desarrollada es:

- ☐ Ciencias Básicas
- ☐ Ciencias Sociales y Jurídicas
- ☐ Ingeniería y Arquitectura

En Cartagena, a 5 de Mayo de 2011

EL COORDINADOR DE LA COMISIÓN ACADÉMICA DEL PROGRAMA

[redacted]

Fdo.: Francisco Ortiz Zaragoza

Comisión de Doctorado

Copyright © 2011 by Juan Sebastián Gómez Díaz
All rights reserved.

Dedicado a mi hermano Alberto,
cuya gran calidad humana me marcó para siempre.

Everything should be made as simple as possible, but not simpler.
Albert Einstein

Acknowledgments

En primer lugar, me gustaría mostrar mi más sincero agradecimiento a Alejandro, mi director de tesis. Tras dar muchas vueltas por el mundo y vivir en distintos países, sé que he tenido el mejor director de tesis posible. No he conocido a ninguna otra persona que tenga ni una humanidad ni una capacidad científica igualable. Ha sido un auténtico placer trabajar con él y espero poder hacerlo en el futuro. Termino mi tesis con la sensación de que estoy y estaré siempre en deuda contigo, Alex.

Me gustaría dar las gracias a todos y cada uno de los miembros del grupo GEAT, actuales (José Luis, David, Fernando, Pedro, Manuel, Mónica, Jose Lorente, Maria, Alejandro Martínez y Raul) y pasados (Javi y Juan Pascual) por los momentos vividos durante estos últimos años. Me gustaría resaltar el apoyo de Mónica y su disposición para ayudarme a modelar matemáticamente cualquier cosa, especialmente en las etapas tempranas de esta tesis. De José Luis, quiero resaltar su gran optimismo, energía y vitalidad, y su desinteresado y constante apoyo técnico ante cualquier duda que pudiera surgir. Destacar tambien la amistad y multiples consejos de David, ante cualquier situación. En especial, quiero dar las gracias a María por su constante apoyo durante la tesis, compartir conmigo sus puntos de vista, conocimientos y por ser capaz de hacerme ver la luz al final del tunel...incluso cuando el tunel se desplomaba sobre mi cabeza.

Además, me gustaría agradecer los buenos momentos pasados con todos los demás compañeros del departamento TIC de la UPCT, y lo mucho que he aprendido de poder escuchar y conversar con personas tan racionales como Leandro o Joan.

Quiero resaltar y agradacer el apoyo del Ministerio de Educación y Ciencia de España, al financiar mediate la una beca FPU (referencia AP2006 − 015) el trabajo realizado en esta tesis. Además, quiero dar las gracias a la Fundación Séneca de la Región de Murcia por apoyar, mediante ayudas, la divulgacion en congresos científicos internacionales de los trabajos realizados.

My most sincere thanks to Prof. Christophe Caloz, who accepted me in his group at the École Polytechnique de Montréal and generously shared with me some of his ideas and visions. I would like to thank all my colleagues of the EM Theory and Applications Research Group for their help, support, and scientific contributions. Specially, I want to deeply acknowledge Mr. Shulabh Gupta, for been a constant source of motivation and positive energy, for the endless technical discussions, and for all the memorable moments we shared outside work. I also want to give special thanks to Mr. Samer Abielmona and Dr. Hoang Nguyen, for their assistance in the realization and measurement of metamaterials, and for transmitting me some of their secret tricks of the engineering art.

I am in deep debt with Attieh, for her constant motivation, her incredible efforts, her friendship and for sharing with me her points of view. I really thank her for the shared moments, both in Canada and in Spain. I also want to dedicate some words to Simone, who was able to cheer me up in our endless coffe breaks. I really doubt that I could have survived in Canada without her help and friendship. Many thanks to all the persons that I have been lucky to meet there in Canada, who offered me countless number of unforgettable moments. An individual mention to each person would be too long, but I sincerely thanks to them all for their friendship.

I would like to express my gratitude to Dr. Thomas Bertuch, for accepted me as his student, and for sharing with me his valuable technical knowledge. Many thanks to Dr. Peter Knott who welcomed me in his department. Also, sincere thanks to all the members of the Antenna Technology and Electromagnetic Modelling department of the FHR Fraunhofer Institute (Germany). Thanks to Mariano, for introducing and taking care of me in the group. Special mention to Marian, for her friendship and for the shared moments inside and outside work. Also, my gratitude to Juan Carlos, Angel, and Carlos, for make me feel like I was at home. In addition, thanks to all other friends that I had the chance to meet in Germany, for making my stage there much more pleasant.

No me olvido de mis compañero de carrera en la Universidad Politécnica de Cartagena, con los que pasé unos años inolvidables. Nombrarlos a todos sería muy largo!. En especial, me gustaría recordar a mi amigo David al que, esté donde esté, siempre recordaré con muchísimo cariño.

Qué decir de mis amigos! Pues que soy una persona muy afortunada por poder tenerlos. En especial, gracias a Juande, por los ya muchos y muchos años de amistad, por estar ahí siempre (ya sea en Canadá, en Alemanía... o en Ontur!), y por aparecer cuando las cosas se tuercen y todo va mal. Ahí es donde se notan los amigos, y tú lo eres de verdad. Gracias a Dani Quirante, por nuestros partidos míticos de tenis, por estar apoyando siempre y ser capaz de adaptarte a cualquier circunstancia, sea la que sea. Cómo olvidarme de Fran! gracias por tantos momentos juntos, y por tantas y tantas conversaciones sin fin, que son capaces de cambiar el mundo. También un recuerdo para mi amigo Dani Bomber, y su motivador punto de vista sobre la vida y el deporte. Manolo! muchas gracias por tu apoyo y por tu gran cualidad: ser capaz de hacerme olvidar la ecuaciones y plantarme de nuevo y de un plumazo en la realidad :). Gracias Alberto, por tu amistad. Muchas gracias también a muchos otros amigos de Murcia, que por razones de espacio no puedo nombrar detalladamente. Y también un recuerdo especial para todos mis amigos de Ontur, pidiendo perdón por todos los momentos en los que no he estado ahí con vosotros.

Muchísimas gracias a ti, Majo, por estar a mi lado, por tu cariño, y por tener un punto de vista alternativo, que no tenía previsto, y que es capaz de cambiar mi modo de pensar. Esta tesis nunca hubiera sido igual sin ti, por lo que, va por ti y en parte, te pertenece.

Mi familia es fundamental en mi vida, esta tesis va por por todos ellos. En especial, a mi padre, Sebastián, el hombre al que mas admiro, por su fuerza y gradísima fortaleza. A mi madre, Reme, a la que quiero con locura, y me apoya y está conmigo incondicionalmente. A mi hermana, por su constante apoyo y comprensión, por estar ahí siempre y acordarse de mi cuando más me hace falta. Un recuerdo para mis abuelos, allá donde estén. Para mi abuela Julia, y para mi abuela Rosa (por su forma de ser y...sus increíbles ojos azules). Y en especial, esta tesis la dedico a mi sobrina Diana, por saber arrancarme una sonrisa sólo con mirarme. Espero saber haberte correspondido: he sido la primera persona en el mundo... en darte a probar chocolate :).

Sinceramente, muchísimas gracias a todos. Esta tesis es por vosotros.

Murcia, Mayo de 2011.

J. Sebastián Gómez Díaz

Abstract

This PhD. dissertation presents a multidisciplinary work, which involves the development of different novel formulations applied to the accurate and efficient analysis of a wide variety of new structures, devices, and phenomena at the microwave frequency region. The objectives of the present work can be divided into three main research lines:

1. The first research line is devoted to the Green's function analysis of multilayered enclosures with convex arbitrarily-shaped cross section. For this purpose, three accurate spatial-domain formulations are developed at the Green's functions level. These techniques are then efficiently incorporated into a mixed-potential integral equation framework, which allows the fast and accurate analysis of multilayered printed circuits in shielded enclosures. The study of multilayered shielded circuits has lead to the development of the novel hybrid waveguide-microstrip filter technology, which is light, compact, low-loss and presents important advantages for the space industry.

2. The second research line is related to the impulse-regime study of metamaterial-based composite right/left-handed (CRLH) structures and the subsequent theoretical and practical demonstration of several novel optically-inspired phenomena and applications at microwaves, in both, the guided and the radiative region. This study allows the development of new devices for ultra wide band and high data-rate communications systems. Besides, this research line also deals with the simple and accurate characterization of CRLH leaky-wave antennas using transmission line theory.

3. The third and last research line presents a novel CRLH parallel-plate waveguide leaky-wave antenna structure, and a rigorous iterative modal-based technique for its fast and complete characterization, including a systematic calculation of the antenna physical dimensions.

It is important to point out that all the theoretical developments and novel structures presented in this work have been numerically confirmed, by the use of both, home-made software and commercial full-wave simulations, and experimentally verified, by the use of measurements from fabricated prototypes.

Resumen

En esta tesis doctoral se presenta un trabajo multidisciplinar, en el que se han desarrollado una serie de formulaciones matemáticas aplicadas al análisis eficiente y riguroso de diversas estructuras, dispositivos y fenómenos físicos en el rango frecuencial de las microondas. Los objetivos que se enmarcan dentro de esta tesis se pueden dividir en tres líneas de investigación diferentes:

1. La primera línea de investigación trata sobre el cálculo de la función de Green de estructuras cerradas multicapa que presenten una sección transversa con geometría convexa arbitraria. Para ello, se han desarrollado tres novedosas técnicas, que han sido formuladas en el dominio espacial. Posteriormente, las funciones de Green obtenidas han sido incluidas dentro de la técnica de la ecuación integral de los potenciales mixtos, para un análisis muy rápido y preciso de circuitos multicapa que se encuentren en una cavidad cerrada. Además, el estudio de circuitos encapsulados multicapa ha permitido el desarrollo de la novedosa tecnología híbrida guia onda-microtira, que presenta importantes ventajas como son su reducido peso, estructura compacta y bajas pérdidas, lo que la hacen una candidata ideal para la industria espacial.

2. La segunda línea de investigación está relacionada con el estudio del comportamiento de líneas de transmisión diestras-zurdas cuando son excitadas por pulsos temporales y la posterior demostración teórica y práctica de una serie de fenómenos físicos y aplicaciones, que son comunes en el campo de la óptica, y que han sido trasladados al dominio frecuencial de las microondas. Este estudio ha permitido el desarrollo de nuevos dispositivos para aplicaciones de banda ancha ó sistemas de comunicación que requieran de una alta transferencia de datos. Además, esta línea de investigación presenta novedosos métodos para la caracterización y posterior análisis de antenas de onda de fuga diestra-zurda, usando la teoría de líneas de transmisión.

3. La tercera y última línea de investigación presenta una novedosa antena de fuga, que está basada en líneas de transmisión diestras-zurdas implementadas mediante una estructura de placas paralelas. Además, se presenta un nuevo método modal iterativo que permite un análisis rápido, preciso y eficiente de este tipo de estructuras, incluyendo la obtención sistemática de las dimensiones físicas de la antena que se requieren para conseguir un determinado comportamiento.

Finalmente, destacar que tanto las formulaciones y desarrollos teóricos propuestos como las nuevas estructuras presentadas en esta tesis han sido validadas de forma numérica, empleando software propio y paquetes comerciales de onda completa, y de forma experimental, usando medidas reales obtenidas de los distintos prototipos fabricados.

Contents

Chapter 1

Introduction

1.1 Motivation and Objectives

The analysis and design of microwave and millimeter wave circuits and antennas is a fundamental step in modern communication systems, such as satellite [Pratt et al., 2002], [Roddy, 2006] or ground mobile communications [Schwartz, 2005]. This task can be faced using several approaches. One interesting possibility is to solve Maxwell's equations [Maxwell, 1865], [Harman, 1995] using some kind of full-wave commercial software, which usually employs methods such as FEM (Finite Elements Method) [Jin and Volakis, 1991], FDTD (Finite Differences Time Domain) [Taflove and Hagness, 2005] or closed packed formulations based on the IE (Integral Equation) technique solved by the MoM (method of moments) [Harrington, 1968], [Mosig, 1989], just to mention a few of them. This will allow to the user the design and posterior fabrication of almost any desired microwave device. However, this option has also some drawbacks. In first place, the use of general full-wave software leads to very high computational times, because this type of software is generic and does not consider the particular features of the structure under consideration. Furthermore, these full-wave simulations do not provide any physical insight, in the sense of a mathematical formulation which can explain the physical phenomena observed. Therefore, sometimes it turns out to be difficult to obtain an optimized solution and to fully understand it, and much more complicated, to propose novel alternatives or approaches to handle a given problem.

Another possibility is to explore Maxwell's equations using some particular technique, adapted to the structure or phenomena under consideration. One possibility here is to use the integral equation method [Mosig, 1989], usually solved by the method of moments [Harrington, 1968]. In this case, the Green's function (or impulse response) [Barton, 1989b] related to the medium (or structure) under analysis is required. Once the Green's functions are known, the deep-insight physics of the problem are revealed. Therefore, it is much easier to fully understand the problem, analyze different solutions and even propose novel approaches to solve it. Furthermore, novel phenomena or effects related to materials, wave propagation, leaky-wave radiation, dispersion, or even transposed from other domains (such as optics) can easily be investigated once their associated Green's functions are known. However, this approach has also some drawbacks. First, it is much more complicated to de-

velop a novel theory particularized to a specific problem than using a commercial software. Second, the theory proposed must be programmed into a computer, in order to obtain the desired solution. And third, this solution must be validated, against full-wave simulation results or measurements, in order to be completely sure about the accuracy of the propose techniques.

In this context, **this PhD thesis presents a multidisciplinary work, which involves the development of different novel formulations** (mostly based on integral equations, but also with components of mode matching [Marcuvitz, 1964], time-domain transmission line approaches, etc). The main objective of the proposed formulations is **to be very accurate and efficient in the analysis of different structures at the microwave and millimeter wave frequency regions**. Then, these formulations are **applied to the deep analysis and quick design of a very wide range of novel devices, applications and phenomena** (such as hybrid waveguide-microstrip technology for space filters, optically-inspired phenomena at microwaves using metamaterials, leaky-wave antennas, etc.) which may find direct use, for instance, in current ultra wide band (UWB) devices, high data-rate communication systems or the demanding space industry. Thereby, *this PhD thesis has both, a strong theoretical and practical components, because most of the devices and phenomena proposed have been fabricated and experimentally verified*. For a simpler comprehension, the objectives of this PhD dissertation are divided into three main research lines:

1. The first research line is devoted to the **computation of Green's functions associated to multilayered cavities with arbitrarily-shaped cross sections** and the proposal of **novel filtering structures**. The first objective is the *accurate and fast analysis of multilayered circuits in shielded enclosures using a mixed-potential integral equation approach*. The idea is to solve the problems and limitations that the current full-wave solvers present when analyzing this type of structures. The second main objective is the *development of novel filtering technologies with specific benefits for the space industry*. For this purpose, the novel *hybrid waveguide-microstrip filter technology* (which is light, compact and low-loss) has been proposed, analyzed and fully demonstrated.

2. The second research line is related to the **impulse-regime analysis of composite right/left-handed (CRLH) structures** [Caloz and Itoh, 2005] and the subsequent **theoretical and practical demonstration of several novel optically-inspired phenomena and applications at microwaves, in both, the guided and the radiative region**. The main objective here is the transposition of phenomena and applications from the optics domain to the microwave regime, taking advantage of the metamaterials properties, to develop novel devices for UWB and high data-rate communications systems. Besides, another important objective of this line is the accurate and simple characterization of current state-of-the-art CRLH leaky-wave antennas (LWAs).

3. The third and last research line proposes **a novel CRLH parallel-plate waveguide (PPW) leaky-wave antenna** and a rigorous **iterative modal-based technique for its fast and complete characterization, including the systematic calculation of the antenna physical dimensions**. The objective here is twofold. First, the development of a novel CRLH LWA structure able to provide advantages over current state of the art antennas, specially concerning the control of the antenna radiation losses. And second, the development of a self-consistent technique able to completely characterize the proposed antenna and especially, *to automatically derive the antenna physical dimensions without requiring the use of commercial full-wave software*.

This PhD. thesis has financially been supported by the Spanish National Grant FPU ("Formacion Profesado Universitario"), with reference AP2006 − 015. **The work has been developed within the framework of the GEAT group** ("Grupo de Electromagnetismo Aplicado a las Telecomunicaciones", in Spanish) headquartered at the Technical University of Cartagena (UPCT). The GEAT group, **leaded by Prof. Alejandro Alvarez-Melcon (main supervisor of this thesis)**, *has ample technical and scientific experience for about* 20 *years*, and it has been very active in the last few years. The main research lines of this *young research group* are integral equation formulations (IE) [Mosig, 1989] solved by the method of moments (MoM) [Harrington, 1968], Green's functions analysis of different structures and media [Álvarez Melcón and Mosig, 2000], [Mosig and Álvarez Melcón, 2003], [Álvarez Melcón et al., 1999], filter theory, synthesis and practical design [Guglielmi et al., 1992], [Cañete-Rebenaque et al., 2004], [Martínez-Mendoza et al., 2008], and leaky-wave antennas [Gomez-Tornero et al., 2005], [Gomez-Tornero et al., 2006b], [García-Vigueras et al., 2010], [Garcia-Vigueras et al., 2011] among others. Therefore, *it provides an excellent research environment*, with special emphasis in theoretical work. Specifically, the group has a strong background on Green's functions computation related to shielded enclosures [Álvarez Melcón and Mosig, 2000], [Gomez-Tornero and Alvarez-Melcon, 2004], [Quesada Pereira et al., 2005a] which constitutes one of the main research lines of this thesis.

Besides, for the successful development of this multidisciplinary work, which includes Green's functions analysis, leaky-wave antennas, metamaterials, optically-inspired phenomena and phased-array theory among other fields, it has been of **extreme importance the collaboration with world leading research groups**. This collaboration, which has been possible thanks to the financial support for international stages provided by the Spanish FPU fellowship, has allowed to learn and take advantage of the know-how, theoretical background, fabrication facilities and expertise from these international research groups. In first place, in order to fully understand the recently developed metamaterial concepts [Caloz and Itoh, 2005], [Eleftheriades and Balmain, 2005], [Marques et al., 2008], **a close collaboration with the ETA (Electromagnetic Theory and Application) research group, leaded by Prof. Christophe Caloz (co-supervisor of this PhD thesis) and headquartered at the Poly-Grames deparment in the Ecole Polytechnique de Montreal, has been established**. Prof. Caloz's group is known to be a leading research group in the field of microwave metamaterials, with key and fundamental contributions in this area [Caloz and Itoh, 2005]. Furthermore, the group activities extend well beyond, covering most of the fields of theoretical, computational and technological electromagnetics engineering, with strong emphasis on emergent and multidisciplinary topics [Gómez-Díaz et al., 2009d], [Gupta et al., 2009a], [Kodera and Caloz, 2009], [Carignan et al., 2009]. As part of this collaboration agreement, I carried out a research stage of one year (from November 2007 to November 2008) at Ecole Polytechnique of Montreal. This has allowed a deep study in the metamaterial nature, providing a fundamental link between optics phenomena and microwaves [Gómez-Díaz et al., 2008a], [Gómez-Díaz et al., 2009b].

In addition, in order to complete the study on leaky-wave antennas [Oliner and Jackson, 2007], [Bertuch, 2007], electromagnetic band-gap (EBG) [Rahmat-Samii and Mosallaei, 2001], [Bertuch, 2006] and phased-array theory [Bhattacharyya, 2006], **an important collaboration with the Fraunhofer Institute for High Frequency Physics and Radar Techniques (Fraunhofer FHR), which is heartquarted at Wachtberg (Germany), has been settled**. This center is known to be a world leader in radar technology, with emphasis on electromagnetic modeling, microwave devices, anten-

nas and sensors. Besides, the FHR Institute counts with an impressive number of technical facilities, with equipment able to fabricate and measure devices working at very high frequencies (Terahertz). As a part of this collaboration, I carried out a research stage of six months (from September 2009 to March 2010) at this Institute, **under the valuable supervision of Dr. Thomas Bertuch**. This has allowed an exhaustive study of phased-array and leaky-wave antennas, and has led to the analysis, design and fabrication of a new type of metamaterial-based parallel-plate waveguide leaky-wave antenna [Gómez-Díaz et al., 2010a], [Gómez-Díaz et al., 2011a], [Gómez-Díaz et al., 2011b].

The importance of the aforementioned international collaborations with respect to this PhD thesis is two fold. First, it has allowed the development of novel electromagnetic theories and formulations [Gómez-Díaz et al., 2008a], [Gómez-Díaz et al., 2009e], [Gómez-Díaz et al., 2011a] for the analysis and design of microwave devices and antennas, **taking advantage of the know-how of various research groups and combining different technical approaches**. Furthermore, it has also provided the adequate framework to find important links between optics phenomena and microwaves using the dispersive behavior of metamaterials [Gómez-Díaz et al., 2009b]. This first step is fundamental in order to ***carry out a multidisciplinary, both theoretical and practical, research project*** as presented in this thesis. Second, **it has allowed to take advantage of the huge fabrication facilities of these international research centers. Therefore, most of the formulations, devices and phenomena which have been derived in this work have been experimentally validated and confirmed**.

1.2 Description and Organization of the Work

This section defines the general context of the present work, the contest of the chapters included in this thesis and how the techniques and concepts developed are placed regarding to the current state of the art. However, due to the wide variety of topics treated, an extensive literature overview is omitted here, and each chapter includes a brief review of the state of the art related to the materials presented in it.

The **first research line, related to multilayered shielded Green's functions, analysis of shielded microwave circuits and filtering structures**, is developed in Chapter 2 and in Chapter 3. The use of shielded enclosures is widely extended in the microwave community (see Fig. 1.1), in order to provide physical support to several devices, avoid unwanted radiation or to obtain immunity against electromagnetic interferences, among other reasons. However, the enclosure produces important electromagnetic effects that must be rigorously considered [Dunleavy and Katehi, 1988b] when analyzing or designing a device. For this analysis, general full-wave methods (such as FDTD [Taflove and Hagness, 2005] or FEM [Jin, 1993]) may be applied. The main problem of such approaches is that they require to mesh the whole cavity, including dielectrics and printed circuits [which is not always easy, due to dimensions difference between the printed circuits (usually small) and the cavity (which may be big)], leading to large execution times. Furthermore, these methods do not provide any physical insight about the cavity response or influence. Another interesting option is to solve this problem using an integral equation formulation [Mosig, 1989] solved by the method of method of moments [Harrington, 1968]. In this case, only the printed circuit must be meshed, leading to faster analysis. However, *it is required to obtain the Green's functions (or impulse-*

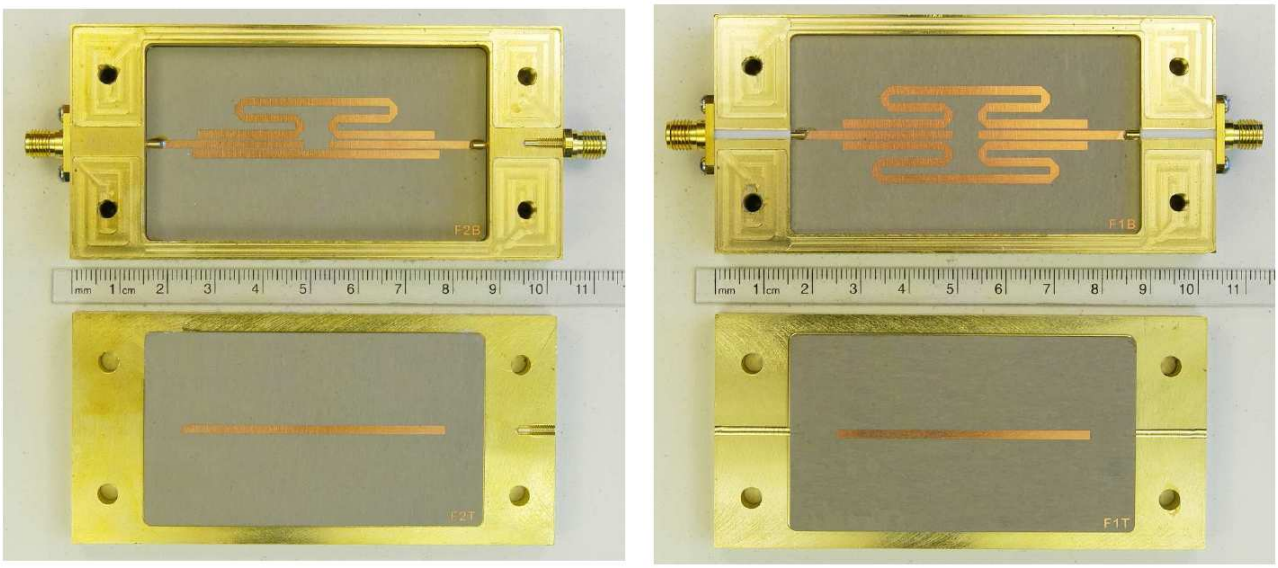

(a) **(b)**

Figure 1.1 – Example of multilayered shielded microwave filters [Cañete-Rebenaque et al., 2011]. (a) Dual-band filter. (b) Pseudo-elliptic filter.

response) related to the multilayered cavity, which is not an easy task. This problem can be formulated either in the spatial domain [Livernois and Katehi, 1989], [Álvarez Melcón and Mosig, 2000] (where the Green's function as expressed as extremely slowly-convergent sum of infinite images) or in the spectral domain [Eleftheriades et al., 1996], [Álvarez Melcón et al., 1999] (which may have convergence problems in some cases, as a function of the cavity and printed circuit dimensions). Besides, these associated Green's functions have only been solved for canonical multilayered geometries, as the rectangular [Álvarez Melcón and Mosig, 2000] or circular [Zavosh and Aberle, 1995].

In this context, Chapter 2 first review the standard techniques (in the spectral and in the spatial domain) found in the literature for the computation of the mixed-potential Green's functions associated to free-space, layered media of infinite transverse dimensions and boxed stratified enclosures. Note that along this work, I employ mixed-potential Green's functions due to their simpler expressions and weaker singularities as compared to the Green's functions related to the fields.

Then, **the chapter presents in detail a fast-convergent spatial domain approach**, based on the work introduced by Prof. Alvarez-Melcon in [Alvarez-Melcon and Mosig, 1999] and in [Quesada Pereira et al., 2005a], **for the Green's functions analysis of convex arbitrarily-shaped multilayered cavities** [Gómez-Díaz et al., 2008c]. The method is based on the use of auxiliary spatial charges or dipoles (spatial images or sources), located outside the cavity under analysis, to impose the boundary conditions for the potentials at discrete points along the cavity contour. Next, the formulation presented is modified, for the case of rectangular enclosures, by using a set of continuous auxiliary sources, which impose boundary conditions along the whole cavity perimeter. *This modification provides a total control on the error committed on the Green's functions calculation, allowing to reduce it to arbitrarily small values*. Furthermore, **the technique is combined with the use of dynamic ground planes**, which leads to mirror spatial images. The use of this method perfectly imposes boundary conditions for the potential on two of the cavity walls, and completely removes any nu-

merical instability provided by the singular behavior of the point source[Gómez-Díaz et al., 2011d]. Besides, this chapter also includes another spatial-domain method for the **rigorous computation of multilayered Green's functions of cavities with triangular right-isosceles cross section** [Gómez-Díaz et al., 2009e]. The technique is based on image theory, and expresses the triangular-shaped Green's functions as a linear combination of boxed Green's functions. Finally, note that, for the sake of validation, the chapter includes many results, such as resonant frequencies of potential pattern distributions, related to the Green's functions analysis of different multilayered cavities. These results are validated using data obtained by commercial full-wave software.

Chapter 3 introduces the mixed-potential integral equation (MPIE), solved by the method of moments, for the analysis of microwave circuits (as these shown in Fig. 1.1). First, the MPIE formulation and procedure [Mosig, 1989] is introduced and explained in detail. Then, the basic steps of the approach are gathered and presented in a organized way, including the geometrical discretizacion of the structure under analysis, Green's functions computation, filling of the MoM matrix, definition of the excitation vectors and the recovering of the system equivalent parameters associated to the structure under analysis.

Usually, the analysis of multilayered shielded circuits using an MPIE approach leads to very high computational times. This is basically due to the slow-convergent behavior of the series arising in the traditional computation of multilayered boxed Green's functions. Even though several approaches have been proposed to increase the efficiency of these series (see [Brezinski and Zaglia, 1991], [Kinayman and Aksum, 1995], [Park et al., 1998], [Park and Nam, 1998], [Gentili et al., 1997] or [Pérez-Soler et al., 2008]), the analysis of shielded circuits is still very time-consuming. In order to overcome this important drawback, **Chapter 3 proposes two novel methods for the efficient implementation of the spatial images technique**, which provides the shielded Green's functions, **into the mixed-potential integral equation framework**. *The first method is based on interpolation* (see [Gómez-Díaz et al., 2008b]), but the idea is not to interpolate the Green's functions, which have fast variations and strong singularities, *but to do this interpolation in an upper abstraction layer, i.e., interpolating the complex values of the charge and dipole spatial images*. This allows to a great reduction of the computational cost required by the method. *The second novel approach proposed in this chapter exploits the fact that the Green's functions computed by the spatial images technique are naturally separated in two parts, source and image contributions*. Using these features, two MoM matrixes are computed separately. The first one contains the singular behavior of the Green's functions and can be evaluated fast using efficient numerical techniques for the computation of the Sommerfeld transformation. The second one contains the contribution of the images, and due to the smooth behavior observed, it can be computed with very limited computational effort (see [Gómez-Díaz et al., 2008c]). *This novel method drastically reduces the computational cost required to the analysis of practical shielded microwave devices*.

The careful study of multilayered cavities and the analysis of circuits placed therein, has led to **the development of the novel hybrid waveguide-microstrip filter technology**. This filter technology combines one resonance, provided by the multilayered cavity (with a specific configuration), with N microstrip resonators, leading to an $N+1$ order filter. *The proposed technology is light, compact, low-lossy, uses the filter package as part of the filter, and allows to implement transversal topologies*. Besides, a survey is presented for the design of this type of filters. **The novel technology proposed is fully validated by using full-wave simulation results and measurements**.

Finally, Chapter 3 also presents a collection of microwave shielded filters analyzed (and in some

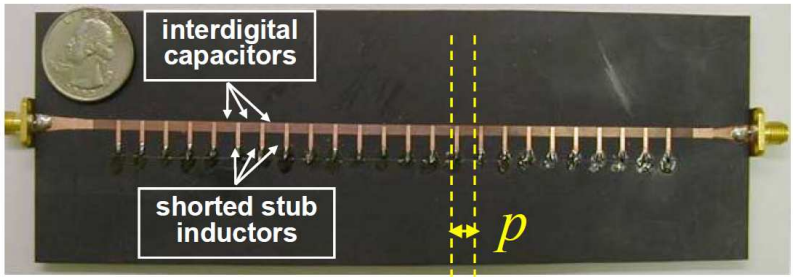

(a)

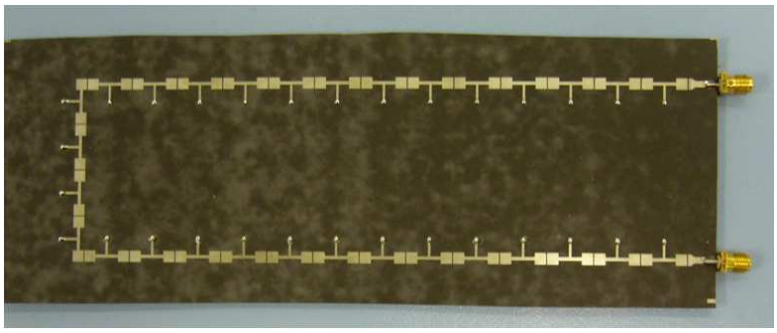

(b)

Figure 1.2 – Example of CRLH transmission lines. (a) Microstrip technology [Caloz and Itoh, 2005]. (b) MIM (Metal Insulator Metal) technology [Abielmona et al., 2007].

cases, also designed) using the proposed techniques. The collection includes examples of the novel hybrid waveguide-microstrip technology, coupled-line filters, and broadside-coupled filters, among others. **The comparison of the results obtained against full-wave simulations data , from commercial packages, and measured results, from fabricated prototypes, fully confirms the accuracy and efficiency of the proposed methods.**

The **second research line** is developed in Chapter 4 and in Chapter 5. This line **is mainly related to the impulse-regime analysis of composite right/left-handed (CRLH) structures and the subsequent theoretical and practical demonstration of several novel optically-inspired phenomena and applications at microwaves, in both, the guided and the radiative region.** In the current microwave state of the art, metamaterials [Caloz and Itoh, 2005], [Eleftheriades and Balmain, 2005], [Marques et al., 2008] have provided novel concepts, phenomena and applications (such as backfire to endfire leaky-wave antennas [Liu et al., 2002], couplers [Nguyen and Caloz, 2007a], [Jarauta et al., 2004], power-dividers [Islam and Eleftheriades, 2008a], phase-shifters [Antoniades and Eleftheriades, 2003a], [Siso et al., 2007], or dual band components [Lin et al., 2004], [Eleftheriades, 2007b], among many others). At microwaves, metamaterials have usually been implemented in planar technology using ***composite right/left-handed transmission lines*** (see [Caloz and Itoh, 2005], [Eleftheriades and Balmain, 2005] and Fig. 1.2), which is a non-resonant approach. Another common implementation is based on split-ring and complementary split-ring resonators [Marques et al., 2008], which is a resonant-type approach. It is interesting to note that this latter implementation can lead to the former, as has recently been demonstrated in [Duran-Sindreu et al., 2009]. Most of the applications and phenomena of metamaterials (as the pre-

viously described) have only been reported in the harmonic regime. However, *the recent emergence of UWB systems [Ghavami et al., 2007] has created a need for novel microwave concepts, phenomena and direct applications in the impulse-regime*. Metamaterial-based CRLH transmission lines[Caloz and Itoh, 2005], which are broadband and highly dispersive in nature, may provide novel and original solutions in this field. *The control of these dispersive properties leads to the* ***dispersion engineering concept****, i.e. the phase shaping of electromagnetic waves to process signals in an analog fashion [Gupta and Caloz, 2009].*

In this context, Chapter 4 first presents a detailed survey of "metamaterials": origins, development, current state of the art, and practical applications. Specifically, an overview of both, bulky and planar, metamaterials is given. Besides, a distinction between the resonant and non-resonant approaches for the design of this type of structures is provided, clearly indicating the main advantages and drawbacks of each alternative. Then, the chapter reviews the state of the art of composite right/left-handed transmission lines. These structures, introduced simultaneously and independently in 2002 by three different research groups (see [Caloz et al., 2002], [Iyer and Eleftheriades, 2002] and [Oliner, 2002]) are based on the periodic loading of a host transmission line by inductive and capacitative elements. This approach is inherently non-resonant, and consequently, low-lossy. One of the main advantages of CRLH TLs is their easy practical implementation using planar technology (such us microstrip, coplanar waveguide, or coplanar stripline). Moreover, this chapter also provides master guidelines [Caloz and Itoh, 2005] for the analysis and design of this type of metamaterial-based transmission lines, and overviews the main CRLH TLs applications in both, the guided and the radiative regime.

Then, **a novel formulation for the impulse-regime analysis of CRLH structures is proposed**. For this purpose, a *closed-form time-domain Green's functions approach is employed to analyze electrically thin CRLH transmission lines and leaky-wave antennas* . The method is first applied to model pulse propagation along dispersive CRLH media [Gómez-Díaz et al., 2009b]. This includes the specific cases of uniform and non-uniform CRLH structures, excited by a single input pulse or a periodic train of input pulses. *The main advantages of this approach are the unconditional stability and fast computation, due to the continuous treatment of time, and the insight into the physical phenomena provided by the Green's functions.* Besides, the method is modified to consider pulse propagation along non-linear CRLH lines. In this case, non-linearity is achieved by loading the CRLH structure with hyper-abrupt diodes, leading to a new unit-cell definition.

Next, the formulation is further extended to study impulse-regime radiation from CRLH leaky-wave antennas. First, **a new circuital condition for the standard CRLH LWA unit cell is proposed to achieve, for the first time, a constant radiation rate in the whole space** [Gómez-Díaz et al., 2011c]. This condition allows a continuous and smooth transition of the radiation losses from the left-handed to the right-handed frequency region. Moreover, it also solves the phase fluctuations that traditionally occur around the CRLH transition frequency due to real radiation losses. Second, **a novel simple theory is given for the harmonic characterization of leaky-wave antennas**. The theory, *which expresses leaky radiation as a function of the currents flowing on each conductor of the transmission line*, provides a fundamental explanation about leaky-wave antennas, in connection with transmission lines. And third, **all the previous developments are combined with the time-domain Green's functions approach previously presented, to efficiently and accurately characterize CRLH LWAs excited by temporal pulses** [Gómez-Díaz et al., 2010b]. Due to the spectral-spatial decomposition property of LWAs [Gupta et al., 2009a], each frequency component of the input signal is radiated to a particular space position, where the time-dependent field evolution can efficiently been retrieved using the

proposed formulation. A single CRLH LWAs and an array of CRLH LWAs (leading to pencil beam pattern) is studied in deep, showing their behavior when excited by different (chirp) modulated input signals.

In Chapter 5, **the formulation previously explained is applied to the development of novel phenomena and applications in the microwave domain, most of them transported from optics** [Saleh and Teich, 2007]. The idea is to exploit the dispersive properties of CRLH TLs (either group velocity or the group velocity dispersion) to obtain these phenomena. The use of *the formulations presented in Chapter 4 is essential, because they allow a fast and accurate analysis of the dispersive structures, whereas the use of commercial full-wave software is extremely time-consuming*. Furthermore, **the practical demonstration (using fabricated prototypes) of the novel phenomena also validates the new theory developed**. The novel phenomena and applications presented in this chapter are: (a) *phenomenology of pulse propagation on dispersive CRLH media* [Gómez-Díaz et al., 2009b], (b) *pulse compression* [Gómez-Díaz et al., 2009b], (c) *temporal Talbot effect* [Gómez-Díaz et al., 2009b], (d) *broadband resonator* [Gómez-Díaz et al., 2009a], (e) *nonlinear effects and automatically balance of CRLH lines* [Gómez-Díaz et al., 2009c], [Gómez-Díaz et al., 2010b], (f) *real time spectrogram analyzer (RTSA) system* [Gupta et al., 2009a] [Gómez-Díaz et al., 2010b], (g) *frequency-resolve electrical gating (FREG) system* [Gupta et al., 2009b] and (h) *spatio-temporal Talbot effect* [Gómez-Díaz et al., 2008a] [Gómez-Díaz et al., 2009d]. Initially, a careful mathematical development is proposed to explain all phenomena/applications. For this purpose, an optical approach has usually been employed [Saleh and Teich, 2007]. Then, a rigorous full-wave validation of all phenomena/applications (using the proposed theory and additional commercial software) is presented. Finally, **measurements are also included to fully demonstrate most of the proposed phenomena and applications**. It is important to point out that **the proposed optically-insipired phenomena/applications are totally original and novel at microwaves**, and some of the proposed effects have never been observed before (as, for instance, the spatio-temporal Talbot effect [Gómez-Díaz et al., 2009d]).

The analogy between the proposed phenomena and applications at microwaves and their corresponded counterpart at optics [Saleh and Teich, 2007] is deduced from the dispersive properties of a CRLH structure . Specifically, *in the guided mode* there is a clear parallelism between the dispersive behavior of a CRLH line and an optical component, which is inherently dispersive (for instance, an optical fiber [Saleh and Teich, 2007]). Therefore, optical phenomena can be easily reproduced at microwaves. In the *radiative mode*, the beam scanning law of the CRLH LWA is analog to a diffraction grating where different spectral components are radiated (or diffracted) at different angles causing spatial dispersion. Besides, note that *the dispersive engineering approach has provided a huge number of novel phenomena and applications at microwaves, with direct impact on current and future UWB systems*.

Finally, the third research line proposes **a novel CRLH parallel-plate waveguide (PPW) leaky-wave antenna** and a rigorous **iterative modal-based technique for its fast and complete characterization, including the systematic calculation of the antenna physical dimensions**. Backward to forward regular leaky-wave antennas [Oliner and Jackson, 2007] are usually designed to operate in the first space harmonic ($\nu = -1$) while metamaterial leaky-wave antennas [Caloz and Itoh, 2005] operates in the fundamental mode ($\nu = 0$). The main advantage of the latter is that it is usually compact, light, and mainly, it is able to scan the whole space (from backfire to endfire, including the broadside direction [Liu et al., 2002]). In order to analyze these types of antennas, circuit models are

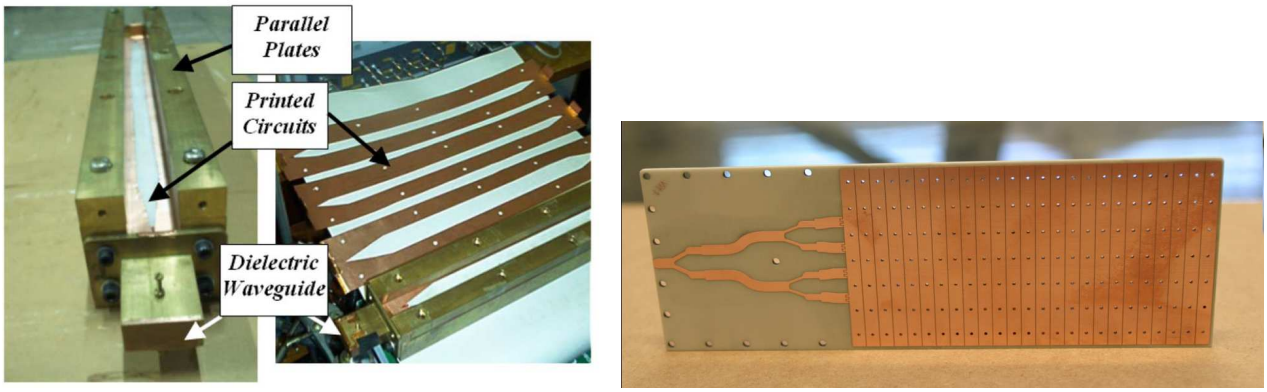

Figure 1.3 – Example of leaky-wave antennas. (a) Hybrid dielectric-waveguide LWA [Gomez-Tornero et al., 2006a]. (b) Proposed parallel-plate waveguide composite right/left-handed LWA [Gómez-Díaz et al., 2011b].

usually employed (see [Caloz and Itoh, 2005] and [Eleftheriades and Balmain, 2005]). These models are able to accurately represent the antenna dispersive behavior [i.e. the phase constant $\beta(\omega)$] but they have difficulties to characterize the amount of radiated power [i.e. leaky rate $\alpha(\omega)$] (on the contrary as other type of LWAs (see Fig. 1.3a), where this radiation rate can easily be obtained [Gomez-Tornero et al., 2006b]). Therefore, the radiation characteristics of the antenna cannot completely be determined with these methods. This is an important limitation of the existing techniques, because the control of the attenuation factor is fundamental for the design of real-life antennas. In addition, a considerable number of very time-consuming full-wave simulations are usually required for the design of balanced CRLH LWAs . This makes the CRLH LWA design procedure a tedious task.

This line is developed in Chapter 6, which first **proposes a novel CRLH leaky-wave antenna** (see Fig. 1.3b). The new structure is composed of a loaded parallel-plate waveguide (PPW). The loading is achieved by using via-holes and slots. In order to successfully analyze the antenna, *a novel dispersive unit-cell circuit is introduced*. This circuit model is able to completely characterize the antenna as a function of frequency, including scattering parameters, radiation angle and losses, and radiation patterns, among all antenna features. Then, to accurately obtain the dispersive parameters of the model, an iteratively-refined modal analysis, based on phased-array theory, is applied. *The method combines a mode-matching technique [Marcuvitz, 1964] with periodic radiating boundary conditions, using Floquet's theorem*. **The proposed analysis is able to automatically derive the antenna physical dimensions in seconds**, without the need to use extremely time-consuming full-wave simulations, leading to a very quick design. Furthermore, *the radiation characteristics of this type of antennas are also investigated in deep, and a novel formulation for the radiated far-field computation is presented.* The frequency-dependent technique is based on an array factor approach of equivalent magnetic sources, accurately retrieve the 1D and 2D radiated electric field, and allows to compute other important quantities related to the antenna, such us radiation patterns, -3dB beam width, directivity, gain, etc. (see [Stutzman and Thiele, 1998]). The formulation inherently takes into account the mutual coupling between the slots, radiation losses, reactive fields and the fluctuations of the radiated power with frequency. **Very good agreement in the 1D and 2D radiation patterns obtained by the**

proposed formulation and the measured results from a PPW CRLH LWA prototype is found, validating both, the novel antenna radiating properties and the proposed theory. *The proposed CRLH LW antenna and subsequent deep-insight analysis provide novel, efficient and easy-design solutions to the antenna community, and it is expected to be ready for practical and commercial applications soon.*

1.3 Original Contributions

In the present work there are some concepts and developments that can be considered as original or innovative contributions to the microwave community. In addition, there are also some descriptions and numerical developments which have been included to keep the coherence and self-consistence of the text. The purpose of this section is to briefly list the main original contributions of this thesis:

Chapter 2 introduces the spatial images technique, applied to Green's functions analysis of multilayered cavities with arbitrarily-shaped cross-section. The main ideas of the technique were originally introduced by Prof. Alvarez-Melcon in [Alvarez-Melcon and Mosig, 1999], and the method was then extended for the specific case of cylindrical multilayered enclosures in [Quesada Pereira et al., 2005a]. The innovation of the present work can be attributed to the complete reformulation of the technique in order to analyze multilayered cavities with convex cross-sections. Besides, in the specific case of rectangular multilayered cavities, the method was further modified by using a set of auxiliary linear sources to impose the potential boundary conditions along the complete cavity perimeter, instead of the use of a discrete set of spatial images. This important modification changes the discrete nature of the technique, leading to a completely continuous method with improved accuracy and stabilities features. Another substantial contribution is the combination of the technique with dynamic ground planes, which perfectly imposes boundary conditions on two of the rectangular cavity walls, and completely removes the problems related to the singular behavior of the point source. Finally, this chapter also introduces a completely novel spatial technique applied to the computation of multilayered Green's functions associated to cavities with right-isosceles triangular cross section.

Chapter 3 proposes two novel methods for the efficient implementation of the spatial images technique into a mixed-potential integral equation framework. These methods drastically reduce the computational cost required for the analysis of practical shielded microwave devices. Besides, this chapter also proposes the new hybrid waveguide-microstrip technology, which combines one resonance, provided by the multilayered cavity, with N microstrip resonators, leading to a $N+1$ order filter. The proposed technology is light, compact, low-lossy, uses the filter package as part of the filter, and allows to implement transversal topologies. Then, several hybrid-waveguide microstrip prototypes have been analyzed, designed and fabricated for the first time, fully demonstrating the usefulness of the proposed technology.

Chapter 4 proposes a time-domain formulation to analyze, for the first time, impulse-regime phenomenology of electrically thin CRLH transmission lines and leaky-wave antennas . In the guided-regime, the formulation is further extended to consider non-linear phenomena, correctly modeling the inclusion of varactors in the CRLH unit-cell . In the radiative-regime, a

new simple circuital condition for the CRLH LWA unit-cell is proposed to achieve, for the first time, a constant radiation rate in the whole space. Besides, a novel leaky-wave characterization, based on contra-directional currents of a simple transmission line is presented. This model provides an additional and easy explanation to understand the complex radiation process associated to this type of antennas.

Chapter 5 rigorously study novel microwave phenomena and applications, most of them transported from optics, exploiting either the group velocity or the group velocity dispersion properties of CRLH TL. The novel phenomena/applications investigated or proposed are: (a) phenomenology of pulse propagation on dispersive CRLH media, (b) pulse compression, (c) temporal Talbot effect, (d) broadband resonator, (e) nonlinear effects and automatically balance of CRLH lines , (f) real time spectrogram analyzer (RTSA) system, (g) frequency-resolve electrical gating (FREG) system, and (h), the spatio-temporal Talbot effect.

Chapter 6 presents the physical structure and the fabrication of a novel CRLH leaky-wave antenna (see Fig. 1.3b). Besides, a completely novel iterative algorithm, based on a new dispersive unit-cell circuit model and on mode-matching techniques, is presented for the fast and accurate design of this type of antennas. Furthermore, the proposed technique allows to obtain the antenna physical dimensions without requiring additional full-wave simulations, leading to a very quick design. Finally, the antenna radiated fields are also accurately retrieved by using a novel array factor approach based on equivalent magnetic linear sources.

For the sake of clarity, a complete list of publications related to the author's novel contributions can be found in Appendix F.

Chapter 2

Green's Functions Analysis of Multilayered Shielded Enclosures

2.1 Introduction

Green's functions owe their name to the British mathematician George Green, which published in 1828 the paper "An Essay on the Application of Mathematical Analysis to the Theories of Electricity and Magnetism" [Green, 1828]. This work introduced novel mathematical concepts applied to the analysis of physical and electromagnetic problems. One of his main contributions was the proposal of a new kind of function, which was employed to solve inhomogeneous differential equations subject to some specific boundary conditions. These functions, called Green's functions, were later successfully applied to a wide diversity of disciplines, such as physics, quantum field theory, statistical field theory, electrodynamics theory, etc.

Nowadays, Green's functions plays an extremely important role in computational electromagnetics (see, for instance, [Harrington, 1961], [Felsen and Marcuvitz, 1973], [Barton, 1989a], [Balanis, 1989], [Collin, 1991], [Tai, 1993], [Dudley, 1994] or [Peterson et al., 1998]), and are commonly applied, together with other mathematical methods, to the analysis and design of microwave and millimeter-wave circuits and antennas.

In this context, Green's functions may be defined as the fields and potentials produced by a unitary charge/dipole embedded in the particular medium surrounding the structure under study [Tai, 1993]. Since they constitute the kernel of any integral equation (IE) formulation (see [Poggio and Miller, 1973], [Mosig, 1989], [Morita et al., 1990] or [Kolundzija and Djordjevic, 2002]), they are of crucial importance in modern computational electromagnetics. Intuitively, a Green's function may be considered as the impulse response of a particular environment. Then, the complete behavior of a real circuit or antenna placed in that media may be obtained by the superposition of many impulse responses by using convolution integrals.

Due to these reasons, there has been a lot of research effort in the study of the Green's functions arising in electromagnetic problems, and many interesting results can be found in the

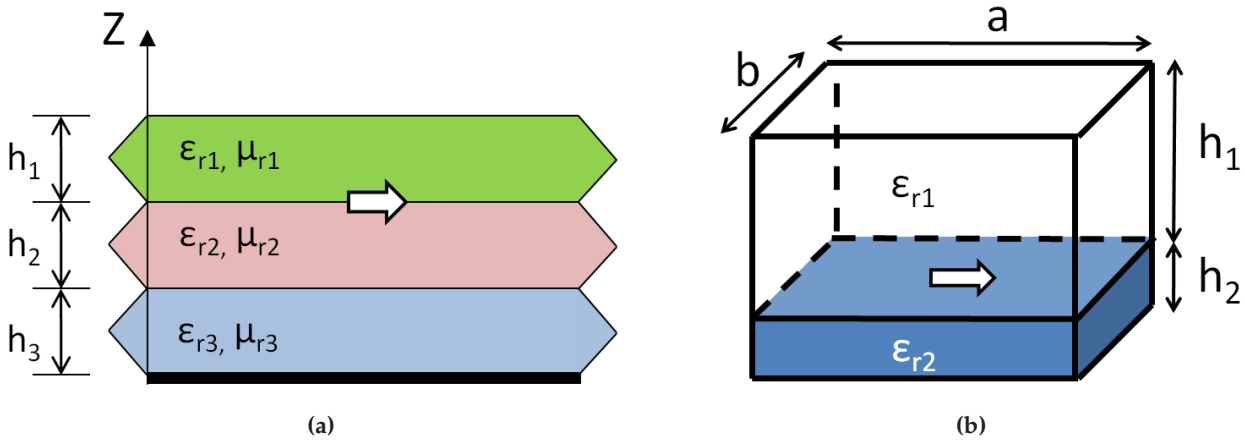

Figure 2.1 – Example of a unitary dipole embedded in two different environments. (a) Multilayered media, with infinite lateral transversal dimensions. (b) Multilayered enclosure.

technical literature (such as those presented in [Felsen and Marcuvitz, 1973], [Barton, 1989a] or in [Peterson et al., 1998]).

In the case of multilayered media (see Fig. 2.1a), the mathematical foundations were given in [Felsen and Marcuvitz, 1973], where it was demonstrated that the use of a double spatial Fourier transformation reduces the original Maxwell's equations to a simple transmission line formalism. Therefore, the multilayered Green's functions are analytically available in the spectral domain, leading to the so-called *spectral Green's functions* (see [Mosig, 1989], [Gay Balmaz and Mosig, 1997] and [Michalski and Mosig, 1997]). In the case of integral equations formulated in the spectral domain (see [Katehi and Alexopoulos, 1985], [Jackson and Pozar, 1985] or [Mesa et al., 1995]) these spectral Green's functions can directly be employed in the analysis of circuits or antennas.

In the case of integral equation formulated in the spatial domain (see [Mosig and Gardiol, 1985], [Mosig, 1989], [Dudley, 1994] or [Bunger and Arndt, 2000], and Chapter 3) the spectral Green's functions must be converted back to the spatial domain, leading to the so-called *spatial Green's functions*. This is done by using the well-known Sommerfeld transformation [Sommerfeld, 1896], which is computationally very intense. In order to accelerate this transformation, a lot of research effort has been carried out for the efficient computation of the spatial-domain multilayered Green's functions. Among the proposed methods, we can mention these techniques which obtain asymptotic expressions of the Sommerfeld integrals in closed-form (see [Marin et al., 1989], [Barkeshli et al., 1990], [Aksun, 1991], [Hoorfar and Chang, 1995], [Aksun, 1996], [Aksun and Dural, 2005], [Yuan et al., 2006], [Boix et al., 2007], [Mesa et al., 2008] or [Alparslan et al., 2010]) and those which perform a numerical representation of the Green's functions (see [Mosig and Gardiol, 1983], [Gay Balmaz and Mosig, 1997], [Mesa and Marques, 1995], [Michalski, 1998], or [Mosig and Álvarez Melcón, 2003]).

In practice, microwave devices are usually located within a shielded enclosure, which provides physical support, immunity against interferences and avoids unwanted radiation. These features have lead to the derivation of boxed multilayered Green's functions (see Fig. 2.1b and [Marcuvitz, 1964], [Felsen and Marcuvitz, 1973], [Mosig, 1989], [Balanis, 1989],

[Eleftheriades et al., 1996] or [Álvarez Melcón and Mosig, 2000]), which can easily be incorporated into integral equation techniques.

On the contrary as free-space [Felsen and Marcuvitz, 1973] or stratified media (see [Mosig, 1989], [Michalski and Mosig, 1997] and [López-Frutos, 2011]), the efficient evaluation of Green's functions in shielded multilayered enclosures is still very challenging. The main reasons are as follows. First, the standard formulation is only able to deal with multilayered cavities with rectangular [Itoh, 1989] or circular [Zavosh and Aberle, 1995] cross-sections. This reduces the generality of the analysis, and avoids its use in practical situations where space is a physical constrain. Second, the infinite sums which arises in the spatial-domain Green's functions are very slowy convergent. Even though several acceleration techniques have recently been proposed (see [Kinayman and Aksum, 1995], [Park and Nam, 1997], [Gentili et al., 1997], [Park et al., 1998], [Park and Nam, 1998], [Pérez-Soler et al., 2008] and Chapter 3.3), the analysis of multilayered printed circuits using this formulation leads to prohibitive simulation times. And third, although efficient algorithms have been presented in the spectral-domain (see [Álvarez Melcón et al., 1999]), the use of a IE approach formulated in the transformed domain still suffers from important convergence issues when the size of the box is large as compared with the mesh employed to discretize the printed circuits.

In this chapter, I address the numerical evaluation of multilayered Green's functions located in shielded enclosures. Specifically, several approaches are presented based on the spatial images concept, introduced by Prof. Alvarez-Melcon in [Alvarez-Melcon and Mosig, 1999] and further extended in [Quesada Pereira et al., 2005a] and in [Quesada Pereira et al., 2005b]. In summary, the novel techniques proposed in this chapter use spatial auxiliary sources to impose the boundary conditions for the potentials along the cavity contour. This allows the fast and accurate computation of spatial-domain Green's functions associated to multilayered enclosures with arbitrarily-shaped convex cross-sections. Then, these Green's functions will be employed in Chapter 3 as building blocks of a mixed-potential integral equation (MPIE) framework [Mosig, 1989], which will be applied to the fast and accurate analysis and design of complex microwave circuits and devices.

In the present work, I am particulary interested in the evaluation of the Green's functions associated to the auxiliary potentials (see [Balanis, 1989] and [Mosig, 1992]). The main advantage of using Green's functions associated to the potentials is that they exhibit weaker singularities ($1/\rho$) as compared with the Green's functions associated to the fields, which exhibit singularities of the order $1/\rho^2$ and higher [Mosig, 1989]. Therefore, the use of the mixed-potentials Green's functions greatly reduces the numerical instabilities associated to the Green's functions singular behavior, leading to a numerically stable spatial-domain MPIE formulation [Mosig and Gardiol, 1985], [Mosig, 1989].

This chapter is organized as follows. In Section 2.2 I briefly review the traditional techniques employed to compute Green's functions, first in free-space, then in unbounded multilayered media and finally, in boxed stratified enclosures.

Then, Section 2.3 derives in great detail the spatial images technique (see [Gómez-Díaz et al., 2008c]), which is applied to the numerical evaluation of Green's functions, and their spatial derivatives, in multilayered enclosures with arbitrarily-shaped cross section. The method consists of placing auxiliary electric dipole and charge images outside the cavity, imposing, at discrete points of the metallic wall, the appropriate boundary conditions for the potentials. This

leads to an accurate approximation of the exact cavity modeling. The presence of dielectric layers and the boundary conditions at the top and bottom covers of closed cavities are taken into account through the Sommerfeld transformation. Besides, the analysis of electrically long structures is performed by using several rings of images, which surrounds the whole cavity at different heights. For the sake of validation, several multilayered cavities are analyzed, obtaining their resonance frequencies and potentials pattern distributions. The results are compared to those obtained by the commercial software HFSS©, showing a very good agreement in all cases.

Next, in Section 2.4, the continuous counterpart of the spatial images technique (see [Gómez-Díaz et al., 2011d]) is proposed for the computation of the multilayered boxed Green's functions and their derivatives. The method employs a set of auxiliary linear distribution of sources to effectively impose the potential boundary conditions along the whole cavity contour. The imposition of these boundary conditions leads to a set of integral equations (IEs), on the unknown distributions of the auxiliary sources, which are solved by applying a method of moments approach. Besides, the technique is combined with the use of dynamic ground planes generating mirror basis functions, which completely remove any singular instability. A convergence/efficiency study, related to the test and basis functions choice, demonstrates the accuracy and efficiency of the proposed technique in all possible situations.

Finally, Section 2.4 proposes a novel method for the Green's functions computation inside multilayered shielded cavities with right isosceles-triangular cross-section. The method, developed again in the spatial domain, is based on image theory. The idea is to use the spatial-domain Green's functions inside a multilayered shielded square box, in order to accurately obtain the Green's functions for the right isosceles-triangular cavity. Image theory is then used to enforce the boundary conditions along the non-equal side of the triangle. It is shown that the new algorithm is very robust, with limited computational effort. For validation purposes, the resonant frequencies and potential patterns of a triangular cavity have been calculated and compared with those obtained by other techniques, showing very good agreement.

It is important to point out that all the techniques proposed here will be employed in Chapter 3 for the analysis and design of several multilayered shielded circuits. There, the use of the novel hybrid-waveguide microstrip filter technology [Martínez-Mendoza et al., 2007], which uses the cavity as a fundamental part of the filter, will be employed to further confirm the accuracy of the derived shielded Green's functions. Besides, full-wave simulations and measured data will also be employed for validation purposes, fully demonstrating the efficiency, accuracy and practical value of the proposed methods.

2.2 Standard Green's Function Formulations

The main purpose of this section is to present a brief overview of the standard mixed-potential Green's function formulation, for the cases of free-space, layered media of infinite lateral dimensions, and stratified boxed enclosures.

From basic electromagnetic theory [Balanis, 1989], [Collin, 1991], it is well-known that the electric and magnetic fields may be expressed by using the auxiliary vector and scalar potentials, as

$$\vec{E} = -j\omega\vec{A} - \nabla\phi_e - \frac{1}{\varepsilon}\left(\nabla \times \vec{F}\right), \tag{2.1}$$

$$\vec{H} = -j\omega\vec{F} - \nabla\phi_m + \frac{1}{\mu}\left(\nabla \times \vec{A}\right), \tag{2.2}$$

where $\vec{A}$, ϕ_e, $\vec{F}$, and ϕ_m are the magnetic vector, electric scalar, electric vector and magnetic scalar potentials, respectively. These last two equations constitute the basis of the mixed-potential integral equations, well-known in the scientific literature [Mosig, 1989], and formulated in detail, for the spatial-domain case, in Chapter 3. Note that the use of the auxiliary potentials in the IE formulation provides several advantages, such as weaker singularities and simpler expressions than the direct use of fields.

In the case of planar structures, on which we are interested, it is possible to obtain the Green's functions related to the potentials [Michalski and Mosig, 1997]. However, note that auxiliary potentials are artificial mathematical quantities, which, initially, can be defined with arbitrariness. Therefore, many possibilities are available to define these potentials [Felsen and Marcuvitz, 1973], [Michalski, 1987], [Michalski and Zheng, 1990]. Among them, we have employed in this work the so-called "Sommerfeld potentials", introduced in [Mosig, 1989].

The potential Green's functions are first presented for the free-space case [Felsen and Marcuvitz, 1973], in Section 2.2.1. There, the potentials generated by a charge/dipole source located in free space are analyzed for any observation point. Then, in Section 2.2.2, the mixed-potential Green's functions associated to sources embedded in planar multilayered media are briefly reviewed. First, the formulation is presented in the *spectral-domain* by using a double spatial Fourier transform [Felsen and Marcuvitz, 1973], [Mosig, 1989], [Michalski and Mosig, 1997]. The main advantage of this approach, using the transformed domain, is that it reduces the original Maxwell equations, related to the multilayered media, into a simple transmission line formalism. Then, the spectral-domain Green's functions are converted back into the *spatial-domain*, by using the Sommerfeld transformation [Sommerfeld, 1896], [Mosig, 1989], [Michalski, 1998], [Mosig and Álvarez Melcón, 2003].

Finally, an overview of the standard Green's functions formalism for multilayered boxed media is given in Section 2.2.3. First, the Green's functions are formulated in the spatial domain by using the image theory [Balanis, 1989]. As a result, an infinite number of spatial images appear with respect to each electrical wall [Itoh, 1989]. Then, the formalism is transformed into the spectral-domain by using the Poisson formula [Collin, 1991], providing the modal formulation of the multilayered boxed Green's functions [Marcuvitz, 1964]. Note that the main drawback of these standard formalisms is that the resulting infinite series present very low convergence rates, which highly limit the direct use of these techniques in practical implementations.

2.2.1 Free-Space Dyadic Green's Functions

The potential Green's functions in free-space are very well-known in the literature [Felsen and Marcuvitz, 1973], [Mosig, 1989], [Alvarez Melcon, 1998], [Stevanovic, 2005]. They are given by the following equations,

$$G_V(\vec{r},\vec{r}\,') = \frac{e^{-jk_0R}}{4\pi\varepsilon_0 R}, \tag{2.3}$$

$$G_W(\vec{r},\vec{r}\,') = \frac{e^{-jk_0R}}{4\pi\mu_0 R}, \tag{2.4}$$

$$\bar{\bar{G}}_A(\vec{r},\vec{r}\,') = \frac{\mu_0 e^{-jk_0R}}{4\pi R}\bar{\bar{I}}, \tag{2.5}$$

$$\bar{\bar{G}}_F(\vec{r},\vec{r}\,') = \frac{\varepsilon_0 e^{-jk_0R}}{4\pi R}\bar{\bar{I}}, \tag{2.6}$$

where G_V and G_W are the electric and magnetic scalar Green's functions and $\bar{\bar{G}}_A$ and $\bar{\bar{G}}_F$ are the magnetic and electric dyadic Green's functions. Besides, in these last equations, k_0 is the free-space wavenumber [Balanis, 1989], R is the distance between the observation ($\vec{r} = x\hat{e}_x + y\hat{e}_y + z\hat{e}_z$) and source ($\vec{r}\,' = x'\hat{e}_x + y'\hat{e}_y + z'\hat{e}_z$) points, defined as

$$R = \sqrt{(x-x')^2 + (y-y')^2 + (z-z')^2}, \tag{2.7}$$

and $\bar{\bar{I}}$ is the dyadic unitary matrix, given by

$$\bar{\bar{I}} = \hat{e}_x\hat{e}_x + \hat{e}_y\hat{e}_y + \hat{e}_z\hat{e}_z = \begin{pmatrix} 1 & 0 & 0 \\ 0 & 1 & 0 \\ 0 & 0 & 1 \end{pmatrix}. \tag{2.8}$$

2.2.2 Green's Functions in Layered Media of Infinite Transverse Dimensions

As previously commented, the mixed-potential Green's functions in layered media are key for the analysis of multilayered structures using an integral equation method [Mosig, 1989]. Here, we briefly summarize the standard procedure to compute these Green's functions. First, the spectral-domain Green's functions are obtained by using an equivalent transmission line network. Then, the Green's functions are converted from the spectral domain to the space domain using the well-known Sommerfeld transformation [Sommerfeld, 1896].

Spectral Domain

The theoretical foundations of the spectral domain approach were given in [Felsen and Marcuvitz, 1973], where it was demonstrated that the Maxwell equations related to the original multilayered problem may be reduced to a one dimensional differential equation using a double spatial Fourier transformation. Besides, this one dimensional differential equation corresponds to the simple well-known transmission line equation [Pozar, 2005].

Therefore, the study of multilayered Green's functions in the spectral domain is reduced to analyze an equivalent transmission line problem [Mosig, 1989], [Mosig, 1992], [Bhattacharyya, 1994], [Michalski and Mosig, 1997], [Alvarez Melcon, 1998]. Then, the Green's functions associated to the sources embedded in the multilayered media are expressed as a function of the voltages and currents in the equivalent network, highly simplifying the analysis procedure.

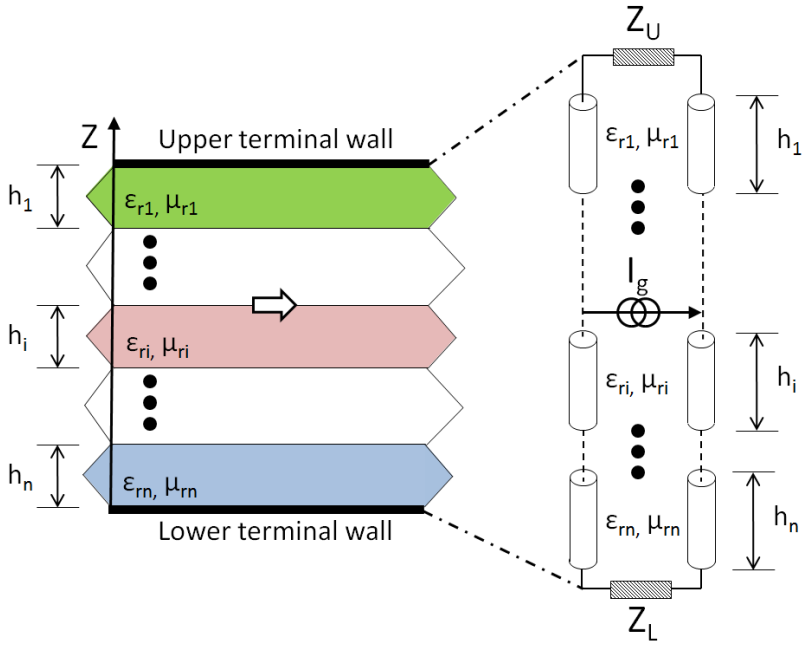

Figure 2.2 – Equivalent transmission line representation of an horizontal electric dipole located inside a multilayered medium. Modified from [Alvarez Melcon, 1998].

An example of this equivalent network representation of the structure is shown, for the case of an horizontal electric dipole, in Fig. 2.2. As can be observed in the figure, every layer of the structure is modeled by a transmission line section. Besides, the walls bounding the structure (which usually represent the free-space or a ground plane) are considered by equivalent lumped impedances. In general [Mosig, 1989], a transversal unitary electric (J_ρ) or magnetic (M_ρ) source is transformed into a parallel current generator [$I_g = 1/(2\pi)$] or into a series voltage generator [$V_g = 1/(2\pi)$] in the equivalent transmission line representation, respectively.

Then, the equivalent transmission line problem must be solved. This can easily be done by using simple transmission line methods, which are extremely efficient (see [Mosig, 1989], [Alvarez Melcon, 1998] or [Pozar, 2005]). Next, the spectral-domain Green's functions are retrieved using the following equations

$$\tilde{G}_V = \tilde{G}_V(k_\rho, z, z') = \frac{\omega}{k_\rho^2}\left[jV_J^{TM}(z) + \frac{V_J^{TE}(z)}{j}\right], \tag{2.9}$$

$$\tilde{G}_W = \tilde{G}_W(k_\rho, z, z') = \frac{\omega}{k_\rho^2}\left[jI_M^{TM}(z) + \frac{I_M^{TE}(z)}{j}\right], \tag{2.10}$$

$$\tilde{G}_A^{xx} = \tilde{G}_A^{xx}(k_\rho, z, z') = \frac{V_J^{TE}(z)}{j\omega}, \tag{2.11}$$

$$\tilde{G}_A^{yy} = \tilde{G}_A^{yy}(k_\rho, z, z') = \frac{V_J^{TE}(z)}{j\omega}, \tag{2.12}$$

$$\tilde{G}_F^{xx} = \tilde{G}_F^{xx}(k_\rho, z, z') = \frac{I_M^{TM}(z)}{j\omega}, \tag{2.13}$$

$$\tilde{G}_F^{yy} = \tilde{G}_F^{yy}(k_\rho, z, z') = \frac{I_M^{TM}(z)}{j\omega}, \tag{2.14}$$

where ρ is the radial source-observer distance, defined by

$$\rho = \sqrt{(x-x')^2 + (y-y')^2}, \tag{2.15}$$

and the spectral radial coordinate k_ρ is given by

$$k_\rho = \sqrt{k_x^2 + k_y^2}, \tag{2.16}$$

where k_x and k_y are the wavenumbers along the x and y directions, respectively.

Note that the voltages and currents (under TM and TE excitations) at the connection points between two transmission line sections provides the potentials at the interfaces of the layered medium.

Finally, it is important to point out that the use of strictly planar electric and magnetic sources, together with the Sommerfeld potentials, reduces to zero seven components ($\tilde{G}^{xy}, \tilde{G}^{yx}, \tilde{G}^{zz}, \tilde{G}^{zy}, \tilde{G}^{zx}, \tilde{G}^{xz}, \tilde{G}^{yz}$) of the the dyadic Green's function vector potentials.

Spatial Domain

In order to apply the integral equation (IE) [Mosig, 1989] for the analysis of multilayered structures, the Green's functions must be available in the spatial domain. Therefore, the spectral-domain Green's functions computed in the previous subsection must be transformed back into the spatial domain. For this purpose, the traditional Sommerfeld (or Fourier-Bessel) equation [Stratton, 1941], [Felsen and Marcuvitz, 1973], [Mosig, 1989] may be used

$$G(\rho, z, z') = S_n\left[\tilde{G}(k_\rho, z, z')\right] = \int_0^\infty J_n(k_\rho \rho) k_\rho^{n+1} \tilde{G}(k_\rho, z, z') dk_\rho, \tag{2.17}$$

where G is a spatial-domain Green's function, J_n is the Bessel function of order n, and $\tilde{G}$ is the spectral-domain Green's function.

In the specific case of mixed-potential Green's functions, the spatial transformation of the different potentials is given by [Alvarez Melcon, 1998]

$$G_V(\vec{r}, \vec{r}\,') = G_V(\rho, z, z') = S_0\left[\tilde{G}_V\right]\Big|_{\vec{r}'}^{\vec{r}} = S_0\left[\tilde{G}_V(k_\rho, z, z')\right], \tag{2.18}$$

$$G_W(\vec{r}, \vec{r}\,') = G_W(\rho, z, z') = S_0\left[\tilde{G}_W\right]\Big|_{\vec{r}'}^{\vec{r}} = S_0\left[\tilde{G}_W(k_\rho, z, z')\right], \tag{2.19}$$

$$G_A^{xx}(\vec{r}, \vec{r}\,') = G_A^{xx}(\rho, z, z') = S_0\left[\tilde{G}_A^{xx}\right]\Big|_{\vec{r}'}^{\vec{r}} = S_0\left[\tilde{G}_A^{xx}(k_\rho, z, z')\right], \tag{2.20}$$

$$G_A^{yy}(\vec{r}, \vec{r}\,') = G_A^{yy}(\rho, z, z') = S_0\left[\tilde{G}_A^{yy}\right]\Big|_{\vec{r}'}^{\vec{r}} = S_0\left[\tilde{G}_A^{yy}(k_\rho, z, z')\right], \tag{2.21}$$

$$G_F^{xx}(\vec{r}, \vec{r}\,') = G_F^{xx}(\rho, z, z') = S_0\left[\tilde{G}_F^{xx}\right]\Big|_{\vec{r}'}^{\vec{r}} = S_0\left[\tilde{G}_F^{xx}(k_\rho, z, z')\right], \tag{2.22}$$

$$G_F^{yy}(\vec{r}, \vec{r}\,') = G_F^{yy}(\rho, z, z') = S_0\left[\tilde{G}_F^{yy}\right]\Big|_{\vec{r}'}^{\vec{r}} = S_0\left[\tilde{G}_F^{yy}(k_\rho, z, z')\right]. \tag{2.23}$$

In the above notation, the superscript ($\vec{r}$) denotes the position vector pointing at the observation point, while the subscript ($\vec{r}\,'$) refers to the position vector pointing at the source point.

Besides, thanks to the symmetry of the problem in the transverse plane, the following identities hold

$$G_A(\vec{r},\vec{r}\,') = G_A^{xx}(\vec{r},\vec{r}\,') = G_A^{yy}(\vec{r},\vec{r}\,'), \tag{2.24}$$

$$G_F(\vec{r},\vec{r}\,') = G_F^{xx}(\vec{r},\vec{r}\,') = G_F^{yy}(\vec{r},\vec{r}\,'). \tag{2.25}$$

The numerical evaluation of these Sommerfeld integrals can be performed by different techniques, such as these presented in [Mosig and Gardiol, 1983], [Mosig and Sarkar, 1986], [Michalski, 1998], [Alvarez Melcon, 1998] or recently in [López-Frutos, 2011]. In this work, the Sommerfeld integrals are computed by the method developed in [Mosig and Álvarez Melcón, 2003].

2.2.3 Green's Functions in Shielded Planar Multilayered Structures

The use of shielded enclosures provides physical support to the microwave devices, immunity against interferences and avoids unwanted radiation. Therefore, the derivation of boxed multilayered Green's functions has attracted much attention in the past, and several contributions on this subject can be found in the literature [Marcuvitz, 1964], [Felsen and Marcuvitz, 1973], [Mosig, 1989], [Balanis, 1989], [Eleftheriades et al., 1996], [Álvarez Melcón and Mosig, 2000]. Here, we briefly review the standard computation of boxed Green's functions in both, the spatial and the spectral domain.

Spatial Domain

The first step for computing the multilayered shielded Green's functions using the spatial domain approach in to obtain the spatial values of any lateral-unbounded stratified Green's function. This can easily be done by using the theory presented in the previous section. Initially, the spectral Green's functions are computed taking into account the top and bottom covers of the cavity. The covers are easily modeled by using short-circuits in the equivalent transmission line network representation (see Fig. 2.3). Then, the Sommerfeld integral is applied to convert back these Green's functions into the spatial domain.

Let us consider a single source placed within the cavity. Using image theory [Balanis, 1989], three images initially appears with respect to the lateral walls (see Fig. 2.4, images close to the cavity). These three images, combined with the original source, represent four basic images (denoted as "BIS": Basic Images Set), which are located at the coordinates $(+x',+y')$,$(-x',+y')$,$(+x',-y')$,$(-x',-y')$. Therefore, we can define the Green's functions provided by this BIS as

$$G_{BIS}(x,y|x',y') = G(x,y|x',y') + s_x G(x,y|-x',y') + s_y G(x,y|x',-y') + s_x s_y G(x,y|-x',-y'), \tag{2.26}$$

where G is the spatial-domain Green's function which takes into account the layered media and the top and bottom covers of the cavity, s_x and s_y are signs functions related to the actual type of the Green's function considered (see Table 2.1), and the dependence with z and z' has explicitly been suppressed for the sake of clarity.

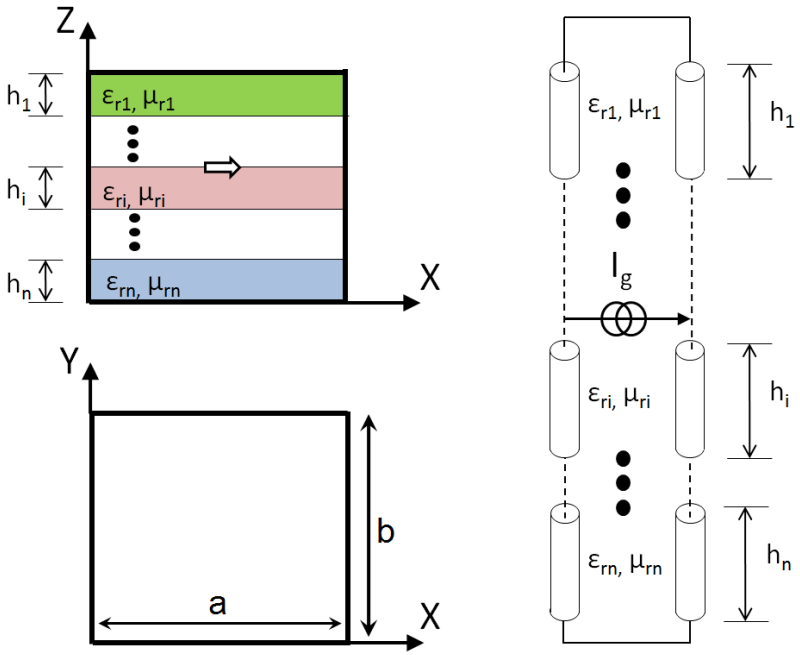

Figure 2.3 – Elementary dipole radiating in a multilayered shielded rectangular enclosure an its transverse equivalent network representation. Modified from [Alvarez Melcon, 1998].

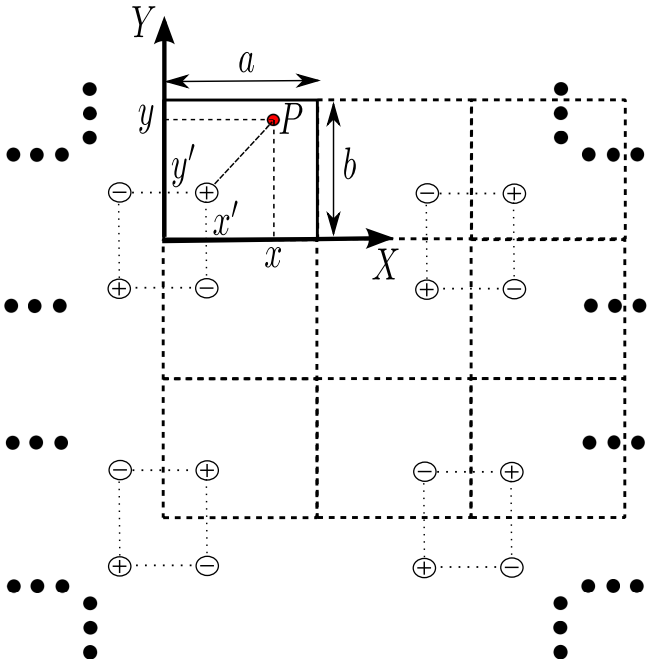

Figure 2.4 – Spatial images for a single unit point charge needed to satisfy the boundary conditions at lateral metallic walls. Reproduced from [Alvarez Melcon, 1998].

The total Green's functions inside the cavity can be just expressed, thanks to the iterative application of image theory over the lateral walls, as an infinite double sum of basic image sets periodically shifted along the x and y directions (see Fig. 2.4). The total boxed Green's function may then been

	s_x	s_y
G_A^{xx}	+1	-1
G_A^{yy}	-1	+1
G_V	-1	-1
G_F^{xx}	-1	+1
G_F^{yy}	+1	-1
G_W	+1	+1

Table 2.1 – Values of the signs associated to all the components of the mixed potential Green's functions

expressed as

$$G_{Box}(x,y|x',y') = \sum_{m=-\infty}^{\infty}\sum_{n=-\infty}^{\infty} G_{BIS}(x,y|x'+2ma,y'+2nb). \tag{2.27}$$

The main advantage of this formula is that the resulting images series converges fast at very low frequencies, or when no dielectric layers are included in the structure. However, as frequency increases, surfaces waves are excited, and convergence is greatly degraded [Alvarez Melcon, 1998]. Therefore, the direct use of this formula within an IE framework requires huge computational resources. In order to increase the convergence rate of this formula, several acceleration techniques are presented and briefly described in Chapter 3.3.

Spectral Domain

A very interesting alternative approach to compute the stratified shielded Green's functions is to apply to Eq. (2.27) the Poisson's summation formula [Collin, 1991], which is given by

$$\sum_{n=-\infty}^{n=+\infty} G(\alpha n) = \frac{\sqrt{2\pi}}{\alpha}\sum_{n=-\infty}^{n=+\infty}\tilde{G}\left(\frac{2n\pi}{\alpha}n\right). \tag{2.28}$$

The use of this formula allows to express Eq. (2.27) as

$$G_{Box}(x,y|x',y') = \sum_{m=0}^{\infty}\sum_{n=0}^{\infty}\tilde{G}(k_{x_m},k_{y_n})f(k_{x_m},x,x')h(k_{y_n},y,y'), \tag{2.29}$$

where $\tilde{G}$ is the corresponding spectral-domain Green's function, which takes into account for the top and bottom cavity covers (see Fig. 2.3). Besides, for a rectangular cavity, the transverse wavenumbers k_{x_m} and k_{y_n} are defined as

$$k_{x_m} = \frac{mx}{a}, \qquad k_{y_n} = \frac{ny}{b}, \tag{2.30}$$

where a and b are the transverse physical dimensions of the cavity (see Fig. 2.3). Finally, the factors f and h are combination of sinusoidal functions, which depend on the actual type of Green's function computed (see Table 2.2).

	$f(k_{x_m}, x, x')$	$h(k_{y_n}, y, y')$
G_A^{xx}	$\cos(k_{x_m}x)\cos(k_{x_m}x')$	$\sin(k_{y_n}y)\sin(k_{y_n}y')$
G_A^{yy}	$\sin(k_{x_m}x)\sin(k_{x_m}x')$	$\cos(k_{y_n}y)\cos(k_{y_n}y')$
G_V	$\sin(k_{x_m}x)\sin(k_{x_m}x')$	$\sin(k_{y_n}y)\sin(k_{y_n}y')$
G_F^{xx}	$\sin(k_{x_m}x)\sin(k_{x_m}x')$	$\cos(k_{y_n}y)\cos(k_{y_n}y')$
G_F^{yy}	$\cos(k_{x_m}x)\cos(k_{x_m}x')$	$\sin(k_{y_n}y)\sin(k_{y_n}y')$
G_W	$\cos(k_{x_m}x)\cos(k_{x_m}x')$	$\cos(k_{y_n}y)\cos(k_{y_n}y')$

Table 2.2 – Form of the f and h functions employed to define the boxed mixed potential Green's functions components.

This is the modal expansion approach of multilayered boxed Green's functions, because the functions f and h are related to the eigenmodes of a rectangular waveguide. In fact, this formulation can also be obtained by using standard infinite waveguide theory [Balanis, 1989], [Pozar, 2005], combined with the imposition of the adequate boundary conditions at the position of the cavity covers [Marcuvitz, 1964], [Alvarez Melcon, 1998]. The main drawback of this formulation is the very slow convergence properties of the associated infinite series, which require the use of many modes to achieve stable results.

2.3 A Spatial Images Technique for the Computation of Green's Functions in Multilayered Convex-Shaped Enclosures

Multilayered shielded Green's functions have usually been computed for rectangular [Railton and Meade, 1992], [Keren and Atsuki, 1995], [Park and Nam, 1997] (see Section 2.2.3) or circular [Zavosh and Aberle, 1995] enclosures. In the first case, the Green's functions can be expressed in terms of spectral domain slowly convergent series of vector modal functions [Dunleavy and Katehi, 1988a]. Other possibilities include spatial domain formulations, for example expressing the Green's functions as slowly convergent series of spatial images [Itoh, 1989]. For circular enclosures, the Green's functions are usually based on spectral-domain techniques, by using the corresponding vector modal series of Bessel functions [Leung and Chow, 1996], [Zavosh and Aberle, 1994]. However, Green's functions inside arbitrarily shaped cavities have never been obtained in the past, and one has to resort to pure numerical techniques, such as finite elements or finite differences, to treat this kind of problems.

Recently, a specially set of truncated images was developed in the spatial domain for the computation of mixed-potential Green's functions associated to parallel-plate waveguides and rectangular multilayered cavities (see [Alvarez-Melcon and Mosig, 1999]). The main idea behind this method is simple and intuitive, and it is based on the two main features that any Green's function must preserve in order to achieve accurate results, namely [Alvarez-Melcon and Mosig, 1999]

1. The singular behavior when $\rho \to 0$.

2. The boundary conditions at all lateral cavity walls.

In the spatial domain, the regular spatial boxed Green's functions [Itoh, 1989], [Alvarez Melcon, 1998] naturally preserve the singular behavior of the source, because they have been constructed using standard Green's functions. What remains is the accurate imposition of the boundary conditions at the metallic walls, which can approximately be done by truncating the infinite number of spatial images and then adjusting the strength of the last images. In this way, the boundary conditions for the fields are satisfied at the cavity walls.

This spatial-domain method was then applied to the numerical computation of shielded Green's functions related to multilayered cylindrical enclosures. In this case, spatial images are located around the circular cavity to enforce the boundary conditions for the potentials. The numerical evaluation of the Green's functions under electric current excitation inside an empty circular cylindrical cavity was described in [Vera Castejón et al., 2004], whereas in [Quesada Pereira et al., 2005a] Green's functions under magnetic currents were studied. Besides, the technique may use the potentials of a stratified medium formulated in the spatial domain with the Sommerfeld integral [Michalski and Mosig, 1997], which allows the analysis of practical multilayered printed circuits. Note that this technique can be seen as a particular case of the "Method of Auxiliary Sources" (MAS) (see [Kaklamani and Anastassiu, 2002] and the references given therein), applied to the computation of Green's functions.

In this context, an important extension of the spatial image method presented in [Alvarez-Melcon and Mosig, 1999] and in [Quesada Pereira et al., 2005a] is proposed here. Specifically, Section 2.3.1 presents the mathematical details of the novel formulation, which allows to compute both the electric scalar potential and the magnetic vector potential dyadic Green's functions, and their associated spatial derivatives, generated by electric currents inside multilayered arbitrarily-shaped convex cavities. For this purpose, the approach is formulated using a cartesian coordinate system which is independent of the cavity shape. The idea of the method is to use charge and dipole images, located outside the cavity, to enforce the proper boundary conditions for the potentials at discrete points along the whole cavity perimeter. This procedure leads to an accurate approximation of the real cavity modeling.

Then, Section 2.3.2 presents a parametric study related to the number of spatial images and their adequate location, both in the cross-section plane and along the height, and the influence of these parameters in the method accuracy. For this purpose, a simple technique is presented to rigourously compute the error committed in the Green's functions computation. From the study, some strategies are proposed in order to increase the accuracy of the method. First, a procedure to automatically place the spatial images outside a given cavity is given. This distribution depends on the shape of the cavity and on the source position, providing low error levels in most situations. It is observed that the accuracy of the computed Green's functions decreases as long as the source is located close to a cavity wall. In fact, the error committed by the technique achieves unacceptable levels when the point source is close to an inner corner of a concave geometry. This problem, which also appears in the MAS technique [Kaklamani and Anastassiu, 2002], limits the practical use of this method to the analysis of arbitrarily-shaped convex cavities. Second, a multi-ring images scheme (see [Quesada Pereira et al., 2005b]) is employed to analyze electrically long structures by sampling the entire cavity at different discrete heights. We show that this technique maintains good accuracy in the imposition of the boundary conditions along the entire cavity height.

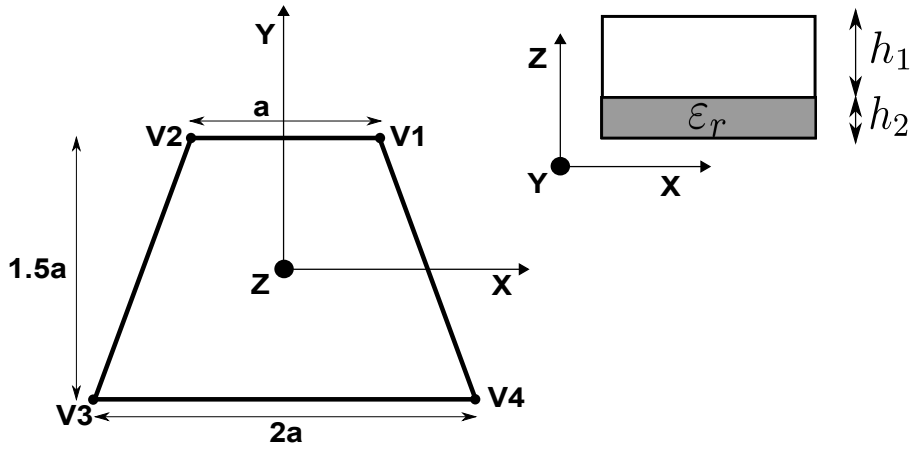

Figure 2.5 – Trapezium-shaped multilayered cavity. $a = \lambda$, $h_1 = 0.02\lambda$, $h_2 = 0.01\lambda$, and $\varepsilon_r = 5.0$,

For the sake of validation, Section 2.3.3 successfully applies the novel image technique to the calculation of the resonant frequencies of arbitrarily convex-shaped multilayered cavities. Then, several multilayered structures (with trapezium, rectangular and triangular-shaped contours) are analyzed. It is shown that, in all cases, the computed resonant frequencies are in excellent agreement with those obtained by the commercial software HFSS©. Furthermore, a comparison between the distribution of the potentials obtained by the spatial images technique and the electric field components (computed by HFSS©) is presented. It is demonstrated that they have the same distribution inside the cavity, because they satisfy the same boundary conditions. Again, excellent agreement between these two completely different methods is found.

It is important to point out that the developed technique will be applied in Chapter 3 for the analysis of multilayered printed circuits located in arbitrarily-shaped cavities. Moreover, that chapter also presents several acceleration techniques which greatly increase the efficiency of the proposed method. Finally, simulations and measured data of real circuits will also be used for validation purposes, further confirming the accuracy and efficiency of the proposed technique.

2.3.1 Theoretical Overview

This subsection presents the formulation required to numerically compute the mixed-potential Green's functions and their associate spatial derivatives inside convex arbitrarily-shaped multilayered cavities under electric current excitation. A trapezium-shaped cavity, shown in Fig. 2.5, is employed to introduce the formulation without lack of generality. Note that the situation is analogous if any other convex geometry is chosen.

The idea of the spatial images technique is to impose the boundary conditions for the potentials at $R \cdot N$ discrete points along the cavity walls, using $R \cdot N$ auxiliary images or sources (where R is the number of rings along the height, and N is the number of spatial images per ring) placed outside the structure (see Fig. 2.6). Then, the strength and orientation of the images are computed, so the proper boundary conditions are satisfied at discrete points of the metallic wall.

In the analysis of completely closed enclosures, the bottom and top covers of the cavity must

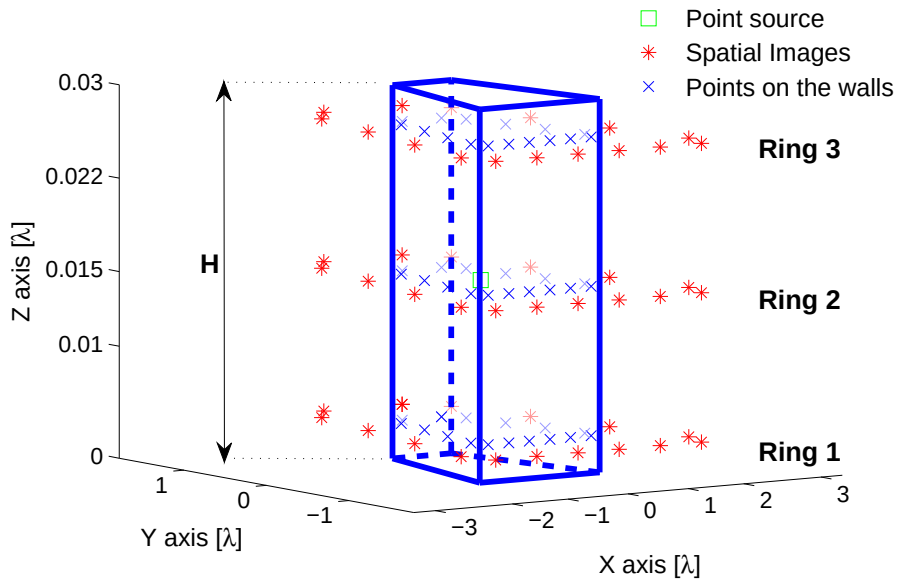

Figure 2.6 – 3D trapezium-shaped cavity view. Rings of auxiliary sources, placed at different heights, are employed to enforce the boundary conditions at the cavity walls.

be included in the formulation. The most efficient way to accomplish this task is to formulate the Green's functions of multilayered media in the spatial domain, using the Sommerfeld transformation ([Michalski, 1998], see Section 2.2.2). In this way, also the presence of dielectric layers inside the cavity can be automatically accounted for. Besides, note that the method imposes the boundary conditions for the potentials considering perfect electric cavity walls. Therefore, the losses due to the finite conductivity of the cavity walls cannot be easily modeled with this formulation. However, the losses in the dielectric substrates are easily included using the spatial-domain multilayered Green's functions formulated as Sommerfeld integrals [Michalski, 1998].

An important question that arises when modeling completely closed enclosures with the spatial images technique is how to treat cavities with electrically large height. In this case, the imposition of the boundary conditions in one cross section of the cavity might not suffice to represent the correct behavior of the fields along the entire height. In order to solve this problem, the use of R rings, each one composed of N auxiliary images, is proposed to analyze electrically long structures (see Fig. 2.6), by sampling the entire cavity at different discrete heights.

In the following subsections, the spatial images formulation is introduced in detail for the computation of the electric scalar and the magnetic vector potentials and their spatial derivatives.

Electric Scalar Potential

The boundary condition that the electric scalar potential must fulfill along a cavity contour C is [Balanis, 1989]

$$\phi_e\big|_C = 0 \rightarrow G_{V_{Cav}}(\vec{r}, \vec{r}\,'_{0,0})\big|_C = 0, \tag{2.31}$$

where $G_{V_{Cav}}$ is the electric scalar potential Green's function inside the multilayered cavity and $\vec{r}\,'_{0,0}$ is the position vector of the point source.

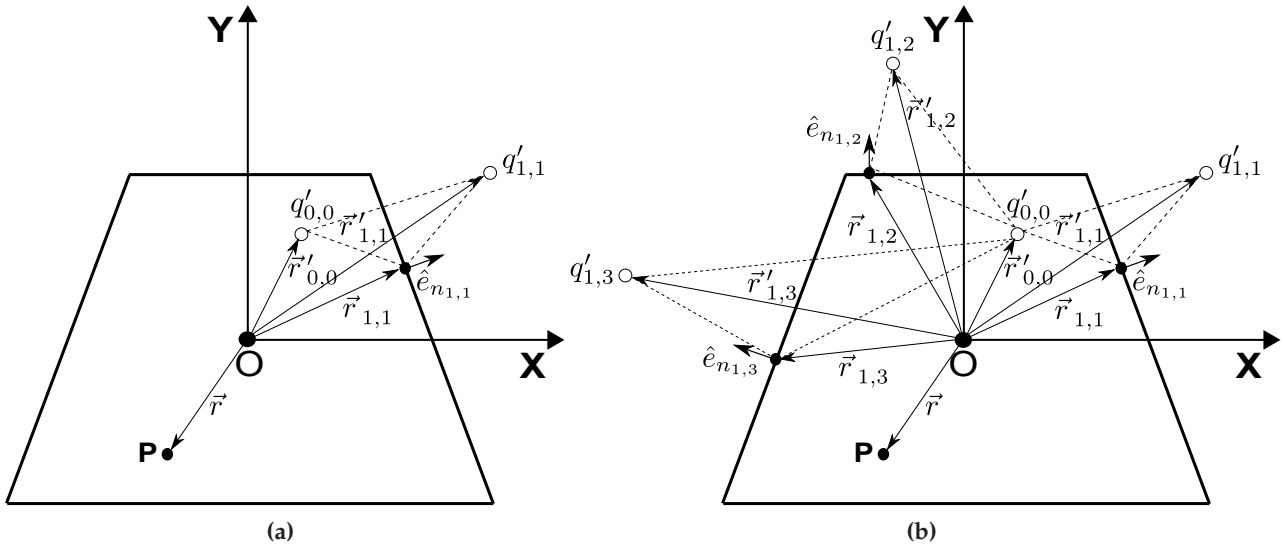

Figure 2.7 – Use of one (a) or three (b) auxiliary charges to enforce the boundary conditions for the electric scalar potential at the cavity contour. O is the origin of the cartesian coordinate system, $q'_{0,0}$ is the original charge source placed inside the cavity, and P is a generic observation point.

Let us a consider that a single source charge is located in the cavity, and that the boundary conditions of the electric scalar potential is enforced at a single discrete point on the cavity (see Fig. 2.7a) by using a unique auxiliary charge image. The complex value of this auxiliary charge can be computing by solving the following equation

$$q'_{1,1} S_0\left[\tilde{G}_V\right]\Big|_{\vec{r}\,'_{1,1}}^{\vec{r}_{1,1}} = -S_0\left[\tilde{G}_V\right]\Big|_{\vec{r}\,'_{0,0}}^{\vec{r}_{1,1}} \quad , \tag{2.32}$$

which, yields

$$q'_{1,1} = \frac{-S_0\left[\tilde{G}_V\right]\Big|_{\vec{r}\,'_{0,0}}^{\vec{r}_{1,1}}}{S_0\left[\tilde{G}_V\right]\Big|_{\vec{r}\,'_{1,1}}^{\vec{r}_{1,1}}}. \tag{2.33}$$

As can be seen in Fig. 2.7a, the combination of the original charge source $q'_{0,0}$ with the auxiliary source $q'_{1,1}$ imposes a zero electric scalar potential at the chosen discrete point of the cavity wall. It is interesting to observe in the previous equation that, in order to set up the numerical procedure, we need to obtain the potentials in the spatial domain. For this purpose, we have employed the zero order Sommerfeld transformation (S_0) of the corresponding spectral domain Green's function ($\tilde{G}_V$), which allows to automatically take into account for the multilayered nature of the structure.

The situation can be extended, for instance, using three auxiliary charges to impose the boundary conditions at three discrete points of the cavity contour, as shown in Fig. 2.7b. In this case, we have

$$\begin{aligned}
q'_{1,1} S_0\left[\tilde{G}_V\right]\Big|_{\vec{r}\,'_{1,1}}^{\vec{r}_{1,1}} + q'_{1,2} S_0\left[\tilde{G}_V\right]\Big|_{\vec{r}\,'_{1,2}}^{\vec{r}_{1,1}} + q'_{1,3} S_0\left[\tilde{G}_V\right]\Big|_{\vec{r}\,'_{1,3}}^{\vec{r}_{1,1}} &= -S_0\left[\tilde{G}_V\right]\Big|_{\vec{r}\,'_{0,0}}^{\vec{r}_{1,1}} \\
q'_{1,1} S_0\left[\tilde{G}_V\right]\Big|_{\vec{r}\,'_{1,1}}^{\vec{r}_{1,2}} + q'_{1,2} S_0\left[\tilde{G}_V\right]\Big|_{\vec{r}\,'_{1,2}}^{\vec{r}_{1,2}} + q'_{1,3} S_0\left[\tilde{G}_V\right]\Big|_{\vec{r}\,'_{1,3}}^{\vec{r}_{1,2}} &= -S_0\left[\tilde{G}_V\right]\Big|_{\vec{r}\,'_{0,0}}^{\vec{r}_{1,2}} \\
q'_{1,1} S_0\left[\tilde{G}_V\right]\Big|_{\vec{r}\,'_{1,1}}^{\vec{r}_{1,3}} + q'_{1,2} S_0\left[\tilde{G}_V\right]\Big|_{\vec{r}\,'_{1,2}}^{\vec{r}_{1,3}} + q'_{1,3} S_0\left[\tilde{G}_V\right]\Big|_{\vec{r}\,'_{1,3}}^{\vec{r}_{1,3}} &= -S_0\left[\tilde{G}_V\right]\Big|_{\vec{r}\,'_{0,0}}^{\vec{r}_{1,3}} \quad .
\end{aligned} \tag{2.34}$$

The values of the complex images charges are obtained by solving the system of linear equations. Again, and as shown in Fig. 2.7b, the combination of the original charge source $q'_{0,0}$ with the auxiliary sources $q'_{1,1}, q'_{1,2}$ and $q'_{1,3}$ imposes a zero electric scalar potential at the chosen discrete points of the cavity wall.

Then, the procedure can be further extended, considering R rings of N images (see Fig. 2.6), which are simultaneously employed to impose the boundary conditions at the cavity walls. In this way, the geometrical details of the cavity contour are taken into account. The following system of linear equations is obtained

$$\sum_{m=1}^{R}\sum_{k=1}^{N} q'_{m,k} S_0\left[\tilde{G}_V\right]\Big|_{\vec{r}\,'_{m,k}}^{\vec{r}_{l,i}} = -S_0\left[\tilde{G}_V\right]\Big|_{\vec{r}\,'_{0,0}}^{\vec{r}_{l,i}} \quad , \qquad (2.35)$$
$$l = 1, 2, \ldots R, \qquad i = 1, 2, \ldots N$$

where all position vectors are shown in Fig. 2.7. With the above notation, we refer to the k^{th} image inside the m^{th} ring, using the position vector $\vec{r}\,'_{m,k}$. In a similar way, we refer to the i^{th} point along the cavity wall inside the l^{th} ring with the position vector $\vec{r}_{l,i}$.

Besides, note that Eq. (2.35) is independent on the geometry of the waveguide, because a rectangular coordinates system is used, and a fixed location of the images and the tangent points is not assumed. The solution of this system of linear equations provides the complex values of the $R \cdot N$ charge images ($q'_{m,k}$), required to impose the boundary conditions of the potential at $R \cdot N$ discrete points on the wall. The final electric scalar potential Green's function inside the cavity is computed by reusing the already computed charge amplitudes, as

$$G_{V_{Cav}}(\vec{r}, \vec{r}\,'_{0,0}) = S_0\left[\tilde{G}_V\right]\Big|_{\vec{r}\,'_{0,0}}^{\vec{r}} + \sum_{m=1}^{R}\sum_{k=1}^{N} q'_{m,k}\, S_0\left[\tilde{G}_V\right]\Big|_{\vec{r}\,'_{m,k}}^{\vec{r}}. \qquad (2.36)$$

It is interesting to observe that the calculation of the cavity Green's functions just requires the evaluation of a fixed number of spatial Green's functions due to isolated images placed inside an infinite multilayered medium.

The proposed formulation also allows the easy computation of the Green's functions spatial derivatives of order n, related to convex arbitrarily-shaped cavities, without requiring an additional computational effort. For this purpose, the derivative of Eq. (2.36) is taken over the the transverse source-observer spatial distance [ρ, see Eq. (2.15)], leading to

$$\frac{\partial^n G_{V_{Cav}}(\vec{r}, \vec{r}\,'_{0,0})}{\partial \rho^n} = S_n\left[\tilde{G}_V\right]\Big|_{\vec{r}\,'_{0,0}}^{\vec{r}} + \sum_{m=1}^{R}\sum_{k=1}^{N} q'_{m,k}\, S_n\left[\tilde{G}_V\right]\Big|_{\vec{r}\,'_{m,k}}^{\vec{r}}. \qquad (2.37)$$

The main advantage of this approach is that the auxiliary charges and their associate complex values are independent of ρ, and they are not affected by the derivative. This means that there is no need to reformulate the problem for this specific case. On the other hand, the only term in the expressions which is affected by the ρ derivative is the Sommerfeld transformation. Specifically, it is known that the derivative of the N-order Sommerfeld transformation is related to the $(N+1)$-order Sommerfeld transformation [Michalski, 1998], as follows

$$\frac{\partial S_N[\tilde{G}]|_\rho}{\partial \rho} = S_{N+1}[\tilde{G}]|_\rho. \qquad (2.38)$$

Finally, note that the spatial derivatives related to the x or y directions can easily be obtained from Eq. (2.37), simply by using the chain's rule of the derivative.

Magnetic Vector Potential

In the evaluation of the magnetic vector potential dyadic Green's functions a similar procedure as in the case of the electric scalar potential is followed. However, the vectorial nature of this potential must carefully be taken into account.

The formulation employs the electric field generated by electric sources, expressed using the mixed potentials formulation as

$$\vec{E} = -j\omega\vec{A} - \nabla\phi_e. \tag{2.39}$$

Using the Lorentz gauge [Balanis, 1989],

$$\nabla \cdot \vec{A} = -j\omega\mu\varepsilon\phi_e, \tag{2.40}$$

the electric field of Eq. (2.39) can be rewritten as

$$\vec{E} = -j\omega\vec{A} + \frac{\nabla(\nabla \cdot \vec{A})}{j\omega\mu\varepsilon}. \tag{2.41}$$

The boundary condition that must be fulfilled is the zero tangent component of the electric field on the cavity walls, which may be expressed as

$$\hat{e}_n \times \vec{E}\big|_C = 0 \rightarrow \vec{E} \cdot \hat{e}_t\big|_C = 0, \tag{2.42}$$

where C represents the cavity contour, and $\hat{e}_n$ and $\hat{e}_t$ are the unit vectors normal and tangent to the cavity walls (see Fig. 2.8), respectively. These vectors are defined as

$$\hat{e}_n = \cos(\varphi)\hat{e}_x + \sin(\varphi)\hat{e}_y, \tag{2.43}$$

$$\hat{e}_t = -\sin(\varphi)\hat{e}_x + \cos(\varphi)\hat{e}_y, \tag{2.44}$$

where the angle φ spans from the x-axis to the perpendicular direction of each cavity wall, as shown in Fig. 2.8.

The idea is to impose the boundary conditions on the potentials, not on the fields. To translate the boundary conditions to the potentials, the mixed potential form of the electric field shown in equation Eq. (2.41) is used. Then, the condition of Eq. (2.42) for the electric field can be split into two different conditions for the potentials, as

$$\hat{e}_n \times \vec{A}\big|_C = 0 \rightarrow \vec{A} \cdot \hat{e}_t\big|_C = 0, \tag{2.45}$$

$$\hat{e}_n \times \nabla(\nabla \cdot \vec{A})\big|_C = 0 \rightarrow \nabla(\nabla \cdot \vec{A}) \cdot \hat{e}_t\big|_C = 0. \tag{2.46}$$

The conditions of the above equations must then be imposed for the $\vec{A}$ potential along the cavity walls, which does not seem to be an easy task. Even though it is possible to impose the condition

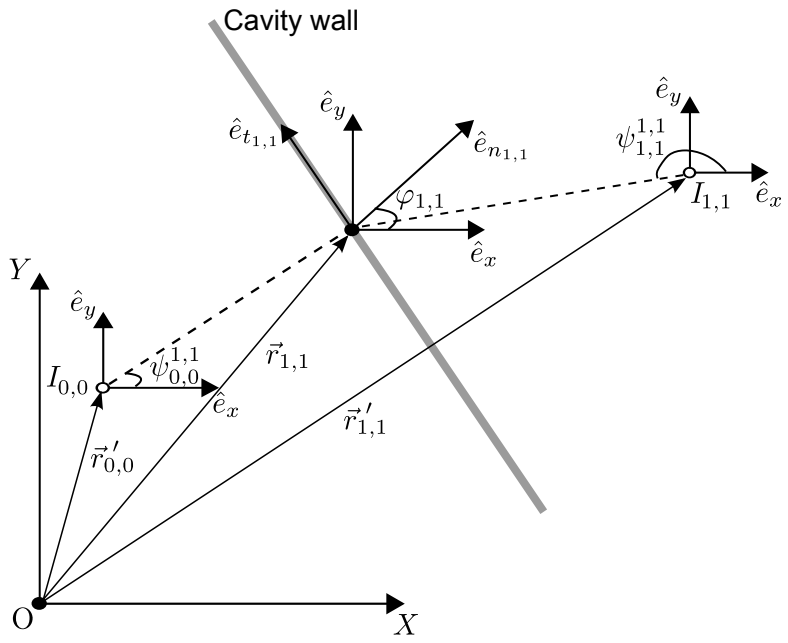

Figure 2.8 – Vectors and angles employed in the imposition of the magnetic vector potential boundary conditions at the point (1,1) of the cavity wall. In this situation, O is the origin of the cartesian coordinate system, $I_{0,0}$ is the source dipole located inside the cavity, $I_{1,1}$ is an auxiliary image dipole, $\hat{e}_{n_{1,1}}$ and $\hat{e}_{t_{1,1}}$ are the normal and tangential unit vectors with respect to the point $(1,1)$ of the cavity wall, $\varphi_{1,1}$ is the angle between the axis x and the vector $\hat{e}_{n_{1,1}}$, and $\psi_{1,1}^{1,1}$ and $\psi_{0,0}^{1,1}$ are the angles which spans from the sources $I_{1,1}$ and $I_{0,0}$ and the point (1,1) on the cavity wall.

of Eq. (2.45) at the cavity contour (using auxiliary dipoles, as in the case of the electric scalar potential) the fulfillment of Eq. (2.46) is not straightforward. For this reason, Eq. (2.46) is rigorously transformed into an equivalent simpler condition, which is easier to be fulfilled by the $\vec{A}$ potential. For this transformation, it is convenient to operate with the normal and tangential components of the magnetic vector potential, as

$$\vec{A} = A_t\hat{e}_t + A_n\hat{e}_n, \tag{2.47}$$

where the scalar values of A_t and A_n are obtained by

$$\begin{aligned} A_n &= \vec{A}\cdot\hat{e}_n = (A_x\hat{e}_x + A_y\hat{e}_y)\cdot\hat{e}_n = +A_x\cos(\varphi) + A_y\sin(\varphi), \\ A_t &= \vec{A}\cdot\hat{e}_t = (A_x\hat{e}_x + A_y\hat{e}_y)\cdot\hat{e}_t = -A_x\sin(\varphi) + A_y\cos(\varphi). \end{aligned} \tag{2.48}$$

Then, the gradient of the magnetic vector potential divergence is obtained as

$$\nabla(\nabla\cdot\vec{A}) = \left(\frac{\partial^2 A_t}{\partial t^2} + \frac{\partial^2 A_n}{\partial n\partial t}\right)\hat{e}_t + \left(\frac{\partial^2 A_t}{\partial n\partial t} + \frac{\partial^2 A_n}{\partial n^2}\right)\hat{e}_n, \tag{2.49}$$

which allows to rewrite the boundary condition of Eq. (2.46) as

$$\nabla(\nabla\cdot\vec{A})\cdot\hat{e}_t\big|_C = \left(\frac{\partial^2 A_t}{\partial t^2} + \frac{\partial^2 A_n}{\partial n\partial t}\right)\Bigg|_C = \frac{\partial^2 A_n}{\partial n\partial t}\big|_C = \frac{\partial}{\partial t}\left(\frac{\partial A_n}{\partial n}\right)\Bigg|_C = 0, \tag{2.50}$$

where the fact that $A_t = 0$ [along the cavity contour, due to Eq. (2.45)] has been employed to simplify the equation.

Besides, the use of the identity

$$\frac{\partial A_n}{\partial n} = (\nabla A_n) \cdot \hat{e}_n, \tag{2.51}$$

helps to simplify Eq. (2.50) to

$$(\nabla A_n) \cdot \hat{e}_n \big|_C = 0. \tag{2.52}$$

In addition, we can further develop this expression as

$$(\nabla A_n) \cdot \hat{e}_n = \left(\frac{\partial A_n}{\partial x} \hat{e}_x + \frac{\partial A_n}{\partial y} \hat{e}_y \right) \cdot \hat{e}_n = \frac{\partial A_n}{\partial x} \hat{e}_x \cdot \hat{e}_n + \frac{\partial A_n}{\partial y} \hat{e}_y \cdot \hat{e}_n = \frac{\partial A_n}{\partial x} \cos(\varphi) + \frac{\partial A_n}{\partial y} \sin(\varphi), \tag{2.53}$$

which, taking into account the normal and tangential components of the magnetic vector potential [see Eq. (2.48)], may be expanded as

$$\begin{aligned}(\nabla A_n) \cdot \hat{e}_n = &+ \frac{\partial A_x}{\partial x} \cos^2(\varphi) + \frac{\partial A_y}{\partial x} \cos(\varphi) \sin(\varphi) + \frac{\partial A_x}{\partial y} \cos(\varphi) \sin(\varphi) + \frac{\partial A_y}{\partial y} \sin^2(\varphi) = \\ &\cos(\varphi) \left[\frac{\partial A_x}{\partial x} \cos(\varphi) + \frac{\partial A_x}{\partial y} \sin(\varphi) \right] + \sin(\varphi) \left[\frac{\partial A_y}{\partial x} \cos(\varphi) + \frac{\partial A_y}{\partial y} \sin(\varphi) \right].\end{aligned} \tag{2.54}$$

At this point, we must keep in mind that, in the proposed method, the total magnetic vector potential is produced by the combination of the potentials generated by isolate dipoles placed on an unbounded stratified media. Therefore, the x and y components of the magnetic vector potential are identical [see Eq. (2.25)], which leads to A_x=A_y. This allows us to introduce a new variable, B', which is defined in the spatial domain as

$$B' = \frac{\partial A_x}{\partial x} \cos(\varphi) + \frac{\partial A_x}{\partial y} \sin(\varphi) = \frac{\partial A_y}{\partial x} \cos(\varphi) + \frac{\partial A_y}{\partial y} \sin(\varphi). \tag{2.55}$$

Besides, in the particular case of the potentials generated by an unique isolate dipole located in an infinite multilayered media, this variable (denoted in this case as B) may be expressed as

$$B = \frac{\partial S_0 \left[\tilde{G}_A \right]}{\partial x} \cos(\varphi) + \frac{\partial S_0 \left[\tilde{G}_A \right]}{\partial y} \sin(\varphi), \tag{2.56}$$

which may also be rewritten in the transformed spectral domain as

$$\tilde{B} = \cos(\phi) j k_x \tilde{G}_A + \sin(\phi) j k_y \tilde{G}_A. \tag{2.57}$$

Then, the use of the Green's functions correspondence between the spectral and spatial domains shown in Table 2.3 (see [Mosig, 1989]), permits to obtain Eq. (2.57) back in the spatial-domain as

$$B = -\cos(\phi) \cos(\psi) S_1 \left[\tilde{G}_A \right] - \sin(\phi) \sin(\psi) S_1 \left[\tilde{G}_A \right] = -S_1 \left[\tilde{G}_A \right] \cos(\psi - \phi), \tag{2.58}$$

where ψ is the angle between the source and observation points (see Fig. 2.8), and S_1 is the first order Sommerfeld transform [Michalski, 1998].

Spectral domain	Spatial domain
$\tilde{G}$	$S_0\left[\tilde{G}\right]$
$jk_x\tilde{G}$	$-\cos(\psi)S_1\left[\tilde{G}\right]$
$jk_x\tilde{G}$	$-\sin(\psi)S_1\left[\tilde{G}\right]$
$jk_xjk_x\tilde{G}$	$\frac{\cos(2\psi)}{\rho}S_1\left[\tilde{G}\right]-\cos^2(\psi)S_0[k_\rho^2\tilde{G}]$
$jk_xjk_y\tilde{G}$	$\frac{\sin(2\psi)}{\rho}S_1\left[\tilde{G}\right]-\frac{1}{2}\sin(2\psi)S_0[k_\rho^2\tilde{G}]$
$jk_yjk_y\tilde{G}$	$-\frac{\cos(2\psi)}{\rho}S_1\left[\tilde{G}\right]-\sin^2(\psi)S_0[k_\rho^2\tilde{G}]$

Table 2.3 – Correspondence between spectral and spatial domain Green's functions

This procedure has allowed to simplify Eq. (2.46) to

$$(\nabla A_n)\cdot\hat{e}_n|_C=\left[\cos(\phi)B'+\sin(\phi)B'\right]|_C=0. \tag{2.59}$$

Therefore, the two boundary conditions that must simultaneously be satisfied at the cavity walls by the magnetic vector potential [see Eq. (2.45) and Eq. (2.45)] can be simplified to the following simpler conditions

$$\begin{aligned}\vec{A}\cdot\hat{e}_t\big|_C=0\rightarrow\left[-A_x\sin(\phi)+A_y\cos(\phi)\right]\big|_C=0,\\ (\nabla A_n)\cdot\hat{e}_n\big|_C=0\rightarrow\left[\cos(\phi)B'+\sin(\phi)B'\right]\big|_C=0.\end{aligned} \tag{2.60}$$

Let us consider a single x-oriented dipole located inside a multilayered cavity, and that the boundary conditions for the magnetic vector potential are first enforced at a unique discrete point on the cavity walls (see Fig. 2.9a). In this case, just the use of a unique auxiliary dipole (I^x) located outside the cavity is required. The superscript x is refereed to the fact that the auxiliary dipole I^x is generated by an original x-oriented dipole inside the cavity under analysis. Besides, note that due to the arbitrary direction of the cavity wall where the boundary conditions are imposed, the auxiliary dipole presents a complex amplitude with an arbitrary direction. This arbitrary-oriented dipole can be simplified by decomposing it into two orthogonal dipoles, oriented along the x and y-directions, as follows (see Fig. 2.9a)

$$I^x=I^{x,x}\,\hat{e}_x+I^{y,x}\,\hat{e}_y, \tag{2.61}$$

where the superscripts (x,x) and (y,x) indicates an auxiliary dipole oriented along the x or y direction and generated by an x-oriented original dipole inside the cavity.

As in the case of the electric scalar potential, we assume that the dipoles are placed on an unbounded multilayered media. To take this into account, the potentials generated by the dipoles, expressed in the spatial domain, are incorporated into the formulation by using the Sommerfeld transformation [Michalski and Mosig, 1997]. In addition, each auxiliary orthogonal dipole has its own complex weight, which can be determined by imposing the conditions of Eq. (2.60). This leads

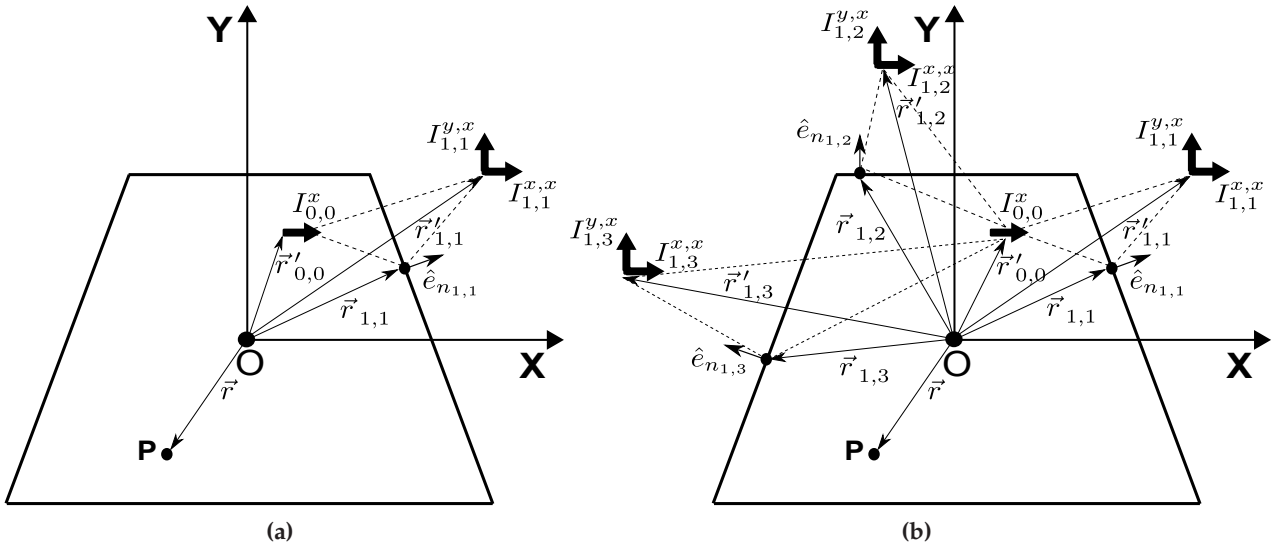

Figure 2.9 – Use of one (a) or three (b) auxiliary arbitrarily-oriented dipoles (decomposed into x and y-oriented dipoles) to enforce the boundary conditions for the magnetic vector potential at the cavity contour. O is the origin of the cartesian coordinate system, $I^{x}_{0,0}$ is the original x-oriented dipole source located inside the cavity, and P is a generic observation point.

to the following system of linear equations

$$\begin{aligned} -\sin(\varphi_{1,1})I^{x,x}_{1,1}S_0\left[\tilde{G}_A\right]\big|^{\vec{r}_{1,1}}_{\vec{r}\,'_{1,1}} + \cos(\varphi_{1,1})I^{y,x}_{1,1}S_0\left[\tilde{G}_A\right]\big|^{\vec{r}_{1,1}}_{\vec{r}\,'_{1,1}} &= \sin(\varphi_{1,1})S_0\left[\tilde{G}_A\right]\big|^{\vec{r}}_{\vec{r}\,'_{0,0}} \quad , \\ \cos(\varphi_{1,1})I^{x,x}_{1,1}B(\vec{r}_{1,1},\vec{r}\,'_{1,1}) + \sin(\varphi_{1,1})I^{y,x}_{1,1}B(\vec{r}_{1,1},\vec{r}\,'_{1,1}) &= -\cos(\varphi_{1,1})B(\vec{r}_{1,1},\vec{r}\,'_{0,0}), \end{aligned} \tag{2.62}$$

where the angles and vectors involved in the formulation are shown in Fig. 2.8 and the variable B [see Eq. (2.58)] is redefined as

$$B(\vec{r}_{l,i},\vec{r}\,'_{m,k}) = -S_1\left[\tilde{G}_A\right]\big|^{\vec{r}_{l,i}}_{\vec{r}\,'_{m,k}}\hat{e}_{n_{l,i}}\cos(\psi^{l,i}_{m,k}-\phi_{l,i}). \tag{2.63}$$

Note that, as in the case of the electric scalar potential, the combination of the original dipole $I^{x}_{0,0}$ with the auxiliary image dipoles ($I^{x,x}_{1,1}$ and $I^{y,x}_{1,1}$) imposes the required boundary conditions at the chosen discrete point on the cavity wall.

The situation can be extended, for instance, imposing the boundary conditions at three discrete points on the cavity wall, as shown in Fig. 2.9b. In this case, the use of three auxiliary arbitrarily-oriented dipoles is required. Again, each auxiliary dipole is decomposed into a set of two orthogonal dipoles, each one with a different complex weight. The final values of these complex weights are retrieved by solving the following system of linear equations

$$
\begin{aligned}
&-\sin(\varphi_{1,1})\left(I^{x,x}_{1,1}S_0\left[\tilde{G}_A\right]\big|^{\vec{r}_{1,1}}_{\vec{r}\,'_{1,1}}+I^{x,x}_{1,2}S_0\left[\tilde{G}_A\right]\big|^{\vec{r}_{1,1}}_{\vec{r}\,'_{1,2}}+I^{x,x}_{1,3}S_0\left[\tilde{G}_A\right]\big|^{\vec{r}_{1,1}}_{\vec{r}\,'_{1,3}}\right)\\
&+\cos(\varphi_{1,1})\left(I^{y,x}_{1,1}S_0\left[\tilde{G}_A\right]\big|^{\vec{r}_{1,1}}_{\vec{r}\,'_{1,1}}+I^{y,x}_{1,2}S_0\left[\tilde{G}_A\right]\big|^{\vec{r}_{1,1}}_{\vec{r}\,'_{1,2}}+I^{y,x}_{1,3}S_0\left[\tilde{G}_A\right]\big|^{\vec{r}_{1,1}}_{\vec{r}\,'_{1,3}}\right)=\sin(\varphi_{1,1})S_0\left[\tilde{G}_A\right]\big|^{\vec{r}_{1,1}}_{\vec{r}\,'_{0,0}}\quad,\\
&-\sin(\varphi_{1,2})\left(I^{x,x}_{1,1}S_0\left[\tilde{G}_A\right]\big|^{\vec{r}_{1,2}}_{\vec{r}\,'_{1,1}}+I^{x,x}_{1,2}S_0\left[\tilde{G}_A\right]\big|^{\vec{r}_{1,2}}_{\vec{r}\,'_{1,2}}+I^{x,x}_{1,3}S_0\left[\tilde{G}_A\right]\big|^{\vec{r}_{1,2}}_{\vec{r}\,'_{1,3}}\right)\\
&+\cos(\varphi_{1,2})\left(I^{y,x}_{1,1}S_0\left[\tilde{G}_A\right]\big|^{\vec{r}_{1,2}}_{\vec{r}\,'_{1,1}}+I^{y,x}_{1,2}S_0\left[\tilde{G}_A\right]\big|^{\vec{r}_{1,2}}_{\vec{r}\,'_{1,2}}+I^{y,x}_{1,3}S_0\left[\tilde{G}_A\right]\big|^{\vec{r}_{1,2}}_{\vec{r}\,'_{1,3}}\right)=\sin(\varphi_{1,2})S_0\left[\tilde{G}_A\right]\big|^{\vec{r}_{1,2}}_{\vec{r}\,'_{0,0}}\quad,\\
&-\sin(\varphi_{1,3})\left(I^{x,x}_{1,1}S_0\left[\tilde{G}_A\right]\big|^{\vec{r}_{1,3}}_{\vec{r}\,'_{1,1}}+I^{x,x}_{1,2}S_0\left[\tilde{G}_A\right]\big|^{\vec{r}_{1,3}}_{\vec{r}\,'_{1,2}}+I^{x,x}_{1,3}S_0\left[\tilde{G}_A\right]\big|^{\vec{r}_{1,3}}_{\vec{r}\,'_{1,3}}\right)\\
&+\cos(\varphi_{1,3})\left(I^{y,x}_{1,1}S_0\left[\tilde{G}_A\right]\big|^{\vec{r}_{1,3}}_{\vec{r}\,'_{1,1}}+I^{y,x}_{1,2}S_0\left[\tilde{G}_A\right]\big|^{\vec{r}_{1,3}}_{\vec{r}\,'_{1,2}}+I^{y,x}_{1,3}S_0\left[\tilde{G}_A\right]\big|^{\vec{r}_{1,3}}_{\vec{r}\,'_{1,3}}\right)=\sin(\varphi_{1,3})S_0\left[\tilde{G}_A\right]\big|^{\vec{r}_{1,3}}_{\vec{r}\,'_{0,0}}\quad,\\
&\cos(\varphi_{1,1})\left[I^{x,x}_{1,1}B(\vec{r}_{1,1},\vec{r}\,'_{1,1})+I^{x,x}_{1,2}B(\vec{r}_{1,1},\vec{r}\,'_{1,2})+I^{x,x}_{1,3}B(\vec{r}_{1,1},\vec{r}\,'_{1,3})\right]\\
&+\sin(\varphi_{1,1})\left[I^{y,x}_{1,1}B(\vec{r}_{1,1},\vec{r}\,'_{1,1})+I^{y,x}_{1,2}B(\vec{r}_{1,1},\vec{r}\,'_{1,2})+I^{y,x}_{1,3}B(\vec{r}_{1,1},\vec{r}\,'_{1,3})\right]=-\cos(\varphi_{1,1})B(\vec{r}_{1,1},\vec{r}\,'_{0,0}),\\
&\cos(\varphi_{1,2})\left[I^{x,x}_{1,1}B(\vec{r}_{1,2},\vec{r}\,'_{1,1})+I^{x,x}_{1,2}B(\vec{r}_{1,2},\vec{r}\,'_{1,2})+I^{x,x}_{1,3}B(\vec{r}_{1,2},\vec{r}\,'_{1,3})\right]\\
&+\sin(\varphi_{1,2})\left[I^{y,x}_{1,1}B(\vec{r}_{1,2},\vec{r}\,'_{1,1})+I^{y,x}_{1,2}B(\vec{r}_{1,2},\vec{r}\,'_{1,2})+I^{y,x}_{1,3}B(\vec{r}_{1,2},\vec{r}\,'_{1,3})\right]=-\cos(\varphi_{1,2})B(\vec{r}_{1,2},\vec{r}\,'_{0,0}),\\
&\cos(\varphi_{1,3})\left[I^{x,x}_{1,1}B(\vec{r}_{1,3},\vec{r}\,'_{1,1})+I^{x,x}_{1,2}B(\vec{r}_{1,3},\vec{r}\,'_{1,2})+I^{x,x}_{1,3}B(\vec{r}_{1,3},\vec{r}\,'_{1,3})\right]\\
&+\sin(\varphi_{1,3})\left[I^{y,x}_{1,1}B(\vec{r}_{1,3},\vec{r}\,'_{1,1})+I^{y,x}_{1,2}B(\vec{r}_{1,3},\vec{r}\,'_{1,2})+I^{y,x}_{1,3}B(\vec{r}_{1,3},\vec{r}\,'_{1,3})\right]=-\cos(\varphi_{1,3})B(\vec{r}_{1,3},\vec{r}\,'_{0,0}).
\end{aligned}
\tag{2.64}
$$

The procedure can be further extended to consider R rings of N auxiliary dipoles (see Fig. 2.6), which are simultaneously employed to impose the boundary conditions at the cavity walls. In this way, the geometrical details of the cavity contour are taken into account. The following system of $(2R \cdot 2N)$ linear equations is obtained

$$
\begin{aligned}
&-\sin(\varphi_{l,i})\sum_{m=1}^{R}\sum_{k=1}^{N}I^{x,x}_{m,k}S_0\left[\tilde{G}_A\right]\big|^{\vec{r}_{l,i}}_{\vec{r}\,'_{m,k}}+\cos(\varphi_{l,i})\sum_{m=1}^{R}\sum_{k=1}^{N}I^{y,x}_{m,k}S_0\left[\tilde{G}_A\right]\big|^{\vec{r}_{l,i}}_{\vec{r}\,'_{m,k}}=\sin(\varphi_{l,i})S_0\left[\tilde{G}_A\right]\big|^{\vec{r}_{l,i}}_{\vec{r}\,'_{0,0}}\quad,\\
&\cos(\varphi_{l,i})\sum_{m=1}^{R}\sum_{k=1}^{N}I^{x,x}_{m,k}B(\vec{r}_{l,i},\vec{r}\,'_{m,k})+\sin(\varphi_{l,i})\sum_{m=1}^{R}\sum_{k=1}^{N}I^{y,x}_{m,k}B(\vec{r}_{l,i},\vec{r}\,'_{m,k})=-\cos(\varphi_{l,i})B(\vec{r}_{l,i},\vec{r}\,'_{0,0}),\\
&\qquad\qquad l=1,2,\ldots R,\qquad\qquad i=1,2,\ldots N.
\end{aligned}
\tag{2.65}
$$

It is important to note that a Sommerfeld transformation of first order (S_1), related to the spatial derivative of the multilayered Green's functions, is involved in the formulation [through the use of the variable B, see Eq. (2.63)]. It is also very important for a correct implementation to note the different vectors and angles employed in the upper equation, which are clarified in Fig. 2.8. Specifically, the angle between the (m,k) dipole and the (l,i) observation point (denoted as $\psi^{l,i}_{m,k}$) is of crucial importance.

Once the system of linear equations is solved, the magnetic vector potential generated by an x-oriented dipole located inside of a multilayered cavity can be recovered by using all the complex

amplitudes of the $2R \cdot 2N$ image electric dipoles ($I^{x,x}_{m,k}$, $I^{y,x}_{m,k}$) as

$$G^{xx}_{A_{Cav}}(\vec{r},\vec{r}\,'_{0,0}) = S_0\left[\tilde{G}_A\right]\Big|^{\vec{r}}_{\vec{r}\,'_{0,0}} + \sum_{m=1}^{R}\sum_{k=1}^{N} I^{x,x}_{m,k}\, S_0\left[\tilde{G}_A\right]\Big|^{\vec{r}}_{\vec{r}\,'_{m,k}}, \tag{2.66}$$

$$G^{yx}_{A_{Cav}}(\vec{r},\vec{r}\,'_{0,0}) = \sum_{m=1}^{R}\sum_{k=1}^{N} I^{y,x}_{m,k}\, S_0\left[\tilde{G}_A\right]\Big|^{\vec{r}}_{\vec{r}\,'_{m,k}}. \tag{2.67}$$

As in the case of the electric scalar potential, it is important to note that all equations are independent of the geometry of the waveguide. This is because a rectangular coordinates system is used, and a fixed location of the images and the tangent points is not assumed.

If the electric unitary dipole inside the cavity is oriented along the y-direction, the same procedure can be followed in order to impose the boundary conditions on the wall. In this case, a similar $2R \cdot 2N$ system of linear equations is obtained

$$\begin{aligned}
-\sin(\varphi_{l,i})\sum_{m=1}^{R}\sum_{k=1}^{N} I^{x,y}_{m,k} S_0\left[\tilde{G}_A\right]\Big|^{\vec{r}_{l,i}}_{\vec{r}\,'_{m,k}} + \cos(\varphi_{l,i})\sum_{m=1}^{R}\sum_{k=1}^{N} I^{y,y}_{m,k} S_0\left[\tilde{G}_A\right]\Big|^{\vec{r}_{l,i}}_{\vec{r}\,'_{m,k}} &= -\cos(\varphi_{l,i}) S_0\left[\tilde{G}_A\right]\Big|^{\vec{r}_{l,i}}_{\vec{r}\,'_{0,0}} \quad , \\
\cos(\varphi_{l,i})\sum_{m=1}^{R}\sum_{k=1}^{N} I^{x,y}_{m,k} B(\vec{r}_{l,i},\vec{r}\,'_{m,k}) + \sin(\varphi_{l,i})\sum_{m=1}^{R}\sum_{k=1}^{N} I^{y,y}_{m,k} B(\vec{r}_{l,i},\vec{r}\,'_{m,k}) &= -\sin(\varphi_{l,i}) B(\vec{r}_{l,i},\vec{r}\,'_{0,0}), \\
l = 1,2,\ldots R, \qquad i = 1,2,\ldots N &
\end{aligned} \tag{2.68}$$

where we can observe that only the excitation vector changes with respect to the system formulated for the x-oriented dipole. The computed image electric dipoles are used to recover the magnetic vector potential inside the cavity, in a similar way as before

$$G^{yy}_{A_{Cav}}(\vec{r},\vec{r}\,'_{0,0}) = S_0\left[\tilde{G}_A\right]\Big|^{\vec{r}}_{\vec{r}\,'_{0,0}} + \sum_{m=1}^{R}\sum_{k=1}^{N} I^{y,y}_{m,k}\, S_0\left[\tilde{G}_A\right]\Big|^{\vec{r}}_{\vec{r}\,'_{m,k}}, \tag{2.69}$$

$$G^{xy}_{A_{Cav}}(\vec{r},\vec{r}\,'_{0,0}) = \sum_{m=1}^{R}\sum_{k=1}^{N} I^{x,y}_{m,k}\, S_0\left[\tilde{G}_A\right]\Big|^{\vec{r}}_{\vec{r}\,'_{m,k}}. \tag{2.70}$$

The proposed formulation also allows the easy computation of the Green's functions spatial derivatives of order n related to the multilayered cavity under analysis, without requiring an additional computational effort. By using Eq. (2.38), the derivatives of the magnetic vector potential are computed over the transversal source-observer spatial distance [ρ, see Eq. (2.15)] as

$$\frac{\partial^n G^{xx}_{A_{Cav}}(\vec{r},\vec{r}\,'_{0,0})}{\partial\rho^n} = S_n\left[\tilde{G}_A\right]\Big|^{\vec{r}}_{\vec{r}\,'_{0,0}} + \sum_{m=1}^{R}\sum_{k=1}^{N} I^{x,x}_{m,k}\, S_n\left[\tilde{G}_A\right]\Big|^{\vec{r}}_{\vec{r}\,'_{m,k}} \quad , \tag{2.71}$$

$$\frac{\partial^n G^{yx}_{A_{Cav}}(\vec{r},\vec{r}\,'_{0,0})}{\partial\rho^n} = \sum_{m=1}^{R}\sum_{k=1}^{N} I^{y,x}_{m,k}\, S_n\left[\tilde{G}_A\right]\Big|^{\vec{r}}_{\vec{r}\,'_{m,k}} \quad , \tag{2.72}$$

$$\frac{\partial^n G^{yy}_{A_{Cav}}(\vec{r},\vec{r}\,'_{0,0})}{\partial\rho^n} = S_n\left[\tilde{G}_A\right]\Big|^{\vec{r}}_{\vec{r}\,'_{0,0}} + \sum_{m=1}^{R}\sum_{k=1}^{N} I^{y,y}_{m,k}\, S_n\left[\tilde{G}_A\right]\Big|^{\vec{r}}_{\vec{r}\,'_{m,k}} \quad , \tag{2.73}$$

$$\frac{\partial^n G^{xy}_{A_{Cav}}(\vec{r},\vec{r}\,'_{0,0})}{\partial\rho^n} = \sum_{m=1}^{R}\sum_{k=1}^{N} I^{x,y}_{m,k}\, S_n\left[\tilde{G}_A\right]\Big|^{\vec{r}}_{\vec{r}\,'_{m,k}}. \tag{2.74}$$

Note that the spatial derivatives related to the x or y-directions can easily be obtained from these equations, simply by using the chain's rule of the derivative.

This main advantage of this approach, as in the case of the electric scalar potential, is that the problem does not need to be reformulated for the computation of the spatial derivatives. This is due to the complex weights of the auxiliary dipoles, which are not affected by this derivative.

2.3.2 Practical Implementation of the Spatial Images Technique

The accuracy of the spatial images technique directly depends on the number of images employed and their adequate distribution around the cavity under analysis. In this subsection, we study the location and number of the spatial images around the structure contour, both in the cross-section plane and in height, in order to determine their influence on the method accuracy. The study is focused on the convergence and error committed in the computation of the electric scalar potential. However, note that a similar study related to the magnetic vector potential would lead to exactly the same conclusions, in terms of both, number and location of auxiliary spatial images.

In order to determine the accuracy of the proposed method, we must be able to exactly know the error committed on the Green's functions computation. This can easily be done by evaluating the fulfillment of the boundary conditions along the cavity contour. In the case of the electric scalar potential, this error is obtained by evaluating Eq. (2.31) along the cavity walls. In the case of the magnetic vector potential, the error is obtained by computing Eq. (2.60) along the cavity contour. In all cases, an ideal situation will provide a zero value for the relevant condition along the whole cavity perimeter.

Moreover, it is extremely important to define an error threshold, to exactly know when the computed Green's functions have enough accuracy. For this purpose, a study related to the practical application of the method has been carried out. In the study, the computed Green's functions have been included into a mixed potential integral equation formulation ([Mosig, 1989], see Chapter 3), which has then been applied to the analysis of shielded microwave filters. After the parametric analysis of many different devices, numerical simulations have shown that the resulting S parameters are convergent if the maximum error committed in the Green's functions computation is below 0.1 for all source locations. The importance of this error threshold is two fold. First, it gives a measure about the quality of any computed Green's functions, and second, it provides practical information about the number of spatial images required to the efficient analysis of shielded multilayered cavities.

It is important to indicate that the accuracy of the method is usually deteriorated when the point source is located close to any cavity wall. This is because the auxiliary spatial images must compensate the singular behavior of the source at that wall. In order to alleviate this problem, a specific distribution of the spatial images, based on image theory, is proposed. Even though the method accuracy using this approach is acceptable, note that a higher error, as compared to the situation where the point source is located far from the walls, is always obtained. A perfect solution to this problem, based on auxiliary ground planes, is proposed in Section 2.4 for the case of rectangular multilayered enclosures. In addition, note that this problem also restricts the use of the spatial images technique to the analysis of multilayered convex-shaped cavities. This is because in the analysis of concave struc-

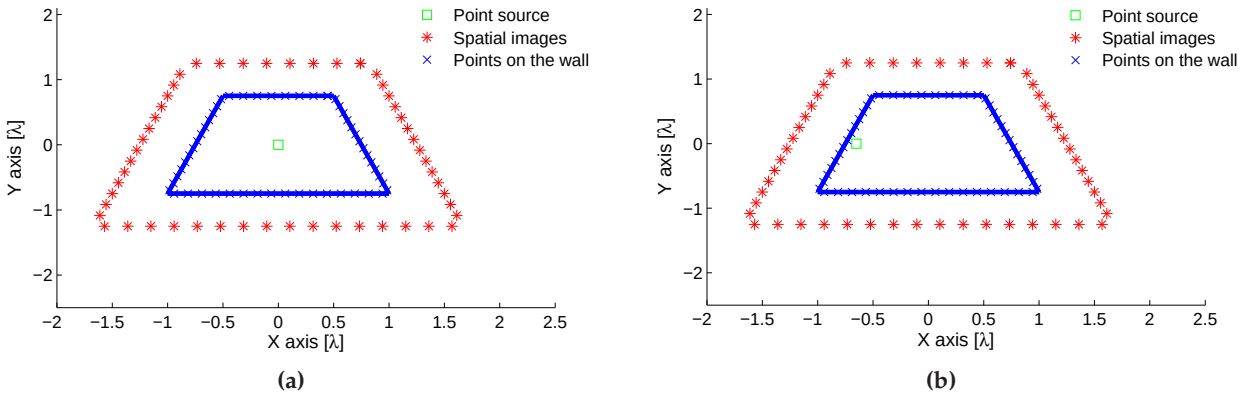

Figure 2.10 – Use of a fix-distance ($d = 0.5\lambda$) algorithm to distribute the spatial images around the trapezium cavity shown in Fig. 2.5. The source is placed at the position $(0, 0, 0.01)\lambda$ (a) and at the position $(-0.65, 0, 0.01)\lambda$ (b).

tures, the set of auxiliary images can not compensate the singular behavior of the point source, which may be placed close to a wall, while keeping a low error level along the whole cavity perimeter. Besides, the inner corners of this type of structures also provide singular behavior to the potentials, which can not easily be compensated by the auxiliary images. Note that this type of problems also arises in other numerical methods, such us in the MAS [Kaklamani and Anastassiu, 2002].

Spatial Images Distribution

In order to implement the spatial images technique, the first step is to discretize the cavity contour. An interesting strategy is to uniformly select discrete points on each segment of the contour, avoiding the corners. This is because in these points the tangent and normal unit vectors, required by the formulation, are not well defined and their use may cause numerical instabilities.

Then, the spatial images must be located around the cavity contour. Since the proposed formulation pretends to be useful for the evaluation of arbitrary geometries, the situation of the images changes as a function of the waveguide shape. A simple way to locate them is to follow the structure contour, with an adequate separation distance. This procedure is shown in Fig. 2.10. However, the exact location of the spatial images might affect the accuracy and numerical stability of the technique, especially when the source point is close to the walls of the cavity (see Fig. 2.10b). This is due to the singular behavior of the source, which can not be compensated by the far-located spatial images. Thereby, although a specific spatial images distribution could provide good accuracy when it is used with a particular type of cavity and source position, the same distribution might not be able to achieve the same accuracy for another cavity shape, or when the source is placed at a different location.

A possible alternative is to use another algorithm to locate the images around the cavity. Specifically, we propose a new procedure which depends on both, the shape of the cavity and on the source position, and provides acceptable accuracy in all situations. A trapezium-shaped cavity is depicted in Fig. 2.11 in order to introduce this new algorithm.

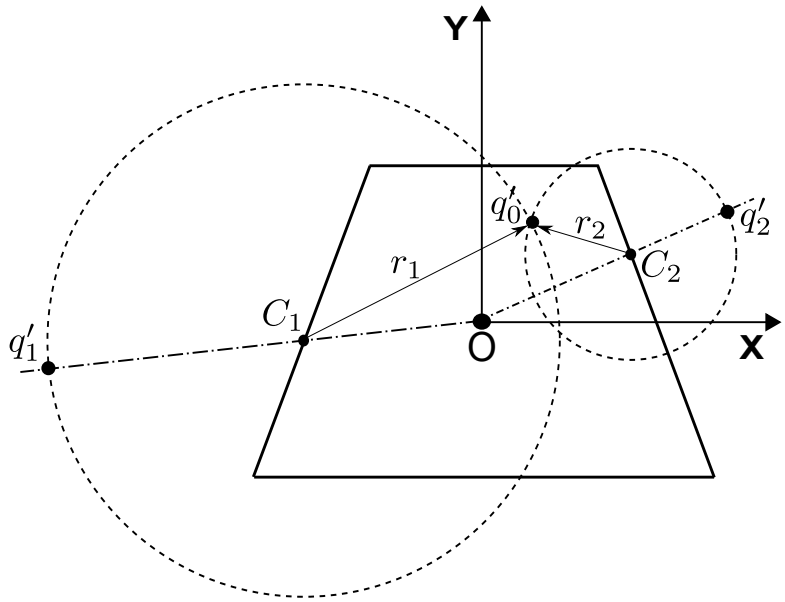

Figure 2.11 – Example of the algorithm employed to locate the auxiliary sources around a cavity contour. The algorithm uses each point of the cavity wall (C_1 and C_2 in this case) as a center of an auxiliary circle, with radius equal to the distance between the circle center and the point source (q'_0). Then, each auxiliary image (q'_1 or q'_2) is located at the intersection between its associated auxiliary circle and the line traced between the cavity center (O) and the point on the cavity wall (C_1 or C_2).

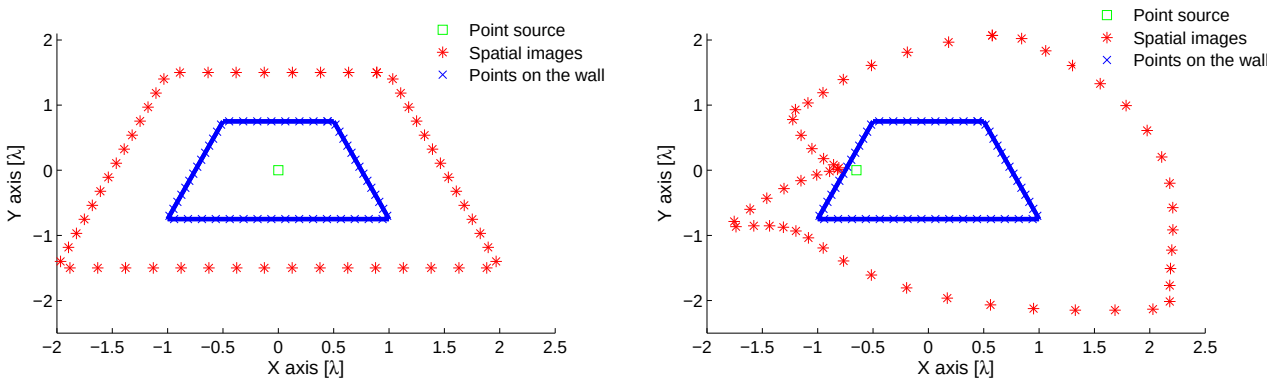

Figure 2.12 – Use of the proposed dynamic image location algorithm to distribute the spatial images around the trapezium cavity shown in Fig. 2.5. The source is placed at the position $(0, 0, 0)\lambda$ (a) and at the position $(-0.65, 0, 0)\lambda$ (b).

The first step of the method consist of sampling the cavity contour at N discrete points. Each of these points will be the center of a virtual circle, with radius equal to the distance to the source position inside the cavity (see Fig. 2.11). To locate each single spatial image, a line is traced from the center of the waveguide to each discrete point at the wall. These lines will intersect the virtual circles at a maximum of two points. The position of the image is selected at the intersecting point falling outside of the cavity. The algorithm is illustrated for two different points C_1 and C_2 in Fig. 2.11. An example of the algorithm behavior, for a large number of spatial images, is also shown in Fig. 2.12. It

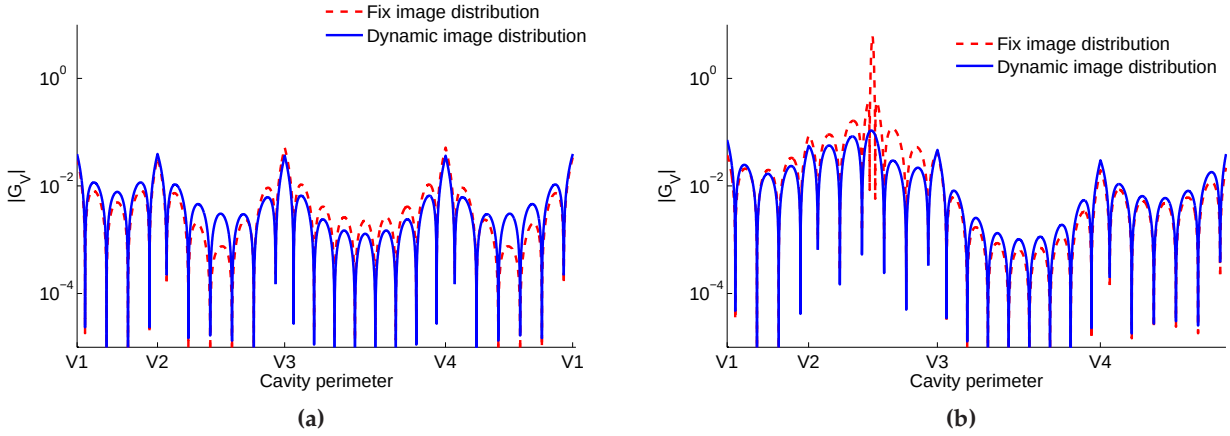

Figure 2.13 – Error committed in the imposition of the G_V boundary conditions [see Eq. (2.31)] along the walls of the cavity shown in Fig. 2.5, as a function of the type of algorithm employed to locate the spatial images. In the analysis, 4 images per λ are employed. V_X denotes the X vertex of the cavity, as indicated in Fig. 2.5. (a) Point source located at $(0, 0, 0)\lambda$. (b) Point source located at $(-0.65, 0, 0)\lambda$.

is important to note that when the source is placed near a cavity wall, the method locates one image close to that wall. We have observed that this situation leads to increased accuracy for source points close to the wall, since this image tends to impose the right boundary conditions locally at the closest wall. An example of this situation is presented in Fig. 2.12b, where we show the final location of the images, obtained with this algorithm, for a situation of a source point placed very close to a wall. We can observe that one spatial image approaches the source point from outside the cavity. This behavior correctly simulates the situation of a source point very close to an infinite ground plane. By image theory, we know that in this case the spatial image must be placed at the same distance from the ground plane as the source [Balanis, 1989]. This behavior of the basic image theory is respected by the new algorithm, leading to an increased accuracy for points close to the cavity walls.

In order to demonstrate the usefulness of the spatial images distribution algorithm, we present in Fig. 2.13a the electric scalar potential around the trapezium cavity contour. For this test, the source point is located at the cavity center. Ideally, the electric scalar potential should always be zero around the cavity wall. In the figure, the presence of zeros clearly indicates the points where the boundary conditions have been enforced. In between these points, higher values of the potential are observed. Besides, note that in Fig. 2.13a several peaks at the corners appear. These peaks are produced by the abrupt changes of the contour direction, that occur close to the corners of the geometry.

In the figure, we compare the results obtained using the new algorithm (see Fig. 2.12a) with the results obtained when the spatial images are placed following the cavity contour at a fixed distance from the wall ($d = 0.5\lambda$, see Fig. 2.10a). As can be observed, the error is maintained very low along the whole cavity contour in all cases. This test shows the numerical stability of the spatial images technique when the source is placed at positions far from the cavity walls.

We have repeated a similar study in Fig. 2.13b, but locating the source point very close to the left wall of the cavity. In this case, the results obtained using the fix location of images (see Fig. 2.10b) provides unacceptable error levels, specially in the wall close to the source. In this same figure, we

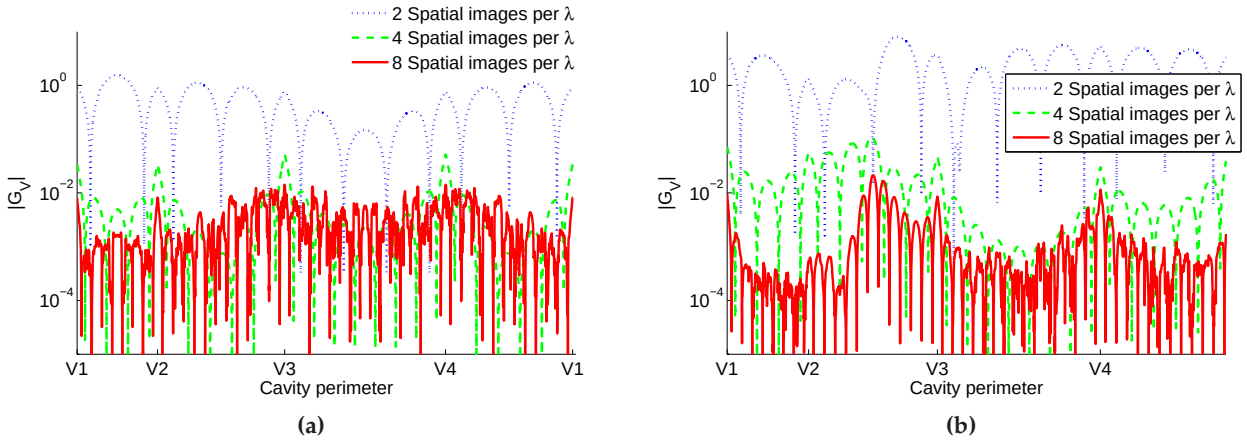

Figure 2.14 – Error committed in the imposition of the G_V boundary conditions [see Eq. (2.31)] along the walls of the cavity shown in Fig. 2.5, as a function of the number of spatial images employed per λ. In the analysis, the dynamic algorithm to locate the spatial images is employed. V_X denotes the X vertex of the cavity, as indicated in Fig. 2.5. (a) Point source located at $(0, 0, 0)\lambda$. (b) Point source located at $(-0.65, 0, 0)\lambda$.

denote with a thick line the potential obtained when the new algorithm is employed to locate the spatial images (see Fig. 2.12b). We can observe that, in this case, the potential around the cavity wall is very small, even along the wall close to the source point. This last result confirms that a clever selection for the location of the images around the cavity leads to an improved convergence and numerical precision in the imposition of the relevant boundary conditions.

There is a physical explanation for the improved accuracy obtained when the new technique to locate the images is used. When the source is close to a wall, the relevant geometrical detail influencing the behavior of the Green's functions is the wall close to the source, which tends to behave as an infinite ground plane, as the source approaches the wall. Using the proposed technique to locate the images, one of the spatial images will be placed in a mirror position to the source point with respect to this wall, which is in agreement with the spatial images solution for an infinite ground plane [Balanis, 1989]. The importance of the algorithm introduced is twofold. First, the algorithm places the spatial images in an automatic fashion for any convex shape of the cavity considered. Second, the accuracy and stability of the algorithm increases for source points very close to the walls, as we have just discussed.

Spatial Images Convergence

Another important issue is the convergence of the spatial images technique versus the number of images employed. In general, we have observed that the use of $3 - 5$ images per λ are enough to achieve good convergence rates. In order to demonstrate this, we present in Fig. 2.14a the electric scalar potential computed along the cavity contour of Fig. 2.5 when 2, 4 and 8 images per λ are employed. In this example, the source is located at the cavity center, and the dynamic algorithm is used to distribute the spatial images around the structure. As can be observed in the figure, the use of 2 images per λ leads to unacceptable error levels. However, as we increase the number of images,

the error is reduced, leading to convergent results. In Fig. 2.14b, we present the same analysis, but locating the point source very close the cavity wall. Similar conclusions as in the previous case can be extracted. The improvement in accuracy when increasing from 4 to 8 spatial images per λ is not very large, indicating that convergence has been reached. Finally, note that the use of many spatial images may lead to ill-conditioned system of equations, which completely destroy the computation of the shielded Green's functions. In order to avoid this problem, a maximum number of 12 images per λ is recommended.

Multiring Rearrangement

Initially, the spatial images technique employs N images to impose the boundary conditions at N discrete points situated at a given cross section of the cavity. However, if the height of the cavity is electrically large, the imposition of the boundary conditions at one cross section plane of the cavity might not suffice to represent the correct behavior of the fields along the whole height. As previously commented, an interesting solution to this problem is to use a total of R rings, each one having N spatial images, to impose the boundary conditions at several discrete heights of the cavity (see Fig. 2.6). Therefore, boundary conditions are imposed on a total of $R \cdot N$ discrete points along the cavity walls.

To show the effectiveness of this idea, we present in Fig. 2.15 the electric scalar potential at the waveguide wall, plotted along the height of the trapezium-shaped cavity introduced in Fig. 2.5. In order to model an electrically long structure, we have modified the thickness of the dielectric layers to $h_2 = 0.2\lambda$ and $h_1 = 0.1\lambda$. The results are given when one, three and four rings of images are included in the calculations. Ideally, the electric scalar potential must be zero along the cavity height, in order to fulfill the boundary conditions. In solid line we include the results when only one ring of images is placed at $z = 0.1\lambda$. We observe that the potential is zero at one point, but the amplitude rapidly grows along the height of the cavity. Via the dash-dotted line, we show the results obtained when three rings of images, placed at heights $z = 0.05\lambda, 0.1\lambda, 0.215\lambda$, are included. We observe that the value of the potential along the substrate height is now smaller. Finally, if we place four rings of images scattered along the cavity height, at positions $z = 0.05\lambda, 0.1\lambda, 0.15\lambda, 0.21\lambda$, the value of the potential remains very low along the whole cavity height. This demonstrates that the boundary conditions can be maintained within a given accuracy, and demonstrates the usefulness of the multi-ring approach to model electrically long cavities.

From the practical point of view, it is interesting to establish a strategy to place the rings of images. In general, a ring can be placed at each interface where the microwave circuits are printed. In this way, the error in the fulfillment of the boundary conditions for the fields at these interfaces will be minimum (they will correspond to the zeros shown in Fig. 2.15). Moreover, the electrical length of the cavity height is fundamental to decide the number of rings to employ. We have observed that a new ring must be placed for each $\lambda/6$ of the cavity height. Furthermore, the presence of dielectric layers may excite new resonant modes. In this case, additional rings can be added to properly model these modes.

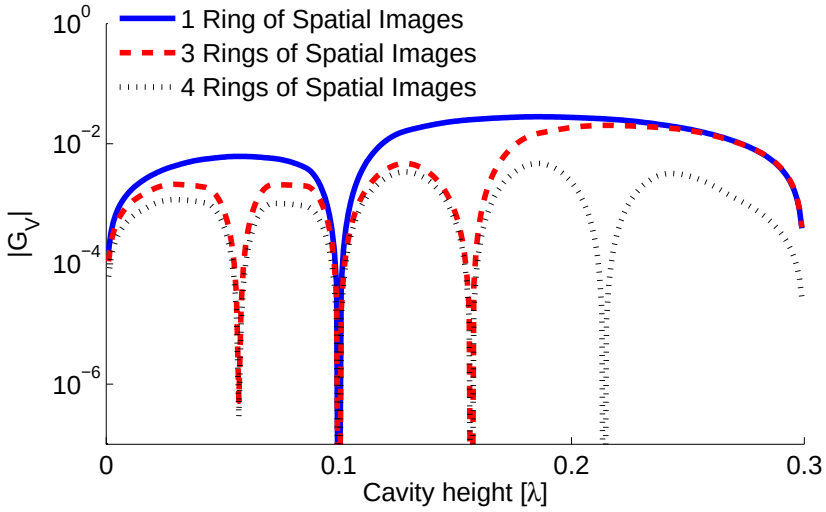

Figure 2.15 – Error committed in the imposition of the G_V boundary conditions [see Eq. (2.31)] along the Z axis of the cavity shown in Fig. 2.5 (using $h_1 = 0.1\lambda$ and $h_2 = 0.1\lambda$) analyzed with one, three, and five rings of spatial images. In the analysis, the dynamic algorithm is employed on each ring to locate 4 spatial images per λ of the cavity contour. The point source is located at the cavity center.

2.3.3 Numerical Validation

This subsection presents some numerical results to validate the spatial images technique. Specifically, the method is applied to the computation of the resonant frequencies associated to several multilayered cavities. Besides, it is demonstrated that the proposed method can also compute the potentials at the cavity resonances, without any convergence problems. Then, several free-noise potential patterns are obtained. In all cases, the results are validated using the commercial software HFSS©.

It is important to keep in mind that the spatial images technique will be also applied in Chapter 3 for the analysis of multilayered printed circuits located in arbitrarily-shaped cavities. There, simulations and measured data will be employed for validation purposes, further confirming the accuracy of the proposed technique.

Multilayered Trapezium-Shaped Cavity

In this first example, the resonant frequencies of the trapezium-shaped cavity shown in Fig. 2.16a are computed. In order to obtain them, the source and an observation points are placed at fixed positions inside the cavity, as shown in Fig. 2.16a. Using these fixed source and observation positions, a frequency sweep is performed. Several peaks are obtained in the potentials response, clearly indicating the resonant frequencies of the cavity. Then, these frequencies predicted by the spatial images method are compared to those obtained by HFSS©. This is shown in Table 2.4, which demonstrates that a high accuracy has been achieved, maintaining in all cases a relative error below 0.1%.

Then, the magnetic vector potential G_A^{xx} is computed, at the dielectric interface plane, at the

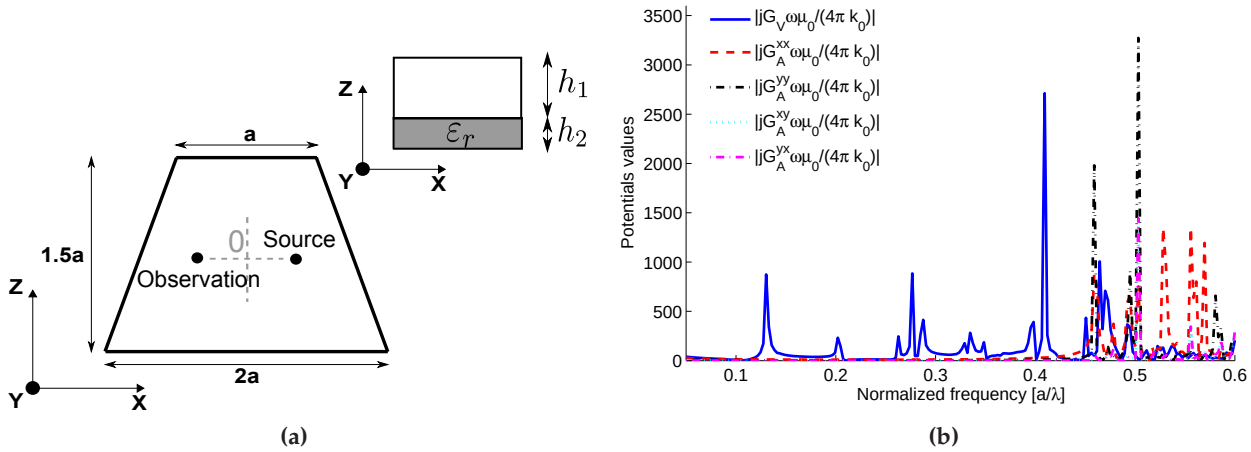

Figure 2.16 – Study of the resonant frequencies associated to the trapezium-shaped multilayered cavity (with parameters $a = \lambda$, $h_1 = 0.2\lambda$ and $h_2 = 0.1\lambda$) shown in (a). O is the origin of the coordinate system. For the study, the mixed-potential Green's functions are computed as a function of frequency at the observation point $(-0.1a, 0, h_2)$, when the source is placed at $(0.1a, 0, h_2)$. Sharp peaks in the response clearly indicate the resonant frequencies (b).

Spatial Images Technique	HFSS©	Absolute difference	Relative difference (%)
0.1305	0.1306	0.0001	0.0766
0.2024	0.2026	0.0002	0.0494
0.2050	0.2049	0.0001	0.0488
0.2628	0.2630	0.0002	0.0760
0.2763	0.2761	0.0002	0.0724
0.2859	0.2861	0.0002	0.0699
0.3281	0.3279	0.0002	0.0610

Table 2.4 – Normalized resonant frequencies (a/λ) of the trapezium cavity shown in Fig. 2.16a, computed with the spatial images technique and validated using HFSS©.

normalized frequency of $a/\lambda = 0.5033$. The results, shown in Fig. 2.17a, are compared with the x-component of the electric field obtained by the commercial software HFSS© at the same frequency and location (see Fig. 2.17b). As can be observed, the same mode distribution is obtained with both methods.

Multilayered Rectangular-Shaped Cavity

In this example, the resonant frequencies of the rectangular-shaped cavity shown in Fig. 2.18 are computed. For this purpose, the same procedure as in the previous case is employed. The resonant frequencies obtained with this method are compared with those obtained by HFSS© in Table 2.5. As can be observed, excellent agreement between these two completely different approaches is found.

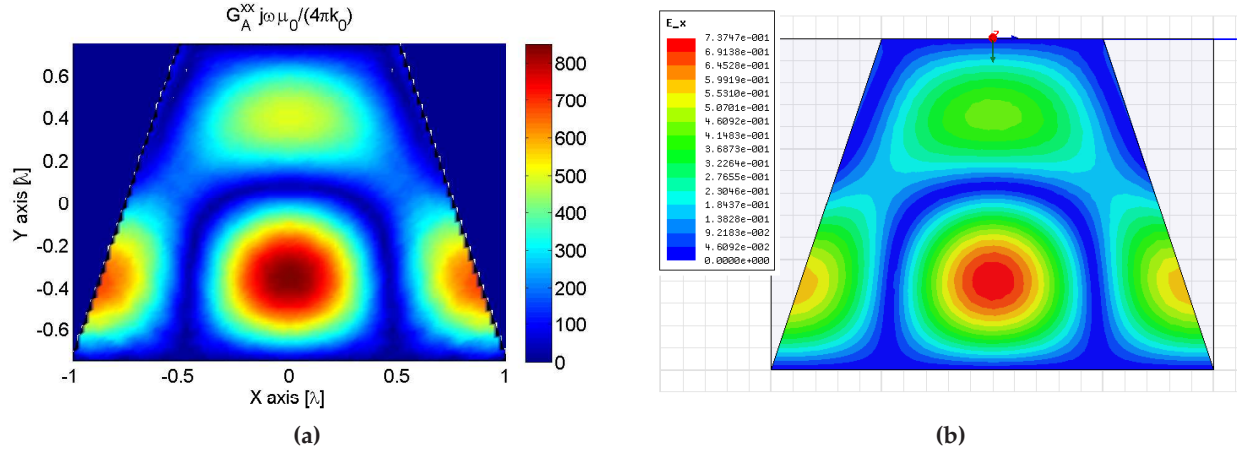

Figure 2.17 – Magnetic vector potential (G_A^{xx}) inside the multilayered trapezium-shaped cavity of Fig. 2.20a obtained with the spatial images technique at the normalized resonant frequency of $a/\lambda = 0.5033$ (a). The x-component of the electric field, computed with the commercial software HFSS© at the same resonant frequency [see (b)], is employed as validation.

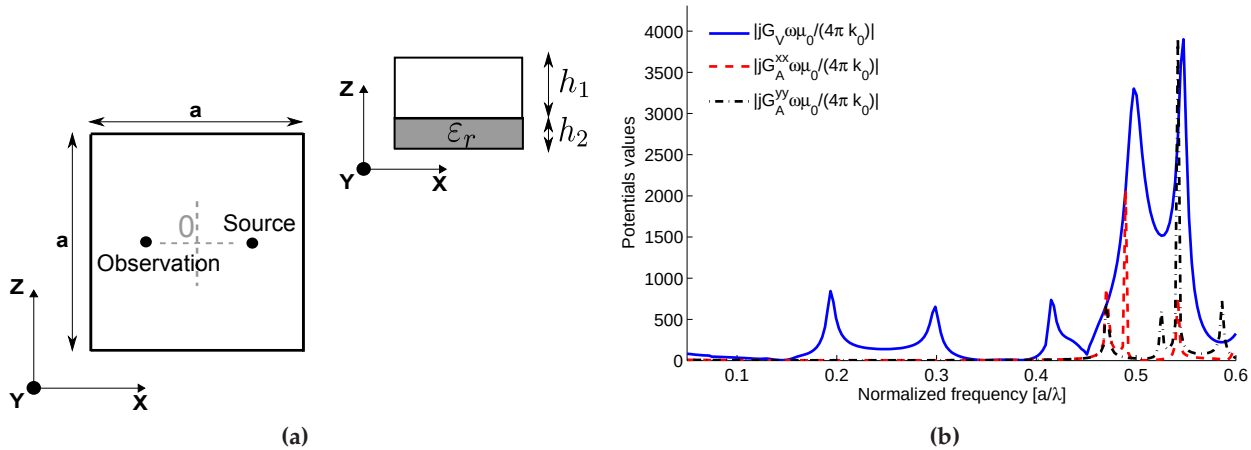

Figure 2.18 – Study of the resonant frequencies associated to the rectangular-shaped multilayered cavity (with parameters $a = \lambda$, $h_1 = 0.2\lambda$ and $h_2 = 0.1\lambda$) shown in (a). O is the origin of the coordinate system. For the study, the mixed-potential Green's functions are computed as function of frequency at the observation point located at $(-0.1a, 0, h_2)$, when the source is placed at $(0.1a, 0, h_2)$. Sharp peaks in the response clearly indicate the resonant frequencies (b).

As a further validation, we present in Fig. 2.19 the electric scalar potential obtained at the normalized resonant frequencies of $a/\lambda = 0.1937$ and $a/\lambda = 0.418$. In the same figure, the results are compared with those obtained by the commercial software HFSS©. In this case, the z-component of the electric field is plotted at the resonant frequencies. The same pattern is obtained by the two

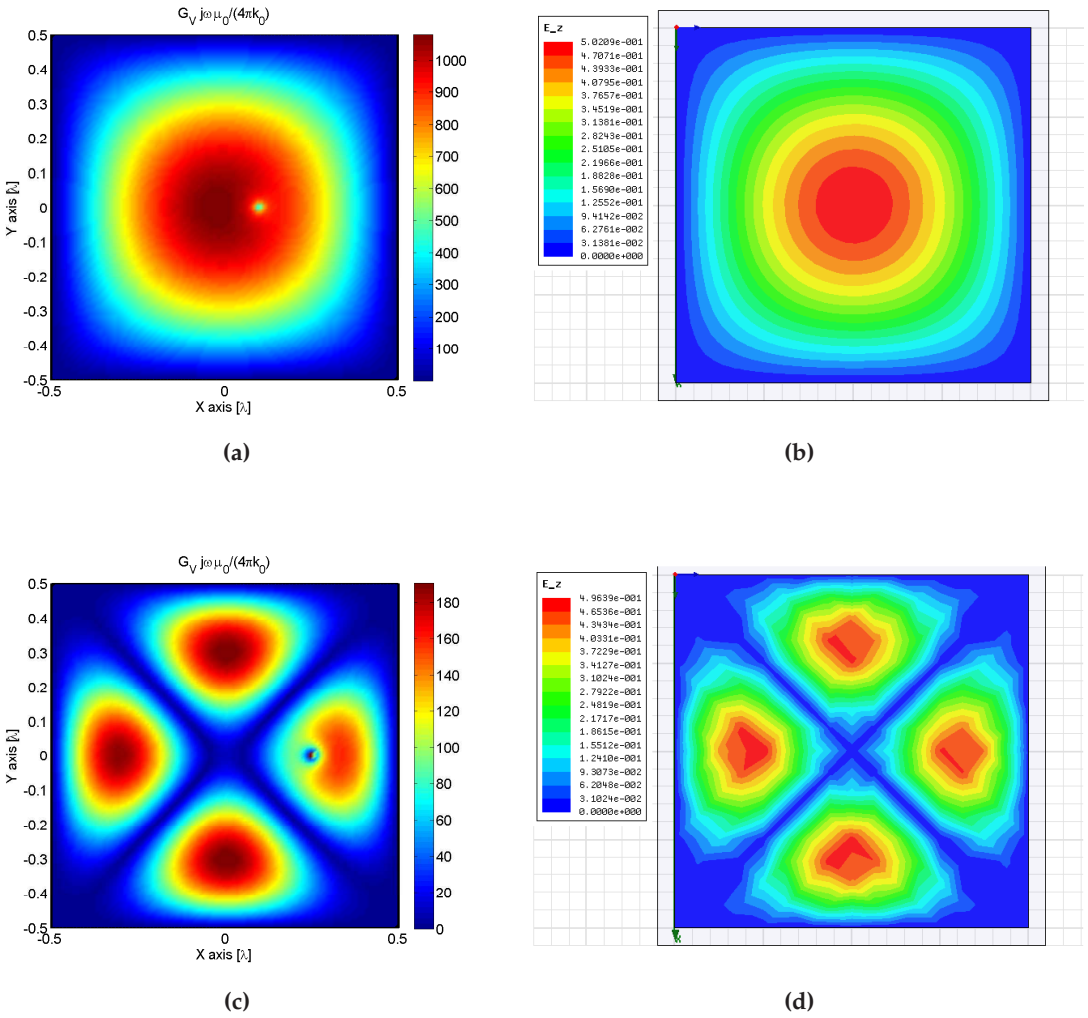

Figure 2.19 – Electric scalar potential (G_V) inside the multilayered rectangular-shaped cavity of Fig. 2.18a obtained with the spatial images technique at the normalized resonant frequencies of $a/\lambda = 0.1937$ (a) and $a'/\lambda = 0.4182$ (c). The z-component of the electric field, computed with the commercial software HFSS© at the same resonant frequencies [see (b) and (d)], is employed as validation.

methods in all cases, fully validating the results obtained by the spatial images technique.

Multilayered Triangular-Shaped Cavity

In this last example, the same procedure as in the previous cases is applied to the triangular-shaped cavity shown in Fig. 2.20, in order to compute the cavity resonant frequencies. Again, the computed frequencies are compared with those obtained by HFSS©. The result of this comparison is shown in Table 2.6, which demonstrates that excellent agreement is found between the two techniques.

Spatial Images Technique	HFSS©	Absolute difference	Relative difference (%)
0.1937	0.1936	0.0001	0.0517
0.2987	0.2989	0.0002	0.0669
0.4182	0.4185	0.0003	0.0716
0.4701	0.4705	0.0004	0.0850
0.4896	0.4890	0.0004	0.0818
0.5254	0.5251	0.0003	0.0571
0.5420	0.5417	0.0003	0.0554

Table 2.5 – Normalized resonant frequencies (a/λ) of the rectangular cavity shown in Fig. 2.18a, computed with the spatial images technique and validated using HFSS©.

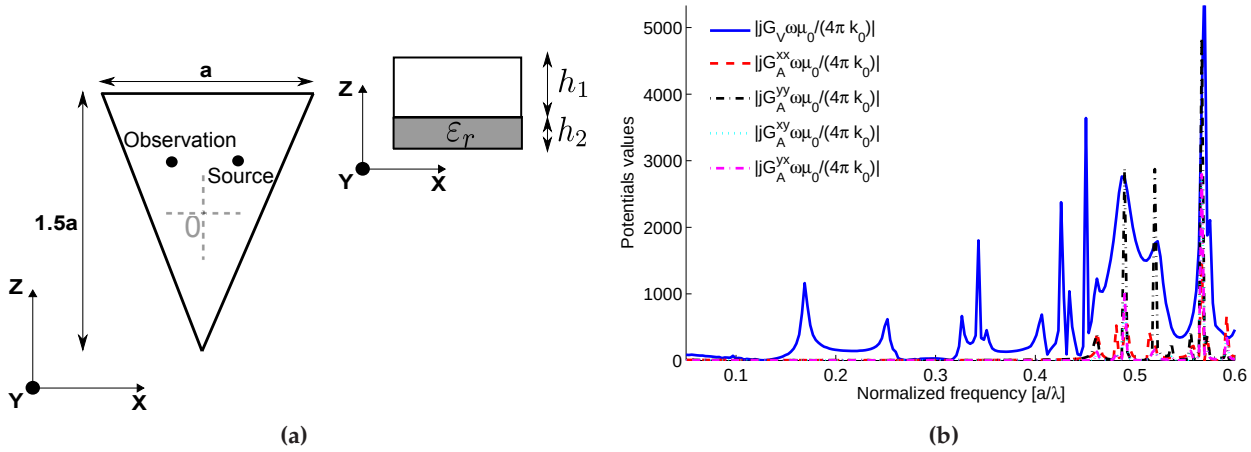

(a) (b)

Figure 2.20 – Study of the resonant frequencies associated to the triangular-shaped multilayered cavity (with parameters $a = \lambda$, $h_1 = 0.2\lambda$ and $h_2 = 0.1\lambda$) shown in (a). O is the origin of the coordinate system. For the study, the mixed-potential Green's functions are computed as function of frequency at the observation point located at $(-0.1a, 0, h_2)$, when the source is placed at $(0.1a, 0, h_2)$. Sharp peaks in the response clearly indicate the resonant frequencies (b).

Finally, the magnetic vector potential G_A^{yy}, computed at the normalized frequency of $a/\lambda = 0.5668$, is shown in Fig. 2.21a at the dielectric interface plane. For the sake of validation, the y-component of the electric field obtained by the software HFSS© is presented in Fig. 2.21b. As can be observed, excellent agreement between the patterns obtained by the two techniques is found.

Spatial Images Technique	HFSS©	Absolute difference	Relative difference (%)
0.1693	0.1694	0.0001	0.0590
0.2521	0.2523	0.0002	0.0793
0.3294	0.3292	0.0002	0.0608
0.3456	0.3453	0.0003	0.0869
0.4045	0.4048	0.0003	0.0741
0.4180	0.4176	0.0004	0.0958
0.4349	0.4352	0.0003	0.0689

Table 2.6 – Normalized resonant frequencies (a/λ) of the triangular cavity shown in Fig. 2.20a, computed with the spatial images technique and validated using HFSS©.

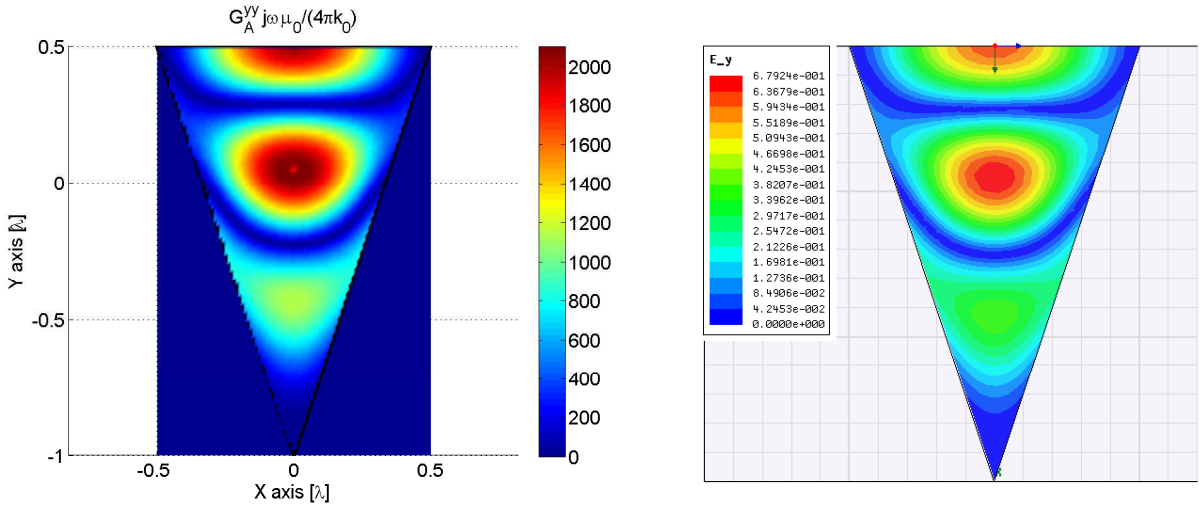

(a) **(b)**

Figure 2.21 – Magnetic vector potential (G_A^{yy}) inside the multilayered triangular-shaped cavity of Fig. 2.20a obtained with the spatial images technique at the normalized resonant frequency of $a/\lambda = 0.5668$ (a). The y-component of the electric field, computed with the commercial software HFSS© at the same resonant frequency [see (b)], is employed as validation.

2.4 Grounded MoM-Based Spatial Technique for the Computation of Green's Functions in Multilayered Shielded Boxes

This section presents the continuous counterpart of the discrete spatial images technique presented in Section 2.3, particularized to the computation of the rectangular boxed multilayered Green's functions and their associated spatial derivatives. The continuous nature of the technique increases the accuracy that can be obtained in the Green's functions computation, with respect to other implementations based on discrete sources [Quesada Pereira et al., 2005a], [Gómez-Díaz et al., 2008c]. Specifically, arbitrarily small errors in the Green's functions computation can be achieved. A refinement in the technique, which exploits the decoupling of the x and y-dyadic components of the Green's functions in rectangular boxes, contributes to further improve the method efficiency.

Instead of discrete auxiliary point sources (as in [Gómez-Díaz et al., 2008c], see Section 2.3), the proposed continuous method uses a set of auxiliary linear distribution of sources to impose potentials boundary conditions along the whole cavity contour. After applying boundary conditions, a set of integral equations (IEs), on the unknown values of the auxiliary sources, is obtained. The IE problem is then solved by using the method of moments (MoM) [Harrington, 1968]. A rigorous study about the impact of the test and basis functions choice on the Green's functions convergence is then presented and discussed, showing a trade-off between accuracy (using roof-top basis/test functions) and speed (using point-matching basis/test functions).

Besides, the method is combined with the use of dynamic ground planes. The ground planes are placed covering two of the cavity walls, as a function of the source position. A set of mirror basis functions are then placed with respect to them. The values of these basis functions are well-known from basic electromagnetic theory [Balanis, 1989], and the effective number of unknowns that need to be numerically calculated is greatly reduced. The combination of the auxiliary and mirror linear sources perfectly imposes the boundary conditions along the two covered cavity walls, whereas these conditions are numerically imposed on the remaining two walls. Note that, following this technique, the convergence problems when the source point is close to a cavity wall or corner are completely eliminated. This is done by placing the ground planes at the two closest cavity walls to the source position. In this way, the boundary conditions will automatically be imposed at these critical planes. By following this strategy, the positions of the ground planes can be dynamically changed, according to the position of the source point inside the cavity. This preserves high accuracy for all positions of the source point.

The proposed spatial technique for the calculation of multilayered boxed Green's functions and their derivatives is described in Section 2.4.1. The method is then numerically validated in Section 2.4.2, where a comparative study about the error in the Green's functions computation versus the different type of test/basis functions employed is given.

Note that, in Chapter 3, the proposed theory will be included into a mixed-potential IE approach (MPIE) [Mosig, 1989] and it will be applied to the analysis of practical shielded microwave circuits, with planar metal patches printed at the dielectric interfaces. There, a careful comparative study will demonstrate that the proposed method is extremely competitive as compared with other numerical techniques known to the author, avoiding any convergence problems.

2.4.1 Continuous Auxiliary Sources Combined with Dynamic Ground Planes

This subsection first carefully describes the grounded MoM-based formulation for the computation of multilayered boxed Green's functions and their n-order spatial derivatives. Then, the location and definition of test and basis functions are carefully analyzed.

Theoretical Overview

Let us consider a multilayered rectangular cavity, which is excited by a point source. The first task is to obtain the Green's functions related to an infinite multilayered medium. This is easily accomplished using the Sommerfeld transformation [Michalski, 1998] applied to the corresponding spectral domain Green's functions ($\tilde{G}$) [Itoh, 1989] (see Section 2.2.2).

Then, the idea is to impose the boundary conditions on the potentials along the cavity contour, C. If the height of the cavity is electrically small, this imposition is performed only at a single height z (which usually corresponds to the air-dielectric interface where the circuit is printed). However, if the height of the cavity is electrically large, the imposition of the boundary conditions in one cross section of the cavity might not suffice to represent the correct behavior of the fields along its height. In this case boundary conditions are imposed on discrete heights ($z = 1...R$) of the cavity (see [Quesada Pereira et al., 2005b], [Gómez-Díaz et al., 2008c], and Section 2.3). This can be viewed as a kind of *point-matching* [Harrington, 1968] technique along the cavity height.

The next step is to introduce a set of auxiliary distributions of linear sources. These sources are located surrounding the cavity under analysis (following the contour C' shown in Fig. 2.22). Here, the term linear is employed to emphasize that a continuous distribution of sources (such as 1D wires) is used, instead of discrete punctual sources as it was previously done (see Section 2.3 and [Gómez-Díaz et al., 2008c]). The auxiliary linear sources are applied to compute both, the electric scalar and the magnetic vector potentials. In each case, the physical nature of the auxiliary linear sources corresponds to the potential under analysis (charge for the electric scalar potential and dipole currents for the magnetic vector potential). The unknown auxiliary distribution of sources are then computed to impose, in conjunction with the original point source, the boundary conditions on the lateral walls. Finally, the Green's functions inside the multilayered rectangular enclosure are recovered with the standard convolution integrals on the relevant sources of the problem

$$G_{V_{Box}}(\vec{r},\vec{r}\,'_{0,0}) = S_0\left[\tilde{G}_V\right]\Big|_{\vec{r}\,'_{0,0}}^{\vec{r}} + \int_{C'} S_0\left[\tilde{G}_V\right]\Big|_{\vec{r}\,'}^{\vec{r}} Q(\vec{r}\,')\partial\vec{r}\,', \tag{2.75}$$

$$G_{A_{Box}}^{xx}(\vec{r},\vec{r}\,'_{0,0}) = S_0\left[\tilde{G}_A\right]\Big|_{\vec{r}\,'_{0,0}}^{\vec{r}} + \int_{C'} S_0\left[\tilde{G}_A\right]\Big|_{\vec{r}\,'}^{\vec{r}} D^x(\vec{r}\,')\partial\vec{r}\,', \tag{2.76}$$

$$G_{A_{Box}}^{yy}(\vec{r},\vec{r}\,'_{0,0}) = S_0\left[\tilde{G}_A\right]\Big|_{\vec{r}\,'_{0,0}}^{\vec{r}} + \int_{C'} S_0\left[\tilde{G}_A\right]\Big|_{\vec{r}\,'}^{\vec{r}} D^y(\vec{r}\,')\partial\vec{r}\,', \tag{2.77}$$

where $Q(\vec{r}\,')$, $D^x(\vec{r}\,')$ and $D^y(\vec{r}\,')$ are the auxiliary set of linear charges and dipoles. Also, (S_0) denotes the zero-th order Sommerfeld transformation, applied to the spectral domain Green's functions for a specific source ($\vec{r}\,'$) and observer point ($\vec{r}$) locations.

The main drawback of this formulation occurs when the point source is located very close to a cavity wall (see Section 2.3.2). In this case, the use of auxiliary sources can not effectively compen-

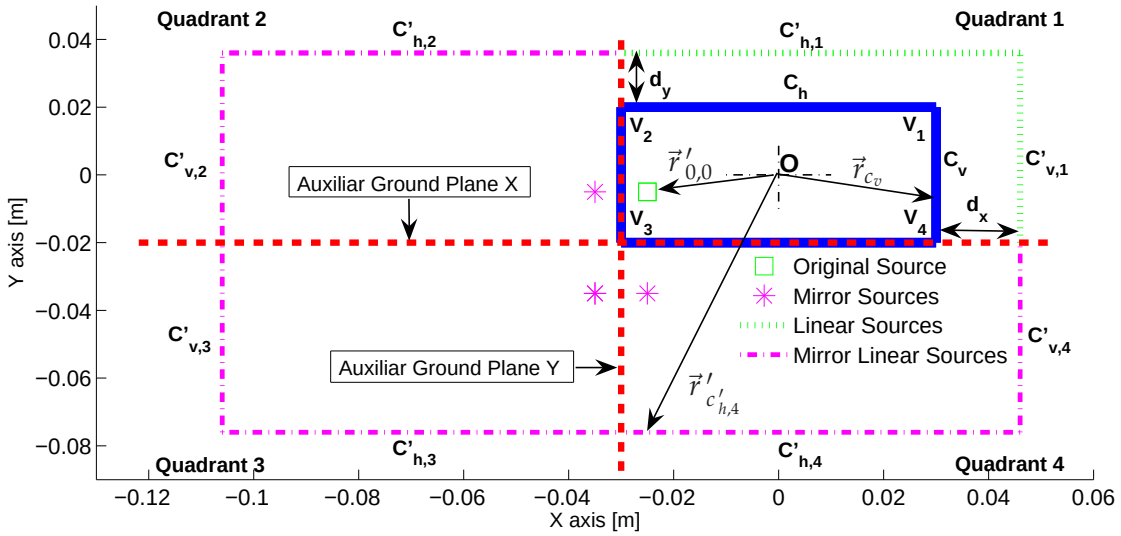

Figure 2.22 – An auxiliary linear distribution of sources ($C'_{h,1}$ and $C'_{v,1}$) is combined with two auxiliary ground planes to analyze a multilayered rectangular enclosure. Mirror linear sources, with respect to the ground planes, appear from the original set of linear sources. Potential boundary conditions are then numerically imposed along the non-covered cavity walls, and are perfectly imposed along the covered walls. The dimensions of the cavity are $60x40$ mm, and it is composed of 2 layers: a dielectric layer ($\epsilon_r = 2.2$ of thickness 3.17 mm), and an air layer (3.0 mm height). The source is placed at the position $(-25, -5, 3.14)$ mm. O is the coordinates origin and cavity center.

sate for the singular behavior introduced by the point source, and important errors in the Green's function computation might occur. This problem can totally be solved using the concept of dynamic ground planes. Using this approach, auxiliary ground planes are located covering two of the cavity walls (the closest to the point source), as can be seen in Fig. 2.22. The auxiliary set of linear sources are then located surrounding only the two non-covered walls, in order to impose there the boundary conditions. A set of mirror linear sources (and also mirror images, related to the original point source) appears with respect to the ground planes. Note that the values of all mirror sources are well-known from basic electromagnetic theory [Balanis, 1989]. The combinations of all sources *perfectly* impose the potential boundary conditions on the covered cavity walls, while these conditions are numerically imposed on the remaining two walls. This completely eliminates the instabilities related to the singular behavior of the source, because the ground planes are dynamically located as a function of the source position, imposing perfect boundary conditions on the critical walls (see Fig. 2.23). In this way, accuracy is preserved for all positions of the source point. Furthermore, this approach drastically decreases the computational effort required, because most of the auxiliary sources are mirror sources, whose values are known, and the size of the final system of linear equations is effectively reduced.

The problem now consists on obtaining the unknown auxiliary linear distribution of sources which are used to impose the required boundary conditions for the potentials at the remaining walls.

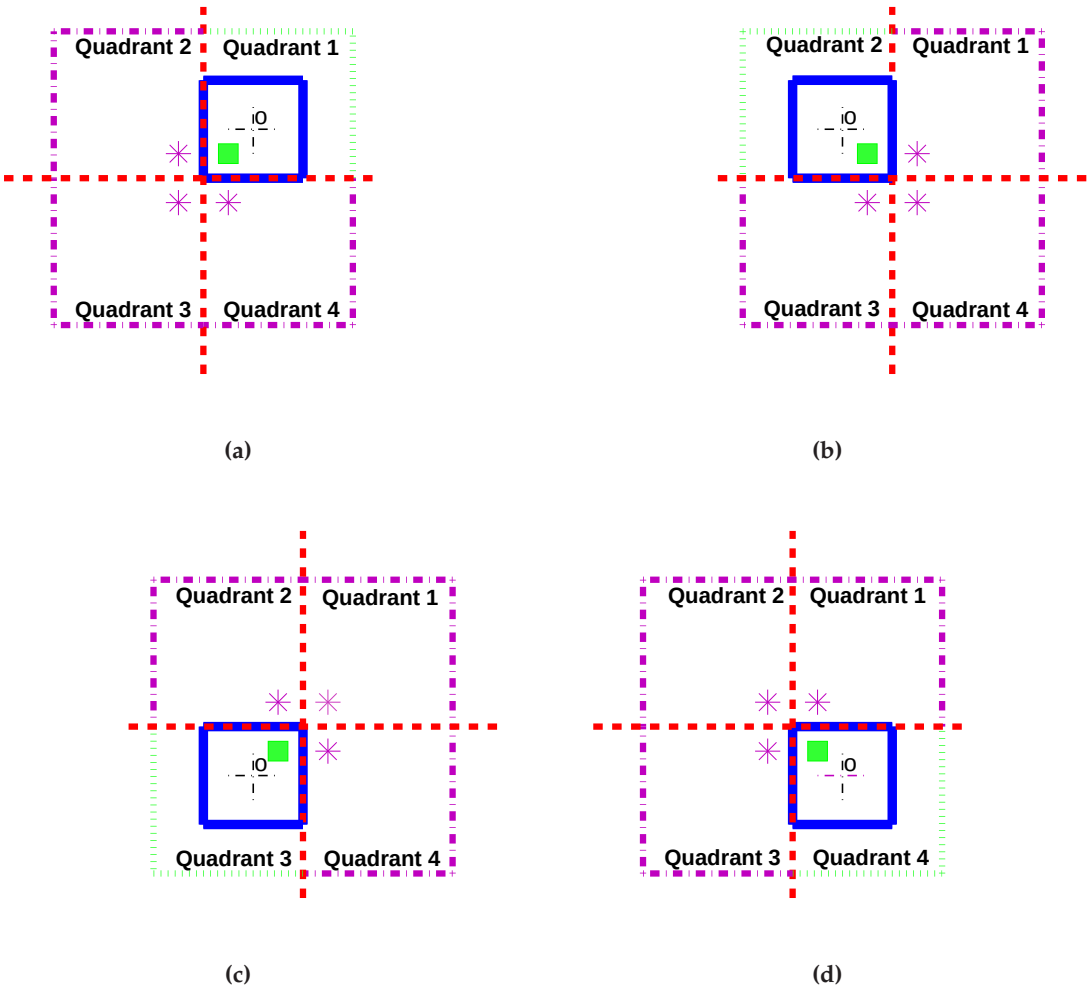

Figure 2.23 – Dynamic position of the auxiliary ground planes as a function of the point source location. The new planes position defines the quadrant where the cavity under analysis is placed, i.e., first (a), second (b), third (c) or forth (d) quadrant. The set of auxiliary linear sources is placed in the same quadrant as the cavity, whereas mirror linear sources appear in all other quadrants.

Specifically, in the case of the electric scalar potential, this condition is

$$G_{V_{Box}}(\vec{r},\vec{r}\,'_{0,0})|_C = 0, \tag{2.78}$$

which combined with Eq. (2.75) yields

$$\left[S_0\left[\tilde{G}_V\right]\Big|_{\vec{r}\,'_{0,0}}^{\vec{r}} + \int_{C'} S_0\left[\tilde{G}_V\right]\Big|_{\vec{r}\,'}^{\vec{r}} Q(\vec{r}\,')\partial\vec{r}\,'\right]\Bigg|_C = 0. \tag{2.79}$$

This last equation has the form of an integral equation [Mosig, 1989], where the auxiliary linear distribution of sources is the unknown. In order to solve this equation, we apply the method of moments [Harrington, 1968], expanding $Q(\vec{r}\,')$ as a sum of basis functions as

$$Q(\vec{r}\,') \approxeq \sum_{m=1}^{R}\sum_{k=1}^{B_V} \alpha_{k,m} \sum_{g=1}^{4} P_{G_V}(\vec{r}\,'_{0,0}, g) f_{V,b,a}^{g,k,m}(\vec{r}\,'), \tag{2.80}$$

		Auxiliary source quadrant [g]			
	Source quad.	Quad. 1	Quad. 2	Quad. 3	Quad. 4
P_{G_V}	1	+	-	+	-
	2	-	+	-	+
	3	+	-	+	-
	4	-	+	-	+
$P^x_{G_A}$	1	+	+	-	-
	2	+	-	-	+
	3	-	-	+	+
	4	-	+	+	-
$P^y_{G_A}$	1	+	-	-	+
	2	-	-	+	+
	3	-	+	+	-
	4	+	+	-	-

Table 2.7 – Signs which must be applied to the auxiliary sources as a function of the quadrants (defined by the ground planes) where the original point source and the auxiliary sources are located.

where R is the total number of rings, B_V is the total number of basis functions, $f^{g,k,m}_{V,b,a}(\vec{r}\,')$ is the basis function (indicated by the letter "b") number k, placed on the ring m, related to the scalar electric potential (V), and located on any (horizontal or vertical) direction a within the g quadrant (with $g = 1, 2, 3, 4$), and $\alpha_{k,m}$ is the weight associated to this basis function. Note that a specific weight $\alpha_{k,m}$ is associated to a particular basis function (k, m), but also to all its mirror basis functions (placed in all quadrants, $g = 1...4$). The adequate sign of each mirror basis function $\left[P_{G_V}(\vec{r}\,'_{0,0}, g)\right]$ depends on the quadrants of the point source and the mirror images, and it is given in Table 2.7.

Introducing Eq. (2.80) into the integral equation, a standard MoM technique yields to the following system of linear equations

$$\sum_{m=1}^{R}\sum_{k=1}^{B_V}\alpha_{k,m}\sum_{g=1}^{4}\int_C\int_{C'_{a,g}} f^{g,i,l}_{V,t,a}(\vec{r})S_0\left[\tilde{G}_V\right]\Big|^{\vec{r}}_{\vec{r}\,'}P_{G_V}(\vec{r}\,'_{0,0}, g)f^{g,k,m}_{V,b,a}(\vec{r}\,')\partial\vec{r}\partial\vec{r}\,' =$$
$$-\sum_{g=1}^{4}\int_C f^{g,i,l}_{V,t,a}(\vec{r})S_0\left[\tilde{G}_V\right]\Big|^{\vec{r}}_{\vec{r}\,'_{0,g}}P_{G_V}(\vec{r}\,'_{0,0}, g)\partial\vec{r}, \qquad (2.81)$$
$$l = 1, 2, 3, \ldots, R; \quad i = 1, 2, 3, \ldots, B_V,$$

where C is the cavity contour, $C'_{a,g}$ are the auxiliary linear sources placed on any (a) direction within the g quadrant, and $\vec{r}\,'_{0,g}$ is the position vector of the original or mirror point source located on the g quadrant (see Fig. 2.22). Note that the formulation also requires the use of test functions, which have been denoted as $f^{g,i,l}_{V,t,a}(\vec{r})$, where t indicates that it is a test function, i is the test function number and l is the number of ring.

After solving the system, the weights of the basis functions ($\alpha_{k,m}$) are recovered. This allows to

express the electric scalar potential inside the multilayered rectangular enclosure as

$$G_{V_{Box}}(\vec{r},\vec{r}\,'_{0,0}) = \sum_{g=1}^{4} S_0\left[\tilde{G}_V\right]\Big|_{\vec{r}'_{0,g}}^{\vec{r}} P_{G_V}(\vec{r}\,'_{0,0},g) + \sum_{m=1}^{R}\sum_{k=1}^{B_V}\alpha_{k,m}\sum_{g=1}^{4}\int_{C'_g} S_0\left[\tilde{G}_V\right]\Big|_{\vec{r}'}^{\vec{r}} P_{G_V}(\vec{r}\,'_{0,0},g) f_{V,b,a}^{g,k,m}(\vec{r}\,')\partial\vec{r}\,'. \tag{2.82}$$

Besides, note that the proposed formulation allows the easy computation of the boxed Green's functions spatial derivatives of order n, without requiring an additional computational effort. Following the procedure presented in Section 2.3, spatial derivatives are taken on Eq. (2.82) over the transverse source-observer spatial distance, ρ, leading to

$$\begin{aligned}\frac{\partial^n G_{V_{Box}}(\vec{r},\vec{r}\,'_{0,0})}{\partial\rho^n} &= \sum_{g=1}^{4} S_n\left[\tilde{G}_V\right]\Big|_{\vec{r}'_{0,g}}^{\vec{r}} P_{G_V}(\vec{r}\,'_{0,0},g) \\ &+ \sum_{m=1}^{R}\sum_{k=1}^{B_V}\alpha_{k,m}\sum_{g=1}^{4}\int_{C'_g} S_n\left[\tilde{G}_V\right]\Big|_{\vec{r}'}^{\vec{r}} P_{G_V}(\vec{r}\,'_{0,0},g) f_{V,b,a}^{g,k,m}(\vec{r}\,')\partial\vec{r}\,'.\end{aligned} \tag{2.83}$$

As commented in Section 2.3, the main advantage of this approach is that basis functions and their associated weights are independent of (ρ), and they are not affected by the derivative. This means that there is no need to reformulate the problem for this specific case, because the same weights computed for the potentials can be used for the derivatives. Besides, note that the spatial derivatives related to the x or y-directions can easily be obtained from these equations, simply by using the chain's rule of the derivative.

Let us suppose that the point source is now an x-oriented dipole. It is interesting to remark that this source, placed inside a rectangular cavity, can not create a y-oriented component. This is because the walls of the cavity are placed either parallel (horizontal) or antiparallel (vertical) with respect to the source, and they do not force the presence of cross-components [Balanis, 1989]. Note that this is a specific situation for the rectangular cavity, and that it does not hold in more general cavities (such as the arbitrarily-shaped convex structures discussed in Section 2.3). Therefore, for the case of a rectangular cavity the y-component of the dyadic Green's functions is directly, and strictly, zero.

In order to compute the x-component of the magnetic vector potential Green's functions inside the multilayered enclosure, the two boundary conditions that must be fulfilled are

$$G_{A_{Box}}^{xx}(\vec{r},\vec{r}\,'_{0,0})\Big|_{C_h} = 0, \tag{2.84}$$

$$\frac{\partial G_{A_{Box}}^{xx}(\vec{r},\vec{r}\,'_{0,0})}{\partial x}\Big|_{C_v} = 0, \tag{2.85}$$

where the suffix h and v denotes horizontal and vertical walls, respectively (see Fig. 2.22).

Analyzing these boundary conditions, one realizes that they are decoupled. This means that the conditions on the horizontal walls are not related to the conditions on the vertical walls. Therefore, the boundary conditions can be imposed separately on each wall, leading to the solution of two linear systems of $B_{A,\xi}$ unknowns (where $B_{A,\xi}$ is the number of basis function related to the wall ξ, with $\xi = h, v$) instead of solving one linear system of $2B_{A,\xi}$ unknowns (as was the approach presented

in Section 2.3 for more general cavities).

Introducing the general expression of the G_A^{xx} component, presented in Eq. (2.76), into Eq. (2.84) and Eq. (2.85), the two following integral equations are obtained

$$\left[S_0\left[\tilde{G}_A\right]\Big|_{\vec{r}\,'_{0,0}}^{\vec{r}} + \int_{C'_h} S_0\left[\tilde{G}_A\right]\Big|_{\vec{r}\,'}^{\vec{r}} D^x(\vec{r}\,')\partial\vec{r}\,'\right]\Bigg|_{C_h} = 0, \tag{2.86}$$

$$\left[S_1\left[\tilde{G}_A\right]\Big|_{\vec{r}\,'_{0,0}}^{\vec{r}} \frac{x-x'_{0,0}}{\sqrt{(x-x'_{0,0})^2+(y-y'_{0,0})^2}} + \int_{C'_v} S_1\left[\tilde{G}_A\right]\Big|_{\vec{r}\,'}^{\vec{r}} \frac{x-x'}{\sqrt{(x-x')^2+(y-y')^2}} D^x(\vec{r}\,')\partial\vec{r}\,'\right]\Bigg|_{C_v} = 0, \tag{2.87}$$

where $\vec{r}\,' = x'\hat{e}_x + y'\hat{e}_y$, $\vec{r}\,'_{0,0} = x'_{0,0}\hat{e}_x + y'_{0,0}\hat{e}_y$, and Eq. (2.38) and the chain's rule of the derivative have been employed for simplification purposes. Note that these two equations are very similar as the one obtained for the electric scalar potential [see Eq. (2.79)], but involving now the auxiliary set of linear dipoles, $D^x(\vec{r}\,')$. The method of moments is employed again to solve these two equations. For this purpose, $D^x(\vec{r}\,')$ is expanded as a sum of basis functions, in the following way

$$D^x(\vec{r}\,') \approx \sum_{m=1}^{R} \sum_{\xi=h,v} \sum_{k=1}^{B_{A,\xi}} \alpha_{k,m}^{x,\xi} \sum_{g=1}^{4} P_{G_A}^x(\vec{r}\,'_{0,0}, g) f_{A_x,b,\xi}^{g,k,m}(\vec{r}\,'), \tag{2.88}$$

where $\alpha_{k,m}^{x,\xi}$ is the weight related to k basis function, placed at the m ring, associated to the x-dipole source (denoted by A_x) and imposed on the ξ wall, and $P_{G_A}^x(\vec{r}\,'_{0,0}, g)$ (see Table 2.7) is the sign associated to each auxiliary source, as a function of the quadrant where it is defined.

Introducing Eq. (2.88) into the two integral equations, a standard MoM technique yields to following systems of linear equations

$$\begin{aligned}\sum_{m=1}^{R}\sum_{k=1}^{B_{A,h}} \alpha_{k,m}^{x,h} \sum_{g=1}^{4} \int_{C_h}\int_{C'_{h,g}} f_{A_x,t,h}^{g,i,l}(\vec{r}) S_0\left[\tilde{G}_A\right]\Big|_{\vec{r}\,'}^{\vec{r}} P_{G_A}^x(\vec{r}\,'_{0,0}, g) f_{A_x,b,h}^{g,k,m}(\vec{r}\,')\partial\vec{r}\partial\vec{r}\,' = \\ - \sum_{g=1}^{4} \int_{C_h} f_{A_x,t,h}^{g,i,l}(\vec{r}) S_0\left[\tilde{G}_A\right]\Big|_{\vec{r}\,'_{0,g}}^{\vec{r}} P_{G_A}^x(\vec{r}\,'_{0,0}, g)\partial\vec{r}, \\ l = 1,2,3,\ldots,R; \quad i = 1,2,3,\ldots,B_A,\end{aligned} \tag{2.89}$$

$$\begin{aligned}\sum_{m=1}^{R}\sum_{k=1}^{B_{A,v}} \alpha_{k,m}^{x,v} \sum_{g=1}^{4} \int_{C_v}\int_{C'_{v,g}} f_{A_x,t,v}^{g,i,l}(\vec{r}) S_1\left[\tilde{G}_A\right]\Big|_{\vec{r}\,'}^{\vec{r}} P_{G_A}^x(\vec{r}\,'_{0,0}, g) f_{A_x,b,v}^{g,k,m}(\vec{r}\,')\partial\vec{r}\partial\vec{r}\,' = \\ - \sum_{g=1}^{4} \int_{C_v} f_{A_x,t,h}^{g,i,l}(\vec{r}) S_1\left[\tilde{G}_A\right]\Big|_{\vec{r}\,'_{0,g}}^{\vec{r}} P_{G_A}^x(\vec{r}\,'_{0,0}, g)\partial\vec{r}, \\ l = 1,2,3,\ldots,R; \quad i = 1,2,3,\ldots,B_A.\end{aligned} \tag{2.90}$$

In the above notation, $C'_{h,g}$ and $C'_{v,g}$ refer to the horizontal and vertical auxiliary linear distribution of sources placed on the g quadrant (see Fig. 2.22). Besides, test functions are also employed in this formulation, which are denoted as $f_{A_x,t,\xi}^{g,i,l}$, following the nomenclature previously defined.

Once the two systems of linear equations have been solved, the weights of the basis functions are recovered, and the x-component of the magnetic vector potential can be expressed as

$$G^{xx}_{A_{Box}}(\vec{r},\vec{r}\,'_{0,0}) = \sum_{g=1}^{4} S_0\left[\tilde{G}_A\right]\Big|^{\vec{r}}_{\vec{r}\,'_{0,g}} P^x_{G_A}(\vec{r}\,'_{0,0},g) + \sum_{m=1}^{R}\sum_{\xi=h,v}\sum_{k=1}^{B_{A,\xi}} \alpha^{x,\xi}_{k,m}\sum_{g=1}^{4}\int_{C'_g} S_0\left[\tilde{G}_A\right]\Big|^{\vec{r}}_{\vec{r}\,'} P^x_{G_A}(\vec{r}\,'_{0,0},g) f^{g,k,m}_{A,b,a}(\vec{r}\,')\partial\vec{r}\,'. \tag{2.91}$$

As in the case of the electric scalar potential, the formulation also allows the easy computation of the Green's functions spatial derivatives of order n related to the multilayered cavity under analysis. By using Eq. (2.38), the derivatives of the magnetic vector potential are computed over the source-observer spatial distance, ρ, as

$$\begin{aligned}\frac{\partial^n G^{xx}_{A_{Box}}(\vec{r},\vec{r}\,'_{0,0})}{\partial\rho^n} &= \sum_{g=1}^{4} S_n\left[\tilde{G}_A\right]\Big|^{\vec{r}}_{\vec{r}\,'_{0,g}} P^x_{G_A}(\vec{r}\,'_{0,0},g) \\ &+ \sum_{m=1}^{R}\sum_{\xi=h,v}\sum_{k=1}^{B_{A,\xi}} \alpha^{x,\xi}_{k,m}\sum_{g=1}^{4}\int_{C'_g} S_n\left[\tilde{G}_A\right]\Big|^{\vec{r}}_{\vec{r}\,'} P^x_{G_A}(\vec{r}\,'_{0,0},g) f^{g,k,m}_{A,b,a}(\vec{r}\,')\partial\vec{r}\,'. \end{aligned}\tag{2.92}$$

Then, the spatial derivatives related to the x or y-directions are easily obtained by using the chain's rule of the derivative.

Finally, note that in the case of a y-oriented dipole located within the multilayered rectangular enclosure, a dual formulation can easily be derived.

Proper Termination of Basis/Test Functions

The use of auxiliary ground planes requires a proper definition and termination of the basis functions employed in the problem. After that, test functions are located along the non-covered walls of the cavity following similar ideas.

In the case of the electric scalar potential, the auxiliary charge must be zero at the ground planes. This condition is enforced by terminating the mesh with an entire basis function. Besides, the sharp corner on the auxiliary sources (contour C' in Fig. 2.22) is handled by employing two half-basis functions, that are interconnected, creating a unique basis function, to enforce continuity of the charge at the corner. This procedure is similar as the usually employed in the IE MoM for the modeling of junctions in the metalizations [Kolundzija and Djordjevic, 2002]. An example of this implementation is shown in Fig. 2.24a.

In the case of the magnetic vector potential, produced by an x-oriented source dipole, a zero value must be physically imposed for the auxiliary current at the x-oriented ground plane, whereas it does not vanish at the y-oriented ground plane [Balanis, 2005]. This is modeled by using an additional half-basis function attached to the y-oriented plane, and by terminating the mesh with an entire basis function on the x-oriented plane. Furthermore, note in Fig. 2.24b that two independent half-basis functions have been employed to treat the corner. These two half-basis functions are not interconnected, because each of them is referred to a different boundary condition and applied into a different IE. However, the presence of these two half roof-top functions at the corner is important,

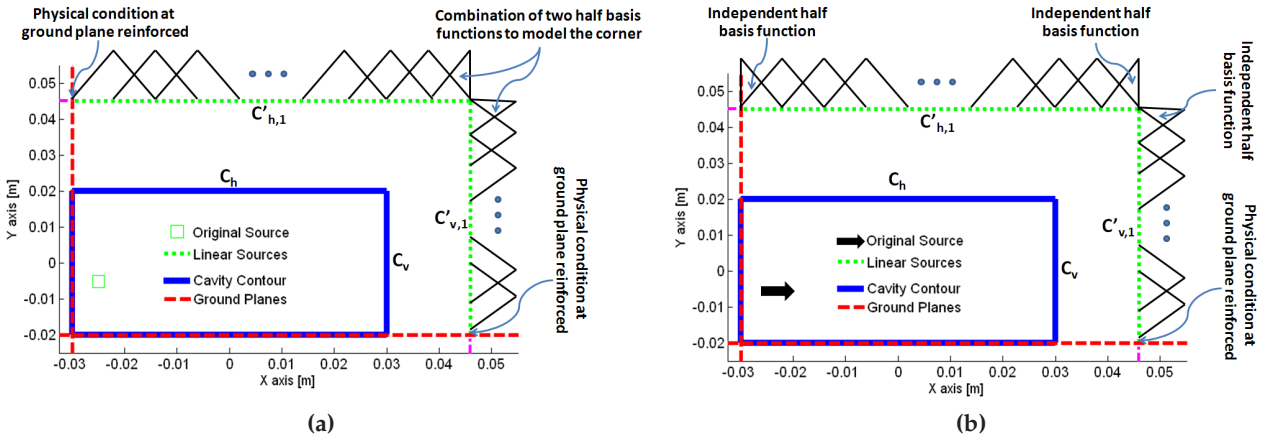

Figure 2.24 – Example of basis functions (rooftops) definition for the G_V (a) and G_A^{xx} (b) computation. In (a) the auxiliary linear charge continuity is enforced at the corner using two interconnected half-rooftops (which makes a unique basis function), meanwhile zero values of the charges are enforced at the ground planes. In (b), a zero value of the potential is forced at the x-oriented plane by terminating the mesh with an entire basis function. Any value of the potential is allowed at the y-oriented plane by inserting there a half-rooftop. The corner is modeled using two isolated half-rooftops.

since the current distribution will in general not be zero at the corner. An example of this implementation is shown in Fig. 2.24b. In the case that the source is a y-oriented dipole, an implementation dual to the proposed for the x-source is employed.

Basis/Test Functions Choice

The derived integral equations are singular-free, thanks to the use of ground planes. Therefore, the convergence of the proposed approach employing different basis/test functions is assured. However, the choice of adequate basis/test functions to solve the proposed IE is very important, and provides a trade-off between accuracy and speed. Three possible choices are presented and discussed below.

The first and simpler option is to use point matching [Harrington, 1968]. In this case, the formulation developed is very similar to the one proposed in Section 2.3, i.e. the auxiliary linear distribution of sources reduces to discrete spatial images/sources, which impose boundary conditions on discrete points along the cavity walls. However, there are two important differences. First, the use dynamic ground planes removes any numerical instability related to the singular behavior of the source, and second, the use of decoupled boundary conditions in the magnetic vector potential allows to solve two systems of linear equations (with $B_{A,h}$ and $B_{A,v}$ unknowns), instead of one system of linear equations with $B_{A,h} + B_{A,v}$ unknowns. The main drawback of point matching is that it may lead to ill-conditioned systems of equations, specially when the number of spatial points employed for the discretization increases. This greatly limits the accuracy of the computed Green's functions. On the other hand, point matching has the important advantage of being extremely fast, because all

integrals which appear in the formulation are reduced to the evaluation of the function at the test point.

The second option studied is to employ linear roof-top for testing, combined with dirac-delta functions for the basis functions. This choice presents an interesting compromise between accuracy and speed. The use of sub-domain test functions impose the boundary conditions on average along the cavity walls (instead of doing it on discrete points), by using a set of discrete sources (or images). Therefore, the overall error committed using this approach is lower than in the previous case. However, this error can not be arbitrarily small, due to ill-conditioned problems that arise in the system of equations when the auxiliary discrete sources become very close. In terms of speed, this approach is slower than the first method, because contour integrals must be numerically evaluated while imposing the boundary conditions. However, the use of auxiliary discrete sources reduces the double integrals to one-dimensional contour integrals. This makes the calculation of the Green's functions also very efficient.

The third and last option proposed is to use linear roof-top test and basis functions. In this case, the error committed can be very small, and it can arbitrarily be reduced by increasing the number of basis/test functions [Harrington, 1968]. This is because the auxiliary linear distribution of sources is able to effectively impose the boundary conditions along the non-covered cavities walls without encountering ill-conditioned situations. Therefore, this method is much more accurate than the previous ones. The main drawback of this approach is that double contour integrals must be performed when imposing the boundary conditions. This makes the computation required intensive. However, several integration schemes can be applied in order to further reduce this computational cost. For instance, most of the auxiliary/mirror sources are placed very far away from the cavity under analysis, and present a smooth behavior, allowing to solve these integrals with little computational effort.

2.4.2 Numerical Validation

This section presents numerical results to validate the proposed technique. For this purpose, the structure shown in Fig. 2.22 is analyzed. This cavity has a thick substrate (3.17 mm), which requires the use of two rings of auxiliary linear sources, the first placed at the dielectric interface and the other placed at a middled height of the substrate ($z = 1.57$ mm).

As commented in Section 2.3, one important advantage of the proposed method is that it allows to exactly know the error committed on the Green's functions computation. This can easily be done by evaluating the fulfilment of the boundary conditions along the cavity contour. In this case, since the use of auxiliary ground planes imposes perfect boundary conditions on the covered walls, only the error committed on the two remaining walls must be examined. For the electric scalar potential, this error is obtained by evaluating Eq. (2.78) along the two non-covered walls. In the case of the magnetic vector potential, the error is obtained by computing Eq. (2.84) for the non-covered horizontal wall and Eq. (2.85) for the non-covered vertical wall. In all cases, an ideal situation will provide a zero value for the relevant condition along the whole cavity perimeter.

The location of the auxiliary linear sources is an important parameter to be considered. In contrast to the approach presented in Section 2.3, the impact of this location on the method accuracy is

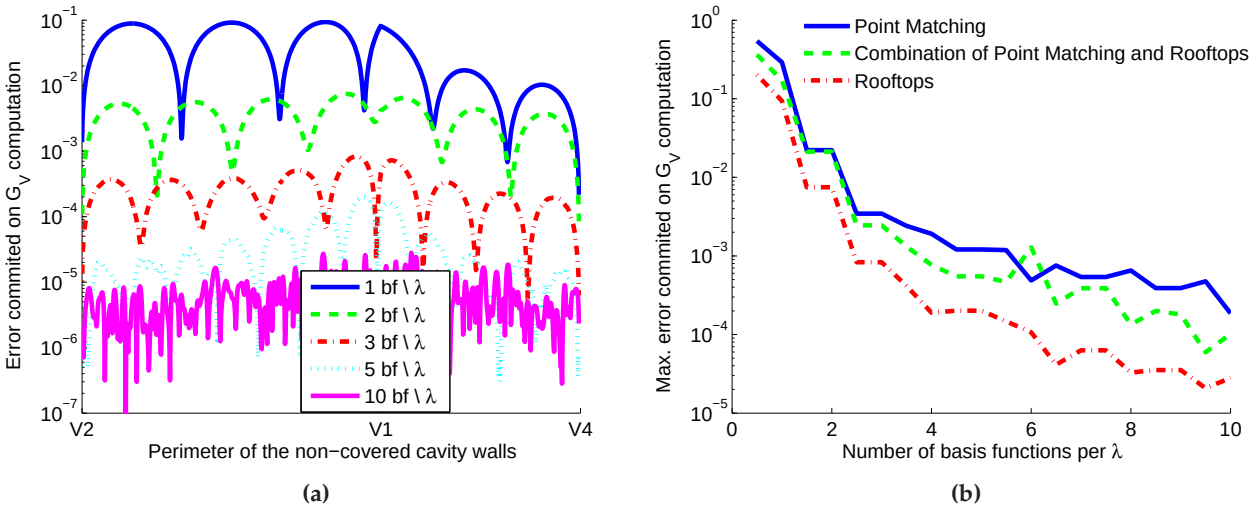

Figure 2.25 – Study of the error committed in the imposition of the G_V boundary conditions at 7 GHz when analyzing the cavity shown in Fig. 2.22. (a) Error committed along the non-covered walls, when different numbers of basis functions (rooftops) per λ are employed. V_X denotes the X-vertex of the cavity, as indicated in Fig. 2.22. (b) Maximum error committed versus the number and type of basis/test functions per λ employed.

very limited, because the proposed approach is singular-free and the method does not have to compensate for the singular behavior of the original source. Therefore, the method is inherently stable as a function of the location of the auxiliary sources. In spite of this, the number of unknowns required to obtain a desired precision varies. If the auxiliary sources are located very close to the cavity walls, their associated singular behavior may degrade the boundary conditions imposition. On the other hand, if the auxiliary sources are located very far away from the walls, the number of unknowns required to achieve a required precision increases, because the auxiliary sources lose effectiveness in representing the fine details of the cavity. Numerical results have shown that values of d_x and d_y (see Fig. 2.22) within the range of $0.2\lambda_0$-$2\lambda_0$ provide good convergence rates using a limited number of test/basis functions. In the following examples, the auxiliary linear sources are always located at the distances $d_x = d_y = 1.5\lambda$.

First, the error committed in the G_V computation at the frequency of 7 GHz is examined. The error is studied along the non-covered cavity walls as a function of the number of basis functions per λ (Fig. 2.25a). In this case, linear rooftop test/basis functions have been employed. As can be observed in the figure, the error is small with just one basis function per λ, and greatly decreases as the number of basis functions is increased. This demonstrates that the method is rapidly convergent, requiring a few number of basis functions to obtain very low errors. In Fig. 2.25b the maximum error is presented for different type and number of basis/test functions. In the case of using a point matching approach, the convergence is slower than in the other cases. This is expected, taking into account the convergence features of point matching inside integral equations [Harrington, 1968]. On the other hand, the use of point matching provides much faster results than the other approaches. In the second case, a combination of rooftops for testing with dirac-delta functions as basis functions

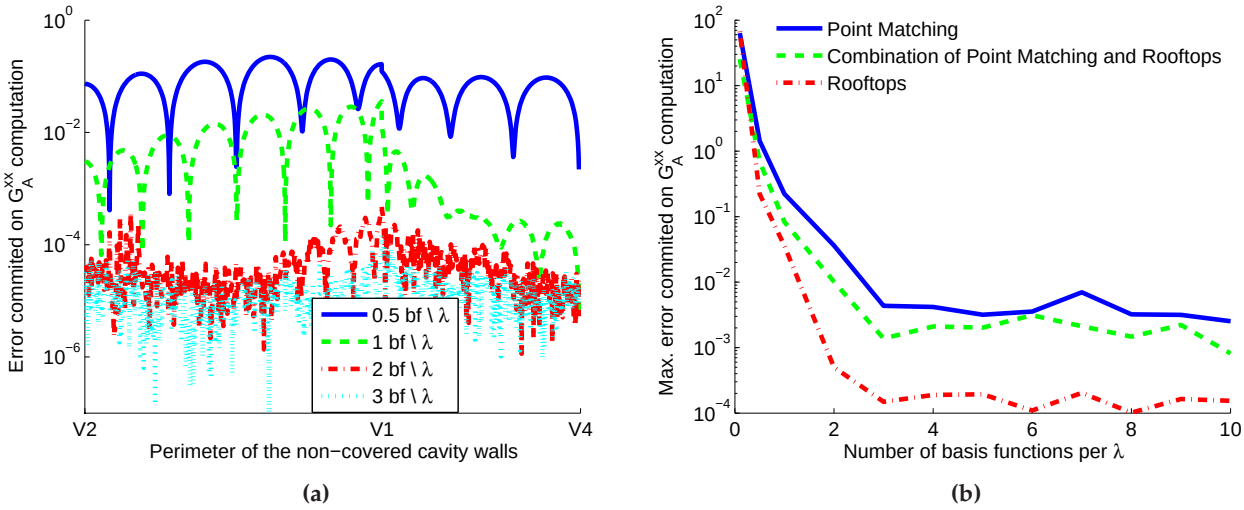

Figure 2.26 – Study of the error committed in the imposition of the G_A^{xx} boundary conditions [Eq. (2.84) and Eq. (2.85)] at 20 GHz when analyzing the cavity shown in Fig. 2.22. (a) Error committed along the non-covered walls, when different numbers of basis functions (rooftops) per λ are employed. V_X denotes the X-vertex of the cavity, as indicated in Fig. 2.22. (b) Maximum error committed versus the number and type of basis/test functions per λ employed.

is employed. This is a trade-off solution, with moderate improvement in the convergence rates and an slightly increase in the computational cost. The last option, which uses rooftop for the basis and test functions, presents the best convergence results. This is expected, because the complete auxiliary distribution of linear sources is employed to impose the boundary conditions along the contour. However, this approach has the drawback to be computationally more intensive than the other two. It is interesting to note that the use of 500 basis/test functions provides an error within the precision of the computer along the complete perimeter, showing that the method is inherently stable (the error can be reduced to arbitrary small values). The use of dirac-delta functions as basis functions can not provide this result, because it leads to an ill-conditioned system of linear equations when the number of basis functions is very high.

Second, the error committed on the G_A^{xx} computation is considered. At the frequency of 7 GHz, the effects of the cavity lateral walls on this potential (for the current location of the point source) are neglectable. However, as the frequency increases, the influence of the lateral walls is more and more important. For this reason, the frequency for the error analysis is set now to 20 GHz, where the lateral walls play a fundamental role in the potentials behavior. Fig. 2.26a shows the error along the cavity contour versus the number of basis functions (rooftops) employed, whereas in Fig. 2.26b a comparison of the maximum error commited, depending on the number and type of test/basis functions, is presented. The analysis of these results leads to the same conclusions as given for the G_V case, and confirms the effectiveness of the proposed approach.

In all cases, the accuracy of the proposed spatial technique depends on the accuracy of the method employed to compute the Sommerfeld transformation [Michalski, 1998]. Therefore, if small errors occurs while computing these transformations, they accumulate and propagate into the

Green's functions. This is specially important in the case of the first order Sommerfeld transformation (S_1), which usually requires more computational effort to achieve very low errors. An example of this error accumulation is shown in Fig. 2.26b, where the minimum error of 10^{-4} on the G_A^{xx} computation is fixed by the maximum error obtained while calculating S_1.

2.5 Green's Function Computation in Multilayered Shielded Cavities with Right Isosceles-Triangular Cross-Section

The spatial images techniques introduced in the previous sections allows the numerical computation of Green's functions in arbitrarily-shaped convex cavities. These approaches were useful approximations to the calculation of the exact Green's functions for these kind of multilayered cavities. In the process, the weights of the fictitious sources are numerically computed to impose the boundary conditions along the cavity walls. This imposition of the boundary conditions needs also to be done along the longitudinal direction (height), for electrically long cavities.

In this section, we present a new rigorous approach for the Green's functions calculation inside a multilayered shielded cavity with right isosceles triangular cross-section. The method is entirely developed in the spatial domain and it is based on image theory. Unlike the previous developed techniques, the method computes the Green's functions rigorously in the whole cavity, without introducing equivalent sources. The key idea is to split a multilayered square shaped box in two right isosceles triangular cavities (namely A and B as shown in Fig. 2.27). Then, we use the spatial domain Green's functions associated to the square cavity to recover the Green's functions related to one of the triangular waveguides. Note that the Green's functions of square cavities can be efficiently computed by using series acceleration techniques [Park and Nam, 1998], [Álvarez Melcón and Mosig, 2000] or by using the accurate method presented in Section 2.4. Once the Green's functions of the square cavity are computed, simple image theory is used to enforce the boundary conditions along the non-equal side of the triangle. In this way, for each point source inside (A), a spatial image will be placed in the other triangular cavity, (B). This image is able to exactly satisfy the boundary condition along the hypotenuse side of the triangular cavity, even along the longitudinal direction (height of the cavity). Finally, the Green's functions inside the triangle (A) are recovered by taking into account the presence of the original and of the image sources in the presence of the auxiliary square cavity.

As in the method presented in the previous sections, the proposed technique uses the concept of spatial images related to the electric scalar and magnetic vector potentials. However, it is important to remark that the present approach exactly satisfies the boundary conditions along the whole cavity wall (even along the height of the enclosure), and therefore it is not an approximation to the modeling of the enclosure. Furthermore, the images are computed using the Green's functions associated to a multilayered shielded square cavity, instead of the usual multilayered infinite medium. On the other hand, the use of this rigorous approach is restricted to the case of multilayered enclosures with triangular right-isosceles cross section.

The usefulness of the proposed technique is demonstrated by obtaining resonant frequencies and potentials patterns of a multilayered cavity with right isosceles triangular cross-section. The results are compared with those obtained by the finite-elements commercial software HFSS©, showing an

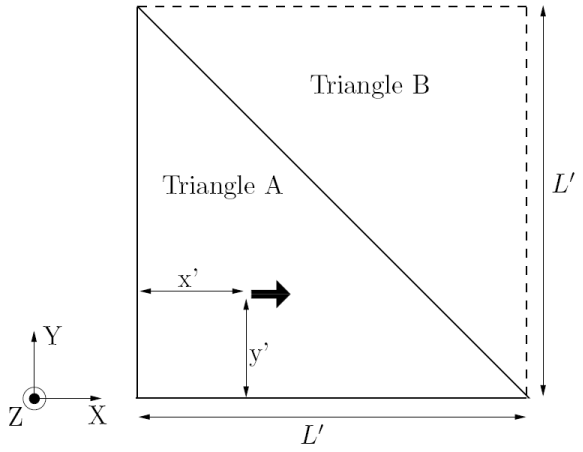

Figure 2.27 – A square box is split in two right-isosceles triangular cavities ("A" and "B"). A unitary electric dipole is placed inside triangle A. $L' = \lambda$, $x' = y' = 0.25\lambda$.

excellent agreement.

Besides, as in the previous sections, note that the proposed method will be applied in Chapter 3 for the analysis and design of shielded microwave filters. There, measured data will be employed to further confirm the accuracy and usefulness of the developed technique.

2.5.1 Theoretical Overview

The geometry for the calculation of the mixed-potential Green's functions is presented in Fig. 2.27. As it can be seen in the figure, an electric unitary dipole is placed inside a right-isosceles triangular metallic cavity (A). The final goal is to compute the Green's functions associated to this triangular cavity (A). To do that, a square cavity, which is composed of the original triangle (A) and of an auxiliary triangle (B) is considered. The Green's functions associated to a multilayered shielded square enclosure, as presented in Fig. 2.27, can efficiently be obtained in the spatial domain using, for instance, the procedure described in [Álvarez Melcón and Mosig, 2000], in [Park and Nam, 1998] or in Section 2.4. These square cavity Green's functions are then used to recover the Green's functions associated to the multilayered triangular cavity (A). To do that, an electric point source (q_e) or an electric unitary dipole (I) is placed inside this cavity (A) [see Fig. 2.28]. Then, the triangle (B) is used to place an exact image of the original source (q'_e or I'). Both original and image sources are computed using the square cavity Green's functions, and therefore, the boundary conditions at the external square walls are automatically satisfied. Finally, the original and image sources are combined to compute the Green's functions associated to the triangular cavity (A). Due to the combination of the original source with its image, the field will also satisfy the boundary conditions at the hypotenuse of the triangular cavity. Since the original and image sources are computed inside a multilayered structure, the final computed Green's functions will also take into account for the substrate layers.

The physical boundary condition to be imposed at the metallic cavity walls is the zero tangent electric field. This boundary condition can also be translated to the potentials. First, the electric scalar potential must vanish along the cavity walls. If a single electric point charge is placed inside the triangle A, the boundary condition will be automatically satisfied along the two external equal sides of

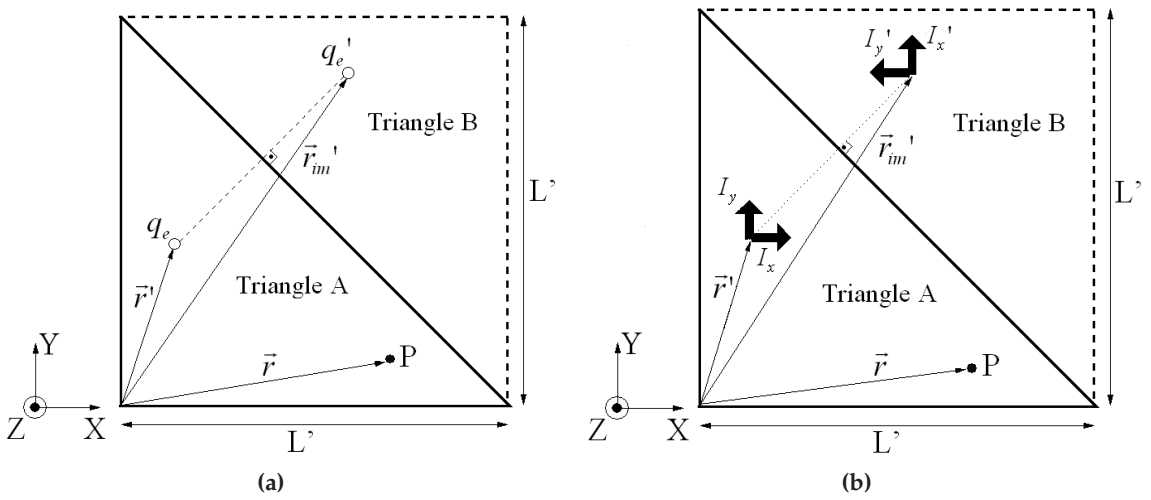

Figure 2.28 – Original and image electric charges and dipole sources used to enforce the boundary conditions for the electric scalar (a) and magnetic vector (b) potentials along the non-equal side of the triangular cavity. Point P is a generic observation point. $L' = \lambda$.

the triangular cavity. This is because these two sides are common to the square cavity used to calculate the basic Green's functions. In order to impose the boundary conditions along the hypotenuse of the triangle, a spatial image of the original source is placed inside triangle B (see Fig. 2.28a). From basic image theory [Balanis, 1989], the value of this new image is the same as the original, but with opposite sign. The combination of both sources will make the electric scalar potential to be zero along the hypotenuse of the triangle, even in the z-direction. Since the image also shares the square cavity sides, the boundary conditions are also satisfied in the other walls. Finally, the electric scalar potential inside the triangular cavity is recovered using a combination of the two sources as

$$G_{V_{Tri}}(\vec{r},\vec{r}\,') = G_{V_{Box}}(\vec{r},\vec{r}\,') - G_{V_{Box}}(\vec{r},\vec{r}\,'_{im}), \tag{2.93}$$

where $\vec{r}$ is a vector pointing towards an arbitrary observation point (P), $\vec{r}\,'$ is the source position (both inside triangle A), and $\vec{r}\,'_{im}$ is the source image position (placed in triangle B). It is important to remark that $G_{V_{Box}}$ is the electric scalar potential inside a square multilayered shielded cavity containing the triangular cavity.

For the evaluation of the magnetic vector potential dyadic Green's function, a similar procedure is followed, but taking into account the vector nature of this potential. Considering two unit dipoles inside triangle A (I_x and I_y, oriented along the x and y axis), two images dipoles can be placed inside triangle B (I'_x and I'_y, oriented along the y and x-axis respectively). These images are used to enforce the boundary conditions along the triangle hypotenuse (see Fig. 2.28b). Again, since all dipoles are placed inside the associated square cavity, the boundary conditions are also imposed along the external walls. By simple image theory, the values of the image dipoles are the same as the original, but their orientations have been rotated by 90 degrees [Balanis, 1989]. The final magnetic

vector potential is recovered using the superposition of all dipoles:

$$G^{xx}_{A_{Tri}}(\vec{r},\vec{r}\,') = G^{xx}_{A_{Box}}(\vec{r},\vec{r}\,'), \tag{2.94}$$
$$G^{yx}_{A_{Tri}}(\vec{r},\vec{r}\,') = G^{yy}_{A_{Box}}(\vec{r},\vec{r}\,'_{im}), \tag{2.95}$$
$$G^{xy}_{A_{Tri}}(\vec{r},\vec{r}\,') = -G^{xx}_{A_{Box}}(\vec{r},\vec{r}\,'_{im}), \tag{2.96}$$
$$G^{yy}_{A_{Tri}}(\vec{r},\vec{r}\,') = G^{yy}_{A_{Box}}(\vec{r},\vec{r}\,'), \tag{2.97}$$

where $\vec{r}$ is a vector pointing towards an arbitrary observation point (P), $\vec{r}\,'$ is the source position (both inside triangle A), and $\vec{r}\,'_{im}$ is the source images position (placed in triangle B). It is worth mentioning that, according to these expressions, an x-directed dipole will produce a y-component of the magnetic vector potential (and viceversa). This cross component is given by the image dipole I'_x, which is oriented along the y-axis. Physically, this cross component is caused by the hypotenuse wall of the triangular cavity.

The computational effort required to evaluate the proposed Green's functions for multilayered triangular cavities represents twice the effort required for the computation of the Green's functions associated to multilayered square cavities, which is the key element of the proposed formulation. Note that for the computation of the latter, different techniques for series acceleration, such as those proposed in [Álvarez Melcón and Mosig, 2000],[Park and Nam, 1998], and in Section 2.4 may be applied.

2.5.2 Numerical Validation

In order to demonstrate the usefulness of the proposed technique, the resonant frequencies and potential patterns of a multilayered triangular cavity are obtained. The results are validated using the data computed by the finite elements commercial software HFSS©.

In Fig. 2.29a a multilayered shielded triangular cavity with right isosceles cross-section is shown. To obtain the resonances of the cavity, the potentials are represented as a function of frequency for a fixed position of source and observation points. In Fig. 2.29b, sharp peaks in the potential response can be observed. These peaks are closely related to the resonant frequencies of the cavity. It is important to remark that at exactly the natural frequencies of the cavity, the value of the potentials will tend to infinity. Consequently, to find the resonant frequencies of the cavity we detect the maximum value of the potentials given by the selected frequency step during the frequency sweep. To study the accuracy of the results, the same study has been performed by the commercial software HFSS©. As it can be seen in Table 2.8, high accuracy has been achieved, maintaining in all cases a relative error below 0.08%, when the frequency step is 0.005λ. It is important to note that the accuracy obtained directly depends on the step length taken by the frequency sweep. When this step becomes smaller, the error decreases. For example, when the frequency step is reduced to 0.0025λ, the maximum relative error is always below 0.04%.

The proposed method can also compute the potentials (even at the cavity resonances) without any convergence problem. To show that this is indeed the case, the electric scalar potential is shown in Fig. 2.30 at the normalized frequency of $\frac{L'}{\lambda} = 0.2851$, where L' denotes the physical length of the two equal sides of the triangle (see Fig. 2.27). Furthermore, the magnetic vector potential G^{yy}_A is depicted

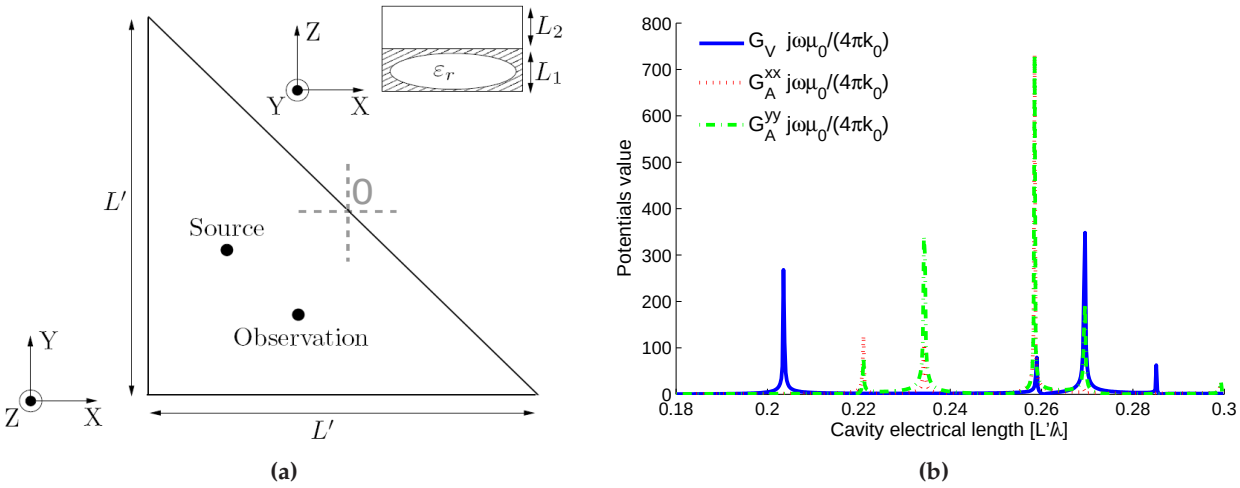

Figure 2.29 – Computation of the resonant frequencies related to a triangular cavity. (a) Multilayered shielded triangular cavity with right isosceles cross-section. $L' = \lambda$, $L_1 = 0.2\lambda$, $L_2 = 0.2\lambda$, $\varepsilon_r = 5.0$. O is the origin of the coordinate system. The point source is placed at the position $(-0.25\lambda, -0.15\lambda, 0.2\lambda)$, and the observation point is placed at $(-0.15\lambda, -0.25\lambda, 0.2\lambda)$. (b) Mixed potentials as a function of the cavity electrical length.

Resonance frequencies, Images Method [GHz]	**Resonance frequencies, HFSS© [GHz]**	**Relative Difference (%)**
0.2035	0.2035	0.0000
0.2210	0.2209	0.0453
0.2342	0.2342	0.0000
0.2585	0.2583	0.0774
0.2588	0.2587	0.0387
0.2695	0.2693	0.0743
0.2851	0.2849	0.0702
0.2991	0.2990	0.0334

Table 2.8 – Resonant frequencies for the triangular cavity shown in Fig. 2.29a.

in Fig. 2.31 at the normalized frequency of $\frac{L'}{\lambda} = 0.2991$. In both cases, a noise-free potential pattern can be observed. Note that the potential values have been normalized, and the representation avoids the singular behavior found at exactly the source position. The same study has been performed using the commercial software HFSS©, obtaining similar results for the z-component (see Fig. 2.30b) and for the y-component (see Fig. 2.31b) of the electric field, respectively.

Finally, in order to verify the boundary conditions for the computed Green's functions, we include in Fig. 2.32 a plot of the magnetic vector potential produced by a y-directed unitary dipole, in

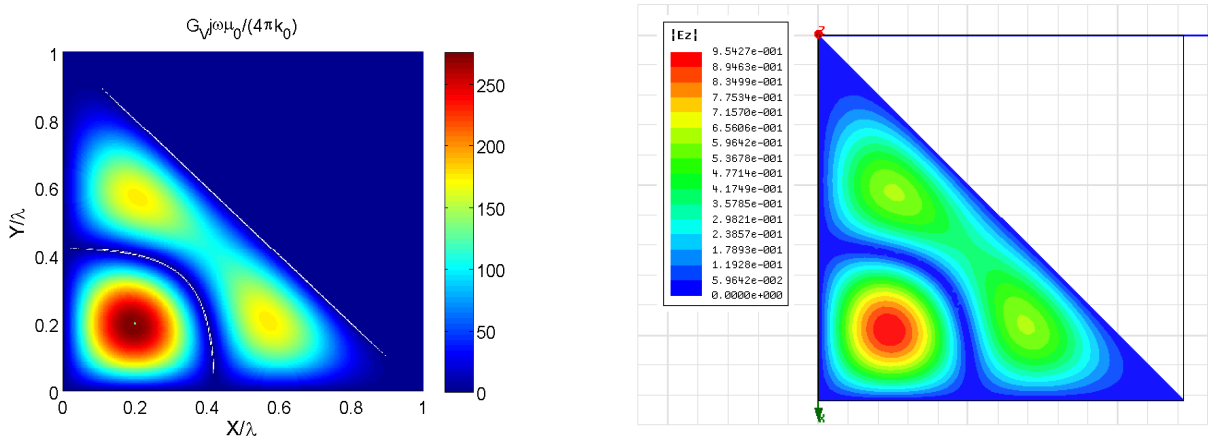

(a) **(b)**

Figure 2.30 – Potential pattern related to the multilayered cavity with a right-isosceles triangular cross-section at the normalized resonant frequency $\frac{L'}{\lambda} = 0.2851$. (a) Electric scalar potential obtained with the proposed technique. The source is placed at the position $(0.2\lambda, 0.2\lambda, 0.2\lambda)$. (b) Z-component of the electric field obtained with the commercial software HFSS©.

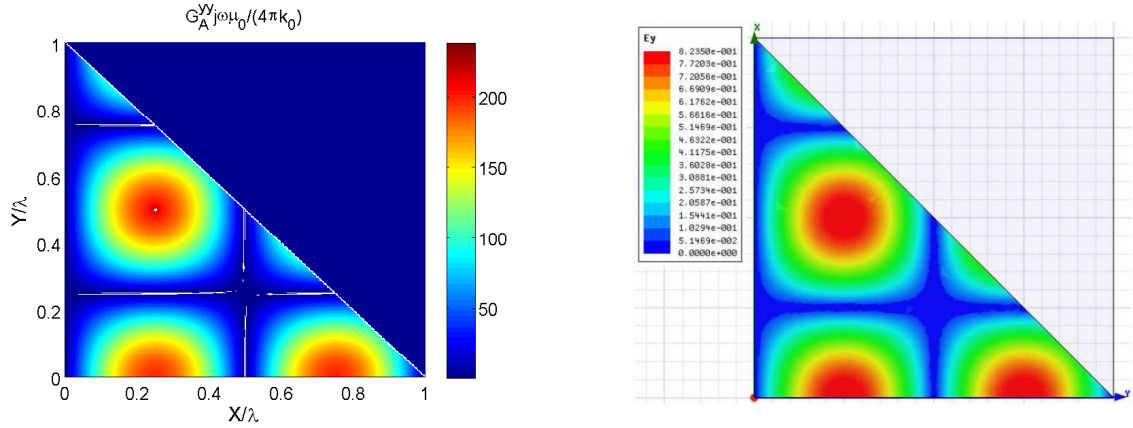

(a) **(b)**

Figure 2.31 – Potential pattern related to the multilayered cavity with a right-isosceles triangular cross-section at the normalized resonant frequency $\frac{L'}{\lambda} = 0.2991$. (a) Magnetic vector potential dyadic component G_A^{yy} obtained with the proposed technique. The source is placed at the position $(0.22\lambda, 0.5\lambda, 0.2\lambda)$. (b) Y-component of the electric field obtained with the commercial software HFSS©.

the same conditions as in Fig. 2.31. We can observe in the figure that the magnetic vector potential remains perpendicular to the three walls of the cavity, therefore fulfilling with accuracy the proper boundary conditions.

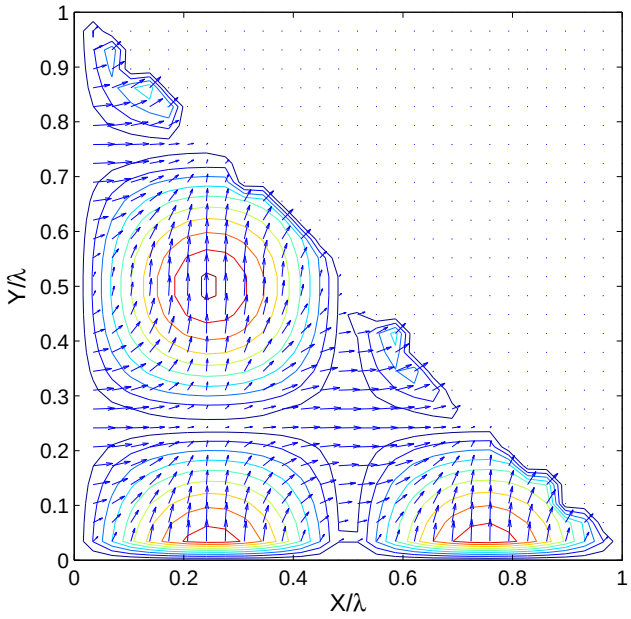

Figure 2.32 – Vector plot of the magnetic vector potential produced by a y-directed unitary dipole in the same conditions as in Fig. 2.31.

2.6 Conclusions

In this chapter I have presented three techniques for the numerical computation of multilayered shielded Green's functions and their associated spatial derivatives. The first technique is formulated in the spatial domain, and employs a set of auxiliary charges and dipoles to impose the boundary conditions for the potentials along the cavity contour. In this way, multilayered cavities with convex arbitrarily-shaped cross sections are efficiently modeled. The presence of dielectric layers and the boundary conditions at the top and bottom covers of closed cavities are taken into account through the Sommerfeld transformation applied to the spectral domain Green's functions. Furthermore, for the analysis of electrically long cavities, the use of several rings of images surrounding the whole cavity at different heights has been proposed. Results reveal that the convergence of the algorithm is achieved with low computational effort, just requiring about 4 spatial images per λ of the structure under analysis. Besides, the proposed algorithm presents the important advantage of providing a measure of the error committed in the imposition of the boundary conditions, which allows to identify and solve possible numerical instabilities. For the sake of validation, the resonant frequencies and potential patterns related to several multilayered enclosures (with different cross-sections, namely trapezium, rectangular and triangular), have been computed and compared to those obtained by the commercial software HFSS©. The excellent agreement found confirms the accuracy of the proposed technique.

The second method is related to the computation of multilayered rectangular boxed Green's functions and their spatial derivatives. The technique combines the use of auxiliary ground planes, which cover two walls of the cavity, with a set of auxiliary linear distribution of sources employed to impose the boundary conditions along the cavity contour. Mirror linear sources appear with respect

to the planes, perfectly imposing boundary conditions on the two covered walls. On the other two walls, a numerical imposition of these conditions has led to a set of integral equations. A convergence study, related to the test and basis functions choice, has been presented and discussed. The numerical results presented have shown that the technique is very fast, inherently stable and avoids any singular behavior. Besides, it has been demonstrated that arbitrarily small errors in the Green's functions computation can be achieved.

The third and last method proposed is related to the numerical evaluation of Green's functions inside multilayered cavities with triangular right-isosceles cross section. The spatial-domain Green's functions for a square multilayered box are used to accurately obtain the Green's function for the triangular cavity. Image theory has then been employed to exactly enforce the boundary conditions for the potentials along the nonequal side of the triangular cavity. Resonant frequencies and potential patterns inside a multilayered triangular cavity have been obtained and validated by using results from the commercial software HFSS©. Again, the excellent agreement found confirms the accuracy of the method.

Thanks to the use of the proposed novel approaches, multilayered shielded Green's functions have been efficiently calculated in many different situations, rigourously taking into account the effects of the lateral walls and their influence on the potentials behavior. The novel methods will be included in Chapter 3 into a mixed-potential integral equation (MPIE), and will be used for the fast analysis of microwave shielded devices. There, full-wave simulations and measured data will fully confirm the accuracy and efficiency of the proposed algorithms.

Chapter 3

Analysis of Multilayered Boxed Circuits and Application to the Design of Hybrid Waveguide-Microstrip Filters

3.1 Introduction

In Chapter 2 of this work I presented several techniques for the calculation of multilayered Green's functions associated to cavities with convex arbitrarily-shaped cross section. In the present chapter, I applied the Green's functions methods previously derived to the analysis and design of multilayered shielded microwave circuits.

Planar technologies, composed of thin metallizations embedded within flat layered media, are one of the main approaches to fabricate circuits in the microwave and millimiter wave domains. The use of closed cavities provides physical support to microwave devices, immunity against electromagnetic interferences and avoids unwanted radiation. However, shielding enclosures also introduces additional effects that must rigorously be taken into account [Dunleavy and Katehi, 1988b], [Dunleavy and Katehi, 1988a], [Faraji-Dana and Chow, 1995]. The accurate and extremely fast analysis of this type of shielded circuits (see Fig. 3.1) is currently a fundamental requirement for modern microwave systems, telecommunication applications and the spatial industry.

In order to analyze and design these devices, general full-wave techniques (such as FEM [Lee et al., 1997], FDTD [Taflove and Hagness, 2005] or TLM [Hoefer, 1985]) may be used. These techniques are able to handle almost any structure, usually obtaining very accurate results. The main drawback of such approaches is that they require to mesh the whole cavity, including dielectrics and printed circuits [which is not always easy, due to dimensions difference between the printed circuits (usually small) and the cavity (which may be big)], leading to large execution times. Furthermore, these methods do not provide any physical insight into the behavior of the structure under study.

One efficient alternative for the analysis of these boxed devices is to em-

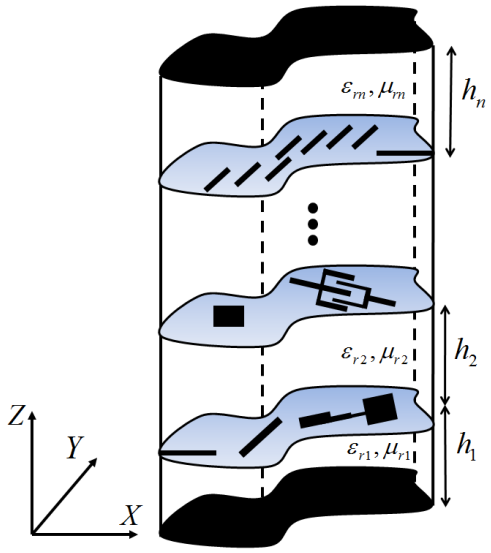

Figure 3.1 – Generic schematic of a shielded multilayered device.

ploy the integral equation (IE) technique [Mosig, 1989], solved by the method of moments (MoM) [Harrington, 1968]. The IE method can be formulated either in the spectral [Jansen, 1985], [Dunleavy and Katehi, 1988a], [Park and Nam, 1997], [Álvarez Melcón and Mosig, 2000], [Bozzi et al., 2001], [Tsalamengas and Fikioris, 2005] or in the spatial domain [Railton and Meade, 1992], [Eleftheriades et al., 1996], [Álvarez Melcón et al., 1999]. The spectral domain, which is widely employed, is usually very efficient, but it presents important convergence problems when the dimensions of the cells employed to discretize the printed circuits are very small as compared to the enclosure. On the other hand, the spatial domain usually expresses the boxed multilayered Green's functions in terms of infinite sums of spatial images, which are very slowly convergent (see Section 2.2.3 of Chapter 2 and [Itoh, 1989]). Even though several acceleration techniques have been proposed to seep-up the convergence of these series (see [Brezinski and Zaglia, 1991], [Kinayman and Aksum, 1995], [Park et al., 1998], [Park and Nam, 1998], [Gentili et al., 1997] or [Pérez-Soler et al., 2008]), the analysis of shielded circuits using spatial domain approaches is still unpractical. Besides, note that, up to date, IE techniques only allows the analysis of printed circuits placed in rectangular or circular [Zavosh and Aberle, 1995] multilayered enclosures.

This chapter is organized as follows. In Section 3.2, I briefly review the Electric Field Integral Equation (EFIE) [Mosig, 1989] which is solved by using the method of moments (MoM) [Harrington, 1968]. Besides, I also give an overview of all the steps required for the numerical implementation of this method. The formulation, based on the works of [Mosig, 1989], [Alvarez Melcon, 1998], [Quesada-Pereira, 2007] is able to analyze a general structure (see Fig. 3.1) composed of an arbitrary number of printed complex circuits. This approach may incorporate any type of spatial Green's functions, such as the free-space Green's functions. However, in order to take into account for the multilayered media and the lateral walls of the structure under analysis, the novel Green's functions developed in Chapter 2 are employed.

Then, in Section 3.3 I present two acceleration techniques for the efficient implementation of the

Green's functions into an IE formulation. The techniques take advantage of the particular features related to the spatial images technique employed to compute the Green's functions. The first technique (see [Gómez-Díaz et al., 2008b]) is based on the bilinear interpolation. Instead of directly interpolate the Green's functions, which have fast variations and strong singularities [Wang et al., 2004], [Pascual García et al., 2006], the idea is to interpolate the complex values of the charge and dipole images, which present a smooth behavior. Then, the final Green's functions are efficiently recovered using the interpolated values of the images. The second method exploits the fact that, in the Green's functions presented in Chapter 2, the source term is naturally separated from the contribution of the spatial images/linear sources that take into account the effects of the cavity lateral walls (see [Gómez-Díaz et al., 2008c]). Using this important feature, two MoM matrixes are computed separately. The first matrix contains the singular behavior, and can be efficiently handled [Michalski, 1998], [Quesada-Pereira, 2007]. The second matrix only contains the images contribution, which presents a very smooth behavior, and it may be computed using very limited computational effort. This matrix decomposition allows the extremely fast IE analysis of multilayered shielded circuits.

In Section 3.3, a novel hybrid waveguide-microstrip technology is presented. This technology arises from the Green's functions study of multilayered shielded enclosures at their resonant frequencies. This filter technology combines one resonance, provided by the multilayered cavity, with N microstrip resonators, leading to a $N+1$ order filter. The proposed technology is light, compact, low-lossy, uses the filter package as a part of the filter, and allows to easily implement transmission zeros. Therefore, it is ideal for space applications. A simple procedure is also presented for the effective design of this type of structures. Then, in order to demonstrate the hybrid waveguide-microstrip technology usefulness, several prototypes printed on different multilayered cavities have been designed, analyzed and fabricated. The analysis and design of these filters have been performed using the methods described in this chapter, and excellent agreement among these results, measurements and full-wave simulations performed with commercial packages have been found in all cases, fully validating the novel filtering structure.

Finally, Section 3.5 presents several examples of microwave shielded circuits. Specifically, coupled-line filters [Guglielmi and Alvarez-Melcon, 1995], broadside-coupled filters [Alvarez-Melcon et al., 2001], and novel designs based on the hybrid waveguide-microstrip technology are investigated in detail. There, the IE formulation described in this chapter, combined with the Green's functions introduced in Chapter 2, is fully validated. Besides, the efficiency of the acceleration techniques presented in this chapter is verified. Specifically, a comparison of the time required to analyze different circuits, using the proposed method and several IE-based alternatives, is presented. The results presented there reveal that the proposed techniques are extremely competitive, in terms of convergence, accuracy and efficiency, as compared with any other technique known to the author.

3.2 Standard Mixed Potential Integral Equation

This section briefly reviews a standard Electric Field Integral Equation (EFIE) [Mosig, 1989] which is solved by using the method of moments (MoM) [Harrington, 1968]. The goal is to obtain a

software tool which allows us to study and analyze multilayered shielded microwave circuits.

The first step is to employ a Mixed-Potential Integral Equation (MPIE) [Mosig, 1989], [Alvarez Melcon, 1998] for the scattering analysis of metal conductors. We have chosen the MPIE formulation instead of the Field Integral Equation (FIE) formulation because it allows a much easier treatment of the Green's function singular behavior. The MPIE formulation requires the computation of the electromagnetic scalar and vector potentials of the problem, under point source excitations (i.e. the so called mixed potentials Green's functions). Following this approach, the electric currents flowing along the conductors of the device are accurately retrieved. Note that this procedure only requires the discretization of the metal patches under consideration, which may be performed using different meshing strategies. Besides, it is important to remark that the metal patches of the structure (not the cavity itself) do not define a closed structure, and therefore, the possibly numerical instabilities related to the EFIE internal resonances are completely avoided [Peterson et al., 1998].

Specifically, in this work a Galerkin version of the MoM has been implemented. Standard rectangular and triangular cells, related to rooftop [Rao, 1980] and Rao-Wilton-Glisson (RWG) [Rao et al., 1982] test and basis functions, are employed for meshing the metal patches. Furthermore, losses in the printed metallizations are also included using the Leontovich boundary condition combined with the concept of the surface impedance of a nonperfect conductor [Pelosi and Ufimtsev, 1996].

The MPIE formulation may incorporate any type of spatial Green's functions, such as the free-space Green's functions. However, in order to take into account for the multilayered media and the enclosure of the structure under analysis, the novel Green's functions developed in Chapter 2 are employed. Note that this step does not require any change in the MPIE formulation, but it allows to automatically incorporate the behavior of the multilayered cavity into the formulation.

The MPIE procedure described in this section, combined with the Green's function analysis presented in Chapter 2, allows the accurate and extremely fast analysis of multilayered shielded circuits, as fully demonstrated in Section 3.5. The rest of this section is organized as follows. Section 3.2.1 presents a detailed derivation of the MPIE formulation. Then, Section 3.2.2 gives an overview of the steps required by any generic IE procedure.

3.2.1 Basic MPIE Formulation

Let us consider a microwave structure composed of an arbitrary number of planar metallic patches printed on a multilayered media, as shown in Fig. 3.2a. The total field within the structure [$\vec{E}(\vec{r})$] is composed of the *impressed* or incident field [denoted as $\vec{E}^i(\vec{r})$] and the field *scattered* by the metal patches [$\vec{E}^s(\vec{r})$], and it may be expressed as

$$\vec{E}(\vec{r}) = \vec{E}^i(\vec{r}) + \vec{E}^s(\vec{r}). \tag{3.1}$$

The standard procedure of IE [Mosig, 1992] applies the equivalence theorem [Balanis, 1989], which replace each metal patch (p) by an equivalent electrical current ($\vec{J}_{s_p}$). This is clearly shown in Fig. 3.2. These equivalent currents also radiates into the structure, generating the scattered field

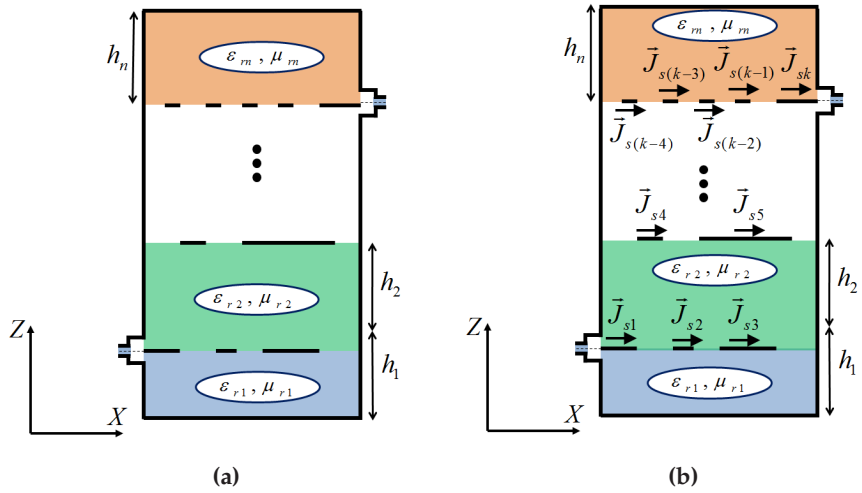

Figure 3.2 – Equivalence theorem. (a) Original multilayered shielded device. (b) Equivalent problem.

$\vec{E}^s(\vec{r})$. This field may be expressed in a mixed-potential form as

$$\vec{E}^s(\vec{r}) = -j\omega\vec{A}(\vec{r}) - \nabla\phi_e(\vec{r}), \tag{3.2}$$

where the auxiliary potentials are defined by

$$\vec{A}(\vec{r}) = \sum_{p=1}^{k} \int_{s_p} \bar{\bar{G}}_A(\vec{r},\vec{r}\,') \cdot \vec{J}_{s_p}(\vec{r}\,')ds'_p, \tag{3.3}$$

$$\phi_e(\vec{r}) = \sum_{p=1}^{k} \int_{s_p} G_V(\vec{r},\vec{r}\,')\rho_{s_p}(\vec{r}\,')ds'_p. \tag{3.4}$$

In these last expressions, k is the total number of metallic surfaces of the structure, $\vec{J}_{s_p}$ and ρ_{s_p} are the equivalent current and charge induced on the metal patch p, which has a surface s_p, and $\bar{\bar{G}}_A$ and G_V are the magnetic dyadic and electric scalar Green's functions associated to the problem. Note that the equivalent current and charge induced on a metal patch p are related by the continuity equation [Balanis, 1989] as follows

$$\nabla' \cdot \vec{J}_{s_p}(\vec{r}\,') = -j\omega\rho_{s_p}(\vec{r}\,'). \tag{3.5}$$

Then, boundary conditions for the fields must be imposed. In the case of a structure such as the one shown in Fig. 3.2, the adequate boundary condition is the vanishing of the tangent electric field on the printed metallic surfaces. This condition may be expressed as

$$\vec{n} \times \vec{E}(\vec{r})\big|_{s_u} = \vec{n} \times \left[\vec{E}^i(\vec{r}) + \vec{E}^s(\vec{r})\right]\Big|_{s_u} = 0, \qquad u = 1,2,\ldots,k, \qquad \text{For all: } s_u \in s_e, \tag{3.6}$$

where s_e represent the collection of all metallic patches.

Besides, note that the goal of the formulation is the analysis of shielded circuits, composed by metallic patches. In this specific situation, there is not any equivalent magnetic current within the

structure, i.e.,

$$\vec{M} = 0. \tag{3.7}$$

Eq. (3.6) assumes that the patches are composed of perfect metals. However, in real cases the metals employed are not perfect, i.e. their associated conductivity is not infinite. In these cases, the finite conductivity of the metals may easily be incorporated to Eq. (3.6) using the impedance (Leontovich) boundary condition [Pelosi and Ufimtsev, 1996], as follows

$$\vec{n} \times \vec{E}(\vec{r})\big|_{s_u} = \vec{n} \times \left[\vec{E}^i(\vec{r}) + \vec{E}^s(\vec{r})\right]\big|_{s_u} = Z_{s_u}\left[\vec{n} \times \vec{J}_{s_u}(\vec{r})\right], \qquad u = 1, 2, \ldots, k, \qquad \text{For all: } s_u \in s_e, \tag{3.8}$$

where the term Z_{s_u} is the surface impedance of the u^{th} metal conductor, and it may be expressed as

$$Z_{s_u} = (1 + j)\sqrt{\frac{\pi f \mu_0}{\sigma_{s_u}}}, \tag{3.9}$$

where f is the frequency, μ_0 is the free-space permeability and σ_{s_u} is the finite conductivity of the metal placed on the surface s_u.

Including Eq. (3.2) into this last equation, the EFIE condition can be expressed as

$$\begin{aligned}\vec{n} \times \vec{E}^i(\vec{r})\big|_{s_u} = \vec{n} \times \Bigg[& Z_{s_u}\vec{J}_{s_u}(\vec{r}) + \sum_{p=1}^{k} j\omega \int_{s_p} \bar{\bar{G}}_A(\vec{r}, \vec{r}\,') \cdot \vec{J}_{s_p}(\vec{r}\,') ds'_p \\ & - \frac{1}{j\omega} \int_{s_p} \left[\nabla G_V(\vec{r}, \vec{r}\,')\right] \left[\nabla' \cdot \vec{J}_{s_p}(\vec{r}\,')\right] ds'_p \Bigg]\Bigg|_{s_u} \\ & u = 1, 2, \ldots, k, \qquad \text{For all: } s_u \in s_e. \end{aligned} \tag{3.10}$$

Note that $\vec{J}_{s_p}$ is the only unknown inside the above integral equation.

The next step is to transform the integral equation into a discrete (matrix) equation, which may easily be solved. For this purpose, we apply the method of moments (MoM) [Harrington, 1968]. In this approach, each unknown (equivalent current $\vec{J}_{s_p}$) is expanded as a linear combination of a set of N_p vector basis functions $\vec{f}_n^{(p)}$. In this work, metallic patches of complex arbitrary shape will be analyzed, and therefore, subdomain basis functions (rooftop [Rao, 1980] and RWG [Rao et al., 1982]) are employed. Following this procedure, the unknown equivalent currents induced in the metallic patches may be expressed as

$$\vec{J}_{s_p}(\vec{r}\,') \approx \sum_{n=1}^{N_p} \alpha_n^{(p)} \vec{f}_n^{(p)}(\vec{r}\,'), \qquad p = 1, 2, \ldots k \qquad \text{For all: } s_p \in s_e, \tag{3.11}$$

where $\vec{r}\,'$ is the position vector of a point inside the printed metallization, N_p is the total number of basis function employed to expand the current on the p^{th} metal patch, and $\alpha_k^{(p)}$ are the unknown coefficients in the expansion of the current on the s_p surface.

Inserting the form of the equivalent induced currents into Eq. (3.10), we obtain

$$\vec{n}\times\vec{E}^i(\vec{r})\big|_{s_u}=\vec{n}\times\left\{\sum_{q=1}^{N_u}Z_{s_u}\alpha_q^{(u)}\vec{f}_m^{(u)}(\vec{r})+\sum_{p=1}^{k}\sum_{n=1}^{N_p}\alpha_n^{(p)}\left[j\omega\int_{s_p}\bar{\bar{G}}_A(\vec{r},\vec{r}\,')\cdot\vec{f}_n^{(p)}(\vec{r}\,')ds'_p\right.\right.$$
$$\left.\left.-\frac{1}{j\omega}\int_{s_p}\left[\nabla G_V(\vec{r},\vec{r}\,')\right]\left[\nabla'\cdot\vec{f}_n^{(p)}(\vec{r}\,')\right]ds'_p\right]\right\}\Bigg|_{s_u}$$
$$u=1,2,\ldots,k,\qquad\text{For all: } s_u\in s_e. \tag{3.12}$$

In this work, the MoM is solved using a Galerkin procedure [Mosig, 1989]. Therefore, we choose as testing functions the same set of functions as we have used before as basis functions. For this purpose, we multiply Eq. (3.12) by the set of test function $\vec{f}_m^{(u)}(\vec{r})$ (with $u=1,2,\ldots k$) and we integrate over the corresponding testing surface, s_u. This leads to the following system of linear equations

$$\int_{s_u}\left[\vec{n}\times\vec{E}^i(\vec{r})\right]\cdot\vec{f}_m^{(u)}(\vec{r})ds_u=$$
$$\vec{n}\times\left\{\sum_{q=1}^{N_u}Z_{s_u}\alpha_q^{(u)}\int_{s_u}\vec{f}_m^{(u)}(\vec{r})\cdot\vec{f}_m^{(u)}(\vec{r})ds_u+\sum_{p=1}^{k}\sum_{n=1}^{N_p}\alpha_n^{(p)}\left[j\omega\int_{s_u}\vec{f}_m^{(u)}(\vec{r})\int_{s_p}\bar{\bar{G}}_A(\vec{r},\vec{r}\,')\cdot\vec{f}_n^{(p)}(\vec{r}\,')ds'_pds_u\right.\right.$$
$$\left.\left.+\frac{1}{j\omega}\int_{s_u}\left[\nabla\cdot\vec{f}_m^{(u)}(\vec{r})\right]\int_{s_p}\left[\nabla'\cdot\vec{f}_n^{(p)}(\vec{r}\,')\right]G_V(\vec{r},\vec{r}\,')ds'_pds_u\right]\right\}$$
$$u=1,2,\ldots k\qquad\text{For all: } s_u\in s_e, \tag{3.13}$$

where the surface divergence theorem [Balanis, 1989] has been applied to transfer the gradient from the scalar potential Green's functions to the testing functions.

Following the Galerkin procedure, the original system of integral equations has been transformed into an algebraic linear system of equations. From this system, the following scalar product, related to the basis function n, defined on the p^{th} metal patch, and to the test function m, defined on the u^{th} metal patch, may be defined as

$$Z_{m,n}^{(u,p)}=\vec{n}\times\left\{Z_{s_u}\int_{s_u}\vec{f}_m^{(u)}(\vec{r})\cdot\vec{f}_m^{(u)}(\vec{r})ds_u+j\omega\int_{s_u}\vec{f}_m^{(u)}(\vec{r})\int_{s_p}\bar{\bar{G}}_A(\vec{r},\vec{r}\,')\cdot\vec{f}_n^{(p)}(\vec{r}\,')ds'_pds_u+\right.$$
$$\left.+\frac{1}{j\omega}\int_{s_u}\left[\nabla\cdot\vec{f}_m^{(u)}(\vec{r})\right]\int_{s_p}\left[\nabla'\cdot\vec{f}_n^{(p)}(\vec{r}\,')\right]G_V(\vec{r},\vec{r}\,')ds'_pds_u\right\}. \tag{3.14}$$

In addition, the known term of the excitation vector can easily be defined as

$$V_{ex}^{(u)}(m)=\begin{cases}\int_{s_u}\vec{f}_m^{(u)}(\vec{r})\cdot\left[\vec{n}\times\vec{E}^i(\vec{r})\right]ds_u, & \text{if}\quad s_u\in s_{ex}\\ 0, & \text{if}\quad\text{Otherwise}\end{cases}, \tag{3.15}$$
$$u=1,2,\ldots k,$$

where the new set s_{ex} has been defined as the set containing all interfaces where input and output ports are placed in order to excite the structure.

The general form of the complete system of linear equation in a matrix fashion may be given as

follows

$$\begin{pmatrix} \bar{\bar{Z}}^{(1,1)} & \bar{\bar{Z}}^{(1,2)} & \dots & \bar{\bar{Z}}^{(1,k)} \\ \bar{\bar{Z}}^{(2,1)} & \bar{\bar{Z}}^{(2,2)} & \dots & \bar{\bar{Z}}^{(2,k)} \\ \vdots & \vdots & \ddots & \vdots \\ \bar{\bar{Z}}^{(k,1)} & \bar{\bar{Z}}^{(k,1)} & \dots & \bar{\bar{Z}}^{(k,k)} \end{pmatrix} \begin{pmatrix} \vec{\alpha}^{(1)} \\ \vec{\alpha}^{(2)} \\ \vdots \\ \vec{\alpha}^{(k)} \end{pmatrix} = \begin{pmatrix} \vec{V}_{ex}^{(1)} \\ \vec{V}_{ex}^{(2)} \\ \vdots \\ \vec{V}_{ex}^{(k)} \end{pmatrix}, \tag{3.16}$$

where the submatrix $\bar{\bar{Z}}^{(u,p)}$ is defined as

$$\bar{\bar{Z}}^{(u,p)} = \begin{pmatrix} Z_{1,1}^{(u,p)} & Z_{1,2}^{(u,p)} & \dots & Z_{1,N_p}^{(u,p)} \\ Z_{2,1}^{(u,p)} & Z_{2,2}^{(u,p)} & \dots & Z_{2,N_p}^{(u,p)} \\ \vdots & \vdots & \ddots & \vdots \\ Z_{N_u,1}^{(u,p)} & Z_{N_u,2}^{(u,p)} & \dots & Z_{N_u,N_p}^{(u,p)} \end{pmatrix}, \tag{3.17}$$

the vector $\vec{V}_{ex}^{(p)}$ is defined as

$$\vec{V}_{ex}^{(p)} = \begin{pmatrix} V_{ex}^{(p)}(1) \\ V_{ex}^{(p)}(2) \\ \vdots \\ V_{ex}^{(p)}(N_p) \end{pmatrix}, \tag{3.18}$$

and the vector $\vec{\alpha}^{(p)}$ is defined as

$$\vec{\alpha}^{(p)} = \begin{pmatrix} \alpha_1^{(p)} \\ \alpha_2^{(p)} \\ \vdots \\ \alpha_{N_p}^{(p)} \end{pmatrix}. \tag{3.19}$$

The inversion of the matrix system in Eq. (3.16) provides the values of the unknown coefficients α_n^p (with $p = 1, 2, \dots k$). These coefficients are then employed to recover the induced electric current on the metal patches defined on the structure.

3.2.2 Steps of a Generic IE Procedure

An standard integral equation procedure may be implemented using different approaches. The following steps are always identified in an standard implementation of a IE-MoM technique [Mosig, 1992], [Alvarez Melcon, 1998], [Stevanovic, 2005].

a) Geometrical Discretization

The IE formulation presented in Section 3.2.1 allows the analysis of circuits composed of complex arbitrarily-shaped printed metallic circuits. Therefore, these complex geometries must be discretized, using triangular or rectangular cells, by efficient meshing techniques. Nowadays, there are many available tools that can perform this

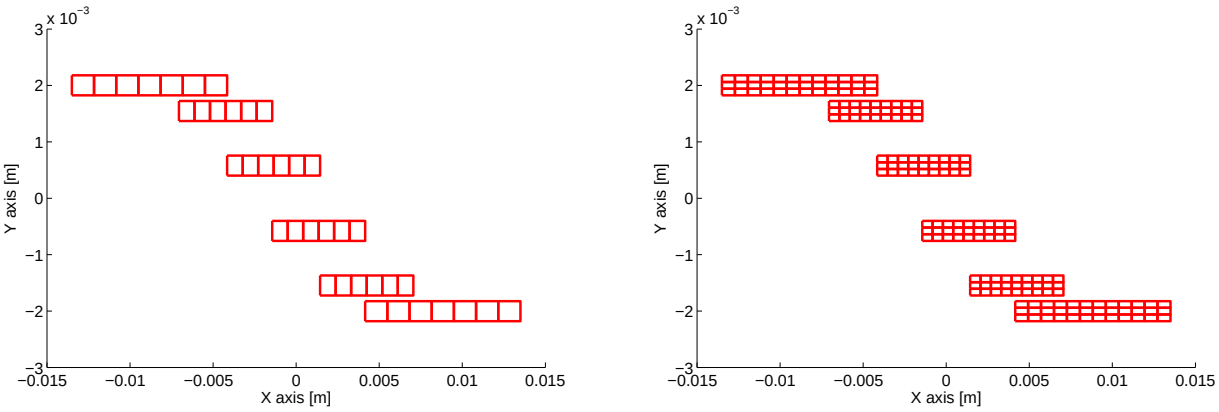

Figure 3.3 – Example of two different meshes employed to discretize a coupled-line 4-poles bandpass filter.

task (such us GiD [International Center for Numerical Methods in Engineering, 2011] or Gmesh [Geuzaine and Remacle, 2011]).

In this thesis, I have used a dedicated meshing software tool developed in [Alvarez Melcon, 1998]. A simple example of the meshing routines employed is shown in Fig. 3.3, which presents a coupled-line 4-poles bandpass filter discretized with one row (a) and a dense (b) mesh strategy.

b) Formulation and Computation of the Green's Functions

As explained in detailed in Chapter 2, the Green's functions represents the impulse response of a specific environment, and consequently, Green's functions are able to completely characterize that environment. The spatial IE implementation described in Section 3.2.1 requires that the Green's functions associated to a particular media must be available in the spatial domain. Besides, the efficient evaluation of these Green's functions for a huge combinations of observer-source pairs is needed in order to analyze microwave circuits in a reasonable amount of time.

In the literature, theare are many extremely efficient techniques for the computation of Green's functions related to free-space and multilayered infinitely-extended media [Balanis, 1989], [Michalski, 1998], [Alvarez Melcon, 1998], [López-Frutos, 2011]. Therefore, the IE analysis of metallic structures placed on these environments is very efficient.

On the other hand, and as explained in Section 2.2.3 of Chapter 2, the computation of Green's functions associated to multilayered boxed media has usually been less efficient in the spatial domain [Itoh, 1989], [Mosig, 1989], [Michalski, 1998], [Alvarez Melcon, 1998] or presents important convergence problems in the spectral domain [Alvarez Melcon, 1998]. Besides, only Green's functions related to rectangular [Park and Nam, 1997] or circular-shaped [Zavosh and Aberle, 1995] multilayered enclosures have been derived to date. Therefore, the fast IE analysis of microwave circuits printed on shielded multilayered media is still a challenging task.

In this work, the IE formulation introduced in Section 3.2.1 is combined with the Green's functions computation described in Chapter 2. Note that these Green's functions are further accelerated with the techniques presented in Section 3.3. This allows the fast analysis and design of microwave shielded circuits. However, note that the described IE formulation also allows to analyze printed circuits placed on other type of media, if the adequate Green's functions are provided.

c) Filling the MoM matrix

The filling of the MoM matrix, defined in Eq. (3.16), represents most of the numerical effort required for the analysis of microwave circuits. As it can be observed from Eq. (3.14), the components of the MoM matrix are scalar products expressed in terms of integrals, which are extended to the subdomain basis and test functions selected in each case. In the IE implemented in this work, rooftop [Rao, 1980] and RWG [Rao et al., 1982] basis and test functions are employed.

There are two basic types of interactions in the MoM matrix. In the case that basis and test functions are defined over non-common cells, the integrals are non singular and they can be numerically integrated using cubature rules [Cools, 1999] specially adapted to triangular or rectangular domains. Further details about this implementation can be found in [Alvarez Melcon, 1998], [Quesada-Pereira, 2007]. In case that the basis and test functions are defined over the same cell, the resulting integrals are singular. In this case, the integral is transformed into polar coordinates, where the Jacobian of the transformation will cancel out the singularity, and the integral can be computed numerically [Morita et al., 1990],[Alvarez Melcon, 1998],[Quesada-Pereira, 2007]. Alternative techniques to treat the singularities are based on the analytical evaluation of the static contribution (see [Wilton et al., 1984] and [Pérez-Soler et al., 2010]).

d) Definition of an excitation vector

The excitation of the input/output ports of the device provides a connection between the real physical world and the mathematical model employed to describe the structure under analysis. The physical excitation provides the vector of independent terms to the IE linear system [see Eq. (3.16)]. Once this linear system of equations is solved, the computed equivalent currents must be translated into physical quantities, such as scattering parameters, impedances, etc.

In this work, the δ-gap excitation model is employed [Eleftheriades and Mosig, 1996], [Alvarez Melcon, 1998]. This simple model is accurate to represent the input/output ports of shielded circuits, which is the goal of this work. However, different excitation models (based on incident plane waves [Stevanovic, 2005] or coplanar waveguide structures [Otero et al., 1997], [Alvarez Melcon, 1998]) may also may used within the IE formulation described in Section 3.2.1, in order to model different situations.

The δ-gap model assumes that each port is excited by a voltage source, with a constant magnitude of V_e along the width of the line, applied over an infinitesimal gap of zero length across the ground plane and the tip of the feeding line. Following this model, the incident (or impressed) excit-

ing field may be expressed as

$$\vec{E}^i(\vec{r}) = V_e \delta(\vec{r} - \vec{r}_e)\hat{e}_e, \tag{3.20}$$

where $\vec{r}_e$ is the position of the e^{th} port and $\hat{e}_e$ is the unit vector normal to the side on which the port is placed. Inserting this last equation into Eq. (3.15), the MoM excitation vector yields non-zero elements only for half basis functions [Alvarez Melcon, 1998]. Is should be noted that the voltage source is restricted to the domain of the conductor, i.e., it only exists along the width of the line where the generator is applied.

e) Solving the matrix equation

The discretization of complex geometries, related to microwave devices, may result into a very large number of unknowns (N). This number completely depends on the type of geometry and also on the number of cells per λ employed for this discretization.

On the contrary as other full-wave techniques (such as FDTD [Taflove and Hagness, 2005] of FEM [Lee et al., 1997]), the MoM matrices are not sparse. Therefore, direct methods for solving large linear equations, such as the LU decomposition [Press et al., 1996a], [Press et al., 1996b], must be employed. These methods have a complexity $\mathcal{O}(N^3)$, while filling the MoM matrix and the Green's functions computation normally have a complexity of $\mathcal{O}(N^2)$ and $\mathcal{O}(N)$, respectively. Therefore, inverting the MoM matrix has usually been considered the bottleneck of the IE approach.

However, this situation has changed over the last years. First, the modeling of complex environments has led to the development of more complicated Green's functions. Second, numerous advances have recently been proposed to solve large and full linear system of equations, such as [Heldrind et al., 2002] or [Rius et al., 2008]. Therefore, the bottleneck of the IE has moved from inverting the MoM matrix to the matrix filling (and the consequent Green's functions computation), specially when the number of unknowns is not very large.

In this work, a standard LU decomposition method [Press et al., 1996a], [Press et al., 1996b] is applied to solve the MoM system of linear equations. This is because the proposed IE approach only require to mesh the printed metallizations of the circuits, which usually requires a limited number of unknowns. In this situation, the LU method is very efficient, because it does not require any preprocessing time as other special technique based on iterative methods. Thereby, the seep-up in the analysis of this type of circuits relies on the efficient computation of multilayered shielded Green's functions and in the filling of the MoM matrix.

f) Recovering equivalent or system parameters of the structure

In order to recover the equivalent or system parameters related to the structure under analysis, a procedure based on standard circuit theory is followed [Mosig, 1989], [Eleftheriades and Mosig, 1996]. Let us assume that the device presents a total of N_g ports. First, each port (e) is excited using a δ-gap model, while the rest of the ports are short-circuited (Y-matrix

definition). Then, the current flowing on the r^{th} port is obtained as

$$I(r,e) = \int_{r_{edge}} \vec{J}_{(s_r),(e)}(\vec{r}\,') \cdot \hat{e}_e, d\vec{r}\,', \tag{3.21}$$

where $\hat{e}_e$ is the unit vector normal to the side on which the r^{th} port is defined, and $\vec{J}_{(s_r),(e)}$ is the current flowing on the metal patch connected to the r^{th} port when the excitation is applied to the e^{th} port. Note that the integration is performed along the r^{th} port edge.

Next, the intrinsic input admittance matrix (dimensions $N_g \times N_g$) is obtained as

$$Y(r,e) = \frac{I(r,e)}{V_e}, \qquad r = 1,2,\dots N_g, \quad e = 1,2,\dots N_g. \tag{3.22}$$

Once the admittance matrix is known, the input impedance related to each port and the scattering parameters can easily be obtained using well-know network equations [Matthaei et al., 1964] [Pozar, 2005]. Note that these relations inherently take into account the reference impedance of the port, required to the scattering parameters computation.

3.3 Acceleration Techniques for the Efficient Green's Function Implementation into an MPIE Formulation

The computation of multilayered boxed Green's functions in both, the spatial [see Eq. (2.27)] or spectral [see Eq. (2.29)] domain is usually a very time-consuming task. This is because the infinite sums involved in these calculations are very slowly convergent. In the case of the spectral domain, Eq. (2.29), the convergence is faster when the observation point is close to the lateral walls, because each term of the modal sum satisfies the boundary conditions on the walls. However, only an infinite number of modes would take into account the singularity at the source point, which leads to a slow convergence of the summation when the observation and source points are close. In the case of the spatial domain, Eq. (2.27), the situation is inverted. This is because the singularity at the source point is inherently considered in the expression, so the convergence is greatly improved when the observation and source points are close. However, only an infinite number of images would perfectly take into account for the boundary conditions imposed on the lateral walls, which leads to a slow convergence ratio when the observation point is close to a cavity wall.

Due to these reasons, the analysis of multilayered shielded circuits using an IE approach usually leads to very high computational times. In order to overcome this important drawback, numerous acceleration techniques have been proposed to seep-up the convergence of the Green's functions summation. A very detailed and complete description on series acceleration can be found in [Brezinski and Zaglia, 1991], whereas [Kinayman and Aksum, 1995] presents and overview of the acceleration methods most commonly employed in electromagnetic problems. In general, acceleration techniques can be divided into two main groups

General Methods: This type of methods can be applied to any infinite series, including these appearing in the formulation of Green's functions. Some examples of these methods are

the Shanks' transformation [Shanks, 1955], [Singh et al., 1990], [Singh et al., 1991], Euler transformation [Hildebrand, 1974], Wynn's ϵ algorithm [Brezinski and Zaglia, 1991], the Levin's T transformation [Singh and Singh, 1993], the Chebyshev-Toeplitz algorithm [Wimp, 1974], [Singh and Singh, 1992b] or the Θ-algorithm [Brezinski, 1982], [Singh and Singh, 1992a].

Specific Methods: This type of methods are derived for the kernel of specific series, and they can only be applied to problems where these series arise. In general, specific methods present less convergence problems and are faster than general methods. Some examples are the Kummer transformation [Brezinski, 1985], [Singh et al., 1990], [Singh and Singh, 1990], the Ewald's transformation [Jordan et al., 1986] or the summation by parts algorithm [Álvarez Melcón and Mosig, 2000], [Mosig and Alvarez-Melcon, 2002].

Nevertheless, only some of these techniques have successfully been applied to the acceleration of the series arising in shielded Green's functions. We can mention here the Ewald transformation [Park and Nam, 1997], [Park et al., 1998], [Park and Nam, 1998], and the Kummer transformation combined with the Poission's summation rule in [Gentili et al., 1997] or combined with the Ewald transformation and the summation by parts technique in [Pérez-Soler et al., 2008]. Unfortunately, the computation of multilayered shielded Green's functions in the spatial domain is still very time-consuming, which highly limits their use in practical IE codes. On the other hand, the IE formulated in the spectral domain [Álvarez Melcón et al., 1999] is very efficient, but it presents important convergence problems when the dimensions of the cells employed to discretize the printed circuits are very small as compared to the enclosure. Furthermore, note that all of these series acceleration techniques and IE implementations are only related to rectangular or circular cavities, whereas no systematic treatment have been proposed for more general shaped structures.

In this context, we propose here two efficient implementations of the multilayered shielded Green's functions derived in Chapter 2 within an IE framework. The proposed methods are specific, because they take advantage of the proposed Green's function formulation features. The first technique is based on the bilinear interpolation. The idea is not to interpolate the Green's functions, which have fast variations and strong singularities [Wang et al., 2004], [Pascual García et al., 2006], but to do this interpolation in an upper abstraction layer, i.e. interpolating the complex values of the charge and dipole images which provide the Green's functions. In this way, the computational cost is reduced, so that practical microwave filters can be analyzed very fast.

The second technique exploits the fact that, in the Green's functions presented in Chapter 2, the source term is naturally separated from the contribution of the spatial images/linear sources that take into account the effects of the cavity lateral walls. Using this important feature, two MoM matrixes are computed separately. The first contains the Green's functions singular behavior and it is evaluated fast using efficient numerical techniques for the computation of the Sommerfeld transformation and specific treatment of the singularities [Quesada-Pereira, 2007]. The second one contains the contribution of the images, and due to the smooth behavior observed, it can be computed with very limited computational effort. This singular and non-singular matrix decomposition leads to an extremely efficient and very accurate IE analysis of multilayered shielded circuits.

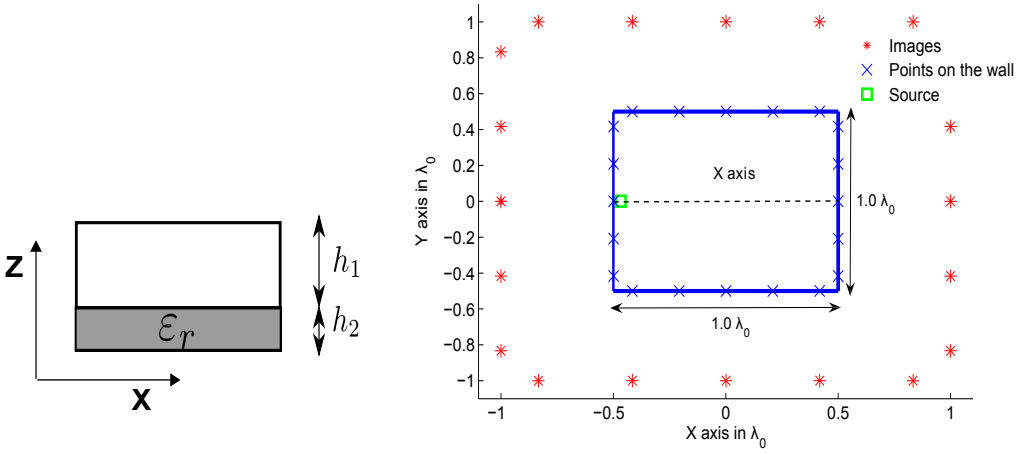

Figure 3.4 – Square cavity used to show the charge/dipole images complex value behavior. The top layer, $h_1 = 0.3\lambda$, is filled by air, whereas the bottom layer, $h_2 = 0.1\lambda$, has a permittivity of $\varepsilon = 9.9$.

3.3.1 Interpolation of the Spatial Images Complex Values

The spatial images technique, proposed in Chapter 2, allows to compute the multilayered shielded Green's functions associated to convex arbitrarily-shaped enclosures. The method employs the infinitely extended multilayered Green's functions in order to impose the appropriate boundary conditions for the fields at discrete points on the lateral cavity walls. For every electric-source point, three systems of linear equations must be solved, finding the weights and orientations of both charge and dipole images, which are needed to fulfill the required boundary conditions. The main disadvantage of the spatial images method is that new exact charge and dipole images must be calculated for every electric source point location, which makes the method presented in Chapter 2 computationally intensive.

The interpolation technique proposed in this section is based on the smooth behavior of the spatial images complex values, as opposed to the behavior of the Green's functions, which present strong singularities and fast variations [Wang et al., 2004], [Pascual García et al., 2006]. To show that this is indeed the case, 20 images, distributed in one ring, are used to analyze a square cavity sketched in Fig. 3.4. The images are situated at fixed points, surrounding the structure. Specifically, they are located at the air-dielectric interface, following the square shape of the structure, and at a distance of $0.5\lambda_0$ with respect to the cavity walls. For the numerical test, the electric source is varied along the x-axis shown in Fig. 3.4. The purpose is to study the behavior of the complex images values when the source moves inside the cavity.

Fig. 3.5a represents the real and imaginary parts of the computed charge values for the tenth (q_{10}) image, when the source is varied along the x-axis shown in Fig. 3.4. It is observed that, except when the source is placed close to a cavity wall, the image complex values present a smooth variation as a function of the source position. Therefore, their values can be easily recovered from discrete samples, if the Nyquist theorem is fulfilled [Oppenheim, 1996]. A similar study is now performed with the x-component of the magnetic vector potential, using unitary electric current sources. Fig. 3.5b

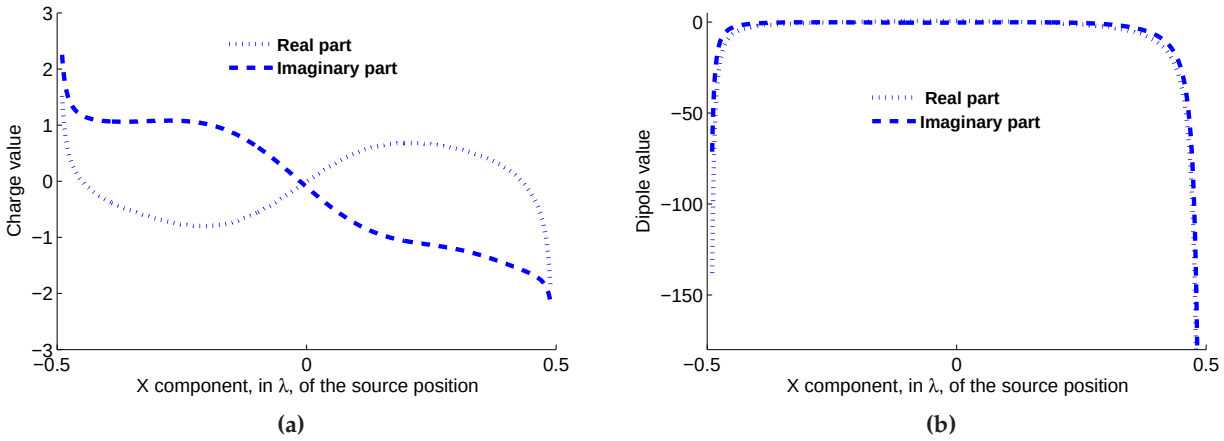

Figure 3.5 – Evolution of the 6^{th} image dipole and 10^{th} image charge complex values versus the source position inside the box depicted in Fig. 3.4.

represents the computed current values for the sixth (I_6^x) dipole image, in a similar situation as before. Also in this case, the response has a smooth behavior when the source point is placed inside the cavity (except when it is located very close to a cavity wall). All other charges and dipoles of the system of images behaves in a similar manner, and are not shown for the sake of space.

Since all the charge and dipole images have a smooth behavior, the idea is to exactly calculate the complex values for four source positions, which correspond to the corners of a rectangular sub-region. Each source has associated $R\,N$ charges images, where R is the number of rings and N is the number of images per ring, and $2\,R\,N$ dipoles images ($R\,N$ oriented along the x-axis and $R\,N$ along the y-axis). The values of the charge and dipole images at the four corners in a generic rectangular sub-region are shown in Fig. 3.6. To find the associated images complex values ($\bar{\bar{Q}}$) of an unknown source, placed in an arbitrary position inside the rectangular sub-region (P_{Int} in Fig. 3.6), the bilinear interpolation can be used as follows:

$$\bar{\bar{Q}}(P_{Int}) \approx \frac{\bar{\bar{Q}}(P_1)}{X_T Y_T} X_2 Y_2 + \frac{\bar{\bar{Q}}(P_2)}{X_T Y_T} X_2 Y_1 + \frac{\bar{\bar{Q}}(P_3)}{X_T Y_T} X_1 Y_2 + \frac{\bar{\bar{Q}}(P_4)}{X_T Y_T} X_1 Y_1, \tag{3.23}$$

where $\bar{\bar{Q}}(P_i)$ denotes the values of the exact charges when the source is placed at the i-th corner of the rectangular sub-region ($i = 1, 2, 3, 4$). Moreover, X_i and Y_i are the coordinates of the interior source point P_{Int}, as shown in Fig. 3.6. Similar expressions are obtained for the dipole images. The interpolated images provide the Green's functions with high accuracy, and with the advantage that only four exact images values must be calculated to recover the Green's functions inside every defined rectangular sub-region.

The error made with the interpolation method directly depends on the region size (see Fig. 3.7). In order to evaluate this error, we present the electric scalar potential (G_V) in Fig. 3.8a and the magnetic vector potential (G_A^{xx}) in Fig. 3.8b, along the observation line shown in Fig. 3.7, when the source is placed at the position $(0.0\lambda_0, 0.65\lambda_0, 0.1\lambda_0)$ (see Fig. 3.7). For validation, results from a spectral

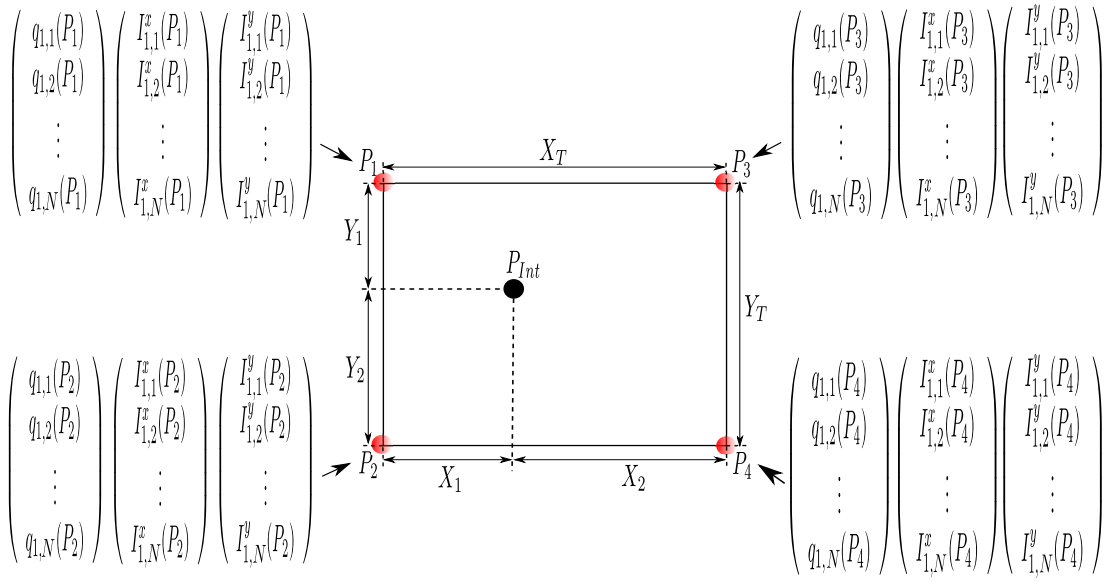

Figure 3.6 – Rectangular interpolation region controlled by four electric-sources placed at the corners. For the sake of compactness, it is assumed that the cavity is analyzed using 1 ring of N images.

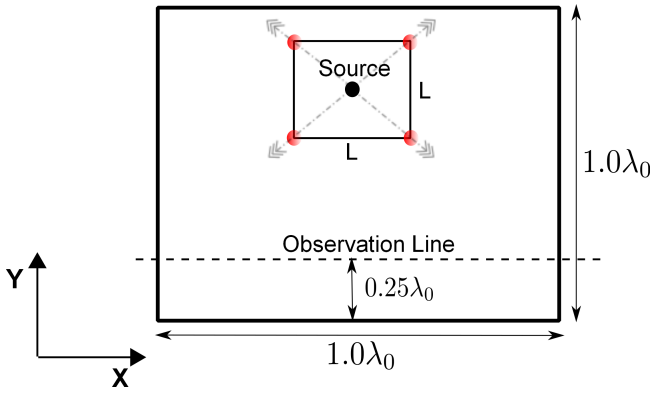

Figure 3.7 – Example of a interpolation square region centered at the source position $(0.0\lambda_0, 0.65\lambda_0, 0.1\lambda_0)$. The length side of the region (L) will change in order to study the interpolation error. The origin of the coordinate system is placed at the center of the cavity, following the notation of Fig. 3.4.

domain approach [Álvarez Melcón and Mosig, 2000], only valid for rectangular cavities, are also included. The charge and dipole image values associated to the source are obtained by interpolation. To do that, an interpolation square region (centered at the source position) is defined, and the length of its side (L) is varied (see Fig. 3.7).

When the length side of the square region is big ($L = 0.15\lambda_0$), the Green's functions obtained by the interpolated images are not accurate. This is due to the error made by the bilinear interpolation. However, as soon as the area of the square region decreases, the Green's Function are recovered with higher precision. It can be observed in Fig. 3.8 that convergence is reached for a side of the square region of $L = 0.07\lambda_0$ (with error below 0.05% in both electric scalar and magnetic vector potentials). We have extended this study along the whole cavity, in order to check the maximum length per wave-

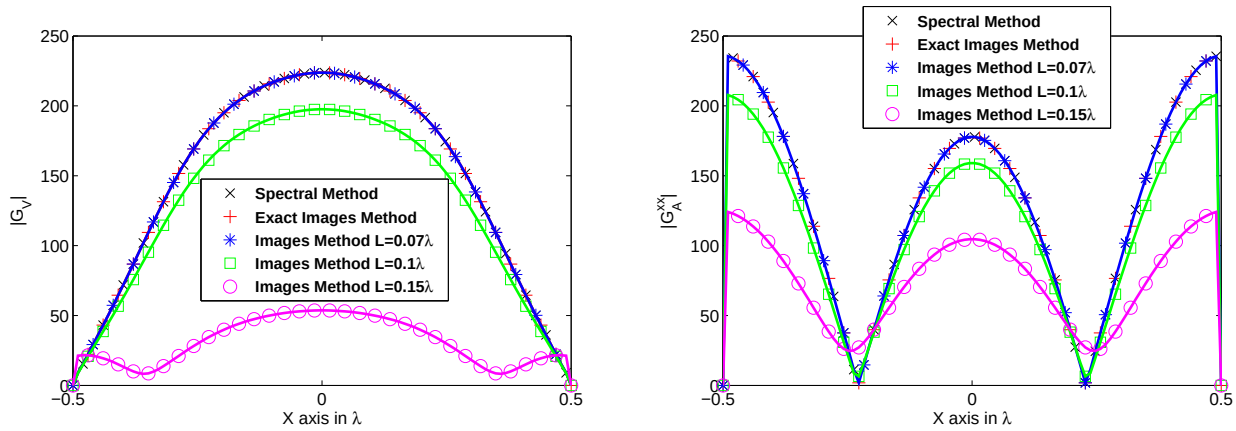

Figure 3.8 – Electric scalar potential ($|G_V|$) (a) and magnetic vector potential ($|G_A^{xx}|$) (b) along the observation line of Fig. 3.7, when the side of the square interpolation region has the values of $L = 0.15\lambda_0$, $L = 0.1\lambda_0$ and $L = 0.07\lambda_0$. Data from a series acceleration technique [Álvarez Melcón and Mosig, 2000] is used as validation.

length of the square region side to obtain an error below 0.1%. In general, convergence is assured when the side of the interpolation region is below $L = 0.05\lambda_0$.

Note that when the source is very close to the cavity walls, a specific spatial images distribution must be employed (see Section 2.3.2 of Chapter 2) in order to obtain accurate results. Also, the dipole images values exhibit faster variations in this case, as it can be observed in Fig. 3.5 for sources very close to the walls. Therefore, the interpolation approach is not used when the source is near to the walls (about $0.05\lambda_0$), in order to avoid very dense sub-regions. Nevertheless, in a practical circuit, most of the mesh cells are not in this situation, and the method proposed can be employed efficiently.

In order to apply the new interpolated Green's functions to the analysis of practical microwave filters, they are incorporated into an MPIE formulation solved by the method of moments (see Section 3.2). The MoM technique usually requires a mesh of the planar circuit with about 10 cells per λ_{eff} [Harrington, 1968]. This method may also impose a higher constraint in some cases, for example when modeling the singular behavior of the transversal currents induced on the microstrip lines. The idea proposed is to use rectangular cells (which will lead to rooftop basis and test functions [Rao, 1980]) for the discretization of the circuit geometry, and then use their corners to define the sub-regions employed in the interpolation procedure. If the printed circuit is discretized with a different type of cells, other interpolation schemes can be employed. In any case, with the interpolation technique, instead of solving millions systems of linear equations needed to perform the MoM analysis with the standard spatial images method, only 4 system of liner equations need to be solved per each cell of the mesh. During the calculation of the MoM matrix elements, the values of the images for every position of the source are rapidly recovered by interpolation.

In practice, the size of a single microstrip circuit cell can be much smaller than the size of the interpolation sub-region. Therefore, each sub-region can control several cells, leading to the idea of a multilevel interpolation approach, as illustrated in Fig. 3.9. This idea will reduce even more the computational cost, specially when very dense meshes are used in the discretization of the circuits.

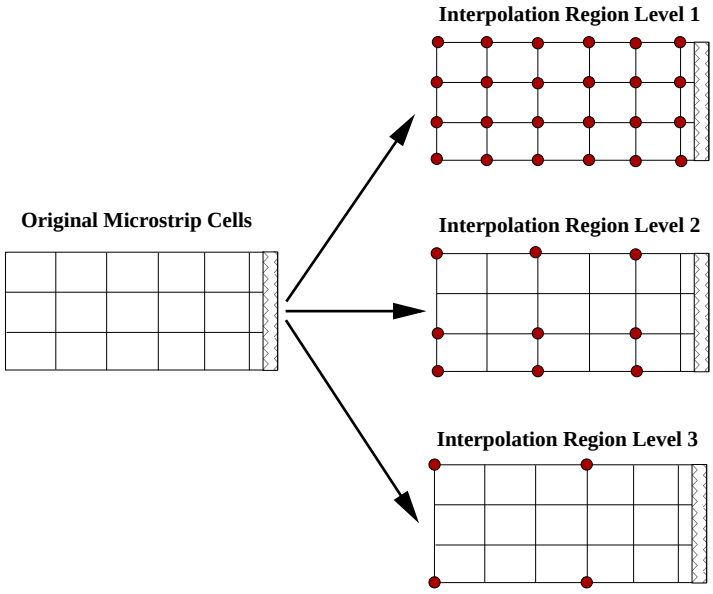

Figure 3.9 – Different interpolation region levels defined over a discretized microstrip line. Region Level 1 controls one cell, Region Level 2 controls four cells and Region Level 3 controls nine cells.

The final errors produced using the one-level or the multilevel interpolation approach are very small. In general, the differences between the original moment matrix and the matrix obtained with the interpolation technique just derived, are always below 0.06%. Moreover, one of the main advantages of the presented technique is that when dense meshes are used, the filling time of the MoM increases almost linearly with the number of cells. This is because the computation of the Green's Function is avoided for each pair of source-observer combinations, and it is only performed at the four corners of each interpolation region.

Finally, in Section 3.5 several multilayered boxed microwave filters are analyzed using the proposed method. There, the results are compared against full-wave commercial software and measured data, fully validating the accuracy and efficiency of the technique.

3.3.2 Singular and Non-Singular MPIE MoM Matrix Decomposition

The direct application of an MPIE MoM procedure (see Section 3.2), combined with the Green's function method proposed in Chapter 2, for the analysis of microwave shielded circuits is computationally very intensive. This is because if $R\,N$-images (distributed on R rings) are employed, one system of linear equation with $R\,N$-unknowns (for the electric scalar potential), and two systems with $2\,R\,N$-unknowns (for the magnetic vector potential), must be solved for any combination of source and observation points.

To circumvent this difficulty, a new integral equation implementation is proposed here based on the special features of the proposed Green's functions formulation. One of the important properties of the spatial images technique is that the source term is naturally separated from the contribution of the images that takes into account for the effects of the cavity lateral walls. Using this important

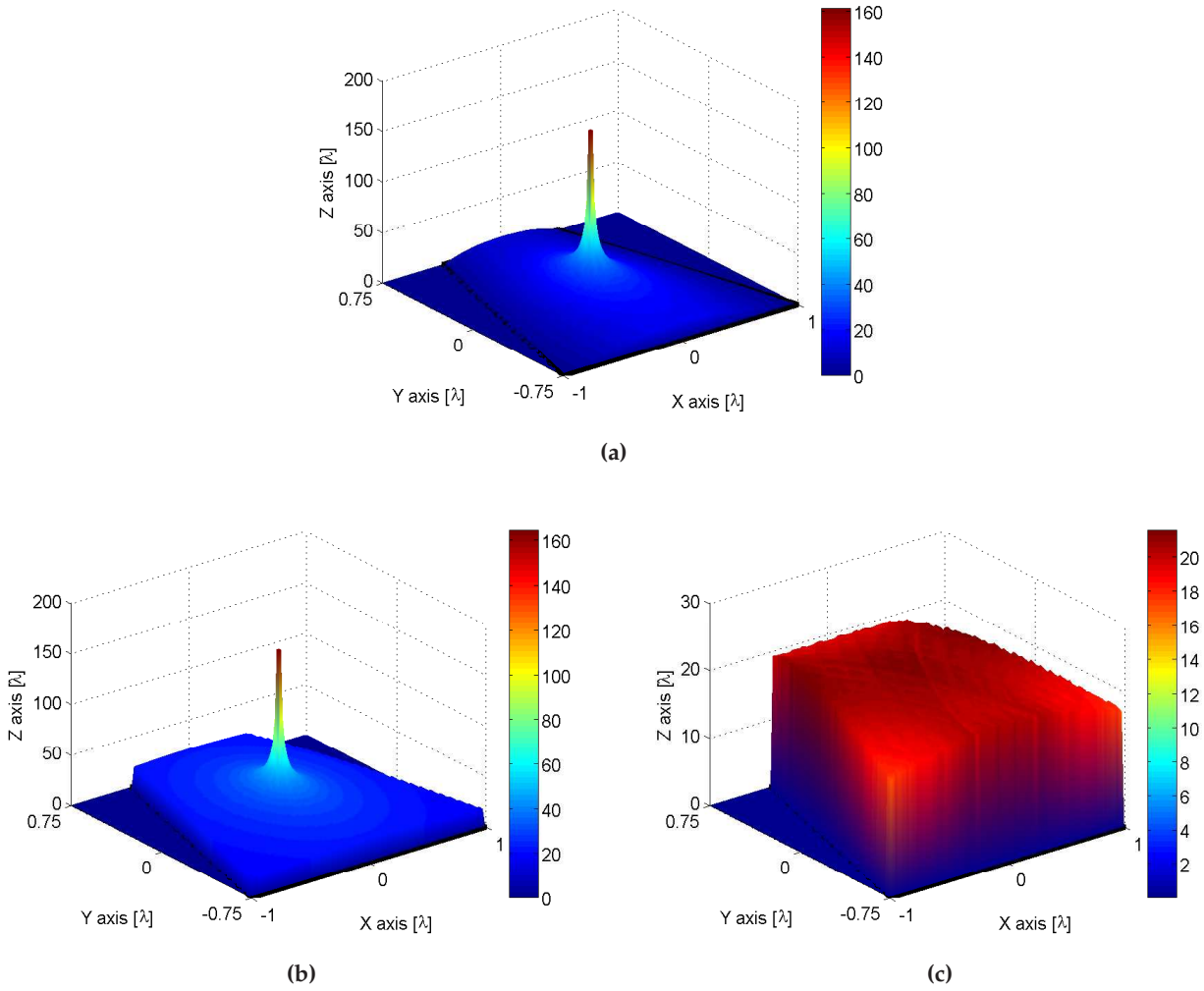

Figure 3.10 – Different contributions to the magnetic vector potential $|G_A^{yy}|$ obtained at the air-dielectric interface of the cavity shown in Fig. 2.5. The source point is placed at the center of the cavity $(0\lambda, 0\lambda, 0.1\lambda)$. (a) Complete $|G_A^{yy}|$ component of the magnetic vector potential. (b) Contribution of the source term to the $|G_A^{yy}|$ component of the magnetic vector potential. (c) Contribution of the images term to the $|G_A^{yy}|$ component of the magnetic vector potential.

feature, the total boxed Green's functions can be naturally expressed in two terms as

$$\bar{\bar{G}}_T(\vec{r},\vec{r}\,') = \bar{\bar{G}}_{Source}(\vec{r},\vec{r}\,') + \bar{\bar{G}}_{Images}(\vec{r},\vec{r}\,'), \tag{3.24}$$

where $\vec{r}\,'$ is the position vector of the source point and $\vec{r}$ denotes the position of the observation point.

In order to demonstrate the behavior of the different components which contribute to the shielded Green's functions, we separately present in Fig. 3.10 the contribution of each component to the calculation of the magnetic vector potential $|G_A^{yy}|$. The analysis is referred to the cavity shown in Fig. 2.5, when the point source is located at the position $(0\lambda, 0\lambda, 0.01\lambda)$. As a reference, the complete $|G_A^{yy}|$ component of the magnetic vector potential is shown in Fig. 3.10a. The source contribution in Eq. (3.24) has a strong singularity, involving fast variations. This is demonstrated in Fig. 3.11b, where we present the G_A^{yy} source contribution to the Green's function. We clearly observe a strong

peak in the potential due to the source located at the center of the cavity. The singular behavior of the source directly depends on the Sommerfeld transformation [Mosig, 1989] for a particular layered structure. To integrate this term, the singularity must be properly handled. However, this term can be computed very fast using standard numerical techniques available for the efficient evaluation of Sommerfeld integrals [Michalski, 1998].

On the other hand, the second term in Eq. (3.24) corresponds to the contribution of the images. It is the evaluation of this term that requires the solution of the systems of linear equations. Fortunately, all images are located outside of the cavity, so they do not contain inside any singular behavior. Consequently, this term exhibits very smooth variations inside the cavity. This is demonstrated in Fig. 3.10c, where we present the same Green's function component as before, but now only the contribution of the images is included. Due to this smooth behavior, this term can be easily integrated with very limited computational effort.

Using these features, two MoM matrixes are computed separately. The first one (Z_{Source}) contains the singular behavior of the Green's functions, and can be evaluated fast using efficient numerical techniques for the computation of the Sommerfeld transformation. The second one (Z_{Images}) contains the contribution of the images, and due to the smooth behavior observed, it can be computed with limited computational effort. Also, there is no singularity in this term, since the images are located outside of the cavity region. Due to these properties, we have observed that in most cases the MoM matrix associated to this term can be integrated using only one point in each of the discretization cells used to represent the geometry of the printed circuit. It is important to remark that with this strategy the value of the spatial images are only calculated when the source is placed at the center of each discretization cell. Using this one point integration rule, the whole MoM matrix can be recovered by a straightforward expression

$$Z_{m,n} = Z_{Source} + Z_{Images} = Z_{Source} + A_m\, A_n\, \vec{f}_m(\vec{r}_{c_m}) \cdot \bar{\bar{G}}_{Images}(\vec{r}_{c_m}, \vec{r}_{c_n}{}') \cdot \vec{f}_n(\vec{r}_{c_n}{}'), \tag{3.25}$$

where A_m and A_n are the areas of the observation and source cells, and $\vec{f}_m(\vec{r}_{c_m})$ and $\vec{f}_n(\vec{r}_{c_n}{}')$ are the test and basis functions. Also, $\bar{\bar{G}}_{Images}$ is the images contribution to the Green's functions evaluated between the center of the observation cell ($\vec{r}_{c_m}$), and the center of the source cell ($\vec{r}_{c_n}{}'$).

The situation when the source is located close to the wall is more complicated. With the spatial images arrangement proposed in Section 2.3.2 of Chapter 2, the images adopt a particular disposition as a function of both the source position and the cavity shape, as can be seen in Fig. 2.12. In this figure, it can be observed that only one image is actually situated very close to the wall.

For this particular situation, the same procedure explained before is extended. The idea is to extract not only the source term, but also the image which is situated close to the wall (with a distance less than 0.08λ). In this way, the Z_{source} matrix contains the singular behavior of the source (placed inside the cavity) and the quasi-singular behavior of the images situated close to the wall (and located outside the cavity). It is important to remark that for the calculation of this matrix, the values of charges/dipoles associated to the quasi-singular images are not recalculated, so the computational cost is still very reduced. In fact, all quasi-singular images values are calculated only once per discretization cell (when the source point is placed at the center of the cell). Then, the values of the extracted images are reused during the calculation of the Z_{source} contribution. This approach leads to an efficient MoM implementation, maintaining in all cases good numerical accuracy.

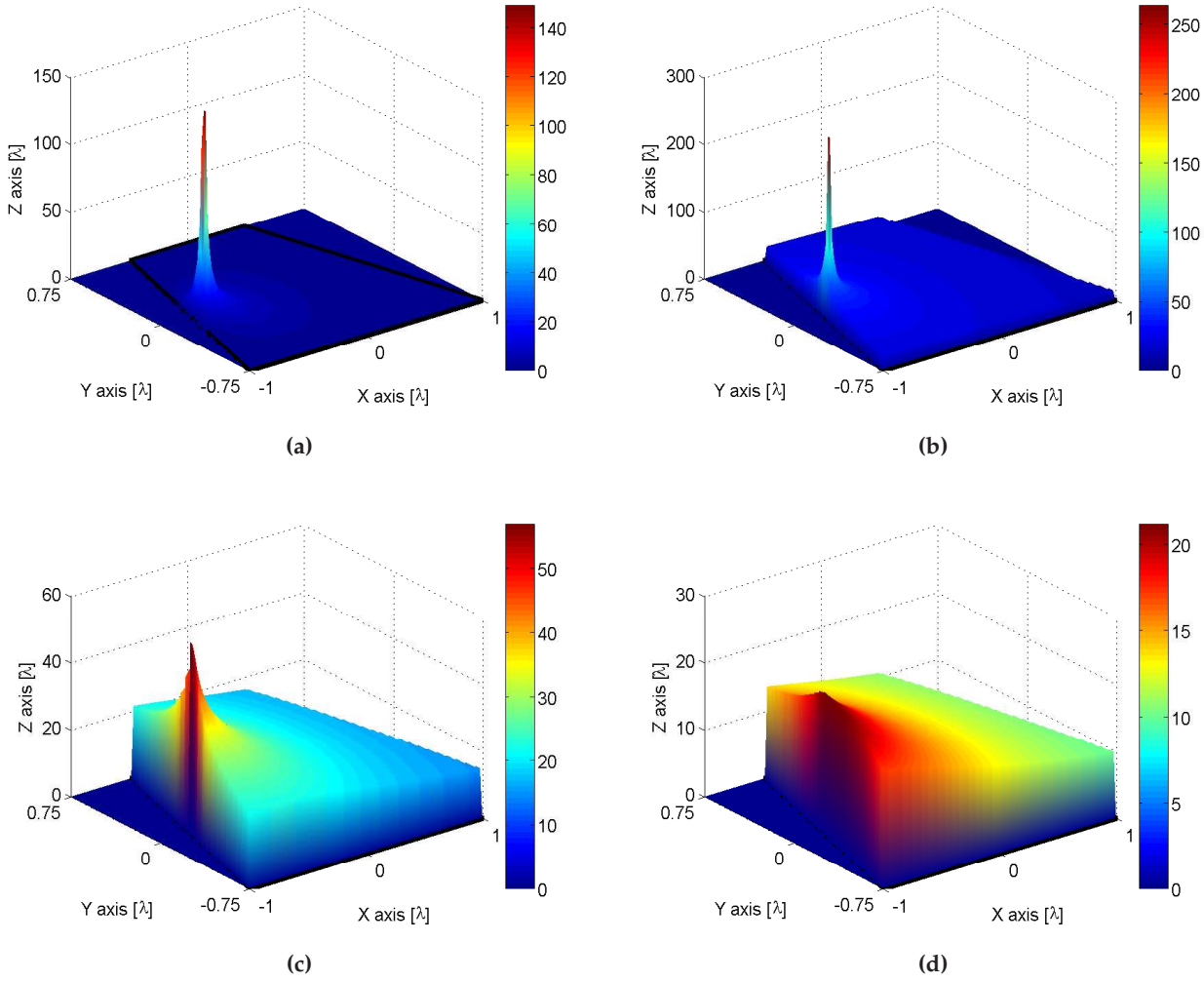

Figure 3.11 – Different contributions to the electric scalar potential $|G_V|$ obtained at the air-dielectric interface of the cavity shown in Fig. 2.5. The source point is placed close to a cavity wall $(-0.7\lambda, 0, 0.01\lambda)$. (a) Total electric scalar potential $|G_V|$. (b) Contribution of the source term to the $|G_V|$. (c) Quasi-singular contribution of the images term to the $|G_V|$. (d) Nonsingular behavior of the images contribution to the $|G_V|$, obtained when the images close to the cavity wall have been extracted.

To further study the features of the proposed method, we present in Fig. 3.11a the electric scalar potential inside the multilayered trapezium-shaped cavity shown in Fig. 2.5, when the source is situated very close to a wall, at the position $(-0.7\lambda, 0.0\lambda, 0.01\lambda)$. It can be observed the singular behavior due to the presence of the source. This singular behavior, due to the singular term of Eq. (3.24), is also explicitly shown in Fig. 3.11b. If we consider only the behavior of the images, the singularity disappears, as it is shown in Fig. 3.11c. However, a quasi-singular behavior raises from the image which is situated close the wall (see Fig. 2.12b). Finally, this image is extracted and added to the singular impedance matrix Z_{source}. In this case, the contribution of the reminder to the electric scalar potential is shown in Fig. 3.11d. This contribution has a smooth behavior, and can be integrated with the one point rule shown in Eq. (3.25).

Besides, note that the procedure described is not a standard extraction of the singular term of the Green's functions, as it was done in previous works [Álvarez Melcón and Mosig, 2000]. Traditionally, the singular behavior of the Green's functions is treated by extracting the asymptotic terms, with subsequent analytical evaluations of the associated static integrals [Arcioni et al., 1997]. On the contrary, with the spatial images technique the source is naturally separated from the other contributions. Once the contribution from the images is treated as described in Eq. (3.25), the isolated source term (Z_{Source}), which provides the singular behavior, can also be treated using other standard asymptotic techniques [Arcioni et al., 1997].

Finally, it is important to point out that with this one point rule, only one system of linear equations with $R\,N$-unknowns and two systems with $2\,R\,N$-unknowns must be solved for each cell of the printed circuit discretization, leading to a very important reduction in the computational cost needed for the analysis of practical shielded circuits. Moreover, the numerical accuracy obtained with this new MoM implementation is very good. In all numerical tests that we have carried out, the relative errors obtained by the new MoM matrix implementation are below 0.01% as compared to a traditional MoM implementation. Section 3.5 will present several multilayered shielded circuits analyzed using the spatial images technique accelerated with the proposed singular and non-singular matrix decomposition method. There, full-wave simulation and measured data will fully validate both, the accuracy and the efficiency of the proposed acceleration techniques.

3.4 Hybrid Waveguide-Microstrip Technology

The development of microwave filters is important to design modern microwave space and terrestrial communication systems [Cameron et al., 2007]. New applications demand more compact and light-weight designs, while keeping the capacity to reject unwanted signals. This necessity of rejection just led to the development of microwave filters whose insertion loss response exhibits transmission zeros at finite frequencies. For this purpose several techniques and different filter topologies have been developed in the last few decades. The introduction of cross-couplings between nonadjacent resonators in the coupling scheme of the filter has been the design method traditionally used to achieve this goal [Cameron, 1999]. Nevertheless, in more recent contributions, alternative schemes for microwave resonator filters have also been proposed [Rosenberg and Amari, 2003].

One of the most outstanding proposed topology was the transversal filter structure, whose coupling matrix can be directly synthesized using the technique presented in [Cameron, 2003]. This structure differs from traditional ones in the fact that multiple input/output couplings are allowed. In addition, no coupling between resonators is introduced. Furthermore, fully canonical filtering functions may be synthesized, if a direct coupling between the source and the load is introduced. With this fully canonical transversal configuration, N transmission zeros can be implemented with a N-th degree filtering function for maximum selectivity.

Several practical implementations of transversal filters have been proposed in the last years. Different examples in printed and waveguide technology can be found in [Rebenaque et al., 2003] and [Guglielmi et al., 2001]. However, the practical implementation of fully transversal topologies is difficult when the order of the filter is high. This is because of the special routing scheme

of transversal filters, where couplings from all the resonators to the input/output ports must be implemented, whilst at the same time inter-resonator couplings must be avoided. This difficulty has limited the practical implementation of transversal topologies to filters of second order [Rebenaque et al., 2003],[Guglielmi et al., 2001],[Amari and Rosenberg, 2003]. When higher order filters are needed, rotations of the original $N+2$ transversal coupling matrix are applied to eliminate undesired couplings, or to create new couplings between resonators [Cameron, 2003], [Liao and Chang, 2007]. When the use of rotations is not possible to achieve a given desired topology, one can still resort to optimization techniques applied to the coupling matrix entries [Amari et al., 2002]. Also, higher order filters can be designed by cascading several sections of second order transversal filters [Guglielmi et al., 2001], [Rebenaque et al., 2004].

This section is focused on the implementation of a novel hybrid microwave filter for high selectivity applications. This technology arise from the deep study of the multilayered shielded circuits and its behavior at resonant frequencies. The proposed structure combines for the first time two different technologies, namely the waveguide and the microstrip technologies. By combining these technologies, very compact structures are obtained since one cavity resonance is combined with the N printed line microstrip resonators, leading to an $N+1$ order filter. Therefore, on the contrary as in the usual microstrip devices, that are designed to operate on a frequency region far from the cavity resonances, the hybrid waveguide-microstrip technology uses the cavity (or filter package) resonance as a fundamental part of the filter response. In addition, the transmission zeros of the filter can be controlled using the different parts of the hybrid structure. In this way, both symmetric and asymmetric responses for maximum selectivity above and/or below the passband can be easily synthesized. In summary, the proposed technology is cheap, light, compact, uses the filter package as a part of the filter and allows to control the frequency position of the transmission zeros. The novel structure is first described in Section 3.4.1, including a simple filter design procedure. Then, in Section 3.4.2, two microwave filters implemented in this technology have been designed and manufactured. Full-wave simulations and measured results will completely validate the use of the new filtering structure for practical applications. Besides, note that this technology will be further employed in Section 3.5, where novel hybrid filters, based on different cavity configurations, are going to be designed, analyzed and manufactured, achieving responses with enhanced features.

It is important to remark that the spatial images technique is an ideal tool for the analysis and design of hybrid waveguide-microstrip filters. This is because the cavity is a key element of the structure. On the contrary as in other full-wave methods (such as FDTD [Taflove and Hagness, 2005] of FEM [Lee et al., 1997]), the cavity is inherently included into the Green's functions, and it does not need to be meshed. This leads to a computationally very efficient analysis of this type of filters using the MPIE technique. Besides, note that an small error in the modeling of the resonant frequencies of the cavity will lead to a wrong design. Therefore, the analysis and design of hybrid waveguide-microstrip filters constitute an excellent benchmark test for the spatial images technique. Furthermore, the use of this tool allows to use arbitrarily-shaped enclosures, which may be of interest in applications where the physical space is an important factor, such as in the space industry.

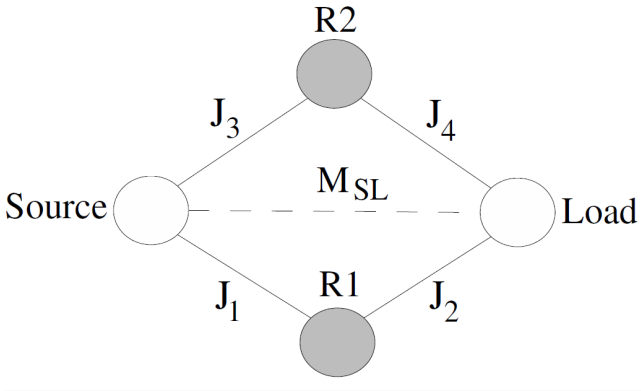

Figure 3.12 – Typical scheme of a Modified Doublet (MD). J_1 to J_4 represent the corresponding couplings between source S, load L, and the resonators. M_{SL} represents the direct coupling from source to load.

	S	1	2	L
S	0	J_1	J_3	M_{SL}
1	J_1	M_{11}	0	J_2
2	J_3	0	M_{22}	J_4
L	M_{SL}	J_2	J_4	0

Table 3.1 – Coupling matrix of the Modified Doublet

3.4.1 Structure Description and Design Procedure

The hybrid structure under study is able to implement either a second or a third [Martínez-Mendoza et al., 2007] order filter responses. Besides, it can also be extended to design dual-band configurations [Martínez-Mendoza et al., 2008].

The simplest configuration of the hybrid waveguide-microstrip filter follows the second order coupling scheme known as the Modified Doublet (MD) topology, which is shown in Fig. 3.12. In the figure, solid line represents coupling between source or load and the resonators, while dashed line represents the direct source-load coupling. The main advantage of this topology consists on the possibility to generate up to two transmission zeros in the insertion loss response of a second order filter. The capability of these structures to implement a maximum number of transmission zeros for a given order of the filter was also recognized in [Cameron, 2003], in the frame of a synthesis technique for transversal filters.

The coupling matrix M of the Modified Doublet, calculated by using the technique described in [Cameron, 2003], is known to be of the form shown in Table 3.1. The terms J_1 to J_4 of the matrix symbolize the couplings between each resonator to the input/output ports. The nonzero diagonal elements in the coupling matrix accounts for differences in the resonant frequencies of the resonators, typical for asynchronous filters [Cameron, 2003]. Furthermore, the coupling parameter M_{SL} represents the direct coupling between source and load. The remaining terms are zero, since there is no cross couplings between resonators.

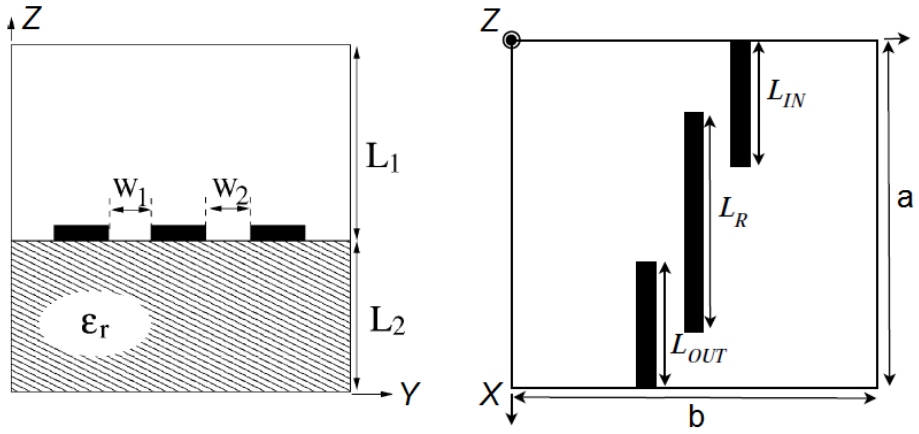

Figure 3.13 – Novel hybrid waveguide-microstrip filter structure.

The proposed hybrid waveguide-microstrip structure for implementing this kind of filters is depicted in Fig. 3.13. In the hybrid structure, the open line microstrip resonator in the printed circuit behaves as resonator R_1 of the Modified Doublet, whereas a hybrid LSM mode excited in the partially filled waveguide behaves as resonator R_2. This mode is TM with respect to the direction normal to the dielectric (z-axis), and is also known as a hybrid LSM mode with respect to the x-axis when studying partially filled waveguides [Collin, 1991].

For our suggested structure, every element of the matrix M can be controlled by means of the dimensions shown in Fig. 3.13. The length of the first resonator, L_r, controls the self-coupling term M_{11} (resonant frequency of the first resonator). The cavity dimensions (a and b) controls the self-coupling term M_{22} (resonant frequency of the second resonator). The couplings between input/output ports and the first resonator, J_1 and J_2, are controlled by adjusting the coupling gaps w_1 and w_2. This is the typical situation of capacitive couplings in standard microstrip line resonators. In addition, the couplings J_3 and J_4 between input/output ports and the second resonator (the resonant mode of the cavity) can be controlled with the adjustment of the port lengths, L_{in} and L_{out}, and of the thickness of the substrate L_2.

On the other hand, it is an established fact that for the Modified Doublet one of the four couplings must be negative. In this specific structure, the sign change in the x-component of the electric field associated to the LSM mode is responsible for this negative coupling. This situation is shown in Fig. 3.14, where the x component of the electric field is shown. As can be observed there, this component of the field has a zero at the center of the cavity, and then changes sign at the side of the output port. It is this change in sign of the x-component of the electric field which synthesizes the negative coupling needed in the Modified Doublet of Fig. 3.12. Besides, it is possible to design the printed resonator to act as a simple half-wavelength open microstrip resonator, since no change in sign is required for R_1.

In case that the hybrid structure implements a transversal configuration, we must assure that the cross-coupling between both resonators (R_1 and R_2) must be null. To explain why the coupling from the LSM mode and the printed line resonator can be neglected, Fig. 3.14 is again useful. Due

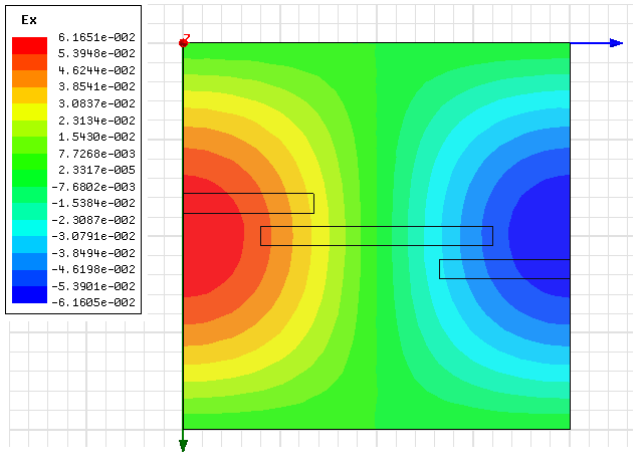

Figure 3.14 – Electric field x-component of the LSM mode inside the rectangular cavity of Fig. 3.13, at the first resonant frequency ($f = 4.56$ GHz). The physical dimensions of the structure are $a = b = 40.0$ mm, $L_1 = 2.62$ mm, $L_2 = 3.14$ mm and $\varepsilon_r = 2.2$.

to the orientation of the printed lines, the x-component of the electric field will be the responsible for the coupling. We can observe in the figure that the printed resonator is placed at the center of the cavity, where the field has a zero. Consequently, the coupling from the LSM mode and the printed resonator will be small. On the contrary, the input/output printed lines are placed where the electric field is maximum, and therefore stronger couplings can be obtained, as required by the transversal topology.

The design procedure to implement a fixed filtering function using the hybrid structure can be carried out by following the idea of separating the design task into several simpler tasks, which was first introduced in [Guglielmi, 1994]. In this way, the value of each dimension of the structure to implement the desired coupling terms can be obtained. First, we compute the $(N+2)$ transversal matrix associated with a fixed second order filter. Next, using the coupling terms of the above $(N+2)$ coupling matrix, that is, the impedance inverters (J_i), the prototype de-normalization process (see for example [Swanson and Macchiarella, 2007]) is applied. This process allows us to obtain the values of the required resonant frequencies of each resonator, in asynchronously tuned filters ($f_{0,k}; k = 1, 2$). The de-normalization process also leads to the values of the required external quality factors ($Q_{e,k}$) of each resonator. Once these values are known, the different resonators in the structure can be isolated to synthesize the required coupling elements. Specifically, we first look for the required frequency response of the resonant LSM mode. To do this, we eliminate the printed line microstrip resonator, and then we adjust the port lengths L_{in} and L_{out}, and the waveguide width b, in order to achieve the required external quality factor and resonant frequency, respectively. Once the LSM resonance has been synthesized, the next step is to look for the required frequency response of the printed line microstrip resonator. Thereby, we add the central microstrip line again and eliminate the presence of the other resonance. To do so, we detune it by setting the waveguide width to a larger value, while we adjust the microstrip line resonator. Now, we can modify the line length L_r and the coupling gaps ω_1 and ω_2, in order to obtain the required resonant frequency and external quality factor, respectively. Once the resonators have been individually synthesized, they are put together to verify that we obtain the desired filtering function inside the passband. However, the transmission

zeros will not probably be located at the specified frequencies, since the direct coupling term M_{SL} still needs to be adjusted. To synthesize it, several iterations of the algorithm just described must be carried out, varying the dimensions L_1 (the height of the cavity), until the transmission zeros are placed at the right locations. In general, we have observed that two or three iterations are usually enough to adjust the positions of the transmission zeros.

The hybrid structure proposed here always has a direct coupling from the input to the output port (entry M_{SL} in Table 3.1). This indeed makes possible to obtain fully canonical responses, with a maximum of transmission zeros. This coupling is related to the excitation of the LSM mode, whose propagation is stopped by the presence of the lateral cavity walls. Accordingly, the direct coupling (M_{SL}) can be controlled with the air layer affecting the propagation of this LSM mode in the partially filled waveguide (L_1 in Fig. 3.13). Using this concept, there is full control in the position of the transmission zeros.

3.4.2 Results and Theoretical Discussion

In this section, two implementation examples of second order transversal filters, using the novel hybrid waveguide-microstrip technology, are presented. The filters follow the coupling scheme of the Modified Doublet (see Fig. 3.12). The results predicted by the coupling matrix theory [Cameron, 2003] will be compared with the results obtained from the electromagnetic analysis of the hybrid structures, using the MPIE formulation presented in Section 3.2 combined with the Green's functions introduced in Chapter 2. Besides, measured results from manufactured prototypes are presented, in order to show the practical validity of the new structure.

Hybrid Waveguide-Microstrip Filter I:
One Transmission Zero Placed on Each Side of the Passband

The first example consist of a second order bandpass filter with -15.0 dB of return loss, and two transmission zeros placed at the frequencies of $f_1 = 4.125$ GHz and $f_2 = 5.146$ GHz. The filter is centered at 4.51 GHz with a bandwidth of 136 MHz. Therefore, this filter presents a response with two transmission zeros asymmetrically located with respect to the passaband. The $(N+2)$ by $(N+2)$ coupling matrix obtained with the theory presented in [Cameron, 2003] is

$$M = \begin{pmatrix} 0 & -0.6852 & 0.7364 & 0.0253 \\ -0.6852 & 1.2723 & 0 & 0.6852 \\ 0.7364 & 0 & -1.2483 & 0.7364 \\ 0.0253 & 0.6852 & 0.7364 & 0 \end{pmatrix}. \tag{3.26}$$

The physical dimensions of the filter have been obtained following the design procedure introduced in the previous section. The final dimensions, using the notation of Fig. 3.13, are $a = b = 40.0$ mm, $L_{in} = L_{out} = 13.5$ mm, $L_r = 24.0$ mm, $L_1 = 2.62$ mm, $L_2 = 3.14$ mm, $w_1 = w_2 = 1.4$ mm, and $\varepsilon_r = 2.2$. We can observe that the dielectric thickness is 3.14 mm. Due to availability, the substrate selected for manufacturing is an RT-DUROID with relative permittivity $\varepsilon_r = 2.2$ and thickness 1.57 mm. In the manufactured prototype, the final dielectric height is achieved by piling up two

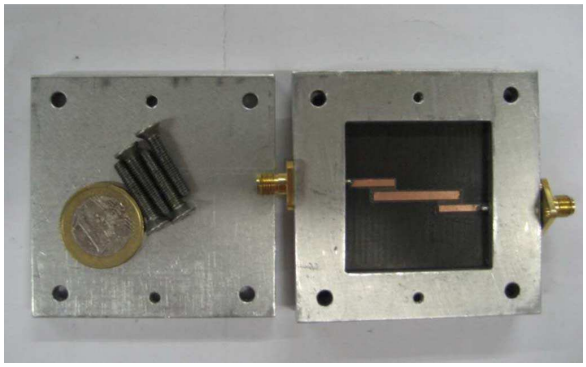

(a)

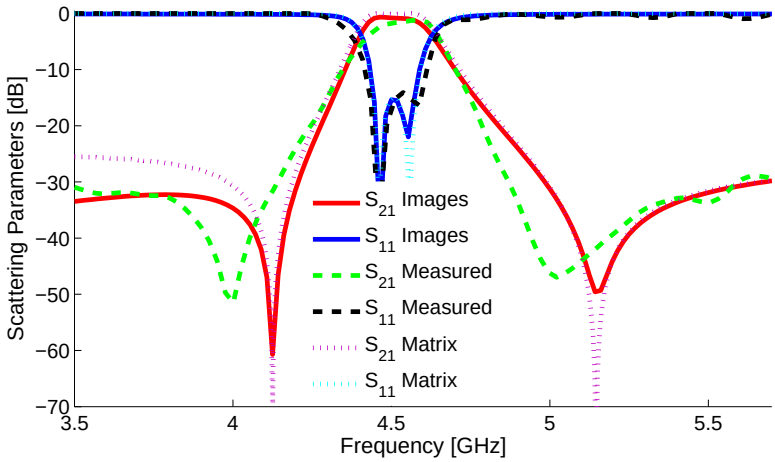

(b)

Figure 3.15 – Hybrid waveguide-microstrip bandpass filter of second order with a transmission zero placed on each side of the passband, following the structure of Fig. 3.13. (a) Aspect of the fabricated breadboard, showing all pieces of the filter. (b) Scattering parameters of the filter, computed with the coupling matrix theory [Cameron, 2003] and with an MPIE formulation combined with the spatial images technique. Measured data is employed for validation.

RT-DUROID substrates of thickness 1.57 mm.

A photograph of the manufactured breadboard is shown in Fig. 3.15a. In Fig. 3.15b we present the results predicted by the coupling matrix theory and the response from a full-wave analysis of the hybrid structure. As previously commented, this analysis is based on the IE approach described in Section 3.2 combined with the spatial images technique introduced in Chapter 2. In the simulations, losses are included in the dielectric substrate $(\tan\delta = 0.004)$, and in the printed metalizations $\sigma = 3 \cdot 10^7\,\Omega^{-1}/\mathrm{m}$. Besides, measured data is included for a complete validation. As it can be observed in the figure, very good agreement among the different responses have been achieved, fully validating the novel hybrid filtering structure.

Results also reveal that the minimum insertion loss of the filter inside the passband is -1.15 dB. Also we can observe a slope in the insertion loss response of the filter. The insertion losses take a

maximum value within the passband of -2.48 dB at the frequency of 4.461 GHz. At the frequency of 4.588 GHz the insertion loss is minimum (-1.15 dB). The slope in the insertion loss response of the filter reveals that a resonator with a higher quality factor has been combined with a resonator of lower quality factor.

Hybrid Waveguide-Microstrip Filter II:
Two Transmission Zeros Placed Above the Passband

The second example consist of a second order bandpass filter with -23.0 dB of return loss, and two transmission zeros placed at the frequencies of $f_1 = 4.8$ GHz and $f_2 = 5.8$ GHz. The filter is centered at 4.435 GHz with a bandwidth of 110 MHz. Therefore, this filter presents a response with two transmission zeros placed on the right side of the passband. The $(N+2)$ by $(N+2)$ coupling matrix obtained with the theory presented in [Cameron, 2003] is

$$M = \begin{pmatrix} 0 & -0.7763 & 1.1472 & 0.0254 \\ -0.7763 & -1.9365 & 0 & 0.7763 \\ 1.1472 & 0 & 1.7985 & 1.1472 \\ 0.0254 & 0.7763 & 1.1472 & 0 \end{pmatrix}. \tag{3.27}$$

The physical dimensions of the filter have again been obtained following the design procedure introduced in the previous section. The final dimensions, using the notation of Fig. 3.13, are $a = 40.0$ mm, $b = 41.46$ mm, $L_{in} = L_{out} = 14.0$ mm, $L_r = 24.96$ mm, $L_1 = 4.10$ mm, $L_2 = 3.14$ mm, $w_1 = w_2 = 1.4$ mm, and $\varepsilon_r = 2.2$. Again, the final dielectric height of the prototype is achieved by piling up two RT-DUROID substrates of thickness 1.57 mm.

A photograph of the manufactured breadboard is shown in Fig. 3.16a. In Fig. 3.16b we present a comparison among the results predicted by the coupling matrix theory, the response from a full-wave analysis of the hybrid structure and measured data. In the simulations, losses are included in the dielectric substrate $(\tan\delta = 0.004)$, and in the printed metalizations $\sigma = 3 \cdot 10^7\ \Omega^{-1}/\text{m}$. As it can be observed in the figure, very good agreement among the different responses is again achieved. This second filter completely validates the proposed filtering structure, fully demonstrating its capability to control the position of the transmission zeros.

3.5 Comparative Study of Multilayered Shielded Microstrip Filters

A software code, based on the MPIE formulation described in Section 3.2 combined with the novel Green's functions computation presented in Chapter 2, has been written for the analysis of multilayered printed circuits in arbitrarily-shaped shielded enclosures. Besides, an efficient implementation of these Green's functions into the MPIE formulation has been achieved using the acceleration techniques introduced in Section 3.3. The result is a software tool computationally very efficient, which can effectively be employed as a CAD tool for the analysis and design of complex multilayered circuits, such as microwave filters.

The goal of this section is to validate the developed CAD tool and to demonstrate the useful-

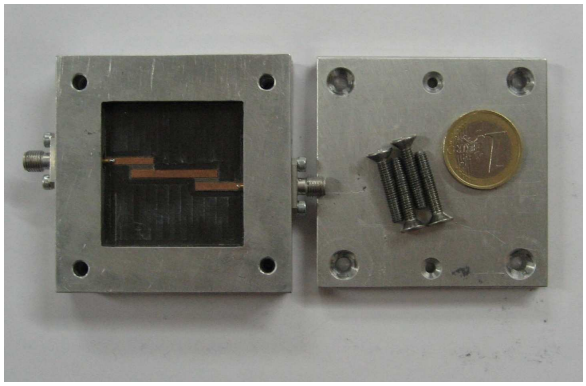

(a)

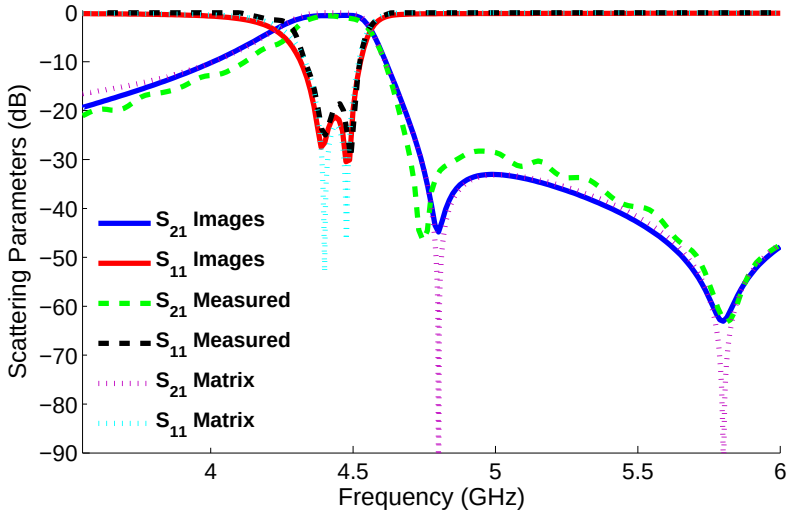

(b)

Figure 3.16 – Hybrid waveguide-microstrip bandpass filter of second order with two transmission zeros placed above the passband, following the structure of Fig. 3.13. (a) Aspect of the fabricated breadboard, showing all pieces of the filter. (b) Scattering parameters of the filter, computed with the coupling matrix theory [Cameron, 2003] and with an MPIE formulation combined with the spatial images technique. Measured data is employed for validation.

ness of the proposed Green's functions when modeling practical multilayered shielded circuits. For this purpose, we present and analyze several practical microwave shielded devices. The analysis is carried out by using the general spatial images technique introduced in Section 2.3 of Chapter 2 in the case of arbitrarily-shaped enclosures, whereas the specific spatial Green's functions formulations presented in Section 2.4 and in Section 2.5 of Chapter 2 are used to treat multilayered cavities with rectangular or triangular-isosceles cross-section, respectively.

First, the accuracy of the method is checked. For this purpose, we present, for each structure under consideration, a comparison of the scattering parameters obtained by the proposed formulation and by different full-wave approaches (such as the commercial software ADS©, a spectral-domain method [Álvarez Melcón et al., 1999] or a neural-network technique [Pascual García et al., 2006]). Be-

sides, measured data obtained from real manufacture hardware further validate the accuracy of the CAD tool.

Second, a comparative study of the proposed method efficiency is presented. For this purpose, the computational time required to analyze each microwave structure is compared against the time required by other full-wave approaches. Besides, the two acceleration techniques introduced in Section 3.3 are carefully examined, leading to the conclusion that the singular/non-singular MPIE matrix decomposition method is, for a given level of accuracy, much more efficient than the Green's function interpolation technique. Note that all the results employed for this study have been obtained with the same computer, based on a 3.06 GHz Pentium IV processor with a total RAM memory of 2 GB, and under exactly the same numerical conditions (in terms of mesh, integration points, etc.).

Note that, in the efficiency study, the time required to compute the Sommerfeld integrals related to the multilayered media is not included. This is because this computation only need to be performed once for a given multilayered configuration. Then, the results from this computation are stored and reused in the analysis or design of any circuit placed on this specific configuration. Therefore, this time is neglectable for the analysis and design of microwave shielded devices (similar as the training time in neural networks approaches [Pascual García et al., 2006]). For the examples analyzed in this section, and using the method presented in [Mosig and Álvarez Melcón, 2003], the time required for this computation ranges from 0.15 to 0.8 seconds per frequency point.

Finally, note that the proposed technique allows the investigation of different microwave filter configurations. Among these configurations, we can point out coupled-line filters, broadside coupled filters (which require a multilayered configuration) or the novel hybrid waveguide-microstrip technology introduced in Section 3.4. In this section we have combined the analysis of shielded microwave filters taken from the literature (as those found in [Guglielmi, 1994], [Alvarez-Melcon et al., 2001], or in [Alvarez Melcon, 1998]) with the design and subsequent analysis of novel filters based on the hybrid waveguide-microstrip technology [Martínez-Mendoza et al., 2007], which exploits the filter package configuration as a key constitutive element of the final filter response.

The rigorous comparative among the different approaches reveals that the proposed technique is extremely competitive, in terms of convergence, accuracy and efficiency, as compared with any other technique known to the author. Therefore, it is an ideal tool for the analysis, design and optimization of shielded microwave circuits.

3.5.1 Example I: 4-Poles Broadside Coupled Filter within a 3-Layer Rectangular Cavity

The first example presents a 4-poles broadside-coupled structure designed as a high-performance microwave filter, which was introduced in [Alvarez-Melcon et al., 2001]. The layout of this filter is shown in Fig. 3.17a. As can be observed from the figure, the circuits are printed on two opposite sides of two dielectric substrates. Note that both, the multilayer configuration and the filter rectangular enclosure, must be rigorously taken into account for an accurate analysis of this structure.

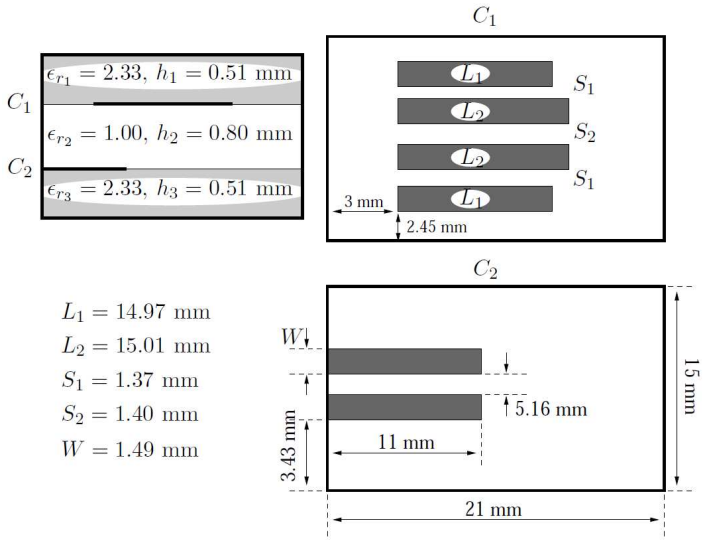

(a)

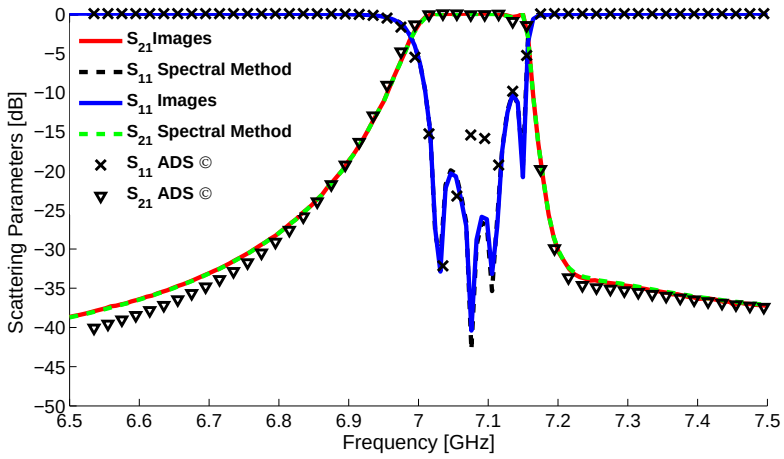

(b)

Figure 3.17 – 4-poles bandpass broadside-coupled filter within a 3 layers rectangular cavity. (a) Filter layout. (b) Scattering parameters computed with the proposed images technique. Full-wave simulation results, computed with ADS© and with the spectral method proposed in [Álvarez Melcón et al., 1999], are employed for validation.

In the analysis, three rows of cells are employed to discretize the printed lines. In this way, the singular behavior of the currents close to parallel edges are correctly modeled. Also, we have used more cells than the strict minimum in the modeling of the printed lines, to obtain high precision in the calculation of the induced currents. Therefore, the sizes of the cells that we use are small, and their side lengths are below the condition $L = 0.05\lambda_0$, allowing the use of the multilevel interpolation scheme (see Section 3.3.1).

In order to analyze this filter, the MPIE formulation is combined with the spatial images technique. For this specific structure, 20 images are placed surrounding the cavity, following the dynamic images location introduced in Section 2.3.2 of Chapter 2. The images are located at the first air-

Technique	Time per frequency point
Original spatial images technique	1336.235 sec.
Spatial images technique + ground planes	342.975 sec.
ADS©	39.234 sec.
Interpolated method first level	18.051 sec.
Interpolated method second level	9.223 sec.
Interpolated method third level	3.652 sec.
Singular/no-singular MPIE matrix decomposition	0.718 sec.

Table 3.2 – Comparison of the time (per frequency point) required by different methods for the analysis of the filter shown in Fig. 3.17. A total of 270 cells are used to discretize the printed circuit.

dielectric interface. First, the filter is analyzed using the original technique, presented in Section 2.3 of Chapter 2. Then, the method is combined with the use of dynamic ground-planes, as specified in Section 2.4.1 of Chapter 2. This increases the accuracy of the method (solving the numerical instabilities when the point source is close to a cavity wall) and reduces the computational cost required by the analysis (in order to achieve the same accuracy level, this technique requires less than half number of unknowns than the regular spatial images method). Then, the two acceleration techniques introduced in Section 3.3 are also employed for the analysis of this filter. The goal is to check the accuracy and the efficiency of these methods. Besides, in order to fully validate the accuracy of the developed techniques, results from a spectral domain approach [Álvarez Melcón et al., 1999] and from the commercial software ADS© are also included.

The scattering parameters of the broadside-coupled filter obtained by the methods described above are shown in Fig. 3.17b. As can be observed in the figure, very good agreement among the very different techniques has been achieved, fully validating the proposed methods. Specially, the agreement between the proposed spatial technique and the spectral domain method [Álvarez Melcón et al., 1999] is remarkable. Note that the results obtained by all spatial-images techniques (with and without acceleration) directly superimpose. Therefore, and for the sake of compactness, we have denoted the results from these methods as "Images" in the figure.

Table 3.2 presents the CPU-times required for all the methods in the analysis of the filter. The original spatial images method spent about 1336 seconds per frequency point, showing the practical limitation of this technique. In fact, the use of this method without any acceleration technique leads to prohibitively long simulations. The combination of this technique with the use of dynamic ground planes increases the method efficiency (to about 342 seconds per frequency point). However, the total time required for the analysis is still very long. The use of the Green's function interpolation scheme (see Section 3.3.1) allows to greatly reduce the total time of the analysis. Specifically, this method is about 98.098% faster than the original technique employing the first-level interpolation, 99.169% with the second-level and 99.682% with the third level, outperforming also the commercial ADS© package. Finally, the use of the singular and non-singular MPIE matrix decomposition method (see Section 3.3.2) achieves the best results, incredibly requiring just 0.7 seconds per frequency point to

analyze this filter. Therefore, this method is more than 5 times faster than the interpolation scheme.

From the results shown in Fig. 3.17b and in Table 3.2, we can conclude

- The spatial images technique is very accurate. The agreement between this method and other full-wave approaches is remarkable.
- The acceleration techniques presented in Section 3.3 are very accurate, and they do not introduce any important variations in the analysis of a practical microwave shielded circuit. In general, a deviation below of 0.1% in the scattering parameters computation is found.
- The singular and non-singular MPIE matrix decomposition method (see Chapter 3.3.2) is the most efficient acceleration algorithm related to the spatial images technique. It is about 5 times faster than the Green's functions interpolation scheme described in Section 3.3.1.
- The use of the dynamic ground planes (see Section 2.4.1 of Chapter 2) is very convenient for the analysis of rectangular multilayered cavities, in terms of both, accuracy and efficiency.

3.5.2 Example II: 4-Poles Coupled-Line Filter. Design I.

The second practical example is a boxed microstrip bandpass filter of fourth order based on coupled line sections presented in [Pascual García et al., 2006], which is sketched in Fig. 3.18a. In the analysis of the filter, we have employed the spatial images technique combined with the use of dynamic ground planes, as described in Section 2.4 of Chapter 2. In addition, the acceleration technique based on the singular and non-singular MPIE matrix decomposition has been applied. For the analysis, 12 images are employed and placed around the cavity at the air-dielectric interface. Besides, the printed circuits are meshed using a total of 104 unit-cells.

Fig. 3.18b presents the filter response obtained by the proposed spatial images technique, the spectral domain method described in [Álvarez Melcón et al., 1999] and by the spatial neural network approach presented in [Pascual García et al., 2006]. As can be observed in the figure, extraordinary agreement among the different techniques has been obtained, fully validating the accuracy of the spatial images method. Note that this structure is specially difficult to be handled by the spectral-domain method, because it has a large box as compared with the size of the printed circuits (which turns out into convergence difficulties [Alvarez Melcon, 1998]).

Table 3.3 presents the CPU-times required for all the methods in the analysis of the filter. It can be seen in the results reported that the accelerated spatial images technique obtains the best computational performance. In particular, the optimized implementation improves the commercial software ADS© by a factor of 27. The proposed technique is even faster than the neural-network method reported in [Pascual García et al., 2006] by a factor of 9. In addition, the neural-network method needs training time, which can be long. This extra computational effort is not needed when the accelerated spatial images approach is used.

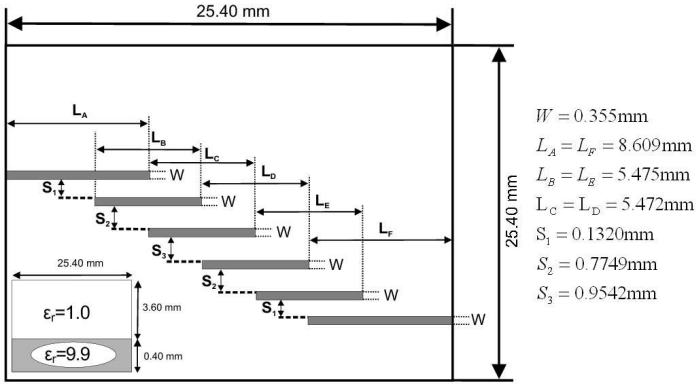

(a)

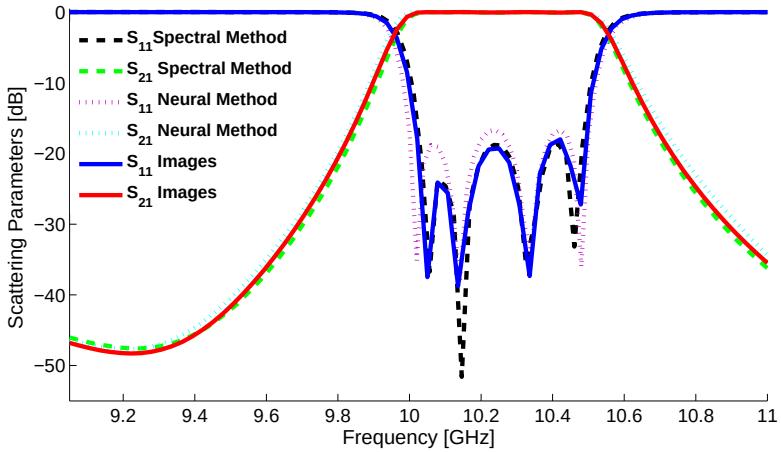

(b)

Figure 3.18 – Boxed microstrip bandpass filter of fourth order based on coupled line sections. Design I. (a) Filter layout. (b) Scattering parameters computed with the proposed images technique. Full-wave simulation data, computed with the spectral method proposed in [Álvarez Melcón et al., 1999] and with the neuronal technique described in [Pascual García et al., 2006], is employed for validation.

Technique	Time per frequency point
Accelerated Spatial Images Technique	0.3567 sec.
Spectral Method [Álvarez Melcón et al., 1999]	9.6439 sec.
Neuronal Network Method [Pascual García et al., 2006]	3.2708 sec.

Table 3.3 – Comparison of the time (per frequency point) required by different methods for the analysis of the filter shown in Fig. 3.18. A total of 104 cells are used to discretize the printed circuit.

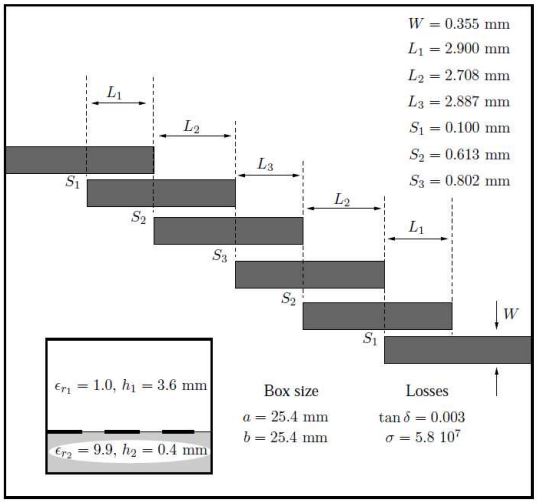

(a)

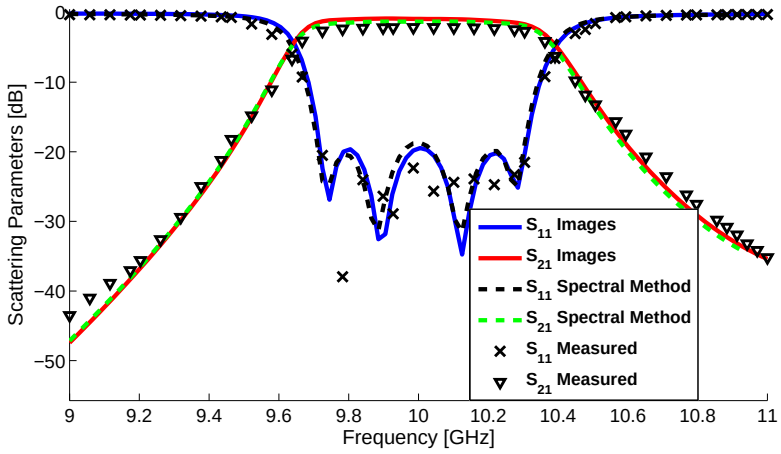

(b)

Figure 3.19 – Boxed microstrip bandpass filter of fourth order based on coupled line sections. Design II. (a) Filter layout. (b) Scattering parameters computed with the proposed images technique. Full-wave simulation data, computed with the spectral method proposed in [Álvarez Melcón et al., 1999], and measured results are employed for validation.

3.5.3 Example III: 4-Poles Coupled-Line Filter. Design II.

The third filter considered is shown in Fig. 3.19a. This filter was initially proposed in [Guglielmi and Alvarez-Melcon, 1995], [Alvarez Melcon, 1998]. The results of the analysis are presented in Fig. 3.19b, where again an extraordinary agreement has been found between the proposed spatial technique and the spectral approach [Álvarez Melcón et al., 1999]. Again, this structure is specially difficult to be handled by the spectral method, because it has a large box as compared with the size of the printed circuits. Besides, note that measured data has been included to further validate the accuracy of the method.

	Accelerated Spatial Images		Spectral Method	
Mesh	*Time per frequency point*	*Basis functions per λ*	*Time per frequency point*	*Modes*
38 cells	0.072 sec	3.0	0.160 sec	20000
76 cells	0.184 sec	3.0	1.209 sec	22500
114 cells	0.328 sec	3.0	9.570 sec	40000
152 cells	0.512 sec	3.0	18.591 sec	50000

Table 3.4 – Comparison of the time (per frequency point) required by the proposed spatial method and an spectral technique [Álvarez Melcón et al., 1999] for the analysis of the filter shown in Fig. 3.19.

Mesh	MPIE formulation (no shield) seconds per frequency point	Accelerated spatial images (shielded) seconds per frequency point	% increment
38 cells	0.0601 sec.	0.0720 sec.	20.0 %
76 cells	0.1480 sec.	0.1844 sec.	24.3 %
114 cells	0.2561 sec.	0.3283 sec.	28.1 %
152 cells	0.3960 sec.	0.5160 sec.	30.3 %

Table 3.5 – Comparison of the time (per frequency point) required to analyze the filter shown in Fig. 3.19a with and without considering the shielded enclosure.

A careful study about the efficiency of the two methods, as a function of the number of discretization cells, is presented in Table 3.4. The proposed spatial method converges in all cases using just 3 basis functions per λ (which turns out into 12 images per ring). On the contrary, the convergence of the spectral method directly depends on the size of the mesh, requiring a very large number of modes in all cases. In terms of efficiency, the proposed spatial technique is always much faster than the spectral approach. For low mesh densities, even though both techniques are quite competitive, the spatial method is more than two times faster. The efficiency distance between the two methods increases with the mesh density, being the spatial technique more than 35 times faster than the spectral approach for the case of a very dense mesh.

In addition, in order to further demonstrate the efficiency of the accelerated spatial images technique, we have analyzed the filter shown in Fig. 3.19a considering the filter with and without the shielded enclosure. In the case that the enclosure is not considered, the formulation reduces to the standard MPIE method (see Section 3.2), which is optimized to perform this type of analysis. Note that in this case the results obtained are not correct, because they neglect the shielding effects [Dunleavy and Katehi, 1988b]. In the case that the enclosure is considered, the same MPIE formulation incorporates the Green's functions proposed in Chapter 2 (which takes into account the shielding effects). This comparative gives an intuitive idea about the additional computational effort required to model the shielding enclosures within an MPIE formulation. The temporal comparative is shown in Table 3.5.

As can be seen in the table, the increment in the computational effort required to incorporate the shielding effects into a standard MPIE formulation is limited. As expected, the influence of the novel

Green's functions is more important when a high density mesh is employed. This makes sense, because the size of the MPIE MoM is bigger and the Green's functions must be computed for more pair of source-observation points. However, note that the time needed to compute the Green's functions for each point source is independent on the mesh size (on the contrary as it occurs in spectral methods [Itoh, 1989], [Álvarez Melcón et al., 1999], where the number of modes to sum up the kernel depends on the cavity size and on the mesh cells dimensions). In the spatial domain approach, the increment in the computational cost is only due to the fact that more point sources in the mesh are considered and must be computed. This comparative demonstrates that the proposed technique is able to efficiently analyze microwave shielded circuits, adding only a very small percentage in the computational effort, as compared with a regular MPIE implementation for planar circuits [Mosig, 1989], and avoiding any convergence issues.

3.5.4 Example IV: 4-Poles Broadside Coupled Filter within a 4-Layer Rectangular Cavity

The fourth structure considered is a broadside coupled filter sketched in Fig. 3.20a. The circuits of the filter are printed on the two dielectric substrates of the multilayer structure. The main advantage of broadside filters is that they allow the introduction of cross couplings between nonadjacent resonators. The cross couplings can then be used to implement transmission zeros that can significantly increase the selectivity of the filters [Alvarez-Melcon et al., 2001].

It is worth mentioning that two rings of spatial images (or auxiliary sources) are needed to obtain accurate results for this structure. This is because the height of this structure is electrically large. The rings are placed at the first and second air-dielectric interfaces (see Fig. 3.20a). In each ring, it is required the use of 3 basis functions per λ (which turns out into 12 images per ring). Besides, note that a total of 150 cells have been employed to discretize the printed circuits. In Fig. 3.20b, a manufactured filter prototype, showing all pieces of the structure, is presented. Simulated versus measured results are included in Fig. 3.20c, showing very good agreement.

The time required by the accelerated spatial-images technique for the analysis of this filter is about 0.85 seconds per frequency point. As a reference, note that the time required by the commercial software ADS© is about 16.25 seconds. Again, the accelerated spatial images if very efficient, outperforming the commercial ADS© package by a factor of 19. In addition, note that the analysis of this filter demonstrate the accuracy of the spatial-images technique to analyze electrically large multilayered structures.

3.5.5 Example V: Hybrid Waveguide-Microstrip Filter using a Multilayered Cavity with a Triangular Cross-Section

As a fifth example, we present in Fig. 3.21a a hybrid waveguide-microstrip filter which uses a multilayered cavity with a triangular-isosceles cross section. As introduced in Section 3.4, this type of filters combines one of the cavity resonances with a printed line microstrip resonance in order to obtain a second order filter response.

As previously commented, this filter follows the Modified Doublet topology (see Fig. 3.12 and

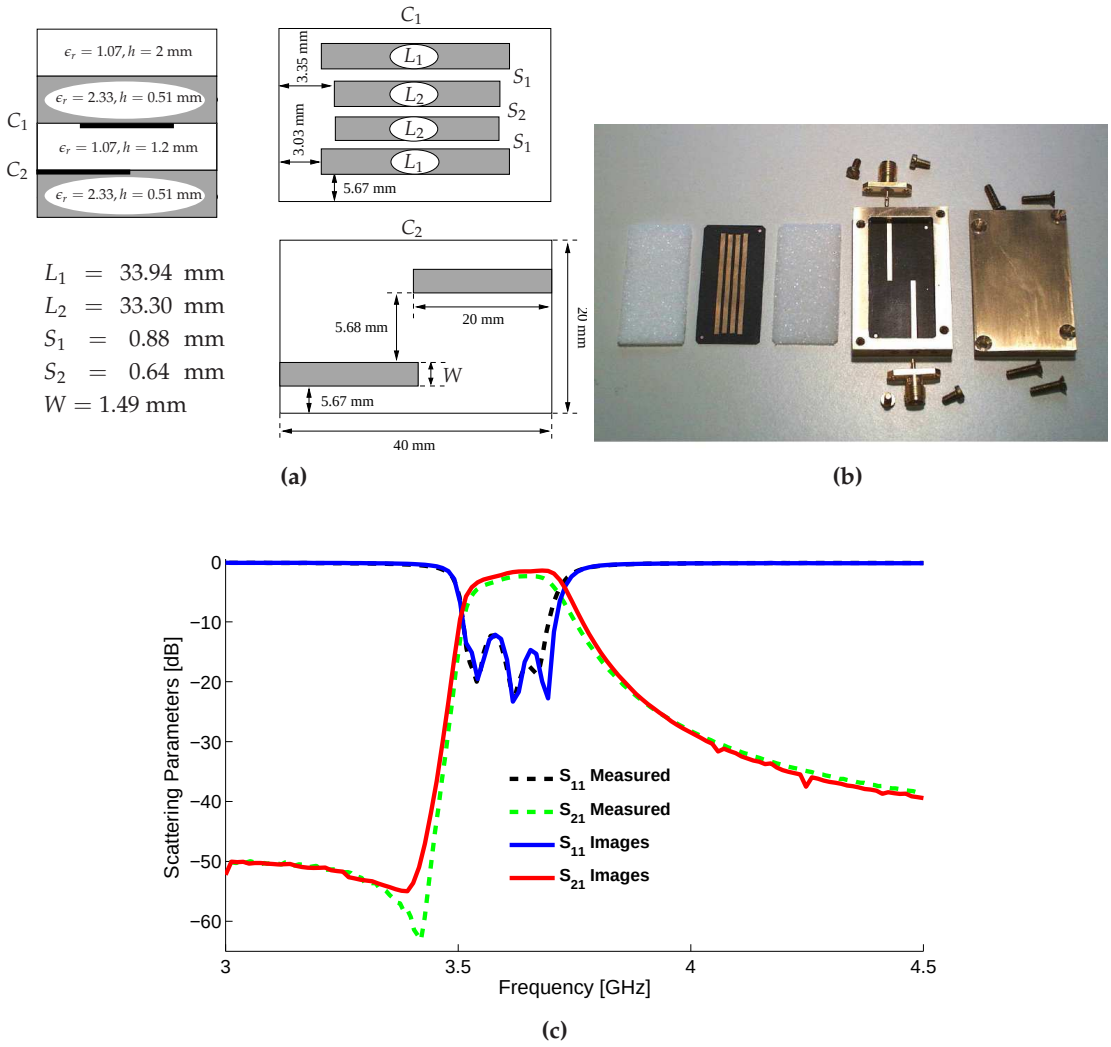

Figure 3.20 – 4-poles bandpass broadside-coupled filter within a 4 layer rectangular cavity. (a) Filter layout. (b) Aspect of the fabricated breadboard, showing all pieces of the filter. (c) Scattering parameters computed with the proposed images technique. Measured data is employed for validation.

[Amari and Rosenberg, 2003]). In our case, we want to design a second order bandpass filter with -10.0 dB of return loss, and two transmission zeros placed at the frequencies of $f_1 = 4.26$ GHz and $f_2 = 5.63$ GHz. The filter is centered at 4.52 GHz with a bandwidth of 180 MHz. Therefore, the proposed filter presents a response with two transmission zeros asymmetrically located with respect to the passaband. The $(N+2)$ by $(N+2)$ coupling matrix obtained with the theory presented in [Cameron, 2003] is

$$M = \begin{pmatrix} 0 & -0.5249 & 0.6487 & 0.0179 \\ -0.5249 & 1.0447 & 0 & 0.5249 \\ 0.6487 & 0 & -0.9477 & 0.6487 \\ 0.0179 & 0.5249 & 0.6487 & 0 \end{pmatrix}. \tag{3.28}$$

It is well known that the Modified Doublet always have one of the four couplings negative. In the proposed configuration, we observe in Fig. 3.22 that the x-component of the electric field, which

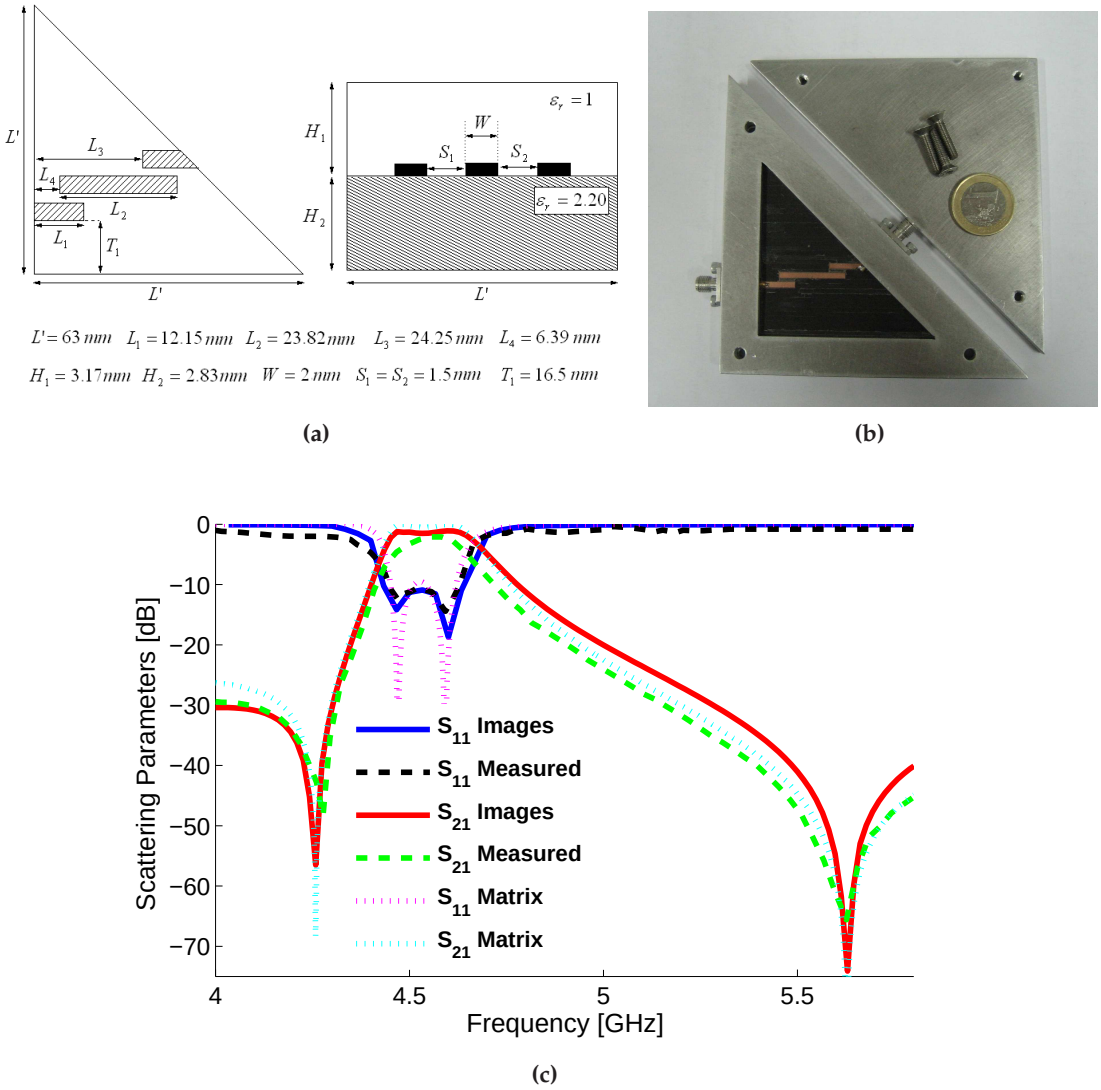

Figure 3.21 – Novel triangular-shaped second-order transversal filter. (a) Filter layout. (b) Aspect of the fabricated breadboard, showing all pieces of the filter. (c) Scattering parameters computed with the proposed images technique. Measured data is employed for validation.

couples to the input/output printed ports, has a zero at the center of the cavity, and then changes sign at the side of the output port. It is this change in sign of the x-component of the electric field, which synthesizes the negative coupling needed in the Modified Doublet. At this point it is interesting to remark that the coupling mechanisms at the input/output ports of the triangular structure are not symmetric, due to the shape of the triangular cavity. This is a difference in behavior as compared to the square cavity (see Section 3.4), where a symmetric coupling between input/output ports always occurs.

In order to design this filter, we follow the procedure guidelines given in Section 3.4. First, the L' dimension of the cavity (related to the physical length of the two equal sides of the triangle, see Fig. 3.21a) is adjusted in order to tune the cavity resonance at the frequency of 4.47 GHz. Then,

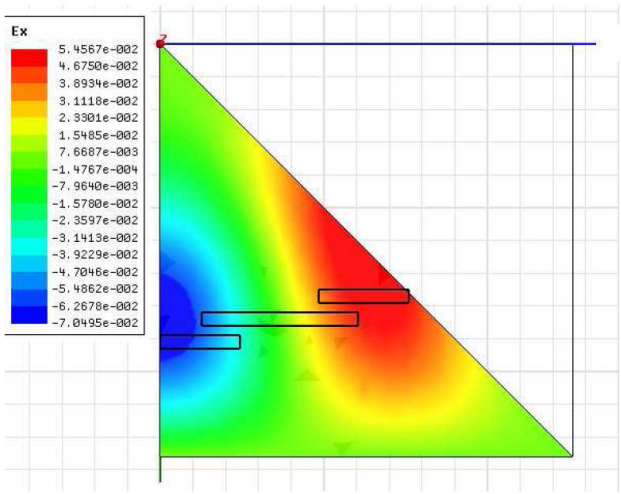

Figure 3.22 – Electric field x-component of the LSM mode inside the triangular cavity, at the first resonant frequency.

the length of the microstrip resonator is individually modified, in order to provide its resonance at the frequency of 4.6 GHz. The final dimensions obtained after the design procedure are shown in Fig. 3.21a. A prototype, shown in Fig. 3.21b, has been manufactured and tested. It is important to remark that the adequate modeling of the triangular multilayered box is essential for this type of filter. This is because one of the resonances of the filter is provided by the partially filled cavity.

Besides, note that other full-wave techniques (such as FDTD [Taflove and Hagness, 2005] of FEM [Lee et al., 1997]) have difficulties in analyzing this filter. This is because of the tight couplings existing between the input and output ports and the printed line resonator, which is difficult to model by a volume mesh. On the contrary, with an integral equation technique these couplings can be modeled more accurately. In this case, only the printed circuits must be meshed, because the multilayered cavity behavior is included into the Green's functions. In Fig. 3.21c we present the response of the filter obtained with the new method. Measured results are also shown for validation purposes. Good agreement between both results can be observed.

The advantages of the proposed triangular-shaped filter as compared to the filter which uses a square cavity are related to the final application. Although the filter response is very similar in both cases, note that the position of the connectors and the size of the box is different. Therefore, this triangular transversal filter may be applied in particular cases, where specific connector positions and size requirements must be satisfied.

3.5.6 Example VI: Hybrid Waveguide-Microstrip Filter using a Multilayered Cavity with a Trapezium-shaped Cross-Section

In this example, we present the design and analysis of a bandpass filter implemented in the hybrid waveguide-microstrip technology, using a multilayered cavity with a trapezium-shaped cross section as a host enclosure. The structure combines one microstrip printed resonator with a resonance of the trapezium-shaped cavity to build up a second order response. It is important to point

out that the modeling of the cavity is a key issue in this structure. Again, this is because the cavity provides one of the resonances of the filter. Consequently, a small error in the modeling of the resonant frequencies of the cavity will lead to a wrong design. The lateral and top views of the filter are shown in Fig. 3.23a.

As previously commented, this type of filters follows the Modified Doublet topology (see Fig. 3.12 and [Amari and Rosenberg, 2003]). In our case, we want to design a second order bandpass filter with -15.0 dB of return loss, and two transmission zeros placed at the frequencies of $f_1 = 4.12$ GHz and $f_2 = 5.3$ GHz. The filter is centered at 4.53 GHz, with a bandwidth of 140 MHz. The $(N+2)$ by $(N+2)$ coupling matrix obtained with the theory presented in [Cameron, 2003] is

$$M = \begin{pmatrix} 0 & -0.6952 & 0.7542 & 0.0220 \\ -0.6952 & 1.3034 & 0.0 & 0.6952 \\ 0.7543 & 0.0 & -1.2765 & 0.7543 \\ 0.0220 & 0.6952 & 0.7543 & 0.0 \end{pmatrix}. \tag{3.29}$$

For the design of the structure, we follow again the guidelines presented in Section 3.4. The trapezium-shaped cavity is first adjusted to obtain a resonance at the frequency of 4.5 GHz. The printed resonator is then optimized to provide the second resonance of the filter. The final filter response is shown in Fig. 3.23c. Good agreement between both measured data and results obtained with the spatial images method is observed. The differences in the minimum insertion loss observed within the passband are mainly due to the cavity losses, which are not considered by the developed spatial images technique. In some cases, these losses can be important since the filter operates with one of the resonances excited in the partially filled cavity.

For the analysis of the structure using the spatial images technique, two rings with 15 images are needed in order to obtain a convergent solution in this cavity. The reason to employ two rings (located at heights of $z = 1.585$ mm and $z = 3.17$ mm) is because the height of this cavity is electrically large. In this case, the use of just one ring of images leads to incorrect results. However, convergence is achieved when using 2 of more rings. This example shows the practical value of the multiring approach (see Section 2.3.2 of Chapter 2) of the spatial images technique.

Finally, note that the microstrip lines were meshed with 150 rectangular cells. The time required for the analysis, using the singular and non-singular MPIE matrix decomposition acceleration method, is about 5 seconds per frequency point. Note that this time is higher as compared with the time required to analyze other microwave shielded circuits. The main reason is that the dynamic ground planes method (see Section 2.4 of Chapter 2), which is specifically designed for rectangular enclosures, can not be applied for this geometry. The dynamic ground plane methods usually requires less than half number of unknowns (providing better convergence rates) as compared with an standard spatial images method, which turns out into a huge decrease of the computational cost required to perform any analysis. Besides, note that no CPU time is given for ADS© since this software can only treat rectangular cavities.

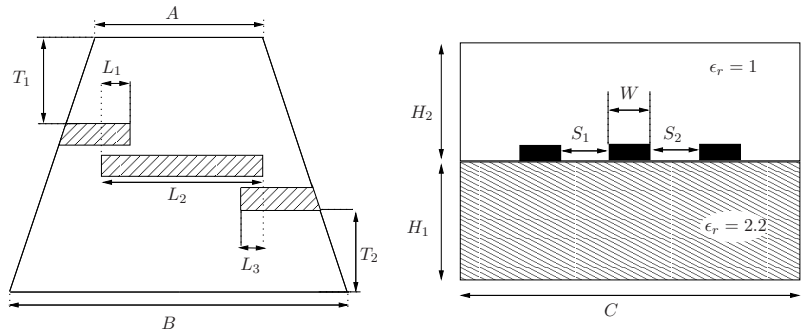

$L_1 = L_3 = 6$ mm, $L_2 = 24$ mm, $H_1 = 3.17$ mm, $H_2 = 2.83$ mm, $A = 27.4$ mm, $S_1 = S_2 = 1.5$ mm, $T_1 = T_2 = 15.5$ mm, $W = 2$ mm, $B = 56$ mm, $C = 40$ mm

(a)

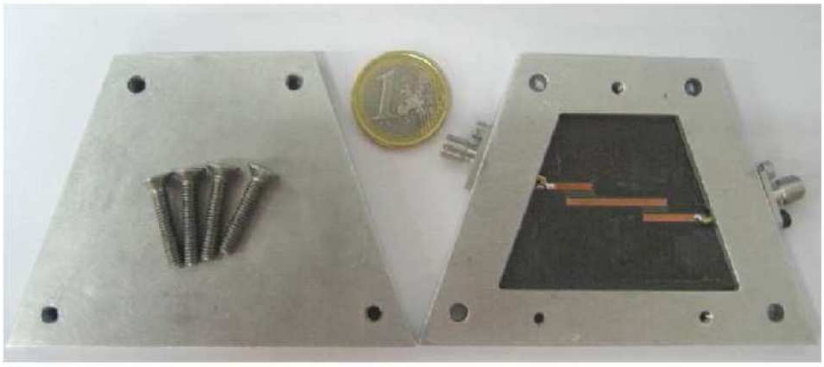

(b)

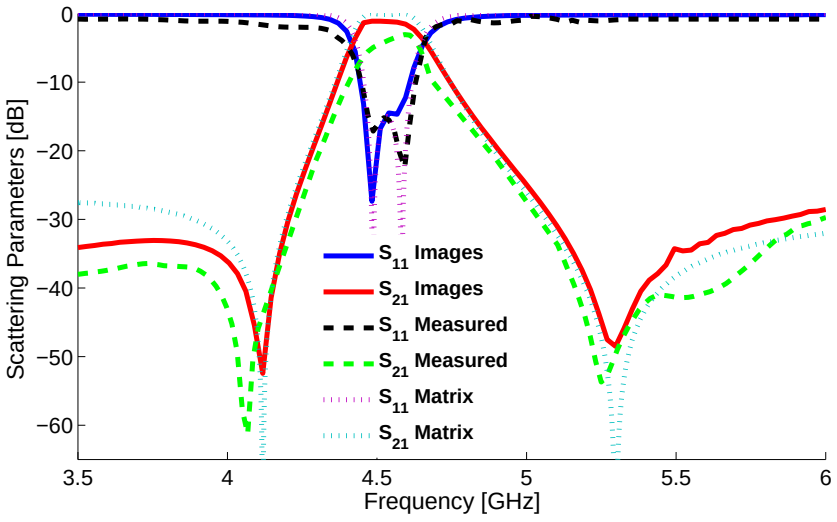

(c)

Figure 3.23 – Novel trapezium-shaped second-order transversal filter. (a) Filter layout. (b) Aspect of the fabricated breadboard, showing all pieces of the filter. (c) Scattering parameters computed with the proposed images technique. Measured data is employed for validation.

3.5.7 Example VII: Dual-Band Hybrid Waveguide-Microstrip Filter using a Multilayered Cavity with a Rectangular Cross-Section

The last filter under consideration is shown in Fig. 3.24a. It is a third-order example of a dual-band hybrid waveguide-microstrip filter [Martínez-Mendoza et al., 2008]. A prototype of the device (see Fig. 3.24b) has been manufactured and tested. The substrate selected for manufacturing is an RT Duroid with relative permittivity of $\varepsilon_r = 2.2$ and thickness of 1.57 mm. The prototype implements a dual bandpass filter with 17 dB of return loss, and three transmission zeros located at 1.4, 4.3, and 4.6 GHz. The center frequency is 4.7 GHz, and its bandwidth is 430 MHz. The $(N+2)$ by $(N+2)$ coupling matrix obtained with the theory presented in [Cameron, 2003], [Martínez-Mendoza et al., 2008] is

$$M = \begin{pmatrix} 0 & -0.575 & -0.533 & 0 & 0 & 0.027 \\ -0.575 & -1.095 & 0 & 0 & 0 & 0.575 \\ 0.533 & 0 & 0.483 & 0.511 & 0 & 0 \\ 0 & 0 & 0.511 & 0.084 & 0.511 & 0 \\ 0 & 0 & 0 & 0.511 & 0.484 & 0.533 \\ 0.027 & 0.575 & 0 & 0 & 0.533 & 0 \end{pmatrix}. \tag{3.30}$$

The dimensions of the designed and manufactured dual-bandpass filter, obtained after optimization, are $a = 40.0$ mm, $b = 34$ mm, $L_{in} = L_{out} = 14.0$ mm, $L_{r_2} = L_{r_3} = 24.54$ mm, $L_1 = 3$ mm, $L_2 = 3.14$ mm, $w_1 = w_2 = 1.8$ mm, and $w_3 = 5$ mm. The final dielectric height of the prototype is achieved by piling up two RT-DUROID substrates of thickness 1.57 mm. This extended thickness is needed to obtain the required high coupling value to the cavity mode (see Section 3.4).

The results of the analysis employing the proposed spatial technique, and a spectral approach [Álvarez Melcón et al., 1999] are presented in Fig. 3.24c. Measured data is included as validation. Note that an extraordinary agreement between the two completely different methods has been obtained. In the simulations, losses are included in the dielectric substrate $(\tan\delta = 0.003)$, and in the printed metalizations $\sigma = 3 \cdot 10^7\,\Omega^{-1}/\text{m}$. The minimum insertion loss of the filter inside the lower passband is 1.3 dB, whereas inside the upper passband the minimum insertion loss increases to 3.45 dB. The high insertion losses in the upper passband are due to the use of a low quality brass material for the manufacturing of the cavity box. The upper passband is formed by a resonant mode excited in this cavity. Therefore, the conductivity of the cavity strongly influences the insertion losses of the upper passband. Consequently, the high insertion losses in the upper passband can be reduced using silver plating techniques on the walls of the shielding cavity.

The filter under analysis is specially difficult to be handled by the spatial images method, because it has a thick substrate and it requires two rings of images. A careful study about the efficiency of the proposed spatial and the spectral domain [Álvarez Melcón et al., 1999] methods, as a function of the number of discretization cells, is presented in Table 3.6. As can be observed, the proposed spatial technique completely converges using 3 basis functions per λ (which turns out into 12 images per ring), independently of the mesh. As expected, the spectral method requires a higher number of modes to converge as the mesh density increases. In terms of efficiency, the proposed spatial method is able to compete against the spectral approach in all cases. For low mesh density, the spectral approach is slightly faster, because it converges summing up a low number of modes. However, as the

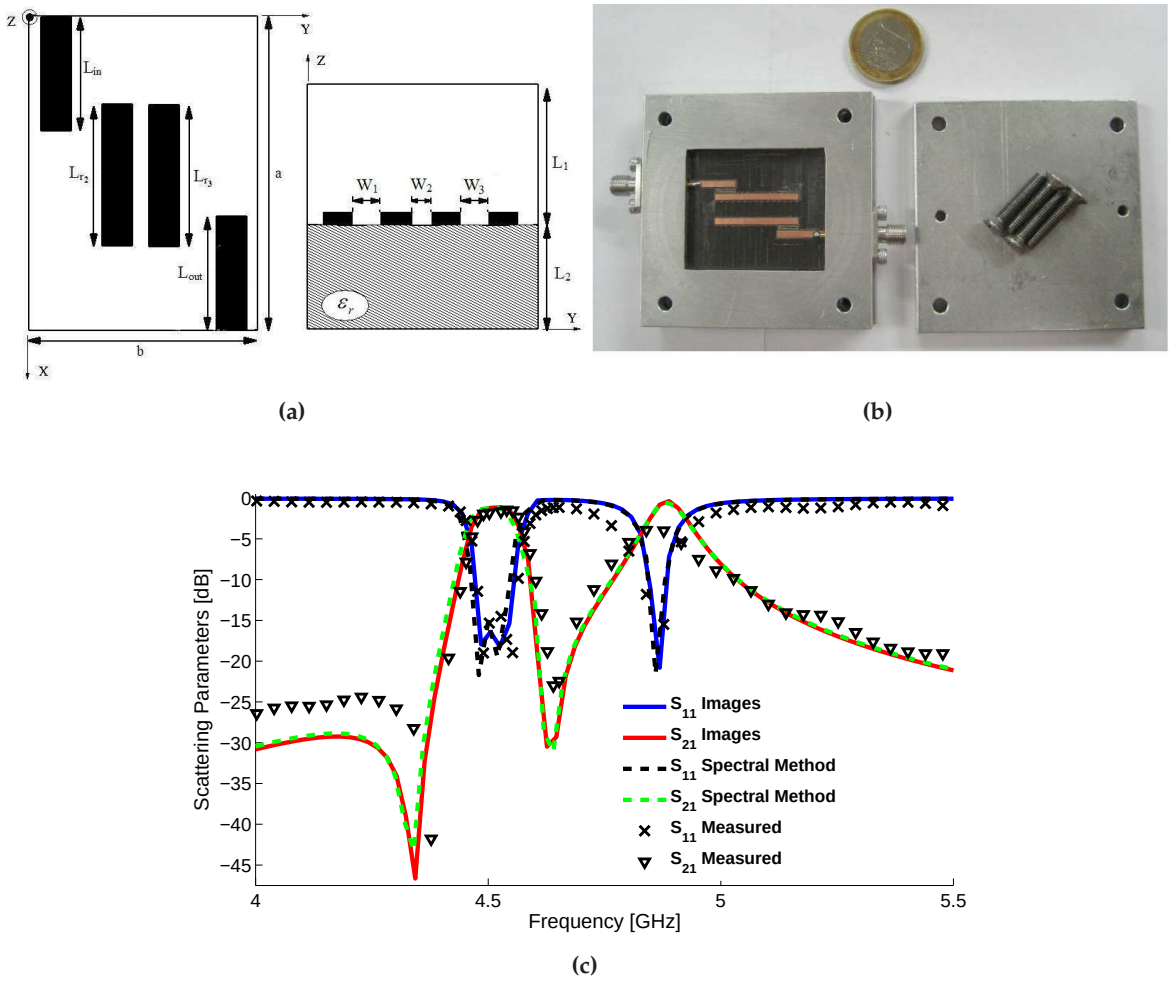

Figure 3.24 – Novel dual-band hybrid waveguide-microstrip filter. (a) Filter layout. (b) Aspect of the fabricated breadboard, showing all pieces of the filter. (c) Scattering parameters computed with the proposed images technique. Full-wave simulation data, computed with the spectral method proposed in [Álvarez Melcón et al., 1999], and measured results are employed for validation.

	Proposed Spatial Method		**Spectral Method**	
Mesh	*Time per frequency point*	*Basis functions per λ*	*Time per frequency point*	*Modes*
45 cells	0.108 sec	3.0	0.075 sec	2500
90 cells	0.312 sec	3.0	0.665 sec	2500
135 cells	0.604 sec	3.0	1.903 sec	3500
180 cells	1.012 sec	3.0	3.909 sec	3500

Table 3.6 – Comparison of the time (per frequency point) required by the proposed spatial method and an spectral technique [Álvarez Melcón et al., 1999] for the analysis of the filter shown in Fig. 3.24.

mesh density increases, the spatial approach becomes more and more efficient (even two and three times faster). This is because an increase in the mesh density only affects the size of the MoM matrix,

but it does not affect to the speed in the calculation of the Green's functions.

3.6 Conclusions

In this chapter, an accurate and efficient CAD tool for the analysis of a wide variety of multilayered shielded printed circuits has been described in great detail. The method is based on a mixed-potential integral equation, which calls for the evaluation of space-domain Green's functions associated to multilayered cavities with convex arbitrarily-shaped cross section. Two acceleration techniques, based on the special features of the spatial images technique employed to compute the Green's functions, have been proposed. It has been shown that the method based on the singular and non-singular MPIE matrix decomposition is much more efficient than the technique based on interpolation of the complex images values. Note that the use of these methods allows an extremely fast and efficient analysis of multilayered shielded circuits.

In addition, a novel hybrid waveguide-microstrip technology has been presented. This technology combines one resonance, provided by the multilayered cavity, with N microstrip resonators, leading to a $N+1$ order filter. The proposed technology is light, compact, low-lossy, uses the filter package as a part of the filter, and allows to implement transversal filters. A simple procedure for the design of this type of filters has been presented. Then, the novel filtering structure has completely been validating, by using full-wave commercial software and fabricated prototypes. Besides, note that the proposed CAD tool is ideal for the analysis of hybrid waveguide-microstrip filters. This is because the proposed Green's functions inherently takes into account for the cavity behavior, and therefore, only the metallic printed circuits must be meshed.

A wide variety of microwave shielded circuits have been then investigated using the proposed CAD tool. Specifically, coupled-line filters, broadside-coupled filters, and novel designs based on the hybrid waveguide-microstrip technology have been analyzed. Excellent agreement between measured data, results from commercial full-wave software and the data obtained by the proposed CAD tool has been achieved in all cases. A careful comparative study has demonstrated that the proposed method is much faster than any other known IE technique, including spectral approaches, avoiding any convergence problem. Therefore, the proposed CAD tool is ideal for the fast analysis, design and efficient optimization of shielded microwave devices.

Chapter 4

Impulse-Regime Analysis of CRLH Structures

4.1 Introduction

In 1967, the Soviet physicist V. Veselago published a theoretical paper [Veselago, 1968] which described wave propagation in media with simultaneously negative permittivity and permeability ($\varepsilon < 0$ and $\mu < 0$). In that paper, this specific type of media was denoted as "LH" (Left-Handed), to express that the electric field, magnetic field, and phase vectors build a left-handed triad, instead of the regular right-handed triad obtained by right-handed ("RH") materials, which are the well-known materials found in nature. Furthermore, many fundamental features and phenomena associated to this novel type of media (such as antiparallel phase and group velocity, frequency dispersion of the constitutive parameters, negative refraction at the interface between a RH and a LH medium, reversal Doppler effect, reversal Vavilov-Cerenkov radiation, reversal Snell's-law, among many others), were carefully presented and explained. After about 30 years, the British physicist J. B. Pendry [Pendry et al., 1999] described how usual right-handed materials can be arranged to obtain macroscopic negative permeability or permeability. For this purpose, traditional materials were periodically loaded with electrically small split-ring resonators or parallel wires, leading to a composite material with $\mu < 0$ or $\varepsilon < 0$, respectively. Soon after, an artificial, effectively homogeneous, structure was proposed by David Smith et al [Smith et al., 2000] [Shelby et al., 2001]. This structure, inspired from Pendry's work, combines both type of periodic loading to simultaneously obtain negative permeability and permittivity, over a specific frequency range. It constitutes the first experimental demonstration of such kind of material, and it has lead to the development of the so-called *bulk metamaterials*. One year later, C. Caloz and T. Itoh [Caloz et al., 2002], G. Eleftheriades [Iyer and Eleftheriades, 2002] and A. Oliner [Oliner, 2002] independently introduced a new approach to obtain these unusual properties on traditional transmission lines, based on the periodical loading of a host line with electrically small and closely spaced series capacitances and shunt inductances. This approach has lead to the development of the so-called *planar metamaterials*, which substantially differs from the bulk media approach. Since these seminar works were published, hun-

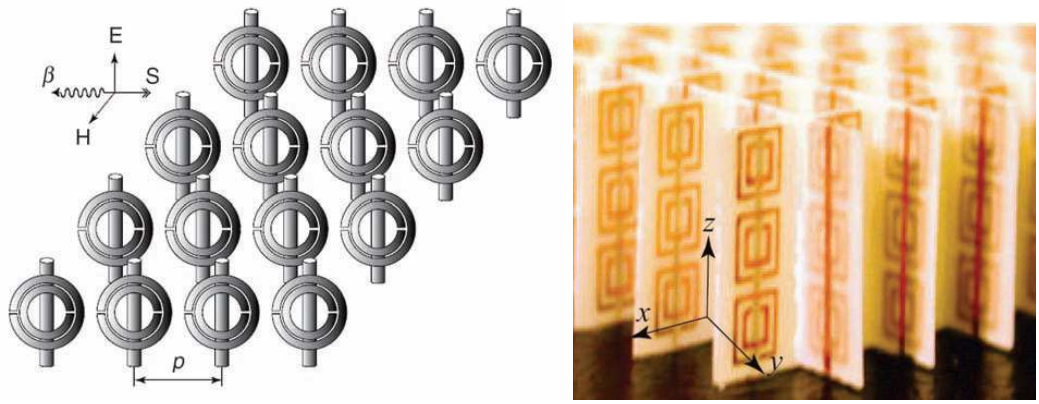

(a) (b)

Figure 4.1 – Resonant particle metamaterial structures, based on split-ring resonator and wire medium. Negative permittivity ($\varepsilon < 0$) is provided by the electric field polarization along the wires, whereas the negative permeability ($\mu < 0$) is provided by the magnetic field polarization in the split-ring resonator. (a) Mono-dimensional structure, reproduced from [Smith et al., 2000] (b) Bi-dimensional structure, reproduced from [Shelby et al., 2001].

dreds of papers, articles and several books have been written about the novel features, phenomena, and applications that this novel type of materials have introduced.

But, what is a metamaterial?. Metamaterials are difficult to define and classify, because the definition and subsequent notation employed to refer to them usually differs from some researches to others, as a function of they background disciplines (optics, microwaves, antennas, filters, etc) [Sihvola, 2007]. In this work, I have used an engineering point of view, which may define electromagnetic metamaterials as "artificial effectively homogeneous electromagnetic structures with unusual properties not readily available in nature" [Caloz and Itoh, 2005], where "an effectively homogenous structure" is related to a structure composed of a combination of discrete unit cells, whose size (denoted as p) is much smaller than the guided wavelength at the frequencies of interest (i.e. $p \ll \lambda_g$). Note the use of the prefix *meta*, which is Greek means "beyond" or "after", suggests the idea that these artificial materials posses properties that transcend those found in nature [Eleftheriades and Balmain, 2005]. These novel properties are obtained from a macroscopical point of view, while the properties of their constitutive unit cells may be different. An intuitive analogy can be made with the taste of an ice-cream: the final taste may be quite different from the sum of taste of ice and cream [Sihvola, 2007].

As previously commented, *bulk metamaterials* were, chronologically, the first metamaterials introduced and experimentally verified. Currently, this technology is mature enough to have an established procedure for its synthesis, analysis and design [Pendry et al., 1999], [Smith et al., 2000], [Engheta and Ziolkowski, 2006], [Carbonell et al., 2011], [Marques et al., 2008]. This approach make a systematic use of split ring resonators (SRRs) to achieve negative permeability, whereas a system of metallic wires is employed to obtain negative permittivity, as shown in Fig. 4.1. This type of metamaterials are based on a *resonant approach*, where the metamaterial behavior is obtained thanks to the resonances of their constitutive elements. Due to this, their initial responses were narrowband

and lossy. Recent studies have shown how to increase their associated bandwith and to reduce their losses, allowing their use in practical applications [Marques et al., 2008]. However, the final structures are still volumetric and heavy. These are fundamental restrictions to its use in microwave applications, where most components and systems have a planar implementation.

The introduction of *planar metamaterials* [Caloz et al., 2002], [Iyer and Eleftheriades, 2002], [Oliner, 2002] in 2002 paved the road to the practical use of metamaterials at microwaves, leading to many prospective engineering applications and allowing their integration into many systems. In contrast to the previous generation of bulk matematerials, this generation follows a *non-resonant approach*. This approach has lead to the development of broadband and low-loss metamaterials in planar technology. One common and practical implementation of such metamaterials is based on the use of composite right/left-handed transmission lines (CRLH TL) [Caloz and Itoh, 2005], which uses simple circuit theory to express the combined left-handed and right-handed behavior of a structure. This has led to an LC-loaded transmitting medium approach, inherently broadband, which can easily be fabricated in microstrip [Caloz and Itoh, 2005] or coplanar waveguide (CPW) [Eleftheriades and Balmain, 2005] technologies, just to mention two of them. On the other hand, another common implementation of planar metamaterials is based on the use of split ring and complementary split ring resonators, following a *resonant approach* [Marques et al., 2008], [Selga et al., 2011]. Initially, this type of planar metamaterials has a narrow band response, due to the use of the constitutive elements resonances. However, there have been a lot of research effort on this area, and a broadband CRLH behavior using resonant elements has finally been achieved [Marques et al., 2008], [Duran-Sindreu et al., 2009].

There are many examples of interesting and groundbreaking applications of planar metamaterials at microwaves, such as multi-band components ([Lin et al., 2004], [Caloz, 2006] or [Eleftheriades, 2007b]), filters and diplexers ([Bonache et al., 2005] [Martín et al., 2003], [Nguyen and Caloz, 2006], [Gil et al., 2007a]), couplers ([Caloz et al., 2004b], [Jarauta et al., 2004], [Nguyen and Caloz, 2007a], [Nguyen, 2010]), power-dividers ([Islam and Eleftheriades, 2008a]), phase-shifters ([Antoniades and Eleftheriades, 2003a] or [Siso et al., 2007]), lenses ([Grbic and Eleftheriades, 2004]) or backfire to endfire leaky-wave antennas ([Liu et al., 2002], or [Grbic and Eleftheriades, 2002a]), just to mention a few of them. A nice review of these and much more applications and devices can be found in metamaterials textbooks, such as [Caloz and Itoh, 2005], [Eleftheriades and Balmain, 2005] or [Marques et al., 2008]. All previously mentioned and most of metamaterials applications operate in the harmonic regime and they have been designed for narrow-band components and systems (even though some of them may support a multi-band operation).

However, the recent explosion of needs for high data-rate wireless links is currently producing a shift from narrow-band radio towards ultra-wideband (UWB) radio operation [Oppermann et al., 2004], [Ghavami et al., 2007]. Therefore, there *is a real need for novel microwave tools, concepts, phenomena and direct applications in the impulse-regime*. Meanwhile the past decades have been focused on the so-called "magnitude engineering" and filter design, a renew interest is currently given to the so-called "dispersion engineering" (which is intended to cover both, dispersion and nonlinearity). In the dispersion engineering approach, the phase is engineered to met some specific requirements in a given frequency range, shaping the electromagnetic waves to process signals

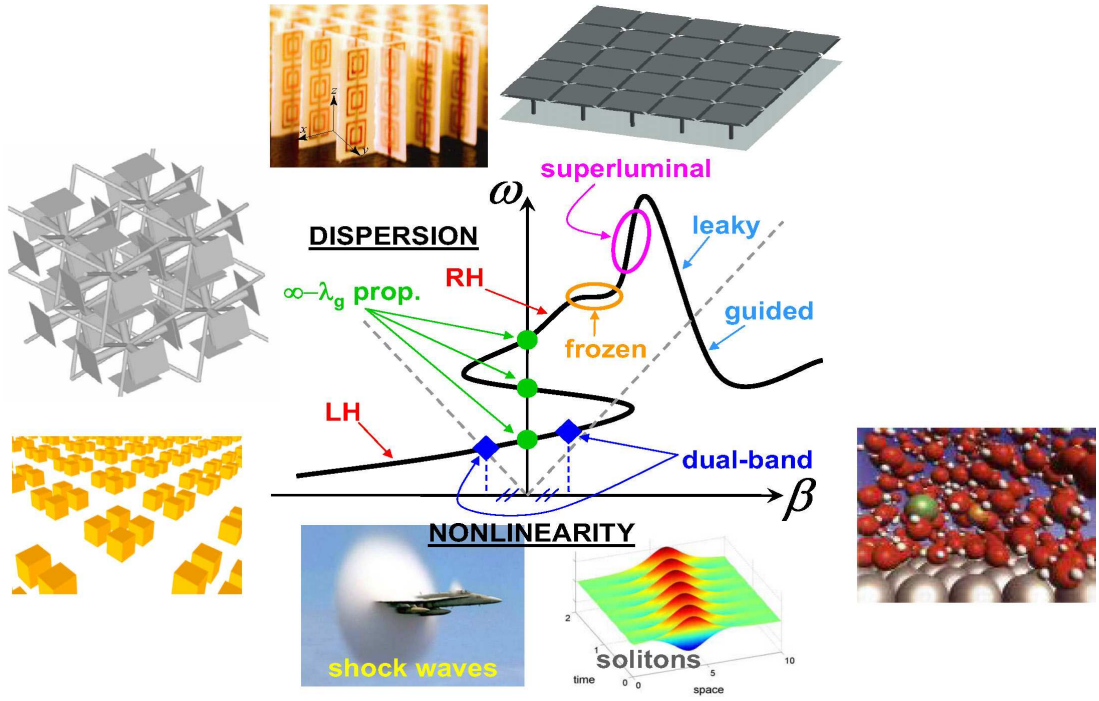

Figure 4.2 – Illustration of the Dispersion Engineering concept using CRLH LTs, showing different dispersive phenomena/applications (some of them directly transposed from optics) which can be obtained at microwaves. Reproduced from [Abielmona et al., 2008].

in an analog fashion [Gupta and Caloz, 2009].

Current dispersion engineering possibilities at microwaves are mainly related to the operation in the guided regime [Nguyen, 2010]. One possibility is the use of surface acoustic waves (SAW) [Wiegel et al., 2002] or magneto static wave (MSW) [Ishak, 1988] devices. The former has the main disadvantage that can only operate at very low frequencies, which greatly limits its use in practical applications [Dolar and Williamson, 1976]. The latter is based on magnetic materials, which are lossy, bulky and require biasing permanent magnets, incompatible with current planar microwave circuits. Other possibility is the use of of multi-section coupling structures [Withers et al., 1985] or chirped microstrip TLs [Laso et al., 2003]. Both approaches have the disadvantage of being completely dependent of the line length, which usually should be long and consequently, very lossy. This problem limits the use of these solutions in practical microwave systems.

In this context of dispersion engineering, the unprecedent, broadband and novel dispersive properties of metamaterial-based CRLH TLs may provide novel and original solutions in both, the guided and the radiative-wave operation modes (some of them are illustrated in Fig. 4.2). However, there has not been a systematic study of the impulse-regime characteristics related to CRLH TLs , and therefore only a few impulse-regime components and systems have been proposed up to now. Some examples of these applications are a Pulse Position Modulation (PPM) system [Nguyen and Caloz, 2008], a tunable pulse delay line [Abielmona et al., 2007], a true time receivers [Nguyen et al., 2008] or a real-time spectrum analyzer [Gupta et al., 2009a].

In this chapter, a time-domain Green's function formulation is presented to model impulse-regime CRLH TLs, in both, the guided and radiative-wave regimes. Initially, in Section 4.2, metamaterial-based composite right/left handed transmission lines are reviewed in detail, summarizing some descriptive formulas and fundamental properties. This brief review is focused on the harmonic-regime CRLH TLs behavior, pointing out some applications in both, the guided and radiative-wave regimes.

Then, Section 4.3 presents a closed-form time-domain Green's function approach to study pulse propagation along electrically thin CRLH TLs (see [Gómez-Díaz et al., 2009b]). The method is based on the transient analysis of 1D transmission lines [Paul, 2007] combined for the first time with the CRLH TL methodology [Caloz and Itoh, 2005], and provides analytical expressions from the inverse Fourier transform of the solutions to the generalized telegrapher's equation. The method explicitly considers the Green's function of the transmission line, leading to an easy treatment of the generator and the load, and allows to consider complex non-uniform lines. The technique is then extended to consider pulse propagation along dispersive and non-linear CRLH lines. For this purpose, the CRLH line is loaded with hyper-abrupt diodes to achieve non-linearity, leading to a new unit-cell model. The non-linear CRLH line is then analyzed cell by cell, obtaining a non-uniform CRLH structure for each discrete time. Furthermore, the time-dependence of the non-linear line as a function of the input signal (which controls the diodes behavior) is rigourously taken into account. The main advantage of the proposed formulation it that it allows an easilly combined treatment of dispersion and non-linearity.

Next, in Section 4.4, the formulation is extended to study impulse-regime radiation from CRLH leaky-wave antennas (LWAs). First, the CRLH LWA radiation features are rigorously analyzed, paying special attention to the radiation at the broadside direction. Specifically, a novel condition of the equivalent series and shunt unit-cell radiators (R, G) is derived in order to achieve a constant full-space radiation rate (see [Gómez-Díaz et al., 2011c]). Second, a deep study on the relationship between leaky modes and the currents induced on the transmission line is presented in the harmonic regime. In the study, the leaky-wave radiation is expressed as a function of the currents flowing on each conductor on the transmission lines. Due to the excitation of leaky modes, these two currents are not in phase (as occurs on regular transmission lines) leading to the far-field radiation. This novel theory provides a fundamental explanation about leaky-wave antennas, in connection with transmission lines, further simplifying the study of these interesting structures. Finally, the novel harmonic theory is transported into the time-domain (see [Gómez-Díaz et al., 2010b]), and applied to analyze impulse-regime CRLH LWAs. Due to the spectral-spatial decomposition property of LWAs [Oliner and Jackson, 2007], each frequency component of the input signal is radiated to a particular space position, where the time-dependent field evolution can efficiently been retrieved using the proposed formulation.

Finally, note that this chapter introduces the basic formulation required to the impulse-regime analysis of CRLH TLs and LWAs, but it does not include any validation of these techniques. Next chapter will employ the proposed formulations to study the impulse-regime phenomenology of CRLH structures, including a theoretical and practical demonstration of several novel optically-inspired phenomena and applications at microwaves, in both, the guided and the radiative regime. There, a careful comparison of the proposed formulation results against full-wave commercial simu-

lations and measurements will demonstrate the validity and accuracy of the novel techniques, which are several order of magnitude faster than purely full-wave methods. The novel techniques keep an excellent agreement with measured data and provide a deep insight into the physics of many impulse-regime phenomena.

4.2 Composite Right/Left-Handed Transmission Lines (CRLH TL)

4.2.1 Introduction

The first planar metamaterial structure was composed of a host transmission line loaded by inductive and capacitative elements [Caloz et al., 2002], [Iyer and Eleftheriades, 2002], [Oliner, 2002]. This transmission line approach, which is inherently nonresonant and low-loss, can be easily implemented in planar technology (such as microstrip or coplanar waveguide, for instance) and provides a practical realization of electromagnetic metamaterials. As in any metamaterial, TL metamaterials are periodic structures composed of unit-cells, whose size must fulfill the condition $p \ll \lambda_g$ (where λ_g is the guided wavelength) ir order to obtain a uniformly homogeneous material.

The circuit model of a unit cell related to a purely left-handed transmission line (LH TL) consists of a simple series capacitance and a shunt inductance, and it provides anti-parallel phase and group velocities [Ramo et al., 1994], [Caloz and Itoh, 2005]. However, this type of "pure" line does not exist in practice, due to the systematic presence of parasitic shunt capacitances and series inductances. These parasitic elements arise from the intrinsic behavior of materials. In order to take into account these effects, the concept of composite right/left-handed transmission lines (CRLH TL) was introduced in [Caloz and Itoh, 2003], [Caloz and Itoh, 2005]. The equivalent circuit model of a CRLH unit-cell is shown in Fig. 4.3a. As a purely LH TL, it is essentially composed of a series capacitor C_L and a shunt inductor L_L (where the L subscript denotes left-handed behavior). Besides, the parasitic nature of the TL circuits at high frequencies are modeled employing a series inductor L_R and a shunt capacitor C_R (where the R subscript denotes right-handed behavior), which complete the unit-cell model. Note that primes are used in the model to denote per-unit-length or time-unit-length units. Specifically, the unit-cell is composed of [Caloz and Itoh, 2005] a RH per-unit-length inductance L'_R (H/m) in series with an LH times-unit-length capacitor C'_L ($F \cdot m$), and a RH per-unit-length capacitance C'_R (F/m) in parallel with an LH times-unit-length inductance L'_L ($H \cdot m$).

The dispersive characteristics of a single CRLH unit-cell, placed inside a periodically infinite environment, are shown in Fig. 4.4a, and Fig. 4.5a, for the unbalanced and balanced cases, respectively. Their characteristics are as follows [Caloz and Itoh, 2005]. At low frequencies, C'_R and L'_R behaves as a short and open circuits, leading to an LH equivalent circuit. This circuit presents a left-handed behavior, with antiparallel phase and group velocities, and a high-pass filter behavior. At high frequencies, the situation is inverted: C'_L and L'_L behaves as a short and open circuits, leading to an RH equivalent circuit. This circuit presents a right-handed behavior, with parallel phase and group velocities, exhibiting a low-pass filter behavior. In a general case, a gap exists between the LH and RH frequency range, leading to an *unbalanced* CRLH line (see Fig. 4.4). However, if the shunt and series resonances of the unit-cell circuits are made equal (which implies $L'_R C'_L = L'_L C'_R$) a *balanced* CRLH line is obtained (see Fig. 4.5). In this case, the frequency gap disappears, and an infinite-wavelength

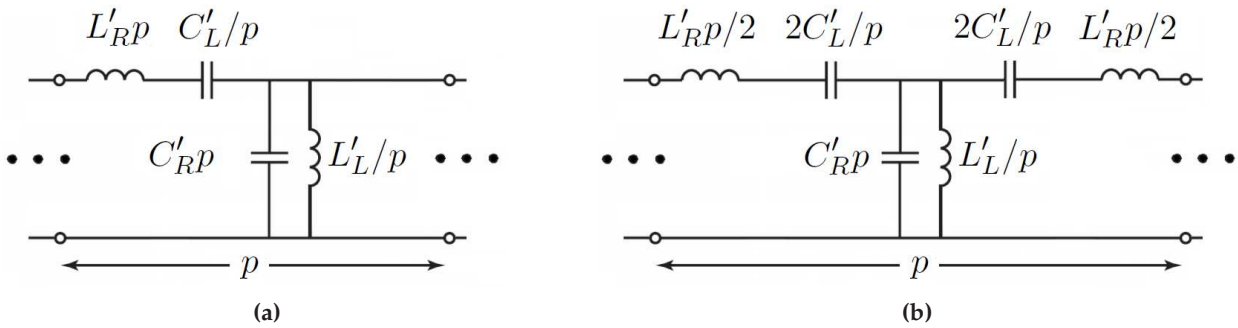

Figure 4.3 – Equivalent unit cell circuit model of a lossless CRLH transmission line. (a) Asymmetric configuration. (b) Symmetric configuration.

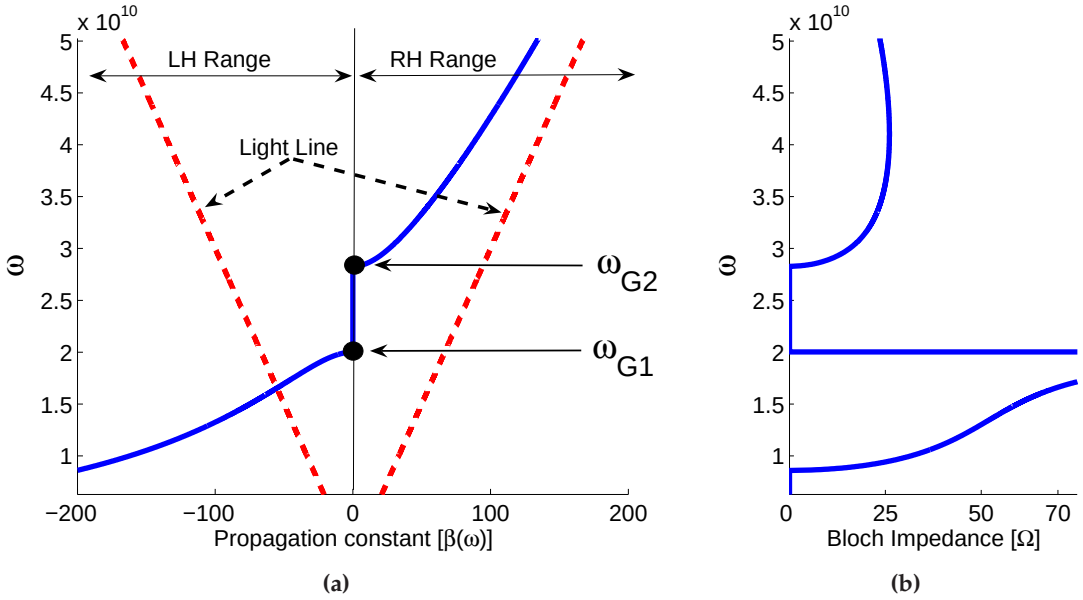

Figure 4.4 – Dispersion diagram (a) and frequency-dependent Bloch impedance (b) related to an *unbalanced* CRLH unit cell placed into a periodically infinite CRLH TL environment. The size of the unit cell is $p = 1$ cm and its circuital parameters are $C_R = C_L = 1.0$ pF, $L_L = 2.5$ nH and $L_R = 1.25$ nH.

($\beta = 0 \rightarrow \lambda_g = \infty$) appears at the so-called transition frequency ω_T. Furthermore, note that a broadband behavior is achieved in this last case. Therefore, the combined LH and RH behavior of the CRLH TL structure operates as a bandpass filter (BPF). Note that the use of a CRLH TL as filter is not optimum in terms of insertion loss, due to the frequency-dependence of the Bloch impedance (see Fig. 4.5b).

Unlike usual RH TL, where the characteristic impedance can be defined at any point along the line, the impedance of a periodic CRLH TL is not well-defined due to the periodic loading of the structure. Instead, a Bloch impedance (related to periodic structures, and which plays the same role as the characteristic impedance for this type of lines [Caloz and Itoh, 2005], [Marques et al., 2008]) is used. This impedance is defined as the impedance obtained at any k^{th} unit-cell terminals. In the

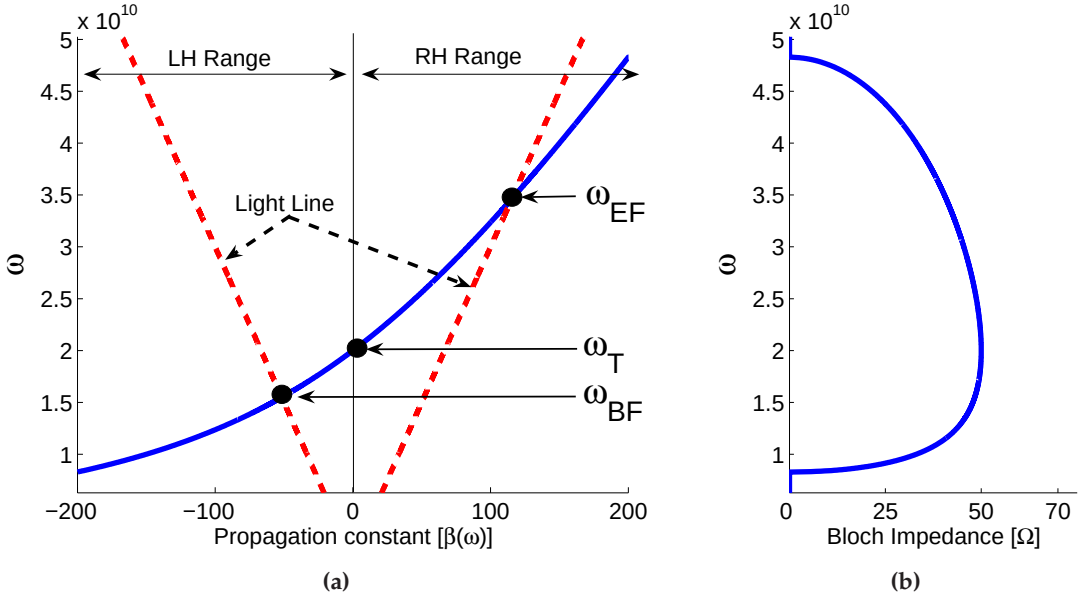

Figure 4.5 – Dispersion diagram (a) and frequency-dependent Bloch impedance (b) related to a *balanced* CRLH unit cell placed into a periodically infinite CRLH TL environment. The size of the unit cell is $p = 1$ cm and its circuital parameters are $C_R = C_L = 1.0$ pF and $L_L = L_R = 2.5$ nH.

case of an unbalanced CRLH TL (see Fig. 4.4b), the Bloch impedance is very frequency-dependent. Besides, the guided wavelength increases when approaching the gap, leading to extreme Bloch impedance values, and avoiding any wave propagation. On the other hand, the Bloch impedance in balanced CRLH TLs (see Fig. 4.5b) is much less frequency-sensitive, and it allows for a broadband matching.

In the case that the homogenous condition for the unit cells is satisfied ($p << \lambda_g$), effective constitutive parameters related to the CRLH line can be obtained [Caloz and Itoh, 2005]. These parameters are frequency-dependent, i.e. $\varepsilon = \varepsilon(\omega)$ and $\mu = \mu(\omega)$. Therefore, this type of transmission lines are *dispersive in nature*. One interesting point here is that, since the CRLH unit-cell can be designed to have a wide variety of values, the dispersive properties of the line can potentially be designed to fulfill some specific requirements. Another point of view to describe CRLH dispersion is related to the group velocity (slope of the dispersion curve), which is also frequency-dependent within the CRLH passband. Furthermore, one incident wave propagating from the source (usually located on the left) towards a load (located on the right) can experience three different types of propagation: *backwards*, when $\omega < \omega_T$, related to the LH behavior of the CRLH TL; *forwards*, when $\omega > \omega_T$, related to the RH behavior of the CRLH TL; and an *infinite-wave phenomena*, related to the transition frequency of the CRLH TL (ω_T) and where the signal's energy flows towards the load without experiencing phase change. The adequate combination of these different types of wave-propagation leads to a extremely rich variety of dispersive properties, which provide novel phenomena and applications at microwaves [Caloz and Itoh, 2005], [Marques et al., 2008].

Another extremely interesting properties of CRLH TLs is that its associated dispersion curve

always penetrates into the *fast-wave region* [Oliner and Jackson, 2007], which is delimited by two lightlines ($\omega = +\beta c$ and $\omega = -\beta c$), as shown in Fig. 4.5a. Therefore, the CRLH TL operates as a *leaky-wave antenna* (LWA) within this frequency band. As compared with other types of LWAs [Oliner and Jackson, 2007], CRLH LWAs are able to radiate from backfire ($\theta = -90^\circ$, where θ is measured from the direction perpendicular to the antenna) [Grbic and Eleftheriades, 2002b] to endfire ($\theta = +90^\circ$), including the broadside direction ($\theta = 0^\circ$) [Liu et al., 2002], [Caloz and Itoh, 2005], as the frequency is scanned from $\omega = \omega_{BF}$ to $\omega = \omega_{EF}$, including the CRLH transition frequency $\omega = \omega_T$ (see Fig. 4.5a). The radiation angle of the main beam of a CRLH TL LWA is approximately given by the scanning law

$$\sin(\theta) \approx \frac{\beta(\omega)}{k_0}, \tag{4.1}$$

where k_0 is the free-space wavenumber. Based on this LWA relationship, each frequency is mapped into a specific angle in space, showing the frequency sensitive nature of CRLH structures.

Finally, note that a broadband CRLH behavior can also be achieved using SSRs [Gil et al., 2007b], [Eleftheriades, 2007a], [Marques et al., 2008]. In this case, the broadband response is achieved using the SRRs outside of their resonances, which mimics the CRLH TL approach by a SRR one. However, CRLH TLs for broadband applications are still preferable, due to their unique performances (up to now), and well-established analysis and design approach.

4.2.2 TL Theory and Useful Formulas

Let us assume that the homogeneity condition ($p << \lambda_g$, where λ_g is the guided wavelength) is satisfied on a CRLH transmission line. This means that a *completely continuous media with CRLH behavior* is available. In this case, the complex propagation constant [$\gamma(\omega) = \alpha(\omega) + j\beta(\omega)$] and Bloch impedance [$Z_B(\omega)$] associated to this type of media may easily be obtained as [Caloz and Itoh, 2005]

$$\gamma(\omega) = \sqrt{Z'Y'} \tag{4.2}$$

$$Z_B(\omega) = \sqrt{\frac{Z'}{Y'}} \tag{4.3}$$

where the per-unit length impedance (Z') and admittance (Y') related to the unit-cell of Fig. 4.3a are defined as

$$Z' = j\omega L_R + \frac{1}{j\omega C_L}, \tag{4.4}$$

$$Y' = j\omega C_L + \frac{1}{j\omega C_R}. \tag{4.5}$$

After some straightforward manipulations, the phase and attenuation constant and the Bloch impedance of this media may be expressed as

$$\beta(\omega) = \frac{s(\omega)}{p}\sqrt{\frac{\omega^2}{\omega_R^2}\left(1-\frac{\omega_{se}}{\omega^2}\right)\left(1-\frac{\omega_{sh}^2}{\omega^2}\right)}, \tag{4.6}$$

$$\alpha(\omega) = 0, \tag{4.7}$$

$$Z_B(\omega) = \sqrt{\frac{L_R}{C_R}\frac{\left(1-\frac{\omega_{se}^2}{\omega^2}\right)}{\left(1-\frac{\omega_{sh}^2}{\omega^2}\right)} - \frac{L_R^2\omega^2}{4}\left(1-\frac{\omega_{se}^2}{\omega^2}\right)^2}, \tag{4.8}$$

where the variables

$$\omega_R = \frac{1}{\sqrt{L_R C_R}} \qquad \text{and} \qquad \omega_L = \frac{1}{\sqrt{L_L C_L}}, \tag{4.9}$$

the shunt and series resonance frequencies

$$\omega_{sh} = \frac{1}{\sqrt{L_L C_R}} \qquad \text{and} \qquad \omega_{se} = \frac{1}{\sqrt{L_R C_L}}, \tag{4.10}$$

and

$$s(\omega) = \begin{cases} -1 & \text{if} \quad \omega < min(\omega_{se}, \omega_{sh}) \quad \text{LH range} \\ +1 & \text{if} \quad \omega > max(\omega_{se}, \omega_{sh}) \quad \text{RH range} \end{cases} \tag{4.11}$$

have been introduced to compact and simplify the notation.

It is important to note that the attenuation constant related to this media is strictly zero, because dielectric, ohmic and radiation losses have been neglected. Besides, note that the previously derived expressions assume a *continuous* CRLH media, which is difficult to obtain in practice. Therefore, they are approximated formulas to model real-life CRLH transmission lines.

Besides, note that CRLH lines are inherently periodic. Therefore, they can efficiently be analyzed using the Floquet's theorem, combined with periodic boundary conditions [Pozar, 2005], [Caloz and Itoh, 2005], [Eleftheriades and Balmain, 2005]. It is important to note that this approach is more accurate than the infinitesimal method (or artificial transmission line) to model CRLH TL. This is because this method effectively takes into account the periodicity of the transmission line, and the CRLH line is treated as a *periodic medium*, which correspons to a practical case. In order to apply this approach, the asymmetrical unit-cell shown in Fig. 4.3a is modified into a symmetrical unit-cell, as shown in Fig. 4.3b. This configuration, which presents the same physical behavior, is preferable for CRLH TLs because it avoids mismatch effects at the connections with externals ports. Employing an ABCD analysis [Pozar, 2005] combined with the Floquet's theorem [Caloz and Itoh, 2005], [Eleftheriades and Balmain, 2005], the complex propagation constant and Bloch impedance of a CRLH unit-cell may be expressed as

$$\gamma(\omega) = \frac{1}{p}\cosh^{-1}\left(1+\frac{ZY}{2}\right), \tag{4.12}$$

$$Z_B(\omega) = \sqrt{\frac{Z}{Y}}\sqrt{1+\frac{ZY}{4}}. \tag{4.13}$$

Besides, note that the above equations tends to Eqs. (4.6)-(4.8) in the long wavelength limit ($p << \lambda_g$). Therefore, the infinitesimal (or artificial transmission line model) can be considered as a limiting approximation of this more rigorous periodic analysis.

In the case of a balanced CRLH unit-cell (i.e. equal and mutually canceling of the series and shunt resonances, which leads to a gapless transition from left-handed to right-handed frequency ranges and implies $L'_R C'_L = L'_L C'_R$), the CRLH transition frequency ω_T (see Fig. 4.5a) is computed as

$$\omega_T = \sqrt{\omega_R \omega_L}, \tag{4.14}$$

and the dispersion relationship is simplified to [Caloz and Itoh, 2005]

$$\beta(\omega) \approx \frac{1}{p}\left(\frac{\omega}{\omega_R} - \frac{\omega_L}{\omega}\right). \tag{4.15}$$

A deeper insight into the CRLH TL propagation constant, and its associated dispersive properties, can be obtained by expanding Eq. (4.15) in Taylor series around a given modulation frequency (ω_0) [Agarwal, 2005],[Abielmona et al., 2008]. This expansion reads

$$\beta(\omega) \approx \frac{1}{p}\left[\beta_0 + \beta_1(\omega - \omega_0) + \frac{1}{2}\beta_2(\omega - \omega_0)^2\right], \tag{4.16}$$

where the terms β_0, β_1 and β_2 are defined as

$$\beta_0(\omega_0) = \left(\frac{\omega_0}{\omega_R} - \frac{\omega_L}{\omega_0}\right), \qquad \beta_1(\omega_0) = \left(\frac{1}{\omega_R} + \frac{\omega_L}{\omega_0^2}\right), \qquad \beta_2(\omega_0) = \frac{\omega_L}{\omega_0^3}, \tag{4.17}$$

and are related to the phase velocity, the nondispersive part of the group velocity, and the group velocity dispersion (or GVD parameter), respectively.

On the other hand, in the case of an unbalanced CRLH TL ($L'_R C'_L \neq L'_L C'_R$), a gap in the propagation constant appears (see Fig. 4.4a). The frequency region of this gap is limited by the frequencies

$$\omega_{G1} = min(\omega_{se}, \omega_{sh}), \tag{4.18}$$

$$\omega_{G2} = max(\omega_{se}, \omega_{sh}). \tag{4.19}$$

The Bloch impedance related to a balanced unit-cell reaches it maximum at ω_T, as [Caloz and Itoh, 2005]

$$Z_B(\omega_T) = \sqrt{\frac{L_R}{C_R}} = \sqrt{\frac{L_L}{C_L}}, \tag{4.20}$$

and decreases as frequency changes from ω_T (see Fig. 4.5b). As a good approximation, Bloch impedance may be considered constant and equal to Eq. (4.20) in a wide frequency range of the CRLH TL bandpass.

The group velocity related to a unit cell within an infinite periodic CRLH TL is obtained as

$$v_g(\omega) = \left(\frac{\partial \beta}{\partial \omega}\right)^{-1} = \frac{p\ \sin[p\,\beta(\omega)]}{(\omega/\omega_R^2) + (\omega_L^2/\omega^3)}. \tag{4.21}$$

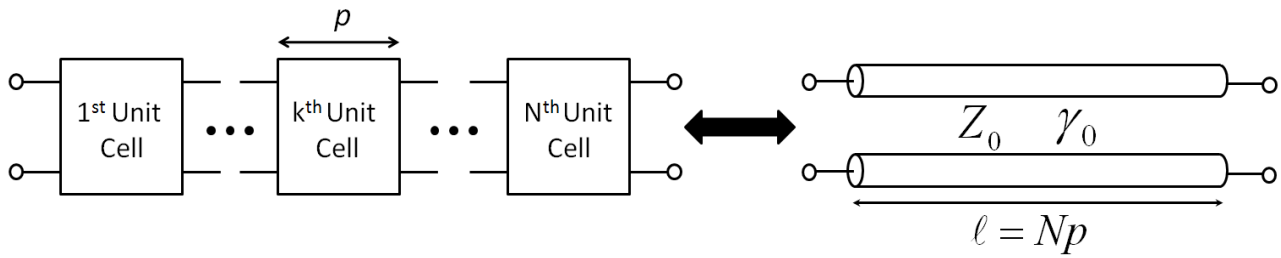

Figure 4.6 – Equivalence between N cascaded unit cells and a transmission line of length ℓ, characterized by an equivalent complex propagation constant γ_0 and Bloch impedance Z_0.

Note that the group velocity is always *positive*, which means that the energy is flowing from the source towards the load. This is not the case of the phase velocity, which can be *positive* (forward propagation, in the RH frequency range) or *negative* (backwards propagation, in the LH frequency range).

Finally, the limits of the CRLH LWA fast-wave region (see Fig. 4.5a) can easily be computed using

$$\omega_{BF} = \frac{\omega_T}{\sqrt{1 + p\omega_R/c}} \qquad \text{and} \qquad \omega_{EF} = \frac{\omega_T}{\sqrt{1 - p\omega_R/c}}, \tag{4.22}$$

which clearly define the frequency region where the CRLH TL acts as a LWA.

Up to now, we have considered the behavior of a single unit-cell, placed within a infinite periodic CRHL TL. This analysis can easily be extended in order to consider a finite structure composed of a total of N unit-cells, which provides a very good approximation of a real CRLH line with finite length (see Fig. 4.6). For this purpose, an $[ABCD]$ matrix, related to the symmetric unit-cell of Fig. 4.3b, is first considered. Note that the use of a symmetric unit-cell configuration is preferred here, in order to exactly have the same input and output impedances and avoid difficult port matching. Then, the ABCD matrix related to the interconnection of N unit cells, and denoted as $[A_N B_N C_N D_N]$, is obtained. This is easily done by multiplying N times the $[ABCD]$ matrix [Pozar, 2005]. Once the $[A_N B_N C_N D_N]$ matrix is obtained, the corresponding scattering parameters can easily be retrieved, using well-known formulas [Pozar, 2005], [Caloz and Itoh, 2005]. Note that this $[S]$ matrix is symmetric ($S_{11} = S_{22}$), due to the use of a symmetric unit-cell configuration. Finally, the complex propagation constant of the finite-length CRLH line is computed as [Caloz and Itoh, 2005]

$$\gamma(\omega) = \alpha(\omega) + j\beta(\omega) = -\frac{ln|S_{21}(\omega)|}{\ell} + j\left\{2\pi m - \phi^{unwrapped}[S_{21}(\omega)]\right\}, \tag{4.23}$$

where $m \in \mathbb{N}$. Note that it is necessary to *unwrap* the phase of S_{21} in order to achieve a continuous propagation constant $\beta(\omega)$. The phase origin, defined as the frequency where $\beta = 0$, must be set at the CRLH transition frequency (ω_T), where this condition is fulfilled. The determination of this phase origin sets the value of the variable m.

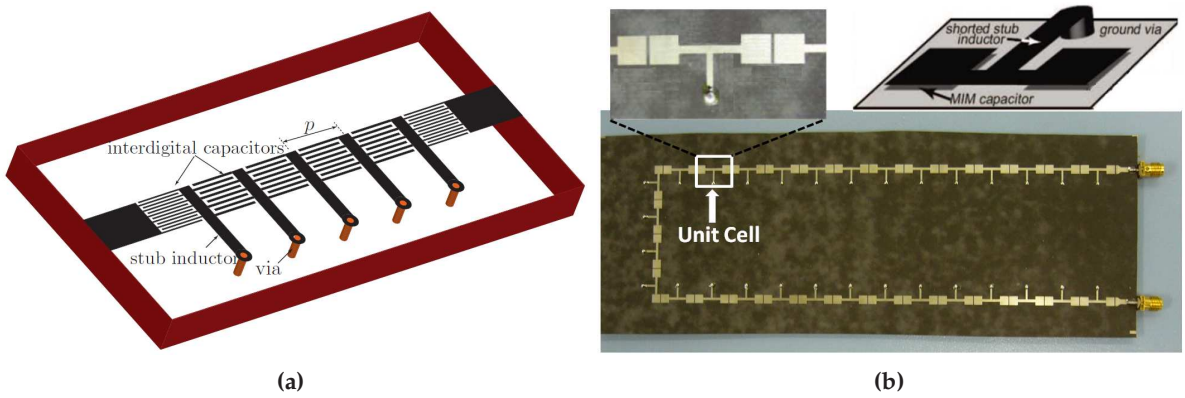

(a) (b)

Figure 4.7 – Examples of planar CRLH transmission lines. (a) Microstrip implementation, based on interdigital capacitors and shorted stub inductors (reproduced from [Nguyen, 2010]). (b) Microstrip implementation, based on Metal Insulator Metal (MIM) capacitors and stub inductors (reproduced from [Abielmona et al., 2007]).

4.2.3 Practical Implementation

One of the main advantages of CRLH TLs is that they can easily be implemented in planar technologies, such as CPW [Eleftheriades and Balmain, 2005] or microstrip [Caloz and Itoh, 2005]. In the CPW case, the host line is loaded by shunt inductors (implemented by the connection between the central strip and the ground planes) and series capacitors (implemented by interdigital geometries or by series gaps).

In this work, all the experimental results have been obtained using CRLH TLs based on a microstrip implementation. The main reasons for this choice are i) microstrip technology allows an easy implementation, leading to excellent results in both the guided and radiative regime, ii) easier interconnection of this line with other microwave components, which are usually implemented in this technology, iii) availability of these lines at the laboratories of Poly-Grames, École Polytechnique de Montréal (Canada), where the measurements where carried out and iv) the excellent *know-how* of Prof. Caloz (cosupervisor of this thesis) and his group in the analysis and design of such lines.

Two examples of microstrip CRLH TLs are shown in Fig. 4.7. In Fig. 4.7a, the microstrip host line is loaded by via-holes (which implements the shunt inductors) and by interdigital capacitors (which implements the series capacitors). This configuration was proposed in [Caloz et al., 2002]. The main drawbacks of this implementation are related to bandwith limitations, due to the existence of transverse resonances associated to the interdigital capacitors (which restrict the use of these lines in wideband or impulse-regime applications), and their asymmetric configuration (which can be solved adding extra complexity in the design process). Recently, a microstrip CRLH TLs based on the use of Metal-Insulator-Metal capacitors was proposed [Nguyen and Caloz, 2006], [Abielmona et al., 2007]. An example of this configuration is shown in Fig. 4.7b. This novel topology solves the problems associated to the interdigital capacitors, allowing an easier and faster design. On the other hand, it is more difficult to fabricate, due to the use of multilayered technology.

4.2.4 Applications

The *non-resonant approach* to obtain *planar metamaterials* has led to the development of many novel and interesting applications at microwaves, most of them in the *harmonic regime*. A possible classification can be made distinguishing between *guided-wave* and *radiative-wave* applications.

In the case of *guided-wave applications*, the CRLH structure operates as a transmission line. Thanks to their exotic dispersion properties, a wide variety of applications appeared in just a few years [Caloz and Itoh, 2005], [Eleftheriades and Balmain, 2005]. Among them, we can highlight the development of multi-band components [Lin et al., 2004], [Caloz, 2006], [Eleftheriades, 2007b], [Caloz and Nguyen, 2007], baluns [Antoniades and Eleftheriades, 2005b] or the straightforward use of CRLH lines as bandpass filters [Islam and Eleftheriades, 2008b], [Nguyen and Caloz, 2006] or diplexers [Horii et al., 2005]. Besides, the unique infinite wavelength property has led to new phase shifters [Antoniades and Eleftheriades, 2003b], [Abdalla et al., 2007], power dividers [Antoniades and Eleftheriades, 2003a], [Antoniades and Eleftheriades, 2005a], [Nguyen and Caloz, 2007b] or zero-th order resonators [Sanada et al., 2004b].

In the case of *radiative-wave applications*, the CRLH structures can be designed as a leaky-wave antennas [Oliner and Jackson, 2007]. Initially, they were designed to radiate at backwards [Grbic and Eleftheriades, 2002b], meanwhile in [Liu et al., 2002] a full-space scanning (from backwards to forwards, including the broadside direction) was demonstrated. These unprecedent radiations features where rapidly exploited in many applications, including electronically scanned antennas [Lim et al., 2004a], [Lim et al., 2005], the use of active elements [Casares-Miranda et al., 2006] (which allows the introduction of tappers designs, providing an important reduction of SSL), dual-band antennas [Caloz et al., 2007], reduction of beam-squinting [Antoniades and Eleftheriades, 2008a] or the use of different types of schemes to increase the antennas efficiency [Nguyen et al., 2009a], [Nguyen et al., 2009b]. Furthermore, CRLH lines can be configured as a resonant antennas [Lai et al., 2007], [Caloz et al., 2008], [Pyo et al., 2009] or monopoles and dipoles [Antoniades and Eleftheriades, 2008b], [Zhu and Eleftheriades, 2009], [Zhu et al., 2010]. A review of some of the above commented antenna applications can be found in [Eleftheriades and Antoniades, 2007] and in [Caloz et al., 2008]

Finally, note that 2*D* and 3*D* configurations of CRLH TLs are also possible. In the case of 2*D*, the first application was related to near field focusing [Iyer et al., 2003] and in the overcoming of the diffraction limit in planar lens [Grbic and Eleftheriades, 2004]. In these last examples, lumped elements were employed. In [Sanada et al., 2004a] the possibility to obtain 2*D* metamaterials avoiding the use of such lumped elements was demonstrated, as long with its use as a CRLH LWA. In addition, a research effort to extend metamaterials to 3*D* has recently been carried out (see [Grbic and Eleftheriades, 2005] or [Zedler et al., 2007], for instance). A nice review of 1, 2 and 3*D* metamaterials concepts and applications can be found in [Caloz, 2009] or in [Eleftheriades, 2009].

4.3 Impulse Regime Analysis of CRLH Transmission Lines

Propagation of electromagnetic short pulses in complex media has been a field of great interest for a long time [Felsen, 1969], [Oughstun, 1991]. Previous research efforts in this field have been mostly theoretical. For instance, pulse distortion in dispersive media has been explained, using asymptotic methods, in correlation with precursor fields in [Heyman and Felsen, 2001], [Oughstun, 2006]. Most practical developments for pulse propagation in dispersive media have been carried out for optical systems, including optical fibers, couplers, switches and soliton devices [Saleh and Teich, 2007]. At microwaves, pulse propagation has been less studied. Generally, the temporal analysis of highly-dispersive linear metamaterial structures is usually performed with time-domain full-wave methods, such as time-domain FEM [Lee et al., 1997], FDTD [Taflove and Hagness, 2005] or TLM [Hoefer, 1985]. However, these accurate techniques require a high computational cost, due to the meshing of the whole geometry under study. In addition, when the dispersive structures also include non-linear elements (such as varactors) this analysis is much more complicated and time-consuming.

In this section a general time-domain Green's function approach is presented for the analysis of pulse propagation in electrically thin CRLH TLs. This method is based on the transient analysis of 1D transmission lines [Paul, 2007] combined for the first time with the CRLH TL methodology [Caloz and Itoh, 2005]. The technique provides analytical expressions from the inverse Fourier transform of the solutions to the generalized telegrapher's equations. The main difference of this approach, with respect to other techniques previously used in dispersion analysis [Felsen, 1969], [Oughstun, 1991], is that the source can be explicitly treated with this formulation thanks to the Green's functions formalism. In this way, it is simple to define useful electrical parameters, such as impedances and reflection coefficients, which are of key importance for the characterization of microwave devices. With this equivalent transmission line simplification of the geometry, the Green's functions are available in closed-form, and directly correspond to the voltages and currents along the transmission line. Furthermore, the specific cases of non-uniform media and periodic train of input pulses, which are useful to model practical devices, are considered. The main advantages of this approach are the unconditional stability and fast computation, due to the continuous treatment of time, and the insight into the physical phenomena provided by the Green's functions.

Then, the method is extended to consider non-linear CRLH TLs. Non-linearity is achieved by replacing the shunt capacitor of the CRLH TL unit cell by a varactor. For the proposed non-linear analysis, time discretization is required. Specifically, the characteristic impedance and propagation constant are re-evaluated at each time for each unit cell of the CRLH TL. The variation of the characteristic impedance of each unit cell is considered, introducing a temporal-dependent mismatch, correctly modeling the nonlinear propagation of the pulse and the small reflected waves between two consecutive unit cells. A non-uniform transmission line is therefore obtained and solved at each particular instant. Next, a novel interpolation scheme has been developed to reduce the computational cost required for the technique while keeping high accuracy. The idea is to interpolate the propagation constant value associated to each unit cell as a function of the variable shunt capacitor, which in turn depends on the modulated input pulse.

As previously commented, this section introduces the basic mathematical treatment of the pro-

posed methods. In Chapter 5 these techniques will be applied to the practical modeling of linear and non-linear guided-wave impulse-regime phenomena and devices, providing physical insight into the problem, fast analysis as compared with other purely numerical techniques, and accurate results. Full-wave simulations and measured data will be employed for validation purposes, further confirming the accuracy of the proposed techniques.

4.3.1 Impulse Regime Analysis of Linear CRLH TL

Many media, ranging from traditional purely right-handed materials to recent CRLH metamaterials [Caloz and Itoh, 2005], can be advantageously analyzed by transmission line theory [Pozar, 2005]. So far, this theory has been applied mostly in the *harmonic* regime, where Green's functions for both the voltage and the current along the line are available [Russer, 2006]. The time-domain Green's function approach provides an extremely efficient tool to analyze *impulse regime* signals along transmission lines. In this case the point source model accurately characterizes a pulse generator, and the computed quantities are the voltages and currents along the line as a function of time. The proposed approach inherently provides broadband analysis without any stability issue. This is particularly beneficial to the case of strongly dispersive media, such as CRLH metamaterials, where novel guided-wave and radiated-wave effects may therefore be easily investigated.

Consider an electric source $\vec{J}(\vec{r},t)$ placed in an arbitrary homogeneous, dispersive, medium. Combining time-domain Maxwell's equations [Collin, 1991],

$$\nabla \times \vec{E}(\vec{r},t) = -\mu \frac{\partial}{\partial t}\vec{H}(\vec{r},t), \tag{4.24}$$

$$\nabla \times \vec{H}(\vec{r},t) = \varepsilon \frac{\partial}{\partial t}\vec{E}(\vec{r},t) + \vec{J}(\vec{r},t), \tag{4.25}$$

the wave equation is obtained as

$$\nabla \times \nabla \times \vec{E}(\vec{r},t) + \mu\varepsilon \frac{\partial^2}{\partial t^2}\vec{E}(\vec{r},t) = -\mu \frac{\partial}{\partial t}\vec{J}(\vec{r},t). \tag{4.26}$$

The spatial-temporal dyadic Green's function $\overline{\overline{G}}(\vec{r},\vec{r}\,';t,t')$ of this equation for a specific medium and a specific source is obtained as the response to a unitary point source $\vec{J}(\vec{r}\,',t') = \delta(\vec{r}\,';t')$. Once this Green's function is known, the electric field may be computed as [Barton, 1989a]

$$\vec{E}(\vec{r},t) = \int\int \bar{\bar{G}}(\vec{r},\vec{r_g}\,';t,t') \cdot \vec{J}(\vec{r_g}\,',t') d\vec{r_g}\,' dt', \tag{4.27}$$

where the spatial-temporal Green's function may be expressed in terms of its inverse Fourier transform

$$\bar{\bar{G}}(\vec{r},\vec{r_g}\,';t,t') = \frac{1}{2\pi}\int_{-\infty}^{+\infty} \tilde{\bar{\bar{G}}}(\vec{r},\vec{r_g}\,';\omega) e^{j\omega(t-t')} d\omega. \tag{4.28}$$

Inserting Eq. (4.28) into Eq. (4.27), yields

$$\vec{E}(\vec{r},t) = \frac{1}{2\pi}\int\int\int \tilde{\bar{\bar{G}}}(\vec{r},\vec{r_g}\,';\omega) \cdot \vec{J}(\vec{r_g}\,',t') e^{j\omega(t-t')} dr'_g dt' d\omega \tag{4.29}$$

This expression is very general. It provides the field radiated by an arbitrary source (in space and time) in an arbitrary dispersive, and possibly nonlinear homogenous medium. Since the spatial-temporal distribution of the source is generally known, only the Green's function needs to be computed to provide the field solution. An analogous formulation may naturally be obtained for the magnetic field.

In case of electrically thin 1D transmission lines (placed along the z direction, as shown in Fig. 4.8), the generator source may be reduced to a point source, greatly decreasing the complexity of the problem. Consider a punctual source placed at the position $\vec{r}_g$, and with a temporal dependence

$$\vec{J}(\vec{r}_g, t') = \vec{\kappa}(\vec{r}_g) I_g(t') = \delta(\vec{r} - \vec{r}_g) I_g(t') \hat{e}_z. \tag{4.30}$$

In this case Eq. (4.29) is reduced to

$$\vec{E}(\vec{r}, t) = \frac{1}{2\pi} \int \int \bar{\bar{G}}(\vec{r}, \vec{r_g}'; \omega) \cdot I_g(t') \hat{e}_z e^{j\omega(t-t')} dt' d\omega. \tag{4.31}$$

At this point, the fourier transform of the temporal source dependence ($\tilde{I}_g(\omega) = \mathfrak{F}\{I_g(t')\}$, where the operator $\mathfrak{F}$ denotes a Fourier transform [Pipes and Harvill, 1971]) is employed. Note that the input pulse is usually modulated at a frequency ω_0, which is included in the $\tilde{I}_g(\omega)$ notation as a $e^{j\omega_0 t}$ term. Besides, a transmission-line Green's function [Russer, 2006] is used to obtain the voltage (V) or to the current (I) along the 1D line, which may be expressed as

$$X(z, t) = \frac{1}{2\pi} \int_{-\infty}^{\infty} \tilde{G}_X(z, z_g; \omega)\, \tilde{I}_g(\omega)\, e^{j\omega t} d\omega, \tag{4.32}$$

where z_g is the source position ($\vec{r}_g = z_g \hat{e}_z$), z is the observation point and $X(z, t)$ denotes the voltage or current along the line (in the z direction), as a function of the Green's functions employed [$\tilde{G}_V(z, z_g; \omega)$ or $\tilde{G}_I(z, z_g; \omega)$, related to the voltage or current, respectively]. It should be noted that the space dependence has been absorbed in the Green's function term, while the temporal information is described by Fourier and inverse-Fourier transforms.

Although expressions for several pulses can be obtained using Fourier relations [Pipes and Harvill, 1971], we will provide an analytical solution for the chirp-modulated Gaussian pulse. This type of pulses are easily generated in practice, are convenient to characterize general broadband systems, and have many applications, such as for instance in radar [Skolnik, 2002] or pulse compression. This pulse may be expressed as

$$I_g(t) = C_0 e^{j\omega_0 t} e^{-\frac{1}{2}(1+jC)\left(\frac{t-t_0}{T_0}\right)^2}, \tag{4.33}$$

where C is the chirp constant, which controls the frequency variation as a function of time, C_0 is a constant amplitude factor, ω_0 is the modulation frequency, T_0 is the temporal width of the pulse, and t_0 is the center of the pulse. Its Fourier transform can be obtained in closed form as

$$\tilde{I}_g(\omega) = j2\pi\sigma C_0 e^{-\frac{\sigma^2}{2}\omega_0^2 + j\omega_0 t_0} e^{\omega(\omega_0\sigma^2 - jt_0)} e^{-\frac{\sigma^2}{2}\omega^2}, \tag{4.34}$$

where the C variable has been absorbed in the σ term,

$$\sigma = \frac{T_0}{\sqrt{1 + jC}}. \tag{4.35}$$

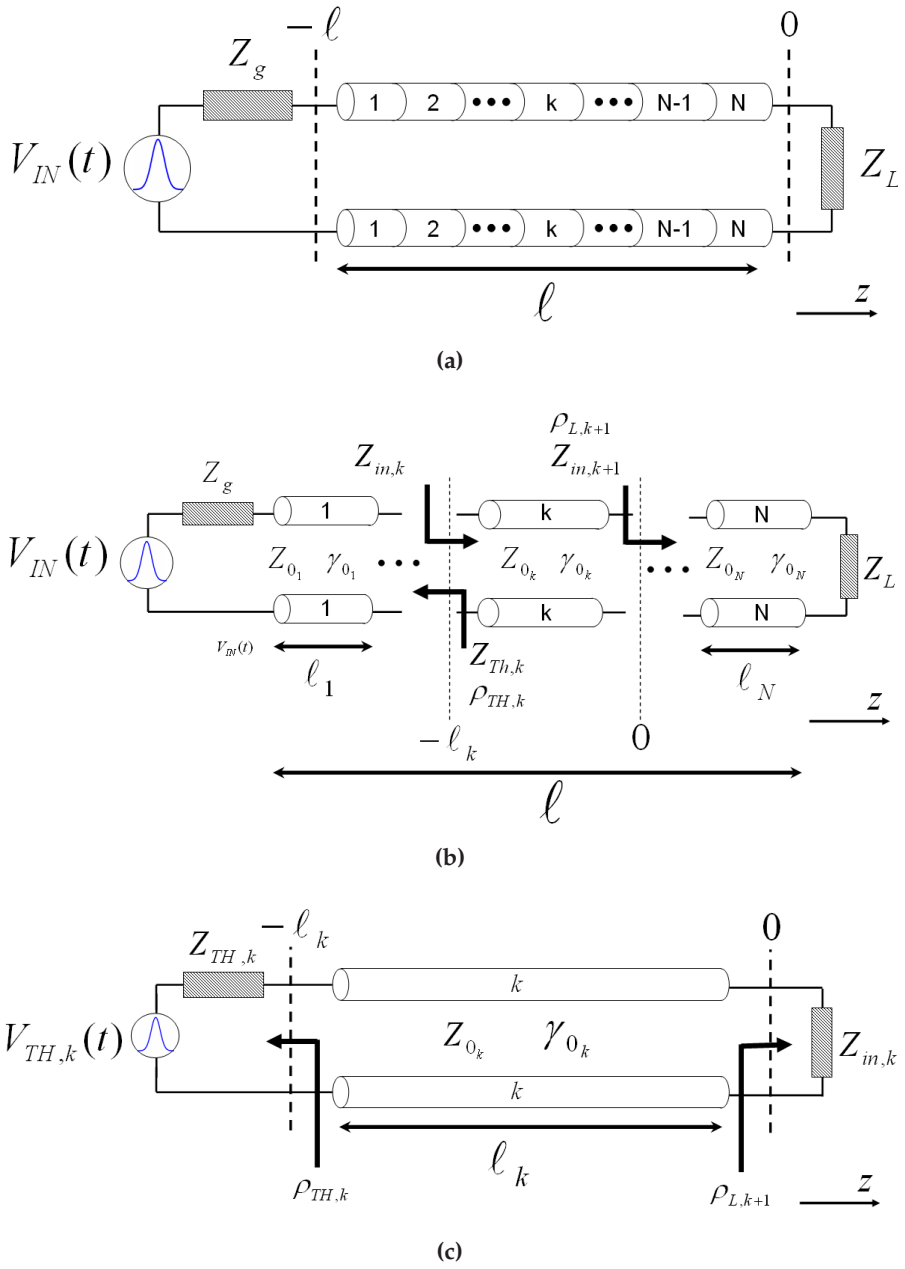

Figure 4.8 – Dispersive artificial transmission line excited by a point source generator. (a) Uniform case. The line, composed of N unit cells, is defined by its characteristic impedance $[Z_0(\omega)]$, complex propagation constant $[\gamma(\omega)]$ and length (ℓ). (b) Non-uniform case. The line is composed of N uniform transmission line sections. Each k^{th} section has its own length (ℓ_k), characteristic impedance $[Z_{0_k}(\omega)]$ and propagation constant $[\gamma_k(\omega)]$. (c) Thévenin equivalent circuit for the k^{th} uniform transmission line section.

Note that Eq. (4.33) reduces to a modulated Gaussian pulse for $C = 0$. This development provides, from its analytical form, insight into more complex temporal signals, which may be expressed as a linear combination of Gaussian pulses.

Matched Transmission Lines

Consider a simple matched transmission line, as shown in Fig. 4.8a (when $Z_g = Z_L = Z_0(\omega), \forall\omega$). In this simple case, the transmission line Green's functions for the voltages and currents may be expressed as

$$\tilde{G}_V(\vec{r},\vec{r}_g;\omega) = e^{-\gamma(\omega)R}, \tag{4.36}$$

$$\tilde{G}_I(\vec{r},\vec{r}_g;\omega) = \frac{e^{-\gamma(\omega)R}}{Z_0(\omega)}, \tag{4.37}$$

respectively, where $\gamma(\omega)$ is the complex propagation constant (or dispersion relation), $Z_0(\omega)$ is the characteristic impedance, and $R = |z - z_g|$ is the distance between the observation point z along the line and the source point z_g (generator).

Using these expressions, the voltage or the current along the line can easily be found with Eq. (4.32). Note that this equation applies to any type of transmission line, including metamaterial CRLH lines [Caloz and Itoh, 2005], provided that the propagation constant [$\gamma(\omega)$] is known. A good approximation for $\gamma(\omega)$ in the infinitesimal limit and valid near the transition region between the LH and RH bands is given by Eq. (4.15), whereas more accurate expressions [Eqs. 4.6-4.7] can be used at frequencies well below and above the transition frequency. In the simplest case, the voltage along the CRLH line may be obtained by inserting Eq. (4.15) into Eq. (4.32). Due to the dispersive behavior of the line, this voltage becomes proportional to

$$V(z,t) \propto \int_{-\infty}^{+\infty} e^{-j\frac{a(t)}{\omega}} e^{b(t)\omega} e^{-c(t)\omega^2} d\omega, \tag{4.38}$$

where $a(t)$, $b(t)$ and $c(t)$ are functions depending on time. This integral expression does not admit an analytical solution to the author knowledge. The numerical treatment required to solve this integral directly depends on the temporal-dependence of the input pulse. For the case of a (chirp) modulated Gaussian pulse, the voltage along the line can be expressed as

$$V(z,t) = V_g \frac{C_0\sigma}{\sqrt{2\pi}\omega_0} e^{-\frac{\sigma^2}{2}\omega_0^2 + j\omega_0 t_0} \int_{-\infty}^{+\infty} e^{-j\frac{\omega'_L}{\omega}} e^{\omega\left[j\left(\frac{1}{\omega'_R}+t-t_0\right)+\omega_0\sigma^2\right]} e^{-\frac{\sigma^2}{2}\omega^2} d\omega, \tag{4.39}$$

where ω'_L and ω'_R are the variables defined in Eq. (4.9), but normalized with respect to the unit-cell length. Although the above expression is not analytical, it admits a fast numerical computation, since 99.9% of the energy in a modulated Gaussian pulse is concentrated in the restricted bandwidth of $(\omega_0 - 5\sigma, \omega_0 + 5\sigma)$.

General non-uniform lines

Consider now the more general case of a nonuniform transmission line medium composed of N uniform transmission line sections (or unit-cells), as shown in Fig. 4.8b. The sections may be different from each other and may be of different type [see Fig. 4.8b]. Therefore, reflections occur due to the transition between two consecutive cells, and different propagation conditions appear at each cell. The Green's function along the k^{th} uniform transmission line section ($z \in [-\ell_k, 0]$, possibly infinitesimal), including generator and load mismatches, reads

$$G_k(z,z' = -\ell;\omega) = A(\omega)\left[e^{-\gamma_k(\omega)z} + \rho_{l,k}(\omega)e^{\gamma_k(\omega)z}\right], \tag{4.40}$$

where [Pozar, 2005]

$$A(\omega) = \frac{V_{Th,k}(\omega) Z_{in,k}(\omega)}{Z_{in,k}(\omega) + Z_{Th,k}} \frac{e^{-\gamma_k(\omega)\ell_k}}{1 - \rho_{l,k}(\omega)\rho_{Th,k}(\omega)e^{-2\gamma_k(\omega)\ell_k}}, \tag{4.41}$$

and

$$\rho_{Th,k}(\omega) = \frac{Z_{Th,k}(\omega) - Z_{0_k}(\omega)}{Z_{Th,k}(\omega) + Z_{0_k}(\omega)}, \tag{4.42}$$

$$\rho_{l,k}(\omega) = \frac{Z_{in,k+1}(\omega) - Z_{0_k}(\omega)}{Z_{in,k+1}(\omega) + Z_{0_k}(\omega)}, \tag{4.43}$$

which was obtained by equating the Green's function evaluated at the input of the k^{th} section, to the Thevenin's voltage evaluated at the same section $V_{Th,k}$ [see Fig. 4.8c]. By recurrently applying Eq. (4.40), the voltage as a function of time may be computed at any point along the nonuniform transmission medium.

Treatment of input periodic signals

The use of periodic input signals is important to model some periodic phenomena or devices, such as the Talbot effect [Azaña and Muriel, 2001] or UWB resonators [Gómez-Díaz et al., 2009a], among many others. For this purpose, the theory previously introduced can easily be extended to consider this type on input signals. A train of (chirp) modulated Gaussian pulses constitute a good example of these periodic signals. In this specific case, the temporal dependence of the source may be extended from Eq. (4.33) to

$$I_g(t) = \sum_{k=-\infty}^{k=+\infty} C_0 e^{j\omega_0 t} e^{-\frac{1}{2}(\frac{t-kT_0}{\sigma})^2}, \tag{4.44}$$

where T_0 is the period rate. The voltage along the transmission line may then be computed as

$$V(z,t) = V_g \frac{C_0\sigma}{\sqrt{2\pi}\omega_0} e^{-\frac{\sigma^2}{2}\omega_0^2} \left[\sum_{k=-\infty}^{k=\infty} e^{j\omega_0 k T_0}\right] \int e^{-\gamma(\omega)z} e^{j\omega t + \omega\omega_0\sigma^2 - \frac{\sigma^2}{2}\omega^2} \left[\sum_{k=-\infty}^{k=\infty} e^{j\omega k T_0}\right] d\omega. \tag{4.45}$$

It is important to note the interchange between the integral and summation operations (which are linear operators), which further contributes to reduce the computational cost required by Eq. (4.45). Furthermore, note that the generalization of this formula to any other type of periodic input signals is straightforward.

4.3.2 Impulse Regime Analysis of Non-Linear CRLH TL

Non-linear transmission lines (NLTL) may be used for a wide variety of applications, ranging from pulse shaping or comb generators, to harmonic generation, among many others [Infeld and Rowlands, 1990], [Olver and Sattinger, 1990], [Rodwell et al., 1991], [Remoissenet, 1994], [Afshari and Hajimiri, 2005]. Usually, non-linear lines are obtained by loading a regular PRH line with hyper-abrupt diodes, which can be lumped elements or even distributed components [Duchamp et al., 2003]. At optics, non-linearity has also led to the development of similar applications [Agarwal, 2005]. In this case, the combination of the dispersive features related to optical

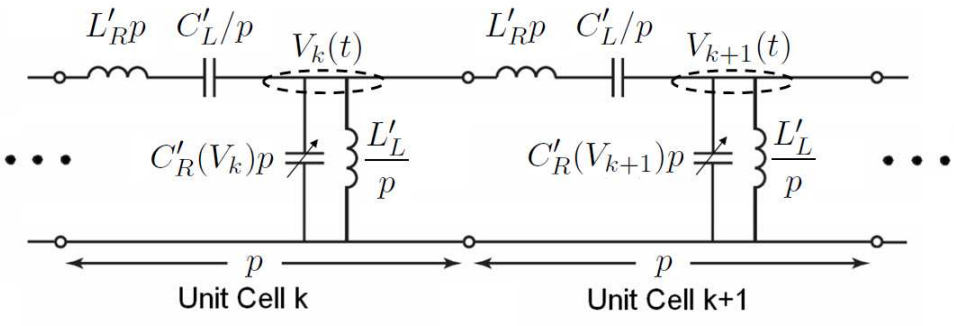

Figure 4.9 – Equivalent circuit model for the non-linear CRLH unit cells k^{th} and $(k+1)^{th}$ (in an asymmetrical configuration, see Fig. 4.3a), where the capacitor C'_R has been replaced by a hyper abrupt diode.

fibers with non-linear effects allows the propagation of solitary waves, also called solitons, which do not suffer from any type of distortion [Lonngren and Scott, 1078]. These waves are specially useful for long-distance communication at optics.

The study of non-liner effects in CRLH lines was first introduced in [Caloz et al., 2004a]. In this type of non-linear lines, the unit cell's shunt capacitor (C_R) is usually replaced by a hyper-abrupt diode, as shown in Fig. 4.9. The wave propagation phenomenology and harmonic generation associated to non-linear metamaterial lines has widely been studied at microwaves, as detailed in [Kozyrev and der Weide, 2005] or [Shadrivov et al., 2008]. Furthermore, it has mathematically been demonstrated the fulfillment of the Schröndinger equation in this media, allowing the existence of solitary waves [Gupta and Caloz, 2007], [Narahara et al., 2007].

However, this type of lines has been usually analyzed in the harmonic regime, and no systematic treatment has been proposed for the analysis and design of practical non-linear metamaterial lines operated in the impulse regime. Note that this type of lines are particulary interesting at microwaves, because they combine dispersion (due to the CRLH behavior) and non-linearity (due to the varactors influence) along the same structure. Therefore, novel phenomena (such as self-phase modulation, the formation of soliton waves, etc) which usually appear in the optics regime [Agarwal, 2005] may be reproduced at microwaves, providing interesting applications. Furthermore, the variation of the varactor's DC bias provides control of the TL's band-gap near the CRLH transition frequency. This can be exploited to electronically balance the line [Caloz and Itoh, 2005].

As already commented, non-linearity is achieved by replacing the shunt capacitor of the CRLH TL unit cell by a varactor. For the proposed non-linear analysis, time discretization is required. Specifically, the characteristic impedance and propagation constant are re-evaluated at each time for each unit cell of the CRLH TL. The time variation of the characteristic impedance of each unit cell is considered, introducing a temporal-dependent mismatch, correctly modeling the nonlinear propagation of the pulse. These impedance variations create small reflected waves between two consecutive unit cells, which are accurately taken into account in the model. A non-uniform transmission line is therefore obtained and solved at each particular instant. Then, a novel interpolation scheme is employed to reduce the computational cost required for the technique. The idea is to interpolate the

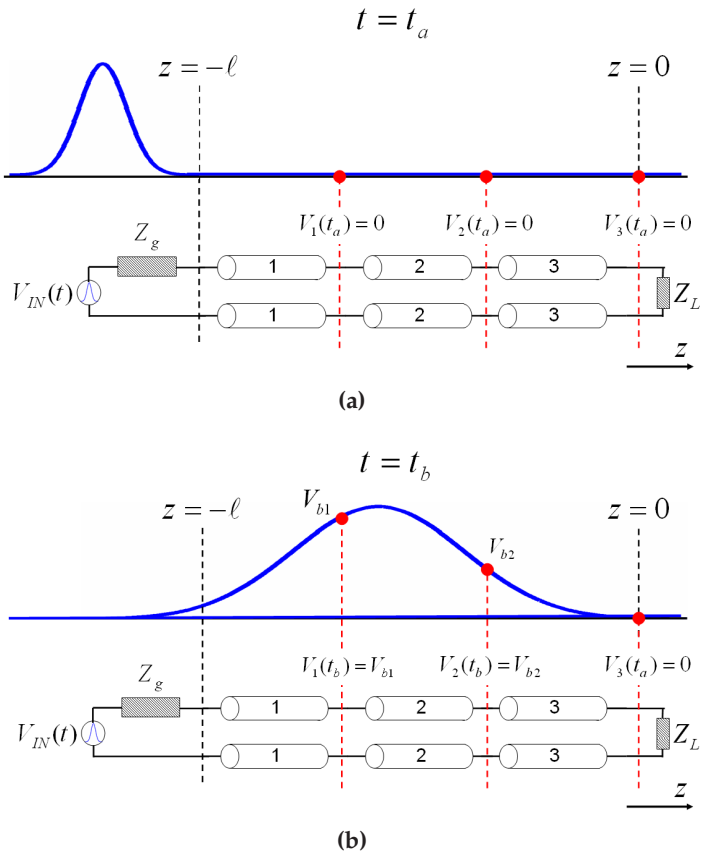

Figure 4.10 – Pulse propagation along a non-linear CRLH transmission line composed of 3 unit cells. The voltage at each unit cell node controls the non-linear behavior of the line. (a) Initial situation, where the time boundary condition imposes a 0 voltage at all unit cell nodes. (b) General situation, where a different voltage is applied to each unit cell node.

propagation constant values as a function of the variable shunt capacitances.

The capacitance introduced by an hyper-abrupt junction diode, which replaces the shunt capacitor of the CRLH unit cell (see Fig. 4.9), depends on the voltage applied at their terminals. Specifically, this type of varactors exhibits the following C-V law

$$C_R(V_k) = \frac{C}{1 + V_k/V_{BIAS}} \simeq C_0 + \eta V_k + \alpha V_k^2, \tag{4.46}$$

where V_k is the voltage at the varactor terminals of the k^{th} unit cell, and V_{BIAS} is the applied bias voltage.

In order to analyze this non-linear line, a time-discretization (with time step Δt) is required. At the initial time ($t = t_a$) a boundary condition of 0 V value along the non-linear line is imposed [see Fig. 4.10a]. Then, at any other time ($t = t_b$) the C_R parameter of the k^{th} unit-cell varies as a function of the voltage present in the previous time at that node [$V_k(t_b - \Delta t)$], which results into an effectively non-uniform medium [see Fig. 4.10b]. This non-uniform medium can be efficiently analyzed with the method presented in Section 4.3.1.

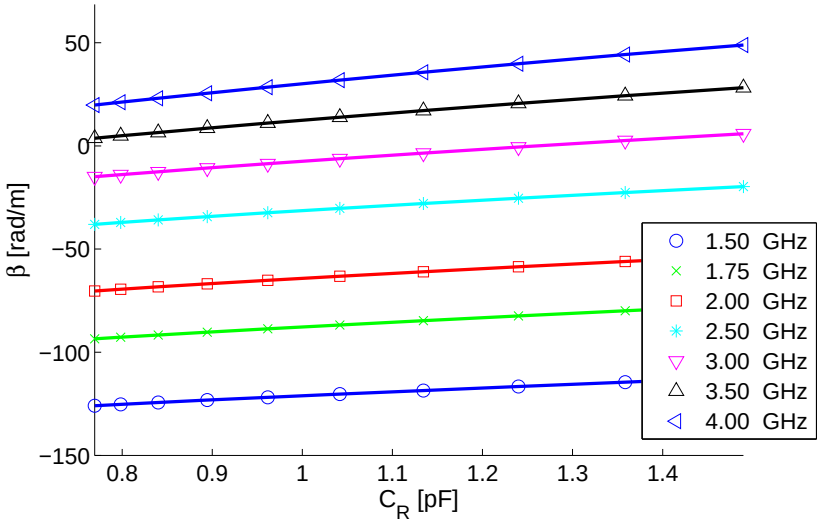

Figure 4.11 – Propagation constant (β) evolution versus the non-linear C_R capacitor, plotted at different frequencies for a single CRLH unit cell. The cell parameters are $C_L = 1.0$ pF and $L_L = L_R = 2.5$ nH.

Thereby, a new propagation constant and a new characteristic impedance must now be computed for each unit cell at any discrete instant of time. The variation of the characteristic impedance creates reflected waves among the unit cells, which are conveniently treated with this method. Moreover, note that the balanced assumption made for the linear case does not hold any more at all times, due to the time-variation of the shunt capacitor. This makes the time-dependent computation intensive.

It is important to mention that the proposed approach is based on the weak nonlinearity assumption [Agarwal, 2005]. As commented, the method assumes that the media is linear at each particular instant. In addition, it also assumes that the variation of the media features (i.e. the influence of the non-linearity) is weak. Therefore, a smooth variation of the unit-cells parameters is required. Then, the use of Eq. (4.32) recovers the temporal evolution of the pulse as it propagates along the line, including the weak non-linear effects. Note that this approach is not appropriate for modeling strong non-linear lines, because in that case the variation of the unit-cell features may be abrupt, and the assumption that the medium is linear at a particular instant may not hold any more [Agarwal, 2005].

This iterative process produces a significant increase in the computational cost as compared to the linear case. In order to reduce it, an interpolation scheme for the computation of the propagation constant is proposed. It is based on the same weak nonlinearity assumption [Agarwal, 2005], which is commonly employed to model non-linear media. Since the input pulse amplitude is known a priori, the possible variations of the shunt capacitor C_R occur in a well-defined range. Under these conditions, the propagation constant of a single unit cell presents a smooth behavior as a function of C_R, as shown for a particular example in Fig. 4.11, and can be efficiently interpolated for an arbitrary C_R value. This simple method provides an important computational cost reduction while maintaining high accuracy.

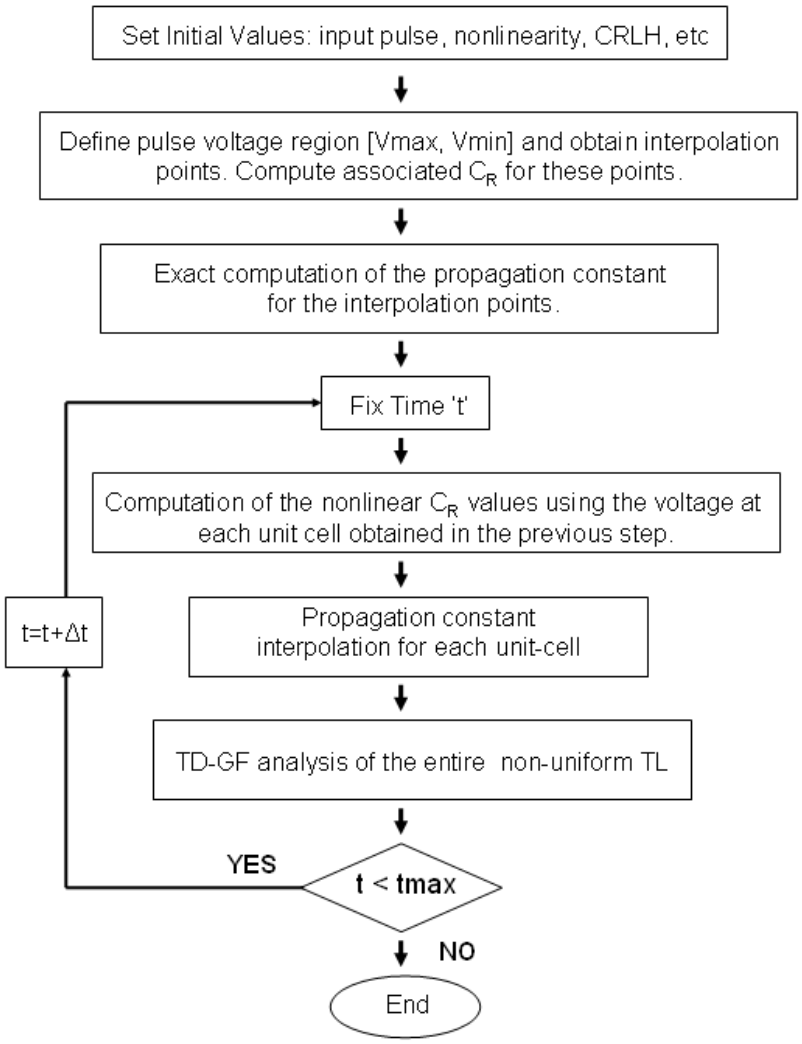

Figure 4.12 – Flowchart of the proposed non-linear time-domain Green's function approach.

The complete iterative process proposed to model pulse propagation along a weak non-linear CRLH transmission line is presented in Fig. 4.12. As can be observed in the flowchart, an analysis of the non-uniform line is performed at each time step. The maximum duration of this step is related to the input signal as

$$\Delta t|_{max} = \frac{1}{2N(f_0 + BW/2)}, \tag{4.47}$$

where f_0 and BW are the modulation frequency and the bandwidth of the input pulse, respectively. The N parameter (with $N \geq 1$) controls the accuracy of the results, and the number of harmonics which can be recovered using this technique.

4.4 Impulse Regime Analysis of CRLH Leaky-Wave Antennas

A CRLH transmission line supports a fast-wave mode [Oliner and Jackson, 2007] which penetrates inside the fast-wave region (see Fig. 4.5a). Therefore, a CRLH structure behaves as a leaky-wave antenna (LWA) [Caloz and Itoh, 2005] when it is excited by a source with a frequency within a range of ($\omega_{BF} < \omega < \omega_{EF}$), where ω_{BF} and ω_{EF} are the fast-wave region limits and they are defined in Eq. (4.22). Since a CRLH line behaves as a LWA, the direction of the radiated main beam follows the LWA scanning law [Oliner and Jackson, 2007], which is given by

$$\sin(\theta) \approx \frac{\beta(\omega)}{k_0}. \tag{4.48}$$

In the above equation, θ is the radiation angle (measured from the perpendicular direction over the CRLH structure) and k_0 is the free-space wavenumber. Fig. 4.13 presents an illustration related to the operation principle of a CRLH LWA. As can be seen in the figure, and following Eq. (4.48), the antenna is able to radiate at backwards [when $\omega < \omega_T$ and $\beta(\omega) < 0$], forwards [$\omega > \omega_T$ and $\beta(\omega) > 0$] and broadside [$\omega = \omega_T$ and $\beta(\omega) = 0$]. Therefore, this type of structures is able to provide a full-space radiation, from backfire ($\theta = -90°$) to endfire ($\theta = +90°$), including the broadside ($\theta = 0°$) direction. As previously commented, the use of CRLH transmission lines as leaky-wave antennas has led to the development of many radiated-wave applications, most of them in the harmonic regime (see [Eleftheriades and Antoniades, 2007] or [Caloz et al., 2008], for instance).

In this section, the radiation features of a CRLH LWA are studied in great detail [Caloz and Itoh, 2005], [Eleftheriades and Balmain, 2005]. For this purpose, the CRLH unit-cell is modified in order to take into account for the possible presence of series and shunt radiators, which provides for the required radiation losses. Then, the propagation and attenuation constants related to this modified unit-cell are obtained in closed-form, in the case of a general structure and in the simplified case of a balanced CRLH line. Next, a simple condition related to the equivalent radiators (R, G) of the LWA unit-cell (see Fig. 4.14) is proposed in order to achieve a constant full-space radiation rate. The derived radiation condition also presents the advantage of solving the phase fluctuations which occur close to the CRLH transition frequency, due to the presence of real radiation losses. Once a single CRLH unit-cell has completely been analyzed, a rigorous transmission line approach related to finite-length CRLH LWAs is presented to explain the radiation mechanism. In the study, the currents flowing on each conductor of a matched CRLH line are related to the total radiation of the antenna. Due to the presence of a fast-wave mode, these two currents are not in antiphase (as usually occurs in regular transmission lines), and it is mathematically demonstrated that this phenomena leads to a net far-field radiation. This simple theory provides a fundamental explanation about leaky-wave antennas in connection with transmission lines.

Then, the impulse-regime transmission line method developed in Section 4.3 is extended in order to analyze CRLH LWAs. Besides, the radiation condition and transmission line theory previously derived are also incorporated into this model. In this approach, the far-field effective radiation current which appears along a CRLH line, when it is excited by an input pulse, is computed as a function of time. This time-domain current turns out into a far-field time-domain radiation, which is rapidly obtained using a Fourier transformation [Pipes and Harvill, 1971]. Due to the spectral-spatial decomposition property of LWAs [Oliner and Jackson, 2007], each frequency component of

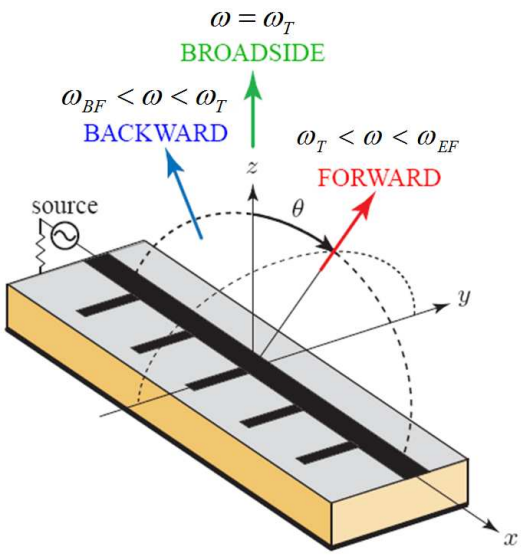

Figure 4.13 – Illustration of a CRLH LWA. The antenna can be configured to radiate at backwards [$\omega < \omega_T$ and $\beta(\omega) < 0$], forwards [$\omega > \omega_T$ and $\beta(\omega) > 0$] or broadside [$\omega = \omega_T$ and $\beta(\omega) = 0$]. Reproduced from [Caloz and Itoh, 2005].

the input signal is radiated towards a particular space position, where the time-dependent field evolution can efficiently been retrieved using the proposed formulation. This approach is especially appropriate to characterize complex radiated-wave UWB phenomena and devices, such as the spatio-temporal Talbot phenomena [Gómez-Díaz et al., 2008a], [Gómez-Díaz et al., 2009d], a real-time spectrum analyzer (RTSA) [Gupta et al., 2009a] or a frequency-resolved electrical gating system (FREG) [Gupta et al., 2009b], just to mention a few of them.

As in Section 4.3, this section basically introduces the mathematical treatment for modeling CRLH LWAs. Then, in Chapter 5, these techniques will be applied to the analysis of radiated-wave impulse-regime phenomena and practical devices. The main advantage of the proposed techniques as compared with other methods from literature (such as full-wave commercial software, TDFEM [Lee et al., 1997] or TDIE [Weile et al., 2004]) is a extremely fast analysis, while keeping high accuracy and physical insight into the problem. Note that full-wave simulations and measurements will be employed in Chapter 5 for validation purposes, further confirming the accuracy of the proposed techniques.

4.4.1 CRLH LWA Unit-Cell Design with Constant Full-Space Radiation Rate

The unit-cell model related to a CRLH transmission line, which operates as a leaky-wave antenna, is shown in Fig. 4.14. It consists of a per unit-length impedance (Z') and a per-unit length admittance (Y'), which may be expressed as

$$Z' = R' + jX' = R' + j(\omega L'_R - \frac{1}{\omega C'_L}), \tag{4.49}$$

$$Y' = G' + jB' = G' + j(\omega C'_L - \frac{1}{\omega L'_R}). \tag{4.50}$$

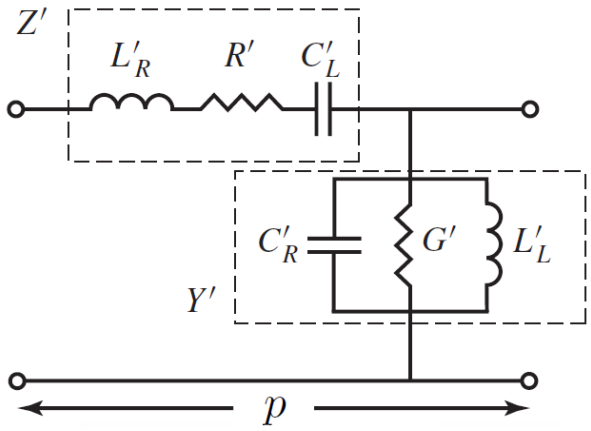

Figure 4.14 – Equivalent unit-cell model of a CRLH transmission line, which operates as a leaky-wave antenna. The series resistance (R′) and the shunt conductance (G′) provide the radiation losses of the antenna. Dielectric and ohmic losses are neglected for simplicity.

The main difference of the CRLH LWA unit-cell as compared with the regular CRLH TL unit-cell (shown in Fig. 4.3a) is the introduction of series and shunt resistors (R',G'), which takes the radiation losses of the antenna into account. In this model, R' and G' are assumed to be constant with frequency inside the fast-wave region. This is an approximation, which is only valid around the central part of the fast-wave frequency region, but it is not accurate close to the edges, where, physically, R' and G' may present important variations as a function of frequency. In addition, note that, for simplicity, dielectric and ohmic losses are neglected in this model. Besides, it is important to keep in mind the use of primes ($'$), which are related to per or times-unit length variables (as introduced in Section 4.2.1, [Caloz and Itoh, 2005]), while non primed quantities denote total values in a whole unit-cell.

Let us assume that the homogenous condition ($p \ll \lambda_g$) is satisfied (where λ_g is the guided wavelength). In the limiting case ($p \to 0$), the complex propagation constant associated to this unit-cell placed in an infinite environment reads [Caloz and Itoh, 2005]

$$\gamma(\omega) = \alpha(\omega) + j\beta(\omega) = \sqrt{Z'Y'}. \tag{4.51}$$

After some tedious but straightforward manipulations, the phase $[\beta(\omega)]$ and attenuation $[\alpha(\omega)]$ constants may be expressed, for the unit cell of Fig. 4.14, as

$$\beta(\omega) = \pm \left(\frac{[(\frac{\omega}{\omega'_{se}})^2 - 1][(\frac{\omega}{\omega'_{sh}})^2 - 1] - R'G'(\frac{\omega}{\omega'_L})^2}{2(\frac{\omega}{\omega'_L})^2} + \frac{\sqrt{[(\frac{\omega}{\omega'_{sh}})^4 + (\frac{\omega}{\omega'_{sh}})^2(G'^2\frac{L'_L}{C'_R} - 2) + 1][(\frac{\omega}{\omega'_{se}})^4 + (\frac{\omega}{\omega'_{se}})^2(R'^2\frac{C'_L}{L'_R} - 2) + 1]}}{2(\frac{\omega}{\omega'_L})^2} \right)^{1/2}, \tag{4.52}$$

$$\alpha(\omega) = \left(\frac{-[(\frac{\omega}{\omega'_{se}})^2 - 1][(\frac{\omega}{\omega'_{sh}})^2 - 1] + R'G'(\frac{\omega}{\omega'_L})^2}{2(\frac{\omega}{\omega'_L})^2} + \frac{\sqrt{[(\frac{\omega}{\omega'_{sh}})^4 + (\frac{\omega}{\omega'_{sh}})^2(G'^2\frac{L'_L}{C'_R} - 2) + 1][(\frac{\omega}{\omega'_{se}})^4 + (\frac{\omega}{\omega'_{se}})^2(R'^2\frac{C'_L}{L'_R} - 2) + 1]}}{2(\frac{\omega}{\omega'_L})^2} \right)^{1/2}. \quad (4.53)$$

For the sake of compactness, we have introduced in these expressions the variables ω_{se} and ω_{sh} [defined in Eq. (4.10)], and the variable ω_L [defined in Eq. (4.9)].

Let us now assume that the CRLH "balanced condition" is satisfied [Caloz and Itoh, 2005]. As explained in Section 4.2.1, this condition implies the mutual cancelation of the series and shunt resonances, allowing a smooth transition from the left-handed to the right-handed frequency range, and it may be expressed as

$$C'_L L'_R = C'_R L'_L. \quad (4.54)$$

Including this last condition into the CRLH unit-cell phase and attenuation constant definitions [Eq. (4.52) and Eq. (4.53)], they may be reduced to

$$\beta(\omega) = \pm \sqrt{\frac{[(\frac{\omega}{\omega'_T})^2 - 1]^2 - R'G'(\frac{\omega}{\omega'_L})^2 + \sqrt{[(\frac{\omega}{\omega'_T})^4 + (\frac{\omega}{\omega'_T})^2(G'^2\frac{L'_L}{C'_R} - 2) + 1][(\frac{\omega}{\omega'_T})^4 + (\frac{\omega}{\omega'_T})^2(R'^2\frac{C'_L}{L'_R} - 2) + 1]}}{2\left(\frac{\omega}{\omega'_L}\right)^2}}, \quad (4.55)$$

$$\alpha(\omega) = \sqrt{\frac{-[(\frac{\omega}{\omega'_T})^2 - 1]^2 + R'G'(\frac{\omega}{\omega'_L})^2 + \sqrt{[(\frac{\omega}{\omega'_T})^4 + (\frac{\omega}{\omega'_T})^2(G'^2\frac{L'_L}{C'_R} - 2) + 1][(\frac{\omega}{\omega'_T})^4 + (\frac{\omega}{\omega'_T})^2(R'^2\frac{C'_L}{L'_R} - 2) + 1]}}{2\left(\frac{\omega}{\omega'_L}\right)^2}}, \quad (4.56)$$

where ω_T is the CRLH transition frequency, defined in Eq. (4.14).

As an illustrative example, consider a CRLH LWA unit-cell with circuital parameters of $C_R = C_L = 1.0$ pF, $L_R = L_L = 2.5$ nH, $R = 5\ \Omega$, $G = 0.04\ \Omega^{-1}$ and a unit-cell length of $p = 1.5$ cm. Note that the radiation losses of this antenna may be important and they can not be neglected (as usually occurs with other circuit models used only for CRLH TLs [Caloz and Itoh, 2005]).

Fig. 4.15a presents the dispersion diagram $[\beta(\omega)]$ for this example. As can be seen in the figure, there are some fluctuations in the phase constant around the transition frequency (even though that the line is balanced). This is due to the effect of real radiation losses, which can not be neglected anymore. Besides, note that the phase constant lies within the fast-wave region as long as frequency increases, which means that this antenna continues to radiate at very high frequencies. In Fig. 4.15b, the attenuation constant $[\alpha(\omega)]$ related to this unit-cell is shown. As can be seen in the figure, it

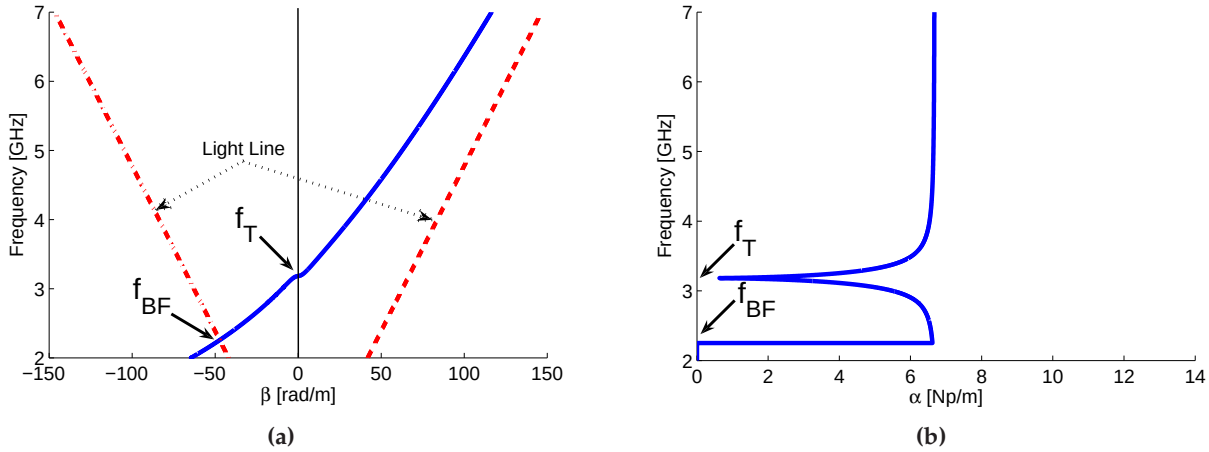

Figure 4.15 – Dispersion diagram (a) and radiation losses (b) associated to a single CRLH LWA unit-cell. The circuital parameters are $C_R = C_L = 1.0$ pF, $L_R = L_L = 2.5$ nH, $R = 5\ \Omega$, $G = 0.04\ \Omega^{-1}$ and the unit-cell length is $p = 1.5$ cm.

presents a step discontinuity at ω_{BF} (which denotes the initial point of the fast-wave region). This non-physical behavior appears because the CRLH LWA circuital-model of Fig. 4.14 is an approximation, which considers that R' and G' are frequency-independent. Specifically, they have a strictly zero value outside of the fast-wave region (no radiation) but a constant and well-defined value inside that region (radiation). However, in a real structure, the values of R' and G' are frequency-dependent, and, after some possible fluctuations, they must gradually tend to zero when approaching the fast-wave region edges. Furthermore, as shown in Fig. 4.15b, the radiation losses suffer an important decrease at the transition frequency (ω_T). This effect implies that the radiation from backfire to end-fire is not constant, and it is usually reduced at the broadside direction (see [Paulotto et al., 2008], [Paulotto et al., 2009]). Besides, it is interesting to note that radiation losses rapidly tends to a finite and well-defined value as long as the frequency is far away from ω_T.

From Eq. (4.56), it is simple to demonstrate that the value of the radiation losses at the transition frequency (ω_T) is [Paulotto et al., 2008]

$$\alpha(\omega_T) = \sqrt{R'G'}. \tag{4.57}$$

Besides, the value of the radiation losses at a frequency different of ω_T (in the limiting case, $\omega \to \infty$) may be expressed as

$$\lim_{\omega\to\infty} \alpha(\omega) = \sqrt{\frac{R'G'}{2} + \omega_T^2 \frac{R'^2 C'_L C'_R + G'^2 L'_L L'_R}{4}}. \tag{4.58}$$

In order to obtain a constant radiation rate in the whole space, the radiation at the broadside direction must be equal to the radiation outside of this direction. In the limiting case, this condition may be expressed as

$$\alpha(\omega_T) = \lim_{\omega\to\infty} \alpha(\omega). \tag{4.59}$$

After some straightforward manipulations, Eq. (4.59) may be reduced to the following simple condi-

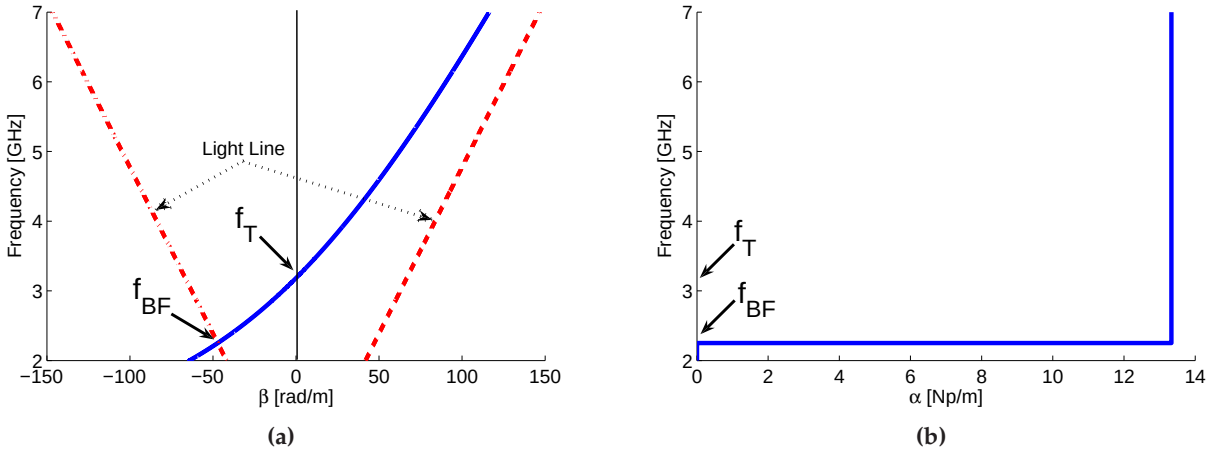

Figure 4.16 – Dispersion diagram (a) and radiation losses (b) associated to a single CRLH LWA unit-cell. The circuit parameters are $C_R = C_L = 1.0$ pF, $L_R = L_L = 2.5$ nH, $R = 5\,\Omega$, $G = 0.2667\,\Omega^{-1}$ (optimized result) and the unit-cell length is $p = 1.5$ cm.

tion

$$\frac{R'}{G'} = \sqrt{\frac{L'_L L'_R}{C'_L C'_R}}. \tag{4.60}$$

The importance of the proposed new $R - G$ condition is two fold. First, this condition forces the CRLH LWA to radiate with the same radiation rate in the whole space (from backfire to endfire), without any decrease at the broadside direction. Physically, this is because the radiated field is a combination from the series and shunt currents along the CRLH LWA unit-cell. This is demonstrated in Fig. 4.16b, where the radiation losses related to the unit-cell model (using the previous circuital parameters) are recomputed employing an optimized value of G [which satisfies Eq. (4.60)]. As can be seen in the figure, radiation losses are constant for all frequencies (inside the fast-wave region). However, note that this circuital model uses frequency independent components, and it only approximates the behavior of a physical structure for frequencies which are not close to the fast-wave region edges. Second, the phase constant is optimized at the transition frequency, solving the fluctuations produced by real radiation losses. This is shown in Fig. 4.16a, which shows the dispersion diagram for this case. In order to further clarify how these phase fluctuations have been removed, Fig. 4.17 presents a detailed zoom of the dispersion diagram at the transition frequency. As can be seen in the figure, the use of non-optimum values of R and G (solid line) leads to phase fluctuations around the transition frequency, which deteriorates the performance at the broadside direction. On the other hand, the use of optimized R and G values (dashed line) completely removes these fluctuations around the transition frequency, and allows a perfect radiation at the broadside direction.

In order to make a real design of a CRLH LWA unit-cell, the series (R') and shunt (G') per-unit-cell resistors must be carefully adjusted. Unfortunately, to the best of our knowledge, there are not CAD expressions to easily link the parameters R' and G' to physical dimensions. Therefore, as in the case of regular CRLH LWA designs, the use of full-wave software is still required to obtain

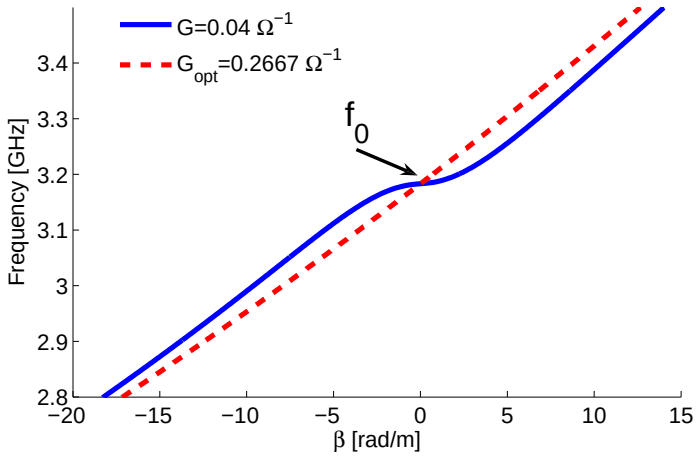

Figure 4.17 – Details of the dispersion diagram around the transition frequency ω_T associated to a single CRLH LWA unit-cell. The circuit parameters are the same as in Fig. 4.15b. The values of the shunt conductance, G, are 0.04 Ω^{-1} (solid line) and 0.2667 Ω^{-1} (dashed line, optimized result).

and optimize these values (see [Paulotto et al., 2008]). However, thanks to the proposed $R' - G'$ condition, the optimization process is simplified, fixing a very clear goal-function to the optimization algorithms. Besides, this condition allows the designer to directly control the total amount of radiation losses (modifying the values of R' and G') while obtaining a more stable CRLH LWA unit-cell design, solving the phase fluctuation around the transition frequency, and maintaining the radiation rate constant in a wide frequency band.

In the following examples, the radiation losses from two different CRLH LWAs taken from the literature are carefully analyzed. Next, the derived $R - G$ condition is applied in each case to obtain the resistance (R') and conductance (G') values which model the CRLH LWA unit-cell. It is then demonstrated that the computed radiation losses i) are completely constant with frequency, ii) do not show any decrease of the radiation efficiency at the broadside direction and iii) agree very well against full-wave simulations and measurements.

Let us examine the work presented in [Paulotto et al., 2008], where a broadside optimization approach of CRLH LWAs based on interdigital capacitors and planar stubs is introduced. Specifically, a parametric full-wave study is presented as a function of the stubs length, achieving an almost constant radiation losses for all beam directions, including broadside. In this case, the derived circuital parameters of the unit-cell were $C_R = 1.47$ pF, $C_L = 0.6$ pF, $L_R = 2.09$ nH, $L_L = 0.85$ nH, $R = 1.18\ \Omega$, $G = 0.4 \times 10^{-3}\ \Omega^{-1}$, with a unit-cell length of $p = 6$ mm. The normalized radiation losses versus frequency for this example, computed using a Bloch-wave periodic approach [Caloz and Itoh, 2005], [Pozar, 2005] are shown in Fig. 4.18 (solid line). This graph reproduces the results presented in [Paulotto et al., 2008]. As can be seen in the figure, the attenuation constant is not completely linear as a function of frequency, and some small variations appear around the transition frequency. This is because the $R - G$ values do not satisfy Eq. (4.60). However, these values are close to the optimum condition. This explains that the optimized antenna of [Paulotto et al., 2008] presents

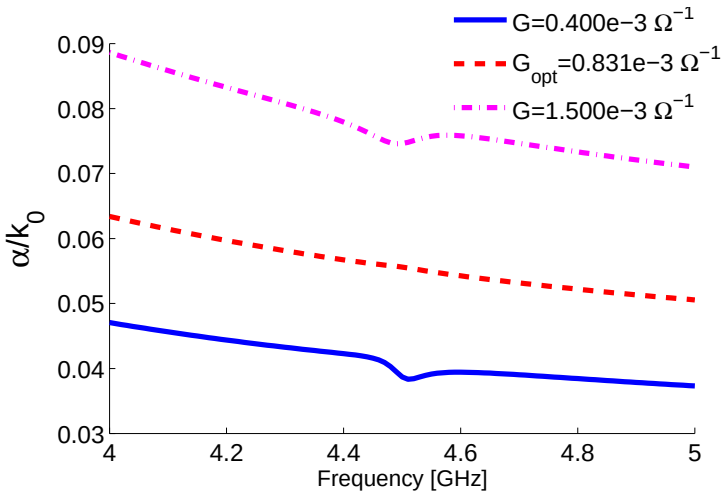

Figure 4.18 – Normalized attenuation constant $[\alpha(\omega)/k_0]$ obtained with a Bloch-wave analysis using a unique unit-cell. The circuital parameters (from [Paulotto et al., 2008]) are $C_R = 1.47$ pF, $C_L = 0.6$ pF, $L_R = 2.09$ nH, $L_L = 0.85$ nH, $R = 1.18\ \Omega$, and the unit-cell length is $p = 6$ mm. The values of the shunt conductance, G, are $0.4 \times 10^{-3}\ \Omega^{-1}$ (solid line, same result as in [Paulotto et al., 2008]), $0.831 \times 10^{-3}\ \Omega^{-1}$ (dashed line, optimized result) and $1.5 \times 10^{-3}\ \Omega^{-1}$ (dashed-dotted line).

an almost constant full-space radiation rate.

At this point, we keep the R value constant, and modify G towards its optimum value ($G = 0.831 \times 10^{-3}\ \Omega^{-1}$). The radiation losses per unit length in this case are also shown in Fig. 4.18 (dashed line). As expected, they are totally linear as a function of frequency, leading to a full-space radiation with constant radiation rate. This result fully demonstrates the usefulness of the new proposed $R - G$ condition. Finally, if we keep increasing the value of G (for instance, $G = 1.5 \times 10^{-3}\ \Omega^{-1}$), the $R - G$ condition is not satisfied anymore, and the radiation losses suffer again variations around the transition frequency (see Fig. 4.18, dashed-dotted line).

Let us now consider the CRLH LW antenna presented in [Liu et al., 2002], [Caloz and Itoh, 2004]. This CRLH LWA is fabricated on microstrip technology, and it is based on interdigital capacitors and via-holes. The line is composed of 24 -6.1 mm long- unit-cells, with circuital parameters of $C_R = 0.5$ pF, $C_L = 0.68$ pF, $L_R = 2.45$ nH and $L_L = 3.35$ nH. The measured attenuation constant [Caloz and Itoh, 2004], $\alpha(\omega)$, is shown in Fig. 4.19 (black '*'). In order to model these radiation losses, the value of R may be modified in order to fit with measurements, keeping the conductance G equal to 0 (this is the approach followed in [Caloz and Itoh, 2004]). A good possibility to fit with the measurement data is to use $R = 3.1\ \Omega$. The attenuation constant computed with these values is also depicted in Fig. 4.19 (solid-line). For this computation, a transmission line (ABCD) matrix approach, combined with the Floquet's theorem, has been applied [Caloz and Itoh, 2005]. As can be seen in the figure, the agreement between simulations and measurements is good in the whole frequency region, with the exception of the frequencies around the transition frequency (ω_T). This is because this model only takes into account the influence of R, whereas the radiation at the broadside direction requires from both, the series and the shunt resistors [R and G, see Eq. (4.57)]. This is further confirmed from the $\alpha(\omega)$-measurements, which do not tend to 0 around the transition frequency, since in the real

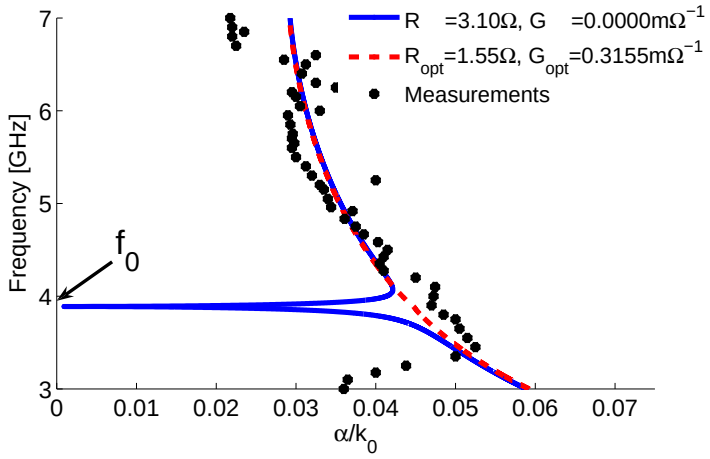

Figure 4.19 – Measured attenuation constant $[\alpha(\omega)/k_0]$ obtained from the 24 -6.1 mm long- unit-cells CRLH LWA prototype presented in [Caloz and Itoh, 2004]. The circuital parameters of the line are $C_R = 0.5$ pF, $C_L = 0.68$ pF, $L_R = 2.45$ nH and $L_L = 3.35$ nH. Simulation results, from a Bloch-wave analysis method, are shown for the case of $R = 3.10\ \Omega$ and $G = 0.0\ \text{m}\Omega^{-1}$ (dashed line), and for the case of $R = 1.55\ \Omega$ and $G = 0.3155\ \text{m}\Omega^{-1}$ (solid line, optimized result).

structure G is close to its optimum value.

At this point, the values of R and G are modified in order to optimize the radiation at the broadside direction. Therefore, the $R - G$ ratio condition introduced in Eq. (4.60) is applied. The derived R and G parameters are $R = 1.55\ \Omega$ and $G = 0.3155\ m\Omega^{-1}$. The computed radiation losses, using these parameters, are shown in Fig. 4.19 (dashed line). As can be seen in the figure, the agreement of the proposed model with respect to measurement is good in the whole frequency range, including the broadside direction. In fact, there is not any decrease of the radiation losses at the transition frequency, as occurs with the measured data. This result demonstrates that the derived $R - G$ condition is indeed required to obtain a constant radiation losses in the whole space, including the radiation at the broadside direction.

Considering CRLH LWAs in general, three configurations are imaginable regarding the distribution of radiation losses over the branches of their unit cells' equivalent circuits. Simplified equivalent circuits representing the three cases are shown in Fig. 4.20. From Eq. (4.57), configuration (a), with radiation losses in both the series and the shunt branch, is the only one that presents radiation losses at the broadside direction different from zero. This means that in order to radiate at the broadside direction, both series and shunt radiation losses must be present [Paulotto et al., 2008]. In any other case [configurations (b) or (c)] the total radiation at this direction is zero.

The field radiated by type (a) CRLH LWAs is a combination of two contributions from the series and shunt currents flowing on the CRLH TL. The CPW-based slot LWA described in [Grbic and Eleftheriades, 2002b] is an example for this type and the proposed equivalent circuit of its unit cell contains both types of radiation losses.

In [Gomez-Tornero et al., 2005] a LWA that uses a rectangular hollow waveguide as host TL is proposed. The inside of the waveguide is coupled to a PPW via asymmetrically placed slots in one

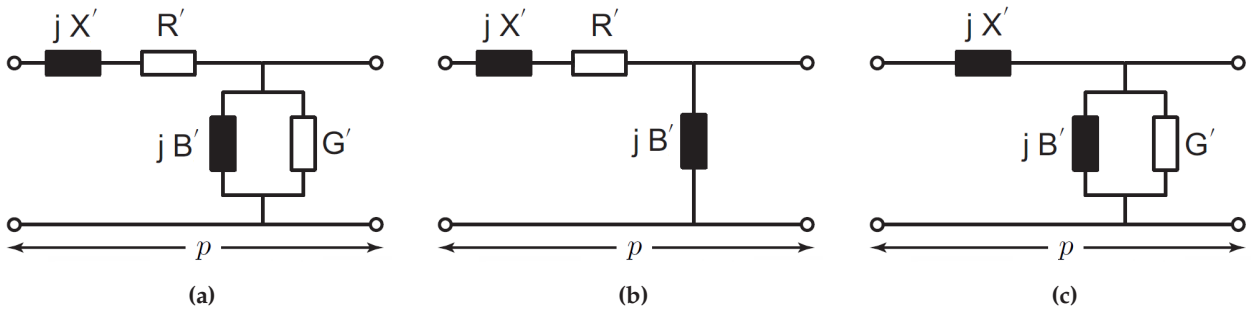

Figure 4.20 – Possible distribution of radiation losses over the series and shunt branches of the unit-cell equivalent circuit. (a) Radiation losses in both series and shunt branches. (b) Radiation losses in series branch only. (c) Radiation losses in shunt branch only.

of the wider waveguide walls. Since the slots are primarily excited by transverse currents of the fundamental TE_{10} waveguide mode, radiation losses should occur only in the shunt branch of an equivalent circuit. Therefore, this LWA is of type (c). As a matter of fact, simulation results presented in [Gomez-Tornero et al., 2005, Fig. 8] exhibit a drop of the attenuation constant to zero at the transition frequency, while the scanning angle indicates a continuous frequency scanning capability.

Finally, the 2-D loaded NRI TL grid LWA analyzed in Section V of [Kokkinos et al., 2006] is of type (b). Its attenuation constant, determined by periodic finite-differences time-domain (FDTD) analysis, drops to zero at the transition frequency. This behavior was reproduced by a periodic analysis of the unit cell's equivalent circuit that contained radiation losses only in its series branches.

4.4.2 Transmission Line Theory of LWA

Let us consider a simple matched transmission line, of length ℓ, fed by a source generator and oriented along the z axis, as shown in Fig. 4.21. The current along this line, at any point "z", may be easily computed using standard transmission line theory [Pozar, 2005] as

$$I(z,\omega) = \frac{V_g}{Z_0(\omega)} e^{-\gamma(\omega)z} + \rho_L \frac{V_g}{Z_0(\omega)} e^{+\gamma(\omega)z} = \frac{V_g}{Z_0(\omega)} e^{-\gamma(\omega)z}, \tag{4.61}$$

where V_g is the maximum voltage provided by the generator, ω is the operating frequency, $Z_0(\omega)$ is the characteristic impedance of the line, ρ_L is the reflection coefficient at the load (which is strictly zero, because the line is completely matched) and $\gamma(\omega)$ is the propagation constant (which may be complex) of the line.

The goal of this section is to compute the electric field radiated by this structure. For this purpose, an spherical coordinate system is employed (see Fig. 4.22). It is very important to distinguish between the angle $\hat{\theta}$ used to denote the elevation angle of the spherical coordinate system [Balanis, 2005] and the angle θ [Oliner and Jackson, 2007], used to measure the angle from the broadside direction to the antenna (see Eq. (4.1) and Fig. 4.13). Besides, we assume that the $1D$ antenna is electrically thin (i.e. its associated x and y dimensions are neglectable).

As previously commented, the transmission line is matched. Therefore, the reflection coefficient

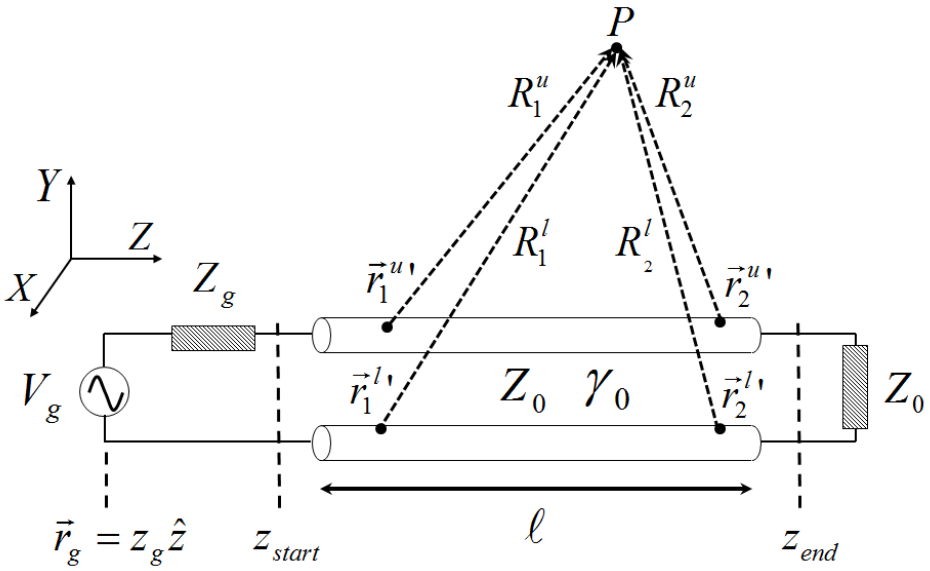

Figure 4.21 – Sketch of a single CRLH transmission line which operates as a leaky-wave antenna. The antenna is placed along the z-axis, it has a length of $\ell = z_{end} - z_{start}$, and it is fed by a punctual generator, placed at $\vec{r} = z_g\hat{e}_z$.

ρ_L is 0, and all the propagating energy is absorbed by the load. This means that only a propagative wave exists along the transmission line. However, it is well-known that transmission lines are composed of two conductors, which are separated by a certain distance [Pozar, 2005]. Therefore, physically, there is a current which is flowing along each conductor. Note that these two currents simultaneously propagate on the conductors, and that they are associated in general to the propagating and reflected waves. A simple possibility to define these two currents is to express them as a function of the transmission line current [see Eq. (4.61)], as follows

$$I_p^u(z,\omega) = I(z,\omega), \tag{4.62}$$

$$I_p^l(z,\omega) = -\xi(\omega) I_p^u(z,\omega) e^{j\chi(\omega)} = -\xi(\omega) I(z,\omega) e^{j\chi(\omega)}, \tag{4.63}$$

where the subscript p denotes that these currents are related to a propagative wave (since in this case $\rho_L = 0$ and there is not any reflected wave) and the superscripts "u" and "l" denote the upper and lower conductor, respectively. Besides, note that the current on the lower conductor is expressed as a function of the current on the upper conductor, with a possible variation in magnitude (related to the variable ξ) and phase (related to the variable χ). Also, the minus sign takes into account that both currents are in opposite physical directions (the current flowing on the lower conductor may be seen as a "return" current [Balanis, 1989]).

It is important to clarify the notation employed to describe the situation under analysis. First, the generator which excites the transmission line is placed at the position $\vec{r}_g$, with $\vec{r}_g = z_g\hat{e}_z$. Second, any point along the line is denoted as $\vec{r}\,'$, with $\vec{r}\,' = z'\hat{e}_z$ (note that $z_{start} \leq z' \leq z_{end}$, see Fig. 4.21). Besides, note that the analysis that is going to be proposed studies the far-field radiation of the transmission line towards an observation point P (denoted as $\vec{r}$, with $\vec{r} = x\hat{e}_x + y\hat{e}_y + z\hat{e}_z$). Therefore, any observation point P must be located in the far-field region of the transmission line [Balanis, 2005],

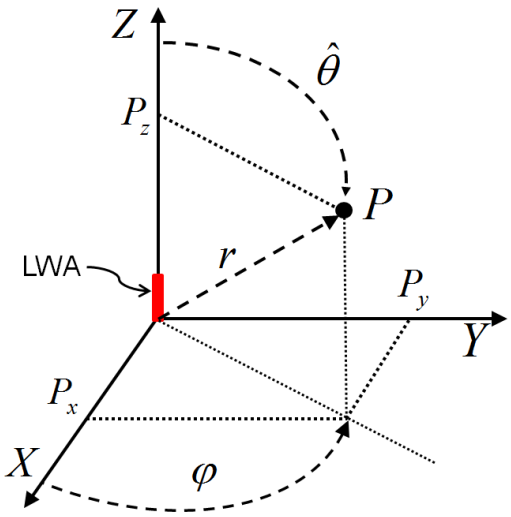

Figure 4.22 – Representation of an electrically thin transmission line leaky-wave antenna oriented along the z axis and an arbitrary observation point "P", in both, cartesian and spherical coordinates [Balanis, 2005].

fulfilling the far-field radiation condition, which is given by

$$R_{ant} = \sqrt{x^2 + y^2 + \left(z - \frac{\ell}{2}\right)^2} > \frac{2\ell^2}{\lambda_0}. \tag{4.64}$$

In this last equation, R_{ant} is the distance between the observation point P (placed at $\vec{r}$) and the transmission line, which can approximately be considered as a point source (placed at the center of the line) from a far-field point of view.

The electric field radiated by the transmission line under study, in the far-field region, is approximately given by [Balanis, 2005]

$$\vec{E}(\vec{r},\omega) \approx -j\omega\vec{A}(\vec{r},\omega), \tag{4.65}$$

where $\vec{A}$ is the magnetic vector potential.

It is important to keep in mind that $\vec{A}$ is related to the physical current which is flowing on the conductors of the transmission line [Balanis, 2005]. Therefore, in the case shown in Fig. 4.21, this potential may be expressed as

$$\vec{A}(\vec{r},\omega) = \frac{\mu_0}{4\pi}\int_{z_{start}}^{z_{end}} \left[I_p^u(z',\omega) + I_p^l(z',\omega)\right] \frac{e^{-jk_0R}}{R} dz'\hat{e}_z, \tag{4.66}$$

where R is the distance between the pair of source-observation points. As can be seen in the Fig. 4.21, each position $\vec{r'}$ along the line may be referred to the upper or to the lower conductor (see points $\vec{r_1^u}'$ and $\vec{r_2^u}'$ in the upper conductor and points $\vec{r_1^l}'$ and $\vec{r_2^l}'$ in the lower conductor), defining different pair of source-observation points for each conductor. However, since we are dealing with electrically thin transmission lines (the distance between the two conductors is neglectable) from a far-field point of view, the positions along the upper and lower conductors are extremely close, and we may consider

that they directly superimpose. Therefore, under these two assumptions, there is a unique distance R between each position along the transmission line and the observation point P.

Besides, note that the two currents which are physically present on the conductor are taken into account to recover the magnetic vector potential. Therefore, from a far-field point of view, we can define an *effective radiation current*, composed by the currents flowing along the two conductors, which completely characterizes the radiation of the transmission line. Specifically, this radiation current may be expressed as

$$I_{rad}(z',\omega) = I_p^u(z',\omega) + I_p^l(z',\omega) = I(z',\omega)\left[1-\xi(\omega)e^{j\chi(\omega)}\right] = \frac{V_g}{Z_0(\omega)}e^{-\gamma(\omega)z'}\left[1-\xi(\omega)e^{j\chi(\omega)}\right]. \tag{4.67}$$

Once this effective radiation current is known, the far-field radiation of a transmission line (which may act as an antenna if the propagation phase lies into the fast-wave region) can easily be recovered using the magnetic vector potential $\vec{A}$ as follows

$$\vec{A}(\vec{r},\omega) = \frac{\mu_0}{4\pi}\int_{z_{start}}^{z_{end}} I_{rad}(z',\omega)\frac{e^{-jk_0R}}{R}dz'\hat{e}_z. \tag{4.68}$$

Let us illustrate the concept of the effective radiation current by using three different examples, which are shown in Fig. 4.23. In the first case, a simple lossless right-handed transmission line is considered (see Fig. 4.23a). Since the line is matched, there is only a propagating wave, which carries the propagating energy towards the load. Physically, there are two currents, one related to each conductor. In fact, both currents have the same magnitude and the same phase, but they flow towards opposite directions. Therefore, the effective radiation current in this case is

$$I_{rad}(z',\omega) = I_p^u(z',\omega) + I_p^l(z',\omega) = I(z',\omega) - I(z',\omega) = 0. \tag{4.69}$$

Including this last equation into Eq. (4.68), it is simple to realize that the far-field radiation from this transmission line is strictly zero. This can also be explained analyzing the fields radiated by the currents flowing on each conductor. Specifically, the far-field electric field radiated by the current from the upper conductor is in antiphase with respect to the electric field radiated by the current flowing along the lower conductor (see Fig. 4.23a). Thereby, the total radiated electric field cancels out. This result is in total agreement with well-known antenna theory [Balanis, 2005].

Let us consider now the case of a dipole, as shown in Fig. 4.23b. In this case, the physical disposition of the transmission line conductors are modified in order to force the currents to flow in phase along the conductors. Therefore, the effective radiation current in this case may be computed as

$$I_{rad}(x',\omega) = \begin{cases} I_p^u(x',\omega) & \text{if} \quad 0 \le x' \le \ell \\ I_p^l(-x',\omega) & \text{if} \quad -\ell \le x' \le 0 \end{cases}. \tag{4.70}$$

First, note that the direction of propagation of the current has been modified from the z to the x axis, due to the physical modification of the structure. Second, note that the effective radiation current coincides with the real current along the dipole [Balanis, 2005]. Therefore, this situation is reduced

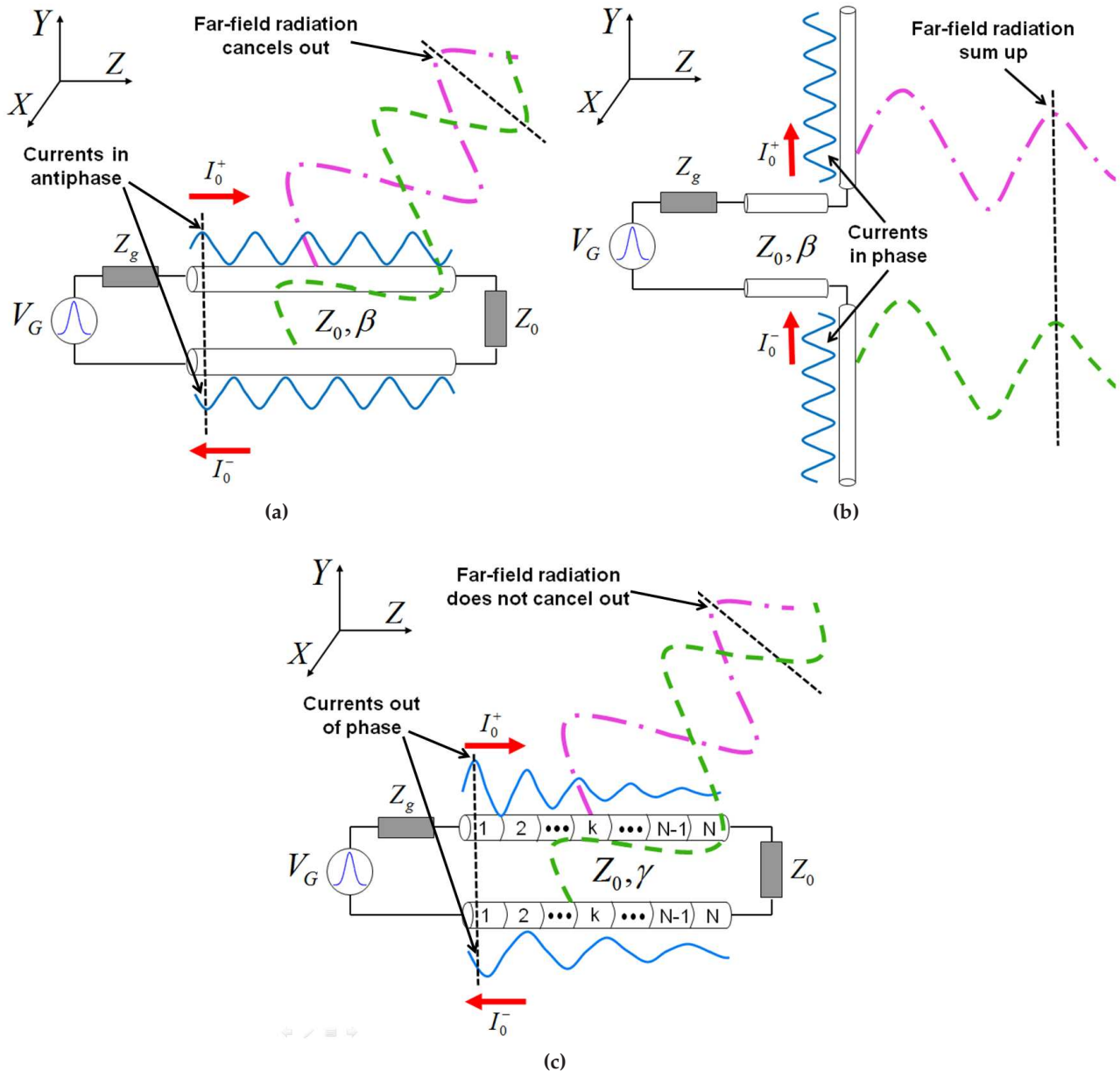

Figure 4.23 – Illustrative example of current distribution and electric field radiation from three different transmission lines. (a) Matched right-handed transmission line. (b) Dipole. (c) Matched transmission-line which behaves as a leaky-wave antenna.

to the analysis of a simple dipole, which is well-known in the literature [Balanis, 2005]. Besides, as compared with the transmission line case, the electric field radiated by the current which flows along each conductor sum up in phase, leading to the total radiation of the dipole (see Fig. 4.23b).

Finally, let us consider the case of a transmission line which acts as a leaky-wave antenna (see Fig. 4.23c). Some examples of these type of structures are CRLH leaky-wave antennas [Caloz and Itoh, 2005] or a simple microstrip line operated in its second mode [Nghiem et al., 1993], [Qian et al., 1999]. As in the previous examples, we assume that the line is matched, so there are not reflected waves. In fact, this situation closely resemble to the first example, where a simple trans-

mission line was analyzed. In that case, the currents flowing on each conductor were in antiphase, leading to an effective radiative current equal to zero and a cancelation of the radiated electric field. However, in this case, it is known that radiated electric field exists at the far-field region. Therefore, the only possibility is that the effective radiation current, defined in Eq. (4.67), does not cancel out for this type of structures. This means that the current flowing along one conductor suffers a change of its phase or magnitude with respect to the current which flows along the other conductor, i.e. *the currents are unbalanced*. Thereby, the radiated electric field associated to one current, flowing along one conductor, is out of phase with respect to the electric field radiated by the current which flows along the other conductor. The combination of both fields leads to the total radiated electric field at the far-field region, which is not zero (see Fig. 4.23c). As we will detail below, this simple transmission line theory, based on unbalanced conductors currents, is able to explain and characterize complex TL LWA radiation phenomena.

The main difference between a TL LWA as compared with a simple lossless TL is the presence of a complex propagation constant $\gamma(\omega) = \alpha(\omega) + j\beta(\omega)$, which is just reduced to a phase constant $\gamma(\omega) = j\beta(\omega)$ in the case of a lossless TL. Therefore, the presence of the radiation losses [$\alpha(\omega)$] unbalances the current which flows alog one conductor with respect to the current which flows along the other conductor. In fact, this current unbalancement due to the presence of radiation losses, may be measured as a function of the variables χ and ξ, which relate the currents on the conductors [see Eq. (4.62) and Eq. (4.63)]. Therefore, the purpose of the following developments is to find a closed-form expression of χ and ξ as a function of the TL LWA characteristics. This will allow to obtain the effective radiation current which flows along the TL LWA, leading to an easy and fast characterization of complex LWA radiation phenomena using simple transmission line theory.

Consider a lossless matched TL LWA, as shown in Fig. 4.23c. From simple TL theory [Pozar, 2005], the total power generated by the source, the power absorbed by the load and the power radiated to free-space are given by

$$P_{source}(\omega) = \frac{|V_g|^2}{2Z_0(\omega)}, \tag{4.71}$$

$$P_{load}(\omega) = \frac{|V_g|^2}{2Z_0(\omega)} e^{-2\alpha(\omega)\ell}, \tag{4.72}$$

$$P_{rad}(\omega) = \frac{|V_g|^2}{2Z_0(\omega)} \left(1 - e^{-2\alpha(\omega)\ell}\right). \tag{4.73}$$

Besides, it is known from antenna theory that the total radiated power by an antenna is given by [Balanis, 2005]

$$P_{rad}(\omega) = \frac{1}{2\eta} \int \int_S |\vec{E}(\hat{\theta}, \phi, \omega)|^2 R^2 \sin(\hat{\theta}) d\hat{\theta} d\phi, \tag{4.74}$$

where $\vec{E}$ is the radiated electric field, η is the free-space impedance, S represents the surface of an sphere which completely surrounds the antenna under analysis, and R is the radius of the sphere (i.e., the distance between the antenna, which is a punctual source from a far-field point of view, and the sphere).

The total radiated power from a transmission line point of view must be equal to the total radiated power from an antenna-theory point of view, i.e.

$$\frac{1}{2\eta}\int\int_S |\vec{E}(\hat{\theta},\phi,\omega)|^2 R^2 \sin(\hat{\theta}) d\hat{\theta} d\phi = \frac{|V_g|^2}{2Z_0(\omega)}\left(1-e^{-2\alpha(\omega)\ell}\right). \tag{4.75}$$

Since the far-field condition has been assumed, several *far-field approximations* [Balanis, 2005] can be applied. First, the radiated electric field is reduced to Eq. (4.65), which in spherical coordinates may be expressed as

$$\vec{E}(\vec{r},\omega) \approx -j\omega A_{\hat{\theta}}(\vec{r},\omega)\hat{e}_\theta = +j\omega A_z(\vec{r},\omega)\sin(\hat{\theta})\hat{e}_\theta, \tag{4.76}$$

where $\hat{e}_\theta$ is the unitary vector in the $\hat{\theta}$ direction.

Second, the distance R between each pair of source-observation points inside the magnetic vector potential [see Eq. (4.66)] may be simplified as [Balanis, 2005]

$$R = \sqrt{x^2+y^2+(z-z')^2} \approx \begin{cases} R_{ant} & \text{for amplitude terms} \\ R_{ant} - z'\cos(\hat{\theta}) & \text{for phase terms} \end{cases}, \tag{4.77}$$

where R_{ant} is the distance between the observation point and the antenna, from a far-field point of view [see Eq. (4.64)].

Combining the far-field approximations with the definition of the effective radiation current I_{rad} [see Eq. (4.67)], the electric-field radiated by a TL LWA in the far-field region may be expressed as

$$\begin{aligned}\vec{E}(\vec{r},\omega) &= \frac{j\omega\mu_0\sin(\hat{\theta})}{4\pi}\int_{z_{start}}^{z_{end}} I_{rad}(z',\omega)\frac{e^{-jk_0R}}{R}dz'\hat{e}_\theta \\ &= \frac{j\omega\mu_0 V_g \sin(\theta)}{4\pi R_{ant} Z_0(\omega)}\left[1-\xi(\omega)e^{j\chi(\omega)}\right]e^{-jk_0R_{ant}}\int_{z_{start}}^{z_{end}} e^{z'[-\alpha(\omega)+j(k_0\cos(\hat{\theta})-beta(\omega))]}dz'\hat{e}_\theta,\end{aligned} \tag{4.78}$$

which, after analytically solving the involved integral, reads

$$\vec{E}(\vec{r},\omega) = \frac{j\omega\mu_0 V_g\sin(\hat{\theta})}{4\pi R_{ant}Z_0(\omega)}\left[1-\xi(\omega)e^{j\chi(\omega)}\right]e^{-jk_0R_{ant}}\frac{e^{\ell[-\alpha(\omega)+j(k_0\cos(\hat{\theta})-\beta(\omega))]}-1}{-\alpha(\omega)+j[k_0\cos(\hat{\theta})-\beta(\omega)]}\hat{e}_\theta. \tag{4.79}$$

In order to compute the total radiated power, the magnitude of the radiated electric field is required. This quantity may be computed as

$$|\vec{E}(\vec{r},\omega)| = \frac{\omega\mu_0|V_g||\sin(\hat{\theta})|}{4\pi R_{ant}Z_0(\omega)}\left|1-\xi(\omega)e^{j\chi(\omega)}\right|\frac{|e^{\ell[-\alpha(\omega)+j(k_0\cos(\hat{\theta})-\beta(\omega))]}-1|}{\sqrt{\alpha^2(\omega)+[k_0\cos(\hat{\theta})-\beta(\omega)]^2}}, \tag{4.80}$$

and the square of this value is obtained as

$$|\vec{E}(\vec{r},\omega)|^2 = \frac{\omega^2\mu_0^2|V_g|^2\sin^2(\hat{\theta})}{16\pi^2R_{ant}^2Z_0^2(\omega)}\left[1+\xi(\omega)^2-2\xi(\omega)\cos(\chi(\omega))\right]\frac{|e^{\ell[-\alpha(\omega)+j(k_0\cos(\hat{\theta})-\beta(\omega))]}-1|^2}{\alpha^2(\omega)+[k_0\cos(\hat{\theta})-\beta(\omega)]^2}. \tag{4.81}$$

Using this last expression, the total radiated power, from an antenna point of view, may be expressed as

$$P_{rad}(\omega) = \frac{\omega^2\mu_0^2|V_g|^2}{32\pi^2\eta Z_0^2(\omega)} \cdot \left[1+\xi(\omega)^2 - 2\xi(\omega)\cos(\chi(\omega))\right] \int\int_S \frac{\sin^3(\hat{\theta})|e^{\ell[-\alpha(\omega)+j(k_0\cos(\hat{\theta})-\beta(\omega))]}-1|^2}{\alpha^2(\omega)+[k_0\cos(\hat{\theta})-\beta(\omega)]^2} d\hat{\theta}d\phi, \quad (4.82)$$

which is independent of the source-observation distance R_{ant}. Exploiting the symmetry properties of the antenna and the sphere S, this last equation can be further reduced to

$$P_{rad}(\omega) = \frac{\omega^2\mu_0^2|V_g|^2}{16\pi\eta Z_0^2(\omega)} \left[1+\xi(\omega)^2 - 2\xi(\omega)\cos(\chi(\omega))\right] \int_0^{\pi} \frac{\sin^3(\hat{\theta})|e^{\ell[-\alpha(\omega)+j(k_0\cos(\hat{\theta})-\beta(\omega))]}-1|^2}{\alpha^2(\omega)+[k_0\cos(\hat{\theta})-\beta(\omega)]^2} d\hat{\theta}. \quad (4.83)$$

For the sake of compactness, the radiated power may be expressed as

$$P_{rad}(\omega) = \frac{\omega^2\mu_0^2|V_g|^2}{16\pi\eta Z_0^2(\omega)} \left[1+\xi(\omega)^2 - 2\xi(\omega)\cos(\chi(\omega))\right] I_{power}(\omega), \quad (4.84)$$

where the variable I_{power} is a real value given by the following integral

$$I_{power}(\omega) = \int_0^{\pi} \frac{\sin^3(\hat{\theta})\left|e^{\ell[-\alpha(\omega)+j(k_0\cos(\hat{\theta})-\beta(\omega))]}-1\right|^2}{\alpha^2(\omega)+[k_0\cos(\hat{\theta})-\beta(\omega)]^2} d\hat{\theta}. \quad (4.85)$$

This last integral does not have an analytical solution, to the best of the author knowledge. However, it is very simple to compute it numerically, because it does not contain any singularity [since in a LWA $\alpha(\omega) > 0, \forall\omega$].

Applying Eq. (4.75), i.e. combining Eq. (4.84) with Eq. (4.73), the variables ξ and χ, which relate the currents flowing on each TL conductor, may be expressed as

$$\xi(\omega)^2 - 2\xi(\omega)\cos(\chi(\omega)) + 1 - \frac{8\pi\eta Z_0(\omega)\left(1-e^{-2\alpha(\omega)\ell}\right)}{\omega^2\mu_0^2 I_{power}(\omega)} = 0. \quad (4.86)$$

At this point, three cases may be analyzed. In the first case, we can consider that currents which flow on the TL LWA conductors have the same magnitude, but they present a variation in their phase. Therefore, the variable $\xi = 1$ and the phase change between the two current may easily be recovered as

$$\chi(\omega) = \cos^{-1}\left[1 - \frac{4\pi\eta Z_0(\omega)\left(1-e^{-2\alpha(\omega)\ell}\right)}{\omega^2\mu_0^2 I_{power}}\right]. \quad (4.87)$$

Besides, it is possible that the currents which flow on the TL LWA conductors have the same phase, but that they present a change in their associated magnitude. In this case, the variable $\chi = 0$

and the amplitude change between the two currents can easily be recovered as

$$\xi(\omega) = 1 - \sqrt{\frac{8\pi\eta Z_0(\omega)\left(1 - e^{-2\alpha(\omega)\ell}\right)}{\omega^2\mu_0^2 I_{power}(\omega)}}. \tag{4.88}$$

Other possibility is that the currents flowing on each conductor presents a change in both, their phase and their magnitude. In this general case, we can not determine the unbalancement from Eq. (4.86), because it is just a single equation with two unknowns. However, for the case of wire antennas, this is not very important to correctly determine the radiated electric field. This is because a linear (wire) antenna just provides a linear polarization of the radiated electric field ($E_r = E_\phi = 0$) [Balanis, 2005]. Therefore, the magnitude values of the electric field can be computed using Eq. (4.80), while the polarization properties are well known. For other more complex antennas, with different degrees and forms of polarizations, it may be necessary to compute both ξ and χ to extract both, the amplitude and the polarization characteristics of the radiated field.

It is important to remark that the proposed approach is able to compute and analyze the radiation from a complex transmission-line based leaky-wave antenna using a simple transmission line theory. The radiated electric field, in the far-field region, is computed using Eq. (4.80). This equation rigorously provides the radiated electric field, correctly recovering the antenna radiation pattern and electric field magnitude values.

The formulation proposed above is relatively simple, numerically stable and easy to compute. However, it can be further simplified assuming that the length of the antenna is large enough to radiate all the input power. This assumption is commonly applied in leaky-wave antennas [Oliner and Jackson, 2007], which are usually designed to radiate more of the 90% of the input energy by increasing the total length of the structure ($\ell \geq 9\lambda$ is a common choice [Oliner and Jackson, 2007]).

If we assume this new condition, Eq. (4.75), which relates the total radiated power from a transmission line and an antenna-theory point of view, is simplified to

$$\frac{1}{2\eta}\int\int_S |\vec{E}^{ap}(\theta,\phi,\omega)|^2 R^2 \sin(\hat{\theta}) d\hat{\theta} d\phi = \frac{|V_g|^2}{2Z_0(\omega)}, \tag{4.89}$$

where the superscript "ap" has been employed to denote that the radiated electric field has been computed for the specific case of an antenna able to radiate all the input power. Besides, note that the right handed term of the above equation is just the total power generated by the source [see Eq. (4.71)], because all the generated power is radiated. The magnitude of the electric field generated in this case may be expressed as

$$|\vec{E}^{ap}(\vec{r},\omega)| = \frac{\omega\mu_0|V_g||\sin(\hat{\theta})|}{4\pi R_{ant} Z_0(\omega)} \left|1 - \xi(\omega)e^{j\chi(\omega)}\right| \frac{1}{\sqrt{\alpha^2(\omega) + [k_0\cos(\hat{\theta}) - \beta(\omega)]^2}}. \tag{4.90}$$

As compared with Eq. (4.80), the expression of the electric field radiated is simplified. This is because the identity

$$\left|e^{\ell[-\alpha(\omega)+j(k_0\cos(\hat{\theta})-\beta(\omega))]} - 1\right| = 1, \tag{4.91}$$

holds when $\ell\alpha(\omega) \to \infty$, i.e. all input energy has been radiated. Mathematically, this is due to the fact that the term $e^{-\ell\alpha(\omega)}$ is real and rapidly tends to 0 when $\ell\alpha(\omega) \uparrow\uparrow$.

The total radiated power in this case may be expressed as

$$P^{ap}_{radiated}(\omega) = \frac{\omega^2\mu_0^2|V_g|^2}{16\pi\eta Z_0^2(\omega)}\left[1+\xi(\omega)^2-2\xi(\omega)\cos(\chi(\omega))\right]\int_0^{\pi}\frac{\sin^3(\hat{\theta})}{\alpha^2(\omega)+[k_0\cos(\hat{\theta})-\beta(\omega)]^2}d\hat{\theta}, \tag{4.92}$$

which for the sake of compactness, can be simplified as

$$P^{ap}_{radiated}(\omega) = \frac{\omega^2\mu_0^2|V_g|^2}{16\pi\eta Z_0^2(\omega)}\left[1+\xi(\omega)^2-2\xi(\omega)\cos(\chi(\omega))\right] I^{ap}_{power}(\omega). \tag{4.93}$$

where the integral I^{ap}_{power} is defined as

$$I^{ap}_{power}(\omega) = \int_0^{\pi}\frac{\sin^3(\hat{\theta})}{\alpha^2(\omega)+[k_0\cos(\hat{\theta})-\beta(\omega)]^2}d\hat{\theta}. \tag{4.94}$$

It is important to note that the integral can be solved analytically, leading to

$$\begin{aligned} I^{ap}_{power}(\omega) = {} & \frac{-2\alpha(\omega)k_0+\alpha(\omega)\beta(\omega)\lg\left(\frac{\alpha(\omega)^2+[\beta(\omega)+k_0]^2}{\alpha(\omega)^2-[\beta(\omega)+k_0]^2}\right)}{k_0^3\alpha(\omega)} \\ & + \frac{[k_0^2+\alpha(\omega)^2-\beta(\omega)^2]\left[\tan^{-1}\left(\frac{\beta(\omega)+k_0}{\alpha(\omega)}\right)-\tan^{-1}\left(\frac{\beta(\omega)-k_0}{\alpha(\omega)}\right)\right]}{k_0^3\alpha(\omega)}. \end{aligned} \tag{4.95}$$

Applying Eq. (4.89) the variables ξ and χ, which relate the currents flowing on each TL conductor, may be expressed as

$$\xi(\omega)^2-2\xi(\omega)\cos(\chi(\omega))+1-\frac{8\pi\eta Z_0(\omega)}{\omega^2\mu_0^2 I^{ap}_{power}(\omega)} = 0. \tag{4.96}$$

As in the previous case, this equation can be solved under two simple assumptions. In the first case, we consider again that the currents which flow on the TL LWA conductors have the same magnitude, but they present a variation in their phase. Therefore, $\xi = 1$ and the phase change between the two currents may be obtained as

$$\chi(\omega) = \cos^{-1}\left[1-\frac{4\pi\eta Z_0(\omega)}{\omega^2\mu_0^2 I^{ap}_{power}(\omega)}\right]. \tag{4.97}$$

On the other hand, it is possible that the currents which flows on the TL LWA conductors have the same phase, but they suffer a change in their magnitude. In this case, $\chi = 0$ and the amplitude change between the two currents may be recovered as

$$\xi(\omega) = 1-\sqrt{\frac{8\pi\eta Z_0(\omega)}{\omega^2\mu_0^2 I^{ap}_{power}(\omega)}}. \tag{4.98}$$

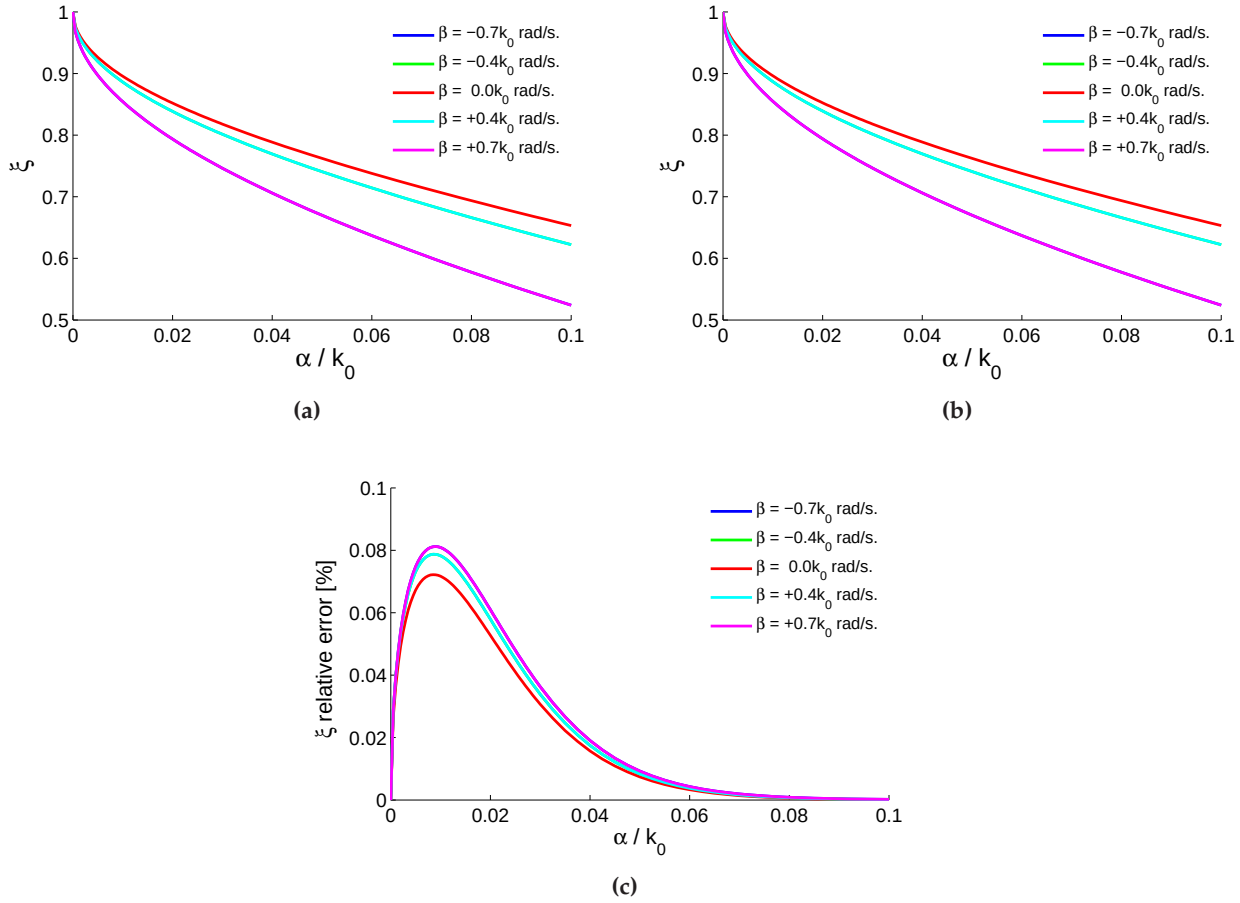

Figure 4.24 – Magnitude change between the currents which flow along the two conductors of a TL LWA (with $\ell = 9\lambda$) as a function of β and α. It is assumed that the currents are in phase ($\chi = 0$). (a) Exact computation of ξ, numerically solving Eq. (4.88). (b) Approximate computation of ξ, using the analytically formula of Eq. (4.98). (c) Maximum percentage error obtained when ξ is computed using the approximate result of Eq. (4.98) instead of the exact formula of Eq. (4.88). Note that ξ only depends on $|\beta|$.

As compared to Eqs. (4.87)-(4.88), Eqs. (4.97)-(4.98) are analytical and they do not involve the computation of any numerical integral. Therefore, they provide simple expressions to understand the phase or amplitude change between the currents flowing on each TL conductors. However, note that these expressions are approximations, which are only accurate when most of the input energy has been radiated by the TL LWA.

Let us consider a long CRLH LWA (with $\ell = 9\lambda$), which is typically able to radiate more than 90% of the input power. In order to fully characterize this structure, the goal is to obtain the values of the variables ξ and χ (which define the unbalacement of the currents flowing on the TL conductors) as a function of the input β and α values. In this way, we can define the currents which are flowing on each TL conductor, and can apply our proposed transmission line theory to characterize LWA radiation phenomena.

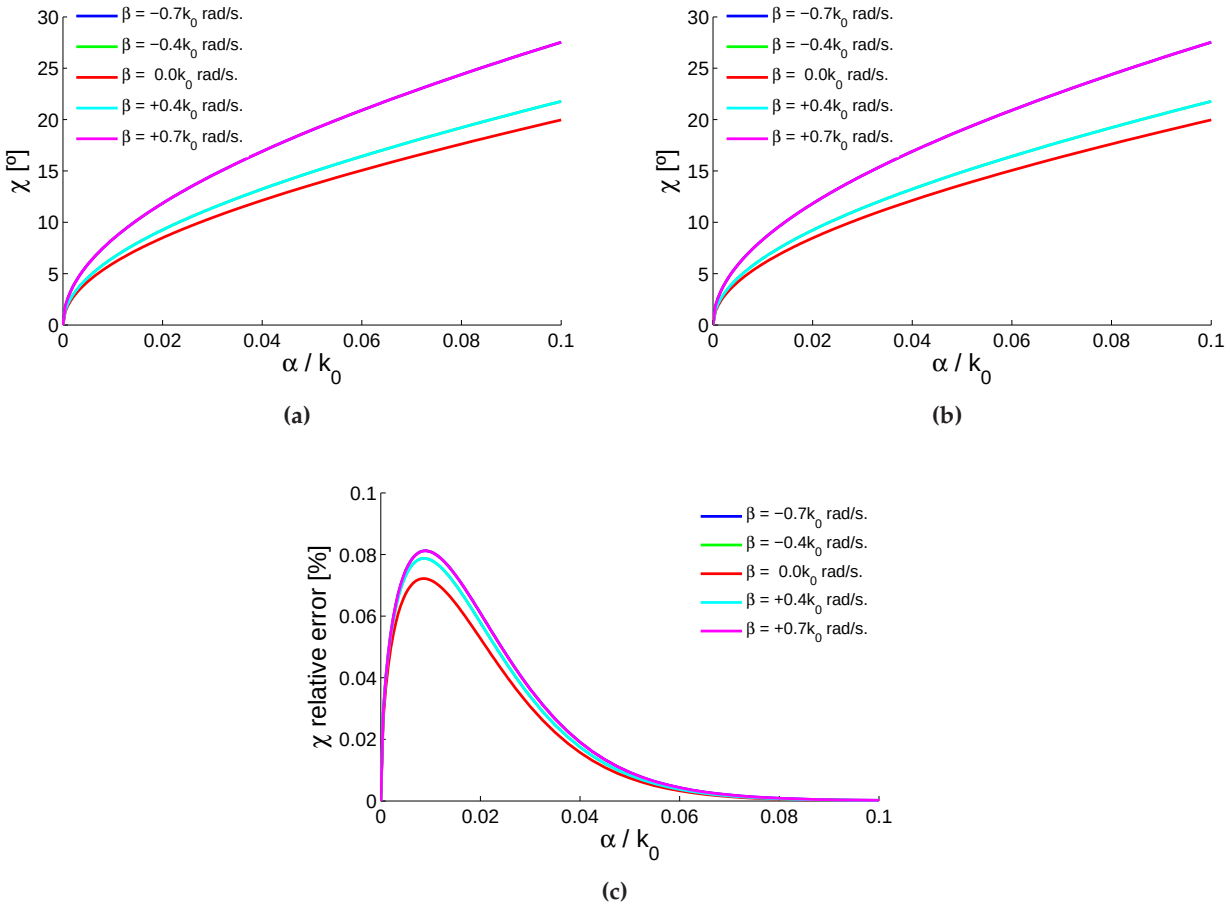

Figure 4.25 – Phase change between the currents which flow along the two conductors of a TL LWA (with $\ell = 9\lambda$) as a function of β and α. It is assumed that the currents have the same magnitude ($\xi = 0$). (a) Exact computation of χ, numerically solving Eq. (4.87). (b) Approximate computation of χ, using the analytically formula of Eq. (4.97). (c) Maximum percentage error obtained when χ is computed using the approximate result of Eq. (4.97) instead of the exact formula of Eq. (4.87). Note that χ only depends on $|\beta|$.

First, we may assume that the phase change between the currents flowing on the two conductors is strictly zero. Then, we can compute the magnitude change between the currents (ξ) for a parametric sweep of the β and α values, normalized with respect to the free-space wavenumber, k_0. This is shown in Fig. 4.24. Specifically, Fig. 4.24a present these data using Eq. (4.88) (exact formula), whereas Fig. 4.24b present the same result using Eq. (4.98) (approximate analytical formula). The error committed in the approximation is very small for all cases, as is demonstrated in Fig. 4.24c.

As can be observed in the figure, the change in magnitude between the currents depends on both, α and β. If the radiation losses are very reduced (i.e. $\alpha \to 0$), the value of ξ tends to 1. This is because the magnitude of the two currents are very close (but flowing on the opposite direction), and the radiated field tends to cancel out. However, as long as the radiation losses increase, the change between the currets magnitude also increases. This means that the currents on the conductors are more unbalanced, leading to the total radiated electric field. Besides, it is also interesting to examine the

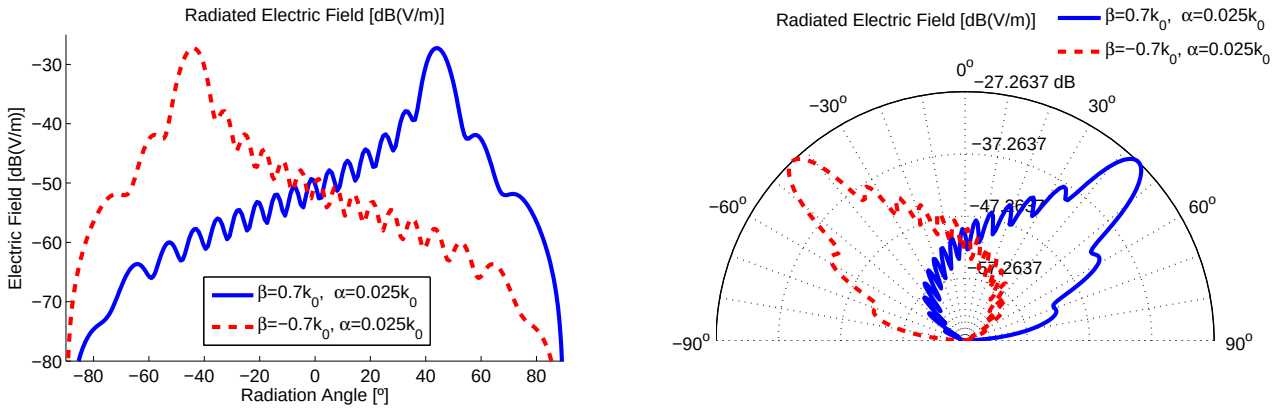

Figure 4.26 – Electric field [dB(V/m)] radiated from a 9λ-long LWA with $\alpha = 0.025k_0$ and $\beta = \pm 0.7k_0$ computed with Eq. (4.80). Observation points are placed at the far-field distance of 1500λ. The radiation angle is measured from the direction perpendicular to the antenna. (a) Cartesian coordinates. (b) Polar Coordinates.

ξ behavior as a function of β. In this case, for the same magnitude change of the currents (i.e. keeping ξ constant), the maximum radiation losses is achieved for $\beta = 0$. Then, α is decreasing as long as the magnitude of β increases. This is because when the radiation angle is close to the endfire or backfire direction, the radiation losses of the structure naturally decreases [Oliner and Jackson, 2007]. Therefore, in order to keep the same α at these directions, it is necessary to increase the unbalance in magnitude of the conductor currents.

A direct consequence of the above comments is that, in order to keep a constant radiation losses for all frequencies, the conductor currents unbalacement must be higher close to the backfire and endfire direction, and lower close to the broadside direction.

Fig. 4.25 present the currents unbalancement in phase (χ), assuming that they have the same magnitude. As can be observed in the figure, the same conclusions about computation, error and behavior versus α and β as explained for the case of Fig. 4.24 are obtained.

Finally, the electric field radiated by a LWA can easily be recovered using Eq. (4.80). It is important to note that this simple TL-based equation is able to recover the magnitude of the electric field (note that, since the radiated fields present a linear polarization, their phase is not relevant), including both, the shape of the radiation pattern and the actual values of field intensity. As an example, the electric field radiated by a 9λ-long LWA at an observation distance of 1500λ is shown in Fig. 4.26, for the cases of $\alpha = 0.025k_0$ and $\beta = \pm 0.7k_0$. As expected, the main beam is radiated towards a backwards ($\beta = -0.7k_0$) or a forward ($\beta = +0.7k_0$) direction, respectively.

This last result confirms that the proposed theory is able to model LWA radiation phenomena from a simple TL point of view. The use of the conductor currents has been introduced in order to model radiation from electrically-thin transmission lines, mathematically demonstrating that these conductor currents must be unbalanced to achieve the desired radiation. This theory provides a novel and fundamental explanation of leaky-wave antennas, providing a physical insight into the problem

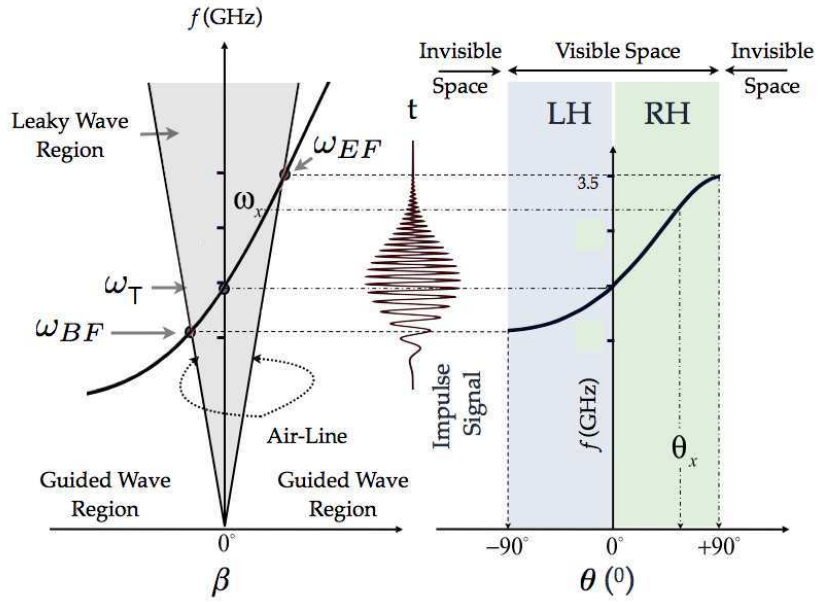

Figure 4.27 – Frequency-space relationship of a CRLH LWA. The dispersion curve is graphically related to its corresponding beam scanning law. Reproduced from [Gupta et al., 2009a].

from a simple TL perspective. As previously explained, this chapter has just introduced the basic theory to model transmission line LWAs. Then, in Chapter 5, the proposed theory will be applied for the analysis and design of different LWA-based devices and phenomena. Besides, that chapter provides and accurate validation of the proposed formulation, in terms of accuracy and speed, with rigorous comparisons against full-wave results and measurements.

4.4.3 Time-Domain Radiation of LWA

This section proposes an impulse-regime analysis of leaky-wave structures. Even though the proposed study is valid for all types of LWAs, we will focus on CRLH LWA structures because they are broadband in nature and they are able to radiate from backfire to endfire, including the broadside direction [Caloz and Itoh, 2005]. As introduced in Section 4.4, a CRLH leaky-wave antenna follows the beam-scanning law of Eq. (4.48). Therefore, each input frequency, which lies inside the fast-wave region, is radiated towards a different direction into space. This situation is explicitly depicted in Fig. 4.27. As can be seen in the figure, there is a unique correspondence between each input frequency [ω_x, with ($\omega_{BF} \leq \omega_x \leq \omega_{EF}$)] and its associated radiation angle (θ_x). Therefore, each frequency is mapped into a different angle in space.

According to Eq. (4.48), if the CRLH LWA is excited by a modulated input pulse, as shown in Fig. 4.28, each spectral component of the signal is radiated towards a different direction in space at any particular instant. Therefore, the CRLH LWA performs an *instantaneous spectral-to-spatial decomposition* of the input pulse [Gupta et al., 2008], [Gupta et al., 2009a]. This decomposition allows to discriminate the various spectral components present in the input signal. In this sense, there is clear parallelism between a CRLH LWA (which usually operates at microwaves) and a diffraction grat-

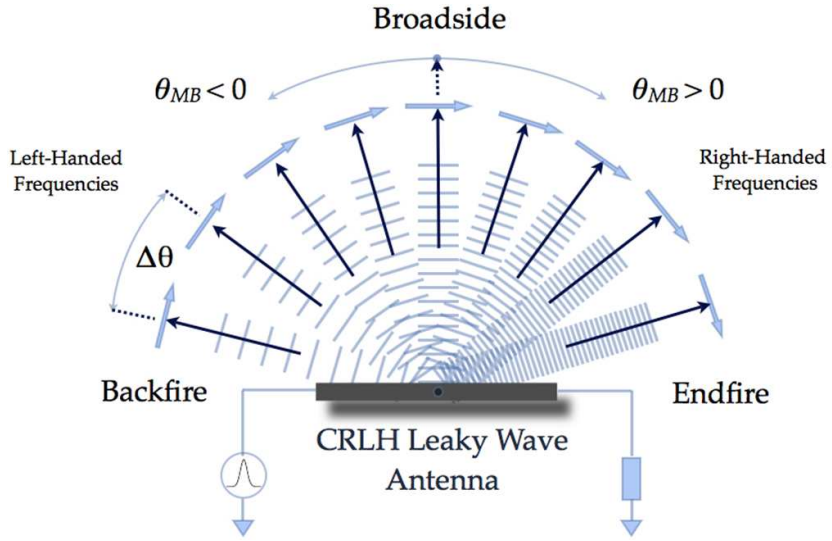

Figure 4.28 – Spectral decomposition of a pulse obtained by the frequency-space mapping property of a CRLH leaky-wave antenna. Reproduced from [Gupta et al., 2009a].

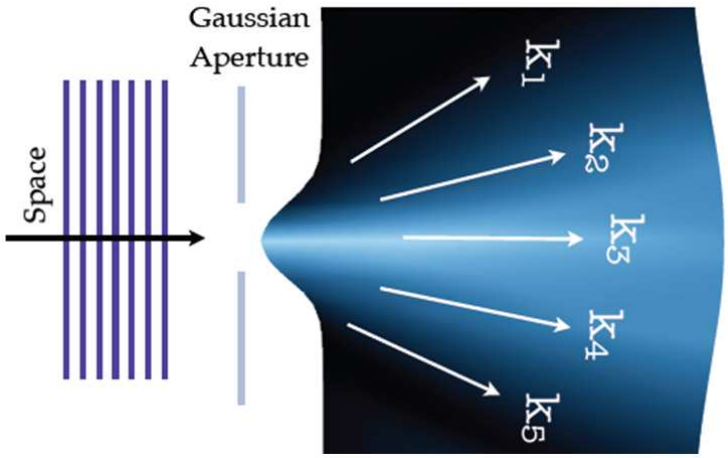

Figure 4.29 – Example of a diffraction grating [Hecht and Zajac, 2003]. The dispersive optical device performs the spatial separation of an incoming wavefront. Each incoming spatial frequency (k_x) is radiated towards a different angle.

ing [Hecht and Zajac, 2003] (Fig. 4.29), which usually operates at the optics regime and radiates each spatial input frequency towards a different direction angle in space. The CRLH LWA main advantage over diffraction gratings is its simple punctual feeding system as compared to the diffraction gratings, which require plane-wave illumination. On the other hand, diffraction gratings are able to operate on a wider frequency range as compared with CRLH LWA, which must be completely re-designed when the input frequency range changes.

The following subsections propose a time-domain formulation to characterize LWAs excited by modulated input pulses. The formulation is first presented for the case of a single antenna, and it is then extended to consider an array of LWAs.

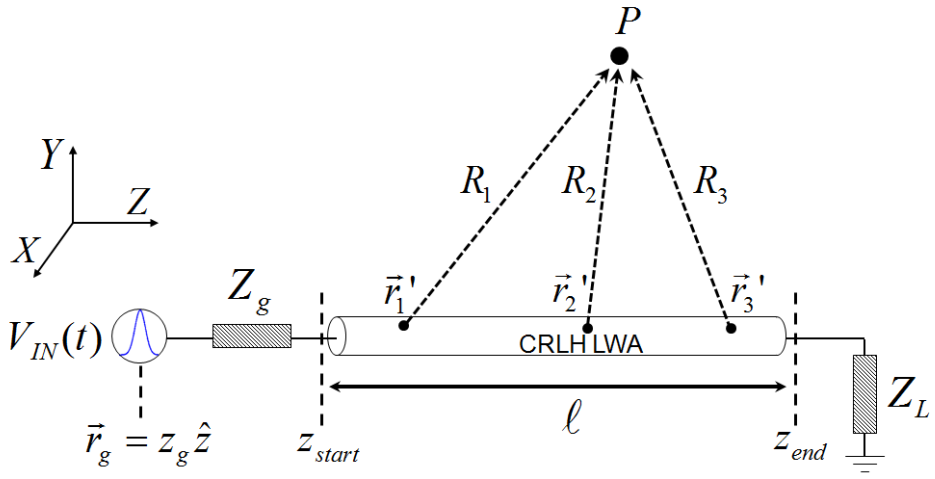

Figure 4.30 – Sketch of a single 1D CRLH LWA. The electrically thin antenna is considered as a linear wire from a far field point of view (see Section 4.4.2). It is placed along the z-axis, it has a length of $\ell = z_{end} - z_{start}$, and it is fed by a punctual generator, placed at $\vec{r} = z_g \hat{e}_z$.

Single LWA

Let us consider a single 1D (or electrically thin) TL LWA, located along the z axis. A sketch of this situation is shown in Fig. 4.30. As in the previous cases, the structure is defined by a characteristic impedance $[Z_0(\omega)]$, a complex propagation constant $[\gamma(\omega) = \alpha(\omega) + j\beta(\omega)]$ and a total length (ℓ, located along the z axis, from z_{start} to z_{end}).

Note that this situation is the same as in the case of Fig. 4.21, but including a change in the source, which now generates time-domain input pulses. Therefore, we will reuse the notation and far-field approximations employed there.

Let us assume that the CRLH LWA is excited by a modulated input pulse. In this case, the time-domain theory developed in Section 4.3 for the analysis of impulse-regime CRLH TL can easily be combined with the *effective radiation current* introduced in Section 4.4.2. Therefore, the *harmonic effective radiation current* defined in Eq. (4.67) transforms into a *time-domain effective radiation current*, which, from a far-field point of view, flows along a CRLH antenna and may be expressed as

$$I_{rad}(z',t) = \int_{-\infty}^{\infty} \tilde{G}_I(z',z_g,\omega)\tilde{I}_g(\omega)\left[1-\xi(\omega)e^{j\chi(\omega)}\right]e^{j\omega t}d\omega. \tag{4.99}$$

In this last equation, $\tilde{G}_I(z',z_g,\omega)$ represents the transmission line Green's function related to the current, $\tilde{I}_g(\omega)$ denotes the Fourier transform of the temporal input pulse, and ξ and χ are related to the unbalancement between the currents which flow on each TL conductor (see Section 4.4.2).

The time-domain behavior of the effective radiation current propagates into the magnetic vector potential, which now reads

$$\vec{A}(\vec{r},t) = \frac{\mu_0}{4\pi}\int_{\omega_{BF}}^{\omega_{EF}}\int_{z_{start}}^{z_{end}} I_{rad}(z',\omega)\frac{e^{-jk_0R}}{R}d\omega dz'\hat{e}_z. \tag{4.100}$$

It is important to remark that the frequency integration limits have been modified with respect to Eq. (4.99). Specifically, the frequency limits directly corresponds to the fast-wave region range ($\omega_{BF} \leq \omega \leq \omega_{EF}$). This is because LWAs are able to radiate spectral components which lies inside this region. Outside of the fast-wave region, this type of structures behaves as a transmission lines (guided-wave region shown in Fig. 4.27) [Caloz and Itoh, 2005]. In the case that this last equation is computed outside of the fast-wave region, it will lead to unphysical results. Besides, note that any losses outside of this frequency region are due to dielectric or ohmic losses, but they are never related to radiation.

Finally, the time-domain electric field radiated by a CRLH LWA can easily be recovered using

$$\vec{E}(\vec{r},t) = \frac{-j\mu_0}{4\pi} \int_{\omega_{BF}}^{\omega_{EF}} \int_{z_{start}}^{z_{end}} \omega I_{eff}(z',\omega) \frac{e^{-jk_0R}}{R} d\omega dz' \hat{e}_z. \tag{4.101}$$

Assuming a matched transmission line and the far-field approximations of Eq. (4.77), i.e. the same situation as in Section 4.4.2, the radiated electric field at the far-field region can be expressed in spherical coordinates as

$$\vec{E}(\vec{r},t) = \frac{j\mu_0 V_g \sin(\hat{\theta})}{4\pi R_{ant}} \int_{\omega_{BF}}^{\omega_{EF}} \frac{\omega \tilde{I}_g(\omega)}{Z_0(\omega)} \left[1 - \xi(\omega) e^{j\chi(\omega)}\right] \frac{e^{\ell[-\alpha(\omega)+j(k_0\cos(\hat{\theta})-\beta(\omega))]} - 1}{-\alpha(\omega) + j[k_0\cos(\hat{\theta}) - \beta(\omega)]} e^{j(\omega t - k_0 R_{ant})} d\omega \hat{e}_\theta. \tag{4.102}$$

The above expression is able to compute the time-domain electric field radiation from a CRLH LWA excited by a modulated input pulse, at any observation point placed in the far-field region. The main features of this closed-form formulation are

- All CRLH LWA radiation features at far-field are taken into account by using a *time-domain effective radiation current*. This current is closely related to the complex propagation constant of the structure (see Section 4.4.2).
- Physical insight into the antenna radiation properties. The Green's function and effective radiation current, related to the CRLH structure, completely define the antenna behavior. These parameters are obtained in closed-form.
- Extremely fast computation, because most expressions are simple and well-behaved integrals (and some of them are analytical for specific input pulses).
- Able to deal with any type of input pulse, providing a continuous temporal output with unconditional stability.

The proposed approach is able to characterize complex radiated-wave UWB phenomena and devices. Specifically, this formulation will be employed in Chapter 5 to model several systems, such as a real-time spectrum analyzer (RTSA) [Gupta et al., 2009a] or a frequency-resolved electrical gating system (FREG) [Gupta et al., 2009b]. It will be shown that the proposed formulation is able to completely characterize these systems with high accuracy. Furthermore, the computational time required for the proposed formulation is in the order of seconds or minutes, whereas full-wave commercial software spends hours or days to carry out the same simulation. This computational cost reduction

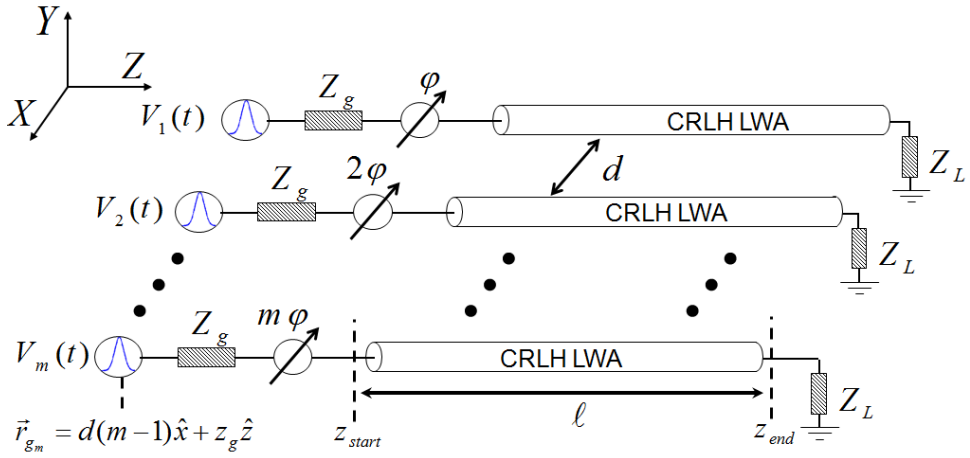

Figure 4.31 – Sketch of an array of m CRLH LWAs. The separation between two consecutive antennas, in the x-axis, is d. Each antenna, p, is placed along the z-axis, it has a length of $\ell = z_{end} - z_{start}$, and it is fed by a punctual generator, placed at $\vec{r}_{g_p} = d(p-1)\hat{e}_x + z_g\hat{e}_z$. Phase shifters are used to provide a phase difference of φ between two consecutive antennas.

allows a fast design of UWB systems. Besides, note that the agreement between full-wave commercial software results, the proposed technique and measurements is excellent. Finally, Chapter 5 will also present a novel UWB phenomena (the spatio-temporal Talbot effect [Gómez-Díaz et al., 2008a] [Gómez-Díaz et al., 2009d]) which employs an array of CRLH LWA operated in the impulse regime. This phenomenon will be theoretically introduced, easily simulated by the proposed time-domain TL LWA theory, and experimentally demonstrated. Note that this complex phenomena is very difficult to simulate using regular full-wave commercial software, due to the extremely large computational cost required to perform a time-domain analysis of 15 to 20 CRLH LWAs.

LWA Array

The derived time-domain formulation related to a single CRLH LW antenna can easily be extended to analyze the time-domain radiation from a CRLH LWA array. The situation in this case is shown in Fig. 4.31. As can be seen in the figure, a total of m CRLH LWAs are combined to obtain the desired array. A phase shift of φ is considered between two consecutive antennas. For simplicity, all antennas are similar and they are defined by the same physical parameters as in the case of the single antenna (see Fig. 4.30). The antennas are placed along the z-axis, and the separation between two consecutive antennas, in the x-axis, is d. Besides, each antenna, p is fed by a generator located at the position $\vec{r}_{g_p} = d(p-1)\hat{e}_x + z_g\hat{e}_z$.

A straightforward modification of Eq. (4.101) allows us to recover the time-domain electric field radiated by a CRLH LWA array as

$$\vec{E}(\vec{r},t) = \frac{-j\mu_0}{4\pi}\int_{\omega_{BF}}^{\omega_{EF}}\int_{z_{start}}^{z_{end}}\omega\sum_{p=1}^{p=m}\left[I_{eff}(z',\omega)e^{j\varphi p}\frac{e^{-jk_0R_p}}{R_p}\right]d\omega dz'\hat{e}_z, \tag{4.103}$$

where R_p is the distance between the observation point P (located at $\vec{r}$) and any point inside the p^{th} antenna [denoted as $\vec{r}\,'_p = d(p-1)\hat{e}_x + z'\hat{e}_z$] and it is defined as

$$R_p = \sqrt{[x - d(p-1)]^2 + (z - z')^2}. \tag{4.104}$$

Assuming that all array elements are matched, and applying the far-field approximations of Eq. (4.77), the radiated electric field of Eq. (4.103) may be expressed in spherical coordinates as

$$\vec{E}(\vec{r},t) = \frac{j\mu_0 V_g \sin(\hat{\theta})}{4\pi} \cdot \int_{\omega_{BF}}^{\omega_{EF}} \frac{\omega \tilde{I}_g(\omega)}{Z_0(\omega)} \left[1 - \xi(\omega) e^{j\chi(\omega)}\right] \frac{e^{\ell[-\alpha(\omega) + j(k_0 \cos(\hat{\theta}) - \beta(\omega))]} - 1}{-\alpha(\omega) + j[k_0 \cos(\hat{\theta}) - \beta(\omega)]} \left[\sum_{p=1}^{p=m} \frac{e^{j(\varphi p - jk_0 R_{ant_p})}}{R_{ant_p}}\right] e^{j\omega t} d\omega \hat{e}_\theta, \tag{4.105}$$

where R_{ant_p} is the distance between the observation point (located at $\vec{r}$) and the antenna p^{th} (which from a far-field point of view, may be considered punctual and located at its center), and it may be expressed as

$$R_{ant_p} = \sqrt{[x - d(p-1)]^2 + (z - \frac{\ell}{2})^2}. \tag{4.106}$$

4.5 Conclusions

In this chapter, I have introduced an impulse-regime analysis of metamaterial-based transmission lines and antennas, with special focus on composite right/left-handed structures. First, I have briefly reviewed the concept of metamaterials, including *bulk* and *planar* metamaterials using both, a *resonant* and a *non-resonant* design approach. Then, I have focused on *composite right/left-handed transmission lines and antennas operated in the harmonic regime*, providing some insight into the physics of these structures and giving some useful formulas for their characterization. Second, I have proposed a novel time-domain analysis of CRLH lines and antennas based on the Green's functions associated to regular transmission lines. Specifically, a novel formulation to describe pulse propagation along dispersive linear and non-linear CRLH lines has been proposed. The proposed theory is able to model complex impulse-regime phenomena, such as dispersion and non-linearity, in a simple, accurate and fast way. Besides, the radiation from CRLH leaky-wave antennas has carefully been studied, including a deep analysis about the radiation at the broadside direction and a novel simple physical explanation, based on transmission line theory, about how these types of antennas are able to radiate. Finally, the previously introduced harmonic method to model the radiation from LWA is reformulated in the time domain, allowing a fast and accurate analysis of the far-field characteristics of CRLH LWAs operated in the impulse-regime.

The main purpose of the proposed formulation is to take advantage of the *dispersion engineering* approach, where CRLH structures, thanks to their broadband nature and dispersive properties, may provide novel and original solutions to engineering problems. Following with this line, and based on the dispersion engineering approach, the next chapter will introduce a wide variety of novel guided and radiative phenomena, devices and applications operated in the impulse-regime and *inspired from*

the optics domain. There, a careful comparison of the results obtained by the formulations proposed in this chapter against full-wave simulations and measurements, will demonstrate that the novel theories are very fast, accurate and provide a deep insight into the physics of the problem in a very simple way.

Chapter 5

Optically-Inspired Phenomena at Microwaves

5.1 Introduction

In Chapter 4 of the presented work I have reviewed basic transmission line (TL) theory of metamaterials (MTM) [Eleftheriades and Balmain, 2005], [Caloz and Itoh, 2005], [Marques et al., 2008], operated in the harmonic regime. As explained there, planar non-resonant transmission line metamaterials exhibit broad bandwidth, dispersive features, low loss and the capability to be integrated with other components and systems. Due to these and other novel properties, metamaterials have led to novel concepts, phenomena and applications (such as backfire to endfire leaky-wave antennas [Liu et al., 2002], couplers [Nguyen and Caloz, 2007a], [Jarauta et al., 2004], power-dividers [Islam and Eleftheriades, 2008a], phase-shifters [Antoniades and Eleftheriades, 2003a], [Siso et al., 2007], or dual band components [Lin et al., 2004], [Eleftheriades, 2007b], among many others). At microwaves, metamaterials have usually been implemented in planar technology using *composite right/left-handed* transmission lines (CRLH TL) [Caloz and Itoh, 2005], which is a non-resonant approach.

Usually, most of the applications and phenomena of metamaterials (as the previously described) have mainly been reported in the *harmonic regime*. However, *the recent emergence of ultra wide band (UWB) systems [Ghavami et al., 2007] has created a need for novel microwave concepts, phenomena and direct applications in the impulse-regime*. Metamaterial-based CRLH transmission lines, which are broadband and highly dispersive in nature, may provide novel and original solutions in this field. The control of these dispersive properties leads to the *dispersive engineering* concept introduced in Chapter 4 (see Fig. 4.2), which consists on the phase shaping of electromagnetic waves to process signals in an analog fashion. In Chapter 4 I have also introduced a novel time-domain Green's function approach to deal with impulse-regime CRLH lines, exploiting the dispersive engineering concept. This formulation constitutes an adequate tool for the analysis and design of UWB CRLH-based devices. Recent examples of these type of components and systems are a Pulse Position Modulation system (PPM) [Nguyen and Caloz, 2008], a tunable pulse delay line [Abielmona et al., 2007], a true time delayer

[Nguyen et al., 2008], compressive receivers [Abielmona et al., 2009] or a Real-Time Spectrum Analyzer (RTSA) [Gupta et al., 2009a]. A nice review of some of these systems and components has been reported in [Gupta and Caloz, 2009].

In the present chapter I explore the impulse-regime phenomenology of CRLH structures and the subsequent theoretical and practical demonstration of several novel optically-inspired phenomena and applications at microwaves, in both, the guided and the radiative regime. The time-domain Green's function approach introduced in Chapter 4 has opened the door to a very fast, but still accurate, analysis of these ***novel microwave phenomena and applications, most of them transported from optics***, exploiting either the group velocity or the group velocity dispersion parameters of CRLH TL. The study can be divided into two main groups, related to the *guided-wave* or *radiative-wave* nature of the proposed phenomena and applications.

1. In the **guided-regime**, the CRLH TL dispersion characteristics provides novel features as compared to conventional transmission lines, which can be exploited in the impulse-regime to obtain new phenomena and UWB applications (see [Gómez-Díaz et al., 2009b]). First, a rigorous study of pulse propagation along CRLH media is presented in Section 5.2. Then, the dispersive properties of the CRLH line are employed to compress pulses (see Section 5.3), with direct use in radar applications. Next, the temporal Talbot effect [Azaña and Muriel, 1999] is introduced, theoretically described and numerically confirmed for the case of CRLH media in Section 5.4. Section 5.5 introduces a novel tunable pulse generator, able to multiply the period rate of an input train of pulses. The analysis of the guided-wave phenomenology related to impulse-regime CRLH is completed in Section 5.6, where a practical study about the combination of non-linear effects with dispersive CRLH media is given.

2. In the **radiative-regime**, CRLH TLs acts as a leaky-wave antenna [Oliner and Jackson, 2007] within the so called "fast wave region", and provides capabilities for full space scanning [from backfire ($\theta = -90^\circ$) to endfire ($\theta = 90^\circ$)] radiation [Liu et al., 2002]. This can be exploited in the impulse-regime, obtaining a *spectral-spatial decomposition* of an input broadband signal, which may lead to novel UWB applications. Specifically, in Section 5.7 the time-domain Green's function approach is employed to efficiently model a Real-Time Spectrum Analyzer (RTSA) [Gupta et al., 2009a] , based on CRLH LWAs, which is able to characterize unknown UWB input signals. Section 5.8 proposes a novel Frequency Resolved Electrical Gating system (FREG), inspired from optics but implemented in the microwave domain, which solves most of the problems related to the finite resolution of CRLH RTSA systems. Finally, in Section 5.9 a completely novel spatio-temporal Talbot phenomena is introduced, mathematically described, numerically confirmed and experimentally demonstrated (see [Gómez-Díaz et al., 2008a] and [Gómez-Díaz et al., 2009d]). Practical applications related to this phenomena include spatial multiplexers, quasi optical devices and wireless array feedings, among others.

The procedure to propose, describe and verify each novel phenomenon or application is as follows. First, a careful description is given. Second, a mathematical development is proposed in order to fully demonstrate all phenomena/applications. For this purpose, an optical approach has usually been adopted [Saleh and Teich, 2007]. Third, the time-domain Green's function method introduced

in Chapter 4 is employed and adjusted in order to model the problem under consideration, obtaining fast results and giving a deep-insight into the physics of the problem. Fourth, a rigorous full-wave simulation of all phenomenon/applications is included to i) demonstrate the presence of the proposed phenomena or the behavior of a specific application, and ii) confirm the accuracy and efficiency of the proposed time-domain approach. For this purpose, a wide variety of commercial software (such as ADS©, CST© or HFSS©, as a function of the type of problem under consideration) is employed. And fifth, an experimental demonstration of most of the proposed phenomena/applications is included. This last step provides a complete verification of the theoretical study, validating its use in real-life environments.

The analogy between the proposed phenomena and applications at microwave and their corresponded counterpart at optics [Saleh and Teich, 2007] is deduced from the dispersive properties of a CRLH structure. Specifically, *in the guided mode* there is a clear parallelism between the dispersive behavior of a CRLH line and an optical component, which is inherently dispersive (for instance, an optical fiber [Saleh and Teich, 2007]). Therefore, optical phenomena can easily be reproduced at microwaves. In the *radiative mode*, the beam scanning law of the CRLH LWA is analog to a diffraction grating where different spectral components are radiated (or diffracted) at different angles causing spatial dispersion. *It is important to remark the use of fabricated prototypes and measurements to demonstrate most of the phenomena*. The measured data is in excellent agreement with the results obtained by the formulation proposed in Chapter 4, validating its practical use. On the other hand, note that *the dispersive engineering approach has provided a huge number of novel phenomena and applications at microwaves, with direct impact on future UWB systems*. This approach has paved the road for a future transposition of many other phenomena and applications from optics to the microwave domain.

5.2 Phenomenology of Pulse Propagation along Dispersive CRLH Media

In this section, the phenomenology of pulse propagation along a CRLH transmission line is studied. As previously stated, the CRLH TL represents a general transmission medium, which is highly dispersive, especially in the LH frequency range. Therefore, it is expected that it provides unusual properties which may lead to novel effects and application in the impulse regime.

The main goal of this section is to experimentally validate the theory presented in Chapter 4. For this purpose, the propagation of a modulated pulse along a CRLH TL is carefully studied. The tunability of the pulse delay as a function of the modulation frequency is demonstrated by measuring the temporal delay from different modulated pulses, leading to a tunable delay system [Abielmona et al., 2007]. Then, the dispersive features of the CRLH TL are further demonstrated monitoring the effects of pulse propagation along a matched and mismatched line, in a cell-by-cell fashion. The measurements included in this section are in excellent agreement with the simulation results provided by the proposed time-domain Green's function techniques (see Chapter 4), allowing their use in the prediction of much more complex dispersive phenomena. Furthermore, they provide physical insight into the impulse regime nature of this type of media.

First, we consider a CRLH transmission line composed of 30 unit cells and with the circuit parameters $C_R = 1.8$ pF, $C_L = 0.9$ pF, $L_R = 3.8$ nH and $L_L = 1.9$ nH (transition frequency

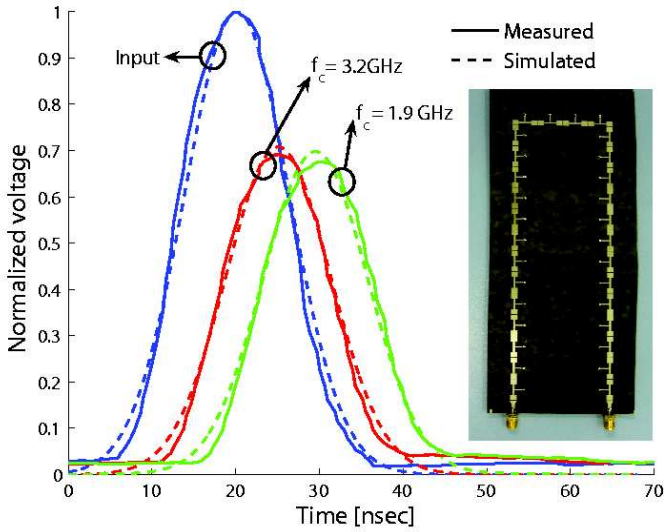

Figure 5.1 – Time-delayed Gaussian waveforms at the input/output of a CRLH transmission line for different carrier frequencies, obtained with the method proposed in Section 4.3 of Chapter 4. Measurement results are also shown for validation. The manufactured CRLH transmission line is shown in the inset.

$f_0 = 2.55$ GHz), excited by a modulated Gaussian pulse ($\sigma = 3.0$ ns, see Appendix A). Fig. 5.1 shows the time-delayed waveforms obtained by the proposed theory for different carrier frequencies, and by experiments using a real-time oscilloscope (Agilent Infiniium DS0871204B). Excellent agreement is observed between theory and experiments.

The group delay frequency function is an important parameter in dispersive systems for analog signal processing applications. This parameter may be computed either in the time domain by determining the time differences between the maxima of the input and output pulses, or in the frequency domain by taking the derivative of the unwrapped phase of the transmission scattering parameter S_{21}. Fig. 5.2 shows the group delay along the same CRLH line and for the same pulse as in Fig. 5.1, computed by the discussed theory using the first approach, and validated by experiment using both approaches. Again, very good agreement is observed between theory and experiment. The small discrepancies between the two measured results may be explained by the tolerance in the localization of the pulse maxima. As it may be seen from these results, the CRLH transmission line acts as an impulse tunable delay system [Abielmona et al., 2007].

To better visualize the dispersion of a pulse along a CRLH dispersive medium, consider now a CRLH transmission line twice as longer as before (60 unit cells), but with the same parameters. To completely validate the discussed theory, this time the line is excited by a modulated square pulse ($f_0 = 2.05$ GHz, $T = 2.2$ ns, see Appendix A). An ABCD matrix approach [Caloz and Itoh, 2005] is employed to compute the propagation constant of the line, taking into account the finite number of unit cells in the experiment. The position-time trajectory of the pulse is presented in Fig. 5.3. Fig. 5.3a shows the computed results, from which two observations may be made: i) at the end of the line, the temporal width of the pulse has increased by a factor of 5 (at 50% of the magnitude), ii) the edges of the square envelope have been rounded off by the band-pass filtering response of the CRLH line.

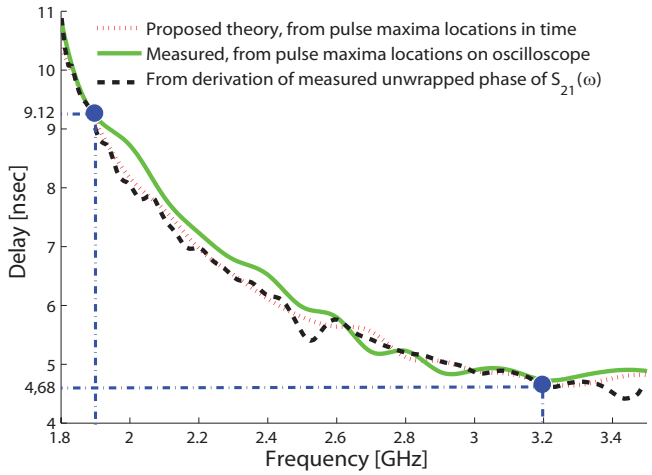

Figure 5.2 – Time delay versus modulation frequency, using the time difference between the maxima of the input and output pulses along the same CRLH line as in Fig. 5.1. Measured data using both, the same procedure as before and unwrapping the phase of $S_{21}(\omega)$, are also shown for validation. The delays obtained in Fig. 5.1 for $f_c = 3.2$ GHz and $f_c = 1.9$ GHz, which are 4.68 and 9.12 ns, correspond to the two highlighted points.

The small ripples near the end of the structure are explained by the Gibbs effect on the input pulse due to the finite computational interval and resolution.

Fig. 5.3b shows the measured result using a high-impedance probe connected to the oscilloscope. The abrupt decrease of the voltage magnitude after the 30th cell is due to the fact that the 60-cell experimental line is in fact constituted of two cascaded 30-cell lines with a small loss in the interconnection. The agreement with theory is reasonable, considering the tolerances of the measurement setup.

Finally, let us investigate the effects of the reflection of a pulse at a discontinuity of a CRLH transmission line. For this purpose, the line is open-ended and it is excited by the same modulated square pulse as in the previous case. The propagation and the reflection of the pulse as a function of space and time is presented in Fig. 5.4. Again, good agreement is observed between the theory (Fig. 5.4a) and the experiment (Fig. 5.4b). It is worth noticing that an interesting interference pattern, between propagating and reflected pulses, occurs near the discontinuity.

5.3 Pulse Compression

One common application of pulse propagation inside a dispersive medium (such as a CRLH medium) is pulse compression. This phenomenon occurs when a chirp-modulated pulse propagates along a line with group delay frequency function opposite to that of the chirp function.

Fig. 5.5a) shows a chirp-modulated Gaussian pulse with a temporal width of $\sigma = 3.0$ ns and a chirp constant of $C = 20$ [Saleh and Teich, 2007] (see Appendix A). Fig. 5.5b), c) and d) present the waveforms along a matched CRLH transmission line excited by this pulse at different locations along the line. At the 5th cell, the pulse is hardly compressed because insufficient dispersion has been

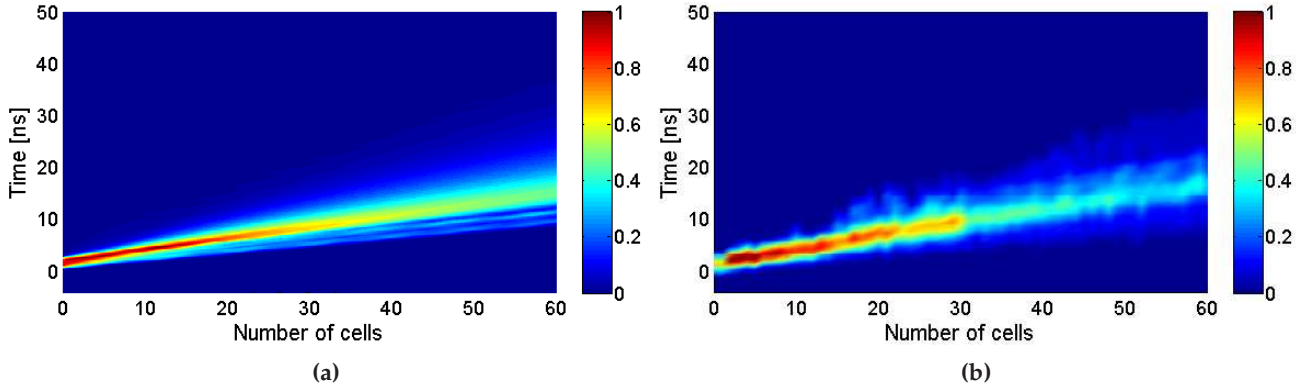

Figure 5.3 – Propagation of a modulated square pulse ($f_0 = 2.05$ GHz, $T = 2.2$ ns, see Appendix A) along a matched CRLH transmission line. The line includes 60 unit cells of length $p = 2.0$ cm and the circuital parameters are $C_R = 1.8$ pF, $C_L = 0.9$ pf, $L_R = 3.8$ nH and $L_L = 1.9$ nH. (a) Simulation. (b) Measurement.

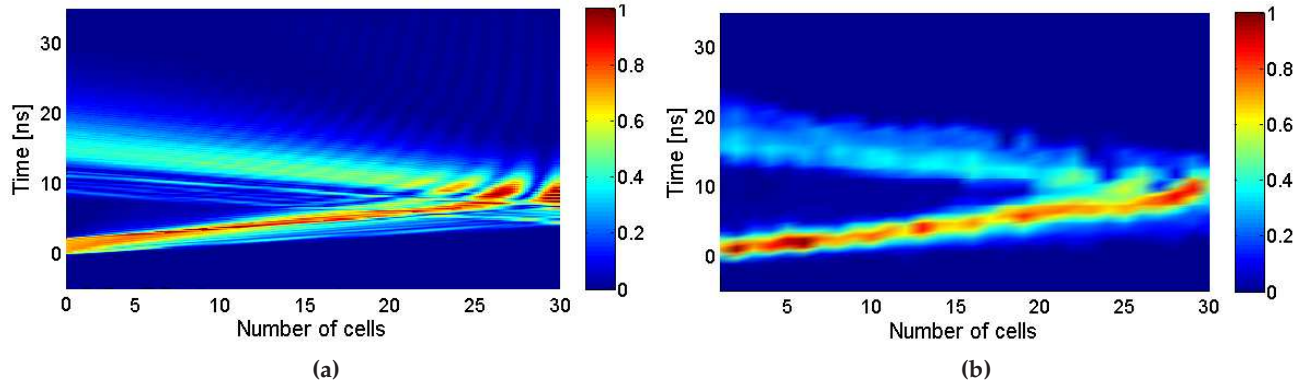

Figure 5.4 – Propagation of a modulated square pulse ($f_0 = 2.05$ GHz, $T = 2.2$ ns, see Appendix A) along an open-ended CRLH transmission line. The line is identical to that of Fig. 5.3 except that it includes only 30 unit cells. (a) Simulation. (b) Measurement.

introduced to compensate for the input chirp. At the 15^{th} cell, the input chirp effect has been canceled and the temporal compression of the pulse is clearly apparent. Note that the reconstruction of the initial pulse is not perfect due to the fact the CRLH group delay is not perfectly linear (see Fig. 5.2). Therefore it cannot exactly compensate for the linear chirp of the input pulse. At the 50^{th} cell, the input chirp has been over-compensated by the CRLH line, and the excess of negative dispersion has resulted in pulse spreading.

Possible applications of CRLH pulse compression include radar [Skolnik, 2002] and microwave imaging systems [Oliver and Quegan, 2004] at arbitrary frequency ranges, due to the scalability of the CRLH line (within technological limitations).

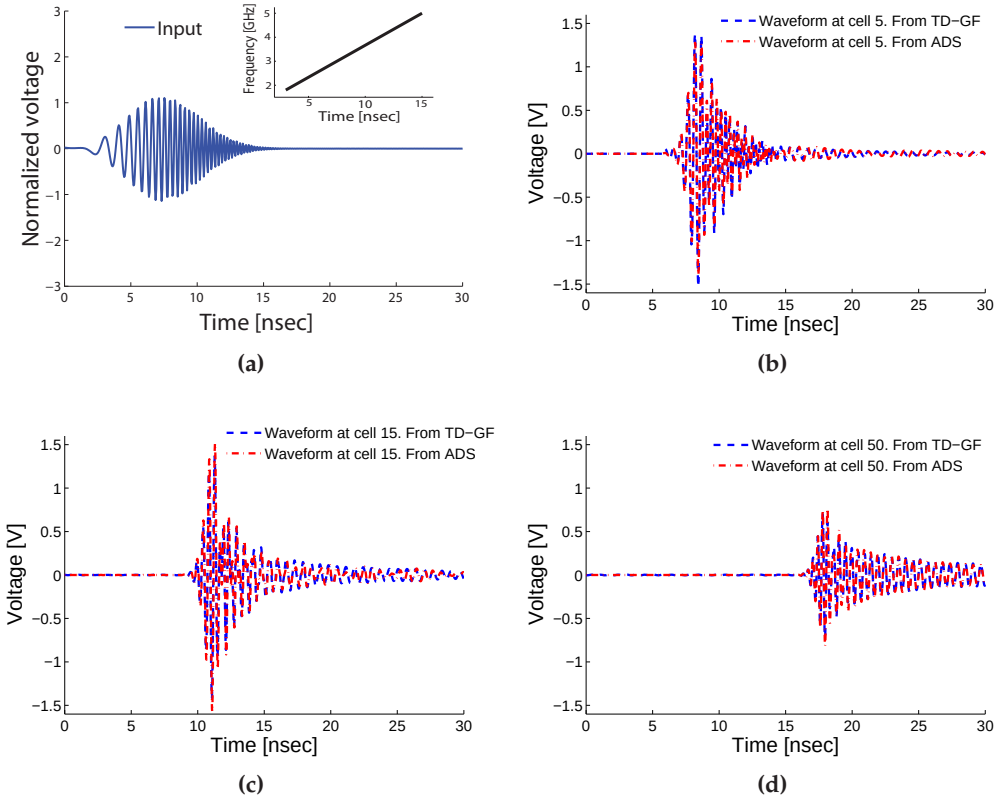

Figure 5.5 – Pulse compression phenomenon in a CRLH TL system excited by a chirp-modulated Gaussian pulse obtained with the time-domain Green's function approach. Results from the commercial software ADS© (see Appendix B) are included as validation.

5.4 Temporal Talbot Effect

5.4.1 Introduction

The Talbot effect is a repetitive constructive interference pattern produced by a dispersive transmission medium with second-order dispersion for a periodic input signal. It was first reported by H. F. Talbot in 1836 for the case of a source with periodic spatial variation [Talbot, 1836]. The temporal counterpart of this effect [Jannson and Jannson, 1981], [Patorski, 1989], [Azaña and Muriel, 1999], [Azaña and Muriel, 2001] occurs when a time-periodic signal is propagating along the same kind of medium. An input pulse train with temporal period T_0 and pulse width ΔT is replicated at the position nz_T ($n \in \mathbb{N}$), where z_T is called the Talbot distance (or self-imaging distance). Also, an increased repetition rate of m pulses per T_0 is obtained at the fractional distances $z_f = (s/m)z_T$ (where $s, m \in \mathbb{N}$), provided that (s/m) is an irreducible fraction, and under the condition that: $m < T_0/\Delta T$ [Azaña and Muriel, 2001]. The temporal Talbot effect has been employed mainly in the optical regime, for applications such as the generation of signals with ultrahigh repetition rate (THz) from slower ranges (GHz) [Azaña and Muriel, 2001], or pulse compression [Berger et al., 2004]

At microwaves, this phenomena is more difficult to reproduce because it requires a second-order broadband dispersive medium. However, the recent introduction of CRLH TLs

[Caloz and Itoh, 2005], which provides a dispersive broadband behavior, may lead to novel scenarios where the temporal Talbot effect and their subsequent applications can be reproduced. This section provides a theoretical demonstration of the temporal Talbot effect in CRLH media, including a full-wave validation of the phenomena at microwaves. Furthermore, the conditions for the phenomena existence in CRLH media are stated, in connection with potential device applications.

5.4.2 Temporal Talbot Effect in CRLH TLs

Intuitively, the temporal Talbot effect occurs when a periodic pulse signal is transmitted through a second order dispersion medium where the neighboring pulses interfere as a result of dispersion so as to produce new temporal components. For the analysis, let us consider a single modulated pulse, denoted by $\Psi(t) = \Psi_0(t)e^{j\omega_0 t}$, where $\Psi_0(t)$ is a slowly varying envelope. The periodic signal is then represented in the time domain, at the position $z = 0$, as

$$A(z=0,t) = \sum_{n=-\infty}^{n=+\infty} \Psi(t - nT_0), \tag{5.1}$$

where T_0 is the repetition rate of the signal. In the spectral domain, the periodic signal becomes discrete, and it can be expressed as

$$\tilde{A}(z=0,\omega) = \omega_r \sum_{n=-\infty}^{n=+\infty} \tilde{\Psi}(\omega = n\omega_r)\delta(\omega - n\omega_r), \tag{5.2}$$

where $\omega_r = 2\pi/T_0$ is the spectral repetition frequency.

On the other hand, the transfer function of a lossless CRLH TL is given by

$$\tilde{H}(z,\omega) = e^{-j\beta(\omega)z}, \tag{5.3}$$

where $\beta(\omega)$ is the CRLH TL propagation constant. As already explained in Section 4.2.2 of Chapter 4, this propagation constant, around the CRLH TL transition frequency, can be approximated as

$$\beta(\omega) = \frac{\omega}{\omega_R} - \frac{\omega_L}{\omega}. \tag{5.4}$$

In the right handed side, the first term provides a simple time delay (or linear frequency phase), whereas the second order term is responsible for the line dispersion. Eq. (5.4) can be further expanded, employing Taylor series, around a modulation frequency (ω_0) as

$$\beta(\omega) = \beta_0 + \beta_1(\omega - \omega_0) + \frac{1}{2}\beta_2(\omega - \omega_0)^2 + O(\omega^3), \tag{5.5}$$

where the term $O(\omega^3)$ is related to the order of the error committed in the approximation, and the term β_n is defined as

$$\beta_n = \left[\frac{\beta^n(\omega)}{\partial\omega^n}\right]\Bigg|_{\omega=\omega_0}. \tag{5.6}$$

Note that Eq. (5.5) is only valid for the case of narrowband pulses (centered at the frequency ω_0 and with bandwidth $\Delta\omega$).

Employing Eq. (5.5), the transfer function of the CRLH TL $\left[\tilde{H}(\omega') = \tilde{H}(\omega = \omega_0 + \omega')\right.$, where a change of variable has been introduced from ω to ω' $\left.\right]$ takes the form

$$\tilde{H}(z,\omega') = \exp\left\{-j\left[\beta_0 + \beta_1\omega' + \frac{1}{2}\beta_2\omega'^2\right]z\right\}. \tag{5.7}$$

In order to derive the Talbot distance, only the third expansion term of the exponential is considered. This is because the first two terms do not provide any information related to the Talbot distance (which is only due to second order dispersion [Azaña and Muriel, 2001]). Specifically, the first term is related to the modulation frequency of the pulse and does not carry any information about the envelope, and the second term represent the group delay (or retarded frame) of the signal.

Using Eq. (5.2) and Eq. (5.7), the spectrum of the signal at the distance z can be written as

$$\begin{aligned}\tilde{A}(z,\omega') =& \omega_r \sum_{n=-\infty}^{n=+\infty} \exp\left\{-j\frac{\beta_2\omega'^2 z}{2}\right\}\tilde{\Psi}(n\omega_r)\delta(\omega' - n\omega_r) = \\ & \omega_r \sum_{n=-\infty}^{n=+\infty} \exp\left\{-j\frac{\beta_2 z}{2}\left(\frac{2\pi n}{T_0}\right)^2\right\}\tilde{\Psi}(n\omega_r)\delta(\omega' - n\omega_r).\end{aligned} \tag{5.8}$$

Note that the appearance of ω' squared term in this equation is due to the quadratic phase factor in the spectral response of the CRLH TL dispersive medium.

Eq. (5.8) reveals that the Talbot effect $\left[\right.$ i.e., $\tilde{A}_z(z,\omega) = \tilde{A}(z=0,\omega)$ $\left.\right]$ occurs under the condition

$$\frac{\beta_2 z}{2}\left(\frac{2\pi n}{T_0}\right)^2 = \pi p, \tag{5.9}$$

where $p \in \mathbb{N}$. The case of the first integer Talbot distance ($p = 1$) is given by

$$z_T = \frac{T_0^2}{2\pi|\beta_2|} = \frac{T_0^2\omega_0^3}{4\pi\omega_L^2}, \tag{5.10}$$

where the identity $\beta_2 = -2\omega_L/\omega_0^3$ [see Eq. (5.6)] has been employed.

The Talbot distance can also be obtained at fractionary distances [Azaña and Muriel, 2001], given by $z_f = (s/m)zT$, where s and m are irreducible integers. At this fractionary distance, the periodic input signal is also self-imaged but with an increase repetition rate by a factor of m. This phenomena corresponds to the fractionary Talbot effect [Azaña and Muriel, 2001]. It is important to note that in the case of a CRLH TL, the basic Talbot distance can be tuned externally by modifying the parameters T_0 and ω_0, without changing the intrinsic parameters of the line.

5.4.3 Numerical Validation and Practical Considerations

After theoretically deriving the Talbot distance related to the CRLH TLs, the phenomena will be verified using the numerical technique proposed in Section 4.3 of Chapter 4 and with commercial full-wave simulations. Consider a balanced lossless CRLH transmission line with circuital parameters $C_R = C_L = 1.0$ pF and $L_R = L_L = 2.5$ nH. A modulated train of Gaussian pulses, with temporal width of $\sigma = 0.75$ ns and period rate of $T_0 = 8$ ns is used to excite the line shown in Fig. 5.6a.

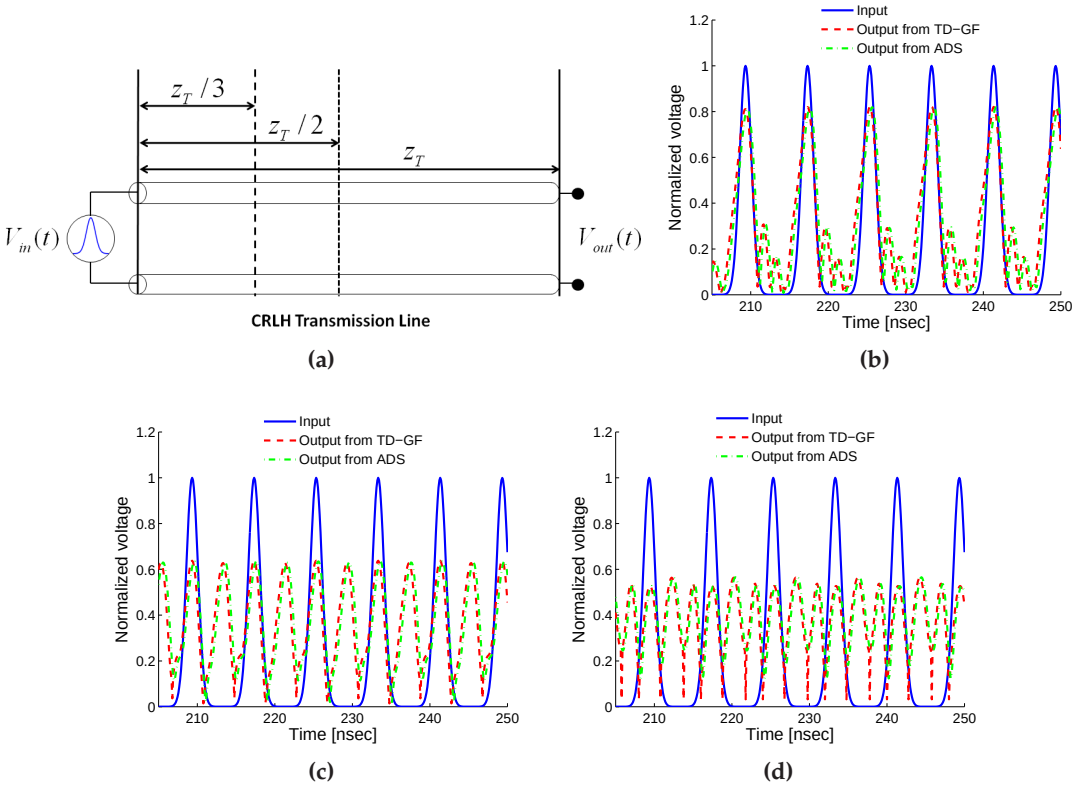

Figure 5.6 – Talbot repetition rate multiplication effect. a) CRLH TL with length corresponding to the basic Talbot distance z_T. b) Reconstruction of the original pulse train at the Talbot distance z_T. c) Repetition rate doubling at the distance $z_T/2$. d) Repetition rate tripling at the distance $z_T/3$. Results obtained from the proposed TD GF approach, and validated using the commercial software ADS© (see Appendix B).

Fig. 5.6b presents the input pulse train and the output pulse train at the Talbot distance z_T. The reconstruction of the initial train of pulses is confirmed, although a small disagreement, due to higher order terms (greater than 2) of the CRLH dispersion relation, is observed between two consecutive pulses. Fig. 5.6c and Fig. 5.6d show the input and output voltages at the fractional Talbot distances of $z_T/2$ and $z_T/3$, respectively. The effect of pulse multiplication is thus clearly confirmed, while the distortion is smaller because less higher-order dispersion effects occur over a shorter distance of propagation.

The practical implementation of Talbot devices based on CRLH transmission lines depends on the technology employed. For instance, with the CRLH parameters used in Fig. 5.6, a microstrip implementation with a typical unit cell size of 1 cm would lead to a Talbot distance z_T of around 17 meters. This is unpractical, specially due to the losses. However, using multilayer technology [Horii et al., 2005], this distance may be dramatically reduced to sizes in the order of several centimeters, while even lower sizes apply for pulse rate repetition multiplication. This decrease in length also decreases the total amount of losses, allowing the Talbot effect to be applied in practical situations, such as the generation of signals with ultrahigh repetition rate or pulse compression[Berger et al., 2004].

5.5 Tunable Pulse Repetion-Rate Resonator

5.5.1 Introduction

Resonators have been widely used in microwaves, with applications ranging from filters or oscillators to tuned amplifiers (see [Pozar, 2005]). Conventionally, purely RH distributed elements are used, providing resonances (ω_m) at the frequencies where the physical length of the structure is multiple of half-wavelength. These devices have been mainly analyzed in the harmonic regime, but little work has been done in the impulse-regime, required in recent developments for ultra wideband (UWB) systems (see, eg. [Ghavami et al., 2007]).

Composite right/left handed (CRLH) transmission line metamaterials (see [Caloz and Itoh, 2005]) may be used as distributed resonators, providing unusual characteristics such as the presence of resonant frequencies out of harmonic ratios, or the zeroth-order resonance. In the latter case, the condition of resonance is independent of the physical length of the structure, as stated in [Sanada et al., 2003] and [Abielmonaa et al., 2006]. The dispersive nature of the CRLH lines may provide interesting broadband solutions. However, the study of this line configured as a resonator has been reported only in the harmonic regime to date.

In this section, a novel broadband CRLH based resonator is proposed. It is shown that the CRLH resonator can support nonuniform discrete spectral resonances due to the nonlinear nature of the CRLH dispersion curve (see [Caloz and Itoh, 2005]). Therefore, the pulse spectral components (broadband excitation with continuous spectrum) inside the resonator are discretized, resulting in periodic temporal signal, with time period being a function of the modulation frequency. The time period of the generated train of pulses depends on the spectral separation of the discrete spectral components, which in turn depends on the modulation frequency. This process can be viewed as a resonant cavity in pulsed lasers in optics, where only discrete modes are being supported, leading to generation of optical pulses (see, eg. [Saleh and Teich, 2007]). Moreover, since a CRLH supports nonuniform resonances, the time period of the generated temporal periodic signal can be tuned externally to obtain various output repetition rates.

Inspired from optical pulsed laser systems and resonant cavities, these concepts are introduced in the microwave domain using impulse-regime CRLH transmission line metamaterials for the first time. Resonator phenomena and various applications are further discussed. The presented results have been computed by the time-domain Green's function approach introduced in Section 4.3 of Chapter 4, and are further validated using commercial full-wave simulators.

5.5.2 Proposed Resonator

In this section, the principle and implementation of the proposed UWB resonator based on CRLH transmission line is presented. Although the resonator principle holds in general for different transmission lines technologies, the use of a CRLH transmission line is proposed, because it provides additional functionalities, such as pulse delay tunability, resulting in variable output repetition rates. This behavior can not be obtained with conventional non-dispersive transmission lines.

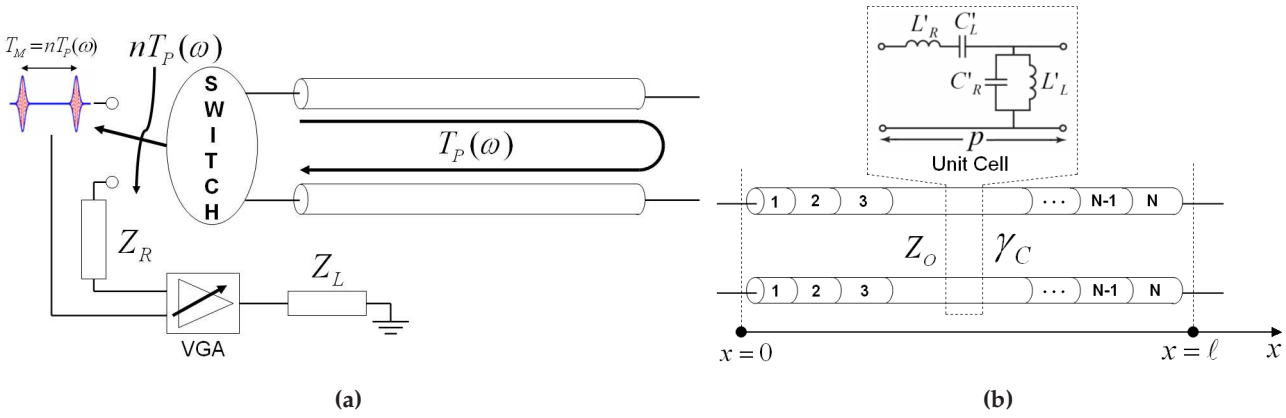

Figure 5.7 – Proposed impulse-regime CRLH resonator and pulse rate multiplicator. (a) Operation principle. (b) CRLH resonator, constituted of N unit cells of length p, with its propagation constant γ_C, characteristic impedance Z_0, and total length $\ell = N\,p$.

Principle

The proposed impulse-regime resonator system is sketched in Fig. 5.7a. The resonator is realized by terminating the transmission line at both ends by an open circuit (see [Pozar, 2005]). Initially, a fast switch injects the input pulse into the resonator (see, eg. [Jin and Nguyen, 2005]). Once the pulse has been injected into the resonator, the switch is set to a high impedance Z_R, which reflects most of the energy back into the line, and transmits only a small amount of energy, which is then amplified, into the load Z_L. The resonator acts as a cavity and therefore supports multiple natural resonances. Due to the broadband nature of the source, all of the cavity resonances lying within the pulse spectrum are excited simultaneously, which results into discretization of the continuous input pulse spectrum.

In time domain, the pulse travels back and forth between the cavity walls (high impedance port terminations, analogous to reflecting mirrors in case of lasers). The signal takes a total time of T_P for completing a single round trip inside the resonator. One of the line termination impedance is designed to be such that when the pulse reaches the end of the line, the high Z_R impedance only transmits a small amount of energy, reflecting the rest of the pulse back to the resonator. This is analogous to having partially reflecting mirrors in optical lasers, with typically high reflectivity around 99%. In order to compensate for the line losses, at the output of the resonator a variable gain amplifier (VGA) can be used (see, eg. [Lee et al., 2007]), which is synchronized with the input pulse generator. After the pulse has covered n-round trips inside the resonator corresponding to a time $T_M = n\,T_P$, n-number of pulses with similar pulse features as that of the input are obtained. Therefore, the system acts as a $1 : n$ pulse burst generator. Moreover, after the n^{th} round trip, the switch at the input changes its position again to connect the generator, in order to introduce a new pulse inside the resonator to produce another burst of n-pulses. As this process repeats itself (synchronized with the output), a constant pulse train at the output is obtained. Consequently, the system also acts as a $1 : n$ repetition rate multiplier.

If the resonator in the system is implemented using conventional right-handed transmission line technologies, the round trip time T_P is fixed (dispersionless). As a result only one repetition rate at

the output is obtained from a given resonator. Therefore, a new line will have to be designed if a different repetition rate is required. To enhance the system features in order to obtain variable repetition rates from the same resonator, a CRLH transmission line can be used. Because of the nonuniform phase response of the CRLH lines, the output time period of the signal can be controlled externally using the modulation frequency of the input signal. The new proposed system, using CRLH lines, is demonstrated and described in the following subsection.

CRLH-TL implementation

A CRLH-TL resonator is depicted in Fig. 5.7b, for an ideal open-ended case . The resonant frequencies (ω_m) of the resonator correspond to these frequencies where the physical length (ℓ) of the line is multiple (m) of half guided wavelength. Since the CRLH-TL is able to provide negative and zero values of the propagation constant (β), the number of resonant modes ($m \in \mathbb{Z}$) are symmetrically defined around $m = 0$ (see [Caloz and Itoh, 2005]). Therefore,

$$\ell = |m|\frac{\lambda}{2} \qquad \text{or} \qquad \beta_m = \frac{m\pi}{\ell}. \tag{5.11}$$

In addition, the field distribution of a particular resonant mode m presents $|m|$ zeros in the standing wave pattern, at the positions

$$x_{k_m} = k\frac{\ell}{m+1}, \qquad k = 1 \ldots m. \tag{5.12}$$

From Eq. (5.11), the resonant frequencies are obtained by sampling the dispersion curve [$\beta(\omega)$] with a sampling rate of π/ℓ. Due to the nonuniform nature of the CRLH dispersion curve, the resonant frequencies are out of the harmonic ratios. Specifically, a compression in the resonant frequencies is obtained in the left-handed region. This can be observed in Fig. 5.8, which shows the dispersion relation for a particular CRLH line, composed of N-unit cells, along with their $(2N-1)$ associated resonances (see the stars in the curve of Fig. 5.8).

In the impulse-regime case, the balanced condition of the CRLH (equal and mutually canceling series and shunt resonances leading to gapless transition from left-handed to right-handed frequency ranges) is required. When the CRLH resonator is excited with a broadband pulse signal, all the resonances falling within the spectral band of the pulse are excited. As a result, the continuous spectrum of the input pulse gets discretized. It is well known from basic signal processing concepts, that this pulse spectrum discretization consequently leads to a pulse periodicity in time. It should be noted that depending on the modulation frequency of the input pulse, variable number of resonances can be excited. Since the spectral separation between these resonances also depends on frequency, different sampling rates can be applied, and the corresponding repetition rate in time will be tunable.

From the time-domain point of view, the tunable periodicity of the pulse can be explained through the temporal pulse propagation inside the CRLH line, which in the infinitesimal limit ($p \to 0$) can be written as

$$v_g(\omega) = \frac{\omega^2\omega'_R}{\omega^2 + \omega'_R\omega'_L}, \tag{5.13}$$

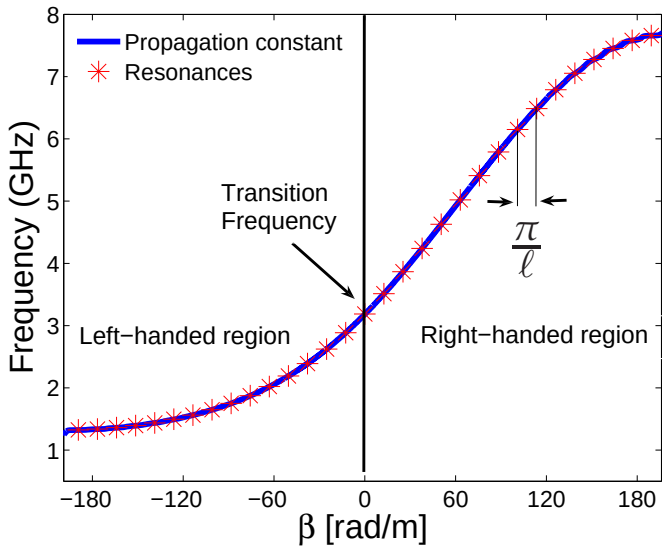

Figure 5.8 – Dispersion relation for the CRLH transmission line resonator of Fig. 5.7b and its resonant frequencies ω_m. The line includes $N = 16$ unit cells of length $p = 1.56$ cm, which leads to $2N - 1 = 31$ resonances. The circuit parameters are $C_R = C_L = 1.0$ pf and $L_R = L_L = 2.5$ nH.

where

$$\omega'_R = \frac{1}{\sqrt{L'_R C'_R}} \quad \text{and} \quad \omega'_L = \frac{1}{\sqrt{L'_L C'_L}}. \tag{5.14}$$

In this last expression L'_R, C'_R and L'_L, C'_L are per-unit-length and times-unit-length parameters of the right-handed and left-handed CRLH contributions, and (p) is the unit cell size, following the notation of [Caloz and Itoh, 2005]. The single round trip time inside the resonator for a pulse is given by

$$T_P(\omega) = \frac{2\ell}{v_g(\omega)}, \tag{5.15}$$

where ℓ is the total length of the physical structure. To determine the controlling parameters of $T_P(\omega)$, the derivative over the modulation frequency is given by

$$\frac{\partial T_P(\omega)}{\partial \omega} = -4\ell \frac{\omega_L}{\omega^3}, \tag{5.16}$$

which shows that the two controlling parameters are:

1. The length of the structure (ℓ). Larger structures provide higher ranges of $T_P(\omega)$. This is shown in Fig. 5.9, where the variation of $T_P(\omega)$ as a function of the number of cells (i.e. ℓ) is presented for a particular CRLH line.

2. The variable ω_L, which provides the dispersion features of the CRLH line.

In order to obtain the accurate expression of the group velocity inside the finite line, the ABCD transmission matrix analysis may be used (see [Caloz and Itoh, 2005]). In this case the propagation

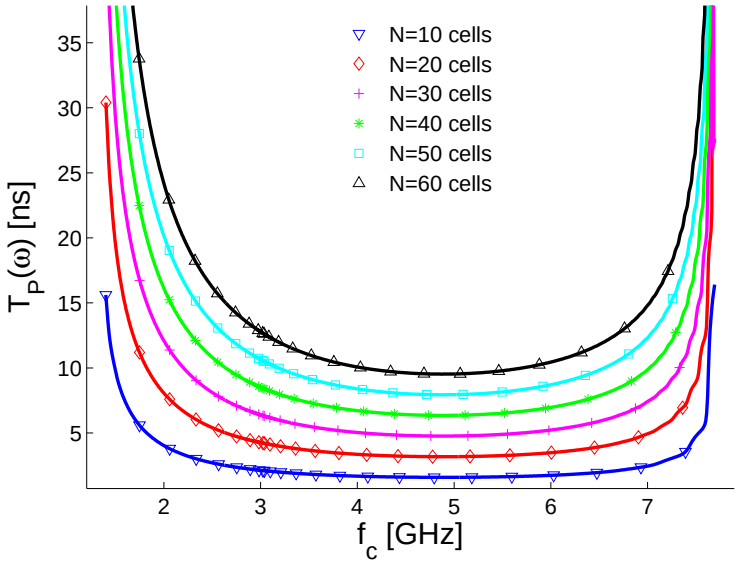

Figure 5.9 – Round trip time $T_P(\omega)$ along the CRLH resonator of Fig. 5.8 for different numbers of cells N, versus the carrier frequency f_c, computed with Eq. (5.15) and Eq. (5.17).

velocity reads

$$v_g = \frac{p\ \sin[p\,\beta(\omega)]}{\omega/\omega_R^2 + \omega_L^2/\omega^3}. \tag{5.17}$$

Note that this expression is valid in all frequency ranges, whereas Eq. (5.13) is only valid near the transition frequency between the RH and LH regions.

5.5.3 Demonstration with modulated Gaussian pulses

In this section, the response of an ideal CRLH resonator excited by modulated Gaussian pulses is presented. We have chosen Gaussian pulses because they are convenient to characterize broadband systems, and are easy to generate in practice. Fig. 5.10 shows the spectral components of a modulated Gaussian pulse as a function of space inside a CRLH transmission line. The pulse [Fig. 5.10a] is modulated at the CRLH line transition frequency to study the resonances at both, the right and left handed regions. In addition, the pulse duration ($\sigma = 0.15$ ns) is chosen to produce a very wideband pulse, in order to excite a large number of resonances. In the spectrum of Fig. 5.10a we can observe some aliasing at low frequencies. Note that the bandpass characteristic of the CRLH line will eliminate this aliasing effect.

First, Fig. 5.10b shows the pulse spectral components along the CRLH line, when it is configured as a transmission line. As expected, all frequencies inside the passband of the line are allowed and can propagate inside the line. On the other hand, Fig. 5.10c represents the pulse spectral components when the line is configured as a resonator. In this case, only discrete frequencies are allowed inside the line, and the pulse spectrum is discretized at the resonant frequencies of the CRLH line. It can be seen that the discrete components are non-uniformly distributed (see Fig. 5.8). It is also noted

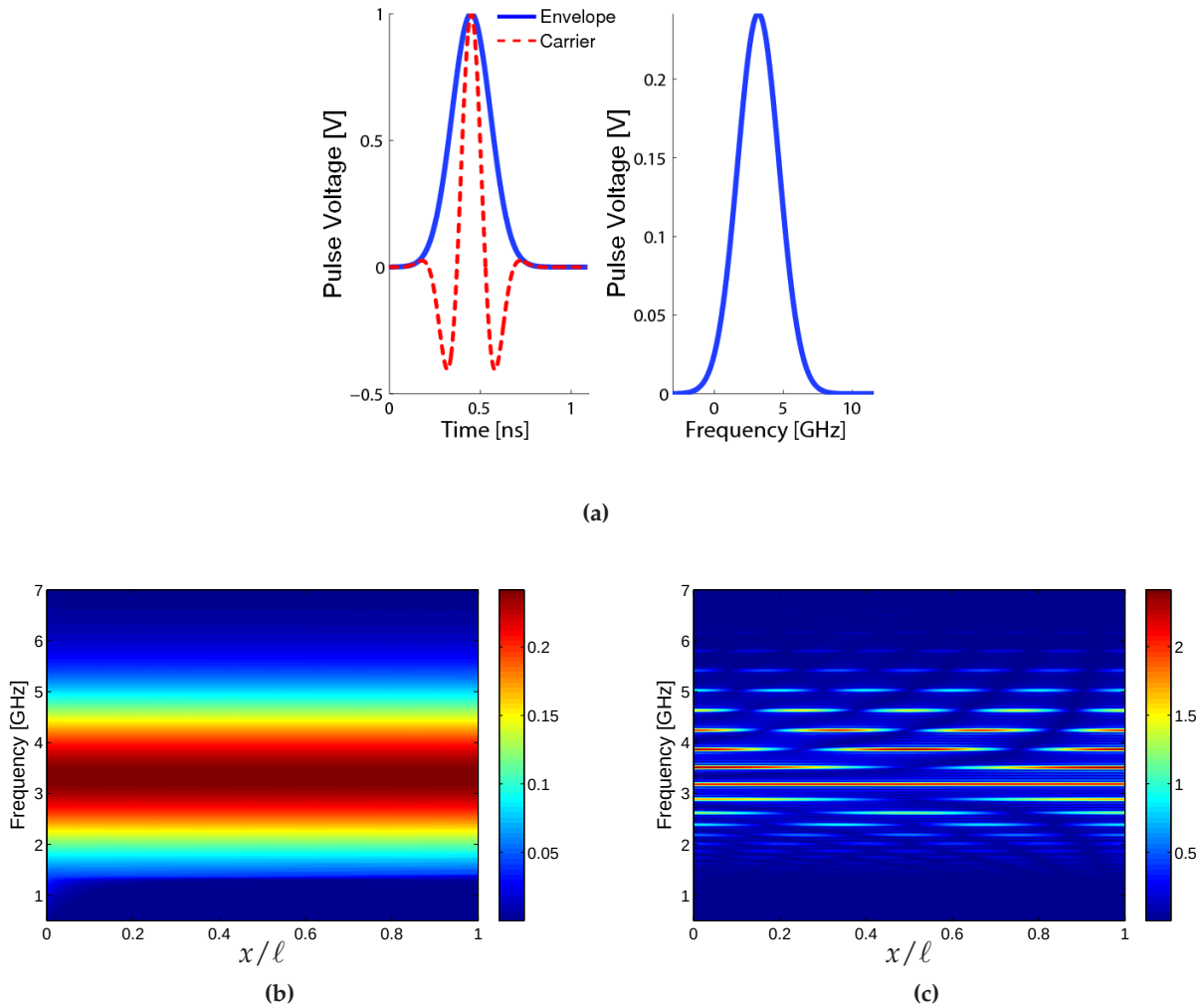

Figure 5.10 – Spectrum evolution of a modulated Gaussian pulse propagating along the CRLH structure of Fig. 5.8. (a) Modulated Gaussian pulse at the input, with carrier frequency $f_c = 3.183$ GHz and temporal width $\sigma = 0.15$ ns (see Appendix A). Both, the pulse envelope and the carrier are shown on the left, while the spectrum of the pulse is shown on the right. (b) Spectrum evolution along the CRLH structure terminated by matched load (transmission line regime). (c) Spectrum evolution along the CRLH structure terminated by an open circuit at both ends (resonator regime).

that at the transition frequency ($f = 3.183$ GHz), the resonant mode $m = 0$ provides a uniform voltage behavior, whereas the rest of the higher order resonances exhibit zeros at the spatial positions indicated by Eq. (5.12).

Fig. 5.11 shows the temporal evolution of a modulated Gaussian pulse ($f_c = 5.0$ GHz, $\sigma = 0.25$ ns, see Appendix A) as a function of space along a CRLH line. Fig. 5.11a presents the pulse propagation when the line is matched. In this case, no reflections occur at the end of the line and all the energy is transmitted. On the other hand, Fig. 5.11b shows the pulse propagation when the CRLH line is configured as a resonator. In this case, multiple reflections can be observed inside the line. It is noted that as the pulse bounce back and forth in the line, there is a gradual decrease in the amplitude level of the pulse due to line losses, which is consistent with the energy conservation.

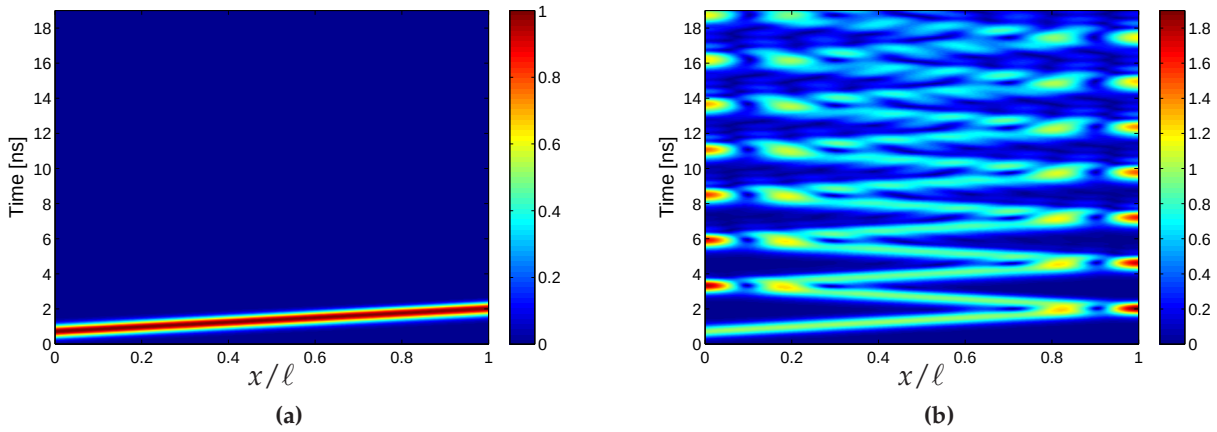

Figure 5.11 – Propagation in time of a modulated Gaussian pulse ($f_c = 5.0$ GHz, $\sigma = 0.25$ ns, see Appendix A), along the CRLH transmission line of Fig. 5.8. (a) Matched line. (b) Open-ended line resonator.

5.5.4 Application: Pulse Rate Multiplication

The proposed CRLH resonator can be configured to extract a small amount of energy, for instance, using a high impedance (Z_R) connected to another circuit (see Fig. 5.7a), or even using a broadband coupled line coupler (see, eg. [Mongia et al., 1999]). Using such small energy extraction mechanism, a train of pulses with similar features as the input is obtained at the output. Note that the frequency components of the generated pulses are exactly the same as in the input pulse, since the resonator is based on linear systems, and therefore no new frequency components are generated in the process (see [Saleh and Teich, 2007]). The maximum pulse bandwidth inside the resonator is related to the features of the CRLH line, which are scalable in frequency as shown in [Caloz and Itoh, 2005]. Specifically, to allow for a good reconstruction of the periodic train of pulses, maintaining the tunability capabilities of the resonator, the number of resonances which should be simultaneously excited by the input pulse must be around one third of the total number of resonances within the operational frequency bandwidth of the line. Note that due to the frequency scalability properties of the CRLH lines, a CRLH resonator may be designed to operate at the desired frequency range, and with the desired maximum pulse bandwidth (with the restrictions of the available technology). As it was previously mentioned, the proposed resonator may also be implemented using non-dispersive right-handed lines. In this case, the resonator could allow for shorter pulses (with higher bandwidth), but losing the tunable behavior of the device.

At the resonator output, the decrease in the pulse amplitudes can easily be compensated using a variable-gain amplifier, for instance that proposed in [Lee et al., 2007], synchronized with the input pulse generator. The main advantage of this approach is that the temporal distance between two consecutive pulses [$T_P(\omega)$] is controlled by the modulation frequency. This is demonstrated in Fig. 5.12, where the pulse waveforms at the output of the CRLH resonator (just before the amplifier) are depicted for different carrier frequencies, showing the tunability property of the resonator. These results have been obtained using the time-domain Green's function approach presented in Section 4.3 of Chapter 4 and are further validated using the commercial software ADS© (see Appendix B).

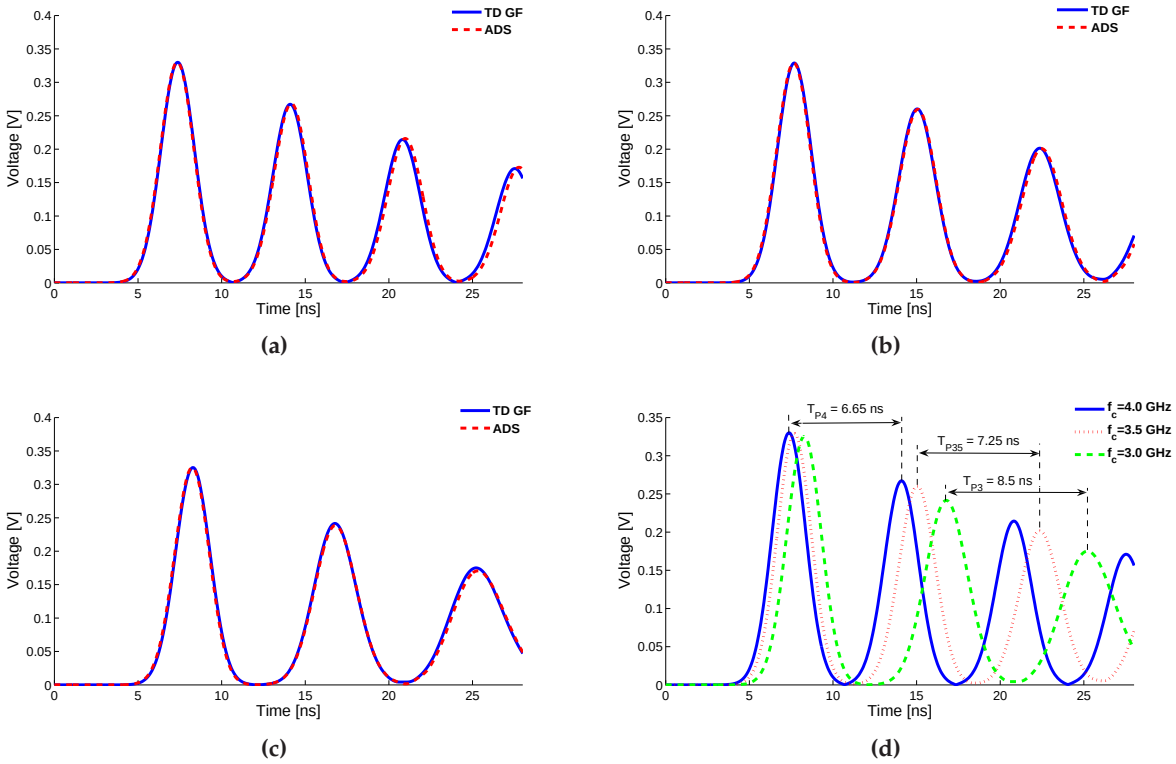

Figure 5.12 – Gaussian waveforms ($\sigma = 1.0$ ns) at the output (Z_R) of the CRLH resonator [Fig. 5.7a] for different carrier frequencies (f_0) showing the tunability of the system. The CRLH line is composed of 40 unit cells with the same circuit parameters as in Fig. 5.8. The generator impedance is $Z_g \approx \infty\ \Omega$ and the load impedance is $Z_R = 500\ \Omega$. Simulation data from the commercial software ADS© (see Appendix B) is included as validation. (a) f_0=4.0 GHz. (b) f_0=3.5 GHz. (c) f_0=3.0 GHz. (d) Results from the three carrier frequencies together, to show the tunability effect.

After several round trips of the pulse, the energy inside the resonator decreases, due to both the losses and the energy extracted from the line. To maintain the same pulse rate [$T_P(\omega)$] at the output, a train of pulses is required in the input, with periodicity $T_M(\omega) = n\,T_P(\omega)$ ($n \in N$). Therefore, the CRLH resonator may be seen as a $1 : n$ pulse rate multiplication device. This is demonstrated in Fig. 5.13, which shows the output of a CRLH resonator when it is excited by a modulated train of pulses, before [Fig. 5.13a] and after [Fig. 5.13b] amplification. Note that the voltage-gain amplifier behavior is well-defined, because the exponential decay of the voltage due to the losses inside the resonator occurs in a relative large and previously known time interval T_M. In practical cases, the number of pulses generated (n) depends on the type of CRLH employed and on the features of the input pulse. In the dispersive (or left-handed) region, the modulation frequency controls the dispersion that the pulse will suffer in time-domain. When this dispersion is important, the final shape of the pulse varies, limiting the repetition rate of the resonator. However, this can be totally compensated using the approach presented in [Schwartz et al., 2008]. In addition, the losses introduced by the line limit the repetition rate in the entire frequency band (both left and right handed regions). Nevertheless, the practical values of (n) are high enough to provide a considerable increase in the repetition rate for most applications, with the additional advantage of tunability.

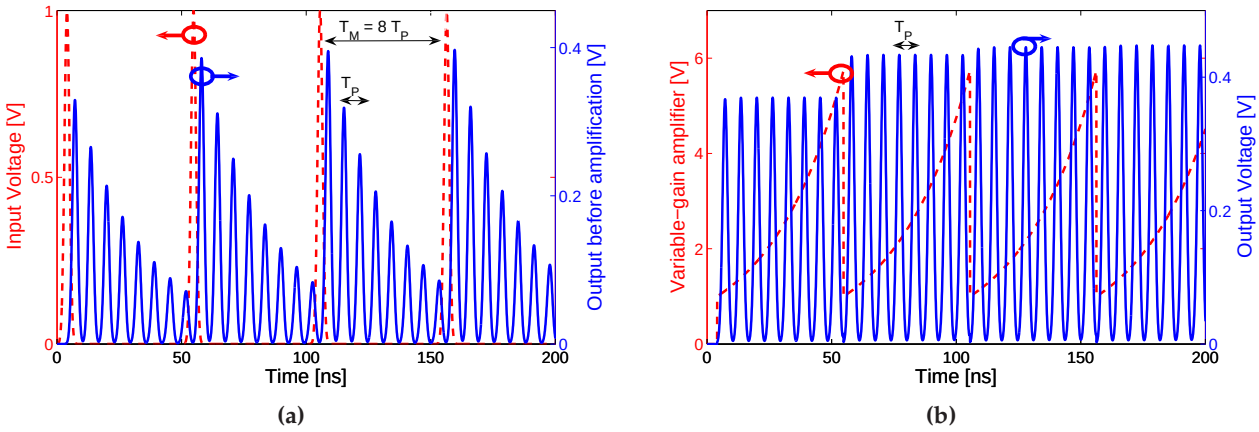

Figure 5.13 – Gaussian waveforms at the output of the CRLH resonator of Fig. 5.12d for a pulse train excitation ($f_c = 5.0$ GHz, $\sigma = 1.0$ ns, $T_P = 6.35$ ns and $T_M = 8T_P$ ns). (a) Input pulse train (dashed) and output pulse train (solid) before amplification (at Z_R). (b) Amplifier gain (dashed) and output pulse train (solid) after amplification (at Z_L).

5.6 Nonlinear Effects and Electronic Balancing of CRLH Lines

5.6.1 Introduction

In this section, the phenomenology of pulse propagation along non-linear CRLH transmission line is examined. As previously stated, CRLH TLs represent a general dispersive medium, specially in the LH frequency range. The dispersion introduced by the CRLH medium is combined with non-linear effects. As explained in Section 4.3.2 of Chapter 4, nonlinearity can easily be achieved using hyper abrupt diodes, which loads the transmission line, leading to the CRLH circuital model shown in Fig. 4.9. The combination of both phenomena, dispersion and non-linearity, leads to novel phenomena (such as self-phase modulation, the formation of soliton waves [Gupta and Caloz, 2007], etc.), which usually appear in the optics regime [Saleh and Teich, 2007], and that may be reproduced at microwaves, providing interesting applications.

The first main goal now is to validate the numerical technique proposed in Section 4.3.2 of Chapter 4, which models pulse propagation along non-linear CRLH TL. For this purpose, the propagation of a modulated pulse along this media is carefully studied and validated using full-wave commercial software. The effects of both phenomena, dispersion and non-linearity, are shown together along the line, confirming the harmonic generation effect. Then, an experimental prototype of a non-linear CRLH line is fabricated and measured. A new unit-cell circuital model is proposed in order to accurately characterize the real line. The variation of the varactor's DC bias is further exploited to provide control of the TL's band-gap near the CRLH transition frequency, which leads to an electrical balancing of the line. Finally, pulse harmonic generation is experimentally demonstrated, showing good agreement with the proposed theory.

Original Method Time [seconds]	*Interpolated Method* Time [seconds]	*Improvement* %
325.57	65.12	≈ 80

Table 5.1 – CPU-time comparison for the pulse propagation computation along a non-linear CRLH, obtained with the original and with the interpolated schemes.

5.6.2 Numerical Validation

The numerical method proposed in Section 4.3.2 of Chapter 4 is able to model pulse propagation taking into account two different phenomena, dispersion and non-linearity. In order to show the practical value of the proposed technique, a modulated Gaussian pulse (with $f_0 = 2.5$ GHz, $V_0 = 1$ V and $\sigma = 0.4$ ns, see Appendix A) is fed into a non-linear CRLH line (composed of 48 unit cells, with unit length equal to $p = 1.56$ cm, circuit parameters $C_0 = C_L = 1.0$ pF and $L_R = L_L = 2.5$ nH and non-linear parameters $\eta = \alpha = 8 \cdot 10^{-13}$, as described in Section 4.3.2 of Chapter 4). This configuration may easily be implemented (for instance, in MIM technology) and provides both, dispersion and non-linearity phenomena.

Fig. 5.14a presents the temporal output waveform of the pulse, computed with the proposed method and validated with the commercial software ADS© (see Appendix B). As can be observed, very good agreement is achieved. Fig. 5.14b depicts the spectrum waveform of the pulse, at the position of $z = 0.7$ m (i.e. in the middle of the non-linear CRLH line, which has been sandwiched by two PRH lines), obtained by both, the proposed technique and ADS©. Again, the agreement between the two different methods is good. In the figure, pulse generation at a frequency multiple of the input pulse is clearly visible, confirming the non-linear behavior of the line. In Fig. 5.14c the temporal propagation of the input pulse (envelope) along the structure is shown. It is interesting to observe the reflected waves along the media, produced by the characteristic impedance fluctuations with time at each unit cell. The pulse spreading, due to the dispersive features of the line, is also clearly visible. Fig. 5.14d presents the spectrum evolution of the pulse along the medium, showing the harmonic generation. Note that the low frequencies of the input pulse have been filtered out by the band-pass behavior of the CRLH line. The explanation of the frequency variations along the line is as follows. Initially, the pulse enters into the non-linear CRLH with a maximum amplitude of V_0, which creates a moderate impedance discontinuity (due to the Bloch impedance variation). This creates reflected waves, as previously commented. In addition, this initial amplitude V_0 also generates harmonics with a maximum of amplitude at the beginning of the line. Then, as long as the pulse is propagating though the medium, the amplitude of the pulse is decreasing, due to the dispersion, consequently decreasing the amplitude of the generated harmonics. Note that an interference pattern occurs in the last CRLH-PRH transition, due to a small temporal dependent impedance mismatch.

The previous results were computed using the interpolated method proposed in Section 4.3.2 of Chapter 4, which directly superimpose with the results from the proposed method without using the interpolation. In Table 5.1 we present a comparison, between the original and interpolated methods, for the time required to compute the results presented in Fig. 5.14. For this computation, we have employed a total of 600 time steps (between 0 and 18 ns) and we have analyzed a total number of 2000 spatial points, uniformly distributed along the 3 mediums (2 PRH and 1 non-linear CRLH composed

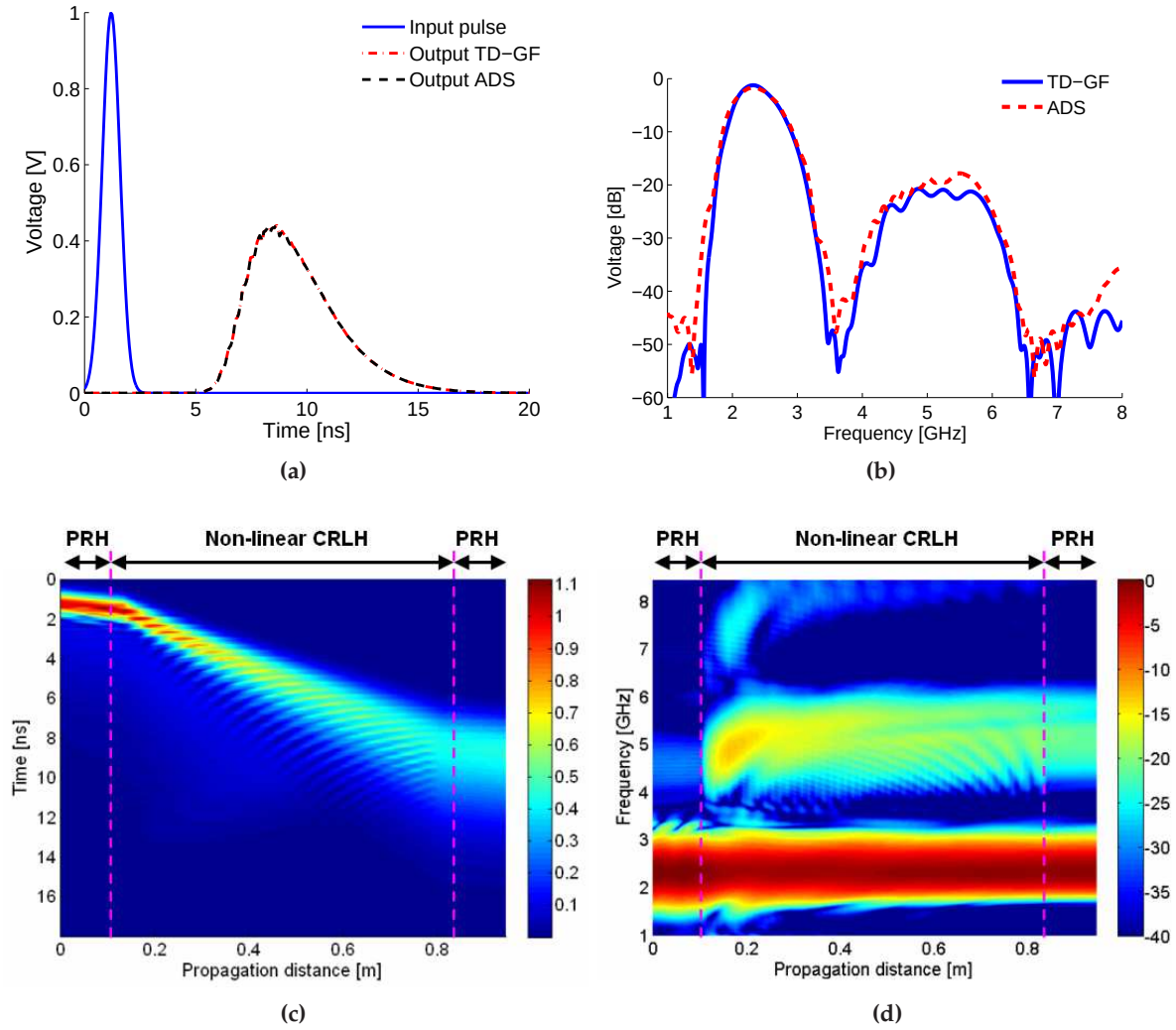

Figure 5.14 – A modulated Gaussian pulse ($f_0 = 2.5$ GHz and $\sigma = 0.4$ ns, see Appendix A) is fed into a non-linear CRLH TL (48 unit cells, with unit length equal to $p = 1.56$ cm, circuit parameters $C_0 = C_L = 1.0$ pF and $L_R = L_L = 2.5$ nH and non-linear parameters $\eta = \alpha = 8 \cdot 10^{-13}$, see Section 4.3.2 of Chapter 4) sandwiched with two conventional right-handed lines. (a) Output waveform (only enveloped shown) provided by the proposed method and validated with ADS© (see Appendix B). (b) Spectrum waveform provided by the proposed method and validated with ADS©, at the distance $z = 0.7$ m. (c) Propagation of the input pulse (envelope) along the lines. (d) Spectrum evolution of the pulse along the lines.

of 48 unit-cells). Note that the exact propagation constant has been calculated just for 11 values of C_R, at each frequency, in order to provide accurate data for the interpolation. These capacitor values are computed following Eq. (4.46) (see Section 4.3.2 of Chapter 4), employing as an input voltage discrete values from a uniform discretization of the input pulse amplitude range. The time required for this computation has already been included in the data shown in Table 5.1. In Fig. 5.15, the maximum relative errors during the propagation constant computation, for different values of frequency, are presented. As can be observed in the figure, the maximum error achieved with the interpolated method is always below 0.1%, due to the very smooth behavior of the CRLH propagation constant

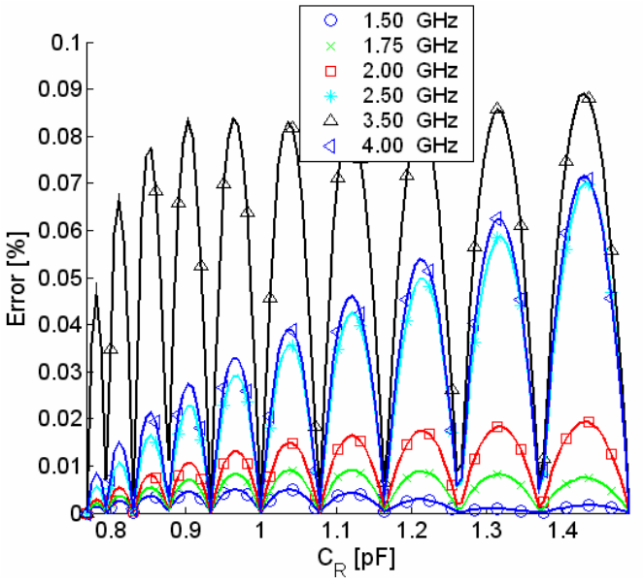

Figure 5.15 – Relative errors between the original and interpolated calculation of the propagation constant, versus C_R for different frequencies.

under weak non-linear conditions. Thereby, the use of the interpolated method is justified, providing an 80% reduction of the computational cost while maintaining high accuracy.

5.6.3 Experimental Demonstration

The practical implementation of a non-linear line is not simple. This is because the CRLH TL should be designed as a balanced line [Caloz and Itoh, 2005] (i.e. mutual cancelation of the series and shut resonances), taking into account the varactor influence. A microstrip prototype of this type of non-linear CRLH TL has been fabricated and tested (see Fig. 5.16). This line is composed of $N = 16$ unit cells of length $p = 1.56$ cm. In this real case, there are more shunt capacitors to consider than just the lumped varactor. Specifically, the microstrip structure itself provides a parasitic capacitance (denoted as C_{RStruc}) which is in shunt with the varactor. Furthermore, due to a limitation on the available varactors, a lumped capacitor (denoted as C_{RLump}) has also been added to increase the overall shunt capacitance of the unit cells (in order to balance the line). Taking into account these considerations, the proposed unit cell circuital model of the non-linear CRLH line of Fig. 5.16 is as shown in Fig.5.17.

This model provides non-linearity through the capacitance provided by the varactor (C_{RVarac}), which varies as a function of the input voltage. Note that the voltage at the varactor terminals [$V_{I_k}(t)$] is different than the voltage at the node of the unit cell [$V_k(t)$]. Specifically, using the formalism of complex signals in time domain as introduced in [Peebles Jr., 1998], it may be expressed as

$$V_{I_k}(t) = V_k(t)\frac{C_{RLump}}{C_{RLump} + C_{RVarac}(t)}. \tag{5.18}$$

In addition, the total shunt capacitance of the non-linear unit cell (equivalent to C_R of a regular

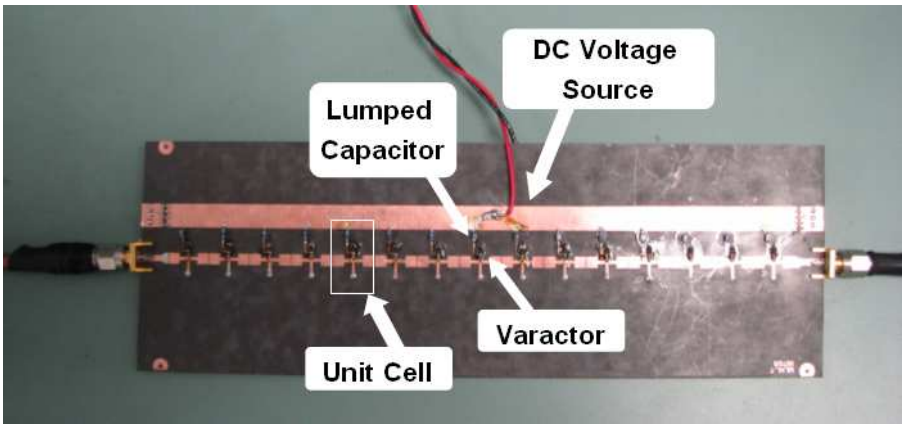

Figure 5.16 – Top view of a microstrip non-linear CRLH prototype, including $N = 16$ unit cells of length $p = 1.56$ cm.

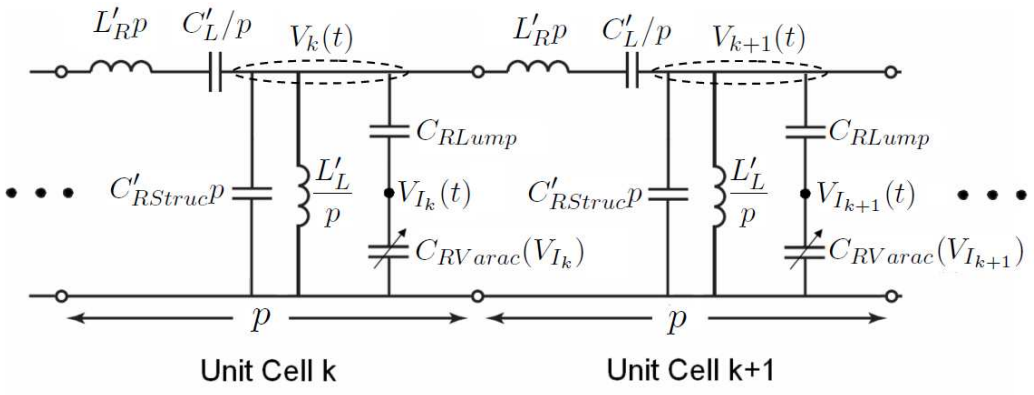

Figure 5.17 – Equivalent circuit model for the non-linear CRLH unit cells k^{th} and $(k+1)^t h$, referred to the prototype shown in Fig. 5.16. The total shunt capacitor (C_R) is composed of $C_{RStruc} = C'_{RStruc}p$ (which depends on the physical structure of the line) in shunt with the series connection of C_{RLump} (lumped capacitor) and C_{Rvarac} (lumped varactor which introduces the nonlinear behavior of the line).

circuital CRLH unit-cell model) may be expressed as

$$C_R(t) = C_{RStruc} + \frac{C_{RLump}C_{RVarac}(t)}{C_{RLump} + C_{RVarac}(t)}. \tag{5.19}$$

Following the proposed non-linear unit-cell model, the circuital parameters which describe a unit-cell of the fabricated prototype are $L_R = 4.5657$ nH, $L_L = 2.0129$ nH, $C_L = 0.80514$ pF, $C_{RStruct}$=1.715 pF and $C_{RLumped}$=1.0 pF. The model of the varactor is MSV34,067-E28/0805-2, which may be characterized as

$$C_{RVarac}(t) = ae^{bV_k(t)} + ce^{dV_k(t)}, \tag{5.20}$$

where $a = 6.849 \cdot 10^{-13}$, $b = -0.4991$, $c = 3.890 \cdot 10^{-13}$ and $d = -0.01694$.

An interesting application of a CRLH TL loaded with varactors is the possibility to electronically balance the line. Specifically, the variation of the varactor's DC bias provides an electrical control

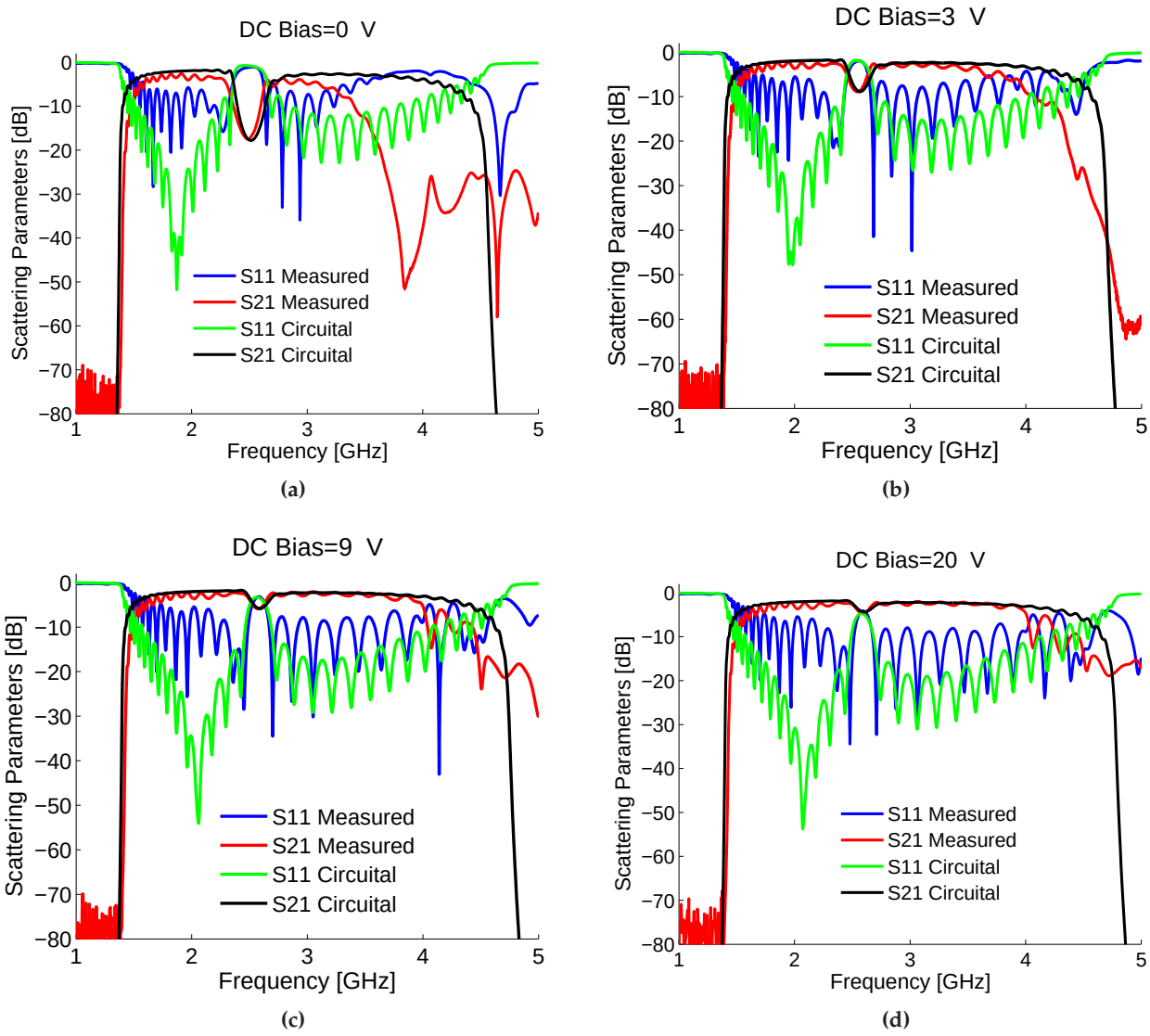

Figure 5.18 – Scattering parameters of the non-linear CRLH transmission line of Fig. 5.16, as a function of the DC Bias voltage. The simulated data has been obtained using a circuit analysis [Caloz and Itoh, 2005], taking into account the proposed non-linear unit cell model (see Fig. 5.17). (a) DC Bias=0 V. (b) DC Bias=3 V. (c) DC Bias=9 V. (d) DC Bias=20 V.

on the band-gap of the transmission line, which arises at the CRLH transition frequency. This is demonstrated in Fig. 5.18, where the scattering parameters of the non-linear line of Fig. 5.16 are shown as a function of the bias voltage. Fig. 5.18a shows the S parameters in the case of $V_{BIAS} = 0$ V. As can be observed, a band gap appears at the transition frequency of the line, i.e. the line is clearly unbalanced (see the gap which appears around the transition frequency, $f = 2.55$ GHz). However, after changing the bias voltage to $V_{BIAS} = 20$ V, the total shunt capacitor of each unit cell is modified, leading to the scattering parameters of Fig. 5.18d. In this case, the band gap is electronically closed, due to the varactor influence (the shunt resonance has been modified and now is able to cancel the series resonance). It is important to remark the very good agreement obtained with the unit

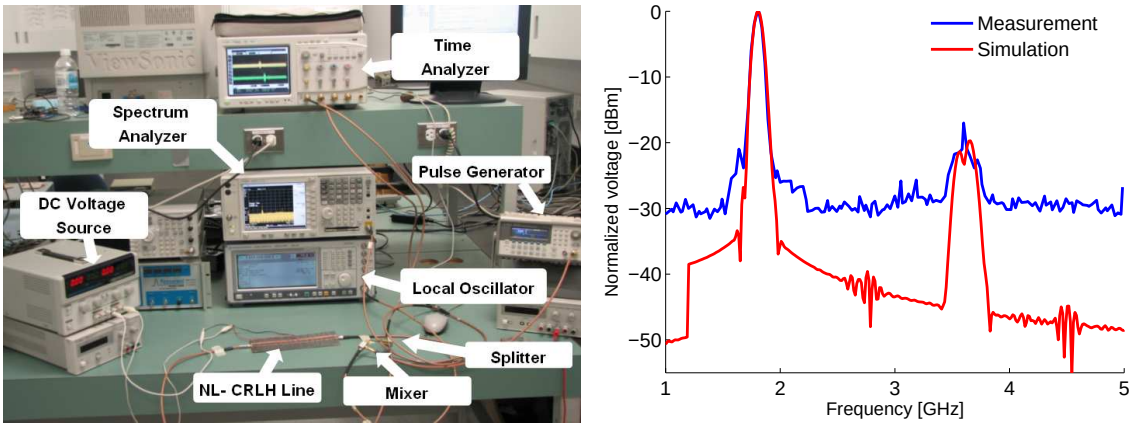

Figure 5.19 – Experimental study of pulse propagation along a non-linear CRLH transmission line. (a) Overview of the entire set-up and equipment employed. (b) Spectrum of a modulated Gaussian pulse ($f_0 = 1.8$ GHz, $\sigma = 4.5$ ns, see Appendix A) after its propagation along the non-linear CRLH transmission line of Fig. 5.16, computed by the non-linear time-domain Green's functions approach and validated against measurements.

cell model proposed in Fig.5.17 as compared with measurements (even in the case of different bias voltages), confirming the accuracy of the proposed model.

In order to further validate the the non-linear formulation proposed in Section 4.3.2 of Chapter 4, pulse propagation along the non-linear line of Fig. 5.16 is studied. In this case, the formulation is modified in order to take into account the novel unit-cell circuital model proposed in Fig. 5.17. The experimental set-up employed for the study is shown in Fig. 5.19a. The Gaussian pulse generated using an arbitrary pulse generator is modulated using a microwave mixer and is then fed into the non-linear CRLH line. Finally, the output pulse is recovered by a spectrum analyzer. Note that a DC voltage source is employed to control the DC bias of the varactor. Fig. 5.19b presents the output spectrum of the modulated Gaussian pulse ($f_0 = 1.8$ GHz, $\sigma = 4.5$ ns and $V_0 = 5$ V) after its propagation along the non-linear CRLH transmission line of Fig. 5.16 ($V_{BIAS} = 5$ V), computed by the non-linear time-domain Green's functions approach and validated with measured data. Note that a new Gaussian pulse, modulated at double frequency of the original (around 3.6 GHz), appears at the output due to the second harmonic generation of the non-linear line. The agreement between simulations and measurements is quite good, especially taking into account the set-up tolerances, thus validating the proposed non-linear method.

5.7 Real Time Spectrogram Analyzer (RTSA) System

5.7.1 Introduction

Ultra wide band (UWB) systems have grown in popularity due to their high data rate capability and their immunity to multipath interference [Ghavami et al., 2007], [Oppermann et al., 2004]. In

most of today's UWB systems, such us radar, security and instrumentation or electromagnetic interfence/compatibility, ultrafast-transient signals are involved. In order to accurately observe and understand such signals, both spectral and temporal information are simultaneously needed. Therefore, a real-time spectrogram analyzer (RTSA) is required to monitor these UWB signals, providing the transient behavior of each instantaneous frequency in real time.

In order to analyze these type of nonstationary signals, joint time-frequency representations may be employed. This type of representation consists on a 2-D plot of a signal, where the energy distribution is related to an image in a time-frequency plane. The joint time-frequency representation provides information related to the temporal evolution of each spectral component, and the exact amplitude and location in time of each frequency. Thus, this representation gives a complete characterization of the signal, including frequency, phase and amplitude response. Therefore, this type of representation is ideal for real-time spectrum analysis. In order to obtain the joint time-frequency representation, several numerical techniques can be employed [Cohen, 1989], with spectrograms and the Wigner-Ville distribution being the most common.

The current state-of-the-art in RTSA systems is based on computing the spectrogram related to an unknown test signal. Spectrograms can be obtained employing either a digital or an analogic approach. The choice of one or other approach depends on the technology and frequency restrictions of the input signal. However, independently of the implementation and technology employed, spectrograms suffer from the fundamental "uncertainty principle" limitation, which states [Cohen, 1989]

$$\Delta t \Delta f \geq \frac{1}{2}, \tag{5.21}$$

where Δf is the bandwidth of the gated signal and Δt is the gate duration. This implies an inherent trade off between time and frequency resolution for all spectrograms.

At microwave frequencies, there are two main approaches to obtain the spectrogram of an unknown input test signal:

Digital RTSAs. The use of short-time Fourier transforms (STFT) [Oppenheim, 1996] is the more usual implementation of RTSA at microwaves. The unknown input signal is periodically time-gated and stored in memory buffers, and the STFT is then applied to each temporal piece of the signal as

$$S(\tau, \omega) = \left| \int_{-\infty}^{+\infty} x(t) g(t-\tau) e^{-j\omega t} dt \right|^2, \tag{5.22}$$

where $g(t)$ is a gate function and $x(t)$ is the unknown input signal. This completely digital approach has two main drawbacks. First, it requires the use of fast processors and large memories. Second, due to the previous restrictions, digital-based RTSA are limited to input signals of only a few hundred megahertz and to spectrograms resolutions of only a few microsecond. Furthermore, a delay due to the computational time is always present. Currently available RTSA are restricted to analyze signals with duration of less than around 50 μs. Therefore, this type of RTSA are not appropriate to characterize UWB signals.

Bank of Filters. In this approach, the unknown input signal is split into different channels and filtered out employing a bank of filters. The filters are designed to have a contiguous central

frequencies. After each filter, a receiver is employed to monitor the temporal evolution of each channel. Finally, the outputs of all filters are combined to generate the desired spectrogram of the unknown input signal [Amin and Feng, 1995]. The main disadvantage of this approach is that it requires a very large number of channels, in order to obtain high frequency resolutions. Consequently, the system is very complex and expensive. Furthermore, extremely narrow-band filters are required in order to implement the bank of filters. This is very challenging, specially at high frequencies. Due to all these restrictions, this RTSA approach has never been implemented or experimentally verified at microwaves.

At optics, RTSAs are usually fabricated employing an analog implementation of the STFT. This is usually obtained by a self-gating process achieved by a nonlinear second-harmonic generating crystal [Trebino, 2002]. Another possibility is the use of Bragg cells [Lee and Wight, 1986].

Recently, an RTSA based on the spectral-spatial decomposition of CRLH LWA was proposed [Gupta et al., 2009a]. In this approach, the CRLH LWA provides an analog implementation of the STFT, in a similar way as it has been implemented in the optical regime. In order to characterize this system, full-wave commercial software may be employed. However, the generation of these results are extremely time consuming due to the complexity of the system and to the temporal nature of the analysis. An interesting and efficient alternative is to employ the theory developed for the modeling of impulse-regime radiation (see Section 4.4.3 of Chapter 4), in order to fully characterize the CRLH LWA RTSA system. For this purpose, the system is first described and analyzed. Then, the results obtained by the proposed numerical technique are validated, first against data from full-wave commercial software, and then against experimental results. It is demonstrated that the proposed approach constitutes an ideal numerical tool to model the analog CRLH LWA RTSA system. It provides not only a fast system modeling technique but also a deep physical insight into the electromagnetic properties of the structure and a complete flexibility in terms of the possible testing pulses.

5.7.2 CRLH LWA RTSA System & Features

The CRLH LWA RTSA proposed in [Gupta et al., 2009a] is shown in Fig. 5.20. The description of the system behavior is as follows. First, the spectral-spatial decomposition of the CRLH LWA is employed to discriminate the frequency components of the input test signal (see Section 4.4.3 of Chapter 4). Second, a set of probes (antenna receivers) monitor the time variation of each frequency component. Finally, a postprocessing step performs the analog/digital (A/D) conversion, the data processing and the display of the spectrogram.

In this RTSA, the CRLH LWA plays a fundamental role. Specifically, its spectral-spatial decomposition property is used to discriminate the frequency components of the unknown input signal. Here, the use of CRLH LWAs [Caloz and Itoh, 2005] over regular LWAs [Oliner and Jackson, 2007] is justified because i) they provide full-space radiation from backfire to endfire in the fundamental mode, offering a simple and real time separation mechanism, ii) they are scalable in frequency and bandwidth, allowing to handle UWB signals, and iii) they provide a simple and compact design and implementation.

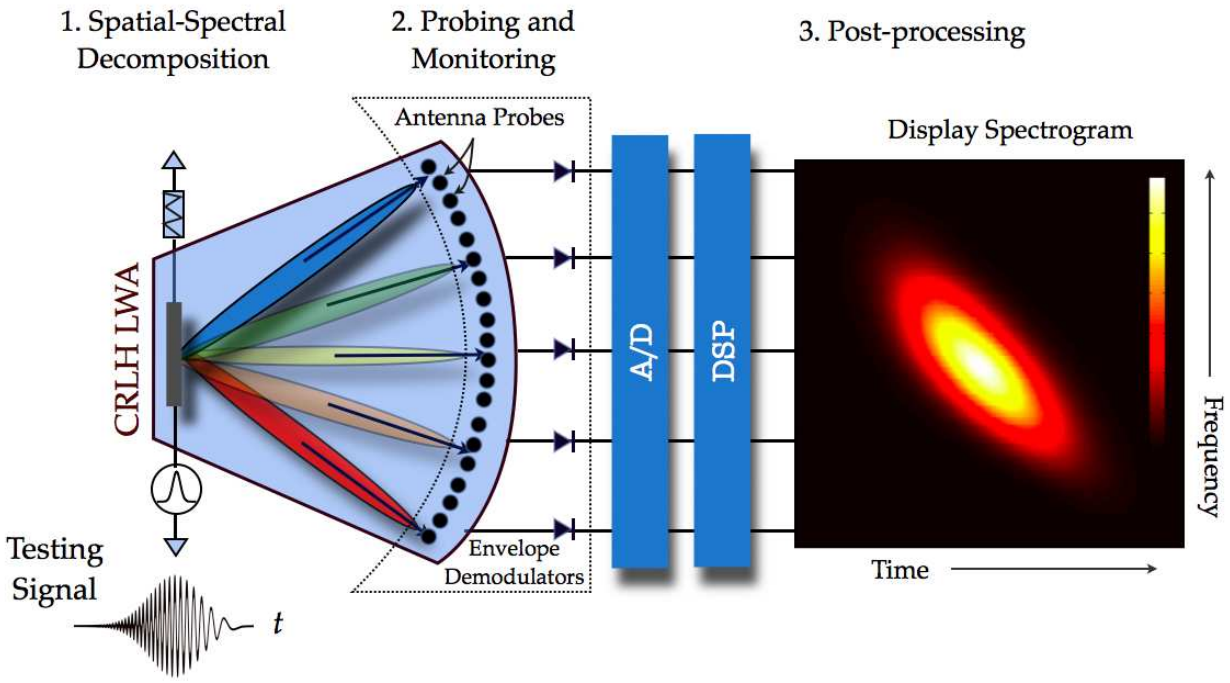

Figure 5.20 – Analog Real-Time Spectrogram Analyzer (RTSA) showing the CRLH LWA, the antenna probes, the envelope detectors, the A/D converters, the DSP block, and the display with the spectrogram. Reproduced from [Gupta et al., 2009a].

Following the impulse-regime behavior of a CRLH LWA (see Section 4.4.3 of Chapter 4 and Fig. 4.28), when a CRLH LWA is excited by a pulse signal, the different spectral components of the input pulse radiate in different directions at any particular instant. Therefore, the CRLH LWA performs an analog spectral to spatial decomposition of the signal, following the beam scanning law of the LWAs [Eq. (4.1)]. In this sense, the CRLH LWA can be seen as a microwave counterpart of an optical diffraction grating, with the advantage that the input signal is fed at a single point of the generator (and it does not require a spatial illumination).

One important step which must be taken before a practical use of the CRLH LWA RTSA system is its calibration. A one-time power calibration procedure is required to take into account for the angular nonuniformity of the radiated signal, due to the actual directive radiation pattern of the CRLH LWA [Caloz and Itoh, 2005]. The power received at each probe location is monitored, and a power normalization vector, as a function of the probe position, is constructed. This vector will compensate for the nonuniform gain profile of the transmitting CRLH LWA and antenna receivers, as well as for free-space losses and possible impedance mismatch. Once the calibration procedure is finished, arbitrary testing signals are recovered as the direct product of the measured signals and the power calibration function.

The analog CRLH LWA RTSA system provides several advantages and benefits as compared with other RTSAs at microwave frequencies. First, this approach is completely analog and real time. Therefore, there is not requirement of large memories and fast processors, just a light postprocessing stage. Second, the same RTSA system can use different CRLH LWAs, in order to be flexible and to

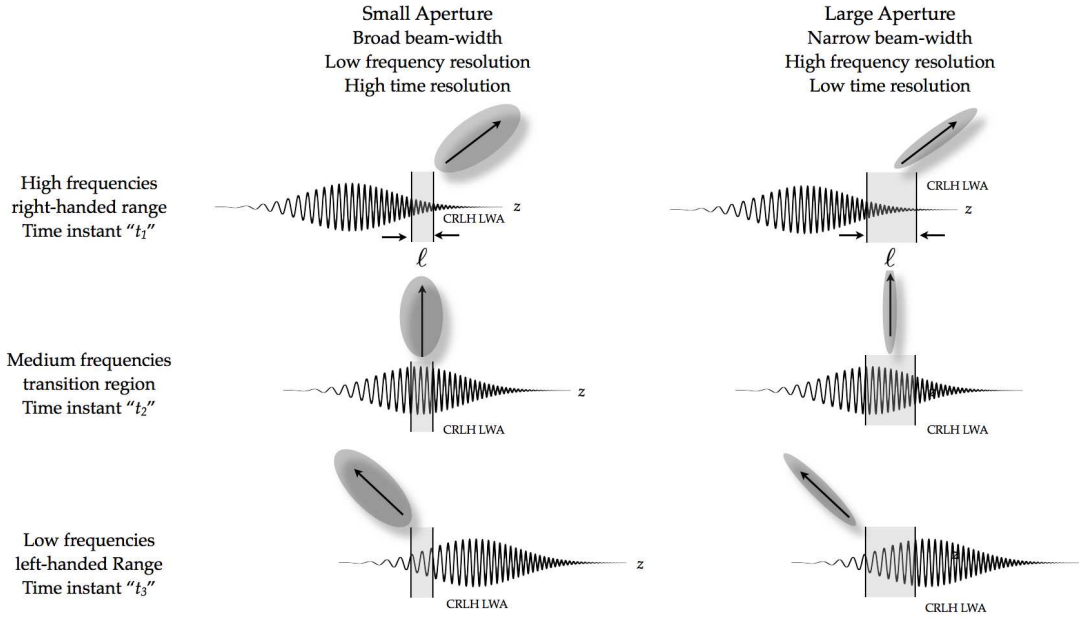

Figure 5.21 – Impact of the LWA size ℓ on the time-frequency resolution of the spectrograms generated by the an analog CRLH LWA RTSA.

cover several frequency ranges. The use of new technologies to fabricate CRLH LWAs allows the use of a wide variety of input signals, from microwave up to potentially millimiter-wave frequencies. Third, the CRLH LWA RTSA system is inherently broadband, and it can be designed to process the 100% of an input signal bandwidth.

On the other hand, the CRLH LWA RTSA system has also to deal with some drawbacks. First, it requires a far-field probe configuration, which makes the system relatively large. However, the system can possibly be compacted employing near-field to far-field transformations (which will add additional postprocessing and will complicate the system). Second, the physical length of the LWA represents a space-gating mechanism which controls the time resolution of the resulting spectrograms. This is clearly shown in Fig. 5.21, where a slice of the signal's spatial waveform is presented on and radiating from the antenna. This space-gated waveform experiences spatial-spectral decomposition from the CRLH LWA where its various spectral components are discriminated in space. The shorter the antenna, the better the sampling of the signal spatial profile, which leads to a better temporal resolution (and vice versa). This space gating is equivalent to a temporal gate of $\Delta t = \ell/v_g$, where v_g is the group velocity along the LWA. Third, the time and frequency resolution also depends on the detector's response time and sampling frequency. Forth, the physical length of the aperture controls the directivity of the LWA (i.e. the frequency resolution of the generated spectrogram). Therefore, the longer the antenna, the better the frequency resolution of the spectrogram (but worse time resolution, as previously explained). Finally, the total number of probes placed in the far field of the antenna also controls the frequency sampling of the spectrogram. Due to this fundamental tradeoff between time and frequency resolutions, *the length of the CRLH LWA antenna is critical*. A particular analog RSTA will have a specific minimum time resolution directly related to this length. However, a commercial analog RTSA could offer CRLH LWAs of different lengths, which could be switched by the user to accommodate different signals.

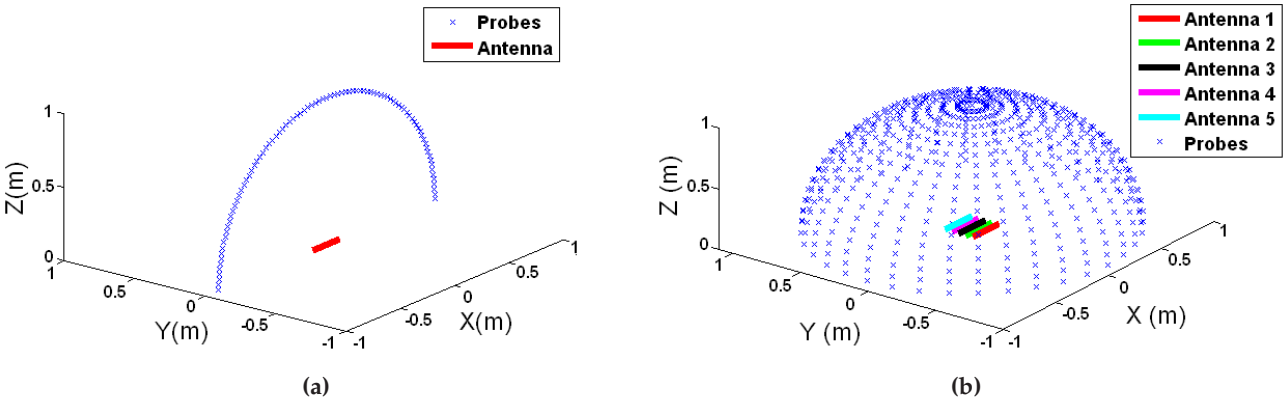

Figure 5.22 – CRLH LWA configuration under study. a) 1D antenna composed by 16 -1 cm- long cells, with CRLH parameters [1] $C_R = 1.8$pF, $C_L = 0.9$pF, $L_R = 3.8$nH, $L_L = 1.9$nH, and with 91 probes placed in a semi-circular far-field configuration. b) 2D antenna array composed by 5 elements separated by 5 cm, and with 1369 probes placed in a semi-spherical far-field configuration.

5.7.3 Numerical Validation & Experimental Demonstration

In this subsection, the time-domain Green's function approach introduced in Section 4.4.3 of Chapter 4 is employed to model a CRLH LWA RTSA. First, the time-domain Green's function approach is validated against full-wave simulations, reproducing simple spectrograms. Then, the formulation is applied to analyze a finite array of LWA, which provides a pencil-beam. Once the formulation has been validated, its use to model a CRLH LWA RTSA is further studied. Initially, the calibration of the RTSA system is numerically performed, as a function of the CRLH LWA employed. Next, several spectrograms related to complex UWB input signals are obtained and the advantages and drawbacks of the proposed method against full-wave commercial software are discussed in detail. Finally, experimental measurements are included to demonstrate the accuracy of the technique developed to model the CRLH LWA RTSA system.

First, the impulse-regime radiation of both a single CRLH LWA and a CRLH LWA array, shown in Fig. 5.22, is studied with the proposed formulation and validated using commercial software. The antenna under study is composed by a total of 16 -1 cm- long unit cells, with circuital parameters of $C_R = 1.8$pF, $C_L = 0.9$pF, $L_R = 3.8$nH and $L_L = 1.9$nH (see Fig. 5.22a). In the case of the CRLH LWA array, it is composed by 5 identical CRLH LWA elements, which are separated a total of 5 cm from each other (on the y-axis, see Fig. 5.22b). The radiation from the antennas are calculated at specific points in space, which corresponds to the probe locations. Therefore, the proposed model does not take into account for the antenna probe receiving pattern, which are just modeled as simple time-domain observation points in space. However, the influence of these patterns can easily be introduced in the formulation.

The antenna shown in Fig. 5.22a is excited by two input pulses. The first pulse is a simple modulated Gaussian pulse, with $f_0 = 3.1$ GHz, $\sigma = 0.5$ ns, whereas the second pulse has the same features, but including a chirp modulation with parameter $C = 1$ (see Appendix A). The radiation is picked

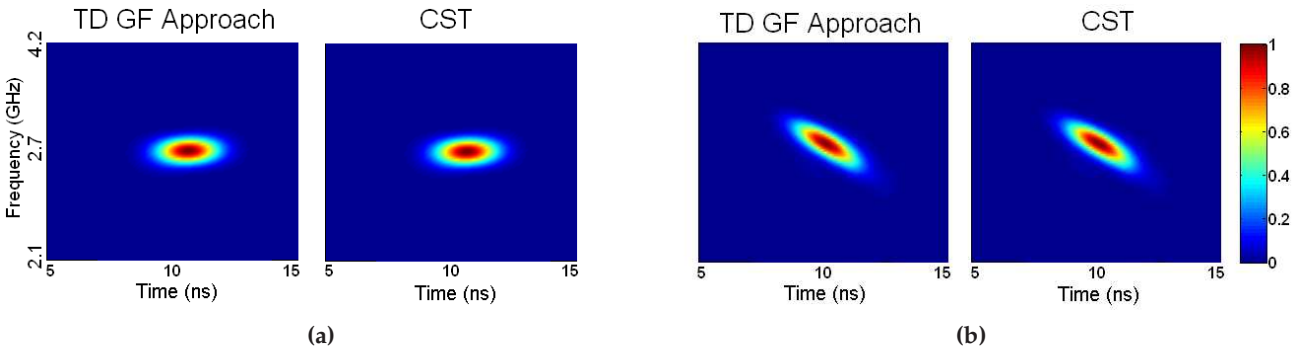

Figure 5.23 – Spectrograms obtained by the proposed time-domain Green's function approach for the 1D CRLH LWA of Fig. 1a, and compared with CST©, results. (a) CW-modulated Gaussian pulse excitation. (b) Chirp-modulated Gaussian pulse excitation.

up by the probes placed in far-field and it is collected in order to compose a spectrogram of the input pulse. As it can be observed in Fig. 5.23, the agreement in the spectrograms obtained by the proposed method and the commercial software CST© is excellent. It is important to remark that the proposed formulation spends about 30 seconds to obtain a single spectrogram, whereas the commercial software CST© lasts about 12 hours to perform this type of simulation (same Pentium IV computer, dual core 2.5 GHz, 2 GB of RAM). Part, but far not all, of this huge computation time reduction is due to the fact that the proposed method uses an equivalent transmission line model of the real antenna.

The proposed formulation has also been applied to analyze the impulse regime response of a CRLH LWA array (see Fig. 5.22b). Specifically, the array is excited by a chirp-modulated Gaussian pulse (with $f_0 = 2.75$ GHz, $\sigma = 0.5$ ns and $C = -3$, see Appendix A). The far-field radiation patterns are presented in Fig. 5.24. Due to the chirp's instantaneous time variation of frequency, the beam is steered as a function of time, providing instantaneous scanning. The analysis was performed in 65.5 minutes, using the proposed time-domain Green's function approach, while CST© failed to produce these results on the same PC due to insufficient computational resources.

Once the proposed formulation has been validated, a complete RTSA system can easily be modeled. For this purpose, consider a CRLH LWA which is composed of 32 unit cells of length $p = 1.0$ cm, with circuital parameters of $C_R = C_L = 1.0$pF and $L_R = L_L = 2.5$nH. In order to complete the analog RTSA system, a total of number of 181 observation probes are placed in a semi-circular configuration, as shown in Fig. 5.22a. The first step to model the RTSA is to perform the calibration of the system. This is necessary to compensate for the different power levels received at each probe [Gupta et al., 2009a], due to the directivity variation with frequency [Caloz and Itoh, 2005]. For the calibration, a narrow-band signal is modulated to the different fast-wave frequencies [following Eq. (4.1) (scanning law)] and subsequently radiated by the LWA. Then, the maximum power received at each probe is stored, obtaining a normalization rule for this particular system configuration. In our example, the calibration data is shown in Fig. 5.25.

After the RTSA system has been calibrated, it can be efficiently used to obtain spectrograms of an unknown input signal. For the method validation, the actual temporal and frequency information

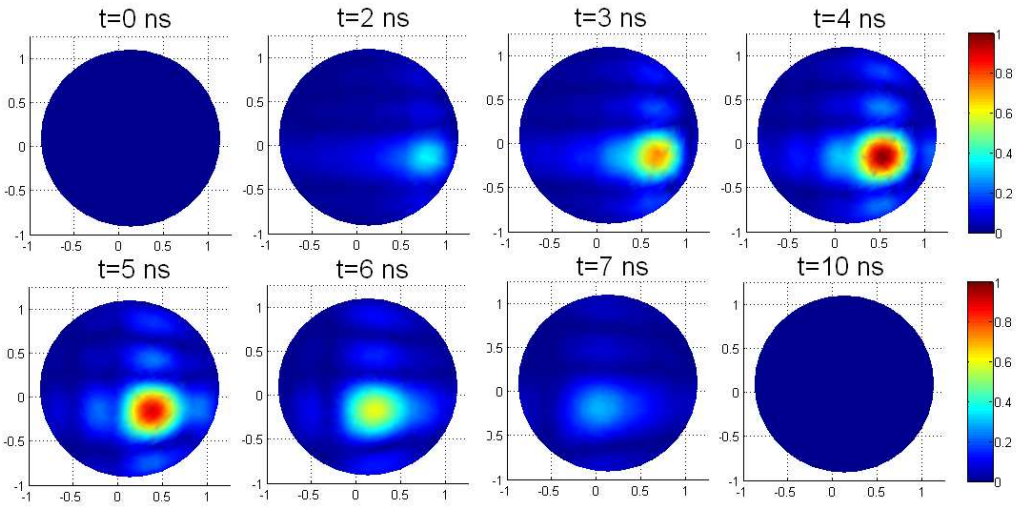

Figure 5.24 – Real-time normalized electric field radiated by the CRLH LWA array of Fig. 5.22b computed by the proposed time-domain Green's function approach (top view of the semi-spherical region) as a function of time for a chirped-modulated Gaussian pulse excitation. The radiation angle from array phase feeding is here of 45° in the yz plane (see Fig. 5.22b).

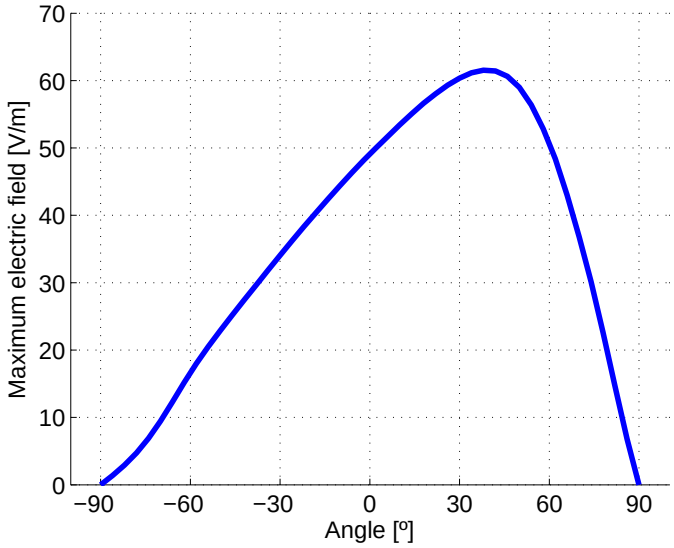

Figure 5.25 – Maximum electric field obtained at the different positions of the probes, used for the calibration of a RTSA system. The CRLH LWA employed is composed of 32 unit cells of length $p = 1.0$ cm, with circuital parameters of $C_R = C_L = 1.0$pF, $L_R = L_L = 2.5$nH.

of an input test signal, previously known, is employed.

In the first example, the CRLH LWA is fed by a signal composed of three modulated Gaussian pulses. The first pulse has a positive-chirp modulation (which means that the modulation frequency is increasing with time), and the third pulse has a negative-chirp modulation. The spectrogram obtained with the proposed method, after calibration, is depicted in Fig. 5.26, including an additional

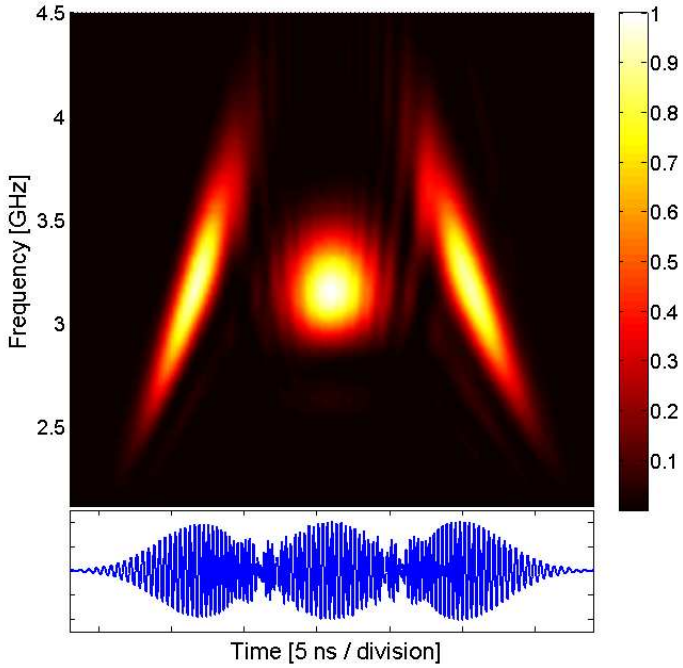

Figure 5.26 – Normalized spectrogram of a three chirp-modulated Gaussian pulses, with chirp parameters $C = -[10, 0, 10]$, modulation frequency $f_0 = 3.19$ GHz and temporal width $\sigma = 1.0$ ns (see Appendix A), computed with the proposed technique. The inset shows the analytical time response of the signal.

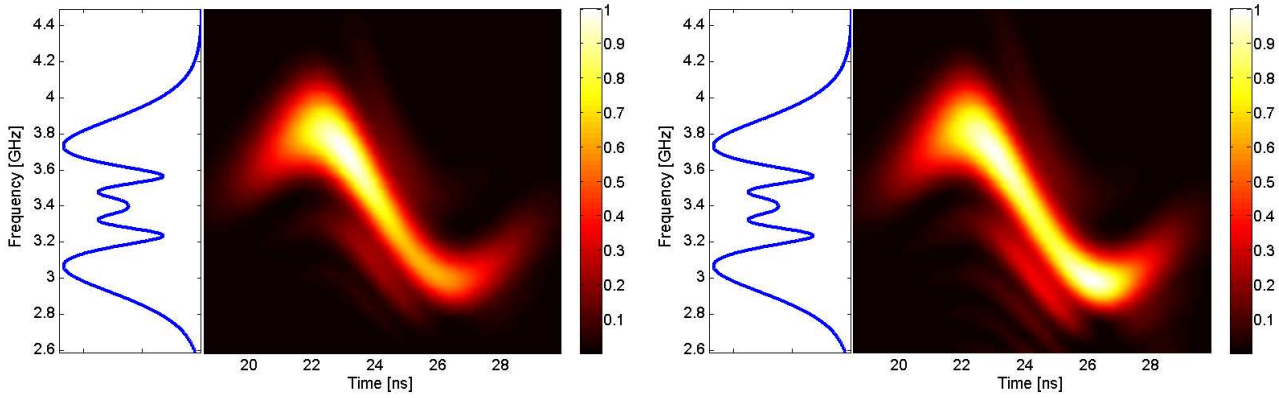

Figure 5.27 – Normalized spectrogram of a self-phase modulated pulse (SPM), with $f_0 = 3.4$ GHz, $m = 1$, $z = 10$ and $\sigma = 1.0$ ns [following the notation of Appendix A]. The inset shows the analytical frequency response of the signal. (a) Without power calibration. (b) Including power calibration.

graph showing the analytical temporal representation of the signal. As can be observed in the figure, the spectrogram follows the signal variations in time (the three pulses are clearly observable) and also, simultaneously, in frequency. It is especially interesting to observe the transition between two consecutive pulses, where frequencies corresponding to different pulses appear at the same instant.

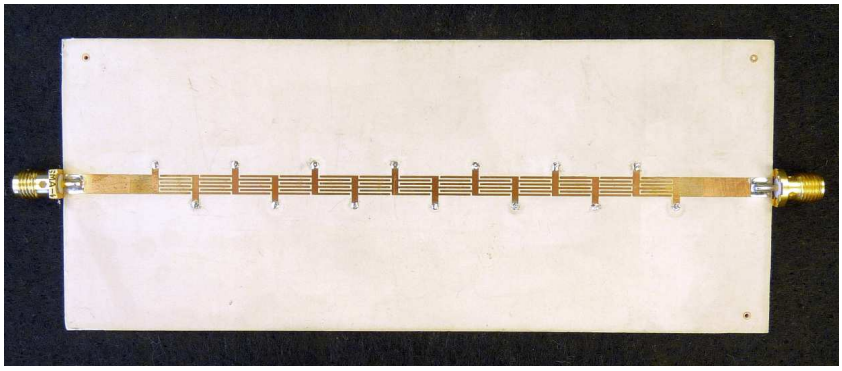

(a)

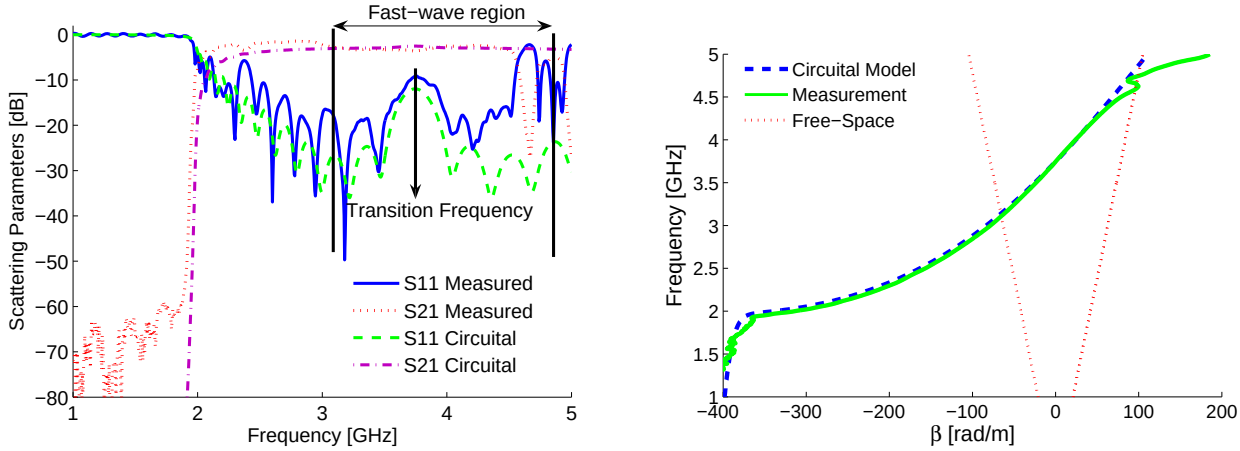

(b) (c)

Figure 5.28 – 1D CRLH LW antenna composed by 14 -0.8 cm- long cells, with circuital parameters $C_R = 1.29$ pF, $C_L = 0.602$ pF, $L_R = 3.0$ nH and $L_L = 1.4$ nH. a) Photo of a microstrip CRLH LWA prototype. b) Scattering parameters. c) Dispersion relation.

In the second example, a self-phase modulated pulse is employed to feed the CRLH LWA. This pulse has strong variations in frequency, as show in Fig. 5.27. The spectrogram has been obtained using the formulation presented, initially without the power compensation [see Fig. 5.27a] and then introducing this correction [Fig. 5.27b]. As can be seen in the figures, the calibration system correctly modifies the spectrogram levels, accurately characterizing the input pulse both in frequency and time. Note that the antenna length plays an important role to frequency discrimination, because it is related to the antenna directivity. A larger antenna, with increased directivity, will also be able to follow the faster frequency variations of the pulse.

The main advantage of the RTSA system is its analogue nature, able to provide real-time spectrogram results in practice. The method proposed here is able to perform a quick (about 30 seconds) and accurate modeling of the system, with deep insight into the CRLH LWA time-radiation properties, and avoiding the extremely time-consuming analysis required in full-wave simulations (usually between $8 - 12$ hours). Therefore, it provides a fast tool to configure an RTSA system and to determine a priory the range of input signals which can accurately be characterized for a given CRLH LWA..

Finally, experimental results from a RTSA prototype are included for a complete system valida-

tion. For this purpose, a CRLH LWA fabricated in microstrip technology and composed of 14 -0.8 cm-long unit cells, with circuital parameters $C_R = 1.29$ pF, $C_L = 0.602$ pF, $L_R = 3.0$ nH and $L_L = 1.4$ nH, is employed. A photo of the fabricated antenna is depicted in Fig. 5.28a, whereas a comparison of the measured and simulated scattering parameters is shown in Fig. 5.28b. Furthermore, Fig. 5.28c presents a simulation-measurements comparison of the antenna dispersion relationship. As can be observed, the CRLH LWA presents its transition frequency at 3.745 GHz. The antenna fast-wave frequency region starts at about 3.1 GHz (related to backfire radiation), and it is extended until 4.7 GHz (related to endfire radiation). Note that several resonances occur within the fast-wave frequency region (close to endfire), degrading the antenna performance. These resonances are due to internal resonances of the interdigital capacitors employed in the antenna prototype [Caloz and Itoh, 2005], and they are not considered in the circuital model of the LWA.

In order to measure the spectrogram of the test signals, a single receiver was used and rotated around the circular far-field trajectory of the system (specifically, between $\theta = -80^\circ$ and $\theta = 80^\circ$ with increments of 5°). The RTSA system is calibrated employing a linear frequency ramp. After calibration, the CRLH LWA is excited by a modulated Gaussian pulse, with FWHM of 3.5 ns. Fig. 5.29 presents a comparison between simulations (obtained by the time-domain Green's function approach) and measurements, as a function of the pulse modulation frequency. It can be observed that a very good agreement is achieved in all cases. First, the pulse modulation frequency is set to 3.3 GHz, which corresponds to backwards radiation. This is clearly shown in the spectrograms of Fig. 5.29a and Fig. 5.29b. Then the modulation frequency is set to the CRLH LWA transition frequency, which corresponds to broadside radiation. As expected, the obtained spectrograms (see Fig. 5.29c and Fig. 5.29d) confirm the change in frequency. Finally, pulse modulation frequency is set to 4.2 GHz, which corresponds to a forward direction. Again the spectrograms show the changes in the pulse frequency, experimentally verifying the RTSA system and confirming the usefulness of the proposed theoretical approach to model this type of analog systems.

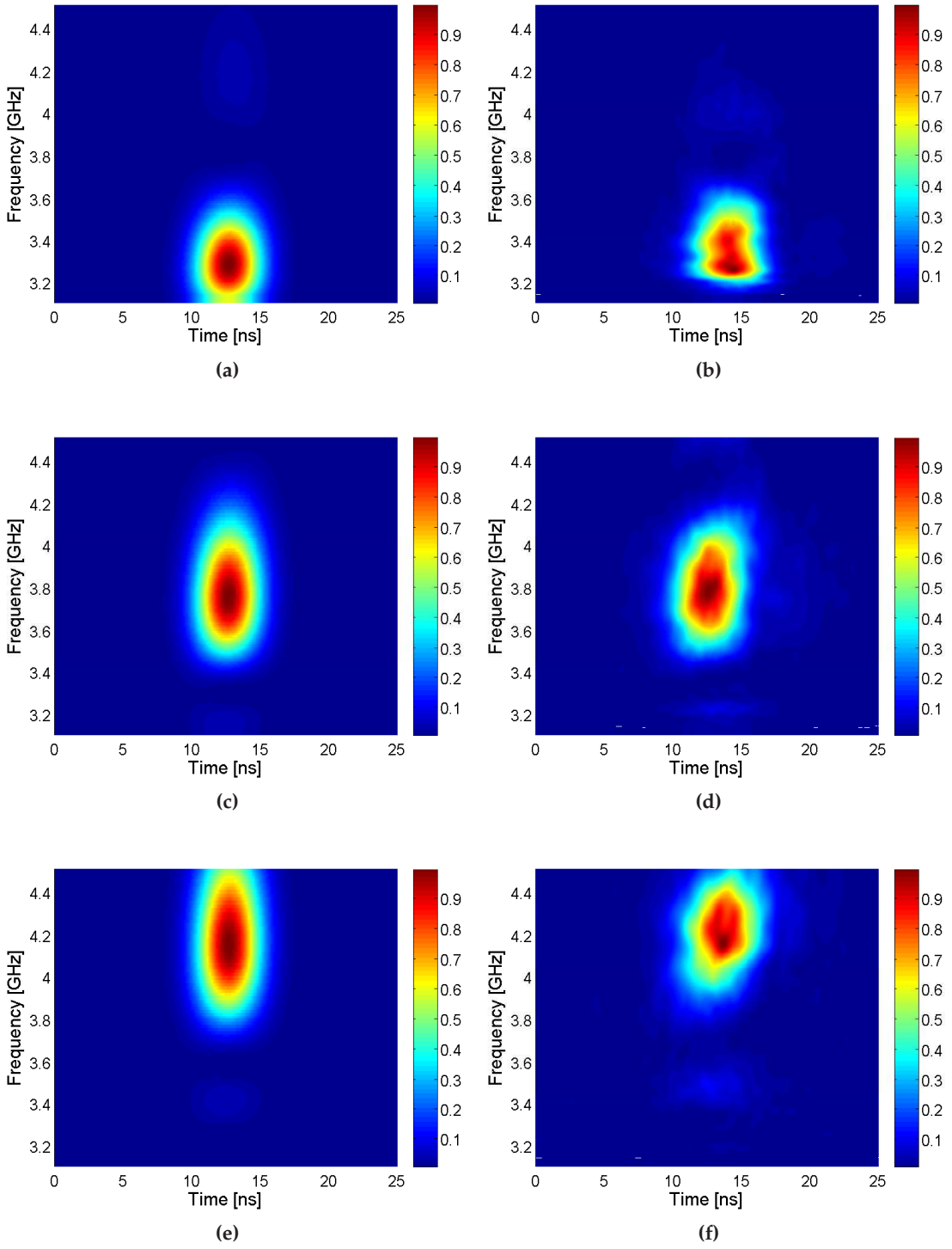

Figure 5.29 – Spectrograms obtained by the proposed RTSA model (figures on the left) and by experiments (figures on the right), employing the CRLH LWA of Fig. 5.28. A modulated Gaussian pulse with $FWHM = 3.5$ ns feeds the antenna. The pulse modulation frequency is set to 3.3, 3.745 and 4.2 GHz, corresponding to backward [(a) and (b)], broadside [(c) and (d)] and forward [(e) and (f)] radiation, respectively.

5.8 Frequency-Resolved Electrical Gating (FREG) System

5.8.1 Introduction

Analog CRLH LWA RTSAs [Gupta et al., 2009a] generate the spectrogram of an unknown input signal in real-time, using the spectral-spatial decomposition property of the leaky-wave antenna, with minimal requirements on computational resources. This system provides important benefits over any other RTSA at microwave frequencies. However, as explained in Section 5.7.2, the time and frequency resolution of the generated spectrograms directly depends on the physical length of the CRLH LWA, which is fixed in a given system. Therefore, a particular antenna can only handle a limited range of input signals, which must fulfil specific time and frequency constrains. This imposes an important limitation to the CRLH LWA RTSA systems.

This section proposes a novel analog approach to obtain spectrograms, where the hardware dependence is suppressed, at the cost of the requirement of periodicity of the input signals. This approach is inspired from a similar system known in optics as Frequency Resolved Optical Gating (FROG) [Trebino, 2002], where a self-gating principle is applied to provide close to ideal spectrograms for arbitrary test signals. Here, we propose a microwave counterpart of the FROG system, which is termed Frequency Resolved Electrical Gating (FREG). This system is very useful for the measurement and characterization of fast-varying non-stationary UWB signals and ultrashort pulses.

5.8.2 FREG System & Features

In order to compute a spectrogram of a signal $x(t)$, a gating function $g(t)$ is required, as was shown in Eq. (5.22). Using a self-gating approach, instead of using a separate time signal as the gate function, the *envelope of the testing signal* itself is used as the gating function, i.e. $g(t) = |x(t)|$. The spectrogram of a signal $x(t)$ is then obtained as

$$S(\tau,\omega) = \left| \int_{-\infty}^{\infty} x(t)|x(t-\tau)|e^{-j\omega t}dt \right|^2 . \tag{5.23}$$

The proposed FREG system, based on this self-gating principle and on the spectral-spatial decomposition property of the CRLH LWA, is depicted in Fig. 5.30. The testing signal, whose spectrogram is to be generated, is split into two channels. One of the channels is envelope detected and passed through a tunable delay line. The two channels are then mixed together. The mixer thus performs the self-gating process at a given time delay instant τ. This self-gated signal is then injected into a CRLH LWA which spectrally resolves it in space. Once the frequency components are separated in space, antennas circularly placed in the far-field of the LWA receive the different frequency components corresponding their angular position. All the received signals are then digitized and summed, before being stored for spectrogram display. This process is repeated for different values of the time delay τ so that the entire test signal is scanned, according to Eq. (5.23), until the spectrogram is fully constructed. Since, the beam scanning law of CRLH LWA is nonlinear in nature, a final post-processing step is required to linearize the spectrogram [Gupta et al., 2009a].

The proposed system exhibits significant advantages over the analog RTSA system and purely digital systems. Due to the self-gating process, neither the time nor the frequency resolutions of the

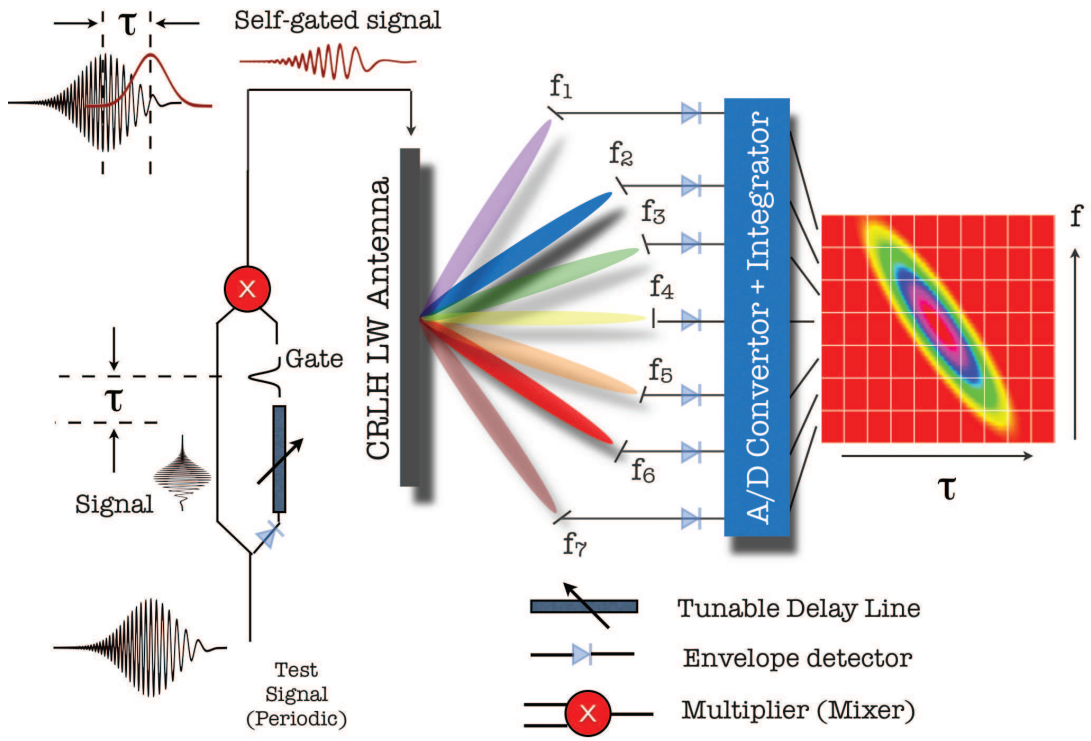

Figure 5.30 – Proposed frequency resolved electrical gating (FREG) system.

generated spectrogram depend on the physical length of the antenna. The time and frequency resolutions are thus dependent only on the time signal itself and the hardware dependence spectrogram is suppressed. The LWA simply plays a role of spectral decomposer which, when longer (higher directivity), provides better separation of frequencies in space.

The choice of the gate duration is an important parameter to achieve an optimal time – frequency resolution in the spectrogram. An optimal gate duration for pulses with dominating phase variations is given by $T_g \approx 1/\sqrt{2|\phi''(t)|}$, where $\phi''(t)$ is the second time derivative of phase [Cohen, 1989]. This duration permits the resolution of the fastest phase variations. For general pulse measurement, a gate duration as short as the testing signal itself or slightly shorter is thus desirable. Since the FREG system is based on self-gating, the gate duration is close to optimal and the corresponding spectrograms are ideal [Trebino, 2002].

Moreover, the proposed system being analog in nature, neither require fast processors nor huge memory buffers, which avoid placing a heavy computational burden on the system. Furthermore, the system is frequency scalable and sufficiently broadband to handle a wide variety of UWB signals. As mentioned above, the length of the LWA controls the spectral decomposition of the gated signal, which is improved as the physical length of the antenna is increased.

Finally, since it uses a multi-shot measurement procedure, where the testing signal is gated sev-

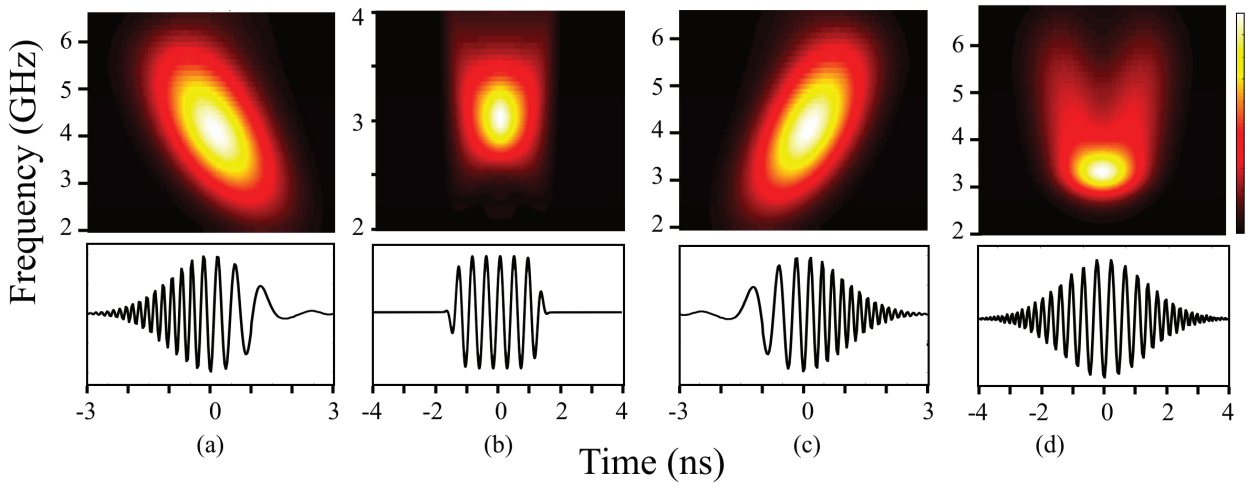

Figure 5.31 – Simulated spectrograms. a) Down-chirped gaussian pulse ($C_1 = -10$, $C_2 = 0$, $f_0 = 4$ GHz). b) Non-chirped super-gaussian pulse ($C_1 = C_2 = 0$, $f_0 = 3$ GHz). c) Up-chirped gaussian pulse ($C_1 = +10$, $C_2 = 0$, $f_0 = 4$ GHz). d) Cubically chirped gaussian pulse ($C_1 = 0$, $C_2 = 0.25 \times 10^{28}$). All pulse have a FWHM duration of 1 ns with a initial pulse offset of $t_0 = 6.5$ ns, and are described using Eq. (A.3) (see Appendix A).

eral times with different time delays τ, the proposed FREG system requires a periodic signal. This is one limitation of the FREG system.

5.8.3 Numerical Validation

In order to simulate the proposed FREG system, the time-domain Green's functions approach presented in Section 4.4.3 of Chapter 4 is employed. The role of this theory is to model the transient CRLH LWA behavior, which provides the spectral-spatial decomposition property and is a key component of the proposed FREG system. Then, the other components of the system are implemented as follows. The envelope of the testing signals are numerically obtained and used as a gating function. The tunable time delay between the replica of the test signal and the gate signal is applied, and the mixer, which performs the self-gating operation, is modeled by a simple mathematical product. The resulting signal is then fed into the CRLH LWA. As a final stage, the temporal radiation computed at the probe locations are integrated as a function of the gate delay (τ), in order to recompose the desired spectrogram.

Once the numerical model of the system is complete, spectrograms obtained from various test signals are computed. For this purpose, consider a 16-cell CRLH LWA with the parameters $C_L = C_R = 1$ pF, $L_L = L_R = 2.5$ nH and a unit cell size of $p = 2$ cm, easily implemented in metal-insulator-metal (MIM) technology [Abielmona et al., 2007]. The various modulated testing pulses are gaussian and supergaussian-type signals which follow Eq. (A.3), described in Appendix A. Fig. 5.31 shows FREG-generated spectrograms. Figs. 5.31(a) and (c) show the spectrograms of a down-chirped and up-chirped gaussian pulses, respectively. A faithful representation of a linear instantaneous

frequency variation is obtained. The spectrogram of a modulated un-chirped super-gaussian pulse is shown in Fig 5.31(b), where the occurrence of all the frequency components of the signal at the same time instant are clearly seen. Finally, Fig. 5.31(d) shows the spectrogram of a cubically chirped (down and up) gaussian pulse. The high frequency components occurring at two different times, characteristic of cubically chirped pulses, can be clearly identified. These few examples demonstrate the capability of the proposed FREG system to analyze a wide variety of non-stationary signals.

It is important to point out that a full-wave simulation of the FREG system is extremely time-consuming. Specifically, the FREG system requires multiple analysis of the impulse-regime response of a CRLH LWA, fed by different input signals. Since each of these analysis lasts between $8-10$ hours, the simulation of a complete FREG spectrogram may easily lasts few days, which is completely prohibitive. On the other hand, the use of the time-domain Green's functions approach reduces this time to a few $(5-8)$ minutes. Furthermore, the use of this numerical tool provides a deep insight into the physics of the system, including an electromagnetic modeling of the antenna and a clear understanding of each step of the proposed FREG system.

Finally, a comparative between the FREG and the RTSA systems is given in Fig. 5.32. The goal of this analysis is to point out the advantages and disadvantages of each method. For the comparative, the same input pulse feeds the RTSA and FREG systems, which are based on identical CRLH LWAs. In the comparative, the number of unit cells N (with size $p = 1.56$ cm and circuital parameters of $C_L = C_R = 1$ pF and $L_L = L_R = 2.5$ nH) of the antenna is modified to perform several tests. The spectrogram results are then given as a function N, i.e. as a function of the total length of the antenna ($\ell = N \cdot p$). For the test, a modulated Gaussian pulse is employed (with $f_0 = 3.0$ GHz and $\sigma = 0.5$ ns). In the figure, the results from the FREG system are placed on the left, whereas the spectrograms computed by the RTSA system are located on the right. First, we set in both systems an antenna with $N = 5$ unit cells, obtaining the spectrograms shown in Fig. 5.32a and Fig. 5.32b. This antenna is physically very short, which turns out into a very low directivity. This leads to a very bad frequency resolution in both spectrograms. On the other hand, this antenna provides an excellent time-gating trade-off, because the energy is radiated as soon as it cames into the antenna, which turns out into an excellent time resolution in the case of the RTSA system. Thereby, the use of a very short antenna leads to generally erroneous spectrograms, due to the wide detection of frequencies which are not part of the input pulse. Second, we modify the CRLH LWA antenna, including now a total of $N = 20$ unit cells. This configuration provides a good frequency resolution in both systems, while the temporal resolution is deteriorated in the RTSA system (due to the use of a longer antenna). The resulting spectrograms are depicted on Fig. 5.32c (FREG) and Fig. 5.32d (RTSA). As it can be observed, the FREG system provides a completely realistic spectrogram, which faithfully reproduces the input signal in terms of frequency and time (location and spreading). On the other hand, the spectrogram obtained by the RTSA has a good frequency resolution, but has some problems dealing with the temporal duration of the pulse. As previously commented, this problem is due to the propagation of the input pulse meanwhile it is being radiated, as graphically illustrated in Fig. 5.21. And third, we simulate the FREG and RTSA systems based on the same CRLH LWA, but composed now of $N = 40$ unit cells. The results are shown in Fig. 5.32e (FREG) and Fig. 5.32f (RTSA). The spectrogram obtained using the FREG system is quite similar to the previous FREG spectrogram ($N = 20$ unit cells), keeping the temporal characteristics but improving the frequency resolution (because a

longer antenna provides higher directivity). All relevant features of the input modulated Gaussian pulse, in terms of frequency and time, can easily be extracted from this spectrogram. However, the RTSA system provides a completely wrong result. This is because of the excessive length of the CRHL LWA, which completely destroy the temporal resolution of the system.

The above comparison demonstrates that the proposed FREG system presents important advantages over the RTSA system, specially in terms on temporal resolution, being able to characterize any unknown UWB input signal. Furthermore, this comparative has shown that the RTSA system can only deal with signals whose characteristics are -at least overall- previously known. On the other hand, the main constrains of the FREG system are the complex equipment required, the requirement of a periodic input signal, and the fact that it is not a completely real-time system.

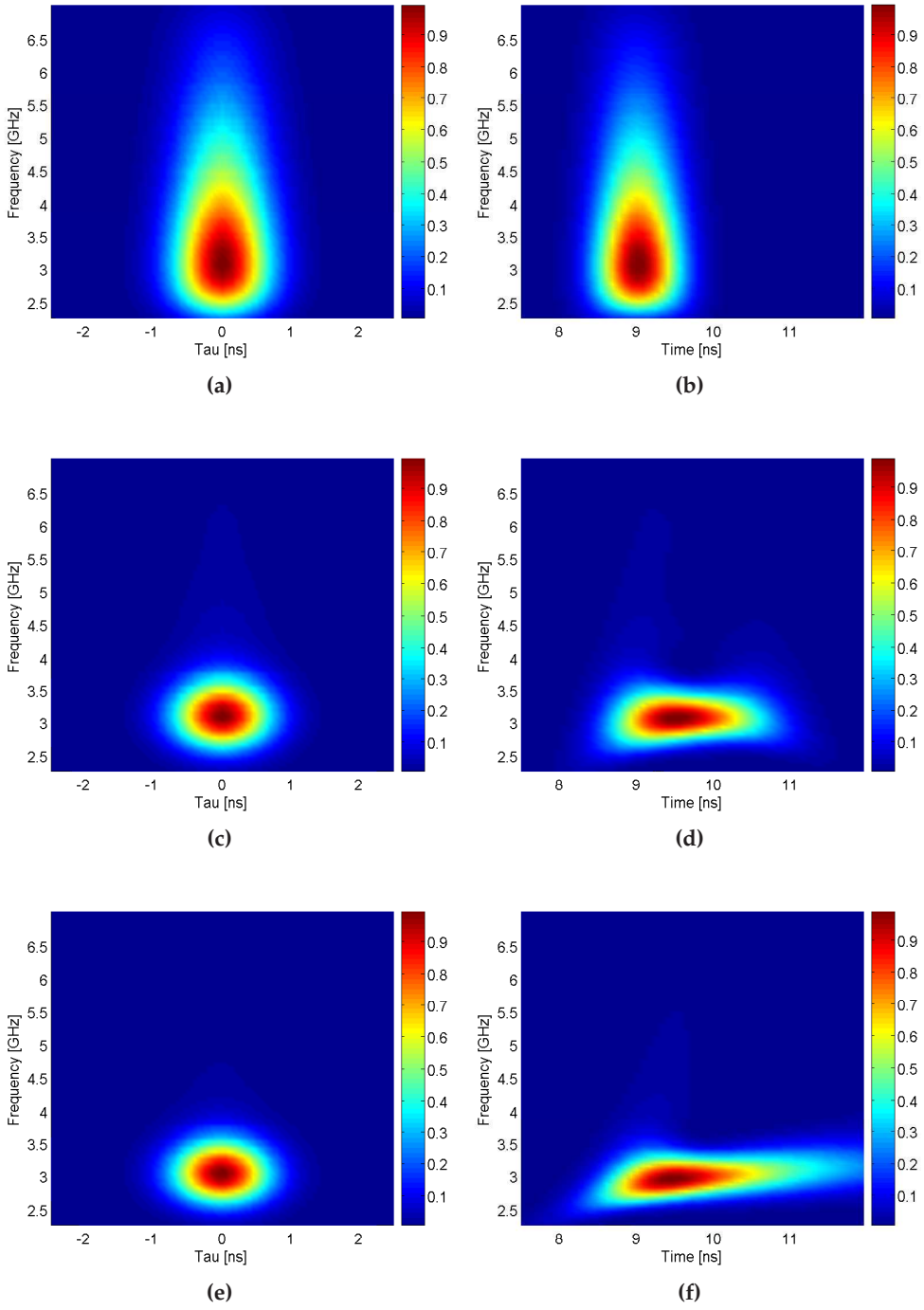

Figure 5.32 – Spectrograms obtained by the proposed FREG (figures on the left) and RTSA (figures on the right) systems, based on identical CRLH LWAs for the different tests. The antennas are composed of different numbers of N cells, with length $p = 1.56$ cm and circuital parameters of $C_L = C_R = 1$ pF and $L_L = L_R = 2.5$ nH. A modulated Gaussian pulse feeds the systems ($f_0 = 3.0$ GHz, $\sigma = 0.5$ ns). The resulting spectrograms are given for the case of $N = 5$ [(a) and (b)], $N = 20$ [(c) and (d)] and $N = 40$ [(e) and (f)] unit cells.

5.9 Spatio-Temporal Talbot Phenomena

5.9.1 Introduction

The Talbot phenomenon was discovered by H. F. Talbot in 1836 [Talbot, 1836]. As was explained in Section 5.4, the spatial Talbot effect occurs when a monochromatic wave is transmitted through (or reflected from) a periodically distributed spatial object. An exact image of the original object appears at a specific distance (called the Talbot distance, z_T) and additional images, with a period multiple of the original object period, appear at fractional distances of z_T. Thanks to the mathematical equivalence between the paraxial Fresnel approximation and the temporal propagation in second-order dispersive medium (such as optical fibers or CRLH media), the Talbot effect posses a temporal counterpart [Azaña and Muriel, 2001]. In this case, an input pulse train is exactly replicated along the dispersive medium at the Talbot distance, and a multiplication of the repetition rate of the periodic signal is observed at fractional Talbot distances.

The spatial Talbot phenomenon has found a wide variety of applications, ranging from array illumination [Lohmann, 1987] or phase locking for laser arrays [Liu, 1989], to the multiplication of the repetition rate of a periodic pulse train [Azaña and Muriel, 1999] or pulse compression [Berger et al., 2004] in the case of the temporal Talbot effect.

In this section, the spatial-temporal Talbot phenomena is introduced. This novel phenomenon, reported in the microwave domain, is based on the combination of the conventional monochromatic spatial Talbot effect and the transient (polychromatic) effect of pulse radiation by a LWA. To produce this phenomenon, an array of CRLH LWAs is fed simultaneously at all of its elements by a modulated pulse (see Fig. 5.33). The beams radiated by the different elements generate an interference pattern which self-image the spatial pulse distribution along the antennas at the Talbot distance. Furthermore, an increase in the repetition rate of this spatial distribution occurs at the fractional Talbot distances. The CRLH LWA, which is sufficiently directive for a given pulse bandwidth, generates a paraxial diffraction (i.e. radiation) of the beams, leading to the spatial Talbot effect. This, combined with the transient nature of the pulsed antenna radiation, leads to the spatial-temporal Talbot phenomenon. In addition, the self-imaging effect replicates the spatial-variation of the pulses as a function of time at each Talbot zones due to the pulses propagation along the CRLH LWAs.

In the next subsection, the general situation of an array of CRLH LWAs fed by a pulse modulated at a particular frequency is studied, and a closed-form solution for the spatio-temporal Talbot distance is given. This distance is equal to the regular spatial Talbot distance for the case of broadside radiation (i.e. modulation frequency set to the transition frequency of the LWA). In addition, note that a change in the modulation frequency provides a variation in the radiation angle (due the scanning law of the LWAs [Oliner and Jackson, 2007]), which also contribute to modify the position of the Talbot distance. This change in the radiation angle can also be exploited to electronically tune the Talbot distance. Moreover, an "aberration frequency region" is defined when the modulation frequency is selected far from the transition frequency of the antenna. Aberrations arise due to higher-order terms of the channel transfer function, and are more important as long as the difference between these two frequencies increases. This affects the self-imaging process, which is progressively distorted, and finally destroyed.

A similar phenomenon, but for the monochromatic case, has been previously reported in the op-

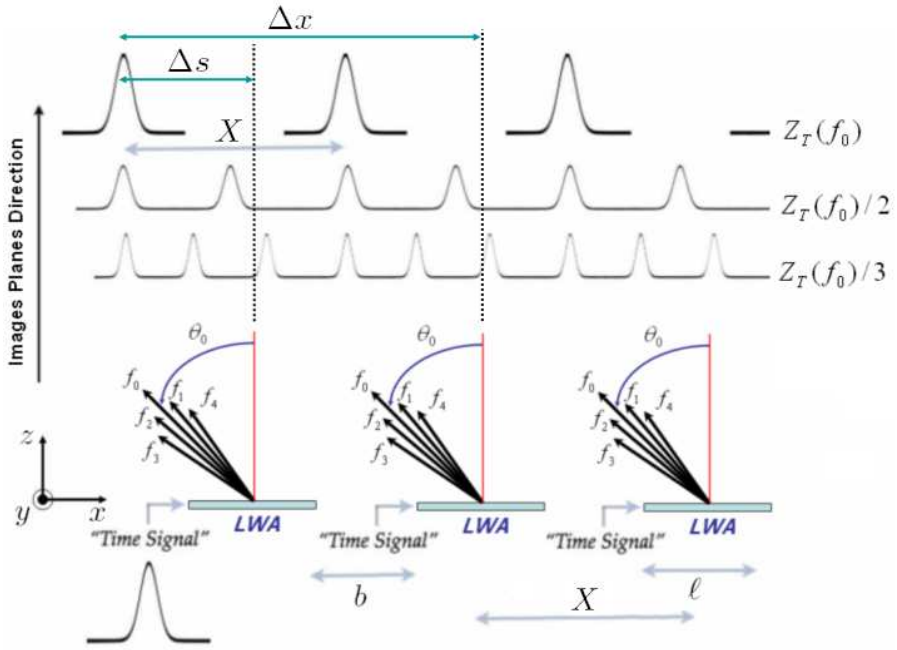

Figure 5.33 – Proposed CRLH LWA array configuration for the investigation of the spatial-temporal Talbot effect. Each antenna radiates the different frequency components of the input modulated pulse to different angles of space. For the sake of simplicity, only the envelopes of the pulses at the main Talbot plane and two fractional Talbot planes are shown.

tical domain, using diffraction gratings [Testorf et al., 1996]. In this case, the diffraction gratings are illuminated with an oblique plane wave. The behavior of the CRLH LWA in the microwave domain is similar to the diffraction gratings in optics, but with several advantages. First, CRLH LWAs are simply fed by an input port. On the contrary, the feeding of the diffraction gratings is more complex, and requires an external device to generate a plane wave. This plane wave is then used to illuminate the diffraction gratings. Second, the CRLH LWA scanning law property [Oliner and Jackson, 2007] electronically performs an off-axis radiation. In the optical domain, the plane-wave generator must be mechanically rotated to achieve a similar type of off-axis radiation [Testorf et al., 1996]. Third, the CRLH LWA is a periodic structure, where the length of the unit cell is electrically very small. Therefore, it does not suffer from important spurious secondary lobes, because it operates in the fundamental space harmonic and the higher space harmonics are very little excited. However, note that the spatio-temporal Talbot phenomenon is only achieved within a particular frequency range. If the phenomenon must be reproduced at a different range, the antennas of the array should be replaced by other antennas designed to operate at that frequency range [Caloz and Itoh, 2005].

The tunable spatio-temporal Talbot phenomenon is then numerically demonstrated using the time-domain Green's function approach presented in Section 4.4.3 of Chapter 4. The self-imaging and the pulse multiplication effects are shown within the tunable frequency region, and the aberrations which arise from off-axis radiation are studied. Finally, an experimental set-up is used to demonstrate, for the first time, this Talbot phenomenon. Specifically, an array of 7 CRLH LWAs is employed to reproduce this effect for the case of broadside radiation at the Talbot distance z_T and also

for the case of off-axis radiation, at the fractional distance $z_T/2$, thereby experimentally validating the proposed theory.

5.9.2 Tunable Spatio-Temporal Talbot Distance

This section presents the detailed mathematical analysis of the spatial-temporal tunable Talbot distance, based on an array of beam-steered metamaterial leaky-wave antennas.

Consider an infinite array of CRLH LWAs, with antenna element spacing b and element length ℓ, where all of the elements are fed simultaneously with the same input pulse, as illustrated in Fig. 5.33. This pulse is modulated at the frequency ω_0 and, assuming the phasor time dependence $e^{+j\omega t}$, it may be expressed as $\Psi(t) = \Psi_0(t)e^{j\omega_0 t}$, where $\Psi_0(t)$ is a slowly varying envelope and ω_0 is the modulation frequency. Due to the time-independence of the Talbot distance [Azaña and Muriel, 2001], the spatial distribution of the field along each CRLH array element, denoted by $A_e(x, z = 0)$, is considered at the fixed time $t = t'$, which may be seen as a "snapshot" of the pulse along the element. Taking all the elements of the *array* into account, the spatial distribution of the field along the overall array takes the periodic form

$$A_a(x, z = 0) = \sum_{p=-\infty}^{+\infty} A_e(x, z = 0) * \delta(x - p\,\Delta x), \tag{5.24}$$

where the symbol "$*$" represents the convolution operation. Taking the spatial Fourier transform of this expression yields

$$\tilde{A}_a(k_x, z = 0) = \Delta k_x \sum_{p=-\infty}^{+\infty} \tilde{A}_e(k_x = p\Delta k_x)\,\delta(k_x - p\Delta k_x), \tag{5.25}$$

where $\Delta k_x = 2\pi/X$ is the spatial repetition frequency and $X = b + \ell$ is the corresponding antenna element spacing (spatial period, see Fig. 5.33).

On the other hand, the transfer function of the CRLH LWA, assuming plane-wave propagation [Oliner and Jackson, 2007], is given by [Saleh and Teich, 2007]

$$\tilde{H}(k_x, z) = e^{-jk_z z} = e^{-j\sqrt{k_0^2 - k_x^2}\,z}, \tag{5.26}$$

where the Helmholtz equation implies the separability condition in the wavenumbers ($k_0^2 = k_z^2 + k_x^2$).

The modulation frequency of the pulse controls the radiation angle (θ), following the CRLH LWA scanning law. When this angle is different from 0°, an off-axis plane-wave propagation in the far-field occurs. In this general case, the spatial frequency is centered around this angle, following the law

$$k_x(\omega) = k_0\,\sin\theta. \tag{5.27}$$

To simplify Eq. (5.26), we can assume that the variation of the angle is relatively small over the frequency bandwidth of the pulse. In addition, due to off-axis propagation, the radiation angle (θ) does not have any restriction, and it may be oriented to any direction.

At this point, we distinguish the radiation angle provided by the modulation frequency of the

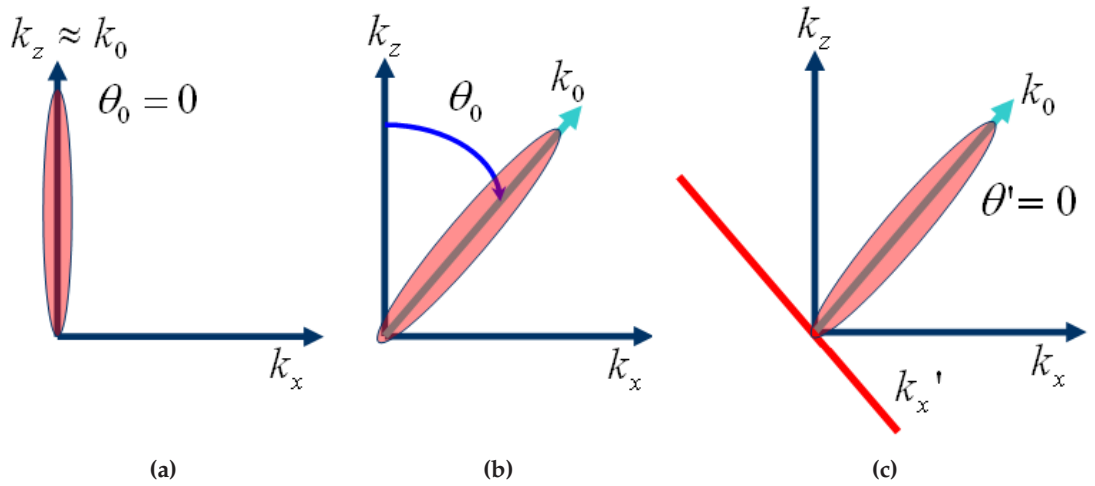

Figure 5.34 – Steered beam radiation in the propagation plane. a) Broadside radiation. b) Radiation in arbitrary direction (off-axis radiation). c) Definition of an auxiliary rotated reference system for the case of off-axis radiation.

pulse, θ_0, and the angle variation provided by the pulse bandwidth, $\Delta\theta$. Taking these two independent contributions into account, the total radiation angle may be defined as

$$\theta(\omega) = \theta_0(\omega_0) + \Delta\theta(\Delta\omega). \tag{5.28}$$

In order to compute the Talbot distance, a change in the coordinate system for the propagation constant is proposed. The idea is to approximate the relationship between the different propagation constants [$k_x(\omega)$ and k_0] with the radiation angle provided by the pulse bandwidth. For this purpose, an auxiliary rotated coordinate system is defined as

$$k_x'(\omega) = k_x(\omega) - k_0 \sin\theta_0. \tag{5.29}$$

This coordinate system depends on the modulation frequency of the input pulse, as graphically illustrated in Fig. 5.34. Inserting Eq. (5.29) into Eq. (5.26), the transfer function of the channel becomes

$$\tilde{H}(k_x, z) = \exp\left\{-j\sqrt{k_0^2 - k_x'^2 - k_0^2\sin^2\theta_0 + 2k_x'k_0\sin\theta_0}z\right\}, \tag{5.30}$$

which, for convenience, may be rewritten as

$$\tilde{H}(k_x, z) = \exp\left\{-jk_0\cos\theta_0\sqrt{1 - 2\frac{\sin\theta_0}{\cos^2\theta_0}\left(\frac{k_x'}{k_0}\right) - \frac{1}{\cos^2\theta_0}\left(\frac{k_x'}{k_0}\right)^2}z\right\}. \tag{5.31}$$

According to the definition of k_x', an auxiliary radiation angle may be defined, using the CRLH LWA scanning law, as

$$\theta' = \sin^{-1}\left[\frac{k_x'(\omega)}{k_0}\right]. \tag{5.32}$$

Independently on the actual radiation direction, for narrow beamwidths we can assume $k'_x \approx 0$, so the ratio k'_x/k_0 is small, and the following approximation holds

$$\theta' \approx \frac{k'_x(\omega)}{k_0}. \tag{5.33}$$

In addition, the square root of Eq. (5.31) may be approximated, using the following Taylor series expansion,

$$\sqrt{1-x} \approx 1 - \frac{x}{2} - \frac{x^2}{8} - \frac{x^3}{16}, \tag{5.34}$$

as

$$\sqrt{1 - 2\frac{\sin\theta_0}{\cos^2\theta_0}\theta' - \frac{1}{\cos^2\theta_0}\theta'^2} \approx 1 - \frac{\sin\theta_0}{\cos^2\theta_0}\theta' - \frac{1}{2\cos^4\theta_0}\theta'^2 - \frac{\sin\theta_0}{2\cos^6\theta_0}\theta'^3 - \frac{5\sin^2\theta_0 + 1}{8\cos^6\theta_0}\theta'^4 - \frac{3\sin\theta_0}{8\cos^6\theta_0}\theta'^5 - \frac{1}{cos^6\theta_0}\theta'^6. \tag{5.35}$$

Note that due to the off-axis radiation, the different components of the Taylor expansion strongly depend on the angle θ_0 (i.e. on the off-axis radiation). In addition, the terms depending on θ^N, with $N \geq 3$, correspond to aberrations. These terms contribute to distort the self-imaging process [Testorf et al., 1996]. The influence of these terms is completely neglectable at the CRLH transition frequency (which corresponds to the broadside direction, where $\theta_0 = 0°$) [Testorf et al., 1996]. However, these aberrations are more and more important as long as the radiation angle θ_0 is different from zero. Since $\theta' \approx 0$, the first aberration term (depending on θ^3) is enough for an accurate characterization of this distortion phenomena. With these considerations, the transfer function of the channel is simplified to

$$\tilde{H}(k_x, z) = \exp\left\{-jk_0[\cos\theta_0 - \tan(\theta_0)\theta' - \frac{1}{2\cos^3\theta_0}\theta'^2 - \frac{sin\theta_0}{2\cos^5\theta_0}\theta'^3]z\right\}. \tag{5.36}$$

Next, the auxiliary angle θ' is linearized around the modulation frequency ω_0, as will be further illustrated later in this section (see Fig. 5.37), as

$$\theta' \approx \xi(\omega - \omega_0), \tag{5.37}$$

where the linearization parameter ξ is defined as

$$\xi = \left.\frac{\partial\theta'}{\partial\omega}\right|_{\omega=\omega_0} = \frac{\partial}{\partial\omega}\left(\frac{k'_x}{k_0}\right) = \frac{c}{\omega_0}\frac{1}{v'_g(\omega_0)}, \tag{5.38}$$

where $v'_g(\omega_0)$ is the group velocity related to the rotated k'_x propagation constant. Introducing the following relationship between the spatial and temporal frequencies

$$v'_g(\omega_0)\,(k'_x - k_{x_0}) \approx (\omega - \omega_0), \tag{5.39}$$

where $k_{x_0} = k_x(\omega_0)$, the angle θ' may be defined as

$$\theta' = \xi\, v'_g(\omega_0)\,(k'_x - k_{x_0}) = \frac{c}{\omega_0}(k'_x - k_{x_0}). \tag{5.40}$$

Therefore, the transfer function of the channel in the rotated coordinate system, $\tilde{H}(k'_x, z)$, may be expressed as

$$\begin{aligned}\tilde{H}(k_x, z) =& \exp\left\{-j\left[\frac{\omega_0}{c}\cos\theta_0 - \tan\theta_0(k'_x - k_{x_0})\right.\right.\\ &\left.\left. -\frac{1}{2\cos^3\theta_0}\frac{c}{\omega_0}(k'_x - k_{x_0})^2 - \frac{\sin\theta_0}{2\cos^5\theta_0}\frac{c^2}{\omega_0^2}(k'_x - k_{x_0})^3\right] z\right\}. \end{aligned} \tag{5.41}$$

In order to derive the Talbot distance, only the third expansion term of the exponential is considered. Note that the first two terms do not provide any information on the Talbot distance. The first term is related to the modulation frequency of the pulse and does not carry any information about the envelope, and the second term represents a k'_x-linear phase factor, equivalent in the spatial-temporal domain to the retarded frame in the time domain. In addition, a forth term appears in this case, due to off-axis radiation. This term does not contribute to the self-imaging process, but it is responsible for additional aberrations. Specifically, the self-imaging process occurs without an important distortion within the following region [Testorf et al., 1996]

$$-25^\circ < \theta < 25^\circ. \tag{5.42}$$

This range is an approximation, which assumes that the aberration terms are negligible inside that region. However, these terms are present at all angles (except broadside) and they will always cause a deviation from the ideal self-imaging process [Testorf et al., 1996]. Note that this angle region does not depend on the separation distance between two consecutive antennas and that, due to the LWA scanning law, leads to different allowed frequency regions for the input pulse, as a function of the particular type of CRLH LWA employed. In addition, note that due to the scanning law of the CRLH LWA, angles outside of the allowed region can be achieved with frequencies higher or lower than the CRLH transition frequency. Therefore, at any other modulation frequency (higher or lower), the aberration terms appear and increase their influence as long as the modulation frequency differs from the CRLH transition frequency.

With the above simplifications and considerations, the transfer function of the system, outside the aberration frequency region, may be rewritten around k_{x_0} as

$$\tilde{H}(k_x^T, z) = \tilde{H}(k'_x = k_{x_0} + k_x^T, z) = \exp\left\{j\frac{k_0}{2\cos^3\theta_0}\frac{c^2}{\omega_0^2}(k_x^T)^2 z\right\}. \tag{5.43}$$

Combining Eq. (5.25) and Eq. (5.43), the output signal radiated at the distance z is expressed in the transformed domain as

$$\begin{aligned}\tilde{A}_r(k_x^T, z) &= \tilde{A}_a(k_x^T, z=0)\,\tilde{H}(k_x^T, z) = \Delta k_x \sum_{p=-\infty}^{+\infty} \tilde{A}_e(p\Delta k_x)\delta(k_x^T - p\Delta k_x)\tilde{H}(k_x^T, z)\\ &= \Delta k_x \sum_{p=-\infty}^{+\infty} \tilde{A}_e(p\Delta k_x)\delta(k_x^T - p\Delta k_x)\, e^{jp^2\phi}, \end{aligned} \tag{5.44}$$

where

$$\phi = \frac{k_0}{2cos^3(\theta_0)}\frac{c^2}{\omega_0^2}\Delta k_x^2 z. \tag{5.45}$$

If the condition

$$p^2\phi = 2\pi q' = 2\pi q p^2, \tag{5.46}$$

with $q, q' \in \mathbb{N}$ (q' varies with p but q is constant), is satisfied, the phase factor in Eq. (5.44) reduces to unity, so that $\tilde{A}_r(k'_x, z) \propto \tilde{A}_a(k'_x, z = 0)$ according to Eq. (5.25), i.e. the field distribution at z (output) is an exact replica of the field distribution at $z = 0$ (input). Therefore, the distance z is the integer Talbot distance, which using $\Delta k_x = 2\pi/X$, yields

$$z_t = \frac{2q'X^2}{\lambda_0}\cos^3\theta_0. \tag{5.47}$$

Some clarifications are needed regarding this tunable Talbot distance. First, additional control over the regular Talbot distance [Talbot, 1836, Azaña and Muriel, 2001] is provided. This may be exploited to tune the position of the Talbot distance, taking advantage of the CRLH LWA scanning law. Second, the new Talbot distance expression directly depends on the radiation angle (θ_0). This behavior is similar to that of a diffraction grating in the optical domain, when illuminated by an oblique plane wave [Testorf et al., 1996]. However, in our case it is the scanning behavior of the CRLH LWA which provides off-axis radiation as a function of frequency. Therefore, it is not required to mechanically rotate a plane-wave generator, as in other optical applications. Third, note that the scanning law depends on the propagation constant of a particular CRLH element (see [Oliner and Jackson, 2007]). Therefore, the tunability of the Talbot distance can also be controlled using a particular antenna with a different scanning law. For the case of broadside radiation, which is common to all antennas and is obtained when the input pulse modulation frequency is set to the CRLH transition frequency, the tunable Talbot distance reduces to the well-known Talbot distance [Talbot, 1836]

$$z_t = \frac{2q'X^2}{\lambda_0}. \tag{5.48}$$

The inverted [$X/2$-shifted Talbot image, obtained by using π instead of 2π in Eq. (5.46)] and fractional spatial-temporal Talbot distances may then be straightforwardly obtained, following the mathematical procedure presented in [Azaña and Muriel, 2001], as

$$z_f = \frac{s}{m}\frac{X^2}{\lambda_0}\cos^3\theta_0, \tag{5.49}$$

where $s, m \in \mathbb{N}$. Specifically, we have $s/m \in \mathbb{N}$ for the integer Talbot distance and its multiples, while s/m is an irreducible rational number for fractional Talbot distances. At fractional Talbot distances, the periodic field distribution along the antenna array [Eq. (5.24)] is reproduced with a repetition rate of m times that of the original distribution. The maximum value of m depends on the spatial width of the pulse distribution along a single antenna X_p [i.e. the width of $A_e(x, z = 0)$], which is typically slightly larger than the spatial width of the input pulse due to CRLH dispersion, and on the spatial repetition frequency X, following the relation [Azaña and Muriel, 2001]

$$m \leq \frac{X}{X_p}. \tag{5.50}$$

If $m > X/X_p$, the imaged pulses overlap in space (spatial aliasing), preventing from the capability of increasing the repetition rate of the original pattern.

It is important to note that the used narrow band assumption of the input pulse leads to the interpretation of the spatial-temporal Talbot effect as a combination of the conventional monochromatic spatial Talbot effect and the impulse nature of the signal, leading to Talbot zones with time-varying patterns as opposed to Talbot planes with time-invariant patterns in the traditional spatial Talbot effect. It should also be noted that since the energy of the pulse is decreasing around its maximum, located at the frequency ω_0, the Talbot zones exhibit a gaussian-like distribution around the maximum at the corresponding centers z_T of the Talbot zones.

Furthermore, note that when the modulation frequency of the input pulse is different from the CRLH transition frequency [Caloz and Itoh, 2005], a spatial shift at the Talbot planes occurs. This spatial shift is due to the off-axis propagation, which induces a lateral shift of the entire radiation given by

$$\Delta x = z_T(f_0)\, \tan\theta_0. \tag{5.51}$$

Besides, it is important to mention that the main contribution to the Talbot distance tunability is due to the change of the frequency itself [see Eq. (5.48)]. However, the frequency change also introduces a variation in the radiation angle, which further modifies the Talbot distance [see Eq. (5.47)], and must rigorously be taken into account for practical designs. In addition, note that the self-imaging process obtained using the off-axis radiation of CRLH LWA is not ideal. This is because of the aberrations found in the description of the free-space transfer function, which cause deviation from the ideal reconstruction of the pulses. The influence of these aberrations is small within the allowed angle region [Eq. (5.42)], but it is always present. Moreover, the narrow-band assumption employed for the paraxial approximation [Eq. (5.33)] and the use of a finite number of antennas for practical cases, also contribute to degrade the quality of the recomposed pulses at the Talbot distance.

Finally, note that the Talbot images reproduce the propagating pulse distribution along the CRLH structures as a function of time. Moreover, a given spatial distribution is imaged *at different times* at the different Talbot distances z_f. The different integer and fractional Talbot distances are known. However, the image formation at each Talbot distance occurs only during a limited time duration, which corresponds to the propagation time of each pulse across each antenna element. To determine the center point of this time duration, we define a reference time t_z as the time required for the pulse to reach the imaging distance from the generator, when it is located at the center of each antenna element. Specifically, this time reads

$$t_z = t_0 + \frac{\text{FWHM}}{2} + \frac{\ell}{2v_g(\omega_0)} + \frac{z_f}{c}, \tag{5.52}$$

where t_0 is the generator switch-on time, FWHM is the full width at half maximum of the pulse (at $t_0 + \text{FWHM}/2$, the maximum of the pulse is at the input of the element), ℓ is the CRLH antenna element length, $v_g(\omega_0)$ is the group velocity at the modulation frequency (at $t_0 + \text{FWHM}/2 + \ell/[2v_g(\omega_0)]$ the pulse is at the center of the element), c is the speed of light, and z_f is the integer or fractional Talbot distance where imaging is considered.

5.9.3 Numerical Validation

In this section, the proposed spatio-temporal Talbot phenomenon is numerically demonstrated employing the time-domain Green's function approach presented in Section 4.4.3 of Chapter 4. First, the phenomenon is studied for the case of broadside radiation (i.e. pulse modulation frequency set to the CRLH LWA transition frequency). This is the simplest situation, because the spatio-temporal Talbot distance reduces to the regular Talbot distance [Talbot, 1836]. Besides, aberrations are not present in this case, and the phenomenon can easily be confirmed. Second, the study is extended to consider off-axis radiation, in order to validate the novel tunable spatio-temporal Talbot distance. This is a more complicated case, because aberrations occurs and may destroy the self-imaging process. A different set of antennas have been employed in each case, in order to further demonstrate that the phenomena can be reproduced with different types of antennas.

The first case corresponds to the broadside radiation of an infinite CRLH LWA array, simultaneously excited by a modulated pulse, whose modulation frequency is set equal to the CRLH LWA transition frequency. In this situation, the spatio-temporal Talbot phenomena should be present, and the corresponding Talbot distance should be the same as in the regular Talbot effect. In order to confirm it, let us consider a CRLH LWA composed of $N = 16$ unit cells of length $p = 1.50$ cm ($\ell = Np$), with the circuital parameters $C_R = 4.5$ pF, $C_L = 2.5$ pf, $L_R = 4.5$ nH and $L_L = 2.5$ nH, corresponding to a transition frequency of $f_0 = 1.50$ GHz [Caloz and Itoh, 2005]. The antenna is excited by an f_0-modulated Gaussian pulse with FWHM of 1.178 ns.

The spatial-temporal Talbot distance with antenna element spacing of $b = 0.5$ m, is computed by Eq. (5.48) as $z_T = 2.738$ m, for an infinite array. In order to validate the proposed analytical approach, Fig. 5.35 presents the magnitude of the field radiated by an array of 20 LWAs at the z_T, $z_T/2$ and $z_T/3$ distances for different radiation directions (z-axis) as a function of the LWA position (x-axis) and of time. For the sake of clarity, only the region of the 10 central antennas is shown. As expected, complete reconstruction of the input spatial periodic distribution is obtained at the integer Talbot distance z_T, and this same distribution with multiplication rate of 2 and 3 is completely reconstructed at the fractional Talbot distances $z_t/2$ and $z_t/3$, respectively. Note that the reconstruction is not perfect, and small distortion effects, due to the truncation of the array (especially at the array edges) and to the high-order dispersive terms, are present. These latter effects are due to the fact that the CRLH structure is not perfectly second-order dispersive in nature, and therefore includes spurious higher-order dispersive terms which alter the reconstruction.

The Talbot patterns observed in Figs. 5.35 are slightly tilted in the $x-$ time plane, with a negative slope. This effect is due neither to a numerical artifact nor to the influence of higher-order dispersion. It is due to the propagation of the pulses along the antenna elements: the energy contributed by the part of the antenna elements closer to the generator is radiated earlier than the energy contributed by the part far from the generator, and therefore reaches the Talbot distance earlier. As it may be observed in the figure, this tilting effect becomes more and more pronounced as the Talbot distances get close to the array, because this represents an increase of the ratio between the antenna element lengths and the radiation distance.

To further characterized the spatial-temporal Talbot phenomenon, let us increase to $b = 0.76$ m

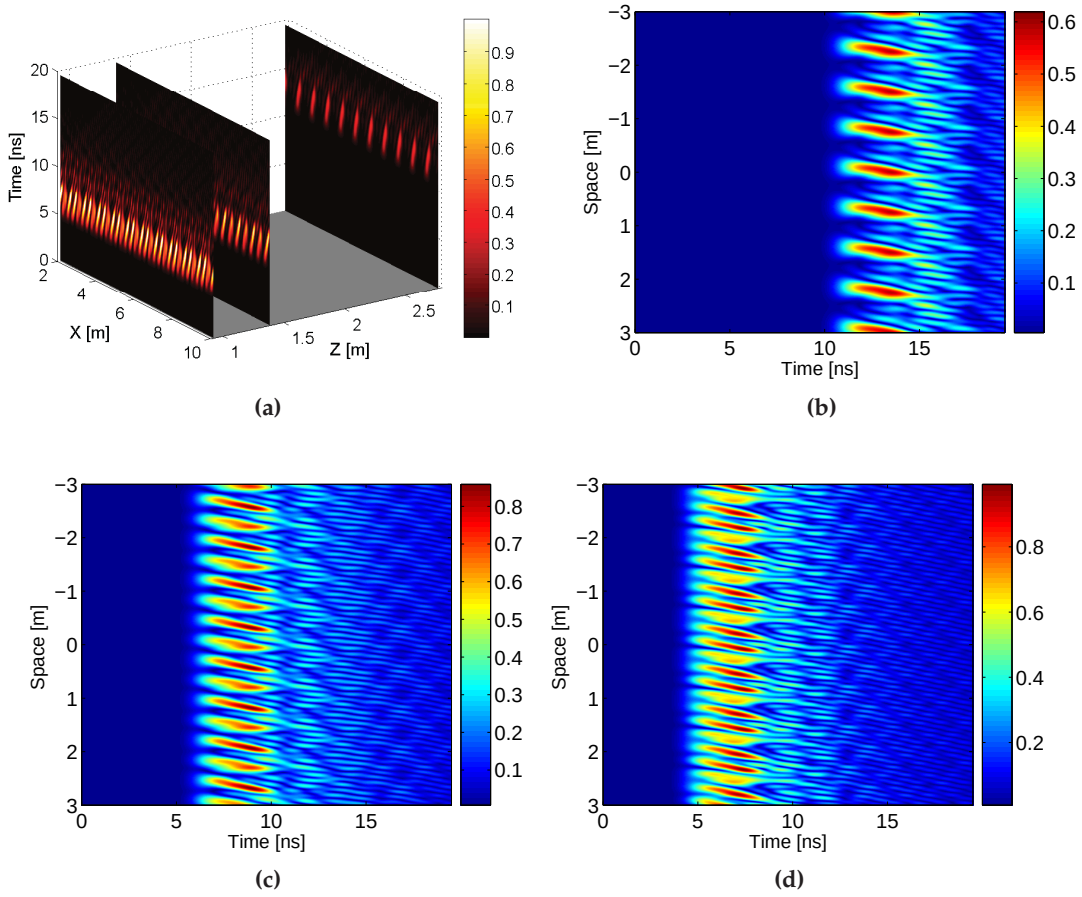

Figure 5.35 – Field (magnitude) radiated by a CRLH LWA array composed of 20 antenna elements (placed at $z = 0$, centered at $x = 0$ and fed by a modulated Gaussian pulse) at different propagation distances (z-axis) as a function of the position x and time. (a) Combined representation at the propagation distances $z_T = 2.738$ m, $z_T/2 = 1.369$ m and $z_T/3 = 0.9127$ m. (b) $z = z_T = 2.738$ m. (c) $z = z_T/2 = 1.369$ m. (d) $z = z_T/3 = 0.9127$ m.

the antenna elements spacing in the array. The new Talbot distance is $z_T = 5.0$ m. Fig. 5.36 presents the radiated field at the distances z_T, $z_T/2$ and $z_T/3$ evaluated at their associated reference times t_z [Eq. (5.52)]. This graph reveals two important facts. First, the repetition rates are in perfect harmonic ratios $(1, 2, 3)$ and perfectly synchronized at t_z. Second, the amplitude of the Talbot pattern decreases for larger distances (from $z_t/3$ to $z_t/2$, z_t, and beyond for multiples), due to free space attenuation, like in the spatial Talbot effect, but unlike in the regular temporal effect.

Once the spatio-temporal Talbot phenomenon has been fully validated, the next step is to demonstrate the tunability of this phenomenon, taking advantage of the CRLH LWA scanning law. For this purpose, and also to confirm that the effect does not depends on the type of antennas employed, we consider now an array of CRLH LWA where each element is composed of $N = 14$ unit cells of length $p = 0.8$ cm ($\ell = Np$), with the circuital parameters $C_R = 1.29$ pF, $C_L = 0.602$ pF, $L_R = 3.0$ nH and $L_L = 1.4$ nH, corresponding to a transition frequency of $f_0 = 3.745$ GHz [Caloz and Itoh, 2005]. Each antenna is excited by a modulated Gaussian pulse with full-width at

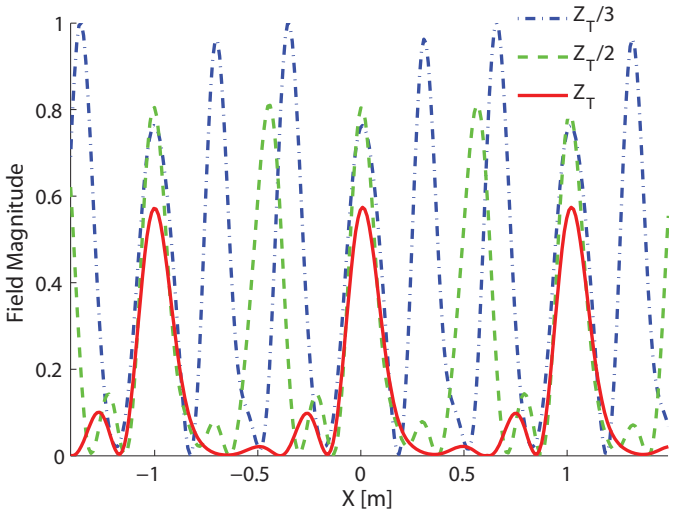

Figure 5.36 – Field (magnitude) radiated by a CRLH LWA array composed of 20 antenna elements (for antenna element spacing of $b = 0.76$ m, placed at $z = 0$, centered at $x = 0$ and fed by a modulated Gaussian pulse) at the distances $z_T = 5$ m, $z_T/2$ and $z_T/3$ computed at their reference time.

half maximum (FWHM) of 3.5 ns. In addition, the radiation of an array composed of 50 elements is considered. This simulates an infinite array around the 10 central antennas, where the results will be again discussed. Initially, we will demonstrate that the approximation employed in Section 5.9.2 are indeed accurate for any pulse modulation frequency. Then, we will focus on the analysis of the spatio-temporal Talbot phenomena results at different frequencies.

The use of the rotated auxiliary propagation constant k'_x provides a fix radiation around the direction ($\theta' \approx 0$), independently of the input pulse modulation frequency. For this purpose, k'_x is dynamically changed as a function of this modulation frequency [Eq. (5.29)]. This effect can be observed in Fig. 5.37, where the auxiliary angle θ', defined in Eq. (5.32), is shown for different modulation frequencies (at broadside, backward and forward). This angle is then linearized around $\theta' = 0°$, using Eq. (5.37). Note that, although in all cases $\theta' = 0°$, the actual radiation direction (θ) changes with the modulation frequency. The linearization procedure provides the paraxial approximation employed for the definition of the tunable Talbot distance. Since it is only valid in the frequency region around $\theta' \approx 0°$, the subsequent mathematical derivations are only valid for the case of narrow-band pulses.

Fig. 5.38 presents the tunable Talbot distance as a function of the input pulse modulation frequency, when the antenna elements spacing is set to $b = 0.388$ m. As it was discussed in the previous section, two frequency regions are clearly observable. The first region, denoted as "Tunable Region", is limited by the allowed angle region of Eq. (5.42), which is translated into frequency through the CRLH LWA scanning law [Eq. (5.27)]. Within this region, the influence of higher-order terms present in the channel transfer function is not very important, and can be neglected. In the second region, denoted as "Aberration Region" (AR), the influence of these terms destroys the self-imaging process and limits the useful frequency region of the tunable spatio-temporal Talbot phenomenon.

In order to validate the tunable Talbot distance, the magnitude of the field radiated by an array

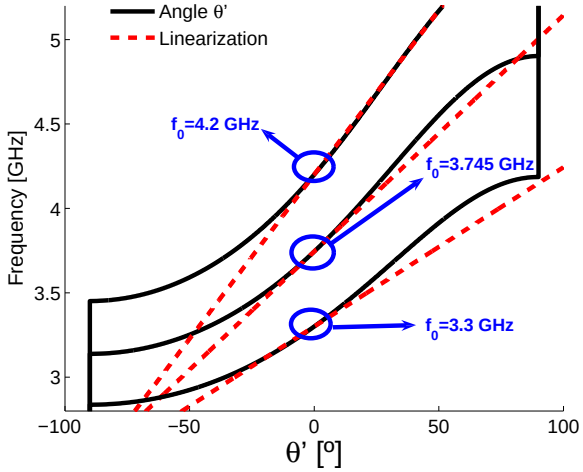

Figure 5.37 – Linearization of the rotated auxiliary angle θ' around broadside ($\theta' = 0$) for different modulation frequencies of the input pulse, computed using Eq. (5.37).

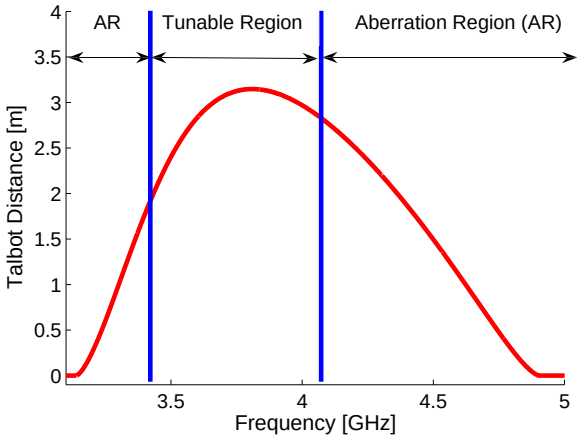

Figure 5.38 – Tunable spatial-temporal Talbot distance as a function of frequency, computed with Eq. (5.47). The circuit parameters of the CRLH LWA employed are $C_R = 1.29$ pF, $C_L = 0.602$ pF, $L_R = 3.0$ nH and $L_L = 1.4$ nH, and the separation distance between two consecutive antennas is $b = 38.80$ cm.

of 50 LWAs at the z_T and $z_T/3$ positions will be shown as a function of the x-axis and of time. For the sake of clarity, only the region of the 10 central antennas is presented.

In Fig. 5.39, the modulation frequency of the input pulse is set to the transition frequency of the CRLH ($f_0 = 3.745$ GHz) which corresponds to broadside radiation. In this case, the influence of the high-order terms is small, leading to a high-quality reconstruction of the pulses, even at the fractional Talbot distance $z_T/3$.

In Fig. 5.40 and Fig. 5.41 the modulation frequency is set to $f_0 = 3.5$ GHz (corresponding to backward radiation) and to $f_0 = 4.0$ GHz (corresponding to forward radiation), respectively. In both cases, the self-imaging phenomenon occurring at the Talbot distance and the pulse multiplication effect occurring at the fractional Talbot distance $z_T/3$ can clearly be observed. However, the

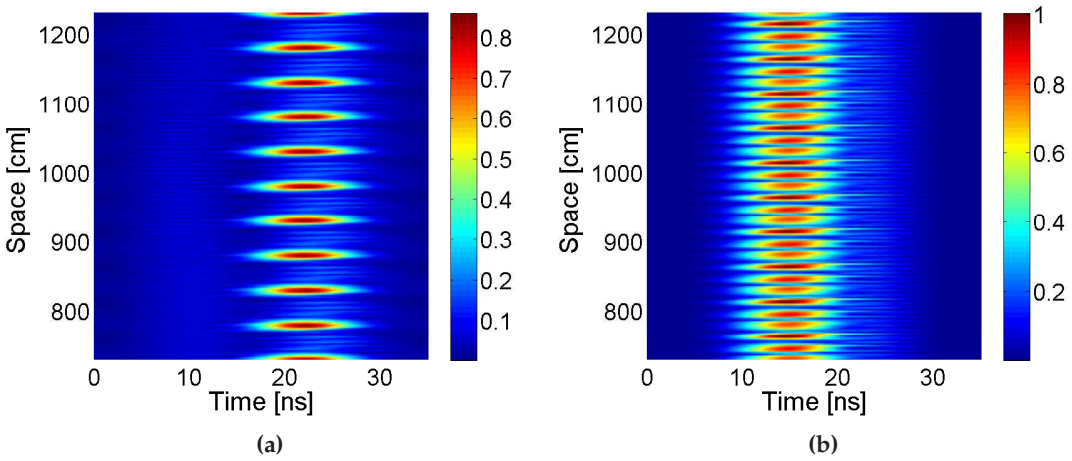

Figure 5.39 – Field (magnitude) radiated by a CRLH LWA array excited by an input pulse with modulation frequency $f_0 = 3.745$ GHz at two different propagation distances (z-axis). a) $z = z_t = 3.1208$ m. b) $z = z_t/3 = 1.0403$ m.

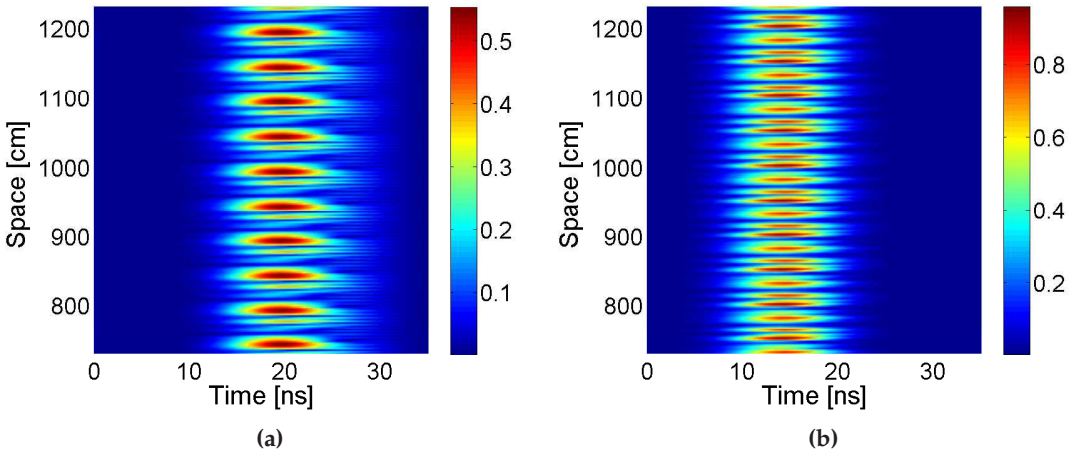

Figure 5.40 – Field (magnitude) radiated by a CRLH LWA array excited by an input pulse with modulation frequency $f_0 = 3.5$ GHz at two different propagation distances (z-axis). a) $z = z_t = 2.430$ m. b) $z = z_t/3 = 0.8100$ m.

reconstruction in this case is not as good as in the case of broadside radiation (see Fig. 5.39), and small distortions and very low-level secondary pulses come out. This is due to the higher-order terms of the channel transfer function, which appear in the off-axis radiation case, degrading the self-imaging process. However, since we are operating in the "Tunable Region" of the Talbot distance (see Fig. 5.38), the influence of these terms is not strong enough to destroy the Talbot phenomenon.

In Fig. 5.42 and Fig. 5.43 the modulation frequency is set to $f_0 = 3.3$ GHz (corresponding to backward radiation) and to $f_0 = 4.5$ GHz (corresponding to forward radiation), respectively. Note that in this case the modulation frequencies employed are in the "Aberration Region", out of the allowed angle range defined by Eq. (5.42). As can be seen in these figures, the self-imaging process

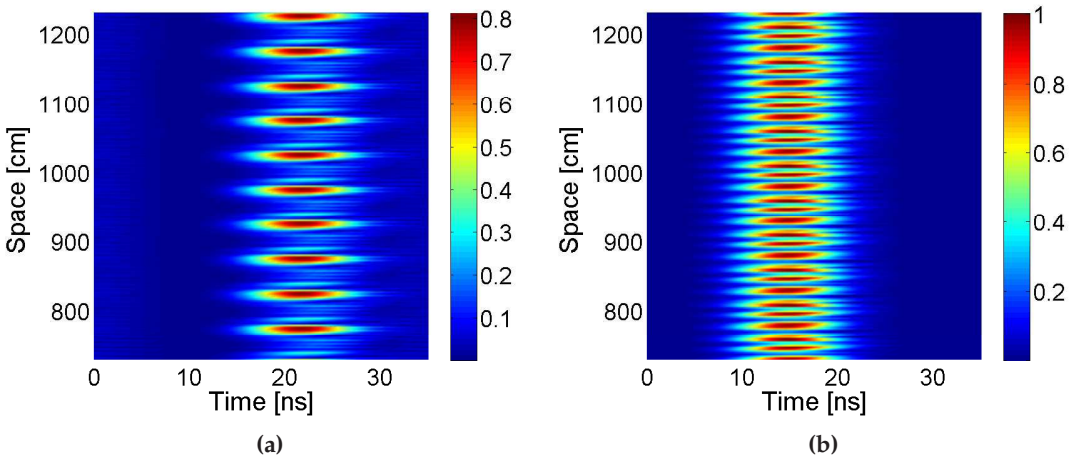

Figure 5.41 – Field (magnitude) radiated by a CRLH LWA array excited by an input pulse with modulation frequency $f_0 = 4.0$ GHz at two different propagation distances (z-axis). a) $z = z_t = 2.926$ m. b) $z = z_t/3 = 0.9753$ m.

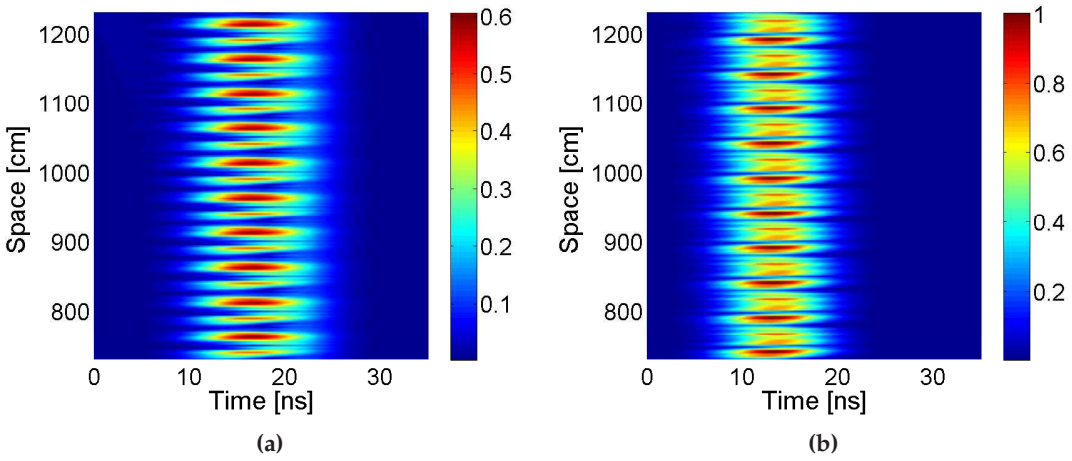

Figure 5.42 – Field (magnitud) radiated by a CRLH LWA array with infinite number of elements excited by an input pulse with modulation frequency $f_0 = 3.3$ GHz at two different propagation distances (z-axis). a) $z = z_t = 1.103$ m. b) $z = z_t/3 = 0.3677$ m.

is not very clear, and the pulses are reconstructed with distortion at the Talbot distance z_T. In the same way, the multiplication pulse effect, which should occur at the fractional distance $z_T/3$, is also destroyed.

Finally, note that a shift in space occurs as a function of the input pulse modulation frequency, following Eq. (5.51). However, taking into account that an infinite (or high enough) number of antennas is considered in the simulations, this shift is not really visible. In fact, in this case only a small shift of the pulses position over the antenna appears (see Fig. 5.33). This shift, denoted Δs, may be

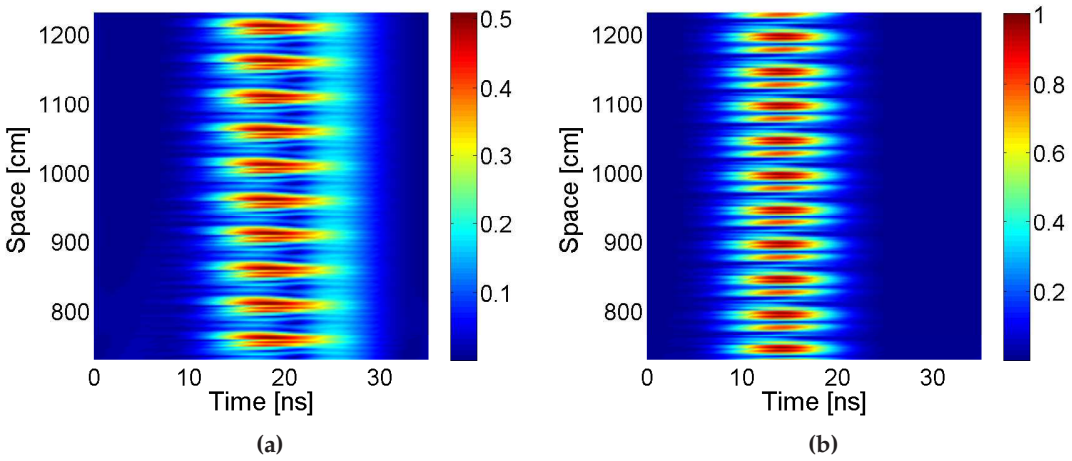

Figure 5.43 – Field (magnitud) radiated by a CRLH LWA array excited by an input pulse with modulation frequency $f_0 = 4.5$ GHz at two different propagation distances (z-axis). a) $z = z_t = 1.221$ m. b) $z = z_t/3 = 0.4070$ m.

calculated as

$$\Delta s = \Delta x - nX, \tag{5.53}$$

where $n \in \mathbb{N}$ is the largest natural number which keeps Δs positive (see Fig. 5.33). For the examples presented in this section, these variations yield $\Delta s = 0.4083, 0.3641, 0.0, 0.3935, 0.0822$ m, corresponding to the modulation frequencies $f_0 = 3.3, 3.5, 3.745, 4.0, 4.5$ GHz, respectively. For instance, consider the pulse located around 783.1 cm for the case of broadside radiation at z_T (see Fig. 5.39a). When the modulation frequency is changed to $f_0 = 3.5$ GHz, the CRLH LWAs begin to radiate at a backward direction. Therefore, that particular pulse is shifted down to a space position around 743.0 cm (see Fig. 5.40), following the space variation predicted with Eq. (5.53).

5.9.4 Experimental Results

This section presents, for the first time, an experimental demonstration of the spatio-temporal Talbot effect. Specifically, this phenomenon has been validated for the case of broadside radiation at the Talbot distance z_T, and also for the case of off-axis radiation, at the fractional distance $z_T/2$, therefore validating the theory proposed in Section 5.9.2.

A diagram of the configuration employed to reproduce the spatio-temporal Talbot phenomenon is sketched in Fig. 5.44. In addition, this figure also shows a picture of the experimental set-up.

The set-up is composed of an arbitrary baseband pulse-generator, which provides a Gaussian pulse. This pulse is then up-converted in frequency using a microwave mixer and a local oscillator. The modulated pulse goes through a Wilkinson power divider [Pozar, 2005], which provides seven identical outputs. Next, seven identical microwave cables are employed to carry the modulated signals to the CRLH LWAs. This step is very important because a small difference in the cables length may destroy the synchronization required to reproduce the phenomenon. The array of 7 CRLH LWA, with an antenna element spacing of $b = 10.8$ cm, simultaneously radiates the modulated pulses. Note

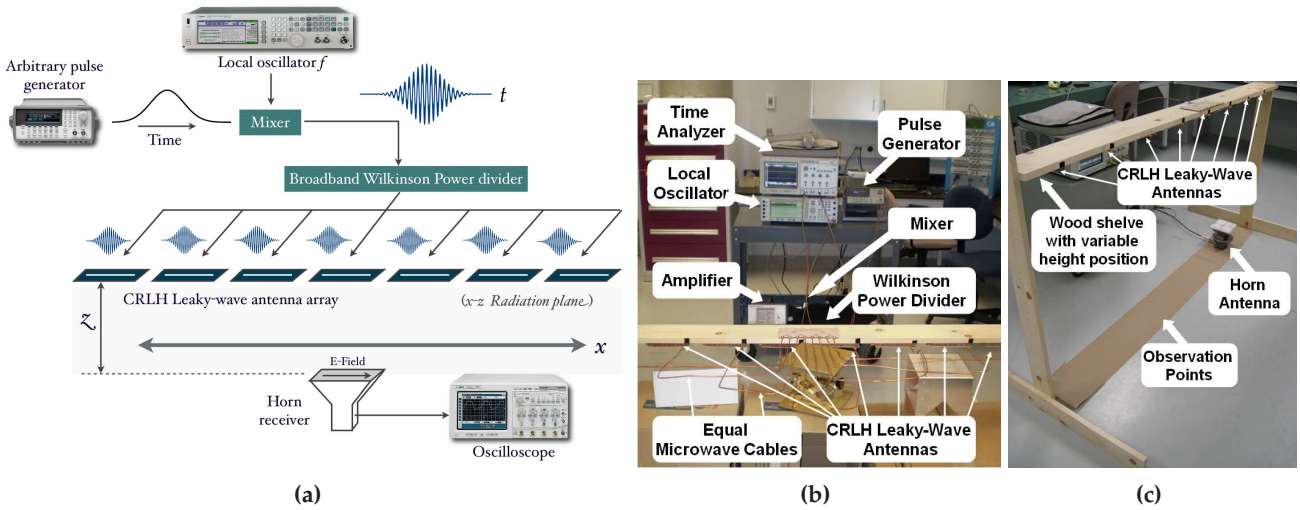

Figure 5.44 – Overview of the entire set-up and equipment employed to reproduce the spatio-temporal Talbot phenomenon. a) Schematic diagram of the proposed experimental set-up. b) Generation, distribution and radiation of the modulated pulses. c) Radiation and reception of the modulated pulses.

that a single CRLH LWAs can be described with the circuit parameters employed in the simulation results of the previous section [$N = 14$ unit cells of length $p = 0.8$ cm ($\ell = Np$), with $C_R = 1.29$ pF, $C_L = 0.602$ pF, $L_R = 3.0$ nH and $L_L = 1.4$ nH]. The same CRLH LWA has also been employed for other radiation problems (see Section 5.7), and it was experimentally analyzed in Fig. 5.28, where a comparison between measured and simulated scattering parameters and dispersion relationship was presented.

As it can be seen in Fig. 5.44, the array of antennas is placed in a wood shelve which can vary its position in height. Therefore, it is simple to place the array at several planes, in order to check the array radiation at different Talbot distances. Finally, the radiation provided by the array is picked up by a horn antenna, placed over the floor. This antenna is moved under the array, along the floor, in order to receive the temporal information of the array radiation as a function of space. For this purpose, a realtime oscilloscope (Agilent Infiniium DS0871204B) is employed.

Fig. 5.45 presents the magnitude of the field radiated by the described CRLH LWA array at the Talbot distance ($z_T = 0.5483$ m), when the modulation frequency of the input pulse is set to $f_0 = 3.745$ GHz. As expected, complete reconstruction of the input spatial periodic distribution is obtained. The agreement between the experimental results and the simulation data is very good, specially considering the high sensitivity of the measuring system.

Finally, Fig. 5.46 presents the magnitude of the field radiated by the described CRLH LWA array at the fractional Talbot distance of $z_T/2 = 0.2874$ m, when the modulation frequency of the input pulse is set to $f_0 = 4.0$ GHz. As expected, double number of pulses is obtained, validating the tunable spatio-temporal Talbot phenomenon at fractional distances. The entire radiation has been shifted-up in space due to the off-axis radiation. This effect is clearly apparent in this situation, because a small number of antennas is employed. This spatial shift can be measured using Eq. (5.51),

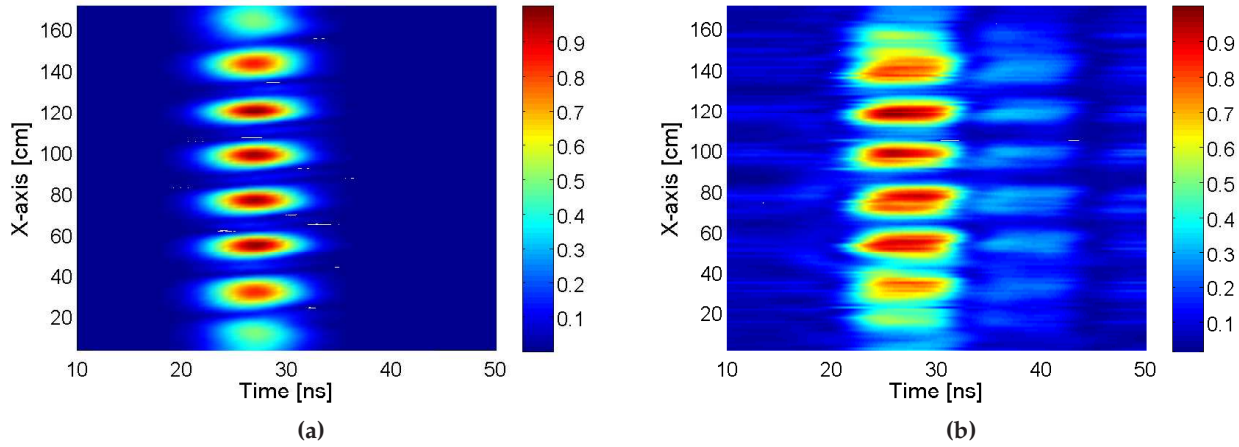

Figure 5.45 – Normalized field (magnitud) radiated by an array of 7 CRLH LWAs elements, excited by an input pulse with modulation frequency $f_0 = 3.745$ GHz at the Talbot distance of $z_T = 0.5483$ m. a) Simulation results. b) Measured data.

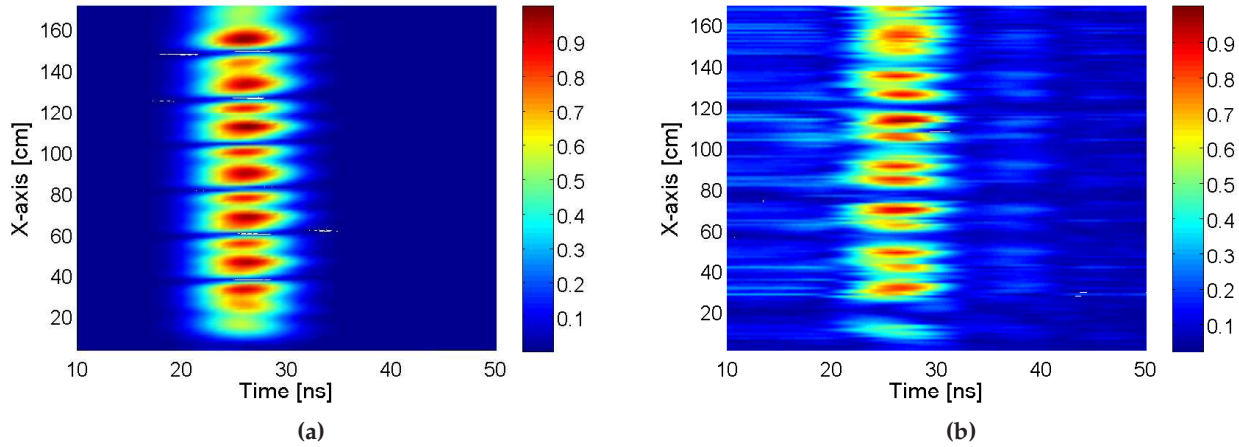

Figure 5.46 – Normalized field (magnitude) radiated by an array of 7 CRLH LWAs elements, excited by an input pulse with modulation frequency $f_0 = 4.0$ GHz at the fractional Talbot distance of $z_T/2 = 0.2874$ m. a) Simulation results. b) Measured data.

yielding $\Delta x = 8.66$ cm.

5.10 Conclusions

In this chapter, I have applied the time-domain Green's function formulation introduced in Chapter 4 to *the development of novel phenomena and applications in the microwave domain, most of them transported from optics*. Instead of the usual magnitude engineering and filter design, a dispersion or phase engineering has been applied (which is related to dispersion and nonlinearity design). In this approach, the dispersive nature and subsequent impulse-regime properties of CRLH transmission lines have been exploited to obtain novel phenomena/applications. Each phenomenon or ap-

plication proposed has theoretically been described, numerically verified, and in most of the cases, experimentally demonstrated. For the analysis, a time-domain Green's formalism has been applied, leading to a fast and accurate analysis, while providing a deep insight into the physics of the problem. Then, the use of time-consuming full-wave commercial software and fabricated prototypes have fully demonstrated the presence and usefulness of the phenomena and applications proposed.

In order to obtain and model the above mentioned phenomena and applications, *the applied dispersion engineering approach has settled a close link between microwaves and optics*. This link is based on the dispersive properties of a CRLH structure, both in the guided and in the radiative regime. In the guided mode, there is a clear parallelism between the inherent dispersion given by an optical component (such as an optical fiber) and a CRLH line. Therefore, the proposed phenomena/applications in this mode reproduces the phenomena/devices which are present in the state of the art at optics. Pulse compression, temporal Talbot effect, a laser-based resonator or the combination of dispersion and non-linear effects are good examples of optical phenomena and devices which have successfully been transported at microwaves. On the other hand, the behavior of a diffraction grating in optics is faithfully reproduced at microwave by a CRLH leaky-wave antenna. Therefore, some phenomena and applications obtained at optics (such as FROG [Trebino, 2002] or the spatial Talbot effect) have also been transported at microwaves, in the radiative mode, leading to the characterization of unknown UWB signals or the development of new spatial multiplexer and wireless array feeding, among others.

The shift from narrow band systems (mostly used in the past) to ultra wide band systems, required by current high date rate wireless communication systems, suggests that the forthcoming decades will experience a major interest on this dispersive engineering approach, providing new, novel and more exciting effects and devices at microwaves.

Chapter 6

PPW CRLH LWAs: Modal-based Analysis, Design and Experimental Demonstration

6.1 Introduction

In Chapter 4 of the present work I have reviewed the basic operation principle of 1D leaky-wave antennas (LWAs) [Oliner and Jackson, 2007], with special focus on metamaterial composite right/left-handed (CRLH) structures [Caloz and Itoh, 2005], [Eleftheriades and Balmain, 2005]. As explained there, this type of LWAs operates using their fundamental guided mode ($\nu = 0$), while conventional LWAs mostly use their first space harmonic ($\nu = -1$) [Oliner and Jackson, 2007]. Besides, these antennas allow to the radiated fan-beam to scan, as a function of frequency, from the backfire towards the endfire directions, including radiation at broadside [Liu et al., 2002] from a single leaky-wave propagation. As previously discussed, all types of CRLH LWAs are based on the same underlying principle, which is the periodic loading of a host transmission line (TL). Typical host TLs are microstrip (MS) lines [Liu et al., 2002],[Lim et al., 2004b], coplanar waveguides (CPW) [Grbic and Eleftheriades, 2002b], or coplanar striplines (CPS) [Antoniades and Eleftheriades, 2008a]. The type of host TL also determines the polarization of the radiated field. LWAs based on MS lines or CPWs generate transverse magnetic (TM) polarization, whereas LWAs comprising CPS lines radiate transverse electric (TE) fields.

These antennas may easily be extended in order to achieve a 2D LWA [Oliner and Jackson, 2007], [Caloz et al., 2011], where the source usually excite the 2D structure from its center and the leaky-wave propagates along the whole surface radiating a conical beam. One interesting example of this type of antennas is the metallo-dielectric surfaces of the mushroom-type [Sievenpiper et al., 1999], [Sievenpiper et al., 2002]. Besides, these structures have successfully lead to 2D CRLH LWAs, which provides a conical-beam with full-space scanning capabilities [Allen et al., 2004], [Caloz et al., 2011].

In order to analyze CRLH LWAs, circuit models are usually employed (see Chapter 4.2, [Caloz and Itoh, 2005], [Eleftheriades and Balmain, 2005]). These models are able to accurately represent the antenna dispersive behavior [i.e. the propagation constant $\beta(\omega)$] but they have difficulties

to characterize the amount of radiated power [i.e. leaky factor $\alpha(\omega)$]. This is because the elements of the circuit model are frequency-independent and they can not accurately characterize the variation of the radiation losses as a function of frequency. Therefore, the radiation characteristics of the antenna cannot completely be determined with these methods. This is an important limitation of the existing techniques, since then the attenuation factor cannot be controlled in the design of antennas for practical applications. In addition, a considerable number of time-consuming full-wave simulations are usually required for the design of CRLH LWAs. This makes the CRLH LWA design procedure a tedious task. Moreover, full-wave analysis does not provide any deep insight into the physics of the radiation phenomena, which is extremely important to understand and to speed-up the design process.

In this chapter, developed during my stage at the Fraunhofer Institute for High Frequency Physics and Radar Techniques (Watchberg, Germany) under the supervision of Dr. Thomas Bertuch, a novel CRLH LWA comprising periodically loaded parallel-plate waveguide (PPW) is proposed (see Fig. 6.1). The PPW loading is achieved by using via-holes and slots. The resulting antenna is planar, low-cost and inherently 2D, because the radiating slots are periodically located along the x direction but they are continuous along the y-direction. Therefore, it is expected that this antenna radiates a pencil-beam with frequency scanning properties. Note that this antenna is different as compared with the 2D structures previously proposed [Oliner and Jackson, 2007], [Caloz et al., 2011]. This is because the proposed structure does not support leaky-wave along the complete structure (i.e., 2D leaky-wave propagation) but only along the x-direction. Then, the 2D behavior of the antenna arises thanks to the finite length of the raditing slots. Therefore, this antenna radiates a pencil-beam, with frequency-scanning capabilities in one plane, instead of the usual conical beam obtained in completely 2D LWAs. The analysis and design of this complex structure may be done using commercial full-wave software. However, the use of this type of software is very time-consuming (especially for the design of a new prototype) and it does not provide any insight into the antenna radiation mechanism.

Instead of using generic full-wave software to study this antenna topology, Section 6.3 presents a novel circuit model for the analysis of PPW CRLH LWAs (see [Gómez-Díaz et al., 2011a]). The elements of the circuit model are determined by an iterative algorithm combined with modal analysis [Harrington, 1961], [Marcuvitz, 1964], [Itoh, 1989]. Specifically, the attenuation factor of the antenna is rigorously computed for the first time using an equivalent radiating structure, which is based on phased-array theory [Bhattacharyya, 2006]. The modal analysis of this structure leads to the accurate definition of a frequency-dependent circuit model, which relates the radiation characteristics with the physical dimensions of the antenna. An iterative algorithm is then proposed to determine the values of the equivalent circuit. The main advantage of the method is that it models and describes in a simple way the complex CRLH LWA radiation phenomena using equivalent dispersive circuits. Furthermore, the proposed approach also serves to compute the physical dimensions of a balanced CRLH unit cell for a particular design. The proposed technique is accurate and very efficient, requiring just minutes to analyze a complete LWA. Besides, a novel formulation to compute the far-field radiation of this type of antennas is presented. The formulation, based on an array factor approach of equivalent magnetic sources, accurately retrieve the 1D and 2D radiated electric field, allowing to compute other important quantities related to the antenna, such us radiation patterns, 3-dB beam width, directivity, and gain [Stutzman and Thiele, 1998].

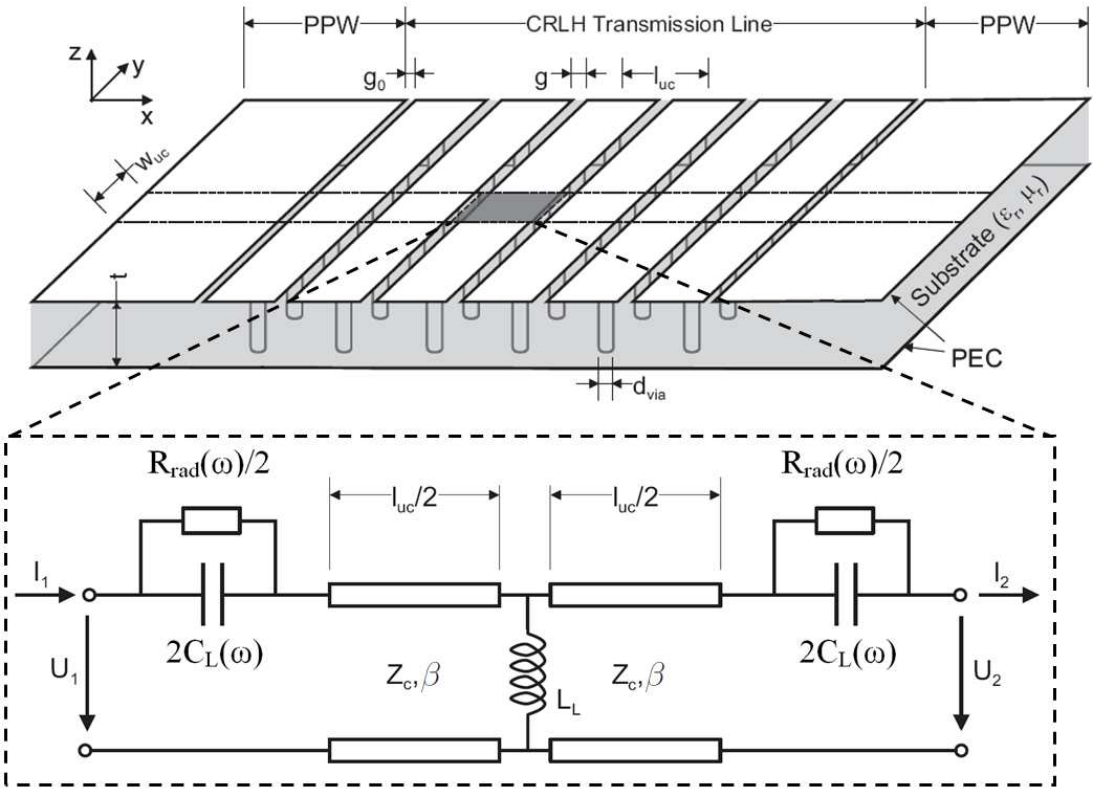

Figure 6.1 – Topology of a CRLH LWA comprising a periodically loaded PPW (top) and equivalent circuit model (bottom) representing a unit cell of the periodic one-dimensional CRLH TL. The loading is obtained by wires and slots. The slots also provide the coupling to free space, which is rigorously modeled by the dispersive lumped elements $C_L(\omega)$ and $R_{rad}(\omega)$.

Then, Section 6.4 presents the design and analysis of two PPW CRLH LWAs. First, the methodology for the the design of a 1D PPW CRLH LWA is carefully introduced by using an example. It is demonstrated that the proposed approach is able to derive the physical dimensions of the structure, leading to a balanced CRLH LWA in a few minutes. Besides, intermediate steps (single unit-cell) and the behavior of the complete antenna are analyzed and compared with the results obtained from full-wave commercial software. Excellent agreement is found, fully validating the proposed design procedure and the method of analysis. Finally, a 2D PPW CRLH LWA is designed, fabricated and measured. The experimental results obtained from the prototype completely validate, for the first time, the radiation mechanism of the antenna. Besides, the good agreement between simulations and measured data fully demonstrate the accuracy of the proposed theory: equivalent dispersive circuit, method of analysis, design methodology and antenna radiation modeling.

6.2 CRLH LWA Comprising Periodically Loaded PPW

The top of Fig. 6.1 shows the topology of the proposed CRLH LWA, including two laterally attached PPW feeding sections. At the bottom an equivalent circuit for the unit cell of the LWA's

CRLH TL section is given. It will be discussed in the next section.

The structure is assumed to be finite in the x- and z-directions and infinitely periodical in the y-direction. Effective wave propagation occurs in the xz-plane. The LWA consists of a planar substrate layer of thickness t with homogeneous and isotropic material characterized by relative permittivity ε_r and relative permeability μ_r. Its back side is completely metalized. The front side is also metalized except for a finite number of parallel and equidistant slots. The first and last slots, used for matching to the input/output ports, have a width of g_0, whereas all other slots have the width g. The metal strips oriented along the y-direction between adjacent slots are connected to the back side metallization by a rectangular grid of metalized via holes with diameter d_{via}. The via holes are placed symmetrically in the center between adjacent slots with a spacing of ℓ_{uc} and w_{uc} along the x- and y-directions, respectively.

The vias and the slots constitute the loading of the PPW and when operated in the proper frequency band the loaded section behaves as a CRLH TL. Note that this CRLH line is attached to two conventional right-handed PPWs at its ends, which constitute the antenna feeding and matching load. Without any slots present, the rectangular grid of via holes creates a so-called artificial dielectric (AD) or wired medium (WM) which exhibits strongly dispersive properties, similar to the ones observed in hollow cylindrical waveguides, including a cut-off frequency $f_{c,WM}$. In the past, open slabs of AD material have been extensively used to create forward scanning LWAs [Bahl and Gupta, 1974, Bahl and Gupta, 1975, Bahl and Gupta, 1976, Bahl and Bhartia, 1980]. The dispersive properties of the AD medium are fundamental for the operation of the proposed CRLH LWA. If the distance t between the metal planes is sufficiently small that only the fundamental parallel plate waveguide mode (PPWM) can propagate in the unloaded PPW, the WM acts like a high pass filter. The cut-off frequency of the WM, $f_{c,WM}$, can be computed resorting to derivations given in [King et al., 1983]. Below cut-off, there is no propagation in the WM and above cut-off the WM supports RH propagation with an effective wave number along the x-direction that is always smaller than the free space wave number k_0.

Introducing the slots in the upper metalization has two effects. On the one hand, a coupling between the region above and the region inside the PPW is established, and on the other hand, a CRLH TL is created which may support left-handed (LH) propagation below the WM cut-off frequency. The coupling of the regions facilitates leaky-wave radiation, provided that the real part of the CRLH TL effective wave number (k_{eff})is smaller than the free space wave number, k_0. At frequencies above $f_{c,WM}$ the propagating mode in the loaded PPW will be RH and thus, forward LW radiation will be observed. Depending on the geometry, below $f_{c,WM}$ the loaded PPW may support LH propagation which will result in backward LW radiation. If the CRLH TL exhibits a "balanced" behavior [Caloz and Itoh, 2005] (see Chapter 4.2.2) , a smooth transition from left-handed to right-handed frequency regions is possible, as frequency varies. However, even in the case that the structure is completely balanced, the antenna presents a reduction in the radiation efficiency at broadside direction. This is because the PPW loading only provides a series resistor in the unit cell equivalent circuit, representing radiation losses, whereas a shunt resistor is also required to efficiently radiate at broadside [Paulotto et al., 2008], as demonstrated in Chapter 4.4.1.

There are other possibilities to derive the proposed CRLH LW antenna, starting ei-

ther from a periodically slotted PPW as in [Lee and Son, 1999] or from mushroom surfaces [Sievenpiper et al., 1999]. For the first option, the homogeneous dielectric filling material of the PPW is replaced by an AD exploiting its dispersive properties. This has the effect of strongly increasing the guided wavelength which facilitates the operation of the LWA in the fundamental mode instead of the first space harmonic as in case of the original periodically slotted PPW. The second option of deriving the CRLH LWA topology starts from a mushroom surface as in [Allen et al., 2004]. For this approach it is important to notice that higher order surface waves or leaky-waves supported by this structure may have their power densities mainly concentrated beneath the artificial surface. This facilitates the excitation of certain higher order TM modes by a laterally connected and monolithically integrated PPW as proposed in [Bertuch, 2007]. The excitation of the mushroom structure beneath the actual surface avoids the interference of parasitic radiation from the feeding structure and the desired LW radiation. In fact, this may be a problem when exciting the LWA by an external feed as proposed in [Sievenpiper et al., 2002, Sievenpiper, 2005], which is solved using the proposed structure.

6.3 Modal-Based Iterative Approach to Analyze PPW CRLW LWAs

The analysis of complex structures, such as the PPW CRLH LWAs described in the previous section and shown in Fig. 6.1, is usually carried out using generic full-wave commercial software, such as HFSS© or CST©, which are based on accurate techniques like FEM [Lee et al., 1997] or FDTD [Taflove and Hagness, 2005], respectively. However, these methods also present some drawbacks. First, they require a very high computational cost because they need to mesh the whole structure under study. Second, it is usually difficult to characterize the leaky-wave behavior of the antenna (complex propagation constant), especially the radiation losses [$\alpha(\omega)$]. And finally, and due to the high computational resources of these programs, it is usually very tedious to make the design of a real antenna and to derive the real physical parameters.

In this section, a modal-based iterative approach is proposed for the analysis of PPW CRLH LWAs. For this purpose, an equivalent dispersive circuit is first derived. The main advantage of this model is the direct correspondence between the dimensions of the real physical structure [see Fig. 6.1 (top)] and the dispersive elements of the circuit [see Fig. 6.1 (bottom)]. In order to determine the values of these elements, an equivalent radiating structure, based on phased-array theory, is employed. This simple structure is then analyzed using a mode-matching approach, and it is analytically demonstrated the link between the radiating structure and the dispersive elements of the circuit. Next, a quickly-convergent iterative algorithm is employed to compute the complex propagation constant associated to the antenna, including the radiation losses. Once the structure has been analyzed, a novel formulation, based on an array factor approach of equivalent magnetic sources, is proposed to compute the 1D and 2D radiation characteristics of the antenna. This last step completes the analysis and radiation study of this type of antennas.

The proposed method presents some advantages over standard full-wave software. First, it is able to model and describe in a simple way the complex CRLH LWA radiation phenomena, including radiation losses, using equivalent dispersive circuits. This provides physical insight into the antenna radiation mechanism, and helps to understand its behavior. Second, the method is much faster than

regular commercial software, allowing the analysis of this type of antenna in just some minutes, instead of hours (or even days) that completely full-wave approaches require. And third, this method allows the fast and accurate design or PPW CRLH LWAs, leading to the physical dimensions of the antenna required to achieve a particular behavior.

Note that the main goal of this section is to derive and explain the proposed modal-based technique. Full-wave results will be employed to validate some partial results, in order to demonstrate the rigorousness of the intermediate steps. However, the final validation of this method is given in the next section, where the proposed approach is employed for the analysis and design of two complete PPW CRLH LWAs. There, full-wave results of the complete design and measured data from a fabricated prototype will completely validate the accuracy and effectiveness of the proposed method.

6.3.1 Equivalent Circuit Model

The equivalent circuit model related to a single unit cell (with length l_{uc} and width w_{uc}) of the CRLH LWA is shown in Fig. 6.1 (bottom). The layout of the equivalent circuit assumes a symmetric composition of the unit cell along the direction of wave propagation. Two right-handed TLs, of length $l_{uc}/2$, have been employed to model the PPW behavior (i.e. the host TL). These TLs are described by their characteristic impedance, Z_c, and propagation constant, β. It is very important to distinguish between β and k_{eff}. The former is related to the host TL (unloaded PPW) and it is typically real, as long as material losses are neglected. The latter is related to the total CRLH unit cell and it is complex, because it also includes the radiations losses of the structure. It may be expressed as

$$k_{eff}(\omega) = \beta_{eff}(\omega) - j\alpha(\omega), \tag{6.1}$$

where $\beta_{eff}(\omega)$ and $\alpha(\omega)$ are the phase constant and radiation losses (leaky) associated to the complete unit-cell, respectively. For convenience, the complex propagation constant is defined here [using $k_{eff}(\omega)$] in a different way as defined in Chapter 4.2.2. However, both definitions of the complex propagation constant may be considered equivalent, since they only differ in a $j = \sqrt{-1}$ term, as demonstrated below

$$e^{jk_{eff}(\omega)} = e^{j[\beta_{eff}(\omega) - j\alpha(\omega)]} = e^{\gamma(\omega)} = e^{\alpha(\omega) + j\beta_{eff}(\omega)}. \tag{6.2}$$

The LH behavior is achieved by a via-hole and by two half-slots (see Fig. 6.1). The loading is modeled in the equivalent circuit with a shunt inductance (L_L) and two symmetrically placed dispersive circuit elements, composed of the parallel connection of a resistor [$R_{rad}(\omega)$] and a capacitor [$C_L(\omega)$]. The parallel connection of the two elements is convenient to represent the radiation mechanism through the slot. In the limiting case of a narrow slot, the capacitor becomes very large, and tends to reduce the radiation by short-circuiting the resistance. This correctly models the radiation reduction that occurs in the real structure for very narrow slots. Note that this dispersive circuit rigorously takes into account the effects of the slot, including the physical parameters of the structure, coupling to free-space, reactive fields, coupling to other slots, radiation losses, and the capacitive behavior required to balance the unit cell. An equivalent radiating structure and the modal analysis employed to derive the values of the equivalent circuit elements, including dispersion, will be explained in the following section.

In order to compute the complex propagation constant of the CRLH unit cell, we represent the equivalent circuit in terms of transmission matrices [Pozar, 2005]. This helps to obtain the value of the shunt inductance L_L for the given geometry, and to determine the complex propagation constant of the unit cell. In the next discussion it is assumed that the physical dimensions of the CRLH unit cell are known. In the following sections, we will explain how to accurately obtain these physical dimensions, without the need to use full-simulations on the complete unit-cell.

The first step required for the analysis is to obtain the characteristic impedance and the propagation constant of the unloaded PPW, related to a single unit cell of length ℓ_{uc} and width w_{uc}. These values may be obtained as

$$Z_c = \frac{t}{w_{uc}} \sqrt{\frac{\mu_r \mu_0}{\varepsilon_r \varepsilon_0}}\,, \tag{6.3}$$

$$\beta(\omega) = \omega \sqrt{\varepsilon_r \varepsilon_0 \mu_r \mu_0}\,, \tag{6.4}$$

where ε_0 and μ_0 are the permittivity and the permeability of vacuum respectively, and ω is the angular frequency. Then, the transmission matrix of the host TL of length $\ell_{uc}/2$ may be expressed as

$$T_{host} = \frac{1}{2} \begin{pmatrix} e^{j\beta\ell_{uc}/2} + e^{-j\beta\ell_{uc}/2} & Z_c \left(e^{j\beta\ell_{uc}/2} - e^{-j\beta\ell_{uc}/2}\right) \\ \frac{1}{Z_c}\left(e^{j\beta\ell_{uc}/2} - e^{-j\beta\ell_{uc}/2}\right) & e^{j\beta\ell_{uc}/2} + e^{-j\beta\ell_{uc}/2} \end{pmatrix}. \tag{6.5}$$

Next, the PPW loaded by a grid of via-holes is considered. This creates an artificial dielectric with strong dispersive properties. Similar to hollow waveguides, where the metallic side walls introduce the same effect, the AD acts like a high pass on the fundamental PPWM. The cut-off frequency $f_{c,WM}$ of the AD can be found by solving (e.g. numerically) the following dispersion equation (see [King et al., 1983])

$$k w_{uc} \tan\left(\frac{k w_{uc}}{2}\right) = \frac{\pi w_{uc}}{\ell_{uc} \ln\left(\frac{\ell_{uc}}{\pi d_{via}}\right)}, \tag{6.6}$$

where $k = 2\pi f_{c,WM} \sqrt{\varepsilon_r \varepsilon_0 \mu_r \mu_0}$ is the intrinsic wave number of the substrate material. Note that the effective wavelength in the AD becomes infinite at the cut-off frequency, which means that the propagation constant tends to zero. Therefore, this frequency corresponds to the transition frequency of a CRLH TL.

The transmission matrix of the shunt inductance is given by

$$T_L = \begin{pmatrix} 1 & 0 \\ \frac{1}{j\omega L_L} & 1 \end{pmatrix}. \tag{6.7}$$

In order to determine the value of the inductance, we will analyze the CRLH unit cell at the transition frequency. At this frequency, the phase shift at the ports of the unit cell becomes zero, and the model of Fig. 6.1 (bottom) reduces to the circuit of Fig. 6.2, as is demonstrated in [Caloz and Itoh, 2005]. The boundary conditions applied to the currents (I_1, I_2) and the voltages (U_1, U_2) may be formulated as

$$\begin{pmatrix} U_1 \\ I_1 \end{pmatrix} = T_{host}\; T_L\; T_{host} \begin{pmatrix} U_2 \\ I_2 \end{pmatrix} = \begin{pmatrix} U_2 \\ I_2 \end{pmatrix}, \tag{6.8}$$

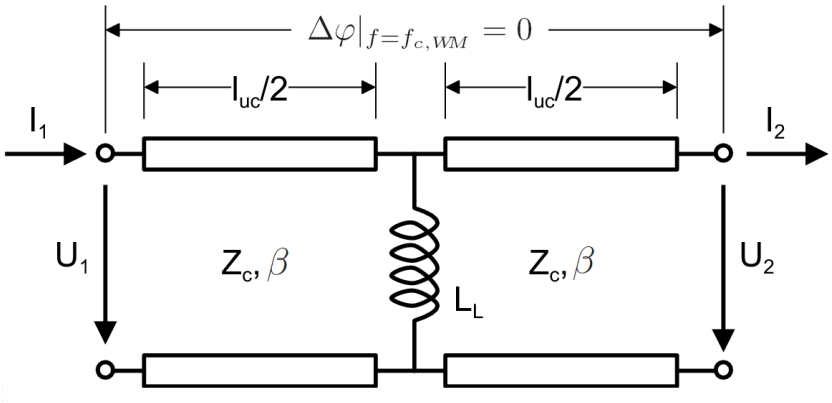

Figure 6.2 – Equivalent circuit model of a unit cell related to a PPW loaded by a periodic grid of wires. The circuit model of Fig. 6.1 reduces to this model at the CRLH TL transition frequency [Caloz and Itoh, 2005], assuming that the cell is balanced.

and L_L is determined by solving

$$\det\left(T_{host}\ T_L\ T_{host} - I\right) = 0, \tag{6.9}$$

where I is the unitary matrix.

The transmission matrix which models the slot in the upper metallization of the host TL is represented by T_{gap}, which will be derived in the next section. The behavior of half of a slot (required to maintain the unit cell symmetry) is obtained as the square root of the T_{gap} matrix, and it is denoted by $T_{gap/2}$.

The transmission matrix associated to the total CRLH unit cell (T_{uc}) is then obtained by a simply multiplication of the transmission matrices related to the unit cell elements, as follows

$$T_{uc} = T_{gap/2}\ T_{host}\ T_L\ T_{host}\ T_{gap/2} = \begin{pmatrix} A_{uc} & B_{uc} \\ C_{uc} & A_{uc} \end{pmatrix}. \tag{6.10}$$

Note that the diagonal elements of T_{uc} are identical, due to the equivalent circuit symmetry.

Applying the Floquet's theorem [Bhattacharyya, 2006], the complex propagation constant (k_{eff}) related to the total unit cell may be then determined by solving

$$\det\left(T_{uc} - e^{jk_{eff}\ell_{uc}} I\right) = 0, \tag{6.11}$$

which yields the complex value of

$$k_{eff} = \frac{\ln\left(A_{uc} \pm \sqrt{B_{uc}C_{uc}}\right)}{j\ \ell_{uc}}. \tag{6.12}$$

Finally, note that the complex propagation constant (k_{eff}) can also be obtained using alternatives approaches (such as the one described in [Marini et al., 2010]), once the different transmission matrixes employed in the analysis are known.

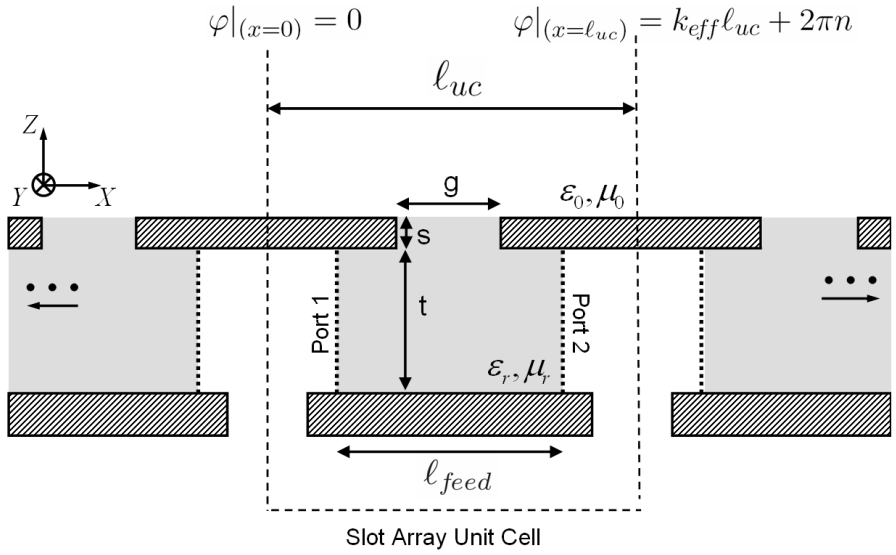

Figure 6.3 – Cross-section of one-dimensional periodic array of infinitely long slots radiating into free space, employed to rigorously model the CRLH LWA radiation mechanism. Periodic boundary conditions in free space are imposed at the limits of the unit cell. Each slot is attached to a PPW T-junction with two PPW ports. Port 1 serves as excitation of the array element.

6.3.2 Equivalent Radiating Structure

In this section, a rigorous computation of the transmission matrix T_{gap}, which characterizes the unit cell slot behavior, is presented. For this purpose, an equivalent phased-array antenna model is employed. It consists of a one-dimensional periodic array of infinitely long slots in a metal plane. At this point, we assume an infinite number of elements (slots) along the x-direction. This assumption is not critical for the analysis of leaky-wave antennas [Oliner and Jackson, 2007], since they are usually several wavelengths long. Using phased-array theory, we assume that all array elements are fed with a progressive phase shift. Each slot is individually attached to a T-junction formed with the PPWs, as shown in Fig. 6.3. In the figure, the dotted line shows the limits of the unit cell. The total length of the whole feeding PPW is ℓ_{feed}, which must be greater than g. Note that the influence of this TL will be removed at the end, in order to characterize an isolated slot in an external array environment. Due to this, it is sufficient to consider a single unit cell (array element) with imposed periodic boundary conditions in free space along the x-direction (see Fig. 6.3). Moreover, the imposed phase shift at a given frequency is determined by the effective wave number of the CRLH TL unit cell as $\Delta\varphi = k_{eff} l_{uc} + 2\pi n$, where k_{eff} was defined in Eq. (6.12) and $n \in \mathbb{Z}$.

Then, the single array element is studied using a multi mode-matching (MM) approach [Harrington, 1961] combined with Floquet's theorem [Bhattacharyya, 2006]. The reason to use a multi-mode analysis is that not only propagative modes, but also evanescent modes must be rigorously taken into account. This is especially important to model the coupling from the PPW to the slot, from where the energy is radiated.

In order to perform the analysis, the equivalent radiating structure of Fig. 6.3 is split into a

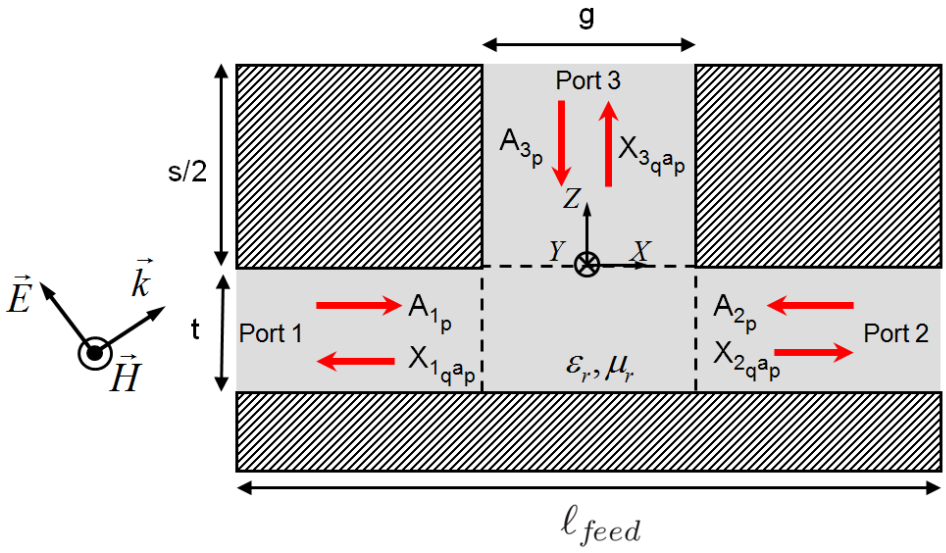

Figure 6.4 – Cross-section of an E-plane T-junction of parallel-plate waveguides.

PPW E-plane T-junction (see Fig. 6.4) and into a slot fed by a vertical PPW (see Fig. 6.5). Then, the general scattering matrix (GSM) [Itoh, 1989], [Pozar, 2005] associated to each individual structure ($GSM_{Tjunction}$ and $GSM_{Aperture}$) is obtained by using mode-matching techniques [Harrington, 1961], [Marcuvitz, 1964], [Itoh, 1989]. Next, both GSMs are combined into a single matrix (GSM_{gap}), related to the total radiating array element. Note that the radiation mechanism of the structure is embedded into GSM_{gap}. At this point, this matrix is further simplified, considering only the fundamental PPW mode. This approximation is accurate, because although evanescent modes couple to the slot and have strong influence on the radiation, they are strongly attenuated as they propagate down the ports. In this way we obtain a matrix S'_{gap}, which contains the scattering parameters related to the total radiating array element. However, we are interested only in modeling the slot. Consequently, we deembed the reference planes of the ports to the plane $x = \ell_{feed}/2$ (as shown in Fig. 6.3), resulting into the scattering matrix S_{gap}. Finally, we perform a simple transformation from the S_{gap} matrix to the transmission matrix T_{gap} [Pozar, 2005].

It can be expected that the magnetic field inside and above the slots in Fig. 6.1 will be primarily polarized parallel to them. Hence, it will be sufficient, in the following modal analysis to consider TM waves. The reference directions of these waves change as a function of the PPW orientation (from x to z-direction according to Fig. 6.4).

The steps to perform the analysis described above are detailed in the next subsections, including a validation of the approach using full-wave simulations.

Modal Analysis of a PPW E-plane T-junction

The E-plane T-junction in a parallel-plate waveguide has extensively been studied in the past [Arndt et al., 1987, Park et al., 1994, Cho, 2003]. A general cross-section of this junction is depicted in Fig. 6.4. In order to build the GSM associated to it, we individually excite each port of the junction with an incident TM mode denoted by A_{a_p} (where $a \in \{1,2,3\}$ is the incident port number and $p =$

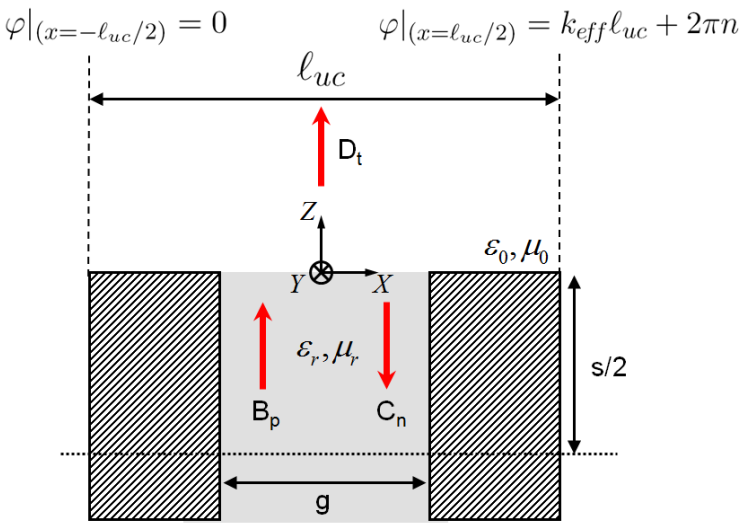

Figure 6.5 – Cross-section of an open-ended parallel-plate waveguide radiating in an array environment. Periodic boundary conditions, related to the complex propagation constant of the complete CRLH LWA unit cell, are imposed in the free-space region.

1...m is the mode number). Then, we obtain the complex mode amplitudes ($X_{b_q a_p}$, where $b \in \{1, 2, 3\}$ is the observation port and $q = 1...m$ is the observation mode) using the analytic series solution method proposed in [Park et al., 1994]. Note that the modal coefficients are referred to the T-junction borders (dashed line in Fig. 6.4), and that these coefficients directly correspond to the generalized scattering parameters. Then, the exact length of the T-junction ports are taken into account by moving the reference plane of each modal coefficient, using

$$S_{b_q a_p} = X_{b_q a_p} e^{-j(k_{a_p}\ell_a + k_{b_q}\ell_b)}, \tag{6.13}$$

where $S_{b_q a_p}$ is a complex mode amplitude related to the origin of the observation (b) and incident (a) ports, ℓ_a and ℓ_b are the lengths of the waveguide sections related to ports a and b (which corresponds to $\ell_{feed}/2 - g/2$ in the case of ports 1 and 2 and to $s/2$ in the case of port 3, as shown in Fig. 6.4), and k_{a_p} and k_{b_q} are the mode wavenumbers.

Modal Analysis of Open-Ended PPW Array

The study of an array of dielectric-filled waveguides radiating into free space has already been performed in the past [Harrington, 1961], [Marcuvitz, 1964]. The structure is shown in Fig. 6.5, including periodic boundary conditions for the free-space radiation. Its simple geometry allows to perform a modal analysis, resorting to the procedures described in [Harrington, 1961] and combined with Floquet's theorem [Bhattacharyya, 2006].

It is important to note that the periodic boundary conditions impose a phase shift of $\Delta\varphi = k_{eff} l_{uc} + 2\pi n$ at the unit-cell limits, where $n \in \mathbb{Z}$ and k_{eff} is the complex wave number associated to the entire CRLH unit-cell [see Fig. 6.1 (bottom)]. This assures that the slot radiation mechanism completely depends on this complex propagation constant, allowing to establish a fundamental relationship between the CRLH TL unit cell and the modal analysis performed of the equivalent radiating

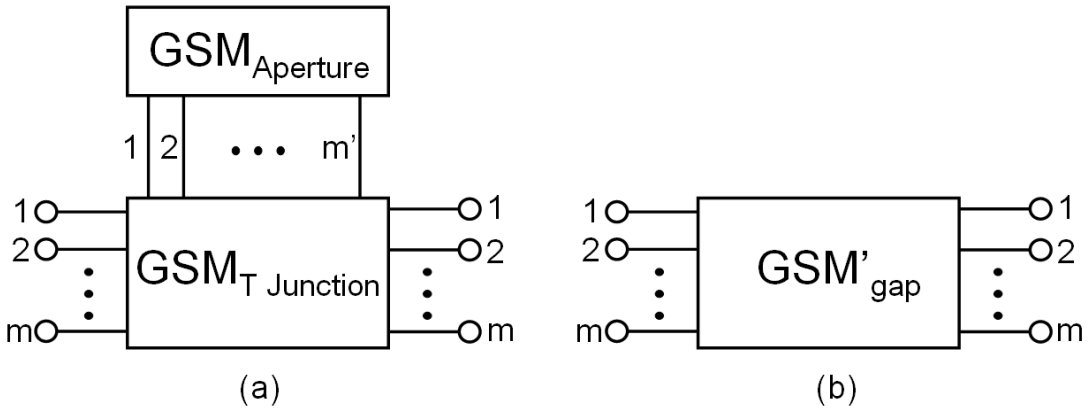

Figure 6.6 – Representation of the equivalent radiating structure of Fig. 6.3 using generalized scattering matrices (GSM). (a) Using the GSM related to the T-junction (see Fig. 6.4) combined with the GSM related to the aperture (see Fig. 6.5). (b) Using a single equivalent GSM.

structure, which are closely inter-related.

Appendix C presents a detailed mode-matching analysis of a partially-filled parallel-plate waveguide radiating within a periodic environment, i.e., of the structure shown in Fig. 6.5. The components of the electromagnetic fields within the PPW and in the free space region are first derived. Applying boundary conditions for the x- and y-components of the fields in the plane $z = 0$, and utilizing the orthogonality properties of the harmonic functions involved in the formulation for the scalar wave potentials, expressions for the modal amplitudes D_t and C_n (see Fig. 6.5) are derived as a function of the excitation mode, B_p. Finally, the generalized scattering matrix ($GSM_{Aperture}$) for the structure of Fig. 6.5 is obtained after performing a modal analysis for each incident mode.

Analysis of the Total Equivalent Structure

The equivalent radiating structure shown in Fig. 6.3 can now easily be modeled using the generalized scattering matrices $GSM_{T_{junction}}$ and $GSM_{Aperture}$, which are connected as indicated in Fig. 6.6(a). This connection can be further simplified, leading to a single matrix GSM'_{gap} (see Fig. 6.6b). For this purpose, a matrix formulation is developed in Appendix D. In resume, the formulation applies boundary condition at the interconnection of the matrices $GSM_{T_{junction}}$ and $GSM_{Aperture}$ (see Fig. 6.6a), allowing to embed the behavior of these two matrices into a unique matrix, GSM'_{gap}, shown in Fig. 6.6(b).

In addition, the GSM'_{gap} matrix is further simplified. Specifically, the scattering parameters for the fundamental PPW mode is considered. Note that the higher order modes have rigorously been taken into account to model the coupling from the T-junction to the slot, and to model the aperture radiation. However, since they are evanescent, they are strongly attenuated while propagating down the ports, and their contributions can be neglected. Therefore, the equivalent radiating structure may now be represented by a simple (2x2) scattering matrix relating the fundamental modes at the two ports (S'_{gap}).

At this point, it is important to remember that the goal is to model the effect of the slot in the PPW (including its radiation characteristics in a periodic environment) in order to be included into the CRLH unit cell model of Fig. 6.1 (bottom). Examining that model, one realizes that the effect of the host parallel-plate waveguide has already been considered. Therefore, we need to shift the reference plane of the last scattering matrix to the position of the slot, which may easily be done as

$$S_{ba} = S'_{ba} e^{j\beta \ell_{feed}}, \tag{6.14}$$

where a, b are the port numbers and β and ℓ_{feed} are the propagation constant of the fundamental mode and physical length related to the feeding parallel-plate waveguide, respectively. This matrix is then transformed into the transmission matrix T_{gap} [Pozar, 2003], which may be expressed as

$$T_{gap} = \begin{pmatrix} T_{11} & T_{12} \\ T_{21} & T_{22} \end{pmatrix}. \tag{6.15}$$

In this last transformation, the PPWcharacteristic impedance [see Eq. (6.3)] has been employed as a reference impedance [Pozar, 2003]. This normalizes the resulting transmission matrix with respect to the unit cell width (w_{uc}).

It is important to note that T_{gap} models the entire radiation mechanism of the equivalent structure (see Fig. 6.3), including radiation losses, coupling to free space, reactive fields, coupling to other slots, and the slot influence within the PPW. Also, note that this matrix relates the electrical behavior of the slot with the physical dimensions of the structure. Finally, the transmission matrix $T_{gap/2}$, employed in Eq. (6.10), is derived as the square root of the T_{gap} matrix, exploiting the concatenation property of two transmission matrices [Pozar, 2003].

A numerical study of T_{gap} reveals that it has the simple form of impedances concatenated in series,

$$T_{series} = \begin{pmatrix} 1 & R'_{rad}(\omega) - \frac{j}{\omega C'_L(\omega)} \\ 0 & 1 \end{pmatrix}. \tag{6.16}$$

This direct correspondence with lumped elements is expected, since the slot radiation losses can be modeled by the resistor, whereas the capacitor takes into account the slot capacitive behavior within the host parallel-plate waveguide as well as the field coupling to free space (reactive fields). In the next sections, it will be demonstrated that the approximation (6.16) is accurate, introducing very small errors. From this matrix, the radiation losses $R'_{rad}(\omega)$ and series capacitor $C'_L(\omega)$ are determined, for a particular angular frequency (ω), as

$$R'_{rad}(\omega) = \mathrm{Re}\{\mathrm{T_{gap}}(1,2)\}, \tag{6.17}$$

$$C'_L(\omega) = \frac{-1}{\mathrm{Im}\{\mathrm{T_{gap}}(1,2)\}!}. \tag{6.18}$$

Then, the series circuit composed of a $R'_{rad}(\omega)$ and $C'_L(\omega)$ is transformed into the shunt circuit [shown in Fig. 6.1(bottom)] using the formulation presented in Appendix E. As previously commented, this representation is preferred because the shunt circuit of a resistor and a capacitance makes easier to understand the slot behavior. Besides, this correspondence with lumped elements allows us to derive the complete equivalent dispersive circuit model related to the PPW CRLH LWA unit cell shown in Fig. 6.1 (bottom).

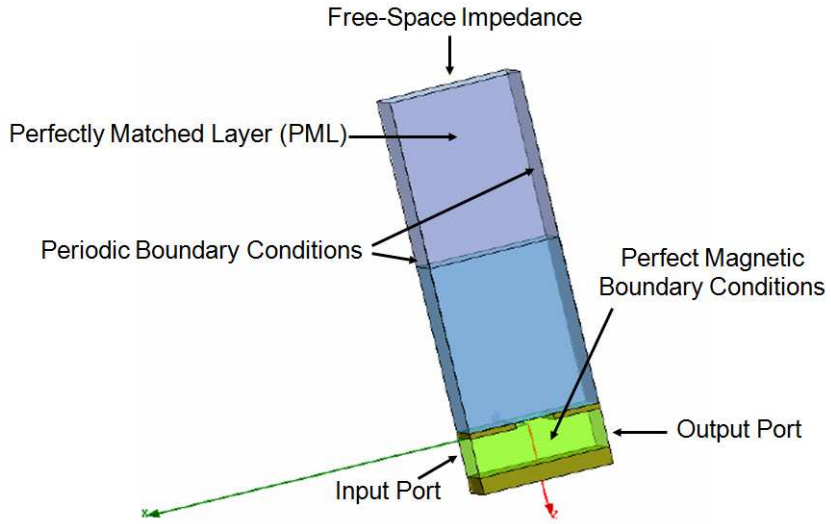

Figure 6.7 – Equivalent radiating structure of a single PPW CRLH LWA unit-cell simulated by Ansoft HFSS©. The types of boundary conditions applied to the side walls of the simulation volume are indicated.

Finally, note that the radiation losses are only modeled by a resistor in the series branch, and that there is no radiation contribution from the shunt branch. As was explained in Chapter 4.4.1, radiation at broadside is only achieved when the radiation losses are distributed over both the series and the shunt branches of the CRLH unit cell. Otherwise, the attenuation constant α tends to zero at the transition frequency, even if the unit cell is balanced. Therefore, it is expected that the type of CRLH LWAs proposed here suffers from an important drop in efficiency when radiating at broadside. However, it is still able to radiate at backward and forward directions, using the fundamental harmonic ($\nu = 0$). Note that although there is a drop in the broadside radiation efficiency, the CRLH TL is still balanced. This means that the propagation constant does not exhibit a bandgap around the transition frequency.

Validation Against Full-Wave Simulations

This section presents a complete validation of the modal technique employed to analyze the PPW CRLH LWA equivalent radiating structure (see Fig. 6.3). For this purpose, let us consider this structure with dimensions $\ell_{uc} = 23.54$ mm, $g = 0.5$ mm, $t = 3.65$ mm and $s = 0.05$ mm. Note that we can chose any value for the length ℓ_{feed}, because the influence of the auxiliary feeding PPW ports is removed in the analysis. For intermediate calculations, we usually set $\ell_{feed} = \ell_{uc}$. For a complete validation of the technique, the scattering parameters S_{11} and S_{21} related to this structure are computed for all possible phase shifts, using the proposed modal approach [Eq. (6.14)]. Then, a model of the equivalent radiating structure has been created in the commercial software Ansoft HFSS© (see Fig. 6.7). Fig. 6.8 presents the comparison between the results computed by both approaches, fully demonstrating that an excellent agreement is obtained in all cases. Also, note that the modal technique needs about 35 minutes to perform this type of analysis, while full-wave simulations spend more than one day to obtain the same results.

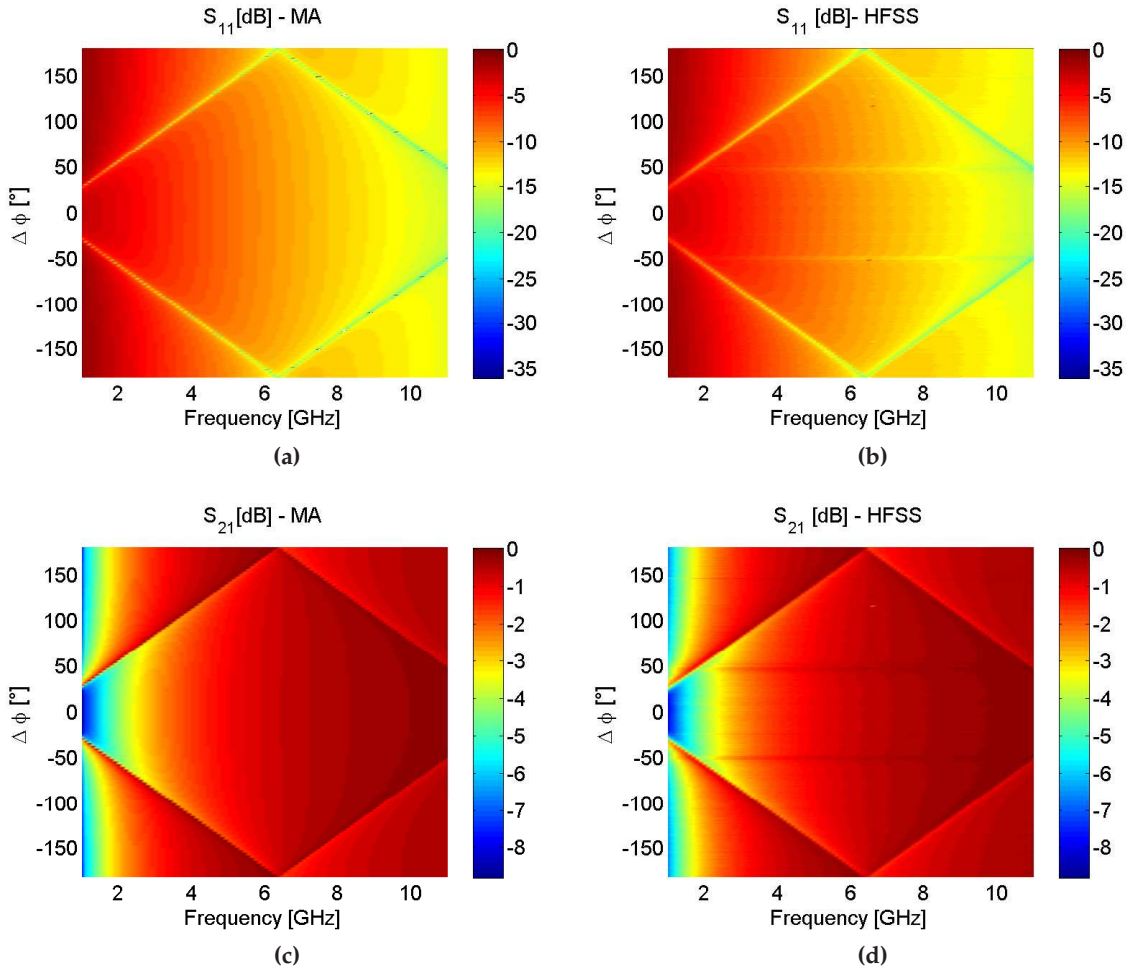

Figure 6.8 – Comparison of the scattering parameters (S_{11} and S_{21}) of the equivalent radiating structure (see Fig. 6.3) computed by HFSS© and by the proposed modal analysis (MA), as a function of both, frequency and phase shift between unit cell elements. The parameters of the unit cell are $\ell_{uc} = 23.54$ mm, $g = 0.5$ mm, $t = 3.65$ mm, and $s = 0.05$ mm.

6.3.3 Iteratively Refined Approach for Complex Propagation Constant Determination

In the previous sections we have explained how to compute the CRLH unit cell complex propagation constant (k_{eff}) as a function of the transmission matrix T_{gap}, and how to compute this matrix as a function of the physical dimensions of the structure and of the CRLH unit cell complex propagation constant (k_{eff}). Therefore, one can easily realize that these variables are closely inter-dependent.

In order to determine the equivalent circuit elements of the CRLH LWA unit cell [see Fig. 6.1 (bottom)], from previously known physical dimensions, an iterative algorithm is proposed. The description of the algorithm flow-chart, shown in Fig. 6.9, is as follows: initially, the non-dispersive elements of the circuit model and the CRLH transition frequency are obtained using the procedures previously described. After that, an initial value of zero is assumed for the complex propagation constant k_{eff} at all frequencies. The transmission matrix T_{gap} is then derived employing the proposed

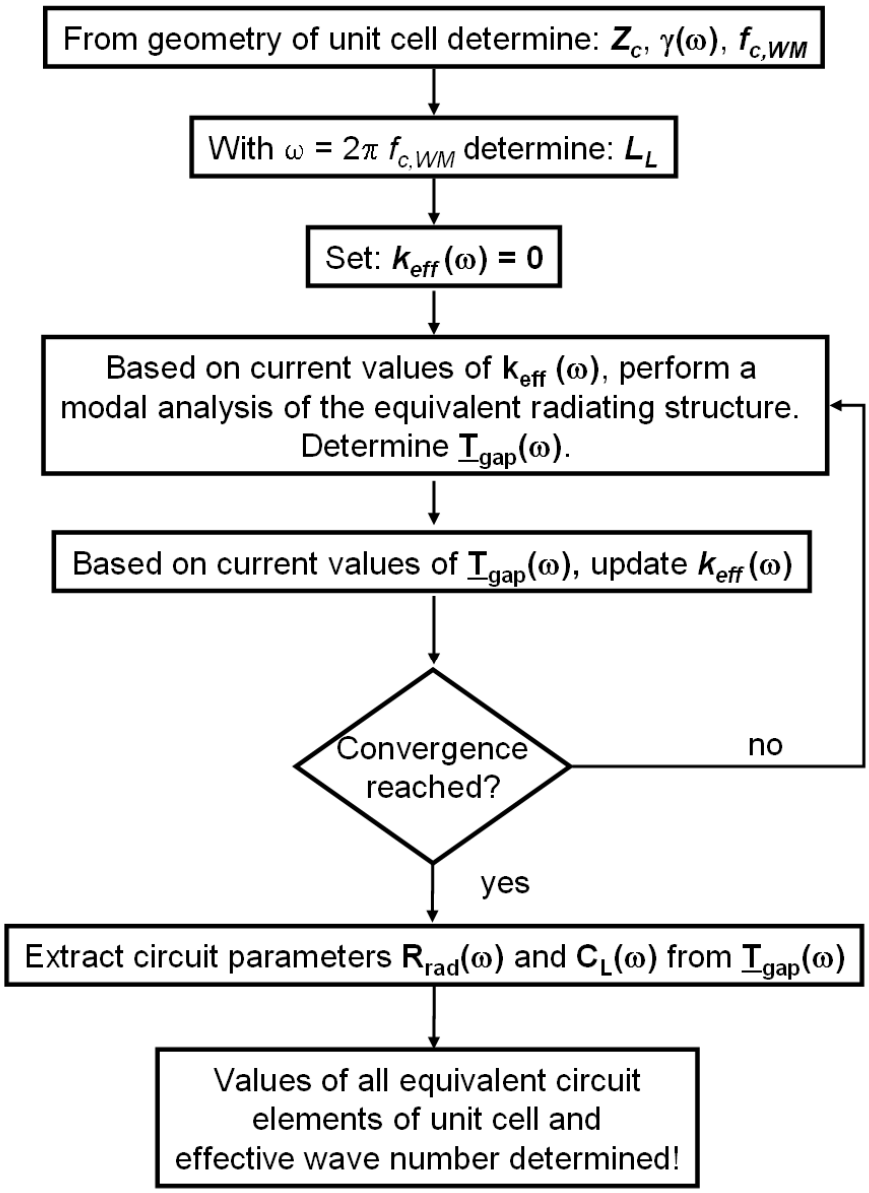

Figure 6.9 – Flow chart of the proposed iterative algorithm that determines the element values of the unit cell equivalent circuit [see Fig. 6.1 (bottom)] and the CRLH TL complex propagation constant.

modal analysis, taking into account k_{eff} and the physical dimensions of the structure. Once this matrix has been obtained, the value of k_{eff} is computed based on the current value of T_{gap}. This procedure is repeated until convergence is reached. This iterative algorithm leads to an accurate model of the slot, through the matrix T_{gap}, and to a final complex propagation constant k_{eff}. In the last step, the frequency dependent values of R_{rad} and C_L are extracted from the transmission matrix T_{gap}. In this way, all circuit parameters related to the unit cell are determined.

It is important to remark that this iterative algorithm is quickly convergent. Numerical simulations demonstrate that 20-30 iterations are enough to achieve a relative error less than 10^{-12} between two consecutive steps over the whole frequency range.

6.3.4 Radiation Characteristics

After applying the iterative modal-based analysis of the PPW CRLH LWA, the complex propagation constant associated to the CRLH TL (k_{eff}) is obtained. This value provides information related to the pointing angle of the antenna, through the phase constant $\beta(\omega)$, and to the beamwidth, through the radiadion losses constant, $\alpha(\omega)$. Then, the radiation properties of the antenna can easily be derived from general LWA theory [Oliner and Jackson, 2007]. However, LWA theory consider a continuous (homogeneous) medium, whereas in the proposed structure (see Fig. 6.1) radiation cames from discrete and well-defined slots. Therefore, the use of general LWA theory to derive the radiation characteristics of the PPW CRLH LWA is an approximation, which entirely depends on the homogenous condition ($p << \lambda_g$, where λ_g is the guided wavelength) and neglects the inherent $2D$ nature of the structure.

Another possibility is to employ the LWA array factor approach proposed in [Caloz and Itoh, 2004]. In this case, the elements of the antenna are considered isotropic radiators, and the feeding of each element (amplitude and phase) is related to the position of the element in the array and the complex propagation constant of the LWA. However, this approach is only able to consider $1D$ or $2D$ discrete structures. Therefore, it is not appropriate to characterize the PPW CRLH LWA proposed here, which presents a continuous nature along the y direction. Besides, regular CRLH equivalent circuits [Caloz and Itoh, 2005] do not consider the frequency variation of their constitutive circuit elements. Therefore, the accuracy of the array factor approach is limited, because it neglects the variation of the mutual coupling between slots and the radiation resistance with frequency.

A very interesting alternative is to consider each slot of the PPW CRLH LWA as an element of a phased array antenna [Bhattacharyya, 2006]. This allows us to rigourously take into account *the periodic nature of the PPW CRLH LWA along the x direction* (i.e., the location of each individual slot over the ground plane) and the *continuous nature of the antenna along the y direction* (i.e., the length of each slot). Since slots are very narrow, they may be approximated by a y-directed magnetic current over a ground plane, which is assumed to be uniform, constant and with a total length of $N_{st}w_{uc}$ (where N_{st} is the number of cells along the y direction and w_{uc} is the width shown in Fig. 6.1). This leads to an equivalent phased-array structure, shown in Fig. 6.10, which presents the same radiation characteristics as the original PPW CRLH LWA.

Another point here is the feeding of each array element. As can be inferred from Fig. 6.1, and was previously demonstrated, each slot of the antenna may be modeled by a frequency-dependent resistor [$R_{rad}(\omega)$], which takes into account for the real radiation losses. Therefore, the current flowing on the n^{th} resistor in the equivalent circuit model [$I_n(\omega)$] is directly responsible for the radiation of the n^{th} slot, and it is considered the feeding of the n^{th} element in the equivalent phased-array configuration. Besides, note that this current inherently takes into account all antenna characteristics, including mutual coupling between the slots and the frequency-dependent radiation losses.

Then, the electric far-field radiated from a PPW CRLH LWA may be obtained by analyzing the radiation from the equivalent problem shown in Fig. 6.10, which yields

$$|\vec{E}(\omega,\hat{\theta},\phi,r)| = E_0(\omega)|\vec{E}_{se}(\omega,\hat{\theta},\phi,r)||AF(\omega,\hat{\theta},\phi)|, \tag{6.19}$$

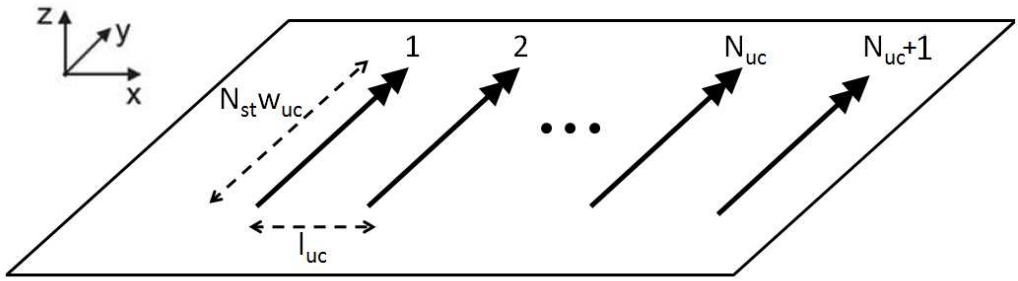

Figure 6.10 – Array of N_{uc} magnetic linear sources of length $N_{st}w_{uc}$, with a separation distance of ℓ_{uc} between two consecutive elements, placed over a ground plane. Each discrete linear source, n, is assumed to be uniformly fed along the y-axis by a complex amplitude, $I_n(\omega)$. This phased array configuration reproduces the radiation behavior of the PPW CRLH LWA (see Fig. 6.1), assuming very narrows slots.

where usual spherical coordinates $(\hat{\theta}, \phi, r)$ have been employed (see Fig. 6.11) and $|E_{se}(\omega, \hat{\theta}, \phi, r)|$ is the absolute electric field radiated by a single element of the array, i.e., the electric field radiated by a linear and uniform magnetic current of length $N_{st}w_{uc}$ placed over a ground plane. This field may be derived analytically as [Stutzman and Thiele, 1998]

$$|\bar{E}_{se}(\omega, \hat{\theta}, \phi, r)| \propto \frac{e^{-jk_0 r}}{2\pi r}\sqrt{\cos^2(\hat{\theta}) + \sin^2(\hat{\theta})\cos^2(\phi)}\,\mathrm{sinc}\left[k_0 \frac{N_{st}w_{uc}}{2}\sin(\hat{\theta})\sin(\phi)\right], \tag{6.20}$$

where k_0 is the free-space wavenumber and the function "sinc(x)" is defined as $\sin(x)/x$.

The term $AF(\omega, \hat{\theta}, \phi)$ is the array factor [Stutzman and Thiele, 1998] [Caloz and Itoh, 2004], which takes into account the combination of $N_{uc}+1$ slots along the x direction. It may be expressed as

$$AF(\omega, \hat{\theta}, \phi) = \sum_{n=1}^{N_{uc}+1} A_n(\omega) e^{jk_0(n-1-N_{uc}/2)\ell_{uc}\cos\theta(\hat{\theta},\phi)}, \tag{6.21}$$

where $\theta(\hat{\theta}, \phi)$ is the angle which spans from the origin of the spherical coordinate system to the projection of the observation point in the $x-z$ plane (i.e., usual angle employed in the LWA scanning law [Oliner and Jackson, 2007], see Fig. 6.11), and it may be defined by

$$\theta(\hat{\theta}, \phi) = \tan^{-1}\left[\frac{\cos(\phi)}{\cos(\hat{\theta})\sin(\phi)}\right]. \tag{6.22}$$

The term $A_n(\omega)$ is the complex amplitude which feds the n^{th} array element, and it is defined by

$$A_n(\omega) = \begin{cases} I_n(\omega)/\sqrt{2} & \text{if} \quad n = 1, N_{uc}+1 \\ I_n(\omega) & \text{if} \quad n = 2, \ldots, N_{uc} \end{cases}. \tag{6.23}$$

Note that the frequency-dependent current $I_n(\omega)$ can easily be derived for a finite structure composed of N_{uc} cells, resorting a simple circuital analysis combined with an ABCD approach [Pozar, 2005]. Besides, note that a $1/\sqrt{2}$ factor appears in the first and last slots because they have

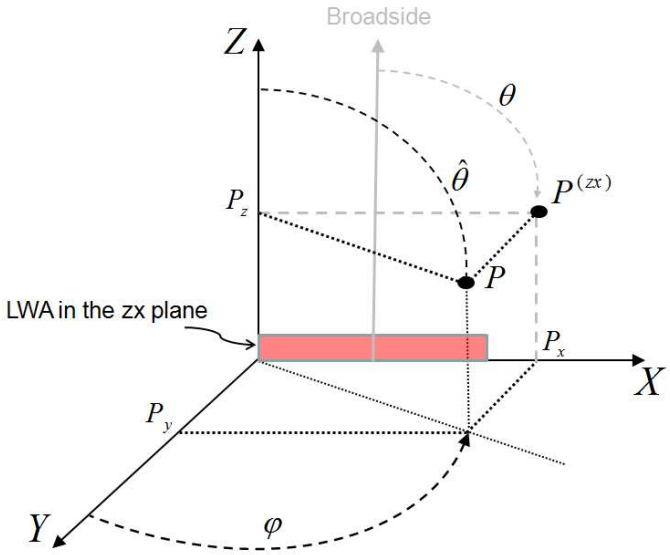

Figure 6.11 – Use of spherical and cartesian coordinates to represent an arbitrary observation point "P" in space. The projection of the point P on the zx-plane, $P^{(zx)}$, is employed to introduce the angle θ, which is measured from the direction perpendicular to the structure under analysis and it is usually employed in leaky-wave antennas [Oliner and Jackson, 2007].

a different width (due to matching reasons) and an associated radiation resistance of $R_{rad}(\omega)/2$, instead of a radiation resistance of $R_{rad}(\omega)$, which is only used for internal slots.

Finally, $E_0(\omega)$ is a normalization term, employed to exactly retrieve the absolute magnitude of the radiated field. This term is expressed as

$$E_0(\omega) = \sqrt{\frac{P_{rad}(\omega)}{P'_{rad}(\omega)}}, \tag{6.24}$$

where $P_{rad}(\omega)$ is the total power radiated by the antenna, computed from the equivalent circuit, and it is defined by

$$P_{rad}(\omega) = \frac{R_{rad}(\omega)N_{st}}{2}\left[\frac{|I_1(\omega)|^2 + |I_{N_{uc}+1}(\omega)|^2}{2} + \sum_{n=2}^{N_{uc}} |I_n(\omega)|^2\right], \tag{6.25}$$

and $P'_{rad}(\omega)$ is a reference power computed from the radiated fields as

$$P'_{rad}(\omega) = \int_{-\pi/2}^{+\pi/2}\int_0^{\pi} \frac{1}{2\eta}|\bar{E}_{se}(\omega,\hat{\theta},\phi,r)|^2|AF(\omega,\hat{\theta})|^2 r^2 \sin\hat{\theta}\, d\hat{\theta}\, d\phi, \tag{6.26}$$

where η is the free-space impedance and the integration has been performed over the upper hemisphere, assuming that the ground plane of the antenna is extended to infinite.

Once the electric field has accurately been obtained, the calculation of parameters such as directivity (D), directive gain (G_D) and realized gain (G_R) of the proposed PPW CRLH LWA may easily be

computed as [Stutzman and Thiele, 1998]

$$D(\omega) = \frac{\max_{\theta}(|E(\omega,\hat{\theta},\phi,r)|^2 r^2)}{P_{rad}(\omega)/(4\pi)}, \tag{6.27}$$

$$G_D(\omega) = D(\omega)\,\frac{P_{rad}(\omega)}{P_{inc}(\omega)\,(1-|S_{11}|^2)}, \tag{6.28}$$

$$G_R(\omega) = D(\omega)\,\frac{P_{rad}(\omega)}{P_{inc}(\omega)}, \tag{6.29}$$

where $P_{inc}(\omega)$ is the power incident on the feeding parallel-plate waveguide, which has a width of $N_{st}w_{uc}$.

The maximum realizable gain, $G_{R,max}$, estimated as in [Pozar, 1994], is

$$G_{R,max} = N_{st}(N_{uc}+1)\frac{4\pi\ell_{uc}w_{uc}}{\lambda_0^2}\sin(\hat{\theta}_{\text{MB}}), \tag{6.30}$$

where λ_0 is the free space wavelength and $\hat{\theta}_{\text{MB}}$ is the angle of the main beam measured from the antenna perpendicular direction.

The PPW LWA radiated electric field computed by Eq. (6.19) presents important advantages over regular array factor approaches [Stutzman and Thiele, 1998], [Caloz and Itoh, 2004]. First, the use of the dispersive equivalent circuit shown in Fig. 6.1 inherently incorporates into the computed electric field all antenna characteristics as a function of frequency, including mutual coupling between slots, radiation losses and the influence of reactive fields. This is usually neglected in other approaches [Caloz and Itoh, 2004], which employs non-dispersive circuital models and consequently neglect the variation of the radiation losses with frequency. Second, the total power radiated by the PPW LWA is obtained as a function of frequency, thanks to the frequency-dependent resistors. Therefore, for a fixed observation distance, the magnitude of the radiation pattern is obtained as a function of frequency. This allows us to obtain the antenna gain and to exactly know on which directions the radiated electric field is more intense. And third, the inherent 2D radiation nature of the antenna is correctly taken into account by the model, leading to a pencil-beam radiation (instead of the usual fan-beam radiated by 1D structures).

6.4 Design and Analysis of 1D and 2D PPW CRLH LWAs

This section presents the design and subsequent analysis of two PPW CRLH LWAs. The antennas have been designed using the iterative modal-based approach introduced in the previous section, without the help of any generic full-wave commercial software. Therefore, it is demonstrated that the approach presented in Section 6.3 is accurate and able to obtain the physical parameters of in practical PPW CRLH LWA designs. Then, the antennas are completely analyzed as a function of frequency, computing the complex propagation constant of the structure, scattering parameters and radiated electric field. As previously commented, two examples are proposed, in order to demonstrate the 1D and 2D radiation characteristics of the proposed antenna.

In the first example, a methodology for the the design of a 1D PPW CRLH LWA is carefully explained. Specifically, all details related to the design of this type of antennas (unit-cell balancing,

determination of the physical dimensions, etc) are extensively given. Then, full-wave commercial software is employed to validate the results obtained with the proposed modal-based approach, including the complex propagation constant of a simple unit-cell (partial results) and the behavior of the complete structure (concatenation of 10 unit-cells). Besides, the 1D radiation characteristics of the structure are presented and analyzed.

In the second example, the designed procedure previously explained is applied to fabricate a 4 rows -14 unit cell long- 2D PPW CRLH LWA prototype. The prototype has been fabricated and measured. The experimental results from the prototype are used to validate, for the first time, the radiation phenomena predicted for this type of antennas. Then, scattering parameters and 1D and 2D radiation are carefully analyzed and compared with the results obtained by the proposed modal-based approach, obtaining good agreement and fully validating the accuracy of the proposed method.

Finally, note that the full-wave and experimental results shown in this section completely validate the topology of the proposed PPW CRLH LWA and the iterative modal-based approach proposed for the design and analysis of these antennas. Besides, the methodology proposed here allows the user to design a PPW CRLH LWA prototype in a few minutes, avoiding the use of time-consuming full-wave commercial software. Furthermore, note that the combination of the 1D and 2D radiation characteristics of the antenna provides a pencil beam pattern, which is able to scan the space as a function of frequency. It is expected that this interesting property, from a low-cost planar antenna, find many applications in real environments.

6.4.1 Design Example I: 1D PPW CRLH LWA and Full-Wave Validation

This section presents a carefully study of a 10 unit-cell long 1D CRLH LWA comprising a periodically loaded parallel-plate waveguide, giving in great detail all the required steps for its design and analysis. Full-wave commercial software is employed to validate the results at each stage, fully demonstrating the validity of the proposed topology and of the modal-based analysis method.

The first step of the analysis is to set the CRLH TL transition frequency, which in this case is 3.0 GHz. Besides, a host waveguide filled by a material with relatively permittivity $\varepsilon_r = 1.12$ is employed. The host guide is loaded by a grid of via-holes with diameter $d_{via} = 1.0$ mm. Applying Eq. (6.6), the unit-cell dimensions (length and width) are $\ell_{uc} = 23.54$ mm and $w_{uc} = 23.54$ mm, respectively. Note that different parameters can be chosen, and they will still lead to a transition frequency of 3.0 GHz. This can easily be done by modifying the data used in Eq. (6.6), providing high versatility in the unit-cell design. However, the CRLH TL homogeneous condition [Caloz and Itoh, 2005] ($\ell_{uc} \ll \lambda_g$ and $w_{uc} \ll \lambda_g$, with λ_g the guided waveguide) must be satisfied in any case.

The next steps of the analysis are as follows. First, the physical dimensions of the waveguide (t) and the slot (g) required to obtain a balanced design are derived. Second, a single unit cell is rigorously analyzed, obtaining its associated complex propagation constant (including radiation losses). Full-wave results from the commercial software HFSS© are employed at this step for validation. Furthermore, it is numerically demonstrated that the approximation employed to extract the frequency-dependent elements R_{rad} and C_L is indeed accurate. Finally, a complete CRLH LWA composed of ten

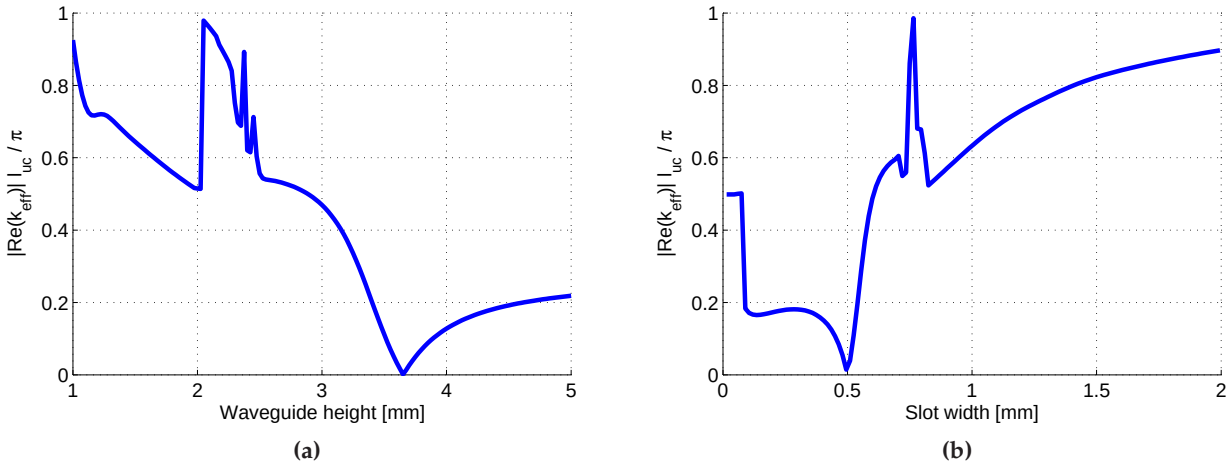

Figure 6.12 – Determination of the physical dimensions of the unit cell required for a balanced CRLH design, i.e. $Re(k_{eff}) = 0$. (a) Evolution of the phase constant as a function of the waveguide height (t), for a fixed value of the slot width ($g = 0.5$ mm.). (b) Evolution of the phase constant as a function of the slot width (g), for a fixed value of the waveguide height ($t = 3.65$ mm.)

unit cells is satisfactorily analyzed using the proposed method and the results are validated using full-wave simulation data, computed by the commercial software CST©. All design steps are given in great detail below.

Balancing the CRLH Unit Cell

In the case of a balanced unit cell, its associated phase constant must be equal to zero at the transition frequency (i.e. $f_{c,WM}$). This allows to obtain a CRLH unit cell with a smooth transition from the left-handed to the right-handed frequency region, avoiding the stopband which appears in the unbalanced case [Caloz and Itoh, 2005] (see Chapter 4.2).

In order to determine the slot and waveguide physical dimensions, we apply the iterative algorithm developed in Section 6.3.3. First, we set some default physical dimensions. In this case, we choose a slot width of $g = 0.5$ mm and a metal thickness of $s = 0.05$ mm, which approximates an infinitesimally thin metal (see Fig. 6.3). The value of g is chosen to make the fabrication process easier. Then, the idea is to obtain the complex propagation constant at the frequency $f_{c,WM}$, for a range of waveguide heights (t). From this analysis we select the thickness value (t) which makes zero the real part of the complex propagation constant (i.e., the phase constant). Fig. 6.12(a) presents this analysis, which yields a final waveguide height of $t = 3.65$ mm. This provides a balanced unit cell design. In order to show that the unit cell is indeed balanced, the procedure is repeated again, but fixing now the waveguide height to the new value ($t = 3.65$ mm) and varying the slot width. The analysis result is shown in Fig. 6.12(b), which demonstrates that $g = 0.5$ mm is indeed the slot width which balances the CRLH unit cell for the given waveguide height ($t = 3.65$ mm). This completes the CRLH unit cell balancing method.

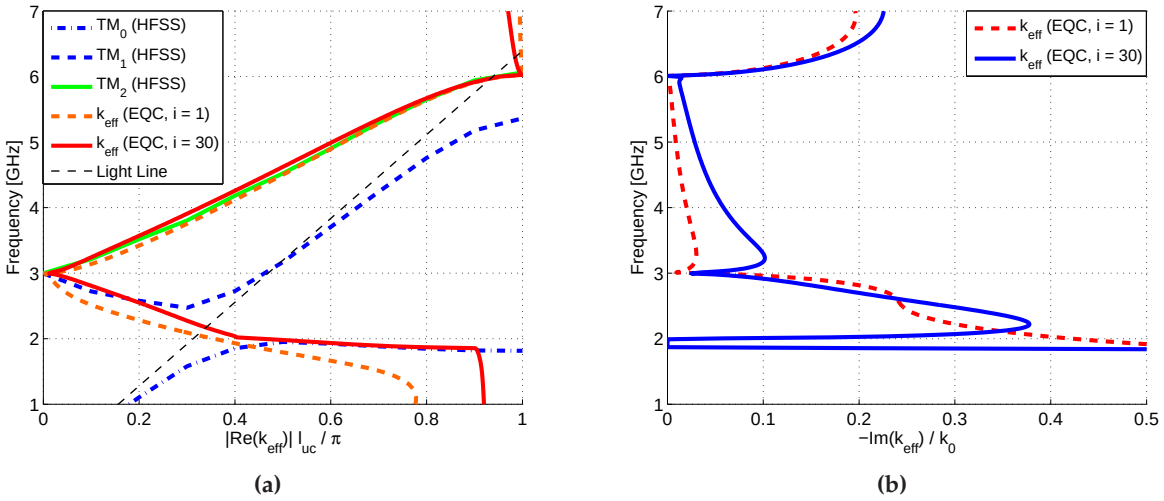

Figure 6.13 – Dispersive behavior of the CRLH LWA under analysis, computed with the proposed iterative algorithm after $i = 1$ and $i = 30$ (convergence reached) iterations. (a) Phase constant diagram, validated using HFSS©. (b) Attenuation (radiation) losses versus frequency.

It is important to remark that the proposed procedure is able to accurately balance the CRLH LWA unit cell, without requiring any full-wave simulations of the complete unit cell. In fact, with the technique proposed the modal analysis is only applied to the slot problem, and not to the complete unit cell structure. Usually, a considerable number of extremely time-consuming full-wave simulations are required to obtain a balanced-design. This is completely avoided using the proposed method, which is able to determine the physical dimensions of a balanced structure in less than 4 minutes. In addition, note that the iterative algorithm is quickly convergent, requiring just eight iterations to obtain a relative error of less than 10^{-12} between two consecutive steps.

Analysis of a Single CRLH Unit Cell

The complex propagation constant of the CRLH unit cell is then obtained for the desired frequency region applying the iterative algorithm. A maximum of 30 iterations are required to obtain convergence (for a relative error below 10^{-12} between two consecutive step for all frequencies). The result of the analysis is shown in Fig. 6.13, for the case of iterations $i = 1$ and $i = 30$ (convergence reached). As it can be observed, a balanced dispersive behavior, with a transition frequency of 3.0 GHz, is clearly obtained. This is further confirmed using simulation data for the dispersion curve, which has been obtained using HFSS©.

In Fig. 6.13(a) it can be observed that the dispersion curve of the TM_2 mode and the RH parts of the TM_1 and of the TM_0 dispersion curve coincide very well with the real part of k_{eff} for $i = 30$. However, there is a discrepancy in the frequency range between 1.95 GHz and 2.5 GHz. This is because the equivalent circuit only reproduces the propagation phenomenon of waves traveling inside the loaded PPW, while the full-wave eigenmode analysis of HFSS© also considers waves which propagate in free-space above the CRLH TL. This leads to a bandgap due to the coupling

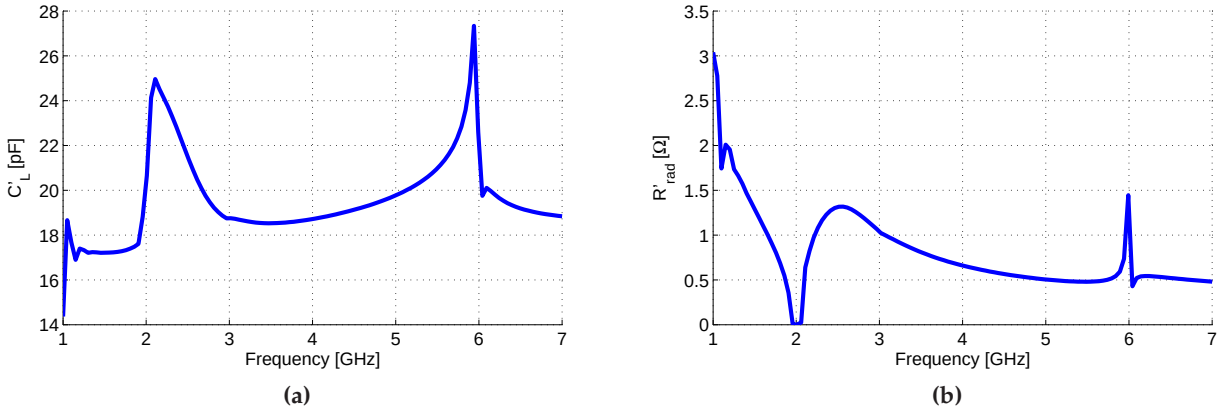

Figure 6.14 – Frequency dependent behavior of the dispersive lumped components which model a slot in a periodic environment, calculated for the CRLH unit cell described in Section 6.4.1 using Eq. (6.17) and Eq. (6.18). (a) Series capacitor $C'_L(\omega)$. (b) Series resistor $R'_{rad}(\omega)$.

between opposite waves propagating above and below the slotted surface (in the case that both types of waves are excited, which occurs in the eigenmode analysis). Note that the equivalent circuit only considers the excitation of the waves traveling inside the CRLH TL, which is correct for predicting the behavior of the proposed LWA.

In Fig. 6.13(b) the radiation losses of the antenna are presented. A significant decrease of the antenna efficiency at the broadside direction (i.e. at the transition frequency of the antenna) can be observed. As explained in Section 6.3.2, this is expected for this type of unit cell configuration. In addition, the computed radiation losses accurately complete the study of the antenna radiation behavior as a function of frequency and of the physical dimensions of the structure. Usually, circuit models [Caloz and Itoh, 2005], [Eleftheriades and Balmain, 2005] are only able to predict the phase constant, and use curve fitting to obtain a frequency-independent resistor value which models the losses. Furthermore, note that usual commercial full-wave software have also difficulties to obtain this parameter in infinitely periodic configurations, because they usually assume a purely real phase shift between the unit cell limits.

In order to complete the analysis, the resistor $R'_{rad}(\omega)$ and capacitor $C'_L(\omega)$ [obtained using Eq. (6.17) and Eq. (6.18)], normalized with respect to the unit cell length ℓ_{uc}, are shown as a function of frequency in Fig. 6.14. It is interesting to note that the bandpass frequency region of the TL (approximately from 2 to 6 GHz) is clearly visible in this figure. In particular, within this frequency range the capacitor exhibits smooth variations, while the value of the radiation resistance experiences a slow decrease. Also, around the lower and upper cut-off frequencies of the structure the capacitance shows an abrupt increase. This is related to a larger stored energy of the structure close to the bandpass edges, very well known in filter theory [Ernst and Postoyalko, 2003].

In addition, note that although the radiation losses decrease at the broadside transition (see Fig. 6.13(b), at 3 GHz) this does not correspond to a decrease of the dispersive lumped resistor value R_{rad}. This is due to the complex relationship between these two quantities, as explained in

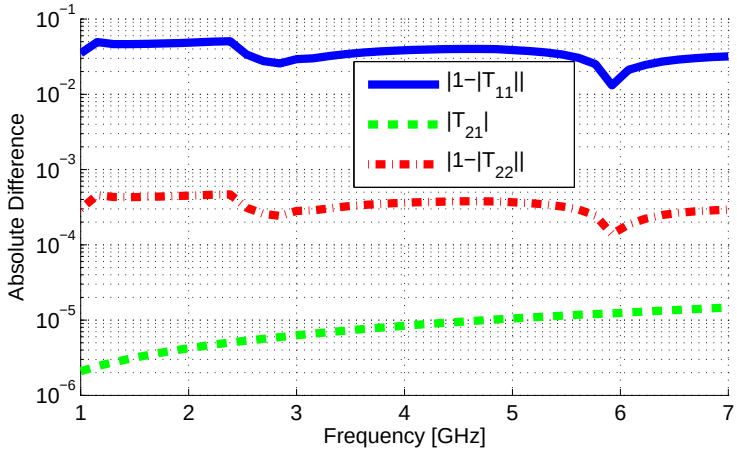

Figure 6.15 – Maximum absolute error of the T matrix elements of the equivalent radiating structure (see Fig. 6.3) with respect to the ideal T matrix related to the equivalent circuit (where $T_{11} = T_{22} = 1$ and $T_{12} = 0$), as a function of frequency.

Section 6.3.2. Furthermore, note that the approximation employed to obtain the dispersive lumped parameters is very accurate. This is demonstrated in two different ways. First, the complex propagation constant obtained using T_{series} [Eq. (6.16), i.e. only with the circuit elements of Fig. 6.1 (bottom)] directly superimpose the full-wave results presented in Fig. 6.13. Second, the maximum absolute error of the terms $T_{gap}(1,1)$, $T_{gap}(2,2)$, and $T_{gap}(2,1)$ [see Eq. (6.15)] as compared with the same elements of T_{series} is very small, as can be observed in Fig. 6.15. This confirms that the proposed dispersive equivalent circuit is indeed accurate.

Analysis of a ten Unit Cells CRLH LWA

Finally, a single strip of width w_{uc} of a complete CRLH LWA consisting of $N_{uc} = 10$ identical unit cells with $g = 0.5$ mm is analyzed combining the single unit cell results obtained in the previous subsection with an ABCD matrix approach [Caloz and Itoh, 2005] (see Chapter 4.2.1). In order to correctly match the antenna, the width of the first and last slots (g_0) must accurately be derived. The goal is to obtain a g_0 width which behaves as a half-slot in the infinite array environment. In this way, the first and last unit-cells of the antenna rigorously follow the equivalent circuit model of Fig. 6.1, and they see the PPW as a kind of continuation of the periodic structure. This leads to a smooth transition from the start/end of the CRLH structure and the unperturbed PPW within the whole frequency range. Following this strategy, the first and last slots present a capacitive behavior close to $2C_L(\omega)$. The approximate value found using this procedure is $g_0 = 0.157$ mm. Furthermore, note that g_0 is responsible for the connection of the CRLH TL to the feeding TL, but it does not influence the propagation and radiation characteristics of the line.

Reference results for the antenna under analysis have been obtained by full-wave time domain simulation using CST Microwave Studio© (MWST). The full-wave model was made up of a strip with perfectly magnetically conducting (PMC) boundary conditions applied to the lateral walls of the simulation volume, in order to represent a laterally periodic structure of infinite extension (see Fig. 6.16).

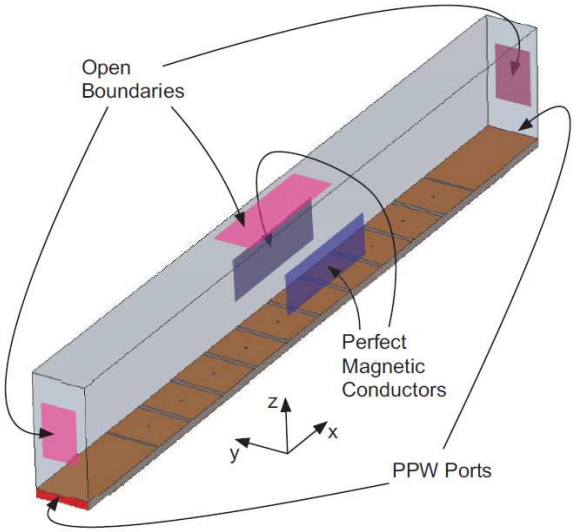

Figure 6.16 – Finite geometry simulated by CST Microwave Studio© consisting of single strip of CRLH LWA covered by an air layer. The types of boundary conditions applied to the side walls of the simulation volume are indicated.

The magnitude of the computed scattering parameters S_{11} and S_{21} and the radiation efficiency $\eta_{rad} = 1 - |S_{11}|^2 - |S_{21}|^2$ (only lossless materials were considered) are plotted in Fig. 6.17. As it can be observed in the figure, a very good agreement between the proposed method and the full-wave simulation is obtained. Furthermore, Fig. 6.18 presents the scanning capabilities of the antenna, as a function of the operating frequency. Specifically, a scanning of the main lobe from the radiation angle $\theta = -45^\circ$ degrees up to $\theta = +60^\circ$ degrees is shown. As expected, a decrease in the radiation efficiency is found at the broadside direction ($\theta = 0^\circ$). Note that the directivity is higher in the RH region ($\theta > 0^\circ$) than in the LH frequency region ($\theta < 0^\circ$). This is related to the fact that the radiation losses [$\alpha(\omega)$] are higher in the LH region (as shown in Fig. 6.13b). Therefore, the input power is radiated in a few unit-cells, leading to a reduced effective length of the antenna (and therefore, a lower directivity). On the other hand, radiation losses are lower at the RH region, and the power is radiated along the whole structure, leading to a larger effective length of the antenna (and, consequently, to a higher directivity).

The above full-wave validations demonstrate that the proposed iterative method is able to efficiently and rigorously analyze PPW CRLH LWAs, taking into account the real physical dimensions of the structure. Furthermore, the proposed method is able to perform the analysis in just six minutes, instead of eight hours required by the full-wave commercial simulations. This allows the application of the proposed modal-based iterative method in the analysis of practical antennas, or even to include this technique into a CAD tool for the analysis, design, and optimization of mushroom based CRLH LWAs.

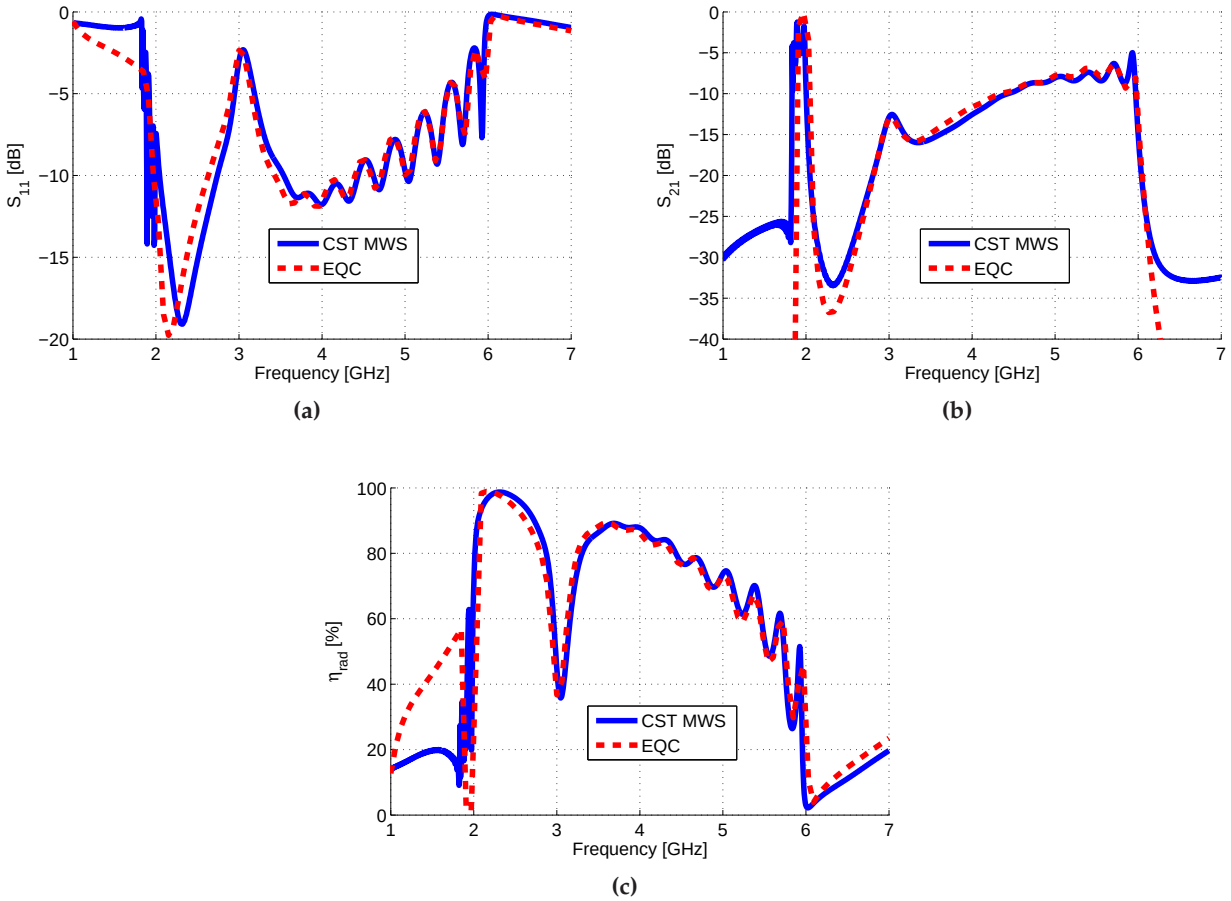

Figure 6.17 – Comparison of scattering parameters and radiation efficiency computed by CST Microwave Studio© (CST MWST) and by the proposed iterative circuit method (EQC) of a single strip CRLH LWA consisting of ten identical reference unit cells.

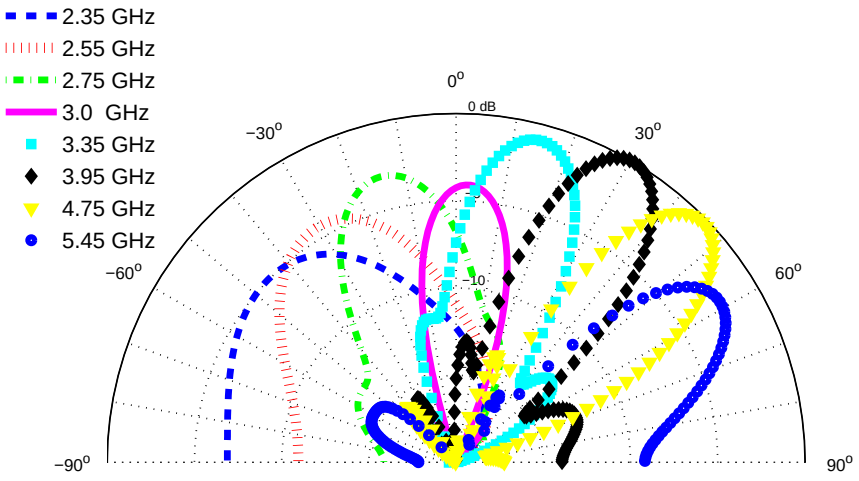

Figure 6.18 – Radiation pattern of the proposed CRLH LWA at different operating frequencies, showing the space scanning capabilities of the antenna.

6.4.2 Design Example II: 2D PPW CRLH LWA and Experimental Verification

This section presents the design, analysis and experimental validation of a PPW LWA composed of 4 rows of CRLH transmission lines, each one with 14 unit-cells. The complete antenna is designed using the method presented in Section 6.3, without the help of any full-wave commercial software. Then, a prototype is manufactured and measured. Very good agreement has been found between measurements and simulations, fully validating both, the antenna radiating phenomena and the proposed modal-based analysis technique.

The first step of the design is to fix the CRLH TL transition frequency, which in this case is set to 9.3 GHz. The dielectric employed, due to availability reasons, has a thickness of $t = 1.525$ mm and a constant permittivity of $\varepsilon_r = 3.38$. This dielectric serves as the host waveguide of the CRLH LWA. Besides, due to fabrication reasons, the diameter of the via-holes is set to $d_{via} = 0.9$ mm. Once these fabrication parameters have been fixed, the use of Eq. (6.6) gives a length and width of the CRLH unit-cell of $\ell_{uc} = 4.15$ mm and $w_{uc} = 7.15$ mm, respectively. Since both dimensions of the unit-cell, length and width, can be adjusted using Eq. (6.6), there is a high flexibility in obtaining a CRLH unit-cell design with the desired transition frequency.

In order to complete the design, we need to derive the physical dimension of the slot, g, which provides a balanced CRLH behavior, i.e., that provides a zero phase constant at the CRLH transition frequency, $Re[k_{eff}(f_{c,WM})] = 0$. For this purpose, following the guidelines given in the previous section, we perform a parametric study of the CRLH phase constant as a function of the slot width g, at the frequency of $f_{c,WM}$. From this analysis, we chose the slot width value which makes zero the CRLH unit-cell phase constant. Fig. 6.19 presents this analysis, which yields a final slot width of $g = 0.61$ mm. This step finishes the CRLH unit-cell design procedure, which has provided all the physical dimensions required to obtain a balanced design. It is important to note that the parametric study required for the unit-cell design has been carried out in just 40 seconds (on a regular 2009 desktop computer), instead of the hours that are usually required by completely full-wave commercial techniques.

Once the CRLH unit-cell has been designed, the next step is to compute the complex propagation constant of the cell within the desired frequency region. For this purpose the iterative algorithm presented in Section 6.3.3 is applied. The analysis is carried out in about 4 minutes (using a 2009 regular desktop computer), requiring about 30 iterations to achieve convergence (relative error below 10^{-12} between two consecutive steps for all frequencies). The results of the analysis are shown in Fig. 6.20. As can be observed in Fig. 6.20(a), the cell is balanced, with a CRLH transition frequency of 9.3 GHz. It is also observed that the LWA start radiating at a frequency around of 7.3 GHz (where the fast-wave region begins) and it continues radiating above 12 GHz. As expected, and as shown in Fig. 6.20(b) and explained in Section 6.3.2, radiation losses are highly mitigated at the broadside direction. Besides, note that radiation losses are larger at the LH frequency region as compared with the RH frequency region. Therefore, the effective length of the antenna is smaller at the LH frequency region (which turns out into a smaller directivity) as compared with the RH frequency region, where the directivity is higher.

After the analysis of a single CRLH unit-cell, a complete PPW CRLH LWA has been fabricated.

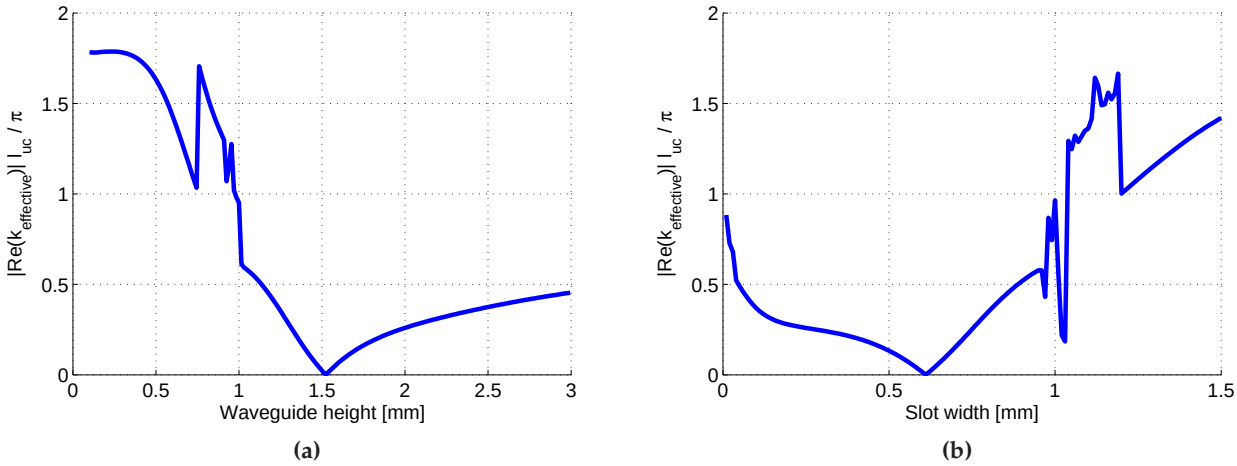

Figure 6.19 – Determination of the physical dimensions of the unit cell required for a balanced CRLH design, i.e. $Re(k_{eff}) = 0$. (a) Evolution of the phase constant as a function of the waveguide height (t), for a fixed value of the slot width ($g = 0.61$ mm.). (b) Evolution of the phase constant as a function of the slot width (g), for a fixed value of the waveguide height ($t = 1.524$ mm.)

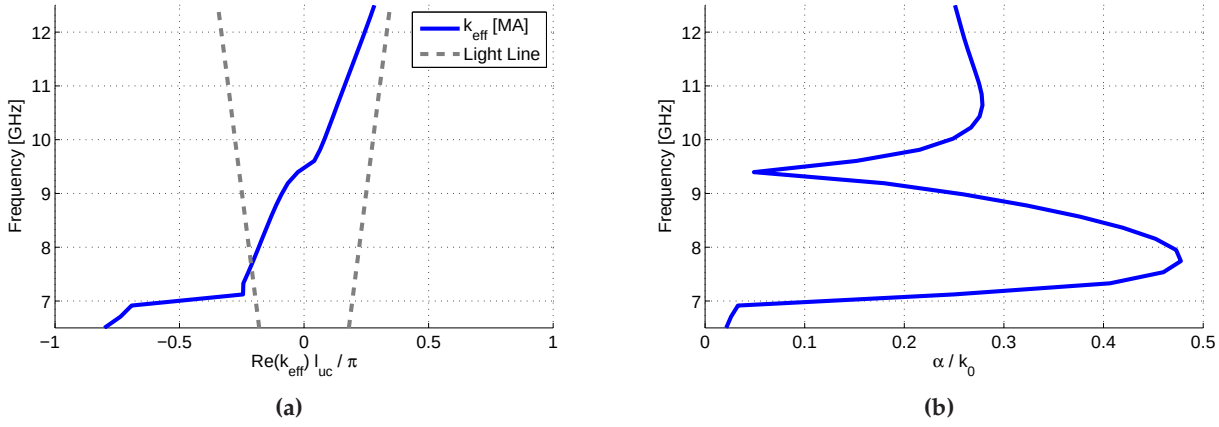

Figure 6.20 – Dispersive behavior of the designed CRLH LWA structure computed with the proposed modal-based approach. (a) Phase constant versus frequency. (b) Attenuation (radiation) losses versus frequency.

The antenna is composed of 4 rows of 14 unit-cells CRLH transmission lines. Each CRLH TL is modeled by using an ABCD approach [Caloz and Itoh, 2005] (see Chapter 4.2.1), which models the concatenation of the 14 unit-cells. All CRLH TLs are simultaneously feed at their input port. The feeding is placed between to consecutive via-holes, in order to reduce reflections. Besides, in order to simulate an infinite medium along the y-direction, additional unfed CRLH TLs have been included at the antenna borders. A photo of the complete fabricated prototype is shown in Fig. 6.21.

Fig. 6.22 presents the simulated return loss (S_{11} parameter) of the antenna, fully validated against experimental results. As can be seen in the figure, the matching of the antenna is very good at the LH

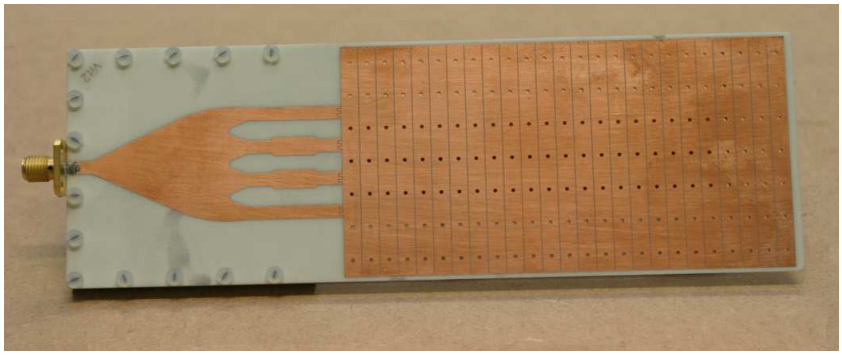

Figure 6.21 – Photo of the PPW CRLH LWA manufactured prototype.

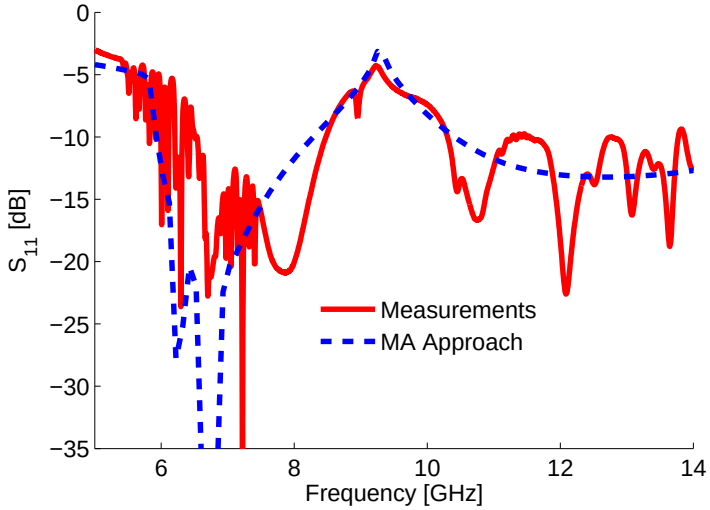

Figure 6.22 – Return loss (S_{11}) of the designed PPW CRLH LWA structure, computed with the proposed modal-analysis approach and validated against measurements.

frequency region, where the energy which propagates into the antenna is completely radiated. This is because the radiation losses are very high at this frequency region [see Fig. 6.20(b)]. On the other hand, the matching of the antenna at the RH frequency region is not so good, but still acceptable (about -10dB). In this region, the return loss presents a response with a ripple. This ripple is related to the reflected waves which appear at the end of the antenna, due to i) the discontinuity between the CRLH medium and free space, and to ii) the fact that the input energy has not completely been radiated, because radiation losses are lower at this frequency band.

Fig. 6.23 presents two radiation diagrams from the designed structure, at the frequencies of 8.4 GHz (radiation towards the backward direction of $-30°$) and of 10.5 GHz (radiation towards the forward direction of $+40°$). The patterns are obtained using Eq. (6.19), and are fully validated employing measured results. As can be observed, good agreement is achieved. Besides, Fig. 6.24 shows the normalized measured electric field, in the E-plane, within the frequency band from 7.0 GHz to 12.5 GHz. It can be observed that the direction of radiation changes from negative to positive angles as frequency increases, correctly following the LWA scanning law. A contour line highlights the region of high radiation intensity. It clearly indicates a continuous scanning frequency range, from

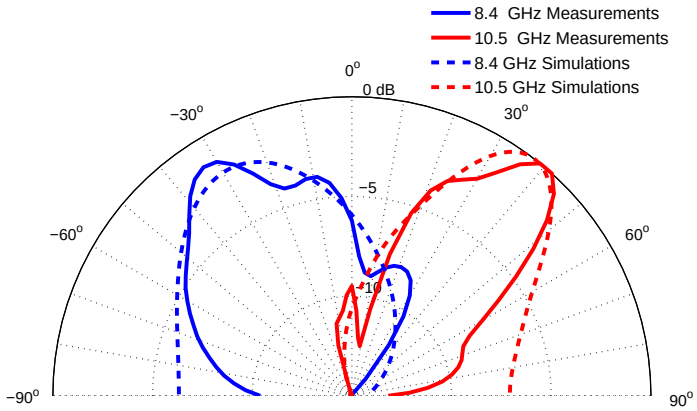

Figure 6.23 – Radiation diagram from the designed PPW CRLH LWA structure obtained using the proposed modal-based approach at two different frequencies ($f = 8.4$ GHz, radiation at backwards, and $f = 10.5$ GHz, radiation at forwards). Measured data is employed for validation purposes.

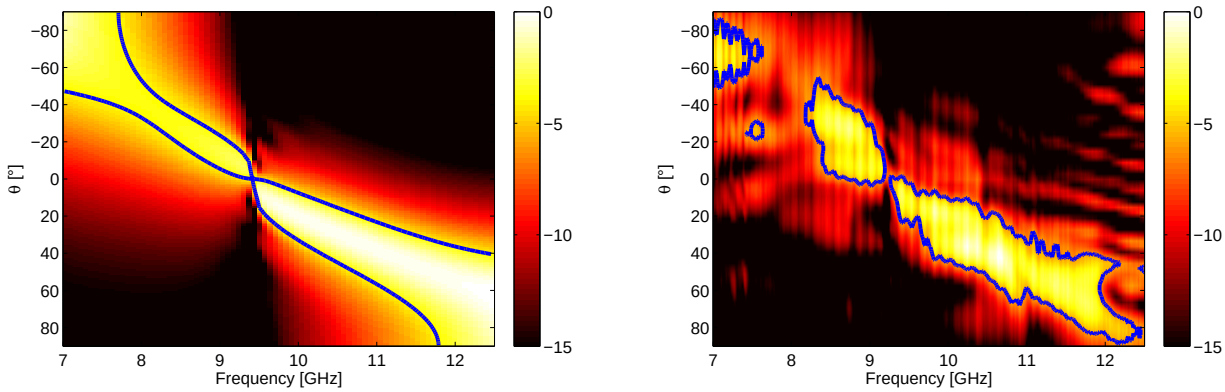

Figure 6.24 – Simulated (a) and measured (b) radiated E-field (normalized) as a function of both frequency and spatial angle (from the direction perpendicular to the antenna). The highlighted radiation main lobe clearly follows the LWA scanning law.

8.1 GHz up to 12.4 GHz, which turns out into a range of radiation angles from $-50°$ up to $80°$. The measured data is in very good agreement with the theoretical results shown in Fig. 6.20(a). As expected, radiation is reduced at the broadside direction (around 9.3 GHz). Besides, it should be noted that secondary lobes pointing backwards appears at the RH frequency region. These lobes are related to the reflected waves which appear at the end of the antenna, and propagate back into the CRLH LWA.

Finally, Fig. 6.25 presents the PPW CRLH LWA electric field radiation at the structure upper hemisphere (top view), obtained at the frequencies of 8.4 GHz (backwards) and of 10.75 GHz (forwards). As can be seen in the figure, a pencil beam appears. This beam type is related to the 2D nature of the antenna, which is continuous along the y direction and periodic along the x direction. Again, good agreement between simulations and measurements is found. Deviations are mainly due to the curvature of the guided wave's phase front when propagating along the loaded PPW, an effect that is not taken into account in the equivalent circuit model, where a straight phase front is assumed.

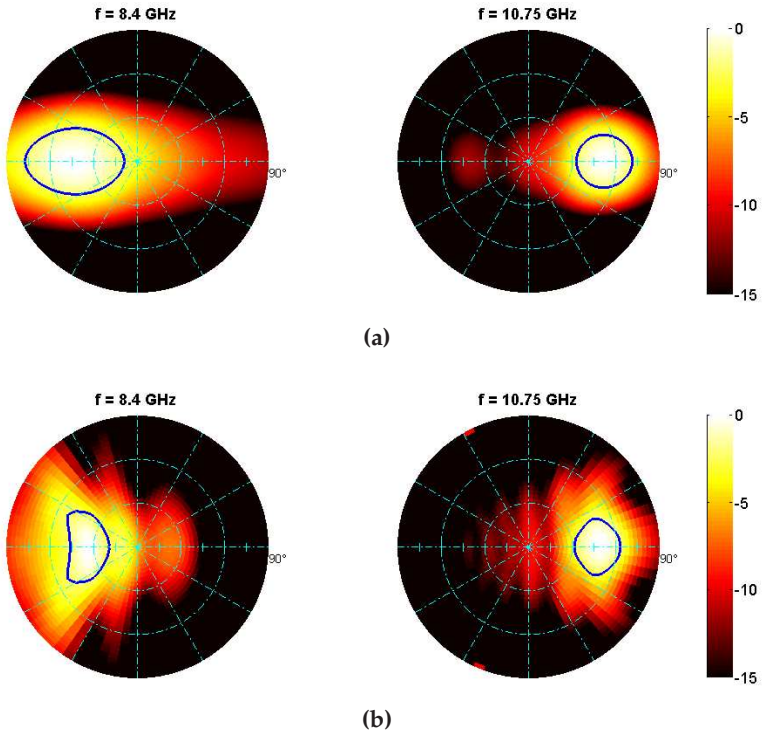

Figure 6.25 – Simulated (a) and measured (b) radiated E-field (normalized) obtained at the antenna far-field upper hemisphere. A pencil beam pattern is clearly visible.

The use of measured data from the fabricated prototype completely validates the radiating phenomena of the proposed CRLH LWA structure. It is important to note that the analysis and design of this type of antennas have been performed using the proposed modal-based iterative approach, without requiring any full-wave commercial software. As it has been shown in this section, the proposed method is able to design a real LWA prototype in only a few minutes, leading to results that are in good agreement with measured data.

6.5 Conclusions

In this chapter, a novel composite right/left-handed leaky-wave antenna comprising a periodically loaded parallel-plate waveguide (PPW CRLH LWAs) has been presented. The antenna loading has been achieved using via-holes and slots. The resulting antenna is planar and inherently $2D$, because the radiating slots are periodically located along the x direction but they are continuous along the y-direction.

In addition, a novel modal-based iterative circuit model for the calculation of the complex propagation constant related to this type of antennas has been proposed. The conventional CRLH unit cell configuration has been modified, including an equivalent circuit which takes into account the coupling of the structure to free-space. This coupling has been modeled employing a unit cell equivalent radiating structure, which is rigorously analyzed using a multi-mode approach combined with Floquet's theorem. The resulting transmission matrix has accurately been represented by lumped elements, leading to a frequency-dependent unit cell model. Then, a quickly-converging iterative

algorithm has been employed to determine the final element values of the unit cell. The proposed technique was found to be accurate, and it can take into account the structure physical dimensions. The technique also allows to obtain a balanced CRLH unit cell design, it is much faster than commercial full-wave simulations, and it provides a deep insight into the physics of the antenna's radiation mechanism. Furthermore, the radiation characteristics of the antenna have been analyzed using a frequency-dependent formulation, which is able to accurately retrieve the radiated electric field, allowing the computation of all antenna parameters: radiation pattern, 3-dB beam width, directivity, gain, etc.

Then, a methodology for the design of practical PPW CRLH LWAs has been introduced. Full-wave simulations and measured results, for two different PPW CRLH LWA designs, have been employed to demonstrate both, the antenna radiation mechanisms and that the developed method is indeed accurate, efficient, and able to provide physical insight into the antenna's behavior.

Finally, note that the proposed antenna is low-cost, low-profile and completely planar. It has been demonstrated that this inherently 2D antenna radiates a pencil-beam, with frequency-scanning capabilities. Due to these interesting antenna's radiation properties and its simple design and analysis, it is expected that the proposed antenna finds practical applications in many real environments.

Chapter 7

Final Conclusions and Perspectives

7.1 Conclusions

This PhD. thesis has been focused on the **development of novel analytical and numerical techniques for the analysis and design of new guiding and radiating structures and optically-inspired phenomena at microwaves.** Through the work, **different approaches** (mostly based on the integral equation technique, but also including other methods, such as mode matching or time-domain transmission lines formulations) **have been proposed for the accurate and efficient analysis of diverse structures operating at the microwave frequency region**. In addition, **these formulations have been applied to the analysis and design of a wide variety of novel microwave devices, applications and phenomena**, such as hybrid waveguide-microstrip filters, temporal and spatio-temporal Talbot effects, or parallel plate waveguide leaky-wave antennas. Finally, *the use of fabricated prototypes has fully demonstrated both, the accuracy and efficiency of the proposed numerical techniques for the analysis of microwave structures, and that the proposed devices/phenomena are indeed adequate and useful to the space industry and to modern ground, mobile, satellite, and UWB high data-rate communications systems*.

For a simple comprehension, the work developed in this PhD. thesis has been divided into three different research lines.

The first research line was mainly related to **the mixed-potential integral equation analysis of multilayered circuits in shielded enclosures**. As it is well-known, the Green's functions associated to the problem under study are the key element of any integral equation formulation. However, even though efficient numerical methods have been developed in the past and are available for the calculation of Green's functions related to unbounded multilayered media, the computation of Green's functions for the shielded version of this problem is still challenging. Generally speaking, an efficient and convergent numerical evaluation of boxed Green's functions cannot be performed neither in the spectral domain nor in the spatial domain, using known techniques. Besides, the methods available in the literature are only valid for the cases of rectangular or circular multilayered enclosures. Consequently, novel algorithms and numerical techniques had to be investigated.

In Chapter 2 of this work, **the numerical evaluation of multilayered shielded Green's func-**

tions, and their spatial derivatives, was addressed and as a result of this study three novel spatial-domain formulations, based on auxiliary sources, have been presented.

The first one, denoted as "spatial images technique", employs a set of auxiliary spatial charges or dipoles (spatial images), located outside the cavity under analysis, to impose the potential boundary conditions at discrete points along the cavity contour. *The proposed technique is able to compute multilayered Green's functions, and their spatial derivatives, associated to cavities with arbitrarily-shaped cross section, requiring just a reduced number of spatial images to achieve numerically convergence*. Furthermore, the approximate technique provides a measure of the error committed in the imposition of the boundary conditions.

The second technique, which is restricted to the case of multilayered rectangular enclosures, presents the continuous implementation of the spatial images technique. In this way, *instead of discrete spatial images, a continuous set of auxiliary sources is employed to impose the potentials boundary conditions along the whole cavity perimeter*. In addition, the method has been combined with *the use of dynamic ground planes*, which *perfectly imposes boundary conditions for the potentials on two of the cavity walls, and completely removes any numerical instability provided by the point source singular behavior*. Note that this technique provides a total control on the error committed on the Green's functions computation, allowing to reduce it to arbitrarily small values.

In last place, the third technique proposed allows the computation of multilayered Green's functions associated to cavities with triangular right-isosceles cross section. The technique is based on image theory, and expresses the triangular-shaped Green's functions as a linear combination of boxed Green's functions. It has been demonstrated that the method is rigorous, stable, and fast convergent.

A common feature of all previous techniques is that they have been developed at the Green's functions level, so the resulting integral equation can easily be solved with an arbitrary discretization scheme. Specifically, these methods are applied in Chapter 3 within a mixed-potential integral equation (MPIE) framework for the analysis of multilayered printed circuits in shielded enclosures. Even though the use of the proposed formulations for the analysis of multilayered shielded circuits leads to very accurate results, it has been observed that these methods are computationally very intensive. In order to circumvent this problem, **two novel techniques have been proposed in Chapter 3 for the efficient implementation of the proposed spatial-domain Green's function approaches within the MPIE formalism**.

The first method is based on the interpolation, not at the Green's functions level but in an upper abstraction layer, i.e. interpolating the complex values of the discrete auxiliary charges or dipole employed to recover the Green's functions. This approximate method provides an important reduction of the computational cost required to the analysis of practical circuits.

The second technique exploits the fact that the developed Green's functions present their singular and non-singular contributions naturally separated. Using this important feature, two different MPIE method of moments matrixes are computed separately. The first matrix is related to the singular behavior, and can be computed very fast using standard techniques. The second one, which contains the influence of the auxiliary sources, is computed with very limited computational effort, due to its smooth behavior. *It has been observed that this approach drastically reduces the computational cost of the MPIE technique, being extremely competitive against any other numerical method known to the author*.

In addition, Chapter 3 have also applied the proposed formulations to the analysis of a wide variety of microwave filters, comparing the results obtained in term of efficiency and accuracy against other full-wave techniques. **Measurements obtained from fabricated prototypes have also been included for a complete validation**. Furthermore, as a consequence of this exhaustive study, Chapter 3 has **introduced the novel hybrid waveguide-microstrip filter technology**. This filter technology combines one resonance, provided by the multilayered cavity (with a specific configuration), with N microstrip resonators, leading to a $N+1$ order filter. *The proposed technology, which have experimentally been demonstrated, is light, compact, low-lossy, uses the filter package as a part of the filter, and allows to implement transversal filters*. Therefore, it is ideal for the space industry.

The second research line presented in this PhD. thesis was mainly related to the **impulse-regime study of composite right/left-handed (CRLH) structures, and the theoretical and practical demonstration of novel optically-inspired phenomena and applications at microwaves**. The introduction of metamaterials in the last decade has led to the development of novel devices and applications, such as leaky-wave antennas, couplers, phase shifters, power dividers, etc. At the microwave regime, metamaterials have usually been implemented by using composite right/left-handed transmission lines (TL), this has led to guiding and radiating devices with superior characteristics as compared with the previous state of the art, such as components with dual/triple/quad-band, enhanced bandwidth, enhanced coupling or leaky-wave antennas with full-space radiation properties. Currently, most of the applications and phenomena of CRLH structures have only been reported in the harmonic regime. However, the emergence of ultra wide band systems requires novel microwave concepts and applications in the impulse regime. Consequently, it was necessary a systematic study of CRLH TLs operated in the impulse regime, where the broadband and highly dispersive nature of metamaterials could provide novel solutions in this field.

In Chapter 4 of this work, **a novel formulation framework has been proposed for the impulse-regime analysis of CRLH structures**. In the guided regime, a closed-form time-domain Green's function method has been used to analyze electrically thin linear and non-linear CRLH transmission lines, excited by a single pulse or by a periodic train of input pulses.

In the radiative regime, *a new circuital condition for the standard CRLH LWA unit cell has been proposed to achieve, for the first time, a constant radiation rate in the whole space*. The novel condition allows a continuous and smooth transition of the radiation losses from the left-handed to the right-handed frequency regions. Besides, a novel simple theory has been presented for the harmonic characterization of leaky-wave antennas. This theory expresses the CRLH LWA radiation losses as a combination of the current flowing on each conductor of the transmission line, providing a fundamental explanation about leaky-wave antennas in connection with transmission lines. In addition, these developments have been combined with the time-domain Green's function approach for the efficient and accurate analysis of CRLH LWA excited by temporal pulses.

Note that the proposed methods are novel, in the sense that the time-domain analysis of such structures have been performed before. In addition, these techniques present interesting features, such as unconditional stability and fast computation, due to the continuous treatment of time, and the insight into the physical phenomena provided by the Green's functions.

Thanks to the novel numerical methods proposed, the possibility for the fast analysis of complex CRLH structures was open. As a consequence, **it was possible to apply the dispersive engineering**

approach (phase shaping of electromagnetic waves to process signals in an analog fashion), i.e. to control the CRLH TL dispersive properties in practical structures. This has been exploited in Chapter 5 for the development of novel phenomena and applications in the microwave domain, most of them transported from optics. Specifically, Chapter 5 has presented the following novel phenomena/devices: (a) *phenomenology of pulse propagation on dispersive CRLH media*, (b) *pulse compression*, (c) *temporal Talbot effect*, (d) *broadband resonator*, (e) *nonlinear effects and automatically balance of CRLH lines*, (f) *real time spectrogram analyzer (RTSA) system*, (g) *frequency-resolve electrical gating (FREG) system* and (h) *spatio-temporal Talbot effect*. In all cases, a detailed mathematical description, following an optical approach, of the phenomena/device has been proposed. Then, **measurements from fabricated prototypes and/or full-wave simulations results have been employed to fully demonstrate the proposed phenomena and applications**, which are completely novel in the microwave regime. Among them, it is important to highlight the spatio-temporal Talbot effect, which was predicted, mathematically modeled and experimentally verified for the first time in the microwave regime. The main applications of this phenomena are related to wireless feeding networks and spatial multiplexors.

Finally, the third research line **have proposed a novel CRLH parallel-plate waveguide (PPW) leaky-wave antenna (LWA), and a new numerical technique for a fast and accurate analysis, design, and characterization of this type of structures**. The introduction of CRLH LWAs during the last decade allowed to obtain antennas able to scan the whole space (from backwards to forwards, including the broadside direction). The analysis of this type of antennas, which are normally fabricated in microstrip or coplanar waveguide technologies, was performed by using circuits models, which are able to accurately take into account for the structure's phase constant. However, due to the structure's complex radiation mechanism, radiation losses are usually neglected, so that the radiation characteristics of this type of antennas can not completely be determined by circuital methods. In addition, a considerable number of very time-consuming full-wave simulations are usually required for the design of balanced CRLH LWAs. Consequently, both, novel CRLH leaky-wave structures, with enhanced features and controllable radiation mechanisms, and numerical techniques which allow the accurate and fast analysis and design of these novel structures, had to be investigated.

A novel PPW CRLH LWA has been presented in Chapter 6. The new structure is composed of a parallel-plate waveguide (PPW) periodically loaded by via-holes and slots. In order to analyze this structure, a novel frequency-dependent unit-cell circuit has been introduced. This circuit model is able to completely characterize the antenna as a function of frequency, including scattering parameters, radiation angle and losses, among all antenna features. In order to obtain the dispersive parameters of the model, an iteratively-refined approach, based on mode-matching, phased-array theory and the use of the Floquet's theorem has been presented. *The proposed technique was found to be accurate, and it can take into account the structure physical dimensions. The technique also allows to obtain a balanced CRLH unit cell design, it is much faster than full-wave simulations, and it provides a deep insight into the physics of the antenna's radiation mechanism*. In addition, the radiation characteristics of this type of antennas have also been investigated in deep, and a novel formulation for the radiated far-field computation has been presented. The frequency-dependent method is based on an array factor approach of equivalent magnetic sources and accurately retrieves the 1D and 2D radiated patterns. **Full-wave simulations and measurements from a fabricated prototype have also been employed to validate both, the antenna radiating characteristics and the proposed techniques**.

I conclude this thesis with the hope that I have made interesting and useful contributions to the microwave community, and that some of the concepts, developments and structures proposed here will find application, in the near coming future, in CAD packages and in modern mobile, satellite and UWB communication systems.

7.2 Perspectives

As in any intensive research activity, the development of the present PhD. dissertation has led to many novel ideas which may contribute to the improvement and future extension of the proposed work. This section briefly specifies these future research lines.

Perhaps, the most straightforward continuation of this work is the extension of the spatial images technique to the more general Green's functions analysis of multilayered enclosures with complete arbitrarily-shaped cross sections (including re-entrant sections). One possibility to carry out this task is to modify the continuous counterpart of the spatial images method, locating the auxiliary sources around the complex contour of the structure. The main problem of this approach is how to handle the singular behavior of the point source, specially when it is placed very close to a cavity wall. Besides, note that the two methods employed to solve this problem in the regular spatial images technique, i.e. the use of a specific algorithm to locate the auxiliary sources and the use of auxiliary ground planes, can not be employed in this case due to the abrupt variations of the cavity contour. However, some strategies based on the extraction of the asymptotic or static parts of the involved singular integrals may lead to accurate solutions (see [Wilton et al., 1984] and [Pérez-Soler et al., 2010].

Another interesting continuation of this work is the application of the spatial images technique for the analysis and design of arbitrarily-shaped cavity backed antennas. In this case, it is required to reformulate the proposed method to compute the multilayered shielded Green's functions for the case of both, electric and magnetic point sources. Then, the integral equation procedure must also be reformulated in order to accurately take into account for the antenna radiation. This may be done my splitting the original problem into two simplest equivalent problems, by using the equivalence theorem. In the first situation, a completely closed cavity, containing both, electric and magnetic sources, should be analyzed. In the second case, the radiation of equivalent magnetic sources placed over a ground plane must be computed. This technique would allow the fast and efficient analysis of cavity-backed antennas employing, for the first time, a completely spatial-domain approach.

Besides, the spatial images technique may also be reformulated to obtain Green's functions of media with different type of boundary conditions, such as perfect electric (PEC), perfect magnetic (PMC), periodic boundary conditions, or a combination of all of them. This modification would allow the accurate analysis of a wide variety of microwave devices and phenomena, such as frequency selective surfaces (FSS), arrays of periodic antennas or CRLH transmission lines and antennas, among many others.

Concerning to the dispersion engineering approach, the main research direction would be the identification of optical phenomena/applications which may be of potential interest at the microwave range. Then, the goal would be to reproduce these phenomena or applications at microwaves, by using the dispersive behavior of CRLH lines combined with the non-linear phenomena achieved by the periodic loading of the line using varactors. On the other hand, it may be useful

to apply some microwave concepts, for instance, related to filter synthesis or antenna arrays, to the development of novel applications at the optic regime.

In the case of UWB applications, one straightforward continuation of the proposed work is the real fabrication of the proposed frequency-resolved electrical gating system (FREG). This would allow the fast and accurate identification (in both, time and frequency) of ultra fast pulses employed by the current UWB systems. The main problem here is the accurate development of extremely precise time-delayers, which is not a simple task.

In the case of harmonic CRLH LWAs, another interesting research direction may be the adequate identification of the antenna radiation mechanism, which in turns also depends on the technology employed for the antenna design (microstrip, CPW, CPS, etc.). This would allow a complete control of the antenna's phase constant and radiation losses, which is extremely important for the design of efficient LWAs. In practice, the radiation losses may be modified around the antenna length (leading to a specific aperture illumination), which would lead to *tapered* leaky-wave antennas (see [Oliner and Jackson, 2007], [Gomez-Tornero et al., 2006a], and [Garcia-Vigueras et al., 2010]). This type of antennas would present some important advantages as compared with regular leaky structures, such as reduced sidelobe levels, beam broadening or focusing properties.

Finally, in the context of the PPW CRLH LWA structure derived in Chapter 6, there are also some possible nice ideas to extend the presented work. First, the analysis of the equivalent radiating structure, which is opened on one side to a free-space periodic environment, is currently performed using a mode-matching technique. An interesting alternative approach is to reformulate the problem by using the integral equation method. In this case, the use of the equivalence theorem would allow to simplify the original problem into two simpler equivalent problems. The first problem is composed by a piece of waveguide, which presents magnetic currents on the top conductor. Then, the second problem is just composed of an equivalent magnetic current radiating into free-space within a periodic environment. This approach would allow the fast analysis of the CRLH PPW LWA equivalent radiating structure, avoiding the relative convergence problems which arise in the mode-matching formulation.

Second, it is important to keep in mind that the proposed method allows to conform the total radiation losses related to each unit-cell. Therefore, it should be relatively easy to make tapered PPW CRLH LWA designs, which, as previously commented, present important advantages in terms of beam shaping and secondary lobe reduction.

And third, an interesting extension of this work would be to accurately shape a desired pencil-beam by controlling the width of each CRLH unit-cell. Furthermore, the incorporation of phase shifters on the feeding lines of each CRLH section would allow a pencil-beam scanning in the complete full-space.

Appendices

Appendix A

Analytical formulas to describe some modulated pulses

The purpose of this appendix is to provide analytical formulas which describe some modulated pulses. These formulas are employed in Chapter 5 to characterize the pulses which excite linear and non-linear dispersive CRLH structures.

A.1 Chirp Modulated Gaussian Pulse

This type of pulses may be described as

$$v(t) = C_0 \mathbf{Re}\left\{\exp\left[j2\pi f_0 t - \frac{1}{2}(1+jC)\left(\frac{t-t_0}{\sigma}\right)^2\right]\right\}, \tag{A.1}$$

where C_0 controls the pulse amplitude, t_0 is the time offset, f_0 is the pulse modulation frequency, σ is related to the pulse duration, and the variable C define the up (when $C > 0$) or down ($C < 0$) chirp modulation. Note that this expression is reduced to a simple modulated Gaussian pulse for the case of $C = 0$. Fig. A.1 presents two examples of this type of pulses.

A.2 Modulated Square Pulse

This type of pulses may be described by

$$v(t) = \begin{cases} C_0 \mathbf{Re}\left\{\exp\left[j2\pi f_0 (t-t_0)\right]\right\} & \text{if} \quad |t-t_0| \leq T/2 \\ 0 & \text{if} \quad |t-t_0| \geq T/2 \end{cases}, \tag{A.2}$$

where C_0 controls the pulse amplitude, t_0 is the time offset, f_0 is the pulse modulation frequency and the variable T define the pulse width. An example of this type of pulses is shown in Fig. A.2.

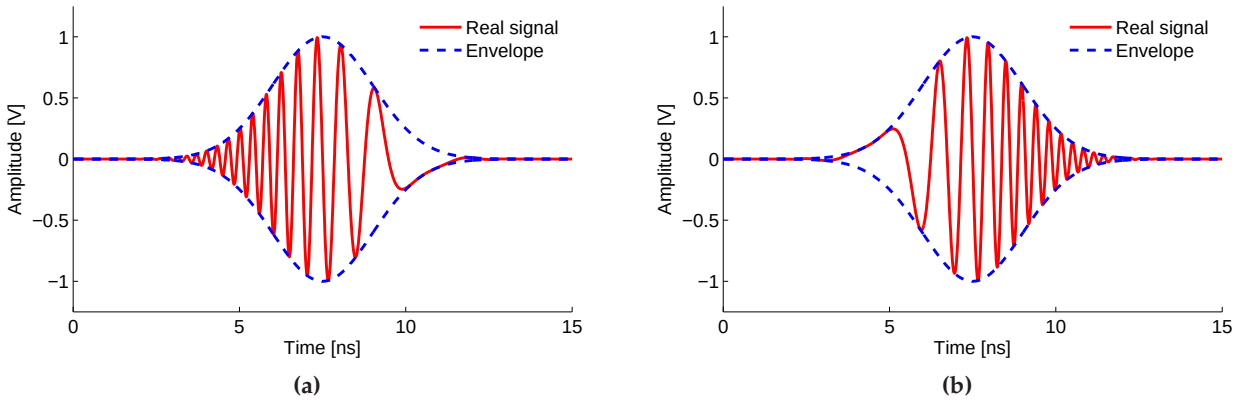

Figure A.1 – Example of chirp-modulated Gaussian pulses, with parameters of $C_0 = 1$, $f_0 = 1.5$ GHz, $\sigma = 1.5$ ns, and $t_0 = 7.5$ ns. (a) Down-chirp Gaussian pulse, with $C = -7$. (b) Up-chirp Gaussian pulse, with $C = +7$.

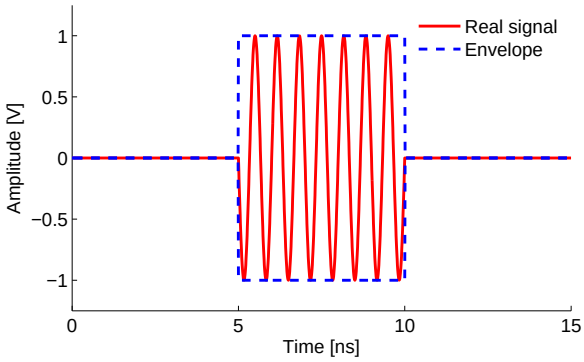

Figure A.2 – Example of a modulated square pulse, with parameters of $C_0 = 1$, $f_0 = 1.5$ GHz, $T = 5$ ns, and $t_0 = 7.5$ ns.

A.3 General Modulated Super-Gaussian Pulse

This type of pulses may be described by

$$v(t) = C_0 \mathbf{Re}\left\{\exp\left[j2\pi f_0 t - \frac{1}{2}(1+jC_1)\left(\frac{t-t_0}{\sigma}\right)^{2m} + jC_2(t-t_0)^3\right]\right\}, \tag{A.3}$$

where C_0 controls the pulse amplitude, t_0 is the time offset, σ is related to the pulse duration, C_1 and C_2 control the linear and quadric chirp modulation, f_0 is the pulse modulation frequency and m is an integer. Fig. A.3 presents two examples of this type of pulses.

A.4 General Non-Linearly Modulated Gaussian Pulse

This type of pulses may be described by

$$v(t) = C_0 \mathbf{Re}\left[U(t)\exp(j|U(t)|^2 z)\right], \tag{A.4}$$

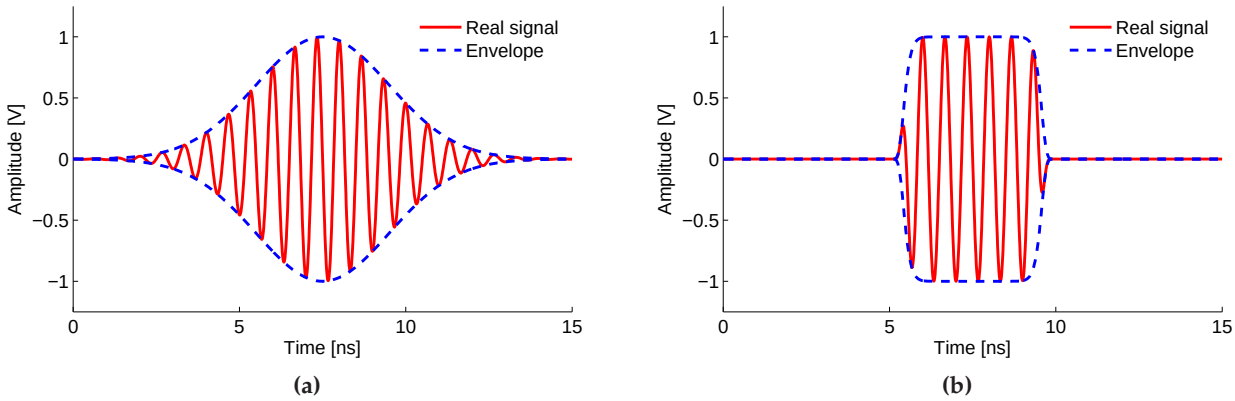

Figure A.3 – Example of modulated super Gaussian pulses, with parameters of $C_0 = 1$, $f_0 = 1.5$ GHz, $C_1 = C_2 = 0$, $\sigma = 2.0$ ns, and $t_0 = 7.5$ ns. (a) $m = 1$, leading to a regular modulated Gaussian pulse. (b) $m = 8$, leading to a modulated super Gaussian pulse.

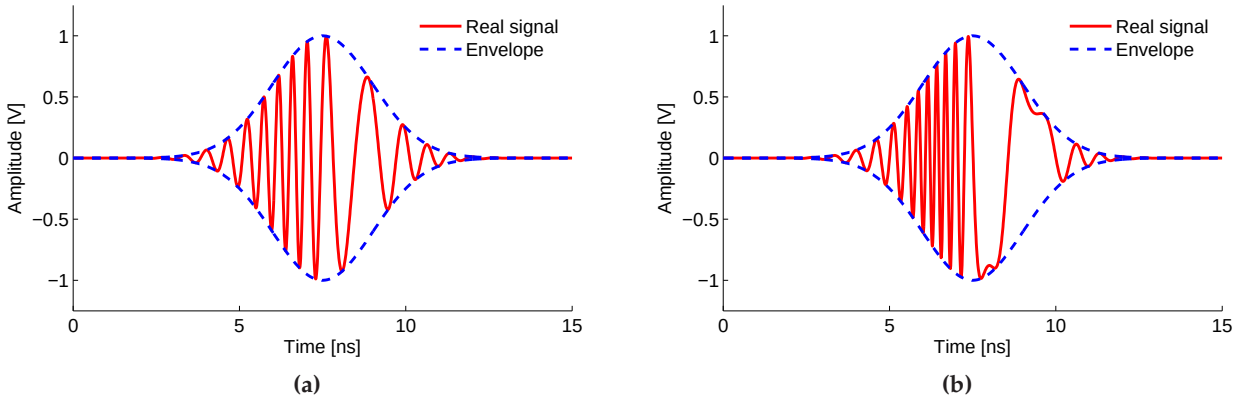

Figure A.4 – Example of non-linear modulated Gaussian pulses, with parameters of $C_0 = 1$, $f_0 = 1.5$ GHz, $C_1 = 0$, $\sigma = 1.5$ ns, and $t_0 = 7.5$ ns. (a) Weak non-linearly modulated Gaussian pulse, with $z = 10$. (b) Strong non-linearly modulated Gaussian pulse, with $z = 25$.

where C_0 controls the pulse amplitude, z is an integer and $U(t)$ is given by

$$U(t) = C_0 \exp\left[j2\pi f_0 t - \frac{1}{2}\left(\frac{t - t_0}{\sigma}\right)^2\right], \tag{A.5}$$

where t_0 is the time offset, f_0 is the pulse modulation frequency, and σ is related to the pulse duration. Fig. A.4 presents two examples of this type of pulses.

Appendix B

Analysis of UWB systems using ADS©

In Chapter 5, the time-domain Green's functions approach proposed in Chapter 4 was employed to model and characterize a wide variety of dispersive and non-linear UWB phenomena and applications at microwaves, such as pulse propagation along CRLH media (see Section 5.2 of Chapter 5), pulse compression (see Section 5.3 of Chapter 5), or the temporal Talbot effect (see Section 5.4 of Chapter 5). In that chapter, the home-made software was validated using measurements from fabricated prototypes (when available) or using simulated results obtained by the commercial software ADS©.

In this appendix, I briefly explain the use of the software ADS© to model UWB phenomena and applications at microwaves. Specifically, I present a description in ADS© (at the system level) of the tunable UWB repetition rate resonator (proposed in Section 5.5 of Chapter 5) and of pulse propagation along non-linear media (see Section 5.6 of Chapter 5). I have chosen these two specific cases because they are the most complicated to model. Any other application or phenomenon (as those described in Chapter 5) can also easily be characterized in ADS© in a similar way.

Finally, note that this appendix does not include any result, just a brief system description of two UWB environments. The explanations of the phenomena and applications, a mathematical justification, and validation results can be found in Chapter 5.

B.1 Tunable Pulse Repetition-Rate Resonator

The features and characteristics of the tunable pulse repetition-rate resonator were presented in Section 5.5 of Chapter 5. In order to fully characterize this device, we have employed the commercial software ADS©. Specifically, the structure presented in Fig. 5.7 is modeled by the circuit model shown in Fig. B.1.

The description of the resonator block diagram in ADS© is as follows. Initially, a baseband Gaussian pulse is generated by a time-domain source (represented in the block "A" of the figure) and modulated using a local oscillator ("B") and a mixer ("C"). The modulated Gaussian pulse propagates

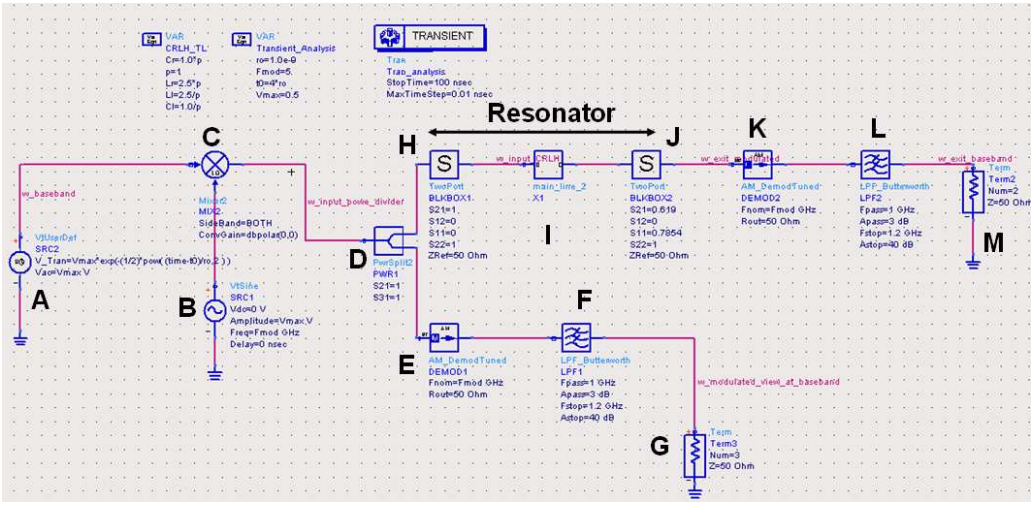

Figure B.1 – Proposed ADS© model of the UWB CRLH-based tunable resonator (see Fig. 5.7a).

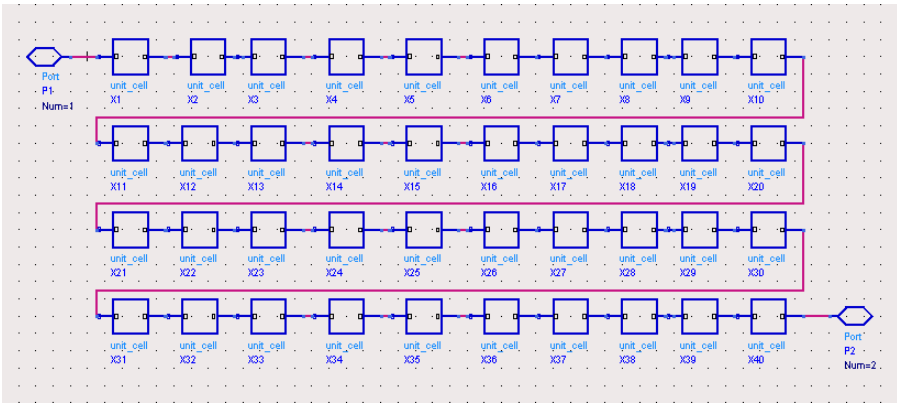

Figure B.2 – Proposed ADS© model of the CRLH transmission line employed in the UWB CRLH-based tunable resonator (see Fig. 5.7b).

into a two different stages, using a splitter ("D"). One of the modulated signals given by the splitter is down-converted to baseband and used as a reference. For this purpose, a demodulator ("E") and a low-pass filter ("F") are employed. The second modulated Gaussian pulse provided by the splitter is used as an input to the actual CRLH resonator. This resonator is composed of two ideal two-ports blocks ("H" and "J") and a CRLH line ("I"). The first block ("H") is configured to propagate all the energy from the splitter towards the CRLH line, and to reflect all the energy which comes from the CRLH line. On the other hand, the block ("J") is configured to reflect back most of the energy towards the line, but also to propagate a small amount of energy to the next stage of the system. In this way, the energy is traveling back and forth between the ideal blocks ("H" and "J"). This configuration, similar to a laser cavity, is able to accurately simulate the behavior of the proposed resonator. In addition, the CRLH line ("I") is modeled using 40 unit cells in a hierarchical configuration, as it can be seen in Fig. B.2. Besides, each unit cell follows the circuit configuration of Fig. 4.3b, which is modeled, using again a hierarchical configuration, as shown in Fig. B.3. Then, the modulated pulse which comes out of the resonator is down-converted to baseband using a demodulator and a low-

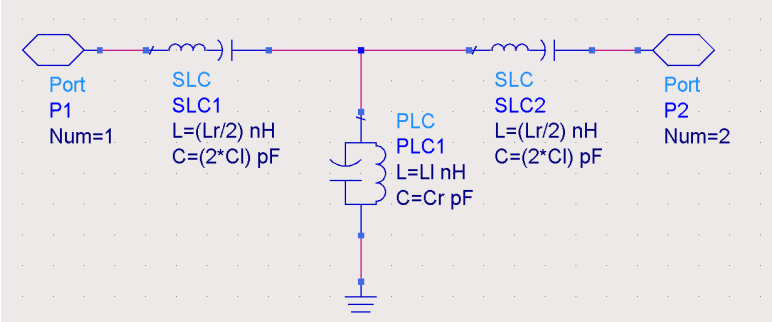

Figure B.3 – Proposed ADS© model of a single CRLH unit-cell.

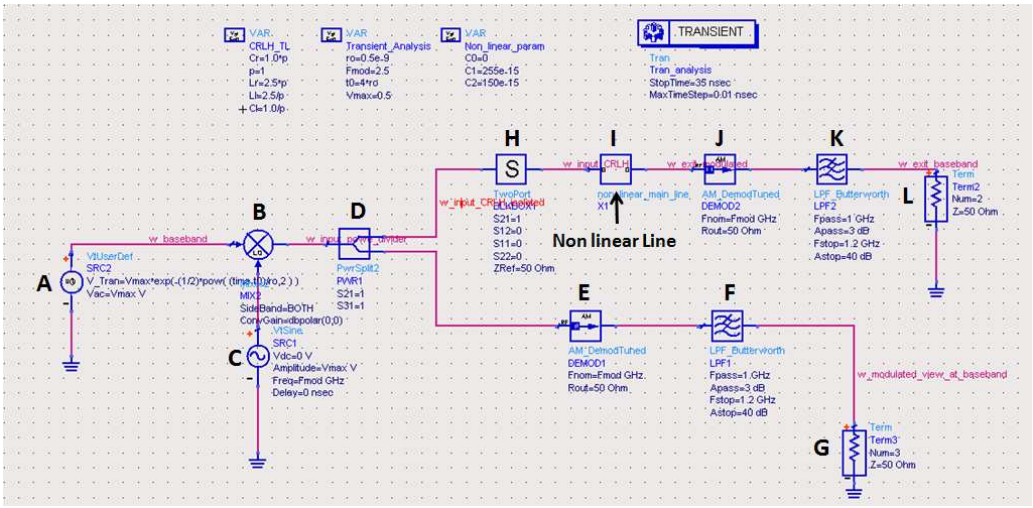

Figure B.4 – Proposed ADS© model of pulse propagation along non-linear CRLH media.

pass filter (blocks "K" and "L"). Note that the final amplification stage of the resonator (see Fig. 5.7a) has not been included in this model for simplicity. Finally, a transient analysis is carried out in order to study the behavior of the complete structure.

B.2 Pulse Propagation along Non-Linear CRLH lines

The features and characteristics of pulse propagation along non-linear CRLH media were presented in Section 5.6 of Chapter 5. In order to fully characterize this phenomena, we have modeled it using the ADS© scheme shown in Fig. B.4.

The description of the model is very similar as in the case of the resonator. First, the generator (block "A" in the figure) provides a baseband Gaussian pulse, which is modulated by using a local oscillator ("B") and a mixer ("C"). The splitter ("D") divides the input pulse into two identical signals. One of these signals is down-converted to baseband [by using a demodulator ("E") and a low-pass filter ("F")] and is used as a reference. The second modulated pulse travels through an ideal two-port block ("H"), which is configured to allows the propagation of the pulse towards the next stage, and

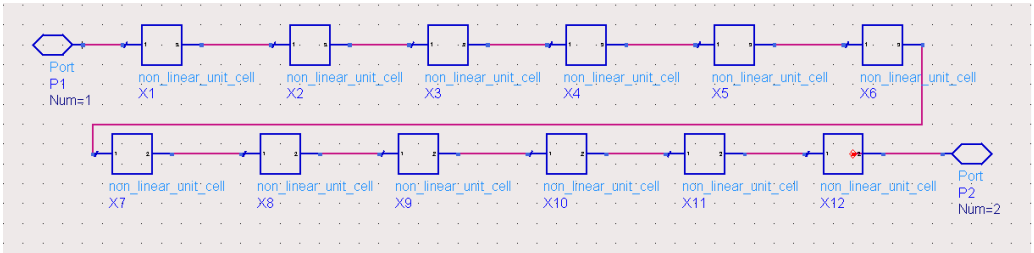

Figure B.5 – Proposed ADS© model of the non-linear CRLH transmission line.

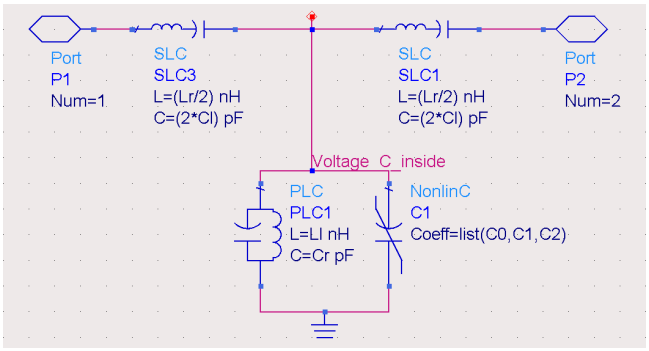

Figure B.6 – Proposed ADS© model of a single non-linear CRLH unit-cell.

absorbs any possible reflected wave coming from there. Then, the pulse is fed into the non-linear CRLH line ("I"), which is modeled by using 12 non-linear unit cells in a hierarchical configuration, as shown in Fig. B.5. Following the hierarchical strategy, each of the non-linear unit-cells has been implemented using the circuital model shown in Fig. B.6. Note that non-linearity is provided by a shunt varactor, which directly depends on the the voltage at the central node of the unit-cell. Finally, the modulated signal which comes out of the non-linear CRLH line is down-converted to baseband using a demodulator and a low-pass filter (blocks "J" and "K").

Appendix C

Mode-matching analysis of a waveguide opened to free space within a periodic environment

C.1 Introduction

The purpose of this Appendix is to present a mode-matching analysis of a dielectric-filled parallel-plate waveguide (PPW) which radiates into free-space in a periodic environment, i.e., the analysis of a single aperture radiating within an infinity periodic array of apertures (see Fig. 6.5). The waveguide is filled by a dielectric with relative permittivity ε_r, and has a width of g. Thanks to the simple geometry of the parallel-plate waveguide, a multi-modal analysis is performed, employing the procedures described in [Harrington, 1961], [Marcuvitz, 1964], [Itoh, 1989] combined with the Floquet's theorem [Bhattacharyya, 2006].

The steps to perform this study are as follows. First, a modal analysis of an open-ended parallel plate waveguide excited by an incident mode is presented. Then, periodic boundary conditions are applied at the edges of the unit-cell in order to model the radiation at free-space within a periodic environment. In both regions, a set of modes are employed to expand the fields. Next, boundary conditions are applied at the waveguide-free space interface, leading to a set of equations related to the electric and magnetic fields. Finally, a mode-matching technique is applied to these equations, determining the complex coefficients associated to the modes employed to expand the fields. All these steps are described in great detail below.

C.2 Modal Analysis of a Waveguide

Let us consider the filled parallel-plate waveguide shown in Fig. C.1, which presents a discontinuity (aperture) at its end. The field within the vertical PPW is expanded in mode functions TM to x (TM_x). The reason of using this expansion set is because in the PPW CRLH LWA structure (see

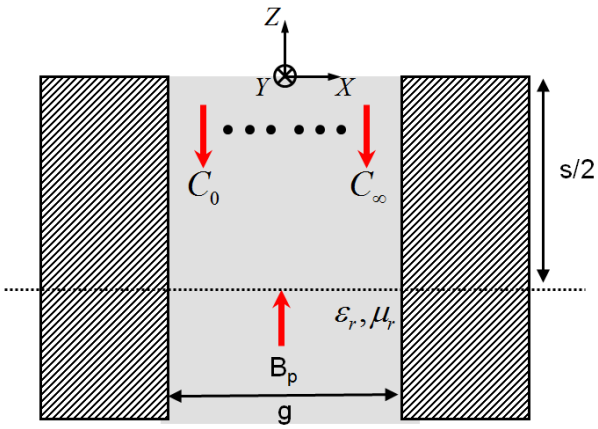

Figure C.1 – Filled parallel-plate waveguide with width g. The guide, analyzed using a set of TM_x modes, is excited by an incident p mode, with amplitude B_p. Reflected modes appear at the waveguide discontinuity (located at $z = 0$), which propagate back towards the waveguide.

Fig. 6.1) the energy propagates along the x direction. Therefore, the complete antenna is excited using a TM_x mode, which is coupled onto the waveguide under analysis. Note that the TM_x set of modes employed to characterize this waveguide are hybrid modes with respect to the direction of propagation within the waveguide, which in this case is z. Due to the use of a TM_x expansion, the magnetic and electric vector potentials in the filled waveguide may be defined as [Harrington, 1961]

$$\vec{F}_{PPW} = 0, \tag{C.1}$$

$$\vec{A}_{PPW} = \psi_{PPW}\hat{e}_x, \tag{C.2}$$

where $\hat{e}_x$ is the unitary vector along the x direction and ψ_{PPW} is the scalar wave potential or wavefunction in the waveguide.

The scalar wave potential can easily be derived applying the corresponding boundary conditions at the PPW borders [Harrington, 1961]. Besides, note that the waveguide is excited by the p^{th} incident TM_x mode, which has an amplitude B_p. This mode propagates along the waveguide until it reaches the aperture. Even though part of the energy is coupled towards free-space, some energy is reflected back towards the waveguide. This reflected field is expanded into an infinite series of modes with complex amplitudes C_n. Taking into account the above comments, the scalar wave potential may be defined as

$$\psi_{PPW} = k_w^{-1} B_p \cos\left[k_{x,p}^w \left(x - \frac{g}{2}\right)\right] e^{-jk_{z,p}^w z} + k_w^{-1} \sum_{n=0}^{n=\infty} C_n \cos\left[k_{x,n}^w \left(x - \frac{g}{2}\right)\right] e^{jk_{z,n}^w z}. \tag{C.3}$$

In this last expression, k_w is the intrinsic wavenumber of the filling material

$$k_w = \omega\sqrt{\varepsilon_0 \varepsilon_r \mu}, \tag{C.4}$$

$k_{x,p}^w$ is the x-oriented wavenumber related to the p^{th}-mode, defined by

$$k_{x,p}^w = \frac{p\pi}{g}, \tag{C.5}$$

and the Helmholtz equation implies separability of the wavenumbers is cartesian coordinates, i.e., $k_w^2 = k_{x,p}^{w2} + k_{z,p}^{w2}$, determining the z-directed wave number related to the p^{th}-mode as

$$k_{z,p}^w = \pm\sqrt{k_w^2 - \left(\frac{p\pi}{g}\right)^2}. \tag{C.6}$$

Note that, since the waveguide presents a parallel-plate configuration with (z-x) in-plane excitation, the wavenumber along the y-direction is directly zero, i.e. $k_{y,p}^w = 0, \forall p$.

The electric and magnetic fields can directly be obtained from the wavefunction of Eq. (C.3) by using [Harrington, 1961]

$$E_x = \frac{1}{j\omega\varepsilon_0\varepsilon_r}\left(-\frac{\partial^2}{\partial x^2} + k_w^2\right)\psi_{PPW}, \tag{C.7}$$

$$E_y = 0, \tag{C.8}$$

$$E_z = \frac{-1}{j\omega\varepsilon_0\varepsilon_r}\frac{\partial^2\psi_{PPW}}{\partial x \partial z}, \tag{C.9}$$

$$H_x = 0, \tag{C.10}$$

$$H_y = \frac{\partial\psi_{PPW}}{\partial z}, \tag{C.11}$$

$$H_z = 0. \tag{C.12}$$

It is important to note that a minus sign has been included in the terms related to a derivative over the direction x. This sign appears [Harrington, 1961] because the direction of propagation is z (see Fig. C.1), whereas the field has been expanded in a set of TM_x modes. Besides, note that the wave inside the structure is not only TM_x, as expected, but also TM_z (due to the parallel plate configuration). This allows us to further simplify the formulation and prevents the formation of TE waves at the waveguide discontinuity.

After some tedious but straightforward developments, the components of the electric and magnetic fields related to the wavefunction of Eq. (C.3) may be rewritten as

$$E_x^w = \frac{jB_p k_{z,p}^w k_{z,p}^w}{\omega\varepsilon_0\varepsilon_r k_w}\cos\left[k_{x,p}^w\left(x-\frac{g}{2}\right)\right]e^{-jk_{z,p}^w z} + \frac{j}{\omega\varepsilon_0\varepsilon_r k_w}\sum_{n=0}^{n=\infty} C_n k_{z,n}^w k_{z,n}^w \cos\left[k_{x,n}^w\left(x-\frac{g}{2}\right)\right]e^{jk_{z,n}^w z}, \tag{C.13}$$

$$E_y^w = 0, \tag{C.14}$$

$$E_z^w = \frac{-B_p k_{x,p}^w k_{z,p}^w}{\omega\varepsilon_0\varepsilon_r k_w}\sin\left[k_{x,p}^w\left(x-\frac{g}{2}\right)\right]e^{-jk_{z,p}^w z} + \frac{1}{\omega\varepsilon_0\varepsilon_r k_w}\sum_{n=0}^{n=\infty} C_n k_{z,n}^w k_{x,n}^w \sin\left[k_{x,n}^w\left(x-\frac{g}{2}\right)\right]e^{jk_{z,n}^w z}, \tag{C.15}$$

$$H_x^w = 0, \tag{C.16}$$

$$H_y^w = j\frac{k_{z,p}^w}{k_w}B_p\cos\left[k_{x,p}^w\left(x-\frac{g}{2}\right)\right]e^{-jk_{z,p}^w z} - \frac{j}{k_w}\sum_{n=0}^{n=\infty} C_n k_{z,n}^w \cos\left[k_{x,n}^w\left(x-\frac{g}{2}\right)\right]e^{jk_{z,n}^w z}, \tag{C.17}$$

$$H_z^w = 0. \tag{C.18}$$

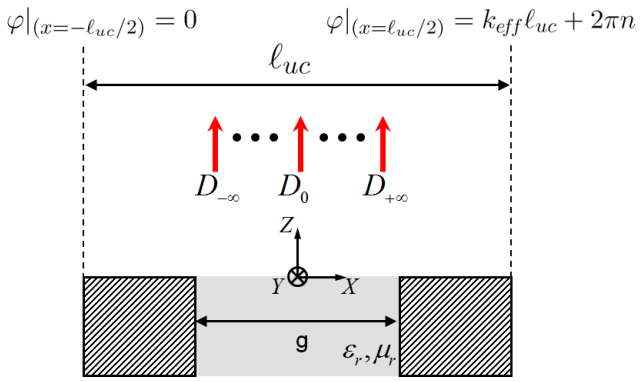

Figure C.2 – Modeling of the free-space radiation of a parallel-plate waveguide placed within a periodic environment. Periodic boundary conditions, related to the complex propagation constant of the complete CRLH LWA unit cell, are imposed in the free space region. Due to periodicity, a discrete set of complex modes (D_t) appears.

C.3 Modal Analysis of a Slot placed within a Periodic Environment

After the energy travels along the waveguide, it reaches the aperture discontinuity, as shown in Fig. C.2. There, some energy is coupled to free space. In this region, the field is expanded in a set of mode functions TM to z (TM_z). This set of modes has been employed because the field which propagates from the waveguide is both, TM_z and TM_x. Therefore, we will match fields from two different regions, expanded using the TM_z set of modes. Note that we have avoided the use of hybrid modes for the mode-matching (TM_x modes, as used inside the waveguide), because it would lead to the generation of hybrid TM_x modes at free-space, which require a more complicated formulation. Using the TM_z expansion set, the magnetic and electric vector potentials in free-space yields

$$\vec{F}_0 = 0, \tag{C.19}$$

$$\vec{A}_0 = \psi_0 \hat{e}_z, \tag{C.20}$$

where $\hat{e}_z$ is the unitary vector along the z direction and ψ_0 is the scalar wave potential or wavefunction in free-space.

It is very important to note that periodic boundary conditions have been applied in free space, at the limits of the unit-cell. This situation models an infinite periodic array of apertures, and can effectively be anaylzed using the Floquet's theorem [Bhattacharyya, 2006]. Using this model and due to periodicity, the field in free-space is expressed as the infinite sum of a discrete set of complex modes D_t, instead of the usual continuous spectrum obtained in the single slot case [Harrington, 1961]. Taking into account the above comments, the scalar potential at free-space may be defined as

$$\psi_0 = k_0^{-1} \sum_{t=-\infty}^{t=\infty} D_t e^{-jk_{x,t}^0 x} e^{-jk_{z,t}^0 z}, \tag{C.21}$$

where k_0 is the free-space wavenumber, and the t^{th} wavenumber along the x direction is determined by

$$k_{x,t}^0 = k_{eff} + t\frac{2\pi}{\ell_{uc}}. \tag{C.22}$$

In this last expression, ℓ_{uc} is the physical length of the unit-cell (see Fig. C.2) and k_{eff} is the effective wavenumber related to the periodic environment (see Chapter 6.3). Specifically, the imposition of this periodic boundary condition assures that the aperture radiation mechanism completely depends on the complex propagation constant of the CRLH TL unit-cell, k_{eff}. Thanks to the separability of the wavenumbers in cartesian coordinates, the z-directed wave number may then be expressed as

$$k_{z,t}^0 = \pm\sqrt{k_0^2 - \left(k_{eff} + t\frac{2\pi}{\ell_{uc}}\right)^2}. \tag{C.23}$$

The electric and magnetic field can directly be obtained from the wavefunction of Eq. (C.21) by using [Harrington, 1961]

$$E_x = \frac{1}{j\omega\varepsilon_0\varepsilon_r}\frac{\partial^2\psi_0}{\partial x\partial z}, \tag{C.24}$$

$$E_y = 0, \tag{C.25}$$

$$E_z = \frac{1}{j\omega\varepsilon_0\varepsilon_r}\left(\frac{\partial^2}{\partial x^2} + k_0^2\right)\psi_0, \tag{C.26}$$

$$H_x = 0, \tag{C.27}$$

$$H_y = -\frac{\partial\psi_0}{\partial x}, \tag{C.28}$$

$$H_z = 0. \tag{C.29}$$

Nota that, as compared with Eqs. (C.13)-(C.18), the minus sign related to the x-directed terms has been suppressed [Harrington, 1961]. This is because the direction of propagation (z) and the modes employed for the expansion set (TM_z) shares the same orientation (z).

After some tedious but straightforward developments, the components of the electric and magnetic fields related to the wavefunction of Eq. (C.21) can be expressed as

$$E_x^0 = \frac{j}{\omega\varepsilon_0\varepsilon_r k_0}\sum_{t=-\infty}^{n=\infty} D_t k_{x,t}^0 k_{z,t}^0 e^{-jk_{x,t}^0 x} e^{-jk_{z,t}^0 z}, \tag{C.30}$$

$$E_y^0 = 0, \tag{C.31}$$

$$E_z^0 = \frac{-j}{\omega\varepsilon_0\varepsilon_r k_0}\sum_{t=-\infty}^{n=\infty} D_t k_{x,t}^0 k_{x,t}^0 e^{-jk_{x,t}^0 x} e^{-jk_{z,t}^0 z}, \tag{C.32}$$

$$H_x^0 = 0, \tag{C.33}$$

$$H_y^0 = \frac{j}{k_0}\sum_{t=-\infty}^{t=\infty} D_t k_{x,t}^0 e^{-jk_{x,t}^0 x} e^{-jk_{z,t}^0 z}, \tag{C.34}$$

$$H_z^0 = 0. \tag{C.35}$$

C.4 Mode-Matching Formulation

The electric and magnetic fields inside the filled waveguide have been defined in Section C.2, whereas the electric and magnetic fields in the periodic free space environment have been defined in Section C.3. This section derives a mode-matching formulation [Harrington, 1961],

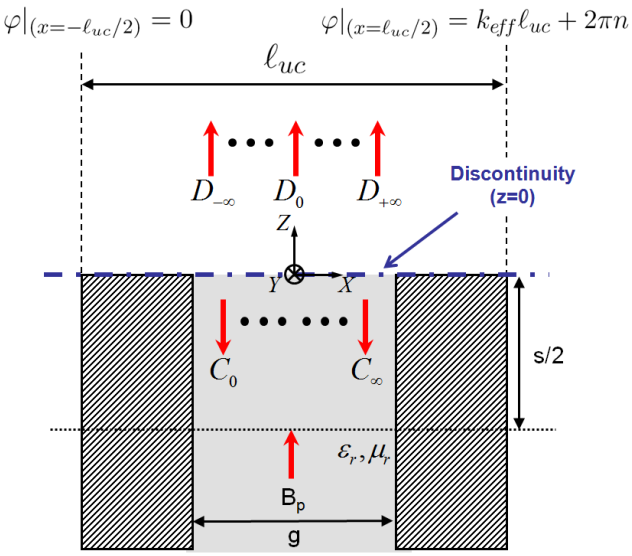

Figure C.3 – Open-ended parallel-plate waveguide radiating in an array environment. Periodic boundary conditions, related to the complex propagation constant of the complete CRLH LWA unit cell, are imposed in the free-space region. The waveguide is excited by the p^{th} mode, B_p, which generates two set of modes: one set is reflected back towards the waveguide (C_n) and the other is coupled to free-space (D_t).

[Marcuvitz, 1964], [Itoh, 1989] to determine the complex amplitudes related to the reflected (to the waveguide, C_n) and transmitted (to free space, D_t) modes, which appear when the waveguide is excited by an incident p^{th} mode.

The first step is to impose boundary conditions at the waveguide discontinuity, i.e., at the position $z = 0$ (see Fig. C.3), for both, the electric and the magnetic fields.

In the case of the electric field, the tangential field must be continuous at the aperture interface. Besides, note that the tangential electric field must be zero at the surface of any perfect electric conductor. Therefore, the boundary condition that must be imposed on the electric field along the discontinuity is

$$E_x^w \text{rect}\left(\frac{x}{g}\right)\Big|_{z=0} = E_x^0\Big|_{z=0} \quad , \tag{C.36}$$

where the function "rect" is defined as

$$\text{rect}(x) = \begin{cases} 0 & \text{if} \quad |x| > \frac{1}{2} \\ 1 & \text{if} \quad |x| < \frac{1}{2} \end{cases} \quad . \tag{C.37}$$

Besides, the tangential components of the magnetic field must be continuous at the aperture interface surface. Note that they will not be zero along the waveguide metallic walls, because possible induced currents placed there could generate a discontinuity on the fields. Imposing the continuity of the tangential magnetic field along the aperture, the following boundary condition is obtained

$$H_y^w \text{rect}\left(\frac{x}{g}\right)\Big|_{z=0} = H_y^0 \text{rect}\left(\frac{x}{g}\right)\Big|_{z=0} \quad . \tag{C.38}$$

Once the boundary conditions have clearly been defined, the next step is to apply the mode-matching technique [Harrington, 1961], [Marcuvitz, 1964], [Itoh, 1989]. For this purpose, we will first developed each boundary condition, and then we will exploit the orthogonality properties of the harmonic functions involved in the formulation for the scalar wave potentials in order to derive the complex coefficient of the modal amplitudes (D_t, C_n), as a function of the excitation mode B_p. These steps are detailed below, for the electric and magnetic fields cases.

C.4.1 Boundary Conditions: Electric Field

The tangential electric field must be continuous along the interface between the waveguide and free-space, i.e., along $z = 0$, as explicitly mentioned in Eq. (C.36). This equation can be further developed as

$$\frac{jB_p k^w_{z,p} k^w_{z,p}}{\omega\varepsilon_0\varepsilon_r k_w} \cos\left[k^w_{x,p}\left(x-\frac{g}{2}\right)\right] \text{rect}\left(\frac{x}{g}\right) + \frac{j}{\omega\varepsilon_0\varepsilon_r k_w} \sum_{n=0}^{n=\infty} C_n k^w_{z,n} k^w_{z,n} \cos\left[k^w_{x,n}\left(x-\frac{g}{2}\right)\right] \text{rect}\left(\frac{x}{g}\right) = \frac{j}{\omega\varepsilon_0\varepsilon_r k_0} \sum_{t=-\infty}^{t=\infty} D_t k^0_{x,t} k^0_{z,t} e^{-jk^0_{x,t}x}. \tag{C.39}$$

Following the mode-matching technique, and in order to exploit the orthogonality properties of the harmonic functions, we multiply both sides of the above equation by $e^{-jm\frac{2\pi}{\ell_{uc}}x}$, where $m \in \mathbb{Z}$. Specifically, we use as auxiliary functions the Floquet's modes which appear on the free-space region. This is because we want to determine the reflected and transmitted coefficients when the excitation comes from the waveguide. The number of auxiliary modes to employ (M) is exactly the same number of modes employed for the fields expansion in the free-space region. Then, we integrate along the discontinuity, i.e. along the x direction (at $z = 0$) from $-\ell_{uc}/2$ towards $\ell_{uc}/2$ [Marcuvitz, 1964], [Itoh, 1989]. In this way, Eq. (C.39) is reformulated as

$$\int_{-\ell_{uc}/2}^{\ell_{uc}/2} \frac{jB_p k^w_{z,p} k^w_{z,p}}{\omega\varepsilon_0\varepsilon_r k_w} \cos\left[k^w_{x,p}\left(x-\frac{g}{2}\right)\right] \text{rect}\left(\frac{x}{g}\right) e^{-jm\frac{2\pi}{\ell_{uc}}x} dx + \int_{-\ell_{uc}/2}^{\ell_{uc}/2} \frac{j}{\omega\varepsilon_0\varepsilon_r k_w} \sum_{n=0}^{n=\infty} C_n k^w_{z,n} k^w_{z,n} \cos\left[k^w_{x,n}\left(x-\frac{g}{2}\right)\right] \text{rect}\left(\frac{x}{g}\right) e^{-jm\frac{2\pi}{\ell_{uc}}x} dx = \int_{-\ell_{uc}/2}^{\ell_{uc}/2} \frac{j}{\omega\varepsilon_0\varepsilon_r k_0} \sum_{t=-\infty}^{t=\infty} D_t k^0_{x,t} k^0_{z,t} e^{-jk^0_{x,t}x} e^{-jm\frac{2\pi}{\ell_{uc}}x} dx. \tag{C.40}$$

After some tedious but straightforward manipulations, the integrals which appear in the above equation may individually be solved as

$$\int_{-\ell_{uc}/2}^{\ell_{uc}/2} \frac{jB_p k_{z,p}^w k_{z,p}^w}{\omega\varepsilon_0\varepsilon_r k_w} \cos\left[k_{x,p}^w\left(x-\frac{g}{2}\right)\right] \text{rect}\left(\frac{x}{g}\right) e^{-jm\frac{2\pi}{\ell_{uc}}x} dx =$$
$$\frac{jB_p k_{z,p}^w k_{z,p}^w}{\omega\varepsilon_0\varepsilon_r k_w} \frac{g}{2}\left[\text{sinc}\left(\frac{g}{2}\left(k_{x,p}^w - m\frac{2\pi}{\ell_{uc}}\right)\right) e^{-jk_{x,p}^w\frac{g}{2}} + \text{sinc}\left(\frac{g}{2}\left(k_{x,p}^w + m\frac{2\pi}{\ell_{uc}}\right)\right) e^{+jk_{x,p}^w\frac{g}{2}}\right], \tag{C.41}$$

$$\int_{-\ell_{uc}/2}^{\ell_{uc}/2} \frac{j}{\omega\varepsilon_0\varepsilon_r k_w} \sum_{n=0}^{n=\infty} C_n k_{z,n}^w k_{z,n}^w \cos\left[k_{x,n}^w\left(x-\frac{g}{2}\right)\right] \text{rect}\left(\frac{x}{g}\right) e^{-jm\frac{2\pi}{\ell_{uc}}x} dx =$$
$$\frac{j}{\omega\varepsilon_0\varepsilon_r k_w} \sum_{n=0}^{n=\infty} C_n k_{z,n}^w k_{z,n}^w \frac{g}{2}\left[\text{sinc}\left(\frac{g}{2}\left(k_{x,n}^w - m\frac{2\pi}{\ell_{uc}}\right)\right) e^{-jk_{x,n}^w\frac{g}{2}} + \text{sinc}\left(\frac{g}{2}\left(k_{x,n}^w + m\frac{2\pi}{\ell_{uc}}\right)\right) e^{+jk_{x,n}^w\frac{g}{2}}\right], \tag{C.42}$$

$$\int_{-\ell_{uc}/2}^{\ell_{uc}/2} \frac{j}{\omega\varepsilon_0\varepsilon_r k_0} \sum_{t=-\infty}^{t=\infty} D_t k_{x,t}^0 k_{z,t}^0 e^{-jk_{x,t}^0 x} e^{-jm\frac{2\pi}{\ell_{uc}}x} dx = \frac{j}{\omega\varepsilon_0\varepsilon_r k_0} \sum_{t=-\infty}^{t=\infty} D_t k_{x,t}^0 k_{z,t}^0 \ell_{uc} \text{sinc}\left(\frac{\ell_{uc}}{2}\left(k_{x,t}^0 + m\frac{2\pi}{\ell_{uc}}\right)\right), \tag{C.43}$$

where the function "sinc" is defined as [Pipes and Harvill, 1971]

$$\text{sinc}(x) = \begin{cases} \frac{\sin(x)}{x} & \text{if} \quad x \neq 0 \\ 1 & \text{if} \quad x = 0 \end{cases}. \tag{C.44}$$

Then, the boundary condition on the electric field imposed at $z = 0$ [see Eq. (C.39)] may be rewritten as

$$\frac{jB_p k_{z,p}^w k_{z,p}^w}{\omega\varepsilon_0\varepsilon_r k_w} \frac{g}{2}\left[\text{sinc}\left(\frac{g}{2}\left(k_{x,p}^w - m\frac{2\pi}{\ell_{uc}}\right)\right) e^{-jk_{x,p}^w\frac{g}{2}} + \text{sinc}\left(\frac{g}{2}\left(k_{x,p}^w + m\frac{2\pi}{\ell_{uc}}\right)\right) e^{+jk_{x,p}^w\frac{g}{2}}\right] +$$
$$\frac{j}{\omega\varepsilon_0\varepsilon_r k_w} \sum_{n=0}^{n=\infty} C_n k_{z,n}^w k_{z,n}^w \frac{g}{2}\left[\text{sinc}\left(\frac{g}{2}\left(k_{x,n}^w - m\frac{2\pi}{\ell_{uc}}\right)\right) e^{-jk_{x,n}^w\frac{g}{2}} + \text{sinc}\left(\frac{g}{2}\left(k_{x,n}^w + m\frac{2\pi}{\ell_{uc}}\right)\right) e^{+jk_{x,n}^w\frac{g}{2}}\right] =$$
$$\frac{j}{\omega\varepsilon_0\varepsilon_r k_0} \sum_{t=-\infty}^{t=\infty} D_t k_{x,t}^0 k_{z,t}^0 \ell_{uc} \text{sinc}\left(\frac{\ell_{uc}}{2}\left(k_{x,t}^0 + m\frac{2\pi}{\ell_{uc}}\right)\right). \tag{C.45}$$

C.4.2 Boundary Conditions: Magnetic Field

The tangential magnetic field must be continuous along the aperture interface, as explicitly mentioned in Eq. (C.38). This equation can be further developed as

$$j\frac{k_{z,p}^w}{k_w} B_p \cos\left[k_{x,p}^w\left(x-\frac{g}{2}\right)\right] \text{rect}\left(\frac{x}{g}\right) - \frac{j}{k_w} \sum_{n=0}^{n=\infty} C_n k_{z,n}^w \cos\left[k_{x,n}^w\left(x-\frac{g}{2}\right)\right] \text{rect}\left(\frac{x}{g}\right) =$$
$$\frac{j}{k_0} \sum_{t=-\infty}^{t=\infty} D_t k_{x,t}^0 e^{-jk_{x,t}^0 x} \text{rect}\left(\frac{x}{g}\right). \tag{C.46}$$

At this point, we follow the same mode-matching procedure introduced in the last section, i.e., we multiply both sides of the above equation by $e^{-jm\frac{2\pi}{\ell_{uc}}x}$, where $m \in \mathbb{Z}$, and then we integrate along the x direction (at $z = 0$) from $-\ell_{uc}/2$ towards $\ell_{uc}/2$ [Marcuvitz, 1964], [Itoh, 1989]. In this way,

Eq. (C.46) is reformulated as

$$\int_{-\ell_{uc}/2}^{\ell_{uc}/2} j\frac{k_{z,p}^w}{k_w} B_p \cos\left[k_{x,p}^w\left(x-\frac{g}{2}\right)\right] \text{rect}\left(\frac{x}{g}\right) e^{-jm\frac{2\pi}{\ell_{uc}}x} dx -$$
$$\int_{-\ell_{uc}/2}^{\ell_{uc}/2} \frac{j}{k_w} \sum_{n=0}^{n=\infty} C_n k_{z,n}^w \cos\left[k_{x,n}^w\left(x-\frac{g}{2}\right)\right] \text{rect}\left(\frac{x}{g}\right) e^{-jm\frac{2\pi}{\ell_{uc}}x} dx =$$
$$\int_{-\ell_{uc}/2}^{\ell_{uc}/2} \frac{j}{k_0} \sum_{t=-\infty}^{t=\infty} D_t k_{x,t}^0 e^{-jk_{x,t}^0 x} \text{rect}\left(\frac{x}{g}\right) e^{-jm\frac{2\pi}{\ell_{uc}}x} dx. \quad \text{(C.47)}$$

After some tedious but straightforward manipulations, the integrals which appear in the above equation may individually be solved as

$$\int_{-\ell_{uc}/2}^{\ell_{uc}/2} j\frac{k_{z,p}^w}{k_w} B_p \cos\left[k_{x,p}^w\left(x-\frac{g}{2}\right)\right] \text{rect}\left(\frac{x}{g}\right) e^{-jm\frac{2\pi}{\ell_{uc}}x} dx =$$
$$j\frac{k_{z,p}^w}{k_w} B_p \frac{g}{2}\left[\text{sinc}\left(\frac{g}{2}\left(k_{x,p}^w - m\frac{2\pi}{\ell_{uc}}\right)\right) e^{-jk_{x,p}^w\frac{g}{2}} + \text{sinc}\left(\frac{g}{2}\left(k_{x,p}^w + m\frac{2\pi}{\ell_{uc}}\right)\right) e^{+jk_{x,p}^w\frac{g}{2}}\right], \quad \text{(C.48)}$$
$$\int_{-\ell_{uc}/2}^{\ell_{uc}/2} \frac{-j}{k_w} \sum_{n=0}^{n=\infty} C_n k_{z,n}^w \cos\left[k_{x,n}^w\left(x-\frac{g}{2}\right)\right] \text{rect}\left(\frac{x}{g}\right) e^{-jm\frac{2\pi}{\ell_{uc}}x} dx =$$
$$\frac{-j}{k_w} \sum_{n=0}^{n=\infty} C_n k_{z,n}^w \frac{g}{2}\left[\text{sinc}\left(\frac{g}{2}\left(k_{x,n}^w - m\frac{2\pi}{\ell_{uc}}\right)\right) e^{-jk_{x,n}^w\frac{g}{2}} + \text{sinc}\left(\frac{g}{2}\left(k_{x,n}^w + m\frac{2\pi}{\ell_{uc}}\right)\right) e^{+jk_{x,n}^w\frac{g}{2}}\right], \quad \text{(C.49)}$$
$$\int_{-\ell_{uc}/2}^{\ell_{uc}/2} \frac{j}{k_0} \sum_{t=-\infty}^{t=\infty} D_t k_{x,t}^0 e^{-jk_{x,t}^0 x} \text{rect}\left(\frac{x}{g}\right) e^{-jm\frac{2\pi}{\ell_{uc}}x} dx = \frac{j}{k_0} \sum_{t=-\infty}^{t=\infty} D_t k_{x,t}^0 g \,\text{sinc}\left(\frac{g}{2}\left(k_{x,t}^0 + m\frac{2\pi}{\ell_{uc}}\right)\right). \quad \text{(C.50)}$$

Then, the boundary condition on the magnetic field imposed at the aperture interface [see Eq. (C.46)] may be rewritten as

$$j\frac{k_{z,p}^w}{k_w} B_p \frac{g}{2}\left[\text{sinc}\left(\frac{g}{2}\left(k_{x,p}^w - m\frac{2\pi}{\ell_{uc}}\right)\right) e^{-jk_{x,p}^w\frac{g}{2}} + \text{sinc}\left(\frac{g}{2}\left(k_{x,p}^w + m\frac{2\pi}{\ell_{uc}}\right)\right) e^{+jk_{x,p}^w\frac{g}{2}}\right] +$$
$$\frac{-j}{k_w} \sum_{n=0}^{n=\infty} C_n k_{z,n}^w \frac{g}{2}\left[\text{sinc}\left(\frac{g}{2}\left(k_{x,n}^w - m\frac{2\pi}{\ell_{uc}}\right)\right) e^{-jk_{x,n}^w\frac{g}{2}} + \text{sinc}\left(\frac{g}{2}\left(k_{x,n}^w + m\frac{2\pi}{\ell_{uc}}\right)\right) e^{+jk_{x,n}^w\frac{g}{2}}\right] =$$
$$\frac{j}{k_0} \sum_{t=-\infty}^{t=\infty} D_t k_{x,t}^0 \, g \,\text{sinc}\left(\frac{g}{2}\left(k_{x,t}^0 + m\frac{2\pi}{\ell_{uc}}\right)\right). \quad \text{(C.51)}$$

C.4.3 Determining the Complex Modal Coefficients

In the previous subsections, we have expanded the fields on the waveguide and on the periodic free-space region as a sum of an infinite number of modes, which are only present in their respective regions. The problem now consists of determining the complex amplitudes of the modal coefficients associated to the fields in each region. Initially, this procedure may lead to an infinite set of linear equations, which can not be handled by a regular computer. Therefore, it is necessary to truncate the number of modes employed to expand the fields in each region, leading to an approximate solution of the problem [Itoh, 1989]. The accuracy of the computed solution should be verified, in order to assure that convergence has been reached. This means that the results should be stable when the number of modes employed increases.

Let us assume that the p^{th} mode is incident on the waveguide (see Fig. C.3). We limit to N the number of modes which propagates back towards the waveguide and to T the number of modes which propagates into free-space. At this point, we can construct a set of linear equations by using the equations derived to impose boundary conditions [see Eq. (C.45) and Eq. (C.51)]. There, for each value of m, two equations are obtained (one related to the electric field, denoted with a superscript "e", and another related to the magnetic field, denoted with a superscript "h"). Finally, a total number of $2M$ equations are obtained as

$$\begin{pmatrix} [b^e] \\ [b^h] \end{pmatrix} B_p + \begin{pmatrix} [c^e] \\ [c^h] \end{pmatrix} [C] = \begin{pmatrix} [d^e] \\ [d^h] \end{pmatrix} [D], \tag{C.52}$$

where B_p is the amplitude of the incident p^{th} mode, $[C]$ and $[D]$ are two matrixes with dimensions $1 \times N$ and $1 \times T$ related to the reflected and transmitted complex modal coefficients, respectively. These matrixes may be represented as

$$[C] = \begin{pmatrix} C_1 & \dots & C_{(N-1)} & C_N \end{pmatrix} \quad \text{and} \quad [D] = \begin{pmatrix} D_1 & \dots & D_{(T-1)} & D_T \end{pmatrix}. \tag{C.53}$$

The matrixes $[b^e]$ and $\left[b^h\right]$ have both dimension of $M \times 1$, and represents complex values which multiply the excitation coefficient, B_p, in the imposition of the electric [see Eq. (C.45)] and magnetic [see Eq. (C.51)] boundary conditions, respectively. These matrixes may be represented as

$$[b^e] = \begin{pmatrix} b^e_{1,p} \\ \vdots \\ b^e_{(M-1),p} \\ b^e_{M,p} \end{pmatrix} \quad \text{and} \quad \left[b^h\right] = \begin{pmatrix} b^h_{1,p} \\ \vdots \\ b^h_{(M-1),p} \\ b^h_{M,p} \end{pmatrix}, \tag{C.54}$$

where each m^{th} element of the $[b^e]$ and $\left[b^h\right]$ matrixes is defined as

$$b^e_{m,p} = \frac{jgk^w_{z,p}k^w_{z,p}}{2\omega\varepsilon_0\varepsilon_r k_w}\left[\operatorname{sinc}\left(\frac{g}{2}\left(k^w_{x,p} - m\frac{2\pi}{\ell_{uc}}\right)\right)e^{-jk^w_{x,p}\frac{g}{2}} + \operatorname{sinc}\left(\frac{g}{2}\left(k^w_{x,p} + m\frac{2\pi}{\ell_{uc}}\right)\right)e^{+jk^w_{x,p}\frac{g}{2}}\right], \tag{C.55}$$

and

$$b^h_{m,p} = j\frac{gk^w_{z,p}}{2k_w}\left[\operatorname{sinc}\left(\frac{g}{2}\left(k^w_{x,p} - m\frac{2\pi}{\ell_{uc}}\right)\right)e^{-jk^w_{x,p}\frac{g}{2}} + \operatorname{sinc}\left(\frac{g}{2}\left(k^w_{x,p} + m\frac{2\pi}{\ell_{uc}}\right)\right)e^{+jk^w_{x,p}\frac{g}{2}}\right], \tag{C.56}$$

respectively.

The matrixes $[c^e]$ and $\left[c^h\right]$ have both dimension of $M \times N$, and represents complex values which multiply the modal coefficients C_n in the imposition of the electric [see Eq. (C.45)] and magnetic [see Eq. (C.51)] boundary conditions, respectively. These matrixes may be represented as

$$[c^e] = \begin{pmatrix} c^e_{1,1} & c^e_{1,2} & \cdots & c^e_{1,(N-1)} & c^e_{1,N} \\ c^e_{2,1} & c^e_{2,2} & \cdots & c^e_{2,(N-1)} & c^e_{2,N} \\ \vdots & \vdots & \ddots & \vdots & \vdots \\ c^e_{(M-1),1} & c^e_{(M-1),2} & \cdots & c^e_{(M-1),(N-1)} & c^e_{(M-1),N} \\ c^e_{M,1} & c^e_{M,2} & \cdots & c^e_{M,(N-1)} & c^e_{M,N} \end{pmatrix} \tag{C.57}$$

and

$$\left[c^h\right] = \begin{pmatrix} c^h_{1,1} & c^h_{1,2} & \cdots & c^h_{1,(N-1)} & c^h_{1,N} \\ c^h_{2,1} & c^h_{2,2} & \cdots & c^h_{2,(N-1)} & c^h_{2,N} \\ \vdots & \vdots & \ddots & \vdots & \vdots \\ c^h_{(M-1),1} & c^h_{(M-1),2} & \cdots & c^h_{(M-1),(N-1)} & c^h_{(M-1),N} \\ c^h_{M,1} & c^h_{M,2} & \cdots & c^h_{M,(N-1)} & c^h_{M,N} \end{pmatrix}, \tag{C.58}$$

where each (m^{th}, n^{th}) element of the $[c^e]$ and $\left[c^h\right]$ matrixes is defined as

$$c^e_{m,n} = \frac{jgk^w_{z,n}k^w_{z,n}}{2\omega\varepsilon_0\varepsilon_r k_w}\left[\text{sinc}\left(\frac{g}{2}\left(k^w_{x,n} - m\frac{2\pi}{\ell_{uc}}\right)\right)e^{-jk^w_{x,n}\frac{g}{2}} + \text{sinc}\left(\frac{g}{2}\left(k^w_{x,n} + m\frac{2\pi}{\ell_{uc}}\right)\right)e^{+jk^w_{x,n}\frac{g}{2}}\right] \tag{C.59}$$

and

$$c^h_{m,n} = \frac{-jk^w_{z,n}g}{2k_w}\left[\text{sinc}\left(\frac{g}{2}\left(k^w_{x,n} - m\frac{2\pi}{\ell_{uc}}\right)\right)e^{-jk^w_{x,n}\frac{g}{2}} + \text{sinc}\left(\frac{g}{2}\left(k^w_{x,n} + m\frac{2\pi}{\ell_{uc}}\right)\right)e^{+jk^w_{x,n}\frac{g}{2}}\right], \tag{C.60}$$

respectively.

In the last case of matrixes $[d^e]$ and $\left[d^h\right]$, they have both dimension of $M \times T$, and represents complex values which multiply the modal coefficients D_t in the imposition of the electric [see Eq. (C.45)] and magnetic [see Eq. (C.51)] boundary conditions, respectively. These matrixes may be represented as

$$[d^e] = \begin{pmatrix} d^e_{1,1} & d^e_{1,2} & \cdots & d^e_{1,(T-1)} & d^e_{1,T} \\ d^e_{2,1} & d^e_{2,2} & \cdots & d^e_{2,(T-1)} & d^e_{2,T} \\ \vdots & \vdots & \ddots & \vdots & \vdots \\ d^e_{(M-1),1} & d^e_{(M-1),2} & \cdots & d^e_{(M-1),(T-1)} & d^e_{(M-1),T} \\ d^e_{M,1} & d^e_{M,2} & \cdots & d^e_{M,(T-1)} & d^e_{M,T} \end{pmatrix} \tag{C.61}$$

and

$$\left[d^h\right] = \begin{pmatrix} d^h_{1,1} & d^h_{1,2} & \cdots & d^h_{1,(T-1)} & d^h_{1,T} \\ d^h_{2,1} & d^h_{2,2} & \cdots & d^h_{2,(T-1)} & d^h_{2,T} \\ \vdots & \vdots & \ddots & \vdots & \vdots \\ d^h_{(M-1),1} & d^h_{(M-1),2} & \cdots & d^h_{(M-1),(T-1)} & d^h_{(M-1),T} \\ d^h_{M,1} & d^h_{M,2} & \cdots & d^h_{M,(T-1)} & d^h_{M,T} \end{pmatrix}, \tag{C.62}$$

where each (m^{th}, t^{th}) element of the $[d^e]$ and $\left[d^h\right]$ matrixes is defined as

$$d^e_{m,t} = \frac{jk^0_{x,t}k^0_{z,t}\ell_{uc}}{\omega\varepsilon_0\varepsilon_r k_0}\text{sinc}\left(\frac{\ell_{uc}}{2}\left(k^0_{x,t} + m\frac{2\pi}{\ell_{uc}}\right)\right) \tag{C.63}$$

and

$$d^h_{m,t} = \frac{jk^0_{x,t}g}{k_0}\text{sinc}\left(\frac{g}{2}\left(k^0_{x,t} + m\frac{2\pi}{\ell_{uc}}\right)\right), \tag{C.64}$$

respectively.

Once the individual matrixes which compose the set of linear equations have clearly been defined, Eq. (C.52) is algebraically manipulated in order to solve the system. Combining the unknown complex coefficients $[C]$ and $[D]$ on one side of the system of equations, one yields

$$\begin{pmatrix} [b^e] \\ [b^h] \end{pmatrix} B_p = -\begin{pmatrix} [c^e] \\ [c^h] \end{pmatrix} [C] + \begin{pmatrix} [d^e] \\ [d^m] \end{pmatrix} [D] = \begin{pmatrix} -[c^e] & [d^e] \\ -[c^h] & [d^h] \end{pmatrix} \begin{pmatrix} [C] \\ [D] \end{pmatrix}. \tag{C.65}$$

Finally, the modal complex coefficients associated to each reflected and transmitted waves can directly be obtained by solving

$$\begin{pmatrix} [C] \\ [D] \end{pmatrix} = \begin{pmatrix} -[c^e] & [d^e] \\ -[c^h] & [d^h] \end{pmatrix}^{-1} \begin{pmatrix} [b^e] \\ [b^h] \end{pmatrix} B_p. \tag{C.66}$$

Appendix D

Concatenation of Scattering Matrixes

The purpose of this appendix is to provide a simple formulation to concatenate two different multi-mode electrical networks defined by their associated scattering parameters. Due to the multi-mode nature of the networks, the situation under analysis can be considered as the combination of two scattering matrixes with a different number of input/output ports, which also have some ports in common [Balanis, 1989]. In this way, each input/output mode may be seen as a different input/output port. Then, the final goal is to obtain a closed-form expression of the equivalent multi-mode scattering matrix. This situation is clearly depicted in Fig. D.1.

Let us consider two different multi-mode networks, defined by their associated scattering parameters. The first network is related to the multi-modal matrix S', which has dimensions $(M+D)\times(M+D)$ (i.e., M input ports and D output ports), whereas the second network is described by the multi-modal matrix S'', which has dimensions $(D+F)\times(D+F)$ (i.e. D input ports and F output ports). As can be seen from this notation (and it is explicitly shown in Fig. D.1a) the two matrixes has a total of D ports in common.

Consider a single matrix, for instance the matrix S'. The matrix is related to an electrical network with two ports (one input port, denoted by the subscript "i", and one output port, denoted by the subscript "o"). Employing the usual incident/reflected wave notation [Pozar, 2005], and taking into account the multi-mode nature of the matrix, S' may be defined as

$$\begin{pmatrix} [b'_i] \\ [b'_o] \end{pmatrix} = [S'] \begin{pmatrix} [a'_i] \\ [a'_o] \end{pmatrix}, \tag{D.1}$$

where $[a'_i]$ is a matrix, with dimension $M\times 1$, related to the incident waves towards the input port, $[b'_i]$ is a matrix, with dimension $M\times 1$, related to the reflected waves from the input port, $[a'_o]$ is a matrix, with dimension $M\times 1$, related to the incident waves towards the output port and $[b'_o]$ is a matrix, with dimension $M\times 1$, related to the outcoming waves from the output port. As previously commented, the dimension of the scattering matrix S' is $(M+D)\times(M+D)$, and it relates the incident and reflected waves, taking into account the input and output ports and the multi-mode nature of the electric network (see Fig. D.2).

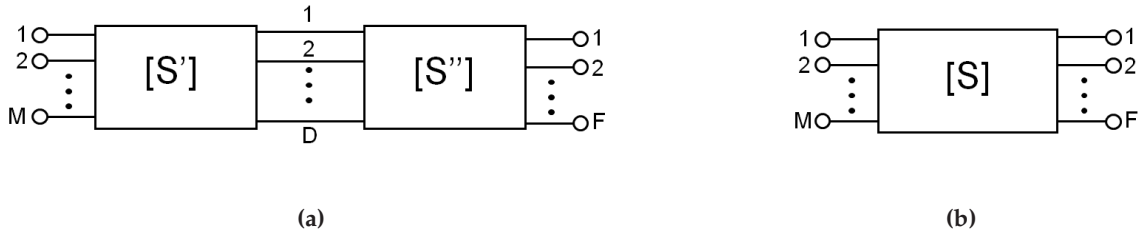

Figure D.1 – Concadenation of two different multi-mode electrical networks defined by their associated scattering parameters. Each input/output mode is seen as an input/output port [Balanis, 1989]. (a) Combination of the matrix S' [dimension: $M \times D$] with the matrix S'' [dimension: $D \times F$]. (b) Equivalent matrix S [dimension: $M \times F$], which reproduces the same electrical behavior as in case (a).

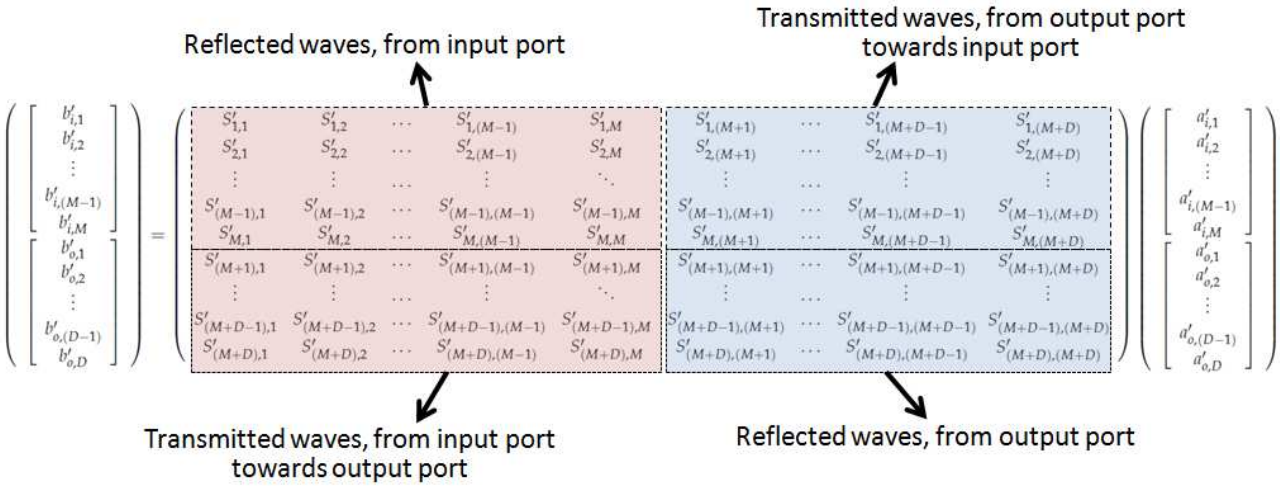

Figure D.2 – Dimensions and characteristics of a multi-mode scattering parameters matrix S' which define a two-port electrical network.

Developing Eq. (D.1), the definition of matrix S' may be rewritten as

$$b'_{i,t} = \sum_{n=1}^{M} S'_{t,n} a'_{i,n} + \sum_{n=1}^{D} S'_{t,(M+n)} a'_{o,n}, \tag{D.2}$$

$$b'_{o,g} = \sum_{n=1}^{M} S'_{(M+g),n} a'_{i,n} + \sum_{n=1}^{D} S'_{(M+g),(M+n)} a'_{o,n}, \tag{D.3}$$

where $t = 1...M$, $g = 1...D$, $a'_{i,N}$ is related to the N^{th} wave which propagates towards the input port (left side of the network S' in Fig. D.1a), and $a'_{o,N}$ is the N^{th} wave which propagates towards the output port (right side of the network S' in Fig. D.1a). A similar notation, $b'_{i,N}$ and $b'_{o,N}$, is followed for the N^{th} waves which cames out from the input and output ports of the network, respectively.

Following this notation, the matrix S'' may be defined as

$$b''_{i,g} = \sum_{n=1}^{D} S''_{g,n} a''_{i,n} + \sum_{n=1}^{F} S''_{g,(D+n)} a''_{o,n}, \tag{D.4}$$

$$b''_{o,w} = \sum_{n=1}^{D} S''_{(D+w),n} a''_{i,n} + \sum_{n=1}^{F} S''_{(D+w),(D+n)} a''_{o,n}, \tag{D.5}$$

where $w = 1...F$ and the use of the double primed sign '' has been included to clearly indicate that the incident/reflected waves are related to the matrix S''.

Fig. D.3 presents a graphical representation of the scattering matrix concatenation, explicitly including the incident and reflected waves on each network. As can easily be inferred from the figure, the waves which came from the output port of the first network are the incident waves which propagate toward the input port of the second network. These are the boundary conditions that must be imposed at the networks interface, in order to combine both scattering matrixes into a unique matrix. Specifically, these conditions may be expressed as

$$b'_{o,x} = a''_{i,x} \quad \text{and} \quad a'_{o,x} = b''_{i,x} \quad \text{for} \quad x = 1...D. \tag{D.6}$$

Applying these boundary conditions in the definition of the scattering parameters, the input and output waves related to each network may be expressed as

$$b'_{i,t} = \sum_{n=1}^{M} S'_{t,n} a'_{i,n} + \sum_{n=1}^{D} S'_{t,(M+n)} b''_{i,n}, \tag{D.7}$$

$$a''_{i,g} = \sum_{n=1}^{M} S'_{(M+g),n} a'_{i,n} + \sum_{n=1}^{D} S'_{(M+g),(M+n)} b''_{i,n}, \tag{D.8}$$

and

$$a'_{o,g} = \sum_{n=1}^{D} S''_{g,n} b'_{o,n} + \sum_{n=1}^{F} S''_{g,(D+n)} a''_{o,n}, \tag{D.9}$$

$$b''_{o,w} = \sum_{n=1}^{D} S''_{(D+w),n} b'_{o,n} + \sum_{n=1}^{F} S''_{(D+w),(D+n)} a''_{o,n}. \tag{D.10}$$

The main goal now is to combine the equations shown above in order to obtain a single scattering matrix (S) which reproduce the same electrical behavior as the concatenation of matrixes S' and S''. For this purpose, we excite the two networks system with an incident wave ($a'_{i,q}$, with $q = 1...M$), which propagates towards the input port of the first network (S' in Fig. D.3). Note that this is the only incoming wave which excites the system (i.e., $a'_{i,h} = 0$, $\forall h \neq q$) with all output ports of the global network matched ($a''_{o,w} = 0$, $\forall w$).

Taking into account this excitation, the waves which propagates from network S'' towards network S' may be expressed as

$$b''_{i,g} = a'_{o,g} = \sum_{n=1}^{D} S''_{g,n} b'_{o,n}. \tag{D.11}$$

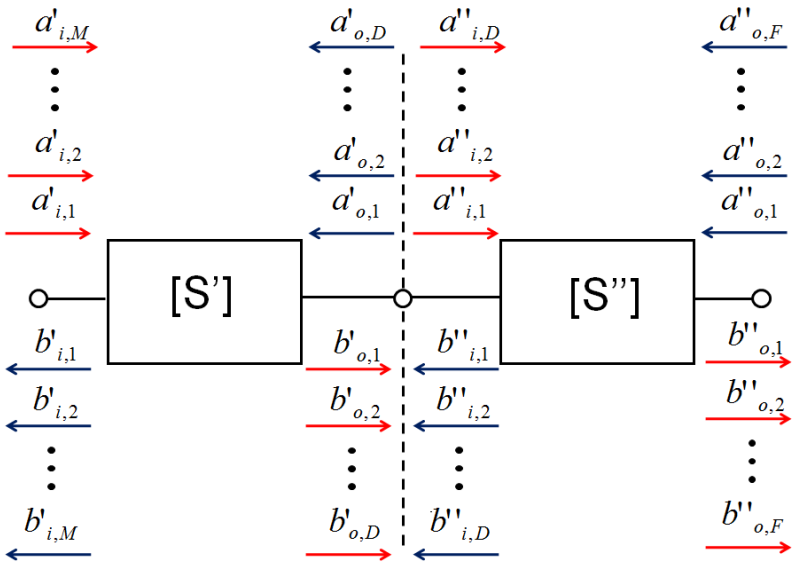

Figure D.3 – Explicit representation of the incident (a) and reflected (b) waves employed for the concatenation of two electrical networks. Each multi-mode network (S' and S'') is defined by its scattering parameters.

Using this last expression, and applying the adequate boundary conditions [see Eq. (D.6)], the reflected waves from the first network (S') may be reduced to

$$b'_{i,t} = S'_{t,q}a'_{i,q} + \sum_{n=1}^{D} S'_{t,(M+n)}b''_{i,n} = S'_{t,q}a'_{i,q} + \sum_{k=1}^{D} b'_{o,k} \sum_{n=1}^{D} S'_{t,(M+n)}S''_{n,k}. \tag{D.12}$$

Employing the same methodology, the waves propagating from network S' towards network S'' may be rewritten as

$$b'_{o,g} = a''_{i,g} = S'_{(M+g),q}a'_{i,q} + \sum_{k=1}^{D} b'_{o,k} \sum_{n=1}^{D} S'_{(M+g),(M+n)}S''_{n,k} = S^{ex1}_{g,q}a'_{i,q} + \sum_{k=1}^{D} b'_{o,k}S^{rw1}_{g,k}, \tag{D.13}$$

where the variables

$$S^{ex1}_{g,q} = S'_{(M+g),q}, \tag{D.14}$$

and

$$S^{rw1}_{g,k} = \sum_{n=1}^{D} S'_{(M+g),(M+n)}S''_{n,k} \tag{D.15}$$

have been introduced for the sake of completeness.

Since $g = 1...D$ (number of ports in common between the network S' and S''), Eq. (D.13) repre-

sents a total of D linear equations, which may easily be expressed in a matrix formulation as follows

$$\begin{pmatrix} b'_{o,1} \\ b'_{o,2} \\ \vdots \\ b'_{o,(D-1)} \\ b'_{o,D} \end{pmatrix} = \begin{pmatrix} S^{ex1}_{1,q} \\ S^{ex1}_{2,q} \\ \vdots \\ S^{ex1}_{(D-1),q} \\ S^{ex1}_{D,q} \end{pmatrix} a'_{i,q} + \begin{pmatrix} S^{rw1}_{1,1} & S^{rw1}_{1,2} & \cdots & S^{rw1}_{1,(D-1)} & S^{rw1}_{1,D} \\ S^{rw1}_{2,1} & S^{rw1}_{2,2} & \cdots & S^{rw1}_{2,(D-1)} & S^{rw1}_{2,D} \\ \vdots & \vdots & \ddots & \vdots & \vdots \\ S^{rw1}_{(D-1),1} & S^{rw1}_{(D-1),2} & \cdots & S^{rw1}_{(D-1),(D-1)} & S^{rw1}_{(D-1),D} \\ S^{rw1}_{D,1} & S^{rw1}_{D,2} & \cdots & S^{rw1}_{D,(D-1)} & S^{rw1}_{D,D} \end{pmatrix} \begin{pmatrix} b'_{o,1} \\ b'_{o,2} \\ \vdots \\ b'_{o,(D-1)} \\ b'_{o,D} \end{pmatrix}. \tag{D.16}$$

Then, the value of each $b'_{o,g}$ wave (i.e., wave coming from network S' towards network S'') may be obtained by solving the following system of linear equations

$$\begin{pmatrix} 1 - S^{rw1}_{1,1} & -S^{rw1}_{1,2} & \cdots & -S^{rw1}_{1,(D-1)} & -S^{rw1}_{1,D} \\ -S^{rw1}_{2,1} & 1 - S^{rw1}_{2,2} & \cdots & -S^{rw1}_{2,(D-1)} & -S^{rw1}_{2,D} \\ \vdots & \vdots & \ddots & \vdots & \vdots \\ -S^{rw1}_{(D-1),1} & -S^{rw1}_{(D-1),2} & \cdots & 1 - S^{rw1}_{(D-1),(D-1)} & -S^{rw1}_{(D-1),D} \\ -S^{rw1}_{D,1} & -S^{rw1}_{D,2} & \cdots & -S^{rw1}_{D,(D-1)} & 1 - S^{rw1}_{D,D} \end{pmatrix} \begin{pmatrix} b'_{o,1} \\ b'_{o,2} \\ \vdots \\ b'_{o,(D-1)} \\ b'_{o,D} \end{pmatrix} = \begin{pmatrix} S^{ex1}_{1,q} \\ S^{ex1}_{2,q} \\ \vdots \\ S^{ex1}_{(D-1),q} \\ S^{ex1}_{D,q} \end{pmatrix} a'_{i,q}. \tag{D.17}$$

After solving the linear system of equations, each $b'_{o,g}$ wave can be expressed as

$$b'_{o,g} = a''_{i,g} = a'_{i,q} f'_{g,q}(S', S''), \tag{D.18}$$

where $a'_{i,q}$ is the excitation wave and $f'_{g,q}(S', S'')$ is a function, which depends on S' and S'', and relates the output and input waves. Note that this function is directly obtained after solving Eq. (D.17).

Finally, the scattering parameters of the equivalent combined network (S, see Fig. D.1) can be expressed as

$$S_{t,q} = \frac{b'_{i,t}}{a'_{i,q}} = S'_{t,q} + \sum_{n=1}^{D} \sum_{k=1}^{D} S'_{t,(M+n)} S''_{n,k} f'_{k,q}(S', S''), \tag{D.19}$$

for the reflection coefficients (input port point of view, modal excitation wave defined by $q = 1...M$ and observation mode defined by $t = 1...M$) and as

$$S_{(M+w),q} = \frac{b''_{o,w}}{a'_{i,q}} = \frac{\sum_{n=1}^{D} S''_{(D+w),n} a''_{i,n}}{a'_{i,q}} = \sum_{n=1}^{D} S''_{(D+w),n} f'_{n,q}(S', S''), \tag{D.20}$$

for the case of the transmission coefficients (i.e., from the input to the output port, with modal excitation wave defined by $q = 1...M$ and observation mode at the output port defined by $w = 1...F$).

The same procedure can be now applied in the case that the incident wave comes from the output port of the second network (S'') and propagates towards the input port of the first electrical network (S'). In this situation, the incident wave is denoted by $a''_{o,z}$, with $z = 1...F$. Note that this is the only incoming wave which excites the system (all other ports are considered to be matched) and,

therefore, $a'_{i,h} = 0\ \forall h$ and $a''_{o,w} = 0, \forall w \neq z$.

Taking into account this excitation, the waves which propagates from network S' towards network S'' may be expressed as

$$b'_{o,g} = a''_{i,g} = \sum_{n=1}^{D} S'_{(M+g),(M+n)} b''_{i,n}. \tag{D.21}$$

Using this last expression, and applying the adequate boundary conditions [see Eq. (D.6)], the reflected waves from the second network (S'') may be expressed as

$$b''_{o,w} = S''_{(D+w),(D+z)} a''_{o,z} + \sum_{n=1}^{D} S''_{(D+w),n} a''_{i,n}, \tag{D.22}$$

where $w = 1...F$.

Employing the same methodology, the waves propagating from network S'' towards network S' may be rewritten as

$$b''_{i,g} = S''_{g,(D+z)} a''_{o,z} + \sum_{n=1}^{D} S''_{g,n} b'_{o,n} = S''_{g,(D+z)} a''_{o,z} + \sum_{k=1}^{D} b''_{i,k} \sum_{n=1}^{D} S'_{(M+n),(M+k)} S''_{g,n}, \tag{D.23}$$

and simplified to

$$b''_{i,g} = S^{ex2}_{g,z} a''_{o,z} + \sum_{k=1}^{D} b''_{i,k} S^{rw2}_{g,k}, \tag{D.24}$$

where the variables

$$S^{ex2}_{g,z} = S''_{g,(D+z)}, \tag{D.25}$$

and

$$S^{rw2}_{g,k} = \sum_{n=1}^{D} S'_{(M+n),(M+k)} S''_{g,z}, \tag{D.26}$$

have been introduced for the sake of completeness.

Eq. (D.24) forms a set of linear equations which can easily be expressed in a matrix way as

$$\begin{pmatrix} 1 - S^{rw2}_{1,1} & -S^{rw2}_{1,2} & \cdots & -S^{rw2}_{1,(D-1)} & -S^{rw2}_{1,D} \\ -S^{rw2}_{2,1} & 1 - S^{rw2}_{2,2} & \cdots & -S^{rw2}_{2,(D-1)} & -S^{rw2}_{2,D} \\ \vdots & \vdots & \ddots & \vdots & \vdots \\ -S^{rw2}_{(D-1),1} & -S^{rw2}_{(D-1),2} & \cdots & 1 - S^{rw2}_{(D-1),(D-1)} & -S^{rw2}_{(D-1),D} \\ -S^{rw2}_{D,1} & -S^{rw2}_{D,2} & \cdots & -S^{rw2}_{D,(D-1)} & 1 - S^{rw2}_{D,D} \end{pmatrix} \begin{pmatrix} b''_{i,1} \\ b''_{i,2} \\ \vdots \\ b''_{i,(D-1)} \\ b''_{i,D} \end{pmatrix} = \begin{pmatrix} S^{ex2}_{1,q} \\ S^{ex2}_{2,q} \\ \vdots \\ S^{ex2}_{(D-1),q} \\ S^{ex2}_{D,q} \end{pmatrix} a''_{o,z}. \tag{D.27}$$

After solving the linear system of equations, each $b''_{i,g}$ wave can be expressed as

$$b''_{i,g} = a''_{o,z} f''_{g,z}(S', S'') \tag{D.28}$$

where $a''_{o,z}$ is the excitation wave and $f''_{g,z}(S', S'')$ is a function, which depends on S' and S'', and relates the output and input waves. Note that this function is directly obtained after solving Eq. (D.27).

Finally, the scattering parameters of the equivalent combined network (S, see Fig. D.1) can be expressed as

$$S_{(M+w),(M+z)} = \frac{b''_{o,w}}{a''_{o,z}} = S''_{(D+w),(D+z)} + \sum_{n=1}^{D}\sum_{k=1}^{D} S''_{(D+w),n} S'_{(M+n),(M+k)} f''_{k,z}(S', S'') \tag{D.29}$$

for the reflection coefficients (output port point of view, modal excitation wave defined by $z = 1...F$ and observation mode defined by $w = 1...F$) and as

$$S_{t,(M+z)} = \frac{b'_{i,t}}{a''_{o,z}} = \sum_{n=1}^{D} S'_{t,(M+n)} f''_{n,z}(S', S'') \tag{D.30}$$

for the case of the transmission coefficients (i.e., from the output to the input port, with modal excitation wave defined by $z = 1...F$ and observation mode at the input port defined by $t = 1...M$).

Appendix E

Transformation between series and shunt R-C circuits

The purpose of this appendix is to derive simple expressions for the lumped components of an R-C series and shunt circuits, in order to achieve the same input impedance in both cases. This situation is clearly depicted in Fig. E.1.

The input impedance of a series R-C circuit [shown in Fig. E.1(left)] is given by

$$Z_{se}(\omega) = R(\omega) + \frac{1}{j\omega C(\omega)}, \tag{E.1}$$

and the input impedance of a shunt R-C circuit [shown in Fig. E.1(right)] is given by

$$Z_{sh}(\omega) = \frac{R_1(\omega)}{1 + j\omega C_1(\omega) R_1(\omega)}. \tag{E.2}$$

The goal now is to obtain the R-C values of the series circuit as a function of the R-C values of the shunt circuit. For this purpose, we can easily equal the input impedances of the circuits, as

$$Z_{se}(\omega) = Z_{sh}(\omega) \rightarrow R(\omega) + \frac{1}{j\omega C(\omega)} = \frac{R_1(\omega)}{1 + j\omega C_1(\omega) R_1(\omega)}. \tag{E.3}$$

After some straightforward manipulations, this last equation may be rewritten as

$$R(\omega) + \frac{1}{j\omega C(\omega)} = \frac{R_1(\omega)}{1 + \omega^2 C_1(\omega)^2 R_1(\omega)^2} + \frac{1}{j\omega \frac{1+\omega^2 C_1(\omega)^2 R_1(\omega)^2}{\omega C_1(\omega) R_1(\omega)^2}}, \tag{E.4}$$

which allows us to clearly express the R-C values of the series circuit as follows

$$R(\omega) = \frac{R_1(\omega)}{1 + \omega^2 C_1(\omega)^2 R_1(\omega)^2}, \tag{E.5}$$

$$C(\omega) = \frac{1 + \omega^2 C_1(\omega)^2 R_1(\omega)^2}{\omega C_1(\omega) R_1(\omega)^2}. \tag{E.6}$$

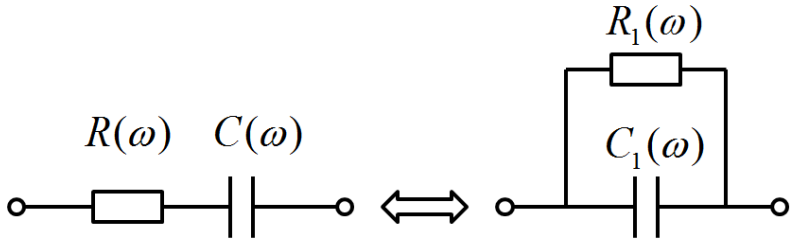

Figure E.1 – Input impedance equivalence between a series and a shunt R-C circuits. The series circuit (left) is composed of a resistor (R) and a capacitor (C), and the shunt circuit is composed of a different resistor (R_1) and a different capacitor (C_1). Note that this transformation depends on frequency.

On the other hand, the input admittance of a series R-C circuit is given by

$$Y_{se}(\omega) = \frac{j\omega C(\omega)}{1 + j\omega C(\omega)R(\omega)}, \tag{E.7}$$

and the input admittance of a shunt R-C circuit is given by

$$Y_{sh}(\omega) = \frac{1}{R_1(\omega)} + j\omega C_1(\omega). \tag{E.8}$$

The goal now is to obtain the R-C values of the shunt circuit as a function of the R-C values of the series circuit. For this purpose, we can easily equal the input admittances of the circuits, as

$$Y_{sh}(\omega) = Y_{se}(\omega) \rightarrow \frac{1}{R_1(\omega)} + j\omega C_1(\omega) = \frac{j\omega C(\omega)}{1 + j\omega C(\omega)R(\omega)}, \tag{E.9}$$

After some straightforward manipulations, this last equation may be rewritten as

$$\frac{1}{R_1(\omega)} + j\omega C_1(\omega) = \frac{\omega^2 C(\omega)^2 R(\omega)}{1 + \omega^2 C(\omega)^2 R(\omega)^2} + j\omega \frac{C(\omega)}{1 + \omega^2 C(\omega)^2 R(\omega)^2}, \tag{E.10}$$

which allows us to clearly express the R-C values of the shunt circuit as follows

$$R_1(\omega) = \frac{1 + \omega^2 C(\omega)^2 R(\omega)^2}{\omega^2 C(\omega)^2 R(\omega)}, \tag{E.11}$$

$$C_1(\omega) = \frac{C(\omega)}{1 + \omega^2 C(\omega)^2 R(\omega)^2}. \tag{E.12}$$

Appendix F

Author's Publications

This PhD. dissertation has introduced novel formulations applied for the analysis of new technologies, devices and phenomena at the microwave regime. The publications of several technical and scientific international papers guarantees the quality and interest of the novel ideas proposed. Specifically, **the work presented in this thesis has contributed to the publication of** 21 **peer-review international journal papers (**14 **of them as a first author),** 4 **invited international conferences (all of them as a first author),** 13 **international conferences (**4 **of them as a first author),** 9 **Spanish national journal papers (**4 **of them as a first author) and** 20 **Spanish national conferences (**10 **as a first author)**.

This appendix gives a list of the main relevant contributions for the scientific community derived from the present work. The acronyms employed to denote and distinguish journals and conferences follows the structure of [*NameNumber*], where *Name* is related to the type of publication [***J*** for peer-review international journal, ***SJ*** for Spanish national journal, ***InvC*** for invited international conference, ***C*** for international conferences and ***SC*** for Spanish national conferences] and *Number* is related to the number of a specific paper within the same type of publication.

F.1 International Refereed Journals

J1 **J. S. Gómez-Díaz**, J. L. Gómez-Tornero, A. Álvarez-Melcón and C. Caloz, "A Simple Transmission Line Model for the Characterization of Leaky-Wave Antennas", IEEE Trans. Antennas and Propagation, [To be submitted].

J2 M. Martínez-Mendoza, **J. S. Gómez-Díaz**, D. Cañete-Rebenaque, A. Álvarez-Melcón and S. Amari, "A Systematic Algorithm for the Design of Hybrid Waveguide-Microstrip Transversal Microwave Filters", IET Microwaves, Antennas and Propagation [Under review. Current status: Accepted subject to minor changes].

J3 **J. S. Gómez-Díaz**, A. Álvarez-Melcón and T. Bertuch, "Radiation Characteristics of Mushroom-like PPW LWAs: Analysis and Experimental Verification", IEEE Antennas and Wireless Propa-

gation Letters [Under review. Current status: Accepted subject to minor changes].

J4 **J. S. Gómez-Díaz**, A. Álvarez-Melcón and T. Bertuch, "A Modal-Based Iterative Circuit Model for the Analysis of CRLH Leaky-Wave Antennas comprising Periodically Loaded PPW", IEEE Trans. Antennas and Propagation, Vol. 59, Issue 4, pp. 1101-1112, April, 2011.

J5 **J. S. Gómez-Díaz**, M. García-Vigueras and A. Álvarez-Melcón, "A Grounded MoM-based Spatial Green's Function Technique for the Analysis of Multilayered Circuits in Rectangular Shielded Enclosures", IEEE Trans. Microwave Theory and Techniques, Vol. 59, Issue 3, pp. 533-541, March, 2011.

J6 **J. S. Gómez-Díaz**, D. Cañete-Rebenaque and A. Álvarez-Melcón, "A Simple CRLH LWA Circuit Condition for Constant Radiation Rate", IEEE Antennas and Wireless Propagation Letters, Vol. 10, pp. 29-32, March, 2011.

J7 D. Cañete Rebenaque, M. Martínez Mendoza, J. Pascual-García, **J. S. Gómez-Díaz**, and A. Álvarez-Melcón, "Novel Implementations for Microstrip Resonator Filters in Transversal and Alternative Topologies", IEEE Trans. Microwave Theory and Techniques, Vol. 59, Issue 2, pp. 242-249, February, 2011.

J8 **J. S. Gómez-Díaz**, S. Gupta, A. Álvarez-Melcón and C. Caloz, "Efficient Time-Domain Análisis of Highly-Dispersive Linear and Non-Linear Meta-material Waveguide and Antenna Structures", IET Microwaves, Antennas and Propagation, Special Issue on APMC 2008, Vol. 4, Issue 10, pp. 1617-1625, doi: 10.1049/iet-map.2009.0205, October, 2010,

J9 M. García-Vigueras, J. L. Gómez-Tornero, G. Goussetis, **J. S. Gómez-Díaz** and A. Álvarez-Melcón, "A Modified Pole-Zero Technique for the Analysis and Design of Waveguides and Leaky-Wave Antennas with Dipole-Based FSS", IEEE Trans. Antennas and Propagation, Vol. 58, Issue 6, pp. 1971-1979, June, 2010.

J10 **J. S. Gómez-Díaz**, S. Gupta, A. Álvarez-Melcón and C. Caloz, "Investigation on the Phenomenology of Impulse-Regime Metamaterial Transmission Lines", IEEE Trans. Antennas and Propagation, Vol. 57, Issue 12, pp. 4010-4014, December, 2009.

J11 **J. S. Gómez-Díaz**, S. Gupta, A. Álvarez-Melcón and C. Caloz, "Tunable Talbot Imaging Distance using an Array of Beam-Steered Metamaterial Leaky-Wave Antennas", Journal of Applied Physics, Vol. 106, 084908, doi: 10.1063/1.3213382, 2009.

J12 **J. S. Gómez-Díaz**, M. Martínez-Mendoza, F. D. Quesada-Pereira and A. Álvarez-Melcón, "Efficient Calculation of the Green's functions for Multi-layered Shielded Cavities with Right Isosceles-Triangular Cross-Section", IET Microwaves, Antennas and Propagation, Vol. 3, Issue 5, pp. 736-741, doi:10.1049/iet-map.2008.0081, August, 2009.

J13 **J. S. Gómez-Díaz**, S. Gupta, A. Álvarez-Melcón and C. Caloz, "Impulse-regime CRLH resonator for Tunable Pulse Rate Multiplication", Radio Sci., 44, RS4001, doi:10.1029/2008RS003991, July, 2009.

J14 J. Pascual-García, F. D. Quesada-Pereira, D. Cañete-Rebenaque, **J. S. Gómez-Díaz** and A. Álvarez-Melcon, “A New Neural Network Technique for the Design of Multilayered Microwave Shielded Bandpass Filters", Int. Journal of RF and Microwave Computer-Aided Engineering, doi: 10.1002/mmce.20363, Vol. 19, Issue 3, pp. 405-415, December, 2008.

J15 **J. S. Gómez-Díaz**, S. Gupta, A. Álvarez-Melcón and C. Caloz, "Spatio-Temporal Talbot Phenomenon using Metamaterial Composite Right/Left-Handed Leaky-Wave Antennas", Journal of Applied Physics, 104, 104901, doi: 10.1063/1.3013905, 2008.

J16 M. Martínez-Mendoza, **J. S. Gómez-Díaz**, D. Cañete-Rebenaque and A. Álvarez-Melcón "Design of Dual-Bandpass Hybrid Waveguide-Microstrip Microwave Filters", IEEE Trans. Microwave Theory and Techniques, Vol. 56, Issue 12, pp. 2913-2920, December, 2008.

J17 **J. S. Gómez-Díaz**, M. Martínez-Mendoza, F. J. Pérez-Soler and A. Álvarez-Melcón, "An Interpolated Spatial Images Method for the Analysis of Multilayered Shielded Microwave Circuits", Microwave and Optical Technology Letters, Vol. 50, N. 9, pp. 2294-2300, September 2008.

J18 F. J. Pérez-Soler, F. D. Quesada-Pereira, **J. S. Gómez-Díaz**, and A. Álvarez-Melcón "Analysis of Inductive Multiport Microwave Devices Employing a Novel Double Parallel Plate Approach", IET Microwaves, Antennas and Propagation, Vol. 2, Issue 2, pp. 171-179, doi:10.1049/iet-map:20070132, March, 2008.

J19 **J. S. Gómez-Díaz**, M. Martínez-Mendoza, F. D. Quesada-Pereira, F. J. Pérez-Soler and A. Álvarez-Melcón, "Practical Implementation of the Spatial Images Technique for the Analysis of Shielded Multilayered Printed Circuits", IEEE Trans. Microwave Theory and Techniques, Vol. 56, Issue 1, pp. 131-141, January, 2008.

J20 M. Martínez Mendoza, **J. S. Gómez-Díaz**, D. Cañete Rebenaque, J. L. Gómez Tornero and A. Álvarez-Melcón, "Design of Bandpass Transversal Filters Employing a Novel Hybrid Structure", IEEE Trans. Microwave Theory and Techniques, Vol. 5, Issue 12, pp. 2670-2678, December, 2007.

J21 **J. S. Gómez-Díaz**, F. D. Quesada-Pereira, J. L. Gómez-Tornero, J. Pascual-García and A. Álvarez-Melcon, “Numerical Evaluation of the Green’s Functions for Arbitrarily Shaped Cylindrical Enclosures and their Optimization by a new Spatial-Images Method", Radio Sci., 42, RS5007, doi: 10.1029/2006RS003588, October, 2007.

F.2 Spanish Journals

SJ1 **J. S. Gómez-Díaz**, M. Martínez-Mendoza, J. A. Lorente-Acosta and A. Álvarez-Melcón, "Nueva Condición Circuital para el Diseño de Antenas CRLH LW que presenten una Tasa de Radiación Constante en todo el Espacio", IV Jornadas Introducción a la investigación (UPCT) [Under review].

SJ2 A. Shahvarpour, C. Caloz, **J. S. Gómez-Díaz**, A. Álvarez-Melcón, D. Cañete-Rebenaque, P. Vera-Castejón, F. D. Quesada-Pereira, J. L. Gómez-Tornero, "Análisis espectral de metasustratos con anisotropía uni-axial y aplicación en el ensanchamiento de la banda de ondas leaky-wave", Espacio-Teleco, UPCT, Ed. Áglaya, ISSN 2171-2042, MU-27-2009, Vol. 2, pp. 146-152, 2011.

SJ3 **J. S. Gómez-Díaz**, M. García-Vigueras, A. Shahvarpour, M. Martínez-Mendoza, J. A. Lorente Acosta, A. Martínez-Ros, M. Jiménez-Nogales, R. Guzmán-Quirós, y A. Álvarez-Melcón, "Antena Leaky-Wave en Guía-Onda basada en Metamateriales: Método de Análisis y Diseño y Validación Experimental", III Jornadas Introducción a la investigación (UPCT), Ed. Áglaya, ISSN 1888-8356, Mu-1618-2008, pp. 80-82, May, 2010.

SJ4 J. A. Lorente Acosta, M. Martínez-Mendoza, **J. S. Gómez-Díaz**, M. García-Vigueras, A. Shahvarpour, A. Martínez-Ros, M. Jiménez-Nogales, R. Guzmán-Quirós, y A. Álvarez-Melcón, "Filtros de Microondas de una Sola Pieza Realizados Mediante Fundido Selectivo por Láser", III Jornadas Introducción a la investigación (UPCT), Ed. Áglaya, ISSN 1888-8356, Mu-1618-2008, pp. 83-85, May, 2010.

SJ5 **J. S. Gómez-Díaz**, M. García-Vigueras, F. D. Quesada-Pereira, J. Pascual-García, D. Cañete-Rebenaque, J. L. Gómez-Tornero, A. Shahvarpour, C. Caloz and A. Álvarez-Melcón "Estudio de la Ingeniería de Dispersión en Microondas empleando Líneas de Transmisión basadas en Metamateriales CRLH", Espacio-Teleco, UPCT, Ed. Áglaya, ISSN 2171-2042, MU-27-2009, Vol. 1, pp. 39-48, December, 2009.

SJ6 **J. S. Gómez-Díaz**, F. D. Quesada-Pereira, F. J. Pérez-Soler, J. Pascual-García, D. Cañete-Rebenaque, M. Martínez-Mendoza, J. L. Gómez-Tornero, C. Caloz and A. Álvarez Melcón, "Estudio de la Propagación y Radiación de Pulsos Temporales en Líneas de Transmisión basadas en Metamateriales CRLH", Telecoforum, UPCT, Ed. Áglaya, ISSN 1698-2924, MU-1447-2004, Vol. 6, December, 2008.

SJ7 P. Vera-Castejón, **J. S. Gómez-Díaz**, F. D. Quesada-Pereira, F. J. Pérez-Soler, J. Pascual-García, D. Cañete-Rebenaque, M. Martínez-Mendoza, J. L. Gómez-Tornero, and A. Álvarez Melcón, "Medidas sobre Canales Analógicos y Digitales de Televisión y su Interpretación para la Correcta Planificación de Sistemas de Recepción", Telecoforum, UPCT, Ed. Áglaya, ISSN 1698-2924, MU-1447-2004, Vol. 6, December 2008.

SJ8 M. Martínez Mendoza, **J. S. Gómez-Díaz**, D. Cañete-Rebenaque, F. J. Pérez-Soler, J. Pascual-García, J. L. Gómez-Tornero, P. Vera-Castejón and A. Álvarez Melcón, "Diseño de Filtros Transversales de Segundo Orden Empleando la Novedosa Tecnología Híbrida Guiaonda-Microstrip", Telecoforum, UPCT, ISSN 1698-2924, Vol. 5, December 2007.

SJ9 P. Vera Castejón, F. D Quesada-Pereira, D. Cañete Rebenaque, J. Pascual García, M. Martínez Mendoza, **J. S. Gómez-Díaz**, F. J. Pérez Soler, J. L. Gómez Tornero and A. Álvarez Melcón "Estudio de las Modulaciones Utilizadas en el Sistema de Televisión Digital Terrestre", Telecoforum, UPCT, ISSN 1698-2924, Vol. 5, Diciembre 2007.

F.3 Invited International Conference Proceeding

InvC1 **J. S. Gómez-Díaz**, S. Gupta, A. Álvarez Melcón and C. Caloz, "Impulse-regime analysis of metamaterial-based leaky-wave antennas and applications", American Electromagnetics Conference, Ottawa (Canada), July 2010. **Invited**.

InvC2 **J. S. Gómez-Díaz**, S. Gupta, A. Álvarez Melcón and C. Caloz, "Numerical analysis of Impulse Regime Phenomena in Linear and Non-Linear Metamaterial transmisión Lines", International Conference on Electromagnetics in Advanced Applications (ICEAA), Turin (Italy), September 2009. **Invited**.

InvC3 **J. S. Gómez-Díaz**, S. Gupta, A. Álvarez Melcón and C. Caloz, "Spatio-Temporal Talbot Effects in Impulse-Regime Metamaterial Leaky-Wave Antennas", European Conference of Antennas and Propagation (EuCap), Berlin (Germany), March 2009. **Invited**.

InvC4 **J. S. Gómez-Díaz**, A. Álvarez Melcón and C. Caloz, "Time-Domain Green's Function Technique for Highly-Dispersive Metamaterial Waveguide and Antenna Structures", Asia-Pacific Microwave Conference (APMC), Hong-Kong (China), December 2008. **Invited**.

F.4 International Conference Proceedings

C1 **J. S. Gómez-Díaz**, A. Álvarez-Melcón and T. Bertuch, "An Iteratively-Refined Circuital Model of CRLH Leaky-Wave Antennas derived from a Mushroom Structure", IEEE Antennas and Propagation Symposium (APS), Toronto (Canada), July 2010.

C2 **J. S. Gómez-Díaz**, M. Garcia-Vigueras, D. Cañete-Rebenaque, F. D. Quesada-Pereira and A. Álvarez-Melcón, "Use of Ground Planes within the Spatial Images Technique: Application to the Analysis of Rectangular Multilayered Shielded Enclosures", IEEE International Microwave Symposium (IMS), Anaheim (California, USA), May 2010.

C3 M. Martínez-Mendoza, **J. S. Gómez-Díaz**, D. Cañete-Rebenaque, A. Álvarez-Melcón and S. Amari, "A Highly Selective Hybrid Waveguide-Microstrip Transversal Microwave Filter", International Workshop on Microwave Filters, Toulousse (France), November, 2009.

C4 S. Gupta, **J. S. Gómez-Díaz** and C. Caloz, "Frequency Resolved Electrical Gating Principle for UWB signal Characterization using Leaky-Wave structures", European Microwave Conference, Rome (Italy), September 2009.

C5 D. Cañete-Rebenaque, M. Martínez-Mendoza, J. Pascual-García, **J. S. Gómez-Díaz** and A. Álvarez-Melcón, "Novel Implementations of Microstrip Resonator Filters in Transversal Topology", European Microwave Conference, Rome (Italy), September 2009.

C6 F. J. Pérez-Soler, F.D. Quesada-Pereira, **J. S. Gómez-Díaz**, M. Martínez-Mendoza, D. Cañete-Rebenaque, J. P. García, J.L. Gómez-Tornero and A. Álvarez Melcón, "Progress in Numerical Techniques Applied to Integral Equation Formulations", VI Iberian Meeting on Computational Electromagnetics, Chiclana (Cadiz, Spain), October 2008.

C7 **J. S. Gómez-Díaz**, A. Álvarez-Melcón and C. Caloz, "Characterization of Pulse Radiation by CRLH Leaky-Wave Antennas using a Time-Domain Green's Function Approach", IEEE Antennas and Propagation Symposium (APS), San Diego (California, USA), July 2008.

C8 F. J. Pérez-Soler, **J. S. Gómez-Díaz**, F. D. Quesada-Pereira, A. Álvarez-Melcón, "New Efficient Acceleration Technique for the Calculation of the Green's Functions in Rectangular Waveg-

uides", IEEE Antennas and Propagation Symposium (APS), San Diego (California, USA), July 2008.

C9 M. Martínez-Mendoza, F. J. Pérez-Soler, **J. S. Gómez-Díaz**, F. D. Quesada-Pereira, A. Alvarez-Melcón and R. J. Cameron, "Enhanced Topology for the Design of Bandpass Elliptic Fileters Employing Inductive Windows and Dielectric Objects", IEEE International Microwave Symposium (IMS), Atlanta (USA), June 2008.

C10 **J. S. Gómez-Díaz**, M. Martínez-Mendoza, F. D. Quesada-Pereira, J. Pascual-Garcia, F. J. Pérez-Soler and A. Álvarez-Melcón "Numerical evaluation of the Green's functions for arbitrarily shaped enclosures", IEEE International Microwave Symposium (IMS), Honolulu (Hawai, USA), June, 2007.

C11 M. Martínez-Mendoza, **J. S. Gómez-Díaz**, D. Cañete-Rebenaque, J. L. Gómez-Tornero and A. Álvarez-Melcón "Design of a Bandpass Transversal Filter Employing a Novel Hybrid Waveguide-Printed Structure", IEEE International Microwave Symposium Digest (IMS), Honolulu (Hawai, USA), June, 2007.

C12 F. J. Perez-Soler, F. D. Quesada-Pereira, **J. S. Gómez-Díaz** and A. Álvarez-Melcón "Efficient Novel Analysis For Inductive Structures With Obstacles Attached To The Waveguide Walls", IEEE Antennas and Propagation Symposium (APS), Honolulu (Hawai, USA), June, 2007.

C13 G. Doménech-Asensi, **J. S. Gómez-Díaz**, J. Martínez-Alajarín and R. Ruiz-Merino, "Synthesis on programmable analog devices from VHDL-AMS", in proceedings of the 13th IEEE Mediterranean Electrotechical Conference (MELECON'2006), pp 27-30, Benalmádena (Málaga, Spain), May, 2006.

F.5 Spanish Conference Proceedings

SC1 **J. S. Gómez-Díaz**, M. García-Vigueras, M. Martínez-Mendoza and A. Álvarez-Melcón "Nueva condición circuital para el diseño de antenas CRLH LW con una tasa de radiación constante", XXVI Simpósium Nacional de la Unión Científica Internacional de Radio URSI [Under review].

SC2 **J. S. Gómez-Díaz**, A. Álvarez-Melcón and T. Bertuch, "Antenas CRLH LWA basadas en Guías de Onda: Análisis Teórico y Demostración Experimental", XXV Simpósium Nacional de la Unión Científica Internacional de Radio URSI, Bilbao (Pais Vasco, Spain), September, 2010,.

SC3 **J. S. Gómez-Díaz**, M. García-Vigueras, D. Cañete-Rebenaque and A. Álvarez Melcón "Uso Combinado de Imágenes Espaciales con Planos de Masa Dinámicos: Aplicación al Análisis de Cavidades Rectangulares Multicapa", XXV Simpósium Nacional de la Unión Científica Internacional de Radio URSI, Bilbao (Pais Vasco, Spain), September, 2010.

SC4 M. García-Vigueras, J.L. Gómez-Tornero, R. Guzmán-Quirós, **J. S. Gómez-Díaz** and A. Álvarez-Melcón "Control de la Radiación de una Antena Leaky-Wave cargada con una Superficie Selectiva en Frecuencia", XXV Simpósium Nacional de la Unión Científica Internacional de Radio URSI, Bilbao (Pais Vasco, Spain), September, 2010,

SC5 **J. S. Gómez-Díaz**, S. Gupta, J. Pascual-García, D. Cañete-Rebenaque, F. D. Quesada-Pereira, C. Caloz and A. Álvarez-Melcón "Resonador CRLH de Banda Ancha: Aplicación para la Multiplicación Sintonizable de la Periodicidad de un Tren de Pulsos", XXIV Simpósium Nacional de la Unión Científica Internacional de Radio URSI, Santander (Cantabria, Spain), September, 2009.

SC6 **J. S. Gómez-Díaz**, S. Gupta, J. L. Gómez-Tornero, M. García-Vigueras, C. Caloz and A. Álvarez Melcón "Efecto Talbot Espacio-Temporal basado en CRLH LWAs: Fundamentos y Validación Experimental ", XXIV Simpósium Nacional de la Unión Científica Internacional de Radio URSI, Santander (Cantabria, Spain), September, 2009.

SC7 J. C. Galindo-Rosique, **J. S. Gómez-Díaz** y A. Álvarez-Melcón "Estudio comparativo y desarrollo de diferentes transiciones Microstrip-SIW", XXIV Simpósium Nacional de la Unión Científica Internacional de Radio URSI, Santander (Cantabria, Spain), September, 2009.

SC8 J. C. Galindo-Rosique, **J. S. Gómez-Díaz** , A. J. Martínbez-Ros, J. L. Gómez-Tornero y A. Álvarez-Melcón "Fenómeno de pared magnética en antenas ranuradas utilizando tecnología SIW", XXIV Simpósium Nacional de la Unión Científica Internacional de Radio URSI, Santander (Cantabria, Spain), September, 2009.

SC9 D. Cañete-Rebenaque, M. Martínez-Mendoza, J. Pascual-García, **J. S. Gómez-Díaz** and A. Álvarez-Melcón, "Nuevas Implementaciones de Filtros Microstrip en Topología Transversal", XXIV Simpósium Nacional de la Unión Científica Internacional de Radio URSI, Santander (Cantabria, Spain), September, 2009.

SC10 M. García-Vigueras, R. Guzmán-Quirós, J.L. Gómez-Tornero, **J. S. Gómez-Díaz** y A. Álvarez-Melcón "Estudio de la dispersión de modos Leaky en guías de onda de placas paralelas cargadas con FSS y AMC con aplicación en antenas Leaky-Wave", XXIV Simpósium Nacional de la Unión Científica Inter-nacional de Radio URSI, Santander (Cantabria, Spain), September, 2009.

SC11 **J. S. Gómez-Díaz**, S. Gupta, M. Martínez-Mendoza, A. Álvarez-Melcón and C. Caloz "Estudio de la Radiación de antenas CRLH Leaky-Wave excitadas por pulsos y Aplicaciones", XXIII Simpósium Nacional de la Unión Científica Internacional de Radio URSI, Madrid (Spain), September, 2009.

SC12 **J. S. Gómez-Díaz**, M. Martínez-Mendoza, F.D. Quesada-Pereira and A. Álvarez-Melcón, "Cálculo Eficiente de la Función de Green en Cavidades Multicapa con Sección Transversal de tipo Rectángulo-Isósceles", XXIII Simpósium Nacional de la Unión Científica Internacional de Radio URSI, Madrid (Spain), September, 2009.

SC13 M. Martínez-Mendoza, D. Cañete-Rebenaque, **J. S. Gómez-Díaz**, F. J. Pérez-Soler, A. Álvarez-Melcón, "Nuevos Filtros Multicapa Basados en Trisectios Empleando Nodos No Resonantes",XXIII Simpósium Nacional de la Unión Científica Internacional de Radio URSI, Madrid (Spain), September, 2009.

SC14 **J. S. Gómez-Díaz**, M. Martínez-Mendoza, J.L. Gómez-Tornero, D. Cañete-Rebenaque and A. Álvarez-Melcón, "Formulación Espacial de la Función de Green en Cavidades de Geometría

Arbitraria", XXII Simpósium Nacional de la Unión Científica Internacional de Radio URSI, Tenerife (Spain), September, 2007.

SC15 **J. S. Gómez-Díaz**, M. Martínez-Mendoza, F. D. Quesada-Pereira, F. J. Pérez-Soler and A. Álvarez-Melcón, "Un Método Eficiente de Interpolación en el Dominio Espacial para el Análisis de Dispositivos de Microondas Encapsulados", XXII Simpósium Nacional de la Unión Científica Internacional de Radio URSI, Tenerife (Spain), September, 2007.

SC16 M. Martínez-Mendoza, **J. S. Gómez-Díaz**, D. Cañete-Rebenaque, J.L. Gómez-Tornero and A. Álvarez-Melcón, "Diseño de un Filtro Transversal Empleando una Nueva Estructura Híbrida Guiaonda-Circuito Impreso", XXII Simpósium Nacional de la Unión Científica Internacional de Radio URSI, Tenerife (Spain), September, 2007.

SC17 M. Martínez-Mendoza, **J. S. Gómez-Díaz**, D. Cañete-Rebenaque, J.L. Gómez-Tornero and A. Álvarez-Melcón, "Efecto del Acoplo Directo en Filtros Transversales Paso Banda de Segundo Orden con todos sus Ceros de Transmisión Situados en el Infinito", XXII Simpósium Nacional de la Unión Científica Internacional de Radio URSI, Tenerife (Spain), September, 2007.

SC18 F. J. Pérez-Soler, F. D. Quesada-Pereira, M. Martínez-Mendoza, **J. S. Gómez-Díaz** and A. Álvarez-Melcón, "Análisis Eficiente de Estructuras Guía Onda Inductivas con Dieléctricos Pegados a las Paredes Mediante una Nueva Formulación Integral de Superficie.", XXII Simpósium Nacional de la Unión Científica Internacional de Radio URSI, Tenerife (Spain), September, 2007.

SC19 J. Pascual-García, F. D. Quesada-Pereira, D. Cañete-Rebenaque, **J. S. Gómez-Díaz** and A. Álvarez-Melcón, "Una Nueva Técnica de Diseño de Filtros de Microondas Multicapa Apantallados Basada en Redes Neuronales", XXII Simpósium Nacional de la Unión Científica Internacional de Radio URSI, Tenerife (Spain), September, 2007.

SC20 **J. S. Gómez-Díaz**, F. D. Quesada-Pereira, J. Pascual-García, D. Cañete-Rebenaque, J.L. Gómez-Tornero and A. Álvarez-Melcón, "Optimización del Cálculo de las Funciones de Green Mediante Imágenes Espaciales", XXI Simpósium Nacional de la Unión Científica Internacional de Radio URSI, Oviedo (Spain), September, 2006.

Index of Terms

Glossary

$*$

Sign to denote the convolution operation.

$A(z,t)$

Temporal representation (in volts) of a periodic signal at the position z.

$AF(\omega,\hat{\theta},\phi)$

Array factor term expressed in spherical coordinates.

$A_a(x,z)$

Spatial distribution of the electric field [at a particular time t (implicit) and at the position z] along the elements of an antenna array, which are placed on the x axis.

$A_e(x,z=0)$

Spatial distribution of the electric field along an array element in a particular time snapshot t (implicit).

B_V

Total number of basis functions employed to compute multilayered boxed electric scalar Green's functions.

$B_{A,\xi}$

Number of basis employed to discretize the wall ξ when computing the boxed Green's function related to the magnetic vector potential.

C'_L

LH times-unit-length capacitance ($F \cdot m$).

C'_R

RH per-unit-length capacitance (F/m).

D^x

In the context of the spatial images technique, auxiliary linear distribution of dipoles employed to compute the boxed multilayered magnetic vector Green's functions generated by an x-oriented source dipole.

D^y

In the context of the spatial images technique, auxiliary linear distribution of dipoles employed to compute the boxed multilayered magnetic vector Green's functions generated by an y-oriented source dipole.

G'

Per unit-length conductance (S/m).

$G^{xx}_{A_{Box}}$

x-component of the multilayered boxed magnetic vector Green's function generated by an x-oriented source dipole.

$G^{xx}_{A_{Cav}}$

x-component of the multilayered magnetic vector Green's function, generated by an x-oriented source dipole, related to a cavity with a convex arbitrarily-shaped cross-section.

$G^{xx}_{A_{Tri}}$

x-component of the multilayered magnetic vector Green's function, generated by an x-oriented source dipole, related to a cavity with triangular cross-section.

$G^{yy}_{A_{Box}}$

y-component of the multilayered boxed magnetic vector Green's function generated by an y-oriented source dipole.

$G^{yy}_{A_{Cav}}$

y-component of the multilayered magnetic vector Green's function, generated by an y-oriented source dipole, related to a cavity with a convex arbitrarily-shaped cross-section.

$G^{yy}_{A_{Tri}}$

y-component of the multilayered magnetic vector Green's function, generated by an y-oriented source dipole, related to a cavity with triangular cross-section.

$G_I(z, z', t)$

Green's function associated to the current along a transmission line.

G_V

Electric scalar Green's function.

$G_V(z, z', t)$

Green's function associated to the voltage along a transmission line.

G_W

Magnetic scalar Green's function.

G_{Box}

Multilayered Green's function related to a cavity with rectangular cross-section.

$G_{V_{Box}}$

Multilayered boxed electric scalar Green's function.

$G_{V_{Cav}}$

Multilayered electric scalar Green's function related to a cavity with a convex arbitrarily-shaped cross-section.

$G_{V_{Tri}}$

Multilayered electric scalar Green's function related to a cavity with triangular cross-section.

$H(z,t)$

Time domain channel transfer function.

I

Current (A).

$I_{m,k}^{x,x}$

Auxiliary dipole number m, located at the k^{th} ring, oriented along the x direction and generated by an original x-oriented dipole source, employed to compute the magnetic vector potential.

$I_{m,k}^{x,y}$

Auxiliary dipole number m, located at the k^{th} ring, oriented along the x direction and generated by an original y-oriented dipole source, employed to compute the magnetic vector potential.

$I_{m,k}^{y,x}$

Auxiliary dipole number m, located at the k^{th} ring, oriented along the y direction and generated by an original x-oriented dipole source, employed to compute the magnetic vector potential.

$I_{m,k}^{y,y}$

Auxiliary dipole number m, located at the k^{th} ring, oriented along the y direction and generated by an original y-oriented dipole source, employed to compute the magnetic vector potential.

$I_g(t)$

Temporal input current provided by a generator (A).

$I_p^l(z)$

Current related to a propagative wave, flowing on the lower conductor of a transmission line.

$I_p^u(z)$

Current related to a propagative wave, flowing on the upper conductor of a transmission line.

$I_{rad}(z', \omega)$

Effective radiation current, from a far-field point of view, which flows along a transmission line.

L'_L

LH times-unit-length inductance ($H \cdot m$).

L'_R

RH per-unit-length inductance (H/m).

N

In the context of the spatial images technique, number of images per ring employed to discretize the contour of a given cavity.

N_g

Total number of ports of a given structure.

N_p

Total number of basis functions employed to characterize the current flowing on the p^{th} metallic patch.

N_{st}

Number of unit-cells along the y direction in a PPW CRLH LWA structure.

N_{uc}

Number of unit-cells along the x direction in a PPW CRLH LWA structure.

P'_{rad}

Reference power radiated by a PPW CRLH LWA.

$P^x_{G_A}(\vec{r}', g)$

Sign of an auxiliary dipole located in the quadrant g, and generated by an x-oriented source dipole.

$P_{G_V}(\vec{r}', g)$

Sign of an auxiliary charge located in the quadrant g.

P_{load}

Total power absorbed by a load.

$P_{radiated}$

Total power radiated to free-space by an antenna.

P_{rad}

Total power radiated by a PPW CRLH LWA.

P_{source}

Total power generated by a source.

Q

In the context of the spatial images technique, auxiliary linear distribution of charges, employed to compute the boxed multilayered electric scalar Green's function.

R

In the context of the spatial images technique, number of rings of images employed to discretize one cavity in height.

R'

Per unit-length resistance (Ω/m).

R_{ant}

Distance between an observation point P (placed at $\vec{r}$) and a linear antenna, considered punctual from a far-field point of view.

S_0

Zero order Sommerfeld transformation.

S_1

First order Sommerfeld transformation.

$S_{b_q a_p}$

Scattering parameter observed at the b port, q^{th} mode, when the port a is excited by the p^th mode.

T_0

Period rate of a periodic temporal signal.

$T_p(\omega)$

Time required for a single round trip inside a UWB CRLH resonator for a give pulse, as a function of frequency.

V

Voltage (V).

V_{BIAS}

DC voltage employed to polarize a varactor .

$V_{ex}^{(u)}(m)$

m^{th} component of the excitation vector employed in the MoM system of linear equations, related to the u^{th} metal patch.

X

In the spatio-temporal Talbot phenomenon context, spatial distance between two consecutive antennas placed within an array.

Z_0

Characteristic impedance (Ω).

Z_B

Bloch impedance (Ω).

$Z_{m,n}^{(u,p)}$

MoM impedance matrix element, related to the basis function n, defined on the p^{th} metal patch, and to the test function m, defined on the u^{th} metal patch.

$\Delta\theta$

Range of spatial directions where the beam of an antenna excited by a pulse is radiated.

$\Psi(t)$

Modulated pulse.

$\Psi_0(t)$

Slowly varying envelope of a baseband pulse.

α

Attenuation constant (Np/m).

$\alpha_n^{(p)}$

In the MPIE context, unknown n coefficient in the expansion of the current on the s_p surface.

$\alpha_{k,m}$

In the spatial images context, complex weight associated to the k^{th} basis function placed on the m^{th} ring.

$\alpha_{k,m}^{x,\xi}$

In the spatial images context, complex weight related to the k basis function, placed at the m ring, associated to an x-oriented auxiliary dipole and imposed on the ξ wall.

$\bar{\bar{G}}_A$

Magnetic dyadic Green's function.

$\bar{\bar{G}}_F$

Electric dyadic Green's function.

$\bar{\bar{Q}}(P_i)$

In the context of the spatial images technique, accelerated by interpolation, complex values of the auxiliary charge images when the source is placed at the i-th corner of the rectangular sub-region ($i = 1, 2, 3, 4$).

β

Phase constant (rad/m).

β_k

Propagation constant related to the k-th mode inside a resonator.

χ

Phase change between the currents which flow along the conductors of a transmission line.

ℓ

Antenna or transmission line length.

ℓ_{uc}

Length of a PPW CRLH LWA unit-cell.

η

Free space impedance.

γ

Complex propagation constant, $\gamma(\omega) = \alpha(\omega) + j\beta(\omega)$.

$\hat{\theta}$

θ component in a spherical coordinate system.

$\hat{e}_n$

Normal unit vector.

$\hat{e}_t$

Tangential unit vector.

λ_g

Guided wavelength.

μ

Permeability.

ω'

Transformed frequency, $\omega' = \omega_0 + \omega$.

ω_0

Modulation frequency of a given pulse.

ω_m

Frequency related to the m resonance inside a resonator.

ω_r

Spectral repetition frequency.

$\overline{\overline{G}}(\vec{r},\vec{r}',t,t')$

Spatio-temporal dyadic Green's function.

ϕ_e

Electric scalar potential (V).

ϕ_m

Magnetic scalar potential (A).

ρ_L

Reflection coefficient at the load.

ρ_{s_p}

Equivalent charge density located on the surface of the p^{th} metallic patch.

σ_{s_u}

Finite conductivity of the metal placed on the surface s_u.

θ

Radiation angle of an antenna main beam, measured from the direction perpendicular to the antenna.

θ'

Antenna radiation angle measured from an auxiliary rotated coordinate system.

$\tilde{A}(z,\omega)$

Spectral representation (in volts/Hz) of a periodic signal at the position z.

$\tilde{A}_a(k_x,z)$

Distribution of the electric field along an antenna array, expressed in the transformed domain, placed at a particular position z.

$\tilde{G}_A^{xx}$

x-component of the spectral-domain multilayered magnetic vector potential Green's function generated by an x-oriented source dipole.

$\tilde{G}_F^{xx}$

x-component of the spectral-domain multilayered electric vector potential Green's function generated by an x-oriented source dipole.

$\tilde{G}_I(z,z',\omega)$

Spectral Green's function associated to the voltage along a transmission line.

$\tilde{G}_V$

Spectral-domain multilayered Green's function related to the electric scalar potential.

$\tilde{G}_V(z, z', \omega)$

Spectral Green's function associated to the voltage along a transmission line.

$\tilde{G}_W$

Spectral-domain multilayered Green's function related to the magnetic vector potential.

$\tilde{H}(k_x, \omega)$

Channel transfer function expressed in the transformed spatial domain.

$\tilde{H}(z, \omega)$

Channel transfer function expressed in the spectral domain.

ε

Permittivity.

$\vec{A}$

Magnetic vector potential ($V \cdot s/m$).

$\vec{B}$

Magnetic Field (T).

$\vec{D}$

Electric Field (C/m^2).

$\vec{E}$

Electric Field (V/m).

$\vec{E}^i$

Incident or impressed electric field (V/m).

$\vec{E}^s$

Scattered electric field (V/m).

$\vec{H}$

Magnetic Field Intesity (A/m).

$\vec{J}$

Current Density (A/m).

$\vec{J}_{s_p}$

Equivalent current density flowing on the surface of the p^{th} metallic patch.

$\vec{f}_n^{(p)}$

n^{th} basis function defined on the p^{th} metallic patch.

$\vec{f}_m^{(u)}$

m^{th} test function defined on the u^{th} metallic patch.

$\vec{r}_g$

Generator position.

$\bar{E}_{se}(\omega, \hat{\theta}, \phi, r)$

Electric field, expressed in spherical coordinates, radiated by a magnetic linear source placed over a ground plane.

$\bar{F}$

Electric vector potential ($A \cdot s/m$).

ξ

In the analysis of leaky-wave antennas, amplitude change between the currents which flow along the conductors of a CRLH transmission line.

$\tilde{\xi}$

In the context of the spatio-temporal Talbot phenomenon, linearization parameter.

b

Antenna element spacing within an infinite array.

c

Speed of light.

f_T

Transition frequency associated to a CRLH line, where $\beta(f_T) = 0$.

f_{BF}

Lower frequency of the fast-wave region, which provides radiation at the backfire direction.

f_{EF}

Highest frequency of the fast-wave region, which provides radiation at the endfire direction.

$f_{V,b,a}^{g,k,m}$

Basis function number k, placed on the ring m, related to the scalar electric potential (V), and located on any (horizontal or vertical) direction a within the g quadrant (with $g = 1, 2, 3, 4$).

$f_{V,t,a}^{g,i,l}$

Test function number i, placed on the ring l, related to the scalar electric potential (V), and located on any (horizontal or vertical) direction a within the g quadrant (with $g = 1, 2, 3, 4$).

$f^{g,k,m}_{A_x,b,\xi}$

Basis function number k, placed on the ring m, related to the magnetic vector potential (A) generated by an x-oriented source dipole, and placed along the wall ξ within the g quadrant (with $g = 1, 2, 3, 4$).

$f^{g,i,l}_{A_x,t,\xi}$

Test function number i, placed on the ring l, related to the magnetic vector potential (A) generated by an x-oriented source dipole, and placed along the wall ξ within the g quadrant (with $g = 1, 2, 3, 4$).

k_0

Free space wavenumber.

k'_x

Auxiliary rotated wavenumber.

k_x, k_y, k_z

Transverse wavenumber along x, y and z axis.

p

Unit-cell length.

$q'_{m,k}$

Auxiliary charge number m, located at the k^{th} ring, employed by the spatial images technique to compute the electric scalar Green's function.

s

Metal thickness.

t

Dielectric thickness.

t_z

Time required for a pulse to reach the imaging Talbot distance from the generator, when it is located at the center of an antenna element.

$v'_g(\omega)$

Group velocity related to the auxiliary rotated k'_x wavenumber.

$v_g(\omega)$

Group velocity as a function of frequency.

w_{uc}

Width of a PPW CRLH LWA unit-cell.

x_{k_m}

Position of the k-th zeros in the m-th standing wave pattern inside a UWB CRLH resonator.

z_T

Integer Talbot distance.

z_f

Fractionary Talbot distance.

AD

Artificial Dielectric.

ADS©

Commercial electromagnetic software based on the method of moments. Distributed by Agilent.

AF

Array Factor term.

Backfire

Direction located at $\theta = -90°$, measured from the direction perpendicular to the structure.

Balanced CRLH unit-cell

CRLH unit cell which present and equal and mutually canceling of the series and shunt resonances, leading to a gapless transition from left-handed to right-handed frequency ranges. This condition implies $C_R L_L = C_L L_R$.

BIS

Basic Image Set.

BPF

Band Pass Filter.

Broadside

Direction located at $\theta = 0°$, i.e. perpendicular to the structure.

CPW

Coplanar Waveguide.

CRLH TL

Composite Right/Left-Handed Transmission Line.

CSRR

Complementary Split Ring Resonator.

CST©

Commercial electromagnetic software based on the finite differences time domain method. Distributed by CST.

CW

Continuous Wave, electromagnetic wave of constant amplitude and frequency.

Dispersive engineering approach

Phase shaping of electromagnetic waves to process signals in an analog fashion.

EFIE

Electric Field Integral Equation.

Endifre

Direction located at $\theta = +90^{\circ}$, measured from the direction perpendicular to the structure.

FDTD

Finite Differences Time Domain method.

FEM

Finite Elements Method.

FIE

Field Integral Equation.

FREG

Frequency-Resolved Electrical Gating system.

FROG

Frequency-Resolved Optical Gating system.

FSS

Frequency Selective Surface.

FWHM

Full Width at Half Maximum of a pulse.

GSM

Generalized Scattering Matrix.

GVD

Group Velocity Dispersion.

Harmonic regime

Operation of a structure/device when it is excited by just a unique frequency.

HFSS©

Commercial electromagnetic software based on the finite element method. Distributed by Ansys.

IE

Integral Equation.

Impulse regime

Operation of a structure/device when it is excited by an input pulse, composed by a set of frequencies.

LH

Left Handed medium, where the electric field, magnetic field and phase vector build a left-handed triad.

LU

Lower and Upper matrix factorization method.

LWA

Leaky Wave Antenna.

MAS

Method of Auxiliary Sources.

MIM

Metal Insulator Metal.

MM

Mode Matching.

MoM

Method of Moments.

MPIE

Mixed-Potential Integral Equation.

MSW

Magneto Static Wave.

MTM

Metamaterial.

PPM

Pulse Position Modulation.

PPW

Parallel-Plate Waveguide.

PPWM

Parallel-Plate Waveguide Mode.

RH

Right Handed medium, where the electric field, magnetic field and phase vector build the regular right-handed triad.

RTSA

Real Time Spectrum Analyzer.

RWG

Rao-Wilton-Glisson. Triangular test or basis function.

SAW

Surface Acoustic Wave.

Spectrogram

Joint time-frequency representation of a signal which consists on a 2-D plot, where the energy distribution is related to an image in a time-frequency plane.

SRR

Split Ring Resonator.

SSL

Side Secondary Lobe.

STFT

Short Time Fourier Transform.

TDIE

Time Domain Integral Equation method.

TLM

Transmission Line Matrix method.

UWB

Ultra Wide Band.

WM

Wired Medium.

Bibliography

[Abdalla et al., 2007] Abdalla, M., Phang, K., and Eleftheriades, G. V. (2007). Printed and integrated CMOS positive/negative index phase shifters using tunable active inductors. *IEEE Transactions on Microwave Theory and Techniques*, 55:1611–1623.

[Abielmona et al., 2007] Abielmona, S., Gupta, S., and Caloz, C. (2007). Experimental demonstration and characterization of a tunable CRLH delay line system for impulse/continuous wave. *IEEE Microwave and Wireless Components Letters*, 17(12):864–866.

[Abielmona et al., 2009] Abielmona, S., Gupta, S., and Caloz, C. (2009). Compressive receiver using a CRLH-based dispersive delay line for analog signal processing. *IEEE Transactions on Microwave Theory and Techniques*, 57(11):2617–2626.

[Abielmona et al., 2008] Abielmona, S., Gupta, S., Nguyen, H. V., and Caloz, C. (2008). Dispersion engineered impulse regime mematerial devices. In *Proc. XXIXth Assembly of Union Radio Science International (URSI)*, Chicago, IL, USA.

[Abielmonaa et al., 2006] Abielmonaa, S., Nguyen, H., and Caloz, C. (2006). CRLH zeroth order resonator (ZOR): Experimental demonstration of insensitivity to losses and to size. In *Asia-Pacific Microwave Conference*, Yokohama, Japan. IEEE.

[Afshari and Hajimiri, 2005] Afshari, E. and Hajimiri, A. (2005). Nonlinear transmission lines for pulse shaping in silicon. *IEEE Journal of Solid-State Circuits*, 40(3):744–752.

[Agarwal, 2005] Agarwal, G. P. (2005). *Nonlinear fiber optics*. Academic Press.

[Aksun, 1991] Aksun, M. I. (1991). A closed-form spatial Green's function for the thick microstrip substrate. *IEEE Transactions on Microwave Theory and Techniques*, 39(2):588–592.

[Aksun, 1996] Aksun, M. I. (1996). A robust approach for the derivation of closed-form Green's functions. *IEEE Transactions on Microwave Theory and Techniques*, 44(5):651–658.

[Aksun and Dural, 2005] Aksun, M. I. and Dural, G. (2005). Clarification of issues on the closed-form Green's functions in stratified media. *IEEE Transactions on Antennas and Propagation*, 53:3644.

[Allen et al., 2004] Allen, C. A., Caloz, C., and Itoh, T. (2004). Leaky-waves in a metamaterial-based two-dimensional structure for a conical beam antenna application. In *IEEE International Microwave Symposium*, volume 1, pages 6–11.

[Alparslan et al., 2010] Alparslan, A., Aksun, M. I., and Michalski, K. A. (2010). Closed-form Green's functions in planar layered media for all ranges and materials. *IEEE Transactions on Microwave Theory and Techniques*, 58(3):602–613.

[Alvarez Melcon, 1998] Alvarez Melcon, A. (1998). *Applications Of The Integral Equation Technique To The Analysis and Sinthesis of Multilayered Printed Shielded Microwave Circuits And Cavity Backed Antennas*. P.h.D. Thesis, Echole Politechnique Federale of Lausanne.

[Alvarez-Melcon and Mosig, 1999] Alvarez-Melcon, A. and Mosig, J. R. (1999). A novel spatial images technique for the analysis of cavity backed antennas. *ACES Journal*, 14(3):91–99.

[Alvarez-Melcon et al., 2001] Alvarez-Melcon, A., Mosig, J. R., and Guglielmi, M. (2001). Broadside couplings for high-selectivity microstrip filters. *Microwave and Optical Technology Letters*, 30:295–302.

[Álvarez Melcón and Mosig, 2000] Álvarez Melcón, A. and Mosig, J. R. (2000). Two techniques for the efficient numerical calculation of the Green's functions for planar shielded circuits and antennas. *IEEE Transactions on Microwave Theory and Techniques*, 48(9):1492–1504.

[Álvarez Melcón et al., 1999] Álvarez Melcón, A., Mosig, J. R., and Guglielmi, M. (1999). Efficient CAD of boxed microwave circuits based on arbitrary rectangular elements. *IEEE Transactions on Microwave Theory and Techniques*, 47(7):1045–1058.

[Amari and Rosenberg, 2003] Amari, S. and Rosenberg, U. (2003). A universal building block for advanced modular design of microwave filters. *IEEE Microwave and Wireless Components Letters*, 13(12):541–543.

[Amari et al., 2002] Amari, S., Rosenberg, U., and Borneman, J. (2002). Adaptive synthesis and design of resonator filters with source/load-multiresonator coupling. *IEEE Transactions on Microwave Theory and Techniques*, 50(8).

[Amin and Feng, 1995] Amin, G. and Feng, K. D. (1995). Short-time fourier transforms using cascade filter structures. *IEEE Transaction on Circuits and Systems II, Analog Digital Signal Processing*, 20(3):631–641–408.

[Antoniades and Eleftheriades, 2008a] Antoniades, M. and Eleftheriades, G. V. (2008a). A CPS leaky-wave antenna with reduced beam squinting using NRI-TL metamaterials. *IEEE Transactions on Antennas and Propagation*, 56(3):708–721.

[Antoniades and Eleftheriades, 2003a] Antoniades, M. A. and Eleftheriades, G. V. (2003a). Compact corporate power divider using metamaterial NRI-TL coupled-line couplers. *IEEE Antennas and Wireless Propagation Letters*, 7:440–442.

[Antoniades and Eleftheriades, 2003b] Antoniades, M. A. and Eleftheriades, G. V. (2003b). Compact, linear, lead/lag metamaterial phase shifters for broadband applications. *IEEE Antennas and Wireless Propagation Letters*, 2:103–106.

[Antoniades and Eleftheriades, 2005a] Antoniades, M. A. and Eleftheriades, G. V. (2005a). A broadband series power divider using zero-degree metamaterial phase-shifting lines. *IEEE Antennas and Wireless Propagation Letters*, 15:808 – 810.

[Antoniades and Eleftheriades, 2005b] Antoniades, M. A. and Eleftheriades, G. V. (2005b). A broadband Wilkinson balun using microstrip metamaterial lines. *IEEE Antennas and Wireless Propagation Letters*, 4:209–212.

[Antoniades and Eleftheriades, 2008b] Antoniades, M. A. and Eleftheriades, G. V. (2008b). A compact multi-band monopole antenna with a defected ground plane. *IEEE Antennas and Wireless Propagation Letters*, 7:652–655.

[Arcioni et al., 1997] Arcioni, P., Bressan, M., and Perregrini, L. (1997). On the evaluation of the double surface integrals arising in the application of the boundary integral method to 3-D problems. *IEEE Transactions on Microwave Theory and Techniques*, 45(3):436–439.

[Arndt et al., 1987] Arndt, F., Ahrents, I., Papziner, U., Wiechmann, U., and Wilkeit, R. (1987). Optimized E-plane T-junction series power dividers. *IEEE Transactions on Microwave Theory and Techniques*, 35(11):1052 – 1059.

[Azaña and Muriel, 1999] Azaña, J. and Muriel, M. A. (1999). Technique for multiplying the repetition rates of periodic trains of pulses by means of a temporal self-imaging effect in chirped fiber gratings. *Optics Lett.*, 24:1672–1674.

[Azaña and Muriel, 2001] Azaña, J. and Muriel, M. A. (2001). Temporal self-imaging effects: theory and application for multiplying pulse repetition rates. *IEEE J. Sel. Top. Quantum Electron*, 7:728–744.

[Bahl and Bhartia, 1980] Bahl, I. J. and Bhartia, P. (1980). Leaky-wave antennas using artificial dielectrics at millimiter wave frequencies. *IEEE Transactions on Microwave Theory and Techniques*, 28(1):1205–1212.

[Bahl and Gupta, 1974] Bahl, I. J. and Gupta, K. C. (1974). A leaky-wave antenna using an artificial dielectric medium. *IEEE Transactions on Antennas and Propagation*, 22(1):119–122.

[Bahl and Gupta, 1975] Bahl, I. J. and Gupta, K. C. (1975). Frequency scanning by leaky-wave antennas using artificial dielectrics. *IEEE Transactions on Antennas and Propagation*, 23(4):584–589.

[Bahl and Gupta, 1976] Bahl, I. J. and Gupta, K. C. (1976). Radiation from a dielectric-artificial dielectric slab. *IEEE Transactions on Antennas and Propagation*, 24(1):73–76.

[Balanis, 1989] Balanis, C. A. (1989). *Advanced Engineering Electromagnetics*. John Wiley and Sons.

[Balanis, 2005] Balanis, C. A. (2005). *Antenna Theory: Analysis and Design. 3rd Edition.* John Wiley and Sons.

[Barkeshli et al., 1990] Barkeshli, S., Pathak, P. H., and Marin, M. (1990). An asymptotic closed-form microstrip surface Green's function for the efficient moment method analysis of mutual coupling in microstrip antennas. *IEEE Transactions on Antennas and Propagation*, 38(9):1374–1383.

[Barton, 1989a] Barton, G. (1989a). *Elements of Green's Functions and Propagation*. Oxford Science Publications.

[Barton, 1989b] Barton, G. (1989b). *Elements of Green's Functions and Propagation: Potentials, Diffusion, and Waves*. Oxford University Press, USA.

[Berger et al., 2004] Berger, N. K., Levit, B. S., Bekker, A., and Fischer, B. (2004). Compression of periodic optical pulses using temporal fractional talbot effect. *IEEE Photonics Technology Letters*, 16(8):1855–1857.

[Bertuch, 2006] Bertuch, T. (2006). Comparative investigation of coupling reduction by ebg surfaces for quasi-static rcs measurement systems. *IEEE Antennas and Wireless Propagation Letters*, 5:231–234.

[Bertuch, 2007] Bertuch, T. (2007). A TM leaky-wave antenna comprising a textured surface. In *Proc. Int. Conf. Electromag. Adv. Appl. (ICEAA)*.

[Bhattacharyya, 1994] Bhattacharyya, A. K. (1994). *Electromagnetic Fields in Multilayered Structures: Theory and Applications*. Artech House, 1st edition edition.

[Bhattacharyya, 2006] Bhattacharyya, A. K. (2006). *Phased Array Antennas : Floquet Analysis, Synthesis, BFNs and Active Array Systems*. Wiley-Interscience, 1st edition edition.

[Boix et al., 2007] Boix, R. R., Mesa, F., and Medina, F. (2007). Application of total least squares to the derivation of closed-form Green's functions for planar layered media. *IEEE Transactions on Microwave Theory and Techniques*, 55:268.

[Bonache et al., 2005] Bonache, J., Gil, I., García-García, J., and Martín, F. (2005). Complementary split ringg resonators for microstrip diplexer design. *Electronics Letters*, 41:810–811.

[Bozzi et al., 2001] Bozzi, M., Perregrini, L., Alvarez-Melcon, A., Gulielmi, M., and Conciauro, G. (2001). MoM/BIŰRME analysis of boxed MMICs with arbitrarily shaped metallizations. *IEEE Transactions on Microwave Theory and Techniques*, 48(12):2227–2234.

[Brezinski, 1982] Brezinski, C. (1982). Some new convergence acceleration methods. *Math. Comput.*, 39:133–145.

[Brezinski, 1985] Brezinski, C. (1985). Integral transforms useful for the accelerated summation of periodic, free-space Green's functions. *IEEE Transactions on Microwave Theory and Techniques*, 33(8):734–736.

[Brezinski and Zaglia, 1991] Brezinski, C. and Zaglia, M. R. (1991). *Extrapolation Methods: Theory and Practice*. North Holland, 1^{st} edition edition.

[Bunger and Arndt, 2000] Bunger, R. and Arndt, F. (2000). Moment method analysis of arbitrarily 3D metallic N-port waveguide structures. *IEEE Transactions on Microwave Theory and Techniques*, 48(4):531–537.

[Caloz, 2006] Caloz, C. (2006). Dual composite right/left-handed (D-CRLH) transmission line metamaterial. *IEEE Microwave and Wireless Components Letters*, 16:585–587.

[Caloz, 2009] Caloz, C. (2009). Perspectives on EM metamaterials. *Materials Today*, 12(3).

[Caloz et al., 2007] Caloz, C., Abielmona, S., Nguyen, H. V., and Rennings, A. (2007). Dual composite right/left-handed (D-CRLH) leaky-wave antenna with low beam squinting and tunable group velocity. *Phys. Stat. Solidi (b)*, 244(4):1219–1226.

[Caloz and Itoh, 2003] Caloz, C. and Itoh, T. (2003). Novel microwave devices and structures based on the transmission line approach of meta-materials. In *IEEE International Microwave Symposium*, Philadelphia, PA, USA.

[Caloz and Itoh, 2004] Caloz, C. and Itoh, T. (2004). Array factor approach of leaky-wave antennas and application to 1-D/2-D composite right/left-handed (CRLH) structures. *IEEE Microwave and Wireless Components Letters*, 14(6):274–276.

[Caloz and Itoh, 2005] Caloz, C. and Itoh, T. (2005). *Electromagnetic Metamaterials: Transmission Line Theory and Microwave Applications.* Wiley and IEEE Press.

[Caloz et al., 2008] Caloz, C., Itoh, T., and Rennings, A. (2008). CRLH metamaterial leaky-wave and resonant antennas. *IEEE Antennas Propagat. Magazine*, 50(5):25–39.

[Caloz et al., 2011] Caloz, C., Jackson, D. R., and Itoh, T. (2011). Leaky-wave antennas. In Gross, F. B., editor, *Frontiers in Antennas: Next Generation Design and Engineering*. McGraw-Hill, 1 edition.

[Caloz et al., 2004a] Caloz, C., Lin, I. H., and Itoh, T. (2004a). Characteristics and potential applications of nonlinear left-handed transmission lines. *Microwave and Optical Technology Letters*, 40(6):471–473.

[Caloz and Nguyen, 2007] Caloz, C. and Nguyen, H. V. (2007). Novel broadband conventional and dual-composite right/left-handed (C/D-CRLH) metamaterials: properties, implementation and double-band coupler application. *App. Physics A*, 87(2):309–316.

[Caloz et al., 2002] Caloz, C., Obake, H., Iwait, H., and Itoh, T. (2002). Transmission line approach of left-handed (LH) materials. In *Proc. USNC/URSI Nat. Radio Sci. Meeting*, page 39, San Antonio, TX.

[Caloz et al., 2004b] Caloz, C., Sanada, A., and Itoh, T. (2004b). A novel composite right/left-handed coupled-line directional coupler with arbitrarty coupling level and broad bandwith. *IEEE Transactions on Microwave Theory and Techniques*, 52(3):980–992.

[Cameron, 1999] Cameron, R. (1999). General coupling matrix synthesis methods for Chebyshev filtering functions. *IEEE Transactions on Microwave Theory and Techniques*, 47:433–443.

[Cameron, 2003] Cameron, R. J. (2003). Advanced coupling matrix synthesis techniques for microwave filters. *IEEE Transactions on Microwave Theory and Techniques*, 51(1):1–10.

[Cameron et al., 2007] Cameron, R. J., Mansour, R., and Kudsia, C. M. (2007). *Microwave Filters for Communication Systems: Fundamentals, Design and Applications*. Wiley-Blackwell.

[Cañete-Rebenaque et al., 2011] Cañete-Rebenaque, D., Martínez-Mendoza, M., Pascual-Garcia, J., Gómez-Díaz, J. S., and Álvarez-Melcón, A. (2011). Novel implementations for microstrip resonator filters in transversal and alternative topologies. *IEEE Transactions on Microwave Theory and Techniques*, 59(2):242–249.

[Cañete-Rebenaque et al., 2004] Cañete-Rebenaque, D., Quesada-Pereira, F. D., Pascual-García, J., Alvarez-Melcon, A., and Marco-Guglielmi (2004). Two compact configurations for implementing transmission zeros in microstrip filters. *IEEE Microwave and Wireless Components Letters*, 14(10):475–477.

[Carbonell et al., 2011] Carbonell, J., Rogla, L. J., Boria, V. E., and Lippens, D. (2011). Design and experimental verification of backward-wave propagation in periodic waveguide structures. *IEEE Transactions on Microwave Theory and Techniques*, 54:1527–1533.

[Carignan et al., 2009] Carignan, L. P., Boucher, V., Kodera, T., Caloz, C., Yelon, A., and Menard, D. (2009). Double ferromagnetic resonance in nanowire arrays. *Applied Phisics Letters*, 52:062504–1:3.

[Casares-Miranda et al., 2006] Casares-Miranda, F. P., Camacho-Peñalosa, C., and Caloz, C. (2006). High-gain active composite right/left-handed leaky-wave antenna. *IEEE Transactions on Antennas and Propagation*, 54(8):2292–2300.

[Cho, 2003] Cho, Y. H. (2003). New iterative equations for an E-plane T-junction in a parallel-plate waveguide using Green's functions. *Microwave and Optical Technology Letters*, 37(7):447 – 449.

[Cohen, 1989] Cohen, L. (1989). Time-frequency distributions-a review. *Proceedings of the IEEE*, 77(2):941–981.

[Collin, 1991] Collin, R. E. (1991). *Field Theory of Guided Waves*. IEEE Press, Piscataway, N.J.

[Cools, 1999] Cools, R. (1999). Monomial cubature rules since Stroud: A compilation, part. 2. *Journal of Computational and Applied Mathematics*, 112(1-2):21–27.

[Dolar and Williamson, 1976] Dolar, V. and Williamson, R. (1976). A continuously variable delay-line system. In *Ultrasonics Symposium*, pages 419–423.

[Duchamp et al., 2003] Duchamp, J. M., Ferrari, P., Fernandez, M., Jrad, A., Mélique, X., Tao, J., Arscott, S., Lippens, D., and Harrison, R. G. (2003). Development of solitons in composite right- and left-handed transmission lines periodically lodaed with schottky varactors. *IEEE Transactions on Microwave Theory and Techniques*, 51(4):1105–1116.

[Dudley, 1994] Dudley, D. G. (1994). *Mathematical Foundations for Electromagnetic Theory*. IEEE Press, New York.

[Dunleavy and Katehi, 1988a] Dunleavy, L. P. and Katehi, P. B. (1988a). A generalized method for analyzing shielded thin microstrip discontinuities. *IEEE Transactions on Microwave Theory and Techniques*, 36(12):1758–1766.

[Dunleavy and Katehi, 1988b] Dunleavy, L. P. and Katehi, P. B. (1988b). Shielding effects in microstrip discontinuities. *IEEE Transactions on Microwave Theory and Techniques*, 36(12):1767–1774.

[Duran-Sindreu et al., 2009] Duran-Sindreu, M., Velez, A., Aznar, F., Bonache, J., and Martin, F. (2009). Application of open split ring resonators and open complementary split ring resonators to the synthesis of artificial transmission lines and microwave passive components. *IEEE Transactions on Microwave Theory and Techniques*, 57(2):3395–3403.

[Eleftheriades, 2007a] Eleftheriades, G. (2007a). Analysis of bandwidth and loss in negative-refractive-index transmission-line (NRI-TL) media using coupled resonators. *IEEE Microwave and Wireless Components Letters*, pages 412–414.

[Eleftheriades, 2009] Eleftheriades, G. (2009). EM transmission-line metamaterials. *Materials Today*, 12(3).

[Eleftheriades, 2007b] Eleftheriades, G. V. (2007b). A generalized negative-refractive-index transmission-line (NRI-TL) metamaterial for dual-band and quad-band applications. *IEEE Microwave and Wireless Components Letters*, 17(6):415–417.

[Eleftheriades and Antoniades, 2007] Eleftheriades, G. V. and Antoniades, M. A. (2007). Antenna applications of negative-refractive-index transmission-line (NRI-TL) structures. *IET Microwaves, Antennas and Propagation*, pages 12–22.

[Eleftheriades and Balmain, 2005] Eleftheriades, G. V. and Balmain, K. G., editors (2005). *Negative-Refraction Metamaterials: Fundamental Principles and Applications*. Wiley & IEEE Press, Hoboken, NJ.

[Eleftheriades and Mosig, 1996] Eleftheriades, G. V. and Mosig, J. R. (1996). On the network characterization of planar passive circuits using the method of moments. *IEEE Transactions on Microwave Theory and Techniques*, 44(3):438–445.

[Eleftheriades et al., 1996] Eleftheriades, G. V., Mosig, J. R., and Guglielmi, M. (1996). A fast integral equation technique for shielded planar circuits defined on nonuniform meshes. *IEEE Transactions on Microwave Theory and Techniques*, 44(12):2293–2296.

[Engheta and Ziolkowski, 2006] Engheta, N. and Ziolkowski, R. W. (2006). *Electromagnetic Metamaterials: Physics and Engineering Explorations*. Wiley-IEEE Press.

[Ernst and Postoyalko, 2003] Ernst, C. and Postoyalko, V. (2003). Prediction of peak internal fields in direct-coupled-cavity filters. *IEEE Transactions on Microwave Theory and Techniques*, 51(1):64–73.

[Faraji-Dana and Chow, 1995] Faraji-Dana, R. and Chow, Y. L. (1995). Accurate and efficient CAD tool for the design of optimum packaging for MMICs. *IEE Proceedings-Microwave Antennas and Propagation*, 142(2):81–88.

[Felsen, 1969] Felsen, L. B. (1969). Transients in dispersive media, part I: Theory. *IEEE Transactions on Antennas and Propagation*, 17:191–200.

[Felsen and Marcuvitz, 1973] Felsen, L. B. and Marcuvitz, N. (1973). *Radiation and Scattering of Electromagnetic Waves*. Prentice-Hall, Englewood Cliffs, New Jersey.

[García-Vigueras et al., 2010] García-Vigueras, M., Gómez-Tornero, J. L., Goussetis, G., Gómez-Díaz, J. S., and Álvarez-Melcón, A. (2010). A modified pole-zero technique for the analysis and design of waveguides and leaky-wave antennas with dipole-based fss. *IEEE Transactions on Antennas and Propagation*, 58(6):1971 – 1979.

[Garcia-Vigueras et al., 2011] Garcia-Vigueras, M., Gomez-Tornero, J. L., Goussetis, G., Weily, A. R., and Guo, J. Y. (2011). Enhancing frequency-scanning response of leaky-wave antennas using high-impedance surfaces. *IEEE Antennas and Wireless Propagation Letters*, 10:7–10.

[Garcia-Vigueras et al., 2010] Garcia-Vigueras, M., Gomez-Tornero, J. L., Guzman-Quiros, R., D.Quesada-Pereira, F., and Alvarez-Melcon, A. (2010). Control of the radiation properties of a fss loaded leaky-wave antenna. In *European Conference on Antennas and Propagation*, Barcelona, Spain.

[Gay Balmaz and Mosig, 1997] Gay Balmaz, P. and Mosig, J. R. (1997). Three dimensional planar radiating structures in stratified media. *Int J Microwave and Millimeter Wave Computer Aided Engineering*, 7(7):330–343.

[Gentili et al., 1997] Gentili, G. G., Garcia Castillo, L. E., Salazar Palma, M., and Pérez Martínez, F. (1997). Green's funcion analysis of single and stacked rectangular microstrip patch antennas enclosed in a cavity. *IEEE Transactions on Antennas and Propagation*, 45(4):573–579.

[Geuzaine and Remacle, 2011] Geuzaine, C. and Remacle, J. F. (2011). Gmsh: a three-dimensional finite element mesh generator with built-in pre- and post-processing facilities. *[Online] http://geuz.org/gmsh/*.

[Ghavami et al., 2007] Ghavami, M., Michael, L. B., and Kohno, R. (2007). *UWB Signals and Systems in Communication Engineering*. J. Wiley & Sons.

[Gil et al., 2007a] Gil, M., Bonache, J., García-García, J., Marterl, J., Martín, F., and Medina, F. (2007a). Design of wide-band semilumped bandpass filters using open split ring resonators. *IEEE Microwave and Wireless Components Letters*, 17:28–30.

[Gil et al., 2007b] Gil, M., Bonache, J., Selga, J., Garca-Garca, J., and Martin, F. (2007b). Broadband resonant-type metamaterial transmission lines. *IEEE Microwave and Wireless Components Letters*, pages 97–99.

[Gómez-Díaz et al., 2010a] Gómez-Díaz, J. S., Álvarez-Melcón, A., and Bertuch, T. (2010a). An iteratively-refined circuital model of CRLH leaky-wave antennas based on a mushroom structure. In *IEEE International Antennas and Propagation Symposium*, Toronto (Canada).

[Gómez-Díaz et al., 2011a] Gómez-Díaz, J. S., Álvarez-Melcón, A., and Bertuch, T. (2011a). A modal-based iterative circuit model for the analysis of CRLH leaky-wave antennas comprising periodically loaded PPW. *IEEE Transactions on Antennas and Propagation*, 59(4):1101–1112.

[Gómez-Díaz et al., 2011b] Gómez-Díaz, J. S., Álvarez-Melcón, A., and Bertuch, T. (2011b). Radiation characteristics of mushroom-like PPW LWAs: Analysis and experimental verification. *IEEE Antennas and Wireless Propagation Letters*. Submitted.

[Gómez-Díaz et al., 2011c] Gómez-Díaz, J. S., Cañete-Rebenaque, D., and Álvarez-Melcón, A. (2011c). A simple CRLH LWA circuit condition for constant radiation rate. *IEEE Antennas and Wireless Propagation Letters*, 10:29–32.

[Gómez-Díaz et al., 2011d] Gómez-Díaz, J. S., Gárcia-Vigueras, M., and Álvarez-Melcón, A. (2011d). A grounded MoM-based spatial Green's function technique for the analysis of multilayered circuits in rectangular shielded enclosures. *IEEE Transactions on Microwave Theory and Techniques*, 59(3):533–541.

[Gómez-Díaz et al., 2008a] Gómez-Díaz, J. S., Gupta, S., Álvarez-Melcón, A., and Caloz, C. (2008a). Spatio-temporal talbot phenomenon using metamaterial composite right/left-handed leaky-wave antennas. *Journal of Applied Physics*, 104:104901–7.

[Gómez-Díaz et al., 2009a] Gómez-Díaz, J. S., Gupta, S., Álvarez-Melcón, A., and Caloz, C. (2009a). Impulse-regime CRLH resonator for tunable pulse rate multiplication. *Radio Science*, 44(doi:10.1029/2008RS003991):1–9.

[Gómez-Díaz et al., 2009b] Gómez-Díaz, J. S., Gupta, S., Álvarez-Melcón, A., and Caloz, C. (2009b). Investigation on the phenomenology of impulse-regime metamaterial transmission lines. *IEEE Transactions on Antennas and Propagation*, 57(12):4010–4014.

[Gómez-Díaz et al., 2009c] Gómez-Díaz, J. S., Gupta, S., Álvarez-Melcón, A., and Caloz, C. (2009c). Numerical analysis of impulse regime phenomena in linear and non-linear metamaterial transmisión lines. In *International Conference on Electromagnetics in Advanced Applications*, Turin, Italy. INVITED.

[Gómez-Díaz et al., 2009d] Gómez-Díaz, J. S., Gupta, S., Álvarez-Melcón, A., and Caloz, C. (2009d). Tunable talbot imaging distance using an array of beam-steered metamaterial leaky-wave antennas. *Journal of Applied Physics*, 106:084908–9.

[Gómez-Díaz et al., 2010b] Gómez-Díaz, J. S., Gupta, S., Álvarez-Melcón, A., and Caloz, C. (2010b). Effcient time-domain análisis of highly-dispersive linear and non-linear metamaterial waveguide and antenna structures. *IET Microwaves, Antennas and Propagation*, 4(10):1617–1625.

[Gómez-Díaz et al., 2008b] Gómez-Díaz, J. S., Martínez-Mendoza, M., Pérez-Soler, F. J., and Álvarez-Melcón, A. (2008b). An interpolated spatial images method for the analysis of multilayered shielded microwave circuits. *Microwave and Optical Technology Letters*, 50(9):2294–2300.

[Gómez-Díaz et al., 2008c] Gómez-Díaz, J. S., Martínez-Mendoza, M., Pérez-Soler, F. J., Quesada-Pereira, F. D., and Álvarez-Melcón, A. (2008c). Practical implementation of the spatial images technique for the analysis of shileded multilayered printed circuits. *IEEE Transactions on Microwave Theory and Techniques*, 56(1):131–141.

[Gómez-Díaz et al., 2009e] Gómez-Díaz, J. S., Martínez-Mendoza, M., Quesada-Pereira, F. D., and Álvarez-Melcón, A. (2009e). Efficient calculation of the Green's functions for multilayered shielded cavities with right isosceles-triangular cross-section. *IET Microwaves, Antennas and Propagation*, 3(15):736–741.

[Gomez-Tornero and Alvarez-Melcon, 2004] Gomez-Tornero, J. L. and Alvarez-Melcon, A. (2004). Nonorthogonality relations between complex hybrid modes: an application for the leaky-wave analysis of laterally shielded top-open planar transmission lines. *IEEE Transactions on Microwave Theory and Techniques*, 52(3):760 – 767.

[Gomez-Tornero et al., 2006a] Gomez-Tornero, J. L., Cañete-Rebenaque, D., Quesada-Pereira, F. D., Pascual-Garcia, J., and Alvarez-Melcon, A. (2006a). Control of leaky-mode propagation and radiation properties in hybrid dielectric-waveguide printed-circuit technology: Experimental results. *IEEE Transactions on Antennas and Propagation*, 54(11):3383–3390.

[Gomez-Tornero et al., 2006b] Gomez-Tornero, J. L., Cañete-Rebenaque, D., Quesada-Pereira, F. D., Pascual-Garcia, J., and Alvarez-Melcon, A. (2006b). Pamela: a useful tool for the study of leaky-wave modes in strip-loaded open dielectric waveguides. *IEEE Antennas and Propagation Magazine*, 48(4):54 – 72.

[Gomez-Tornero et al., 2005] Gomez-Tornero, J. L., Quesada-Pereira, F. D., and Alvarez-Melcon, A. (2005). Analysis and design of periodic leaky-wave antennas for the millimeter waveband in hybrid waveguide-planar technology. *IEEE Transactions on Antennas and Propagation*, 53(9):2834–2842.

[Grbic and Eleftheriades, 2002a] Grbic, A. and Eleftheriades, G. (2002a). Experimental verification of backward-wave raidation from a negative refraction inderx metamaterial. *Journal of Applied Physics*, 92:5930–5935.

[Grbic and Eleftheriades, 2004] Grbic, A. and Eleftheriades, G. (2004). Overcoming the diffraction limit with a planar left handed transmission line lens. *Physical Review Letters*, page 107402.

[Grbic and Eleftheriades, 2005] Grbic, A. and Eleftheriades, G. (2005). An isotropic three-dimensional negative refractive index transmission line metamaterial. *Journal of Applied Physics*, 98:043106.

[Grbic and Eleftheriades, 2002b] Grbic, A. and Eleftheriades, G. V. (2002b). Leaky CPW-based slot antenna arrays for millimeter-wave applications. *IEEE Transactions on Antennas and Propagation*, 50(11):1494–1504.

[Green, 1828] Green, G. (1828). An essay on the application of mathematical analysis to the theories of electricity and magnetism. *T. Weelhouse*.

[Guglielmi, 1994] Guglielmi, M. (1994). A simple CAD procedure for microwave filters and multiplexers. *IEEE Transactions on Microwave Theory and Techniques*, 42(7):1347–1352.

[Guglielmi and Alvarez-Melcon, 1995] Guglielmi, M. and Alvarez-Melcon, A. (1995). Multimode network analysis of planar transmission lines. *IEEE Transactions on Microwave Theory and Techniques*, 43(11):2621–2626.

[Guglielmi et al., 2001] Guglielmi, M., Jarry, P., Kerherve, E., Roquebrun, O., and Schmitt, D. (2001). A new family of all-inductive dual-mode filters. *IEEE Transactions on Microwave Theory and Techniques*, 49(10):1764–1769.

[Guglielmi et al., 1992] Guglielmi, M., Molina, R., and Alvarez-Melcon, A. (1992). Dual-mode circular waveguide filters without tuning screws. *IEEE Antennas and Propagation Magazine*, 2(11):457–458.

[Gupta et al., 2009a] Gupta, S., Abielmona, S., and Caloz, C. (2009a). Microwave analog real-time spectrum analyzer (rtsa) based on the spatial-spectral decomposition property of leaky-wave structures. *IEEE Transactions on Microwave Theory and Techniques*, 57(12):4010–4014.

[Gupta and Caloz, 2007] Gupta, S. and Caloz, C. (2007). Dark and bright solitons in left-handed nonlinear transmission line metamaterials. In *IEEE MTT-S International Microwave Symposium*, Honolulu, Hawai, USA. IEEE.

[Gupta and Caloz, 2009] Gupta, S. and Caloz, C. (2009). Analog signal processing in transmission line metamaterial structures. *RadioEngineering*, 18(2):155–167.

[Gupta et al., 2008] Gupta, S., Caloz, C., and Abielmona, S. (2008). CRLH leaky-wave real-time spectrum analyzer (RTSA) with unrestricted time-frequency resolution. In *IEEE MTT-S International Microwave Symposium*, Atlanta. IEEE.

[Gupta et al., 2009b] Gupta, S., Gómez-Díaz, J. S., and Caloz, C. (2009b). Frequency resolved electrical gating principle for UWB signal characterization using leaky-wave structures. In *39th European Microwave Conference*, Rome, Italy.

[Harman, 1995] Harman, P. M. (1995). *The Scientific Letters and Papers of James Clerk Maxwell Vol. II 1862-1873*. Cambridge University Press, U.K.

[Harrington, 1961] Harrington, R. F. (1961). *Time-Harmonic Electromagnetic Fields*. McGraw-Hill, New York.

[Harrington, 1968] Harrington, R. F. (1968). *Field Computation by Moment Methods*. The MacMillan Company, New York.

[Hecht and Zajac, 2003] Hecht, E. and Zajac, A. (2003). *Optics*. Barnes & Noble.

[Heldrind et al., 2002] Heldrind, A., Rius, J. M., and Ligthar, L. (2002). New block ILU preconditioner scheme for numerical analysis of very large electromagnetics problems. *IEEE Transactions on Magnetics*, 38(2):337–340.

[Heyman and Felsen, 2001] Heyman, E. and Felsen, L. B. (2001). Gaussian beam and pulsed-beam dynamics: complex-source and complex-spectrum formulations within and beyond paraxial asymptotics. *J. Opt. Soc. Am.*, 18:1588–1611.

[Hildebrand, 1974] Hildebrand, F. B. (1974). *Introduction to Numerical Analysis*. McGraw-Hill, New York.

[Hoefer, 1985] Hoefer, W. J. R. (1985). The transmission line matrix method; theory and applications. *IEEE Transactions on Microwave Theory and Techniques*, 33(10):882–893.

[Hoorfar and Chang, 1995] Hoorfar, A. and Chang, D. C. (1995). Closed-form solution to Green's functions in microstrip problems with a thin substrate. *Radio Science*, 30(2):343–351.

[Horii et al., 2005] Horii, Y., Caloz, C., and Itoh, T. (2005). Super-compact multilayered left-handed transmission line and diplexer application. *IEEE Transactions on Microwave Theory and Techniques*, 53(4).

[Infeld and Rowlands, 1990] Infeld, E. and Rowlands, G. (1990). *Nonlinear Waves, Solitons and Chaos*. Cambridge Univ. Press., Cambridge, U.K.

[International Center for Numerical Methods in Engineering, 2011] International Center for Numerical Methods in Engineering (2011). Gid, the personal pre and pos proccesor. *[Online] http://www.gidhome.com/*.

[Ishak, 1988] Ishak, W. (1988). Magnetostatic wave technology: a review. *Proceedigs of the IEEE*, 76(2):171–187.

[Islam and Eleftheriades, 2008a] Islam, R. and Eleftheriades, G. V. (2008a). Compact corporate power divider using metamaterial NRI-TL coupled-line couplers. *IEEE Microwave and Wireless Components Letters*, 18(7):440–442.

[Islam and Eleftheriades, 2008b] Islam, R. and Eleftheriades, G. V. (2008b). An elliptic-type bandpass filter and a bandstop notch filter inspired by the metamaterial NRI-TL topology. *Electronic Letters*, 44:1470–1472.

[Itoh, 1989] Itoh, T. (1989). *Numerical Techniques for Microwave and Millimeter-Wave Passive Structures*. Wiley-Interscience.

[Iyer and Eleftheriades, 2002] Iyer, A. K. and Eleftheriades, G. (2002). Negative refractive index metamaterials supporting 2-D waves. In *IEEE International Microwave Symposium Digest*, pages 412–415, Seattle, WA, USA.

[Iyer et al., 2003] Iyer, A. K., Kremer, P. C., and Eleftheriades, G. (2003). Experimental and theoretical verification of focusing in a large, periodicially loaded transmission line negative nefractive index metamaterial. *Opt. Express*, pages 696–708.

[Jackson and Pozar, 1985] Jackson, R. W. and Pozar, D. M. (1985). Full-wave analysis of microstrip open-end discontinuities. *IEEE Transactions on Microwave Theory and Techniques*, 33:1026–1042.

[Jannson and Jannson, 1981] Jannson, T. and Jannson, J. (1981). Temporal self-imaging effect in single-mode fibers. *J. Opt. Soc. Am.*, 71:1373–1376.

[Jansen, 1985] Jansen, R. H. (1985). The spectral-domain approach for microwave integrated circuits. *IEEE Transactions on Microwave Theory and Techniques*, 33:1043Ű1056.

[Jarauta et al., 2004] Jarauta, E., Laso, M. A. G., Lopetegi, T., Falcone, F., Beruete, M., Baena, J. D., Bonache, J., Gil, I., Garcia-Garcia, J., Marcotegui, A., Martin, F., Marques, R., and Sorolla, M. (2004). Metamaterial microstrip backward couplers for fully planar fabrication techniques. In *12th International Conference on Terahertz Electronics*.

[Jin, 1993] Jin, J. (1993). *The Finite Element Method in Electromagnetic*. Wiley, New York.

[Jin and Volakis, 1991] Jin, J.-M. and Volakis, J. L. (1991). A finite element-boundary integral formulation for scattering by three-dimensional cavity-backed apertures. *IEEE Transactions on Antennas and Propagation*, 39(1):97–104.

[Jin and Nguyen, 2005] Jin, Y. and Nguyen, C. (2005). A 0.25-mm CMOS T/R switch for UWB wireless communications. *IEEE Microwave and Wireless Components Letters*, 15:502–504.

[Jordan et al., 1986] Jordan, K. E., Richter, G. R., and Sheng, P. (1986). An efficient numerical evaluations of the Green's functions for the helmholtz operator in periodic structures. *J. Comput. Phys.*, 63:222–235.

[Kaklamani and Anastassiu, 2002] Kaklamani, D. I. and Anastassiu, H. T. (2002). Aspects of the method of auxiliary sources (MAS) in computational electromagnetics. *IEEE Antennas and Propagation Magazine*, 44(3):54 – 72.

[Katehi and Alexopoulos, 1985] Katehi, P. B. and Alexopoulos, N. G. (1985). Frequency-dependent characterization of microstrip discontiuities in millimiter-wave integrated circuits. *IEEE Transactions on Microwave Theory and Techniques*, 33:1029–1035.

[Keren and Atsuki, 1995] Keren, L. I. and Atsuki, K. (1995). Three-dimensional analytical electrostatic Green's functions for shielded and open arbitrarily multilayered medium structures and their application to analaysis of microstrip discontinuities. *IEICE Transactions on Electronics*, E78-C(10):1366–1371.

[Kinayman and Aksum, 1995] Kinayman, N. and Aksum, M. I. (1995). Comparative study of acceleration techniques for integrals and series in electromagnetic problems. *Radio Science*, 30(6):1713–1722.

[King et al., 1983] King, R. J., Thiel, D. V., and Park, K. S. (1983). The synthesis of surface reactance using an artificial dielectric. *IEEE Transactions on Antennas and Propagation*, 31(3):471 – 476.

[Kodera and Caloz, 2009] Kodera, T. and Caloz, C. (2009). Uniform ferrite-loaded open waveguide structure with crlh response and its application to a novel backfire-to-endfire leaky-wave antenna. *IEEE Transactions on Microwave Theory and Techniques*, 57(4):784–795.

[Kokkinos et al., 2006] Kokkinos, T., Sarris, C. D., and Eleftheriades, G. V. (2006). Periodic FDTD analysis of leaky-wave structures and applications to the analysis of negative-refractive-index leaky-wave antennas. *IEEE Transactions on Microwave Theory and Techniques*, 54(4):1619–1630.

[Kolundzija and Djordjevic, 2002] Kolundzija, B. and Djordjevic, A., editors (2002). *Electromagnetic Modeling of Composite Metallic and Dielectric Structures*. Artech House Publishers.

[Kozyrev and der Weide, 2005] Kozyrev, A. B. and der Weide, D. W. V. (2005). Nonlinear wave propagation phenomena in left-handed transmission-line media. *IEEE Transactions on Microwave Theory and Techniques*, 53(1):238–245.

[Lai et al., 2007] Lai, A., Leong, K. M. K. H., and Itoh, T. (2007). Infinite wavelength resonant antennas with monopolar radiation pattern based on periodic structures. *IEEE Transactions on Antennas and Propagation*, 55(3):868–876.

[Laso et al., 2003] Laso, M., Lopetegi, T., Erro, M., Benito, D., Garde, M., Muriel, M., Sorolla, M., and Guglielmi, M. (2003). Real-time spectrum analysis in microstrip technology. *IEEE Transactions on Microwave Theory and Techniques*, 51(3):705–717.

[Lee and Son, 1999] Lee, C. W. and Son, H. (1999). Periodically slotted dielectrically filled parallel-plate waveguide as a leaky-wave antenna: E-polarization case. *IEEE Transactions on Antennas and Propagation*, 47(1):171–178.

[Lee et al., 2007] Lee, H. D., Lee, K. A., and Hong, S. (2007). A wideband CMOS variable gain amplifier with an exponential gain control. *IEEE Transactions on Microwave Theory and Techniques*, 55(6):1363–1373.

[Lee et al., 1997] Lee, J. F., Lee, R., and Cangellaris, A. C. (1997). Time-domain finite element methods. *IEEE Transactions on Antennas and Propagation*, 45:430–442.

[Lee and Wight, 1986] Lee, J. P. Y. and Wight, J. S. (1986). Acoustooptic spectrum analyzer: Detection of pulsed signals. *Appl. Opt.*, 25(2):193–198.

[Leung and Chow, 1996] Leung, K. W. and Chow, K. Y. (1996). Analysis of hemispherical cavity-backed slot antenna. *Electronics Letters*, 32(16):1430–1431.

[Liao and Chang, 2007] Liao, C.-K. and Chang, C.-Y. (2007). Microstrip realization of generalized Chebyshev filters with box like coupling schemes. *IEEE Transactions on Microwave Theory and Techniques*, 55(1):147–153.

[Lim et al., 2004a] Lim, S., Caloz, C., and Itoh, T. (2004a). Electronically-scanned composite right/left-handed microstrip leaky-wave antenna. *IEEE Microwave and Wireless Components Letters*, 14(6):277–279.

[Lim et al., 2004b] Lim, S., Caloz, C., and Itoh, T. (2004b). A reflecto-directive system using a composite right/left-handed (CRLH) leaky-wave antenna and heterodyne mixing. *IEEE Microwave and Wireless Components Letters*, 14(4):183–Ű185.

[Lim et al., 2005] Lim, S., Caloz, C., and Itoh, T. (2005). Metamaterial-based electronically controlled transmission line structure as a novel leaky-wave antenna with tunable angle and beamwidth. *IEEE Transactions on Microwave Theory and Techniques*, 53(1):161–173.

[Lin et al., 2004] Lin, I. H., De Vincentis, M., Caloz, C., and Itoh, T. (2004). Arbitrary dual band components using composite right/left-handed transmission lines. *IEEE Transactions on Microwave Theory and Techniques*, 52(4):1142–1149.

[Liu, 1989] Liu, L. (1989). Lau cavity and phase locking of laser arrays. *Opt. Lett.*, 14:1312–1314.

[Liu et al., 2002] Liu, L., Caloz, C., and Itoh, T. (2002). Dominant mode leaky-wave antenna with backfire-to-endfire scanning capability. *Electron. Lett.*, 38(23):1414–1416.

[Livernois and Katehi, 1989] Livernois, T. G. and Katehi, P. B. (1989). A generalized method for deriving the space-domain Green's function in a shielded, multilayered substrate structure with applications to MIS slow-wave transmission lines. *IEEE Transactions on Microwave Theory and Techniques*, 37(11):1761–1767.

[Lohmann, 1987] Lohmann, A. W. (1987). An array illuminator based on the talbot-effect. *Optik*, 79:41–45.

[Lonngren and Scott, 1078] Lonngren, K. and Scott, A. F. (1078). *Solitons in Action*. Academic Press, 1st edition.

[López-Frutos, 2011] López-Frutos, A. (2011). *Cálculo Eficiente de Funciones de Green Periódicas y no Periódicas en Medios Homogéneos y Medios Multicapa*. P.h.D. Thesis, Universidad de Sevilla.

[Marcuvitz, 1964] Marcuvitz, N. (1964). *Waveguide Handbook*. MIT Radiation Laboratory Series, Boston, Massachusetts, USA.

[Marin et al., 1989] Marin, M., Barkeshli, S., and Pathak, P. H. (1989). Efficient analysis of planar microstrip geometries using a closed-form aymptotic representation of the ground dielectric slab Green's function. *IEEE Transactions on Microwave Theory and Techniques*, 37(4):669–679.

[Marini et al., 2010] Marini, S., Coves, A., Boria, V., and Gimeno, B. (2010). Efficient modal analysis of periodic structures loaded with arbitrarily shaped waveguides. *IEEE Transactions on Microwave Theory and Techniques*, 58(3):529–536.

[Marques et al., 2008] Marques, R., Martín, F., and Sorolla, M., editors (2008). *Metamaterials with Negative Parameters: Theory, Design and Microwave Applications*. Wiley, Hoboken, NJ.

[Martín et al., 2003] Martín, F., Bonache, J., Gil, I., García, J., and Marqués, R. (2003). Novel microstrip bandpass filters based on complementary split-ring resonators. *IEEE Transactions on Microwave Theory and Techniques*, 54:265–271.

[Martínez-Mendoza et al., 2007] Martínez-Mendoza, M., Gómez-Díaz, J. S., Cañete-Rebenaque, D., and Álvarez-Melcón, A. (2007). Design of bandpass transversal filters employing a novel hybrid structure. *IEEE Transactions on Microwave Theory and Techniques*, 5(12):2670–2678.

[Martínez-Mendoza et al., 2008] Martínez-Mendoza, M., Gómez-Díaz, J. S., Cañete-Rebenaque, D., and Álvarez-Melcón, A. (2008). Design of dual-bandpass hybrid waveguide-microstrip microwave filters. *IEEE Transactions on Microwave Theory and Techniques*, 56(12):2913–2920.

[Matthaei et al., 1964] Matthaei, G. L., Young, L., and Jones, E. M. T. (1964). *Microwave Filters, Impedance-Matching Networks, and Coupling Structures*. Artech House, 1nd edition edition.

[Maxwell, 1865] Maxwell, J. C. (1865). A dynamical theory of the electromagnetic field. *Philosophical Transactions of the Royal Society of London*, 155:459–512.

[Mesa et al., 2008] Mesa, F., Boix, R. R., and Medina, F. (2008). Closed-form expressions of multilayered planar Green's functions that account for the continuous spectrum in the far field. *IEEE Transactions on Microwave Theory and Techniques*, 56:1601–1610.

[Mesa and Marques, 1995] Mesa, F. and Marques, R. (1995). Integral representation of spatial Green's function and spectral domain analysis of leaky covered strip-like lines. *IEEE Transactions on Microwave Theory and Techniques*, 43(4):828–837.

[Mesa et al., 1995] Mesa, F., Marques, R., and Horno, M. (1995). An efficient numerical spectral domain method to analyze a large class of nonreciprocal planar transmission lines. *IEEE Transactions on Microwave Theory and Techniques*, 40(8):1630–1641.

[Michalski, 1987] Michalski, K. (1987). On the scalar potential of a point charge associated with a time-harmonic dipole in a layered-medium. *IEEE Transactions on Antennas and Propagation*, 35(11):1630–1641.

[Michalski, 1998] Michalski, K. (1998). Extrapolation methods for Sommerfeld integral tails. *IEEE Transactions on Antennas and Propagation*, 46(10):1405–1418.

[Michalski and Mosig, 1997] Michalski, K. A. and Mosig, J. R. (1997). Multilayered media Green's functions in integral equation formulations. *IEEE Transactions on Antennas and Propagation*, 45(3):508–519.

[Michalski and Zheng, 1990] Michalski, K. A. and Zheng, D. (1990). Electromagnetic scattering and radiation by surfaces of arbitrary shape in layered media, part I: Theory. *IEEE Transactions on Antennas and Propagation*, 38(3):335–344.

[Mongia et al., 1999] Mongia, R., Bahl, I., and Bhartia, P. (1999). *RF and Microwave Coupled-Line Circuits*. Artech House, 1^{st} edition.

[Morita et al., 1990] Morita, N., Kumagai, N., and Mautz, J. (1990). *Integral Equation Methods for Electromagnetics*. Artech House, Boston, USA.

[Mosig, 1992] Mosig, J. (1992). Review of radio science. In Stone, R., editor, *Integral-equation technique for three-dimensional microstrip structures*. URSI-Oxford Science Publications, Oxford, 1 edition.

[Mosig and Gardiol, 1983] Mosig, J. M. and Gardiol, F. E. (1983). Analytical and numerical techniques in the Green's functions treatment of microstrip antennas and scatters. *IEE Proceedings*, 130(2):175–182.

[Mosig and Gardiol, 1985] Mosig, J. M. and Gardiol, F. E. (1985). General integral equation formulation for microstrip antennas and scatteres. *IEE Proceedings*, 132(7):424–432.

[Mosig and Sarkar, 1986] Mosig, J. M. and Sarkar, T. K. (1986). Comparison of quasi-static and exact electromagnetic fields from a horizontal electric dipole above a lossy dielectric backed by an imperperfect ground plane. *IEEE Transactions on Microwave Theory and Techniques*, 34(4):379–387.

[Mosig, 1989] Mosig, J. R. (1989). *Integral Equation Technique*. Wiley Interscience Publication, New York.

[Mosig and Alvarez-Melcon, 2002] Mosig, J. R. and Alvarez-Melcon, A. (2002). The summation by parts algorithm - a new efficient technique for the rapid calculation of certain series arising in shielded planar structures. *IEEE Transactions on Microwave Theory and Techniques*, 50(1):215–218.

[Mosig and Álvarez Melcón, 2003] Mosig, J. R. and Álvarez Melcón, A. (2003). Green's functions in lossy layered media: Integration along the imaginary axis and asymptotic behavior. *IEEE Transactions on Antennas and Propagation*, 51(12):3200–3208.

[Narahara et al., 2007] Narahara, K., Nakamichi, T., Suemitsu, T., Otsuji, T., and Sano, E. (2007). Development of solitons in composite right- and left-handed transmission lines periodically lodaed with schottky varactors. *Journal of Applied Physics*, 102:024501.

[Nghiem et al., 1993] Nghiem, D., Williams, J. T., and Jackson, D. R. (1993). Existence of a leaky dominant mode on a microstrip line with an isotropic substrate: theory and measurement. In *IEEE International Microwave Symposium Digest*, Atlanta, USA.

[Nguyen, 2010] Nguyen, H. V. (2010). *Advances in Composite Right/Left-Handed Transmission Line Components, Antennas and Systems*. P.h.D. Thesis, Échole Politechnique de Montréal.

[Nguyen et al., 2009a] Nguyen, H. V., Abielmona, S., and Caloz, C. (2009a). Highly efficient leaky-wave antenna array using a power-recycling series feeding work. *IEEE Antennas and Wireless Propagation Letters*, 8:441–44.

[Nguyen and Caloz, 2006] Nguyen, H. V. and Caloz, C. (2006). Broadband highly selective bandpass filter based on a tapered coupled-resonator (TCR) CRLH structure. *European Microwave Association*, 2:44–51.

[Nguyen and Caloz, 2007a] Nguyen, H. V. and Caloz, C. (2007a). Generalized coupled-mode approach of metamaterial coupled-line couplers: Coupling theory, phenomenological explanation, and experimental demonstration. *IEEE Transactions on Microwave Theory and Techniques*, 55(5):1029–1039.

[Nguyen and Caloz, 2007b] Nguyen, H. V. and Caloz, C. (2007b). Tunable arbitrary N-port CRLH infinite wavelength series power divider. *Electronic Letters*, 43(23).

[Nguyen and Caloz, 2008] Nguyen, H. V. and Caloz, C. (2008). CRLH delay line pulse position modulation transmitter. *IEEE Microwave and Wireless Components Letters*, 18(8):527–529.

[Nguyen et al., 2009b] Nguyen, H. V., Parsa, A., and Caloz, C. (2009b). Power-recycling feedback system for maximization of leaky-wave antennas radiation efficiency. *IEEE Transactions on Microwave Theory and Techniques*, 58(7):1641–1650.

[Nguyen et al., 2008] Nguyen, V. H., Abielmona, S., and Caloz, C. (2008). Analog dispersive time delayer for beam-scanning phased array without beam-squinting. In *IEEE International Antennas and Propagation Symposium*, San Dielgo, California, USA.

[Oliner, 2002] Oliner, A. A. (2002). A periodic-structure negative-refractive index medium without resonant elements. In *Proc. USNC/URSI Nat. Radio Sci. Meeting*, page 41, San Antonio, TX.

[Oliner and Jackson, 2007] Oliner, A. A. and Jackson, D. R. (2007). Leaky-wave antennas. In Volakis, J. L., editor, *Antenna Engineering Handbook*. McGraw-Hill, New York, 4 edition.

[Oliver and Quegan, 2004] Oliver, C. and Quegan, S. (2004). *Understanding Synthetic Aperture Radar Images*. SciTech Publishing Inc.

[Olver and Sattinger, 1990] Olver, P. J. and Sattinger, D. H. (1990). *Solitons in Physics, Mathematics, and Nonlinear Optics*. Springer-Verlag., New York.

[Oppenheim, 1996] Oppenheim, A. V. (1996). *Signals and Systems*. Prentice Hall.

[Oppermann et al., 2004] Oppermann, I., Hämäläinen, M., and Iinatti, J. (2004). *UWB Theory and Applications*. John Wiley & Sons.

[Otero et al., 1997] Otero, P., Eleftheriades, G. V., and Mosig, J. R. (1997). Modeling the coplanar transmission line excitation of planar antennas in the method of moments. *Microwave and Optical Technology Letters*, 16(4):219–225.

[Oughstun, 1991] Oughstun, K. E. (1991). Pulse propagation in a linear, causally dispersive medium. *IEEE Transactions on Antennas and Propagation*, 79(10):1379–1390.

[Oughstun, 2006] Oughstun, K. E. (2006). *Electromagnetic and Optical Pulse Propagation 1: Spectral Representations in Temporally Dispersive Media*. Springer Series in Optical Sciences.

[Park et al., 1994] Park, K. H., Eom, H. J., and Yamaguchi, Y. (1994). An analytic series solution for E-plane T-junction in parallel-plate waveguide. *IEEE Transactions on Microwave Theory and Techniques*, 42(2):356 – 358.

[Park and Nam, 1997] Park, M.-J. and Nam, S. (1997). Rapid calculation of the Green's function in the shielded planar structures. *IEEE Microwave and Guided Wave Letters*, 7(10):326–328.

[Park and Nam, 1998] Park, M.-J. and Nam, S. (1998). Rapid summation of the Green's function for the rectangular waveguide. *IEEE Transactions on Microwave Theory and Techniques*, 46(12):2164–2166.

[Park et al., 1998] Park, M.-J., Park, J., and Nam, S. (1998). Efficient calculation of the Green's function for the rectangular cavity. *IEEE Microwave and Guided Wave Letters*, 48(3):124–126.

[Pascual García et al., 2006] Pascual García, J., Quesada Pereira, F. D., Cañete Rebenaque, D., Gómez Tornero, J. L., and Álvarez Melcón, A. (2006). A neural-network method for the analysis of multilayered shielded microwave circuits. *IEEE Transactions on Microwave Theory and Techniques*, 54(1):309–320.

[Patorski, 1989] Patorski, K. (1989). The self-imaging phenomenon and its applications. *Progress in Optics XXVII (Elsevier Science)*, pages 1–108.

[Paul, 2007] Paul, C. R. (2007). *Analysis of Multiconductor Transmission Lines*. Wiley-IEEE Press, 2^{nd} edition edition.

[Paulotto et al., 2009] Paulotto, C. S., Baccarelli, P., Frezza, F., and Jackson, D. R. (2009). A novel technique for open-stopband suppression in 1-D periodic printed leaky-wave antennas. *IEEE Transactions on Antennas and Propagation*, 57(7):1894–1906.

[Paulotto et al., 2008] Paulotto, S., Baccarelli, P., Frezza, F., and Jackson, D. R. (2008). Full-wave modal dispersion analysis and broadside optimization for a class of microstrip crlh leaky-wave antennas. *IEEE Transactions on Microwave Theory and Techniques*, 56(12):2826 – 2837.

[Peebles Jr., 1998] Peebles Jr., P. Z. (1998). *Radar Principles*. Wiley-Interscience, 605 Third Avenue, New York, N. Y.

[Pelosi and Ufimtsev, 1996] Pelosi, G. and Ufimtsev, P. Y. (1996). The impedance boundary condition. *IEEE Antennas and Propagation Magazine*, 38(1):31 – 35.

[Pendry et al., 1999] Pendry, J. B., Holden, A. J., Robbins, D. J., and Stewart, W. J. (1999). Magnetism from conductors, and enhanced non-linear phenomena. *IEEE Transactions on Microwave Theory and Techniques*, 47(11):2075–2084.

[Pérez-Soler et al., 2010] Pérez-Soler, F. J., Quesada Pereira, F. D., Álvarez Melcón, A., Gimeno, B., Esbert, V. E. B., and Perregrini, L. (2010). Analytical evaluation of the static MoM terms for volume and surface rectangular domains. *IEEE Antennas and Wireless Propagation Letters*, 9(2):87–90.

[Pérez-Soler et al., 2008] Pérez-Soler, F. J., Quesada Pereira, F. D., Rebenaque, D. C., Álvarez-Melcón, A., and Mosig, J. R. (2008). A novel efficient technique for the calculation of the Green's functions in rectangular waveguides based on accelerated series decomposition. *IEEE Transactions on Antennas and Propagation*, 56(10):3260–3270.

[Peterson et al., 1998] Peterson, A. F., Ray, S. L., and Mittra, R. (1998). *Computational Methods for Electromagnetics*, page 451. IEEE Press.

[Pipes and Harvill, 1971] Pipes, L. A. and Harvill, L. R. (1971). *Applied Mathematics for Engineers and Physicist*. McGraw Hill, 3rd edition.

[Poggio and Miller, 1973] Poggio, A. J. and Miller, E. K. (1973). *Integral Equation Solutions of Three-dimensional Scattering Problems*. Pergamon Press, Oxford.

[Pozar, 2005] Pozar, D. (2005). *Microwave Engineering*. John Wiley and Sons, 3rd edition.

[Pozar, 1994] Pozar, D. M. (1994). The active element pattern. *IEEE Transactions on Antennas and Propagation*, 42(8):1176–1178.

[Pozar, 2003] Pozar, D. M. (2003). Analysis and design of cavity coupled microstrip couplers and transitions. *IEEE Transactions on Microwave Theory and Techniques*, 51(3):1034–1044.

[Pratt et al., 2002] Pratt, T., Bostian, C. W., and Allnutt, J. E. (2002). *Satellite Communications*. Wiley.

[Press et al., 1996a] Press, W. H., Teukolsky, S. A., Vetterling, W. T., and Flannery, B. P. (1996a). *Numerical Recipes in Fortran 77, The Art of Scientific Computing*. Cambridge University Press, The Pitt Building, Trumpington Street, Cambridge CB2 IRP.

[Press et al., 1996b] Press, W. H., Teukolsky, S. A., Vetterling, W. T., and Flannery, B. P. (1996b). *Numerical Recipes in Fortran 90, The Art of Parallel Scientific Computing*. Cambridge University Press,, The Pitt Building, Trumpington Street, Cambridge CB2 IRP.

[Pyo et al., 2009] Pyo, S., Han, S. M., Baik, J., and Kim, Y. (2009). A slot-loaded composite right/left-handed transmission line for a zeroth-order resonant antennas with improved efficiency. *IEEE Transactions on Microwave Theory and Techniques*, 57(11):2775–2782.

[Qian et al., 1999] Qian, Y., Chang, B. C. C., Itoh, T., Chen, K. C., and Tzuang, C. K. C. (1999). High efficiency and broadband excitation of leaky mode in microstrip structure. In *IEEE International Microwave Symposium Digest*, Anaheim, USA.

[Quesada-Pereira, 2007] Quesada-Pereira, F. (2007). *Avances en Técnicas Numéricas de Resolución de Ecuaciones Integrales en Electromagnetismo*. P.h.D. Thesis, Universidad Politécnica de Cartagena.

[Quesada Pereira et al., 2005a] Quesada Pereira, F. D., Vera Castejón, P., Cañete Rebenaque, D., Pascual García, J., and Álvarez Melcón, A. (2005a). Numerical evaluation of the Green's functions for cylindrical enclosures. *IEEE Transactions on Microwave Theory and Techniques*, 53(1):94–105.

[Quesada Pereira et al., 2005b] Quesada Pereira, F. D., Vera Castejón, P., Gómez Tornero, J. L., Cañete Rebenaque, D., Pascual García, J., and Álvarez Melcón, A. (2005b). Analysis of microstrip to circular waveguide transitions by a new spatial images method. *Microwave and Optical Technology Letters*, 45:563–568.

[Rahmat-Samii and Mosallaei, 2001] Rahmat-Samii, Y. and Mosallaei, H. (2001). Electromagnetic band-gap structures: Classification, characterization, and applications. In *11th IEE International Conference on Antenna and Propagation*, Manchester, UK.

[Railton and Meade, 1992] Railton, C. J. and Meade, S. A. (1992). Fast rigorous analysis of shielded planar filters. *IEEE Transactions on Microwave Theory and Techniques*, 40(5):978–985.

[Ramo et al., 1994] Ramo, S., Whinnery, J. R., and Duzer, T. V. (1994). *Fields and Waves in Communication Electronics*. John Wiley and Sons, 3rd edition.

[Rao, 1980] Rao, S. M. (1980). *Electromagnetic Scattering and Radiation of Arbitrarily-Shaped Surfaces by Triangular Patch Modeling*. P.h.D. Thesis, University of Mississippi.

[Rao et al., 1982] Rao, S. M., Wilton, D. R., and Glisson, A. W. (1982). Electromagnetic scattering by surfaces of arbitrarily shape. *IEEE Transactions on Antennas and Propagation*, 30(5):409–418.

[Rebenaque et al., 2003] Rebenaque, D. C., Melcon, A. A., and Guglielmi, M. (2003). A new simple microstrip open-loop resonators filter for high selectivity applications. In *IEEE MTT-S International Microwave Symposium*, pages 1603–1606, Philadelphia, Pennsylvania, USA. IEEE. No. TH-1B-3.

[Rebenaque et al., 2004] Rebenaque, D. C., Pereira, F. Q., Tornero, J. L. G., Melcon, A. A., and Guglielmi, M. (2004). A new family of microstrip open-loop resonator filters for high selectivity applications. *Microwave and Optical Technology Letters*, 43(5):450–455.

[Remoissenet, 1994] Remoissenet, M. (1994). *Waves Called Solitons: Concepts and Experiments.* Springer-Verlag, Berlin, Germany.

[Rius et al., 2008] Rius, J. M., Parrón, J., Heldring, A., Tamayo, J. M., and Úbeda, E. (2008). Fast iterative solution of integral equations with method of moments and matrix decomposition algorithm. *IEEE Transactions on Antennas and Propagation*, 56(8).

[Roddy, 2006] Roddy, D. (2006). *Satellite Communications*. McGraw-Hill Professional.

[Rodwell et al., 1991] Rodwell, M. J. W., Kamegawa, M., Yu, R., Case, M., Carman, E., and Giboney, K. (1991). GaAs nonlinear transmission lines for picosecond pulse generation and millimeter-wave sampling. *IEEE Transactions on Microwave Theory and Techniques*, 39(7):1194–1204.

[Rosenberg and Amari, 2003] Rosenberg, U. and Amari, S. (2003). Novel coupling schemes for microwave resonator filters. *IEEE Transactions on Microwave Theory and Techniques*, 50(12):2896–2902.

[Russer, 2006] Russer, P. (2006). *Electromagnetics, Microwave Circuit and Antenna Design for Communications Engineering*. Artech House.

[Saleh and Teich, 2007] Saleh, B. E. A. and Teich, M. C. (2007). *Fundamentals of Photonics*. Wiley-Interscience, 2nd edition edition.

[Sanada et al., 2003] Sanada, A., Caloz, C., and Itoh, T. (2003). Novel zeroth-order resonance in composite right/left-handed transmission line resonators. In *Asia-Pacific Microwave Conference*, Seoul, Korea. IEEE.

[Sanada et al., 2004a] Sanada, A., Caloz, C., and Itoh, T. (2004a). Planar distributed structures with negative refractive index. *IEEE Transactions on Microwave Theory and Techniques*, 52:1252–1263.

[Sanada et al., 2004b] Sanada, A., Caloz, C., and Itoh, T. (2004b). Zeroth order resonance in the left-handed transmission line. *IEICE Trans. Electron.*, 87-C:1–7.

[Schwartz et al., 2008] Schwartz, J. D., Arnedo, I., Laso, M. A. G., Lopetegui, T., Azaña, J., and Plant, D. (2008). An electronic UWB continuosly tunable time-delay system with nanosecond delay. *IEEE Microwave and Wireless Components Letters*, 18(2):103–105.

[Schwartz, 2005] Schwartz, M. (2005). *Mobile Wireless Communications*. Cambridge University Press, U.K.

[Selga et al., 2011] Selga, J., Rodriguez, A., Gil, M., Carbonell, J., Boria, V. E., and Martin, F. (2011). Towards the automatic layout synthesis in resonant-type metamaterial transmission lines. *IET Microwaves, Antennas and Propagation*, 4:1007–1015.

[Shadrivov et al., 2008] Shadrivov, I. V., Kozyrev, A. B., Weide, D. W., and S.Kivshar, Y. (2008). Tunable transmission and harmonic generation in non-linear metamaterials. *Applied Phisics Letters*, 93:161903.

[Shanks, 1955] Shanks, D. (1955). Non-linear transformations of divergent and slowly convergent sequences. *J. Math. Phys.*, 34(3):1–42.

[Shelby et al., 2001] Shelby, R. A., Smith, D. R., and Schultz, S. (2001). Experimental verification of a negative index of refraction. *Science*, 292(5515):77–79.

[Sievenpiper, 2005] Sievenpiper, D. (2005). Forward and backward leaky wave radiation with large effective aperture from an electronically tunable textured surface. *IEEE Transactions on Antennas and Propagation*, 53(1):236–247.

[Sievenpiper et al., 2002] Sievenpiper, D., Schaffner, J., Lee, J. J., and Livingston, S. (2002). A steerable leaky-wave antenna using a tunable impedance ground plane. *IEEE Antennas and Wireless Propagation Letters*, 1:179–182.

[Sievenpiper et al., 1999] Sievenpiper, D., Zhang, L., Jimenez Broas, R. F., Alexópolous, N. G., and Yablonovitch, E. (1999). High-impedance electromagnetic surfaces with a forbidden frequency band. *IEEE Transactions on Microwave Theory and Techniques*, 47(11):2059–2074.

[Sihvola, 2007] Sihvola, A. (2007). Metamaterials in electromagnetics. *Metamaterials*, 1(1):2–11.

[Singh et al., 1990] Singh, S., Richards, W. F., Zinecker, J. R., and Wilton, D. R. (1990). Accelerating the convergence of series representing the free space periodic Green's functions. *IEEE Transactions on Antennas and Propagation*, 38(12):1958–1962.

[Singh et al., 1991] Singh, S., Richards, W. F., Zinecker, J. R., and Wilton, D. R. (1991). On the use of Shank's tranform to accelerate the summation of slowly convergent series. *IEEE Transactions on Microwave Theory and Techniques*, 39(3):608–610.

[Singh and Singh, 1990] Singh, S. and Singh, R. (1990). Application of transform to accelerate the summation of periodic free-space Green's functions. *IEEE Transactions on Microwave Theory and Techniques*, 38(11):1746–1748.

[Singh and Singh, 1992a] Singh, S. and Singh, R. (1992a). A convergence acceleration procedure for computing slowly converging series. *IEEE Transactions on Microwave Theory and Techniques*, 40(1):168–171.

[Singh and Singh, 1992b] Singh, S. and Singh, R. (1992b). On the use of Chebyshev-Toeplitz algorithm in accelerating the numerical convergence of infinite series. *IEEE Transactions on Microwave Theory and Techniques*, 40(1):171–173.

[Singh and Singh, 1993] Singh, S. and Singh, R. (1993). On the use of Levin's T-transform in accelearting the summation of series representing the free-space periodic Green's function. *IEEE Transactions on Microwave Theory and Techniques*, 41(5):884–886.

[Siso et al., 2007] Siso, G., Gil, M., Bonache, J., and Martin, F. (2007). Application of metamaterial transmission lines to design of quadrature phase shifters. *Electronics Letters*, 43(20):1098–1100.

[Skolnik, 2002] Skolnik, M. (2002). *Introduction to Radar Systems*. McGraw-Hill.

[Smith et al., 2000] Smith, D., Padilla, W. J., Vier, D., Nemat-Nasser, S., and Schultz, S. (2000). Composite medium with simultaneously negative permeability and permittivity. *Physical Review Letters*, 84:4184–4187.

[Sommerfeld, 1896] Sommerfeld, A. (1896). Mathemathische theorie der diffraction. *Mathemathische Annalen*, 47(319):317–374.

[Stevanovic, 2005] Stevanovic, I. (2005). *Modeling Challenges in Computational Electromagnetics: Large Planar Multilayered Structures and Finite-Thickness Irises*. P.h.D. Thesis, Echole Politechnique Federale of Lausanne.

[Stratton, 1941] Stratton, J. A. (1941). *Electromagnetic Theory*. McGraw-Hill, New York.

[Stutzman and Thiele, 1998] Stutzman, W. L. and Thiele, G. L. (1998). *Antenna Theory and Design. 3rd Edition.* John Wiley and Sons.

[Swanson and Macchiarella, 2007] Swanson, D. and Macchiarella, G. (2007). Microwave filter design by synthesis and optimization. *Microwave Magazine*, pages 55–69.

[Taflove and Hagness, 2005] Taflove, A. and Hagness, S. C. (2005). *Computational Electrodynamics: The Finite-Difference Time-Domain Method*. Artech House.

[Tai, 1993] Tai, C. (1993). *Dyadic Green's Functions in Electromagnetic Theory*. IEEE Press, New York.

[Talbot, 1836] Talbot, H. F. (1836). Facts relating to optical science no. IV. *Philos. Mag.*, 9:401–407.

[Testorf et al., 1996] Testorf, M., Jahns, J., Khilo, N. A., and Goncharenko, A. M. (1996). Talbot effect for oblique angle of light propagation. *Optics Comm.*, 129:167–172.

[Trebino, 2002] Trebino, R., editor (2002). *Frequency-Resolved Optical Gating: The Measurement of Ultrashort Laser Pulses*. Springer.

[Tsalamengas and Fikioris, 2005] Tsalamengas, J. L. and Fikioris, G. (2005). Rapidly converging spectral-domain analysis of rectangularly shielded layered microstrip lines. *IEEE Transactions on Microwave Theory and Techniques*, 51(6):1729–1734.

[Vera Castejón et al., 2004] Vera Castejón, P., Quesada Pereira, F. D., Cañete Rebenaque, D., Pascual García, J., and Álvarez Melcón, A. (2004). Numerical evaluation of the Green's functions for cylindrical enclosures by a new spatial images method. In *IEEE MTT-S International Microwave Symposium*, Forth Worth, Texas.

[Veselago, 1968] Veselago, V. G. (1968). The electrodynamics of substances with simultaneously negative values of ϵ and μ. *Soviet Physical Uspekhi*, 10(4):510–514.

[Wang et al., 2004] Wang, H. G., Chan, C. H., and Tsang, L. (2004). A new multilevel Green's function interpolation method for large scale EM simulations in RF ICs. In *IEEE International Antennas and Propagation Symposium*, pages 1183–1186.

[Weile et al., 2004] Weile, D. S., Pisharody, G., Chen, N., Shanker, B., and Michielssen, E. (2004). A novel scheme for the solution of the time-domain integral equations of electromagnetics. *IEEE Transactions on Antennas and Propagation*, 52(1):283–295.

[Wiegel et al., 2002] Wiegel, R., Morgan, D. P., Owens, J. M., Ballato, A., Lakin, K. M., Hashimoto, K., and Ruppel, C. C. W. (2002). Microwave acoustic materials, devices and applications. *IEEE Transactions on Microwave Theory and Techniques*, 50:738–749.

[Wilton et al., 1984] Wilton, D. R., Rao, S. M., Glisson, A. W., Schaubert, D. H., Al-Bundak, O. M., and Butler, C. M. (1984). Potential integrals for uniform and linear source distributions on polygonal and polyhedral domains. *IEEE Transactions on Antennas and Propagation*, 32(3):276–281.

[Wimp, 1974] Wimp, J. (1974). Toeplitz arrays, linear sequence transformations, and orthogonal polynomials. *Numer. Math*, 23:1–17.

[Withers et al., 1985] Withers, R., Anderson, A., Green, J., and Reible, S. (1985). Superconductive delay-line technology and applications. *IEEE Transactions on Magnetics*, 21(2):186–192.

[Yuan et al., 2006] Yuan, M., Sarkar, T. K., and Salazar-Palma, M. (2006). A direct discrete complex image method from the closed-form Green's functions in multilayered media. *IEEE Transactions on Microwave Theory and Techniques*, 54:1025.

[Zavosh and Aberle, 1994] Zavosh, F. and Aberle, J. T. (1994). Infinite phased arrays of cavity-backed patches. *IEEE Transactions on Antennas and Propagation*, 42(3):390–398.

[Zavosh and Aberle, 1995] Zavosh, F. and Aberle, J. T. (1995). Single and stacked circular microstrip patch antennas backed by a circular cavity. *IEEE Transactions on Antennas and Propagation*, 43(7):746–750.

[Zedler et al., 2007] Zedler, M., Caloz, C., and Russer, P. (2007). A 3-D isotropic left-handed metamaterial based on the rotated transmission-line matrix (TLM) scheme. *IEEE Transactions on Microwave Theory and Techniques*, 57(12):2930–2941.

[Zhu et al., 2010] Zhu, J., Antoniades, M. A., and Eleftheriades, G. V. (2010). A compact tri-band monopole antenna with single-cell metamaterial loading. *IEEE Transactions on Antennas and Propagation*, 58(4).

[Zhu and Eleftheriades, 2009] Zhu, J. and Eleftheriades, G. V. (2009). Dual-band metamaterial-inspired small monopole antenna for wifi applications. *Electronic Letters*, 45(22).

List of Figures

List of Tables